GREAT SALT LAKE AND THE BONNEVILLE BASIN: GEOLOGIC HISTORY AND ANTHROPOCENE ISSUES

Edited by Michael D. Vanden Berg, Richard L. Ford, Carie Frantz, Hugh Hurlow, Kellen Gunderson, and Genevieve Atwood

2024
Utah Geological Association
Publication 51

2024
Utah Geological Association
Publication 51

GREAT SALT LAKE AND THE BONNEVILLE BASIN: GEOLOGIC HISTORY AND ANTHROPOCENE ISSUES

Edited by Michael D. Vanden Berg[1], Richard L. Ford[2], Carie Frantz[2], Hugh Hurlow[1], Kellen Gunderson[3], and Genevieve Atwood[4]

Published by
Utah Geological Association
P.O. Box 520100
Salt Lake City, Utah 84152-0100
www.utahgeology.org

The Utah Geological Association gratefully acknowledges the AAPG-Rocky Mountain Section Foundation for their support of this publication and the associated field trip.

Cover photo: Exposed Holocene microbialite mounds near Lakeside, western Great Salt Lake, Utah. Photo by Michael Vanden Berg

Cover design and layout by Cheryl Wing

ISBN 978-0-99800142-7-2

[1]Utah Geological Survey
michaelvandenberg@utah.gov
hughhurlow@utah.gov

[2]Weber State University
rford@weber.edu
cariefrantz@weber.edu

[3]Zanskar Geothermal & Minerals
kellen.gunderson@gmail.com

[4]Earth Science Education
genevieveatwood@comcast.net

LAND ACKNOWLEDGEMENT

We acknowledge that the watershed of Great Salt Lake and the Bonneville Salt Flats is the traditional and ancestral homeland of the Shoshone, Paiute, Goshute, and Ute peoples. The Utah Geological Association recognizes and respects these sovereign nations and their traditions, cultures, and histories. We, the editors and authors of this book, honor the enduring relationship that exists between Indigenous peoples and the lands we discuss in this volume, a history that spans over ten thousand years dating back to the Fremont and other ancestral peoples of the Great Basin. Utah's Indigenous peoples were the original stewards of the systems and landscapes that are the focus of this guide and were witnesses to many of the changes discussed in this volume. Today, descendants of the original stewards of these lands are critical partners in the work ahead to understand, preserve, and protect our natural world and geoheritage for generations to come.

CONTENTS

PUBLICATIONS OF THE UTAH GEOLOGICAL ASSOCIATION

Most of these publications are for sale at UTAH DEPARTMENT OF NATURAL RESOURCES MAP AND BOOKSTORE, 1594 W. North Temple, P.O. Box 146100, Salt Lake City, Utah 84114-6100. Telephone: 888-UTAHMAP or 801-537-3320; fax: 801-537-3395; web: mapstore.utah.gov. PDFs of more recent books (UGA-43 and later), and individual papers, can be purchased on the UGA website at www.utahgeology.org.

UGA-1	Environmental Geology Tour of the Wasatch Front, road logs, edited by L.S. Hilpert, 1971.
UGA-2	Plateau-Basin and Range Transition Zone, Central Utah, edited by J.L. Baer and E. Callaghan, 1972.
UGA-3	Geology of the Milford Area, edited by L.F. Hintze and J.A. Whelan, 1973.
UGA-4	Energy Resources of the Uinta Basin, 1974.
UGA-5	Proceedings of the First International Conference on the New Basement Tectonics, Salt Lake City (June 3-7, 1974), 1976.
UGA-6	Guidebook to Geology of the Oquirrh Mountains and Regional Setting of the Bingham Mining District, Utah, 1976.
UGA-7	Guidebook to Mineral Deposits of Southwestern Utah, edited by D.R. Shawe, International Association on the Genesis of Ore Deposits Meeting, Field Excursion C-2, 1978.
RMAG/UGA	Basin and Range Symposium and Great Basin Field Conference, edited by G.W. Newman and H.D. Goode, 1979. (co-produced with Rocky Mountain Association of Geologists).
UGA-8	Henry Mountains Symposium, edited by M.D. Picard, 1980.
UGA-9	Central Wasatch Geology, 1981, field trip.
UGA-10	Overthrust Belt of Utah, Symposium and Field Conference, edited by D.L. Nielson, 1982.
UGA-11	Overthrust Belt of Utah, Programs and Abstracts, edited by T.L. Britt, 1982.
UGA-12	Geology and Energy Resources, Uinta Basin of Utah, edited by M.D. Picard, 1985.
UGA-13	Geology of Northwest Utah, Southern Idaho, and Northeast Nevada, edited by G.J. Kerns and R.L. Kerns, Jr., 1984.
UGA-14	Orogenic Patterns and Stratigraphy of North-Central Utah and Southeastern Idaho, edited by G.J. Kerns and R.L. Kerns, Jr., 1985.
UGA-15	Thrusting and Extensional Structures and Mineralization in the Beaver Dam Mountains, Southwestern Utah, edited by D.T. Griffen and W.R. Phillips, 1986.
UGA-16	Cenozoic Geology of Western Utah, Sites for Precious Metal and Hydrocarbon Accumulations, edited by R.S. Kopp and R.E. Cohenour, 1987.
UGA-17	Geology and Hydrology of Hazardous-Waste, Mining-Waste, Waste-Water, and Repository Sites in Utah, edited by G.E. Cordy, 1989.
UGA-18	Energy and Mineral Resources of Utah, edited by M.L. Allison, 1991.
UGA-19	Geology of East-Central Utah, edited by T.C. Chidsey, Jr., 1991.
UGA-20	Hydrocarbon and Mineral Resources of the Uinta Basin, Utah and Colorado, edited by T.D. Fouch, V.F. Nuccio, and T.C. Chidsey, Jr., 1992.
UGA-21	Engineering and Environmental Geology of Southwestern Utah, edited by K.M. Harty, 1992.
UGA-22	Oil and Gas Fields of Utah, edited by B.G. Hill and S.R. Bereskin, 1993.
UGA-23	Cenozoic Geology and Geothermal Systems of Southwestern Utah, edited by R.E. Blackett and J.N. Moore, 1994.
UGA-24	Environmental and Engineering Geology of the Wasatch Front Region, edited by W.R. Lund, 1995.
UGA-25	Geology and Resources of the Paradox Basin, edited by A.C. Huffman, Jr., W.R. Lund, and L.H. Godwin, 1996.
UGA-26	Modern and Ancient Lakes: New Problems and Perspectives, edited by J.K. Pitman and A.R. Carroll, 1998.
UGA-27	Geology of Northern Utah and Vicinity, edited by L.E. Spangler, 1999.
UGA-28	Geology of Utah's Parks and Monuments, 1st Edition, edited by D.A. Sprinkel, T.C. Chidsey, Jr., and P.B. Anderson, 2000.
UGA-28-2	Geology of Utah's Parks and Monuments, 2nd Edition, edited by D.A. Sprinkel, T.C. Chidsey, Jr., and P.B. Anderson, 2003.
UGA-28-3	Geology of Utah's Parks and Monuments, 3rd Edition, edited by D.A. Sprinkel, T.C. Chidsey, Jr., and P.B. Anderson, 2010.
UGA-29	Geologic Road, Trail, and Lake Guides of Utah's Parks and Monuments, edited by P.B. Anderson and D.A. Sprinkel, 2001.

UGA-29-2	Geologic Road, Trail, and Lake Guides of Utah's Parks and Monuments, 2nd Edition, edited by P.B. Anderson and D.A. Sprinkel, 2004.
UGA-29-3	Geologic Road, Trail, and Lake Guides of Utah's Parks and Monuments, 3rd Edition, edited by P.B. Anderson and D.A. Sprinkel, 2012.
UGA-30	The Geologic Transition, High Plateaus to Great Basin – the Mackin Volume, edited by M.C. Erskine, J.E. Faulds, J.M. Bartley, and P.D. Rowley, 2001. (published with the Pacific Section of AAPG).
UGA-31	Ground Water in Utah, Resource, Protection, Remediation, edited by L.E. Spangler, 2004.
UGA-32	Mining Districts of Utah, edited by R.L. Bon, R.W. Gloyn, and G.M. Park, 2006.
UGA-33	Uinta Mountain Geology, edited by C.M. Dehler, J.L. Pederson, D.A. Sprinkel, and B.J. Kowallis, 2005.
UGA-34	Geology of Northwestern Utah, edited by K.M. Harty and D.E. Tabet, 2006.
UGA-35	Field Guide to Geologic Excursions in Southern Utah, edited by W.R. Lund, 2007.
UGA-36	Central Utah—Diverse Geology of a Dynamic Landscape, edited by G.C. Willis, M.D. Hylland, D.L. Clark, and T.C. Chidsey, Jr., 2007.
UGA-37	Hydrocarbon Systems and Production in the Uinta Basin, Utah, edited by M.D. Longman and C.D. Morgan, 2008.
UGA-38	Geology and Geologic Resources and Issues in Western Utah, edited by B.T. Tripp, K. Krahulec, and J.L. Jordan, 2009.
UGA-39	Geology of South-Central Utah, edited by S.M Carney, D.E. Tabet, and C.L. Johnson, 2010.
UGA-40	Sevier Thrust Belt—Northern and Central Utah and Adjacent Areas, edited by D.A. Sprinkel, W.A. Yonkee, and T.C. Chidesy, Jr., 2011.
UGA-41	Selected Topics in Engineering and Environmental Geology in Utah, edited by M.D. Hylland and K.M. Harty, 2012.
UGA-42	The San Rafael Swell and Henry Mountains Basin: Geologic Centerpiece of Utah, edited by T.H. Morris and R. Ressetar, 2013.
UGA-43	Geology of Utah's Far South, edited by J.S. MacLean, R.F. Biek, and J.E. Huntoon, 2014.
UGA-44	Geology of Utah's Uinta Basin and Uinta Mountains, edited by M.D. Vanden Berg, R. Ressetar, and L.P. Birgenheier, 2015.
UGA-45	Resources and Geology of Utah's West Desert, edited by J.B. Comer, P.C. Inkenbrandt, K.A. Krahulec, and M.L. Pinnell, 2016.
UGA-46	Geology and Resources of the Wasatch: Back to Front, edited by W.R. Lund, S.H. Emerman, W. Wang, and A. Zanazzi, 2017.
UGA-47	Geofluids in Utah, edited by S.H. Emerman, B. Bowen, S. Simmons, and S. Schamel, 2018.
UGA-48	Geosites, edited by M. Milligan, R.F. Biek, P.C. Inkenbrandt, P. Nielsen, 2020.
UGA-49	Publication was cancelled, number not used.
UGA-50	The Lacustrine Green River Formation: Hydrocarbon Potential and Eocene Climate Record, edited by M.D. Vanden Berg, R. Brinkerhoff, J.E. Birdwell, E.A. Jagniecki, and L.P. Birgenheier, 2022.
UGA-51	Great Salt Lake and the Bonneville Basin: Geologic History and Anthropocene Issues, edited by M.D. Vanden Berg, R.L. Ford, C. Frantz, H. Hurlow, K. Gunderson, and G. Atwood, 2024.

PRESIDENT'S MESSAGE

On behalf of the members of the Utah Geological Association (UGA), I invite you to engage with the cutting-edge science presented in this guidebook. The UGA is a non-profit, all-volunteer organization of geologists and other geoscientists who share a common interest in Utah's geology. The purpose of the UGA is to increase and disperse geological information to the scientific community and promote public awareness of the usefulness of geology in general. Publication of our guidebook series is one of the principal ways that we fulfill our mission, and we are very proud of UGA Publication 51, Great Salt Lake and the Bonneville Basin: Geologic History and Anthropocene Issues. We are also very excited to offer this guidebook as a free, open-source publication. This is an important "first" for our association and we hope this will promote the wide dissemination of the important and timely science presented in this volume.

As a geomorphologist and Quaternary geologist, I was aware of the basic geologic history of Pleistocene Lake Bonneville and its Holocene remnant, Great Salt Lake, even before my family and I moved to Salt Lake City in 1992. Shortly after my arrival I had the very good fortune to audit several of the late Don Currey's (1934-2004) graduate seminars on Lake Bonneville and the Great Basin at the University of Utah. I was also an early member of the advisory board of FRIENDS of Great Salt Lake during this time. During my 25-year career at Weber State University, I viewed and contemplated Great Salt Lake almost every evening during my homeward commute from Ogden to Salt Lake City. Thus, even though my research did not focus on this system, I was a student of the Lake and very much aware of its importance. Jump to 2022. As UGA's President-Elect, I was very pleased when the Governing Board agreed that our 2023/2024 guidebook should focus on this critical and threatened biogeochemical system. I am very grateful that Michael Vanden Berg (Utah Geological Survey) agreed to serve as lead editor. Michael recruited a dedicated and talented editorial team (Carie Frantz, Hugh Hurlow, Kellen Gunderson, and Genevieve Atwood), which in turn recruited authors engaged in current research and shepherded their manuscripts through the peer-review process in a timely fashion. Thank you all.

I would also like to thank the AAPG Rocky Mountain Section Foundation for their very generous grant to the UGA in support of Publication 51 and its associated fall field trip. UGA's 2023 field trip (October 20-21) to Great Salt Lake and the Bonneville Salt Flats, co-sponsored by the Utah Geological Survey (UGS), was a big success. Field trip leaders Michael Vanden Berg (UGS) and Jeremiah Bernau (Chevron) organized and executed an informative and enjoyable trip that shared the results of recent and ongoing research. Day 1 focused on biogeochemical processes operating in the south arm of Great Salt Lake, which the participants circumnavigated by driving across the railway causeway. This was an exciting first for many participants, including myself. Day 2 focused on the Bonneville Salt Flats, its hydrology, geochemistry, and management issues. The 29 participants, with 12 different affiliations, enjoyed great science and beautiful fall weather. Five university students participated and the RMS-AAPG grant enabled the UGA to offer them a substantial discount on their registration fee.

Great Salt Lake attained a new record-low water-surface elevation in November 2022 (see Rowland and Freeman, this volume, for details). The subsequent media coverage, legislative activity during the 2023 session, and local community response – along with UGA's efforts to produce Publication 51 – made 2023 "the year of the lake" for many of us. I give a final thank you to everyone who is working for a sustainable future for this vital ecosystem through science-based decisions.

With gratitude,
Richard L. ("Rick") Ford
2022-2023 UGA President

EDITORS' MESSAGE

What do you think about when someone mentions Great Salt Lake? Stinky, gross, crusty, wasteland, a place to visit once, but not to return—these are common perceptions, but did you know that Great Salt Lake:

- √ is an important stopover point in North American for millions of migratory birds;
- √ hosts the vast majority of wetland acreage in Utah;
- √ contains the world's largest accumulation of Holocene microbialites;
- √ is the only producer of magnesium metal in North America;
- √ is one of two places in the U.S. that produces lithium, a vital mineral for the transition to clean energy;
- √ contributes to the "Greatest Snow on Earth" in the form of lake effect snow;
- √ produces significant quantities of potash, which is a vital fertilizer needed to grow our food; and
- √ is the number one producer of brine shrimp cysts, which are used in aquaculture facilities worldwide.

Like most terminal saline lakes around the world, the public pays little attention when the lake is "behaving". During these times, scientists are quietly conducting their research, some outdoor enthusiasts are recreating on its waters and along the shores, and industry hums along business as usual. However, every so often the lake goes outside of "normal". When this happens, everyone stands up and takes notice. In the mid-1980s, the lake went outside of "normal" and reached very high levels, threating shoreline communities and infrastructure. Significant actions were taken to tame the high-water levels, including installing massive pumps on the west side to send water into the Bonneville desert. Through the 1990s and 2000s, the lake went back to a state of "behaving" and most people again overlooked our finicky neighbor.

The lake is once again behaving outside of "normal", this time with historic low lake levels. We think everyone can agree that low lake levels pose a risk to Utah citizens in the form of dust emissions, reduced snowpack, threatened wildlife, and impacts to industrial activity. It is in this environment of low lake level and increased attention that the Utah Geological Association proudly releases Publication 51. This new compilation of 14 timely research papers on Great Salt Lake and older Lake Bonneville will hopefully contribute to the new body of scientific work that can help inform those charged with managing this unique resource.

The editors greatly appreciate the authors for being willing to share their knowledge and write such informative papers. We would also like to thank Cheryl Wing, our fantastic and very patient graphic artist for formatting all the papers and other materials with care and attention to detail. In addition, acknowledgement goes to the American Association of Petroleum Geologists Rocky Mountain Section Foundation for providing funding for this book and the associated field trip. Finally, we would like to thank the UGA and all its many volunteers for all their hard work promoting the wonderful geology of Utah.

Michael Vanden Berg, Rick Ford, Carie Frantz, Hugh Hurlow, Kellen Gunderson, and Genevieve Atwood

UGA 51 Editors

DEDICATION

J. Wallace ("Wally") Gwynn, Ph.D.
(May 30, 1940 – July 15, 2021)

Utah Geological Association Publication 51 is dedicated to the career and memory of Dr. John Wallace Gwynn—Wally to his family, friends, and colleagues. Those who had the pleasure of working with Wally fondly remember his infectious smile and enthusiasm, coupled with a depth of knowledge and strong desire to help others.

Wally was born and raised in Salt Lake City, Utah, and attended the University of Utah, where he majored in mineralogy and geology. After completing his doctorate in 1970, Wally worked as a mineral exploration geologist for Phelps Dodge Corporation and as a research geologist for AMAX and Great Salt Lake Minerals. In 1975 Wally joined the Utah Geological Survey (UGS) as a saline-minerals geologist, a position he held for 34 years until his retirement in 2009. In retirement Wally worked as a private consultant on several potash projects in Utah.

Wally's Ph.D. dissertation focused on the tar-sand resources of Uintah and Grand counties, and he continued this work with the UGS. Wally also investigated and published reports on the oil-well brines of the Uinta and Paradox basins, subsurface brines of the Sevier Lake area, and low-temperature geothermal resources along the Wasatch Front. However, the bulk of Wally's UGS career was spent investigating and publishing on the brines and mineral resources of Great Salt Lake; he was the Survey's Great Salt Lake expert for more than 30 years and the author of numerous UGS publications about the Lake. In addition, Wally edited two major compilation volumes about Great Salt Lake during his UGS career: Great Salt Lake: A Scientific, Historical and Economic Overview (Utah Geological and Mineral Survey Bulletin 116, 1980) and Great Salt Lake: An Overview of Change (Utah Department of Natural Resources Special Publication, 2002).

Great Salt Lake was Wally's true scientific passion. He was dogged in his systematic collection of geochemical data, going out onto the lake month after month to document the chemistry and physical properties of the Lake's water layers. The lake data he collected during his UGS tenure is foundational and still in use today. During the 1980s high stand, he was called upon by the Department of Natural Resources to offer guidance with respect to the advisability and consequences of the West Desert pumping project. Wally was all about the data and very generous with his time and expertise, serving on numerous technical committees and responding to inquiries from state and federal agencies, industries, and the general public. Even in retirement Wally followed developments at the Lake. In his interactions, Wally was a kind, patient, and soft-spoken person, and in his work, he was a dedicated geoscientist and public servant.

The Holocene Great Salt Lake and Pleistocene Lake Bonneville System: Conserving our Geoheritage for Future Generations

Marjorie A. Chan[1], Charles G. Oviatt[2], Bonnie K. Baxter[3], Basil Tikoff[4], and Genevieve Atwood[5]

[1]*Department of Geology and Geophysics, University of Utah, Salt Lake City, Utah, marjorie.chan@utah.edu*

[2]*Department of Geology, Kansas State University, Manhattan, Kansas*

[3]*Great Salt Lake Institute, Westminster University, Salt Lake City, Utah*

[4]*Department of Geoscience, University of Wisconsin, Madison, Wisconsin*

[5]*Earth Science Education, Salt Lake City, Salt Lake City, Utah*

10.31711/ugap.v51i.132

ABSTRACT

The modern (Holocene-age) Great Salt Lake (GSL) and Pleistocene Lake Bonneville of the Bonneville Basin (BB) together make a geosite (GSL-BB system) of exceptional scientific, cultural, aesthetic, and societal value. GSL is the largest saline lake in the Western Hemisphere and a sensitive recorder of climate. For millennia, this distinctive salty water body has been a dynamic and complex natural ecosystem, including an important waterway for birds and other wildlife and an archive of environmental change and history. Lake Bonneville is a seminal part of the history of science in the United States through the work of G.K. Gilbert, who in the 1870s and 1880s developed both critical scientific concepts (e.g., isostasy) and methods (e.g., multiple working hypotheses), which are still employed today. GSL is a major tourist attraction, an economic driver, and a place of scientific exploration. Yet today, the GSL is in grave danger of near total desiccation due to a combination of factors: human removal of waters that would normally replenish the lake, climate change, and other environmental pressures. Over the past few decades there has been a growing international movement to recognize and respect our geoheritage, by raising visibility and protection of high-priority geosites. The GSL-BB system is a geoheritage site that urgently needs our protection.

GEOHERITAGE CONCEPT

An International Movement

Over several decades, a growing international geoconservation movement recognizes that exceptional geological sites need to be protected and managed as part of our geoheritage. The Geological Society of America Position Statement (Geological Society of America, 2022) defines geoheritage sites as areas with geologic features of significant scientific, educational, cultural, and/or aesthetic value. These sites are key to advancing knowledge and support the broad understanding of the environment, its geodiversity and biodiversity, and the factors that influence climate change (see America's Geoheritage II workshop proceedings, 2021 https://nap.edu/26316). Although biodiversity is notably visible to the public, the geologic setting – its geodiversity and the convergence of geographic to environmental conditions – commonly form the underpinnings and context for biodiversity. The extensive and rapidly expanding body of literature on geoheritage is too extensive to detail here (e.g., see summaries of Brilha, 2015, 2018; Reynard and Brilha, 2018; Brilha and others, 2018).

The United States is endowed with many sites that embody a rich geoheritage. The U.S. and State Park systems have had an important impact on the conservation movement, but there has been growing recognition for more coordinated global recognition of natural sites. Thus, geoheritage calls for global communication and cooperation, and provides the context that covers much of the science and education related to important geosites, while also embracing ethics, outreach, inclusivity, protection, and management. Geoheritage also relies on modern technology to understand and model how natural systems are impacted. As Earth scientists, we understand Earth systems, with their change and interrelationships, and feedbacks in time and space. We must be caretakers and advocates for GSL, as we have both the knowledge and responsibility to help balance nature and societal needs.

Geosite Locality

In the Basin and Range province, ancient Lake Bonneville (Figure 1A) covered much of western Utah during the last glacial maximum. The modern GSL (Figs. 1B, C) is the recent version of the closed-basin GSL-BB system, which, during the past few

million years, has been dominated by various saline to hypersaline lakes similar to Holocene GSL. Between 30,000 and 13,000 yr BP the lake system was deeper and more extensive (Lake Bonneville) and was dominated by freshwater (Figure 1D, Currey and others, 1984). There is much interest in the GSL as shown by the considerable literature covering more than a century, including this volume (also see Gilbert, 1886, 1890; Oviatt and Shroder, 2016a). The significant runoff that resulted from the wet winter of 2022-2023, does not significantly ameliorate the long-term decline in water level of the GSL.

For centuries, GSL has been the largest saline lake in the Western Hemisphere, recording a history of change (Madsen, B.D., 1989; Gwynn, 2002a). But now in the Anthropocene, drying of GSL (Figs. 1B, C) and the probability of it disappearing, leaving behind a bowl of toxic dust with a few pools of salty water, has understandably raised alarm (e.g., Flavelle, 2022). With growing pressures of urbanization in Utah, the geologic features in Antelope Island State Park in Davis County, Utah, provides one of the few sites left to easily access the GSL and see the context of its history over millennia, including the cyclic rises and falls of GSL and Lake Bonneville. This paper focuses on the broad spectrum and overview of geoheritage values and why it is important to protect the GSL.

GEOHERITAGE VALUES

Cultural and Historical Value

The GSL-BB system has significant cultural as well as historical value because of the role that the landscape played for indigenous peoples as well as in the subsequent exploration of the west by European Americans. Humans have occupied the Great Basin for thousands of years. Native American tribes that have lived in the GSL region, and that are still an important presence, include the Western Shoshone, Goshute, Ute, Paiute, and Washoe peoples (National Park Service, 2015). The landscape was a vital resource where native people hunted and gathered for sustenance, and the GSL watershed provided an exceptional bounty (e.g., Madsen, D.B, 1989). Today many tribal descendants feel an important connection to the land, particularly where open spaces retain much of their original, natural expression.

In the 19th century with expansion and exploration of the west by European Americans (e.g., Stegner, 1954), early scientific studies included the documentation of Lake Bonneville, based on studies of its shorelines, deltas, and sediments by renowned American geologist G. K. Gilbert (1886, 1890). His careful studies on foot and horseback allowed him to deduce that valley floors were previously covered by water and the isolated mountain ranges had been islands and peninsulas in a Pleistocene water body he named "Lake Bonneville." Gilbert used the Bonneville basin to investigate the idea of isostasy (equilibrium adjustments of Earth's crust to changing distributions of weight at the surface, in this case the growth and eventual loss of the water load of Lake Bonneville). Individual shorelines of Lake Bonneville vary in elevation with the highest elevations occurring where the lake was deepest (the weight of the water in the lake depressed the underlying crust, and when the water evaporated, the crust rebounded). This work was the case example for Gilbert to illustrate the methodology of multiple working hypotheses to overcome bias in human reasoning (Gilbert, 1886). His recognition of the dynamic equilibrium of landforms and his correlation of shoreline elevations was seminal to understanding the complex interplay of isostasy and basin tectonics. Gilbert identified and quantified evidence of shoreline superelevation and effects of fetch on shoreline elevations of GSL and Lake Bonneville. Because of Gilbert's work, the GSL-BB system represents a seminal part of the history of science in America.

Gilbert used his experiences in this basin to understand distinctive shoreline barriers, terraces, and spits, and he chronicled the causal changes in hydrology based on rises and falls of Lake Bonneville and the highstands of GSL during the 1870s compared to falling levels of GSL during the 1880s. Remarkably, Gilbert's seminal work has been an inspiration to people all over the world who have studied the history of closed-basin lakes. To be able to retrace Gilbert's thoughts and walk in his footsteps has deep meaning for those who value historical significance. Many Bonneville shorelines are now being rapidly lost or covered due to urbanization, but Antelope Island State Park preserves near-pristine records of these ancient shorelines.

Scientific and Educational Value

The GSL-BB system encompasses a rich geoheritage (Figure 2) and contains many classic textbook geologic features and landscapes, that are significant to both education and research. Much of the specific science is detailed in other papers of this volume.

Geomorphology and Ice Age History

The geoheritage value of the Bonneville basin's prominent ice-age landforms is explained in more detail in other publications (Chan and Currey 2001;

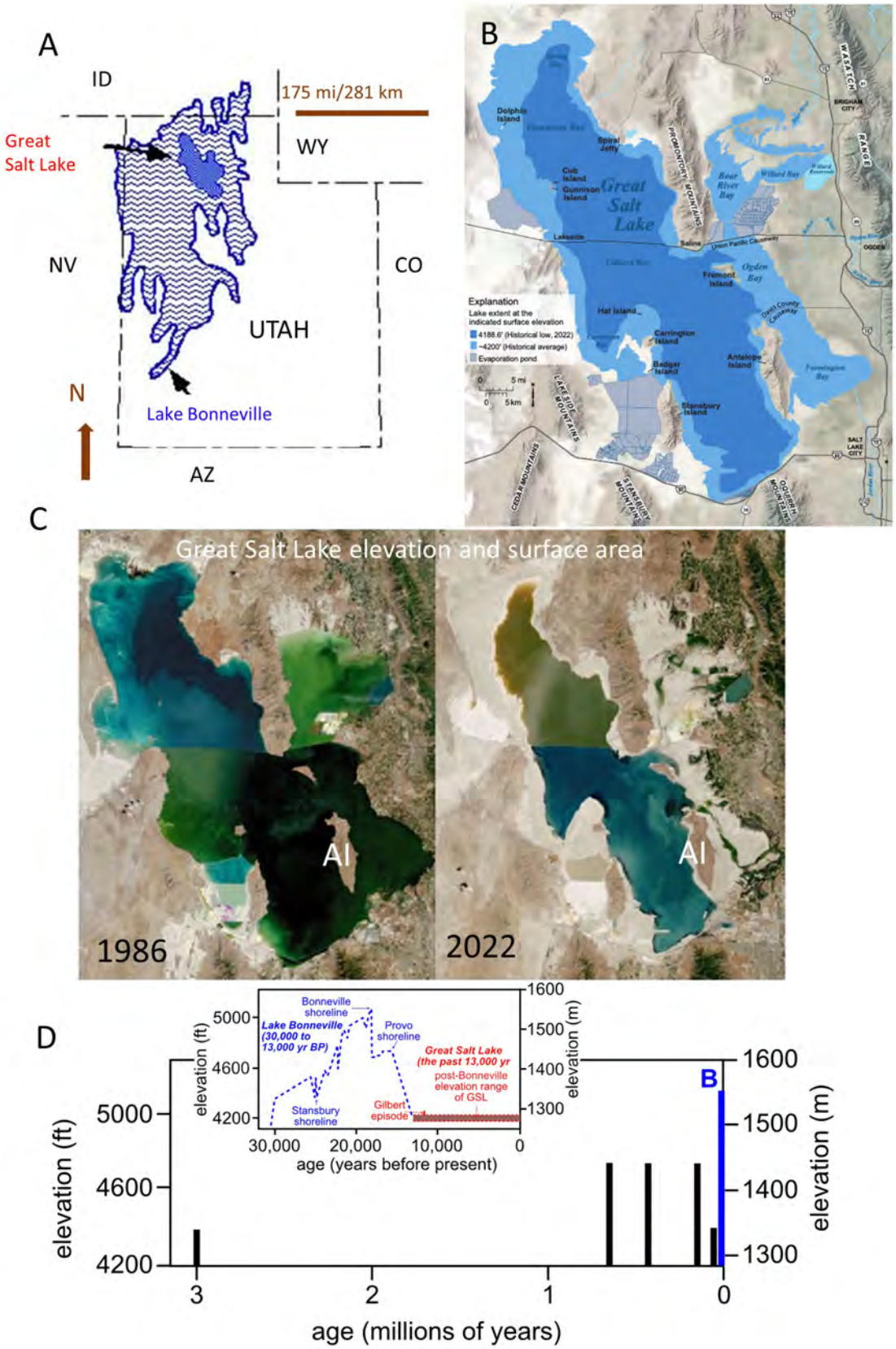

Figure 1. *The GSL-BB system. A. Location of GSL and Lake Bonneville in western Utah. B. Overview map of GSL showing the historic average elevation, and the new 2022 historic low (Figure from Clark and Baxter, 2023.) C. Corresponding Landsat satellite imagery of GSL elevations showing the record high of GSL in 1986 at left vs. historic low in 2022. AI = Antelope Island. Images (Images are public domain.) D. Known Bonneville basin lake cycles. The blue line labeled B in the main graph marks the Bonneville deep-lake cycle. Vertical black bars represent older deep-lake cycles. The base of the main graph is the elevation of modern GSL. Inset shows the shoreline history of Lake Bonneville (blue) and GSL (red) with named shorelines (also see Figure 3). (Inset figure from Oviatt and Shroder, 2016a).*

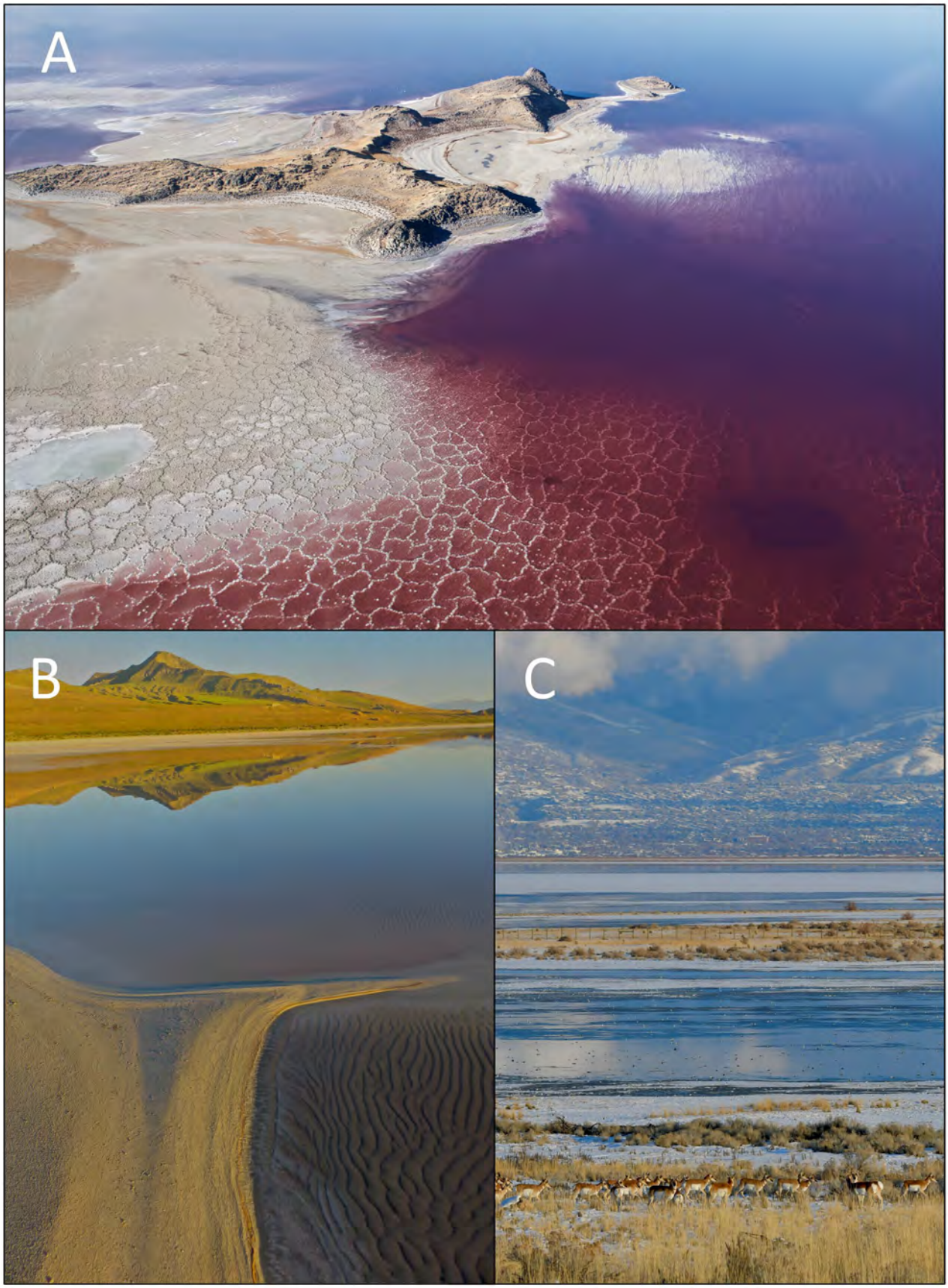

Figure 2. *The GSL-BB system has many geoheritage values including historical, scientific, educational, aesthetic, economic, and societal. A. Polygonal cracks south of Gunnison Island. B. Colorful imagery at Antelope Island. C. GSL lies at the intersection of urban and natural settings (Antelope Island looking east, herd of antelope in the foreground). GSL is a major attraction that draws tourists. GSL enhances the quality of life in the Salt Lake Valley. Images: J. Long.*

Chan and others, 2003; Chan and Godsey, 2004, 2016). Since Lake Bonneville was the largest pluvial lake in the Western Hemisphere (that is, it was caused by climate change and an increase in effective moisture in the basin and was not fed by glacial meltwater), it is a natural laboratory for study (Figure 3), bolstered by the well-dated shorelines that provide a precise lake hydrograph linked to Pleistocene climate change. Study of the GSL-BB has unparalleled analog value for many other large lake systems. The varied character of the lake is a result of climate change in the basin, causing the lake to range from small and hypersaline to large and nearly fresh. Because the basin is so big and deep relative to the amount of water that enters the system, the lake has remained hydrographically closed for most of its history.

Connecting Lake Bonneville and GSL to lakes farther back into the Pleistocene, subsurface cores like the Burmester core (Eardley and others, 1973; Oviatt and others, 1999), tell the story of only four deep-lake cycles during the past 800,000 years. Lake Bonneville was the most recent of those deep-lake cycles, and the deepest because it had the benefit of input from the upper Bear River and rivers in Cache Valley, which were diverted into the basin after 50,000 yr BP. All together those four deep-lake cycles took up less than 10% of the past 800,000 yr — the rest of the time the lake was shallow, similar to the historic GSL (Oviatt and Shroder, 2016b). Prior to 800,000 yr BP, the lake system stayed at low levels back to about 3 million years ago. Thus, other than the four deep-lake cycles, the history of the GSL-BB system indicates that our modern view of GSL is typical of the past few millions of years — a shallow hypersaline lake in a desert environment.

The combination of geomorphic and the sediment records are valuable analogs for other large lake studies, in part because the record in the GSL-BB system is so intact, with distinctive markers of change over documentable spatial and temporal scales. The landscape expressions are also analogs to understanding geologic processes and applying them to regions of Mars (e.g., Chan and others, 2016).

GSL Ooids

GSL is known as the world's largest lacustrine carbonate depositional system (Baskin and others, 2022). Distinctive carbonate ooids (Figure 4) — coated grains formed where waves agitate the lake bottom sediment — of GSL are long-standing world class examples. These sand-size features form when fine-grained particles, such as brine-shrimp pellets or tiny sand grains, become coated with successive thin, concentric layers of calcium-carbonate crystals (crystals of the mineral aragonite arranged radially outward from the center of the ooid; e.g., Sandberg, 1975; Figure 4A). Recent work of Lincoln and others (2022) suggests that the radial pattern is derived from recrystallization. The GSL ooids contrast with other classic examples, such as Bahamian ooids that have calcium carbonate crystals arranged parallel to the grain coatings rather than radially. Oolitic sand is commonly cemented into beachrock (Figure 4B), which is an indicator of lithification along older shorelines, with cementation aided by microbial activity (Lincoln and others, 2022).

Microbialites

Microbialites are organo-sedimentary mounds formed by the actions of complex microbial mats (Burne and Moore, 1987; Lindsay and others, 2017), and GSL has an extensive distribution in the high-salinity water (Baskin and others, 2022; Carney and Vanden Berg, 2022; Pedone and others, 2023). Photosynthesis by cyanobacteria and sulfate metabolism by other microorganisms create conditions that precipitate calcium carbonate (Burne and Moore 1987). In addition, the extra-polymeric substance (EPS; a term commonly used by people who study microbialites) secreted by the cyanobacteria trap carbonate sediment, which creates a substrate on which new mats grow toward sunlight, hence the mound shape. Some microbialites follow older polygonal crack patterns (Figure 4), possibly because they are texturally different sites that might enhance biomediated growth, but microbialites also occur as individual mound buildups (Figure 5) up to 1.5 m high that cover as much as a quarter of the lake floor (Chidsey and others, 2015; Vanden Berg, 2019; Baskin and others, 2022; Wilcock and others, 2024).

Microbialite growth is sensitive to water chemistry and depth (light), wave energy, substrate, and other environmental factors (Kanik and others, 2020). Cyanobacteria-based mats represent the earliest fossilized life form on Earth; layered and mounded accumulations of microbialites are well-preserved in carbonate rocks in the geologic record. The longevity and adaptability of microbialites accounts for their distribution on our planet in modern extreme environments, such as GSL. The study of GSL microbialites has implications for the search for biosignatures on Mars (Noffke, 2015; Chan and others, 2019; Gill and others, 2023).

Mineralogy and Mirabilite

Evaporite minerals such as halite (NaCl) have a long history of being extracted from GSL waters

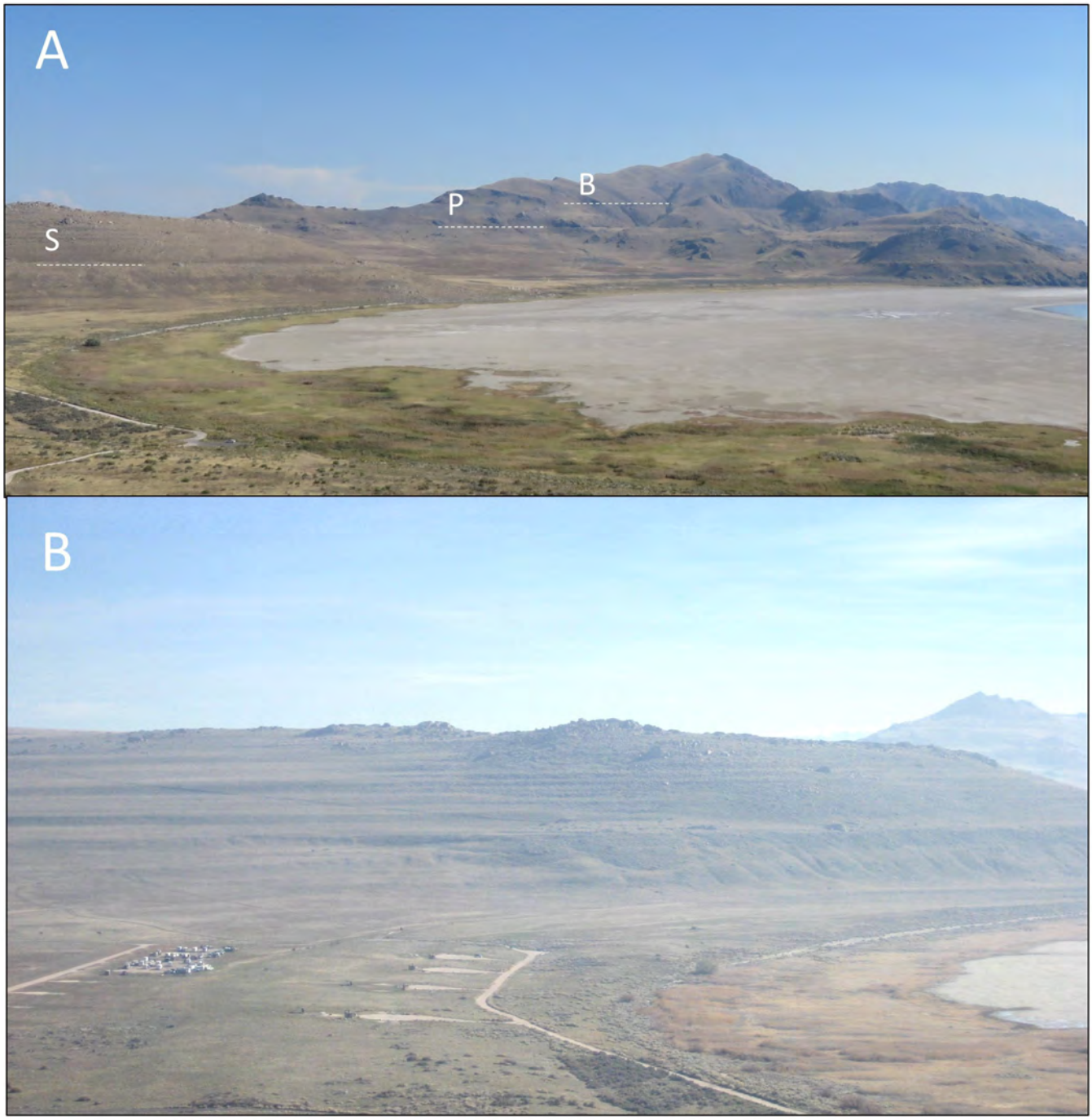

Figure 3. *Shorelines of Lake Bonneville in Antelope Island State Park preserved at White Rock Bay and superimposed on the mountain bedrock. The landforms are a valuable record of geologic history and climate change. A. Prominent shorelines (photo taken in 2014): S = Stansbury shoreline, B = Bonneville shoreline, P = Provo shoreline. B. Many shorelines formed during the rising and falling phases of Lake Bonneville, here showing well-preserved examples between the Stansbury and Provo shorelines on this hillside; GSL at far right (barely in sight; photo taken in 2012). Images: M. Chan.*

(Gwynn, 2002b). Additionally, unusual cold-water, saline-lake minerals, such as mirabilite (hydrated sodium sulfate, $Na_2SO_4 \cdot 10H_2O$, also known as Glauber's salt), occur in spring mounds that are visible during winter months (Figure 6). Groundwater seems to be partially dissolving a subsurface mirabilite layer, and then the mirabilite minerals are reprecipitated at the surface where spring water emerges. Once the sodium-sulfate-rich spring water hits the cold winter air, mirabilite crystals form and build up a collection of small, mounded terraces, with beautiful crystals (Figure 6) that are stable only in sub-freezing dry environments. Some of the mirabilite-rich springs have colorful pools that are being studied for the associated microbial life (e.g., Jagniecki and others, 2021; Gill and others, 2023). These unusual mineralogies have implications for astrobiology and understanding life in extreme environments.

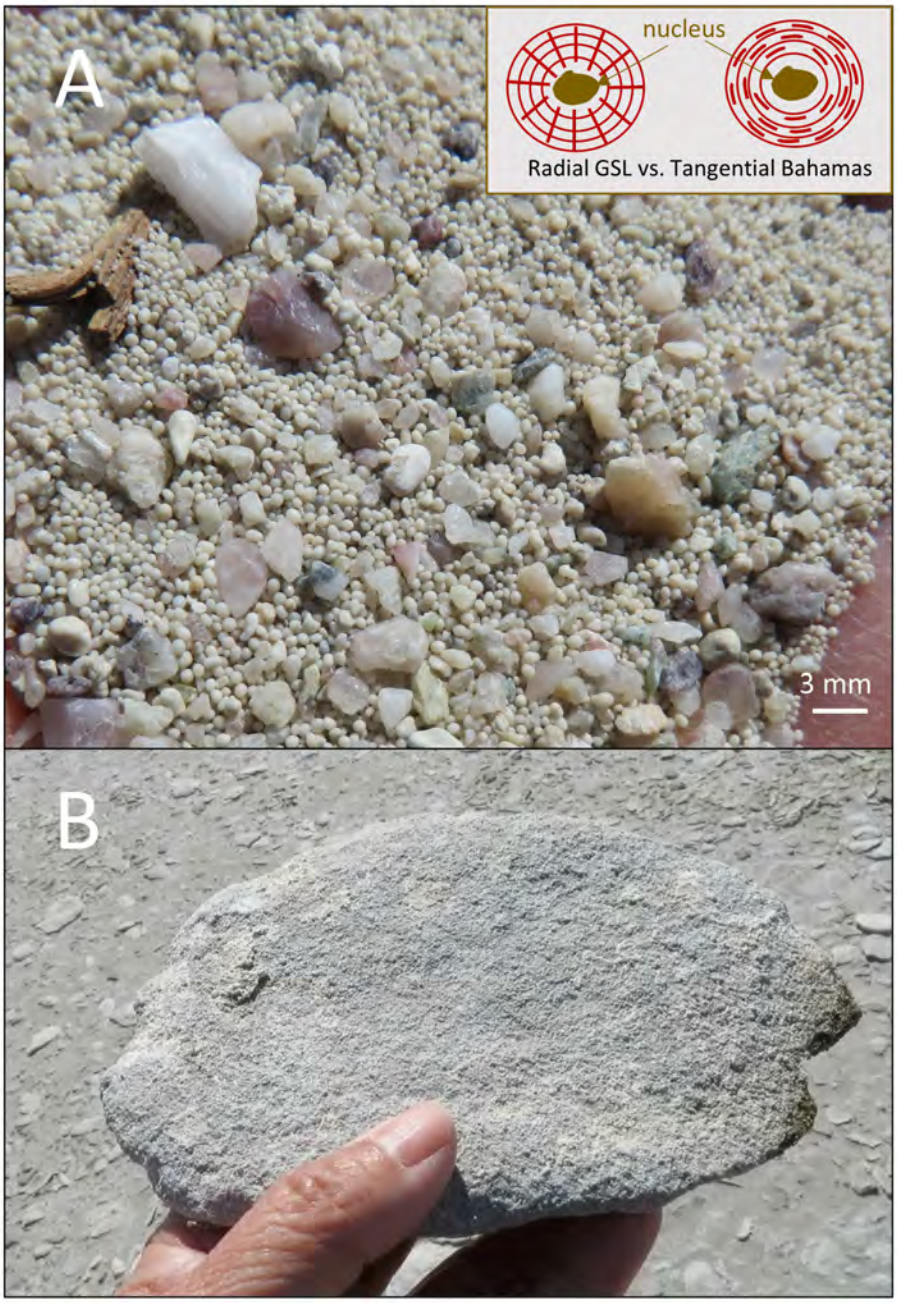

Figure 4. *Distinctive GSL features from the north side of Antelope Island that have scientific value. A. Loose spheroidal oolitic sand (mostly ~ 0.2 to 0.5 mm diameter) with scattered weathered siliciclastic granules derived from nearby bedrock exposures; diagrammatic inset shows GSL radial structure of GSL ooids vs. the common marine tangential structure exemplified in Bahama ooids. B. Cemented beachrock composed of oolitic sand. Images from Bridger Bay, Antelope Island, M. Chan.*

Ecosystem Significance

GSL is a delicately balanced ecosystem (Figure 7). The extreme conditions of GSL gives rise to a rich biodiversity and a special set of lifeforms, including brine shrimp and brine flies and the microorganisms that feed them, which have implications for understanding life adaptations in extreme environments (Baxter and Butler, 2020). The GSL provides important food and shelter to over 10 million migrating birds (Sorenson and others, 2020; GSLEP, 2022), in addition to generating billions of dollars in revenue from tourism and the brine-shrimp industry (Bioeconomics, 2012).

Life on Earth needs water, yet water in the GSL watershed has been extracted and diverted for many purposes, such as for growing alfalfa and building housing subdivisions and supporting infrastructure. This has significantly impacted the inflow and replenishment of the lake, which has been drying and could

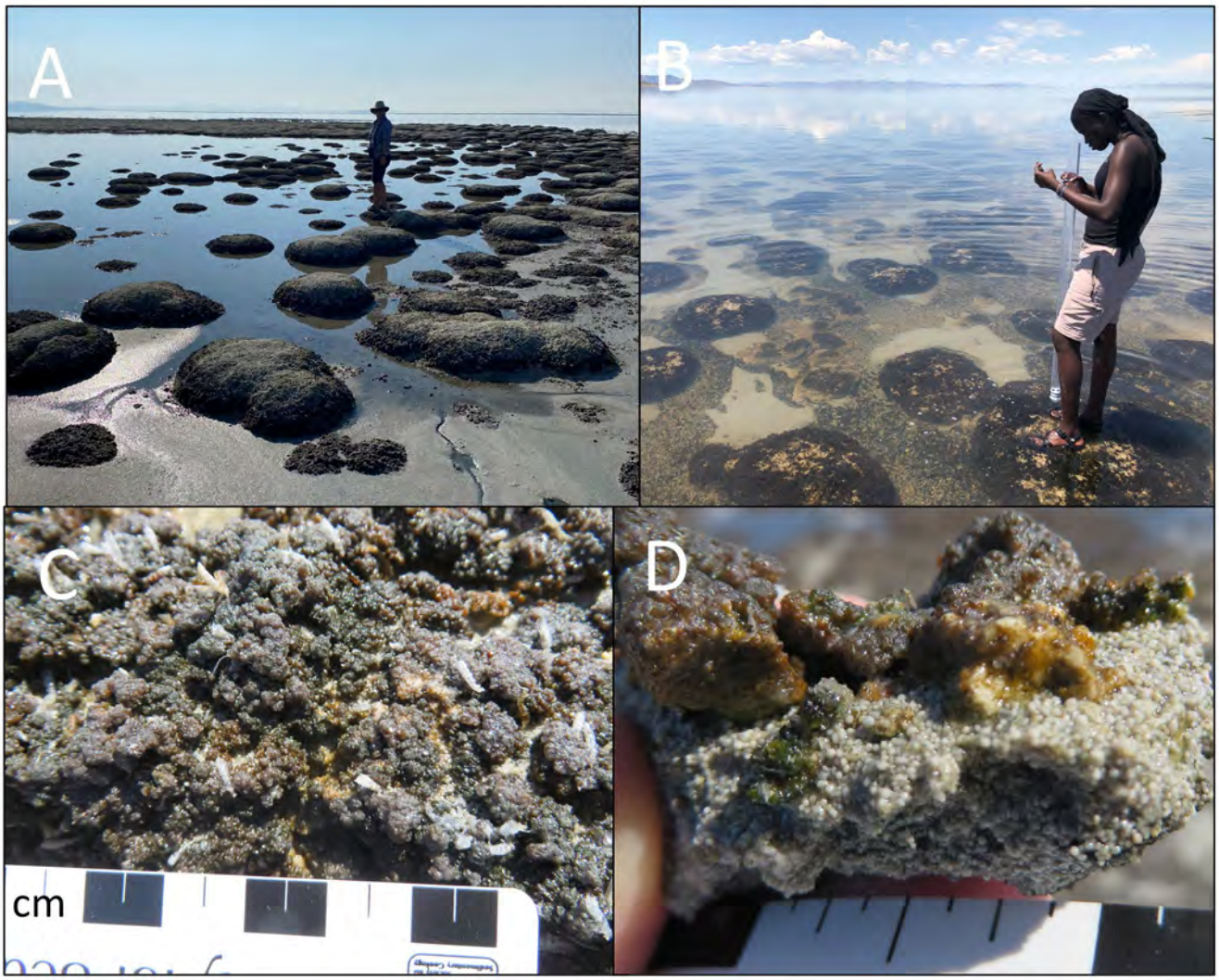

Figure 5. *Microbial mounds of GSL at Bridger Bay, Antelope Island State Park have important implications for understanding early life, with applications to astrobiology. A. and B. buildups; C. and D. cyanobacteria growth holding together oolitic sand grains, with some elongate brine-fly pupae cases. Images A, B: B. Baxter. Images C, D: M. Chan.*

potentially leave a basin of toxic dust that could impact regional communities (Flavelle, 2022). Declining GSL water levels threaten economic activity, public health in adjacent communities and ecosystems of GSL (Larsen, 2022; Great Salt Lake Strike Team report, 2023). It is clear that strategies to improve water management and increase deliveries to the lake are critical. GSL is an extreme ecosystem of biodiversity and geodiversity that is too important to lose.

Societal Value

There is no doubt that the GSL and the Bonneville Basin comprise an aesthetical geoheritage landscape that is visually appealing and that inspires a sense of awe and wonder (Figure 8). The landscape of GSL, enhanced by open space and the natural setting of flora and fauna, has cultural and historical roots, and impacts economic development and tourism as well as quality of life. Shrinking water levels of GSL have put this ecosystem into a state of crisis. Diminishment of the GSL will threaten wildlife and further degrade Utah's air quality.

Society needs geoheritage sites like GSL because these sites are critical to advancing knowledge about water, climate and environmental changes, evolution of life, minerals and resources, and other aspects of the nature and history of Earth (Geological Society of America, 2022). Numerous studies show that nature and the outdoors provide positive impacts on mental health and cognition (e.g., Bratman and others, 2019; Weir, 2020). GSL is an outdoor classroom that enhances public understanding and engagement with science (Figure 8), while providing recreational areas that improve quality of life, as well as economic support to local and regional communities as tourist destinations and as vital mineral and water resources.

CONCLUSIONS

Drying of Pleistocene Lake Bonneville, which ended about 13,000 years ago, left both ancient shore-

Figure 6. *Mirabilite mounds and terrace structures (A, B), with large, cm+ scale crystals growing in cold colorful pools (C, D - colored green by cyanobacteria) at White Rock Bay, Antelope Island State Park. These mineralogies have important implications for life in extreme environments. Winter images (2020): A-C: M. Chan. Image D: D. Eby.*

lines and the modern GSL, the largest saline lake in the Western Hemisphere. This GSL-BB system, as a whole, is a unique and valuable geoheritage archive of climate change and an extreme ecosystem that is often underappreciated and is now under threat of being lost. The GSL-BB hosts world class examples of landforms related to climate history, ooids, microbialite mounds, and evaporite minerals (e.g., halite and mirabilite). The microbialite and mirabilite features have implications for astrobiology and understanding life in extreme environments. Specifically, geoheritage sites like GSL are critical to the geoscience profession, to conserve sites of geoscience importance related to Earth processes, Earth history, and history of geologic thought. These sites are the training ground for the next generation of environmental scientists who will grapple with global societal issues and the complexities and balance of nature. The biodiversity and geodiversity of GSL and the Bonneville Basin make this a remarkable geoheritage jewel of Utah's west desert.

ACKNOWLEDGMENTS

We gratefully acknowledge professional photographer Joel Long for use of his Great Salt Lake images, and reviewers Mark Milligan and Thomas Casadevall.

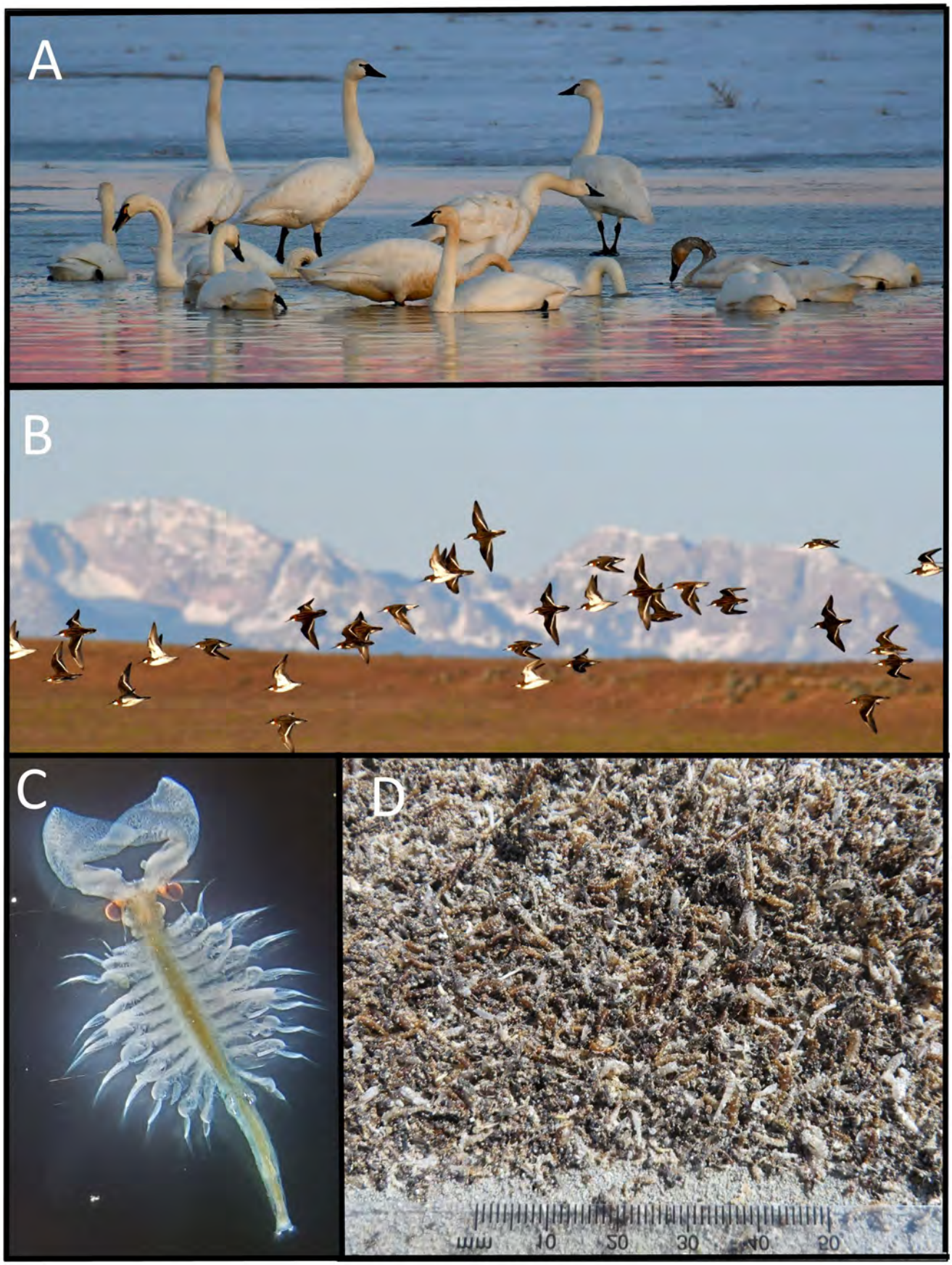

Figure 7. *GSL is a delicately balanced ecosystem. Waterfowl at Farmington Bay Wildlife Refuge on the eastern edge of GSL include migratory populations of Tundra Swans (A) and Phalaropes (B). C: a male GSL brine shrimp with impressive claspers; brine shrimp produce eggs/cysts that are harvested from the lake and sold in aquaculture shops (e.g., fish food), and they provide food for migratory birds. D: Brine-fly detritus, including pupae cases along the beach of Bridger Bay, Antelope Island State Park. Images A, B: J. Long. C: Bridget Dopp. D: M. Chan.*

Figure 8. *GSL is an outdoor laboratory for science, enjoyment of nature, and societal quality of life. Tourists and residents alike find refreshment and a sense of wonder and learning at GSL, Bridger Bay, and Antelope Island State Park. The Stansbury shoreline is visible on the slopes of Buffalo Point in the background in A. Many people enjoy GSL (B, C) year-round. Image A: M. Chan. B, C: J. Long.*

REFERENCES

America's Geoheritage II, 2021, America's Geoheritage II: Identifying, developing, and preserving America's natural legacy, Proceedings of a workshop: U.S. National Academies of Sciences, Engineering, and Medicine. https://nap.edu/26316

Baskin, R. L., Della Porta, G., & Wright, V. P., 2022, Characteristics and controls on the distribution of sublittoral microbial bioherms in Great Salt Lake, Utah: Implications for understanding microbialite development: The Depositional Record, v. 8 no. 1, p. 39-66.

Baxter, B.K. and Butler, J.K., editors, 2020, Great Salt Lake Biology: A Terminal Lake in a Time of Change: Springer, Cham, Switzerland, 537 p.

Bioeconomics, 2012, Economic Significance of the Great Salt Lake to the State of Utah. Accessed Feb-

ruary 14, 2023: https://deq.utah.gov/great-salt-lake-advisory-council/activities-great-salt-lake-advisory-council

Bratman, G.N., Anderson, C.B., Berman, M.G., Cochran, B., De Vries, S., Flanders, J., Folke, C., Frumkin, H., Gross, J.J., Hartig, T. and Kahn Jr, P.H., 2019, Nature and mental health: An ecosystem service perspective: Science advances v. *5*, no. 7, p.eaax0903. DOI: 10.1126/sciadv.aax0903

Brilha, J., 2015, Inventory and quantitative assessment of geosites and geodiversity sites: a review: Geoheritage, v. 1, p. 1867–2477.

Brilha, J., 2018, Geoheritage: inventories and evaluation, *in* Reynard, E., and Brilha, J., editors, Geoheritage: Elsevier, p. 69-85.

Brilha, J., Gray, M., Pereira, D.I. and Pereira, P., 2018. Geodiversity: An integrative review as a contribution to the sustainable management of the whole of nature: Environmental Science & Policy, v. 86, p.19-28.

Burne, R.V., Moore, L.S., 1987, Microbialites: organosedimentary deposits of benthic microbial communities: Palaios, v. 2, no. 3, p. 241–254.

Carney, S., and Vanden Berg, M.D., 2022, Geosites: Microbialities of Bridger Bay, Antelope Island, Great Salt Lake: Utah Geological Survey Notes, v. 54, n. 1. https://geology.utah.gov/map-pub/survey-notes/geosights/geosights-microbialites-of-bridger-bay-antelope-island-great-salt-lake/

Chan, M. A., and Currey, D. R., 2001, Geoantiquities: Earth History in the Urban Landscape: Utah Geological Survey Notes, v. 33, n. 1, p. 8.

Chan, M.A., and Godsey, H., 2004, Geoantiquities: Concepts and applications for education in the urban landscape: Journal of Geological Education v. 52, p. 445-452. http://www.nagt.org/nagt/jge/abstracts/nov04.html

Chan, M.A., Currey, D.R., Dion, A. and Godsey, H., 2003, Geoantiquities – in the urban landscape (Chapter 2): *in* Heiken, Fakundiny, G.R., and Sutter, J., editors, Earth Science in the City: A Reader: American Geophysical Union monograph. ISBN 0-87590-299-5, p. 21-42.

Chan, M.A. Godsey, H.S., 2016, Lake Bonneville geosites in the urban landscape: Potential loss of geological heritage (Ch. 23): *in* Oviatt, C.G., and Shroder, J.F., editors, Lake Bonneville: A Scientific Update, Elsevier, p. 617- 633.

Chan, M. A., Hinman, N. W., Potter-McIntyre, S. L., Schubert, K. E., Gillams, R. J., Awramik, S. M., Boston, P. J., Bower, D. M., Des Marais, D. J., Farmer, J., Jia, T. Z., King, P. L., Hazen, R. M., Léveillé, R. J., Papineau, D., Rempfert, K. R., Sánchez-Román, M., Spear, J. R., Southam, G., Stern, J.C., and Cleaves, H. J., 2019, Deciphering biosignatures in planetary contexts: Astrobiology, v. 19, no. 9, p. 1075-1102. https://doi.org/10.1089/ast.2018.1903

Chan, M.A., Jewell, P.W., Parker, T., Okubo, C., Ormo, J., and Komatsu, G., 2016, Pleistocene Lake Bonneville as an analog for extraterrestrial lakes and oceans: *in* Oviatt, C.G., and Shroder, J.F., editors, Lake Bonneville: A Scientific Update, Elsevier, p. 571-597.

Chidsey, T.C.J., Vanden Berg, M.D., and Eby, D.E., 2015, Petrography and characterization of microbial carbonates and associated facies from modern Great Salt Lake and Uinta Basin's Eocene Green River Formation in Utah, USA, *in* Microbial Carbonates in Space and Time: Implications for Global Exploration and Production: Geological Society of London Special Publication, v. 418, p. 261-286. https://doi.org/10.1144/SP418

Clark, D.L., and Baxter, B.K., 2023, Great Salt Lake's Gunnison and Cub Islands come into focus: Utah Geological Survey Notes, January 2023, https://geology.utah.gov/map-pub/survey-notes/gsl-gunnison-cub-islands/

Currey, D.R., Atwood, G., Mabey, D.R., 1984, Major levels of Great Salt Lake and Lake Bonneville: Utah Geological Mineral Survey Map 73.

Eardley, A.J., Shuey, R.T., Gvosdetsky, V., Nash, W.P., Picard, M.D., Grey, D.C, and Kukla, G.J., 1973, Lake cycles in the Bonneville basin, Utah: Geological Society of America Bulletin, v. 84, p. 211-216.

Flavelle, C., 2022, As the Great Salt Lake dries up, Utah faces an "environmental nuclear bomb": New York Times. https://www.nytimes.com/2022/06/07/climate/salt-lake-city-climate-disaster.html (accessed Feb. 2023)

Geological Society of America, 2022, Geoheritage Position Statement: https://www.geosociety.org/gsa/positions/position20.aspx (accessed Feb. 2023)

Gilbert, G.K., 1886, The inculcation of scientific method by example, with an illustration drawn from the Quaternary geology of Utah: American Journal of Science, v. 31, no. 184, p. 284-300.

Gilbert, G.K., 1890, Lake Bonneville: U.S. Geological Survey Monograph 1, 438 p.

Gill, K.K., Jagniecki, E.A., Benison, K.C., and Gibson, M.E., 2023, A Mars-analog sulfate mineral, mirabilite, preserves biosignatures: Geology, doi:10.1130/G51256.1.

Great Salt Lake Strike Team report, 2023, A synthesized resource document for the 2023 Utah General Legislative Session (February 8, 2023) https://www.scribd.com/document/624426841/GS-FinalAssess-v27-4# (accessed Feb. 2023)

GSLEP, 2022, Great Salt Lake Ecosystem Program:

Birds of Great Salt Lake: Utah Division of Wildlife Resources, https://wildlife.utah.gov/gslep/wildlife/birds.html (accessed Feb. 2023)

Gwynn, J.W., editor, 2002a, Great Salt Lake: An overview of change: Utah Geological Survey, Special Publication of the Utah Department of Natural Resources, 584 p.

Gwynn, J.W., 2002b, The extraction of mineral resources from Great Salt Lake, Utah: History, developmental milestones, and factors influencing salt extraction, *in* Gwynn, J.W., editor, Great Salt Lake: An overview of change: Utah Geological Survey, Special Publication of the Utah Department of Natural Resources, 584 p.

Jagniecki, E., Rupke, A., Kirby, S. and Inkenbradt, 2021, Salt crust, brine, and marginal groundwater of Great Salt Lake's North Arm (2019 to 2021): Utah Geological Survey Report of Investigation 283, Utah Department of Natural Resources, 44 p.

Kanik, M., Munro-Ehrlich, M., Fernandes-Martins, M.C., Payne, D., Gianoulias, K., Keller, L., Kubacki, A., Lindsay, M.R., Baxter, B.K., Vanden Berg, M.D. and Colman, D.R., 2020, Unexpected abundance and diversity of phototrophs in mats from morphologically variable microbialites in Great Salt Lake, Utah: Applied and Environmental Microbiology, v. 86, no. 10, p. e00165-20.

Larsen, L., 2022, The Great Salt Lake's ecological collapse has begun: Salt Lake Tribune https://www.sltrib.com/news/environment/2022/11/08/great-salt-lakes-ecological/ (accessed Feb. 2023).

Lincoln, T.A., Webb, S.M., Present, T.M., Magyar, J.S., and Trower, E.J., 2022, Microbial activity and neomorphism influence the composition and microfabric of ooids from Great Salt Lake, UT: The Sedimentary Record, v. 20, no. 1, https://doi.org/10.2110/001c.56183

Lindsay, M.R., Anderson, C., Fox, N., Scofield, G., Allen, J., Anderson, E., Bueter, L., Poudel, S., Sutherland, K., Munson-McGee, J.H., Van Nostrand, J.D., Zhou, J., Spear, J.R., Baxter, B.K., Lageson, D.R., Boyd, E.S., 2017, Microbialite response to an anthropogenic salinity gradient in Great Salt Lake, Utah: Geobiology, v. 15, no. 1, p. 131–145.

Madsen, D.B., 1989, A grasshopper in every pot: Natural History, v. 7, p. 22-25.

Madsen, B.D., editor, 1989, Exploring the Great Salt Lake: The Stansbury Expedition of 1849-50: University of Utah Press, Salt Lake City, Utah, 889 p.

National Park Service, 2015, Historic tribes of the Great Basin, https://www.nps.gov/grba/learn/historyculture/historic-tribes-of-the-great-basin.htm (accessed Feb. 2023)

Noffke, N., 2015, Ancient sedimentary structures in the < 3.7 Ga Gillespie Lake Member, Mars, that resemble macroscopic morphology, spatial associations, and temporal succession in terrestrial microbialites. Astrobiology, v. *15*, no. 2, p.169-192.

Oviatt, C.G., and Shroder, J.F., Jr., editors, 2016a, Lake Bonneville: A Scientific Update, Elsevier, 696 p.

Oviatt, C.G., and Shroder, J.F., Jr., 2016b, Introduction *in* Oviatt, C.G., and Shroder, J.F., Jr., editors, Lake Bonneville: A Scientific Update, Elsevier N.Y., p. xxv-xxxvi.

Oviatt, C. G., Thompson, R. S., Kaufman, D. S., Bright, J., and Forester, R. M., 1999, Reinterpretation of the Burmester core, Bonneville basin, Utah: Quaternary Research, v. 52, p. 180-184.

Pedone, V.A., Oviatt, C.G., and McGee, D., 2023, Late Quaternary carbonate microbialite complex on the west shore of Great Salt Lake Utah, USA: Journal of Quaternary Science, v. 38, no. 3, p. 319-332.

Reynard, E., and Brilha, J., 2018, Geoheritage: Assessment, Protection, and Management, Elsevier, 482 p.

Sandberg, P.A., 1975, New interpretations of Great Salt Lake ooids of ancient non-skeletal carbonate mineralogy: Sedimentology, v. 22, p. 497-537. https://doi.org/10.1111/j.1365-3091.1975.tb00244.x

Stegner, W., 1954, Beyond the Hundredth Meridian: John Wesley Powell and the Second Opening of the West: Houghton Mifflin, Boston, MA, 438 p.

Vanden Berg, M.D., 2019, Domes, rings, ridges, and polygons: Characteristics of microbialites from Utah's Great Salt Lake: Sedimentary Record, v. 17, no. 1, p. 4–10.

Weir, K., 2020, Nurtured by nature: American Psychological Association, v. 51, p. 50. https://www.apa.org/monitor/2020/04/nurtured-nature

Wilcock, L., Frantz, C.M., and Vanden Berg, M.D., 2024, Use of remote imagery to map microbialite distribution at Great Salt Lake, Utah: Implications for microbialite exposure, in Vanden Berg, M.D., Ford, R., Frantz, C. Hurlow, H., Gunderson, K., and Atwood, G. (eds.), Great Salt Lake and the Bonneville Basin: Geologic History and Anthropocene Issues: Utah Geological Association Publication 51.

Late Neogene and Quaternary Lacustrine History of the Great Salt Lake-Bonneville Basin

Charles G. Oviatt
[3]Department of Geology, Kansas State University, Manhattan, Kansas, joviatt@ksu.edu

10.31711/ugap.v51i.133

ABSTRACT

The Great Salt Lake-Bonneville basin has contained lakes for many millions of years and has been hydrographically closed for most of its history. Lakes in the lacustrine system have ranged from saline to fresh, and from shallow to deep. Tectonics, specifically crustal extension, which began roughly 20 million years ago as part of the formation of the Basin and Range Province, is the cause of lake-basin formation. Much of the rock record of lakes from Miocene time is faulted and has been eroded and/or buried. Pliocene and Quaternary lakes are better known. For much of the past ~5 Ma the basin has probably appeared similar to today, with a shallow saline terminal lake in a dry desert surrounded by mountains. Freshwater marshes and fluvial systems existed on the basin floor during part of the past ~5 Ma, probably were caused by the lack of inflow from the upper Bear River during the Neogene Period and most of the Pleistocene Epoch (that river was diverted into the basin during the Late Pleistocene), combined with a warm and dry climate. The largest deep-lake cycles were caused by changes to a cold and wet climate, which affected the water budget of the lake system and were correlated with periods of global glaciation.

Based on limited data, the total length of time deep lakes existed in the basin is thought to be less than 10% of the past ~773 ka. Lake Bonneville, the most-recent of the deep-lake cycles, was probably the deepest and largest manifestation of the lake system in the history of the basin. Named deep-lake cycles during the past ~773 ka, are Lava Creek (~620 ka), Pokes Point (~430 ka), Little Valley (~150 ka), Cutler Dam (~60 ka), and Bonneville (~30 -13 ka).

Of the Quaternary deep-lake cycles, only Lake Bonneville is represented by lacustrine landforms, outcrops, and cores of offshore deposits; no landforms from older deep-lake cycles exist (some may be buried under Lake Bonneville deposits but are not visible at the surface), and pre-Bonneville lakes are represented by sediments in limited outcrops and drill holes (including a set of cores taken by A.J. Eardley in the mid 20th century). During the past ~773 ka, deep-lake cycles were correlated with changes in the total volume of global glacial ice; the available evidence indicates that prior to ~773 ka deep-lake cycles were rare.

INTRODUCTION

This paper discusses lakes of Pliocene through Quaternary age (Figure 1) that have occupied the Great Salt Lake-Bonneville basin (GSL-BB). The GSL-BB is located in the eastern Basin and Range Province and is part of the Great Basin (Figure 2). All lakes in the GSL-BB during its long history, which includes the past 15 or 20 million years (Ma, mega annum; Figures 1 and 2), should be thought of as parts of a single lacustrine system — this concept is extrapolated from that of Atwood and others (2016), who applied it to Lake Bonneville (LB) and post-LB Great Salt Lake (GSL). Lake size varied over time in response to tectonic and climatic changes; sometimes the lake was shallow and saline to hypersaline, and uncommonly it grew in depth, volume, and surface area to become brackish to fresh.

An important observation emphasized in this paper is that during the Pliocene and Quaternary Epochs the GSL-BB lacustrine system spent more time as a shallow lake than as a deep lake; deep-lake versions of the system have been relatively short lived and uncommon. A more quantitative approach to this observation is discussed below.

It is not possible to give precise definitions of "deep lake," and "shallow lake," but for this paper, "deep" lakes are regarded as being much bigger than modern GSL. In this general sense, "deep" lakes might range from a lake roughly the size of the Cutler Dam (CD) lake (see below for discussions of named lakes in the GSL-BB), roughly 60 m higher than the average elevation of modern GSL (1280 m), to the size of LB, almost 350 m higher than modern GSL in the middle of the basin. "Shallow" lakes would look similar to modern GSL, with average maximum depth near 10 m, but might be shallower than that or several tens of meters higher. With lake level constantly changing in the closed basin (on time scales longer than a few weeks), lake size is difficult to precisely define if shorelines are not available.

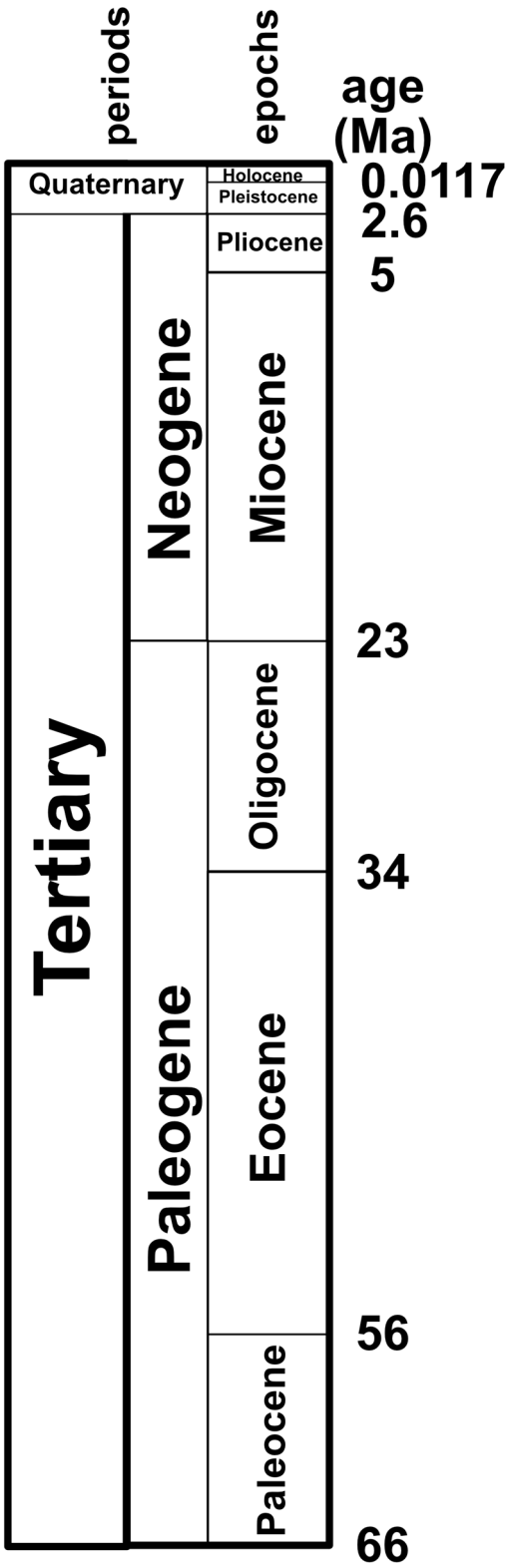

Figure 1. *Approximate ages (in Ma) for subdivisions of the Cenozoic Era (after Walker and others, 2018). In recent interpretations, the Tertiary Period (as it was called for many years) is now regarded as consisting of two geologic periods, the Paleogene and Neogene. The events discussed in this paper occurred during the Neogene and Quaternary Periods (the Miocene, Pliocene, Pleistocene, and Holocene Epochs).*

For this paper, the GSL-BB includes the subbasins that collectively comprise the Bonneville basin of Late Pleistocene to modern age. The subbasins are: (1) the Great Salt Lake (GSL) basin, (2) the Great Salt Lake Desert (GSLD) basin (separated from GSL by low divides), and (3) the Sevier basin (Figure 2). Major streams entering the system are the Sevier and Beaver Rivers in the Sevier basin, and the Provo/ Jordan, Weber, and Bear Rivers in the GSL basin (Figure 2). All these rivers head in the high mountains and plateaus along the eastern margin of the basin. No major rivers flow into the GSLD basin, although a few rivers that are ephemeral today, were probably perennial during deep-lake episodes (streams such as Thousand Springs Creek, Grouse Creek, and Deep Creek [the Deep Creek that heads in eastern Nevada] built impressive deltas into LB). An upward component of groundwater flow (Stephens, 1974; Fitzmayer and others, 2004), and the observation that the mud of the mudflats is moist everywhere (except maybe for a few centimeters at the surface where the wind has dried it), indicates that the modern GSLD is a gigantic groundwater-discharge, or evapotranspiration area (in springs flow is concentrated).

Within the subbasins are smaller closed basins, such as Puddle Valley and Tule Valley in the GSLD basin, and Cedar Valley and Rush Valley in the GSL basin. All these hydrographically closed basins and subbasins exist because of Neogene and Quaternary faulting. The Wasatch fault bounds the eastern margin of the GSL-BB and the Great Basin (and Basin and Range Province), and has the greatest total offset of any fault system in the GSL-BB. The Wasatch fault accounts for the major mountain front of the Wasatch Range. The maximum thicknesses of Neogene and Quaternary sediment in the GSL-BB vary from place to place, and the sediments may be ~4 km thick, or more, in some places (Hintze and Kowallis, 2021). Details of the faulting history are beyond the scope of this paper, but faulting is an important long-term control on the lacustrine history.

This paper summarizes what is currently known about the lacustrine history of the GSL-BB for the past ~5 Ma. As is typical of geologic information, more is known about relatively recent events than about older events. The shapes and sizes of the older lacustrine basins within the GSL-BB are poorly known because of continued tectonic deformation.

MIOCENE TECTONICS AND DEPOSITION

Extension associated with the Neogene and Quaternary tectonics of the Basin and Range Province, including the GSL-BB in the eastern part of the Prov-

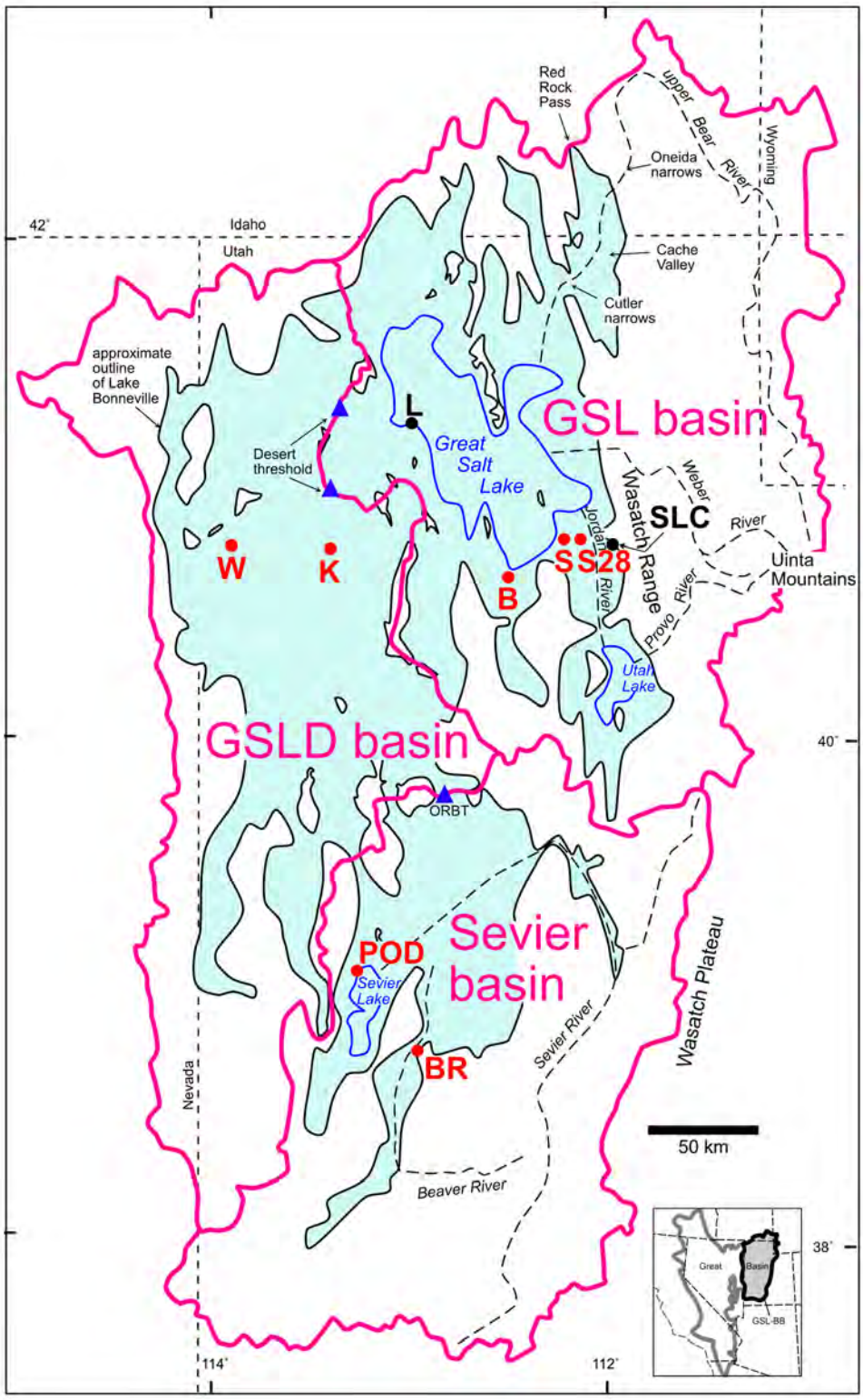

Figure 2. *Map showing approximate modern drainage divides for the subbasins within the GSL-BB. Pleistocene drainage divides were probably similar, but drainage divides for Neogene basins are not known. The GSLD basin has less than a meter of closure and it is separated from the GSL basin by two low thresholds, which are nearly imperceptible on the mudflats at identical elevations (1285 m); when first discussed by Eardley and others (1957) only one threshold, the southern one, was recognized and was called the "Desert threshold" (in some cases it is now called the "Eardley threshold"). The approximate outline of LB (the Bonneville shoreline) is shown for reference, as are major rivers that entered the basins from the east side. Modern lakes are labeled. Approximate locations of the Eardley cores and the Sevier-basin cores are shown with red dots (S28 = S28; S = Saltair; B = Burmester; K = Knolls; W = Wendover; POD = Pit of Death; BR = Black Rock). The low point on the divide between the Sevier basin and the GSLD, is the Old River Bed threshold (ORBT); flow from the Sevier basin entered the GSLD basin during the Late Pleistocene. Major rivers are shown schematically with dashed lines. L = Lakeside; SLC = Salt Lake City.*

ince, began roughly 20 Ma (Hintze and Kowallis, 2021). By at least 15 Ma, lake basins had begun to form in the eastern Basin and Range Province (Patton and Lent, 1980; Taylor and Bright, 1987; Oaks and others, 1999; Bortz, 2002; Janecke and others, 2003; Long and others, 2006; McClellan and Smith, 2020). Despite ongoing tectonism and many details of the topography that have changed between late Neogene time and the present, the general configurations of mountains and basins is probably similar now to what it was 5 Ma ago (Hintze and Kowallis, 2021). Some significant regional-scale changes have occurred in the SLC-BB during the time period in question, such as river diversions that have changed the water budgets of lakes (discussed below).

The Basin and Range Province is still tectonically extending today (WGUEP, 2016; Utah Geological Survey, 2023). Thick accumulations of lacustrine and associated deposits of Miocene age are exposed in such areas as Cache Valley, Utah and Idaho (Oaks and others, 1999; Janecke and others, 2003; McClellan and Smith, 2020), and Goose Creek, ID and NV (Perkins and others, 1995), and in many other places within or near the modern GSL-BB. Janecke and others (2003) present good evidence that Neogene lake basins developed in the area now called northeastern Utah and southeastern Idaho, many of which were associated with the evolving Bannock detachment fault system. It is likely that multiple individual basins were integrated into one large GSL-BB by Pleistocene times in response to continuing tectonism during the several-million-year period, but the details of the lacustrine history are still being discovered. Although there is no question that Miocene lakes existed in the GSL-BB, the outlines of individual basins and the shorelines of those old lakes are not preserved or are covered.

The GSL-BB is large (Figure 2), but it's not an ocean basin — because of the huge spatial variability in geology, biology, topography, etc., within the basin, a core taken from one point, or one outcrop, are unlikely to contain sediments that look similar to those in cores or outcrops several kilometers away. One core or outcrop, although it may contain valuable information, is not likely to record the geologic history of the entire basin. To construct a complete geologic history of the basin, information from multiple sources throughout the lake basin needs to be integrated, a process that takes a long time and efforts by multiple generations of scientists.

WATER BUDGET

The water budget of lakes in the GSL-BB is a fundamental consideration. Although precise measurements for many of the variables in water-budget equations for modern lakes are available, the values of important variables for older lakes can only be generally estimated. Water budget (or balance) can be expressed in many ways, but a simple equation shows water inflows equal to water outflows, plus-or-minus changes in storage of water in the lake (Hutchinson, 1957).

In the case of a hydrographically closed lake, water does not exit the system except by evaporation (there is no river or groundwater outflow). GSL is a closed-basin (or terminal, or endorheic) lake, so it has no surface outflow, and groundwater outflow is assumed to be zero (Arnow and Stephens, 1990). The relationship between volume and surface area (and elevation) in the modern GSL-BB is nearly linear (Wambeam, 2001). For most of its history the GSL-BB has been hydrographically closed and short-term changes in lake level have been correlated with changes in climate.

TECTONICS AND PALEOCLIMATE IN THE BONNEVILLE BASIN

The rate of tectonic deformation and sediment infilling compared to the water balance should be considered in tectonic basins (Bohacs and others, 2000). If climate in a basin favors a positive water balance, where inflows exceed outflows, a basin might appear to be open, but if tectonic subsidence of the basin floor is relatively rapid and the rate of sediment infill is low the basin might remain hydrographically closed even if inflows exceed outflows. The GSL-BB would be classified as "underfilled" by Bohacs and others (2000, their Figure 7; Bernau, 2022). In an underfilled basin plenty of space is available for water and sediment to accumulate, and that large volume of unfilled space keeps the basin from overflowing. In hydrographically closed basins, the water that remains in the basin after most of it has evaporated becomes increasingly salty over time (Hardie and Eugster, 1970).

Over its many-million-year history, the GSL-BB has remained underfilled with respect to sediment, and hydrographically closed most of the time. The rate of tectonic deformation in the GSL-BB is great enough that only one period is known where the basin was hydrographically open while remaining sedimentologically closed. This occurred when Late Pleistocene LB was overflowing at Red Rock Pass into the Snake River drainage basin as the Provo shoreline formed (Gilbert, 1890). During that period (possibly about 1000 to 3000 years in duration) climate was cooler and wetter than today and the lake was deep.

Neogene climate of the GSL-BB was probably similar to that of today, although the mean annual precipitation may have been generally lower and temperature somewhat higher (Moutoux, 1995; Moutoux and Davis, 1995, their Figures 3 and 4; Davis and Moutoux, 1998; Davis, 2002). These paleoclimate interpretations were based on pollen from samples of cuttings from drill holes in GSL (Table 1); the dating was not precise, but the pollen allowed for interpretations of generalized climatic conditions during the Pliocene and Early Pleistocene time.

Quaternary climate in the GSL-BB has been widely variable (Rhode, 2016). When deep-lake cycles occurred, climate was relatively cool and wet and during times when the lake system was shallow, climate was relatively warm and dry (Davis and Moutoux, 1988; Rhode, 2016).

FRESH- TO BRACKISH-WATER MARSHES ON THE BASIN FLOOR

Kowalewska and Cohen (1998), in an analysis of ostracodes (small crustaceans, typically about 1 mm in size) from cuttings taken from the same GSL drill holes that yielded the pollen samples mentioned above, found evidence of freshwater wetlands (marshes) and fluvial environments at various locations on the floor of the basin at different poorly dated times during the past 5 Ma. During the Holocene, the water of GSL has been hypersaline and has not supported ostracodes (Thompson and others, 2016), but at the locations of the drill holes studied by Kowalewska and Cohen (1998), freshwater conditions existed at times, and at other times the same places were occupied by shallow lakes, some of which were saline. Just the presence of freshwater ostracodes on the floor of the GSL-BB, which are not part of deep-lake faunas (Delorme, 1969; Forester, 1987), indicates hydrologic conditions much different than those of today.

Kowalewska and Cohen (1998) compared their ostracode results with pollen results described by Moutoux and Davis (1995), and they were not able to find meaningful correlations between the ostracode interpretations and pollen interpretations of the paleoclimate in the GSL-BB. One possibility to help explain why marshes and/or freshwater fluvial systems might appear low in the basin if it was hydrographically closed, is that, because of local tectonic activity, the basin floor was probably not smooth and uniform, but instead consisted of multiple shallow depressions separated by low ridges and hills. Fresh river water could flow into some depressions (and feed freshwater marshes and/or streams), but not into others, which might contain shallow saline lakes. The number and distribution of drill holes from which cut-

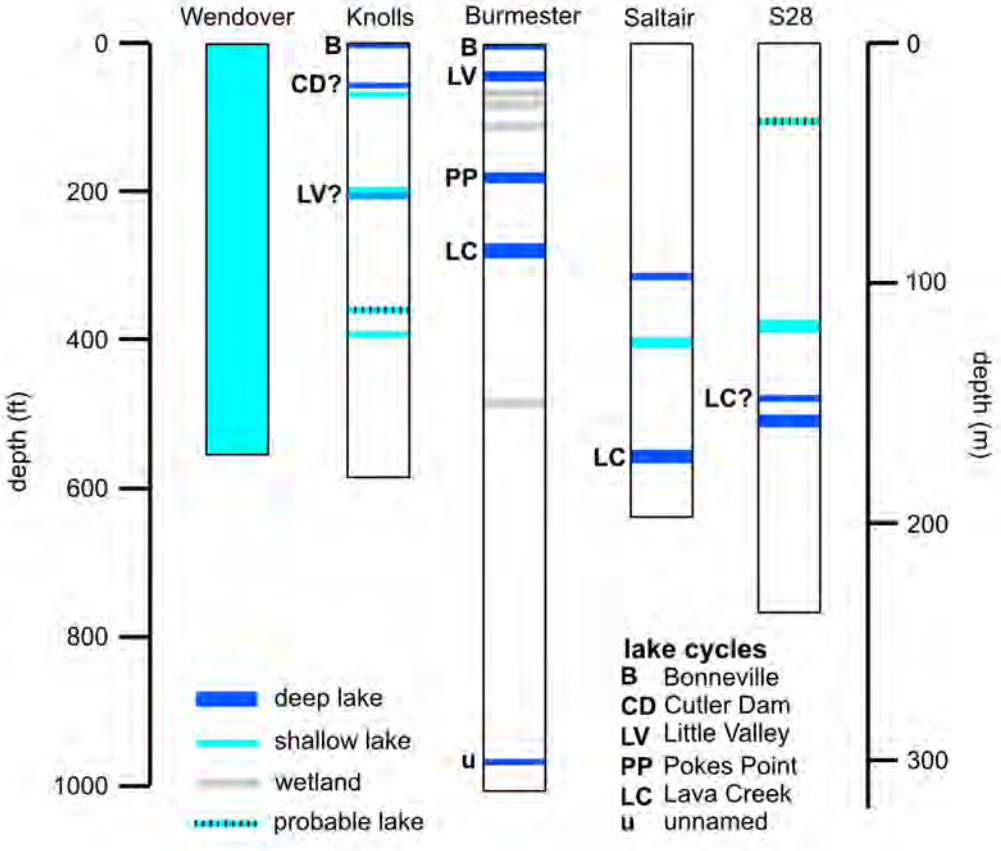

Figure 3. *The Eardley cores. This figure was assembled using data from published (Eardley and Gvosdetsky, 1960; Eardley and others, 1973; Williams, 1994; Oviatt and others, 1999) and unpublished sources (Shuey, 1971; Thompson and Oviatt, 1995, notes from core examinations; J. Bright, D.S. Kaufman, and R.M. Forester-- late '90s data on ostracode faunas and amino acid results for samples collected by Thompson and Oviatt).*

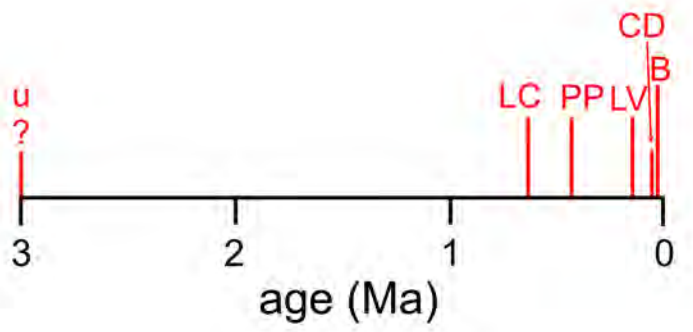

Figure 4. *Known lakes in the GSL-BB larger than modern GSL during the past 3 Ma. Chronologic data are from the Burmester core for the Bonneville, Little Valley, Pokes Point, Lava Creek, and unnamed lake cycles (Oviatt and others, 1999; unpublished information); the age of the CD lake cycle is from Kaufman and others (2001). The X axis of the graph marks the approximate elevation of modern GSL (~1280 m), and the vertical scale, which represents the relative maximum elevations of lakes, is not shown on the figure because insufficient information is available for most lake cycles. Approximations of the upper elevation limits of the CD and LV lake cycles are based on outcrops of lacustrine sediment. The upper elevation limits of the PP and LC lake cycles are interpreted as being similar to that of the LV lake cycle. The elevation of the unnamed lake cycle at about 3 Ma is unknown, but based on the ostracode fauna in sediments of that age from the Burmester core, the lake probably did not rise higher than the CD lake cycle. B = Bonneville, CD = Cutler Dam, PP = Pokes Point, LC = Lava Creek, u = unnamed lake cycle.*

tings were obtained is not sufficient to determine if this explanation is viable; also the available geochronological control is not good enough to make reliable correlations between cores. In a different data set (core GSL00-4; Balch and others, 2005, their Figure 6), the youngest ostracode fauna from a freshwater marsh on the basin floor is on the order of ~45 ka (kilo [1000] annum; presumably prior to the diversion of the upper Bear River and Cache Valley tributaries into GSL (see discussion below).

An important contributing cause of the appearance of marshes and/or freshwater fluvial systems on the basin floor involves the diversion into the GSL-BB of the upper Bear River plus the rivers that drain Cache Valley. These rivers contribute water and dissolved solids to modern GSL. The precise ages of incisions of canyons along the path of the Bear River have not been totally resolved, but it's likely that the incisions occurred during the Late Pleistocene.

According to Pederson and others (2016, their Table 2.1) Oneida Narrows (Figure 2; on the topographic divide of Cache Valley) was fully incised, allowing the upper Bear River to enter Cache Valley, based on optically stimulated luminescence ages, after 55.0 ± 5.6 ka and before 48.9 ± 6.9 ka (a round number near the middle of that overlapping range is 50 ka). Prior to the incision of Oneida Narrows, the upper Bear River had a complicated history involving flow into the Portneuf River (a tributary of the Snake River) and ponding upstream from Oneida Narrows to form Lake Thatcher (Gilbert, 1890; Bright, 1963; Pederson and others, 2016).

Another canyon through which the upper Bear River now flows into the GSL-BB is the Cutler narrows ("gate of Bear River," Gilbert, 1890, his Plate XXX), where the upper Bear River plus its Cache Valley tributaries exit Cache Valley. The exact timing of the incision of Cutler narrows, and the mechanism of the incision, has not been determined, but all the incision (it's possible the incision occurred in stages?) probably was not completed until sometime after the CD lake cycle (that is, after ~60 ka; Oviatt and others, 1987; Kaufman and others, 2001; Oaks and others, 2024).

The incision of Cutler narrows was traditionally interpreted to be the result of superposition probably combined with antecedence (Williams, 1958; Maw, 1968). The word "anteposition" was coined by Hunt (1982) to describe situations where incision began with superposition and continued because of tectonic uplift across the path of the river. Williams (1958), Maw (1968), and Hunt (1982) did not give specific ages or directly discuss which river was superposed to ultimately create Cutler narrows. Movement on the Wasatch and West Cache Valley fault zones would easily account for tectonic uplift of the Junction Hills bedrock block across a superposed river. If the anteposition interpretation were correct, however, the river that was superimposed across the Cutler divide could not have been the Bear River if the upper Bear did not incise Oneida narrows and enter Cache Valley until about 50 ka. More work is needed on the geologic history of the Cutler narrows.

Oaks and others (2018; 2024) suggested the presence of lakes in Cache Valley separate from lakes in the GSL-BB, but the precise ages and characteristics of those Cache Valley lakes have not been determined. This study adopts the relative age of incision of Cutler narrows as younger than the CD lake cycle and older than the LB lake cycle (possibly close to 30 ka, but this has not been scientifically tested).

The upper Bear River, plus the total discharge of rivers that enter Cache Valley from the nearby mountains, plus discharge from the Malad River, accounts for about a third of the modern annual inflow to GSL (Oviatt and others, 1987; Arnow and Stephens, 1990). Without input from the upper Bear River plus the Cache-Valley rivers, the river inflow to the GSL-BB lake system would have been significantly reduced.

Table 1. *Drill holes in the Great Salt Lake and Sevier basins that contain sediments of pre-LB age.*

Drill Hole ID	Collection Year	Latitude (°N)	Longitude (°W)	Elevation (m)	Depth of Hole (m)	Age at Bottom of Hole (Ma)	Core or Cuttings	Reference
GSL96-6	1996	41.0	112.4	1272	9	0.044	core	Thompson and Oviatt, unpublished, 1995-2022; Thompson and others, 2016
GSL96-4	1996	41.0	112.5	1272	5.5	0.04	core	Thompson and Oviatt, unpublished, 1995-2022
GSL00-4	2000	41.1	112.6	1271	120	0.280	core	Schnurrenberger and others, 2001; Balch and others, 2005
C	~1980	41.0	112.4	1272	5.5	0.035	core	Spencer and others, 1984; Thompson and others, 1990
AMOCO 1	?	41.5	112.8	?	?	?	cuttings	Moutoux, 1995
AMOCO 2	?	41.4	112.8	?	?	?	cuttings	Moutoux, 1995
AMOCO 3	?	41.4	112.8	?	?	?	cuttings	Moutoux, 1995
AMOCO 4	?	41.4	112.7	?	?	?	cuttings	Moutoux, 1995
AMOCO 5	?	41.4	112.7	?	?	?	cuttings	Moutoux, 1995
AMOCO 6	?	41.4	112.7	?	?	?	cuttings	Moutoux, 1995
AMOCO 7	?	41.4	112.6	?	?	?	cuttings	Moutoux, 1995
AMOCO 8	?	41.1	112.7	?	?	?	cuttings	Moutoux, 1995
AMOCO 9	?	40.9	112.3	?	?	?	cuttings	Moutoux, 1995
AMOCO 10	?	40.8	112.3	?	?	?	cuttings	Moutoux, 1995
South Rozel (J)	?	41.4	112.6	1272	?	~5	cuttings	Moutoux, 1995; Kowalewska and Cohen, 1998; Davis, 2002
Gunnison (P)	?	41.3	112.7	1270	?	~5	cuttings	Moutoux, 1995; Kowalewska and Cohen, 1998; Davis, 2002
Indian Cove (I)	?	41.3	112.6	1271	?	~5	cuttings	Moutoux, 1995; Kowalewska and Cohen, 1998; Davis, 2002
Bridge	?	41.2	112.5	?	?	?	cuttings	Moutoux, 1995; Davis, 2002
Carrington Island (H)	?	41.0	112.5	2171	?	~5	cuttings	Moutoux, 1995; Kowalewska and Cohen, 1998; Davis, 2002
Sandbar (N)	?	40.7	112.4	?	?	~2.3	cuttings	Kowalewska and Cohen, 1998
S28	1960	40.9	112.2	1286	224	~0.9	core	Shuey, 1971; Eardley and Gvosdetsky, 1960; Williams, 1994; Thompson and Oviatt, unpublished, 1995
Saltair	1956	40.8	112.1	1282	198	~0.8	core	Shuey, 1971; Eardley and Gvosdetsky, 1960; Williams, 1994; Thompson and Oviatt, unpublished, 1995
Burmester	1970	40.7	112.5	1285	307	~3.4	core	Shuey, 1971; Eardley and others, 1970; Williams, 1994; Oviatt and others, 1999; Thompson and Oviatt, unpublished, 1995
Knolls	1960	40.7	113.3	1289	152	~0.9	core	Shuey, 1971; Williams, 1994; Thompson and Oviatt, unpublished, 1995
Wendover	1960	40.7	113.9	1285	171	~1.7	core	Shuey, 1971; Williams, 1994; Thompson and Oviatt, unpublished, 1995; Bright and others, 2022
Clive	2019	40.7	113.1	1307	187	?	cuttings	Stantec, unpublished, 2019; Oviatt, unpublished, 2019
Black Rock	1993	38.7	112.9	1503	273	~3	core	Thompson and others, 1995
Pit of Death	1993	39.0	113.2	1383	140	~3.1*	core	Thompson and others, 1995

*This core contains an unconformity @~140 m, below which is a ~6 Ma tephra.

If the climate in the GSL-BB basin were dryer than today during the late Neogene and Pleistocene (except during deep-lake cycles), it is likely that climatically induced river inflow to the GSL would have been reduced at that time (following the logic of Bekker and others, 2014, who studied tree-ring reconstructions of late Holocene streamflow in the Weber River and the connections with climate). Climatically reduced inflow, combined with the lack of inflow from the Bear and Cache-Valley rivers, would have caused lakes in the GSL-BB to be smaller compared to Holocene GSL, and that reduced input would likely increase the probability of streams feeding marsh systems in isolated depressions on the basin floor.

The information reported by Balch and others (2005) suggests that the hydrologic budget of GSL about at 45 ka was different than it is today. The difference in budget could have been that the Bear and Cache Valley rivers were not entering GSL 45 ka, and/or that climate was dryer at that time, during marine oxygen isotope stage (MIS) 3. MIS 3 was an interglacial period.

It is interesting and seemingly paradoxical that a hypersaline condition for the lake system in the GSL-BB (such as modern GSL) probably requires the inflow volume to be relatively high compared to that required for freshwater marshes to appear on the basin floor. It's clear that a decrease in water inflow to the lake causes lake level to decline; if inflow were to decrease sufficiently a hypersaline lake would cease to exist. In 2023, the upper Bear River and Cache Valley rivers are contributing water to GSL, and the lake is dropping to alarmingly low levels, partly because of the very warm and dry climate we are now experiencing, but mostly because of water diversions by humans from the inflowing rivers before the water gets to GSL (Abbott and others, 2023). If the upper Bear River and Cache-Valley rivers were not presently entering GSL, what would be the condition of the lake in 2023?

PLIOCENE TO LATE PLEISTOCENE DEPOSITION

Sevier basin cores

The Sevier basin (Figure 2) has been part of the larger GSL-BB for at least the past ~3 Ma. Two sediment cores from the Sevier basin record sedimentation during the period from ~3 Ma to a few thousand years younger than the Brunhes/Matuyama paleomagnetic boundary (Thompson and others, 1995), currently dated at 773 ka (Channell and others, 2010). These two cores, the Black Rock and Pit of Death cores (Table 1; Figure 2), contain sediments of shallow lakes and muddy (playa) depositional systems. No deposits of deep lakes were encountered in those cores, an observation that is consistent with observations from the GSL basin farther north and reinforces the interpretation that lakes in the GSL-BB were low or did not exist during the period from ~3 Ma to 773 ka. The deep-lake cycle at about 3 ka in the GSL-BB probably did not get high enough to flood into the Sevier basin; the elevation of the topographic divide between the GSL basin and the Sevier basin (ORBT, Figure 2) was probably on the order of 1400 m.

Eardley cores

During the 1950s and 1960s, Armand J. Eardley, who was a professor of geology at the University of Utah, oversaw the drilling of four deep holes and the acquisition of sediment cores from those drill holes. The cores were called S28, Saltair, Burmester, Knolls, and Wendover (Figure 2; Table 2). Eardley and his colleague, Vasyl Gvosdetsky (University of Utah), published a description and interpretation of one of the cores (the Saltair core; they also commented on the S28 core; Eardley and Gvosdetsky, 1960). R.T. Shuey, a colleague of Eardley's at the University of Utah, obtained funding from the National Science Foundation (NSF) to study the paleomagnetism of the sediments in the Eardley cores and wrote an unpublished report for NSF (Shuey, 1971). In 1973, Eardley and a group of colleagues, published a description and interpretation of part of the Burmester core (Eardley and others, 1973). Lister (1975) described ostracodes from the Saltair and S28 cores. S.K. Williams, a Ph.D. student of B.P. Nash (also at the University of Utah and a coauthor on the Eardley and others, 1973, paper), studied the volcanic ashes from the cores and published important information about the Eardley cores (Williams, 1994).

In 1995, R.S. Thompson (USGS) and C.G. Oviatt (Kansas State University) examined the five Eardley cores looking for evidence of deep-lake cycles based on the presence of carbonate marl deposited in deep lakes and deep-lake ostracode faunas. In 1999 Oviatt and colleagues published a brief description and reinterpretation of the upper ~110 m of the Burmester core (younger than the Brunhes/Matuyama geomagnetic boundary; Oviatt and others, 1999). As part of that work, J. Bright and D.S. Kaufman (Northern Arizona University), and R.M. Forester (USGS), studied ostracode faunas and ostracode amino acid racemization in most of the Eardley cores, and some of that information was published in Oviatt and others (1999). More recently J. Bright and colleagues studied amino acid racemization in ostracodes from the Wendover

Table 2. *Information about the Eardley cores*

core ID	PLSS[1]	latitude[2]	longitude[2]	elevation (m)	depth (m)	sed. rate (m/Ma)[3]	approx. age at bottom (Ma)	year of drilling	recovery	references
S28	SW1/4, SE1/4, Sec. 28, T1N, R2W	40.79	112.07	1286	223	230	~0.9	1960	0% in some sections, up to 40% in others	Shuey (1971); Williams (1994)
Saltair	SE1/4 Sec. 25, T1N, R3W	40.79	112.20	1282	198	260	~0.8	1956	50%	Eardley and others (1963); Shuey (1971); Williams (1994)
Burmester	SE1/4, Sec. 7, T2S, R5W	40.65	112.45	1286	306	3.4-2.6 Ma: 90 m/Ma; 2.6-0 Ma: 120 m/Ma	3.4	1970	90%	Shuey (1971); Eardley and others (1973); Williams (1994); Oviatt and others (1999)
Knolls	SW1/4, Sec. 15, T1S, R13W	40.72	113.30	1289	152	170	0.9	1960	30%	Shuey (1971); Williams (1994)
Wendover	SE1/4, Sec. 15, T1S, R18W	40.74	113.87	1285	171	130	1.7	1960	50% < ~120 m; 15% > ~120 m	Shuey (1971); Williams (1994)

[1]PLSS = Public Land Survey System
[2]datum for latitude/longitude coordinates is WGS84.
[3]data from Williams (1994); approximate sedimentation rates

core (Bright and others, 2022), the only core not studied for that purpose in the 1990s. Davis (2002) published pollen diagrams that had been constructed from data from the Wendover and Knolls cores in the 1960s, but which had not been previously published.

The Eardley cores are now completely dried out. They have been stored in cardboard boxes and sampled multiple times by different people for different purposes. Observations about the geologic history of the core sites, which would have been possible when the cores were fresh, are now difficult. The Eardley cores are now archived at the Utah Geological Survey Core Research Center.

The usefulness of the Eardley cores is limited because some of the core sections have crumbled. Although drilling technology has been vastly improved since the 1960s, the cost of drilling and the acquisition of even one new core that might build on what has been learned from the Eardley cores, would be huge. However, the scientific information (geologic, biologic, paleoclimatic, etc.) that could be obtained from a new core would be invaluable.

The following sections give summaries of published and unpublished information and interpretations concerning the Eardley cores (Figures 3 and 4; Tables 1 and 2). Eardley did not publish anything related to two of the cores (Knolls and Wendover). No independent studies of the sediments or changing depositional environments represented in the Knolls and Wendover cores have been published.

When Bob Thompson and I examined all the Eardley cores in 1995, we found that the core sections had not been split and the surviving sections of the cores were covered with dried mud from the drilling operations. In order to examine the sediments, we had to look at the ends or break apart dried core sections or scrape off the mud from the surfaces. We found this to be true for all the cores, including the Saltair and Burmester, so it was unclear to us how Eardley and his colleagues had observed any of the sediments in the cores.

S28 and Saltair cores

These Saltair and S28 cores were taken near each other (Figure 2; Tables 1 and 2). Although some important information about pre-LB lake cycles is preserved in these cores (Eardley and Gvosdetsky, 1960; recognizing that interpretations of global Quaternary history have changed considerably since the 1950s), the amount and quality of information about the lacustrine history of the GSL-BB the cores can provide is not great. Both the S28 and Saltair cores were drilled at locations dominated by the Jordan River and its precursors and were not suitable as complete records of sedimentation in GSL-BB lakes.

Deposits of the LB cycle are not present in either the S28 or Saltair cores, and it would now be difficult to determine whether LB sediments were not preserved at the coring sites or if LB sediments simply were not recovered during the drilling operations. Deposits of some older deep-lake cycles are present in the cores and deposits of some deep-lake cycles are missing. Although Lister (1975) defined some new ostracode species based on samples from the S28 and Saltair cores, and his descriptions of ostracodes are excellent and useful, he did not indicate the depths of the samples or say anything about the depositional environments of the samples he examined.

Burmester core

The Burmester core is the longest Eardley core at 306 m and covers the greatest amount of time (the age at the base of the core is ~3.4 Ma; Williams, 1994). In our examination of the core in 1995 we found many buried calcic soils, some with enough soil carbonate to whiten the core for many meters.

Eardley and others (1973; their Figure 1) showed 17 deep-lake cycles during Brunhes time based on their work on the Burmester core, whereas Oviatt and others (1999) found evidence in the Burmester core for only four deep-lake cycles during the same time period (an age of 750 ka for the Brunhes/Matuyama geomagnetic boundary was estimated by Eardley and others, 1973; in 2023 the age of that geomagnetic boundary is considered to be ~773 ka [Channell and others, 2010]). In the upper ~3 m of the Burmester core Eardley and others (1973; their Figure 1) interpreted the sediments as representative of shallow to dry lakes, overprinted by a soil, but Oviatt and others (1999; their Figure 1) found deposits of LB in that interval, including the Hansel Valley basaltic ash (Miller and others, 2008), which was erupted during the early transgressive phase of LB.

Recovery was good in the Burmester core (90%; Table 2) and that core has provided ages for middle and Late Pleistocene deep-lake cycles in the basin (Figure 4). The approximate drilling site of the Burmester core is low in the basin, but it is on land, not in the GSL, and no deposits of shallow lakes are preserved in the Burmester core.

Knolls core

The LB marl is present in the Knolls core. However, in a shallow pit about 4 km west of the approximate location of the Knolls core, only about 80 cm — approximately the lower half — of the LB marl (Gilbert's, 1890, white marl) are present, and the upper half has been deflated (Oviatt and others, 2020). It

is unknown how much of the LB marl is present in the Knolls core and the section may not be complete. Sediments of pre-LB deep-lake cycles are present lower in the Knolls core, although it is not known if those deep-lake stratigraphic units are truncated or complete. Most of the core is dominated by sediments of shallow lakes (similar to the Wendover core, described below).

Wendover core

In the Wendover core the LB marl is completely absent, as are deposits of pre-LB deep lakes (unpublished observations by Thompson and Oviatt, 1995, and by Oviatt and D.L. Clark, 2019-2022; Bright and others, 2022; Clark and others, 2023; Bernau and others, 2024). Drilling recovery was not good (Table 2), but no non-lacustrine deposits have been observed; deposits of shallow lakes dominate the core. The Wendover core helps demonstrate the importance of deflation in the GSLD (Bernau, 2022; Bernau and others, 2023, this volume), but does not help with determining when deep-lake cycles occurred.

The sediments in the Wendover and Knolls cores reveal important information about the pre-LB history of the GSL-BB. In both cores, the most common sediment types are carbonate mud (grain sizes of clay, silt, some fine sand) and oolitic sands, where most of the oolitic grains are rod shaped. Also present are irregularly shaped carbonate lumps and gypsum grains (both primary and secondary precipitates). Some carbonate mud units (not the ones dominated by rod-shaped ooids) contain the ostracode *Limnocythere staplini*, but no other ostracode species are present.

L. staplini lives in brackish water with relatively low alkalinity. In this basin this means the lake was less than a few tens of meters deep — if it rose higher the water would have become diluted and other ostracode species would appear. The rod-shaped ooids probably indicate the presence of brine shrimp (Eardley, 1938); spherical ooids probably formed abiotically in the wave-agitation zone of a shallow saline lake (Eardley, 1938). These sediments indicate that in pre-LB times, lakes in the GSLD were shallow and varied in dissolved-solid content from being saline-enough to support brine shrimp at times (too saline for ostracodes), to being brackish and supporting ostracodes at other times (but no brine shrimp). Taking into account the poor recovery of the Wendover and Knolls cores (Table 2), the observations suggest that deposition in shallow lakes dominated in the GSLD for thousands or millions of years. Although dated shorelines of pre-LB lakes in the GSLD have not been found (and may not exist), fluctuating lakes with an average elevation of roughly 1300 ± 10 m would be suitable candidates for producing this kind of sedimentary record. A rise of GSL to about 1300 m today would cause widespread flooding and destruction of human infrastructure in the GSL part of the basin, but from a geologic perspective 1300 m is close to the average level of GSL. While “1300 m” is an arbitrarily chosen elevation, it’s within the possible range of elevations of closed-basin lakes that periodically flooded the GSLD during pre-B time.

This range of elevations is close to the maximum elevation of the latest-Pleistocene Gilbert-episode lake (~1297 m). The Gilbert-episode lake (about 12,000 years ago) formed after LB had evaporated, and was part of GSL. In the GSLD the Gilbert-episode lake was strongly influenced by fresh, cold water that flowed into the GSLD from the Sevier basin along the Old River Bed (Palacios-Fest and others, 2021; they referred to the Gilbert-episode lake as the "Old River Bed delta lake"), but in the GSL part of the system the same shallow lake was brackish (Thompson and others, 2016). Similar pre-LB lakes in the GSL-BB with elevations in the range of 1300 ± 10 m should be considered part of ancestral GSL, but it is unknown whether freshwater from the Sevier basin entered the GSLD in pre-LB times.

DISCUSSION

Figure 4 shows an estimate of the ages of known deep-lake cycles in the GSL-BB based primarily on data from the Eardley cores (Oviatt and others, 1999). Figure 5 shows correlations between deep-lake cycles in the GSL-BB and MISs (ages summarized by Lisiecki and Raymo, 2005). Deep lakes, other than the ones that have been documented so far, may have risen and fallen during additional even-numbered MISs during Brunhes time (even-numbered stages were glaciations, odd-numbered stages were interglacials), but further investigations are needed to decipher details. If samples of vein-fill calcite and aragonite from outcrops at Lakeside were deposited during deep-lake cycles, they may suggest deep-lake cycles during MIS 8 and MIS 10 (D. McGee, MIT, personal communication, 2019)(Figure 5).

It is possible to estimate the proportion of time that deep-lake cycles occupied the GSL-BB during the Brunhes geomagnetic Chron (730-0 ka). If each of the four largest deep-lake cycles lasted the same length of time as the Bonneville cycle, about 17 ka, the total proportion of time that deep-lake cycles occupied the GSL-BB during the past 773 ka was roughly 9%. Only one deep-lake cycle is poorly known from the period between 3 Ma and 773 ka (based on limited information from the Burmester core), and, based on its ostracode fauna, the lake

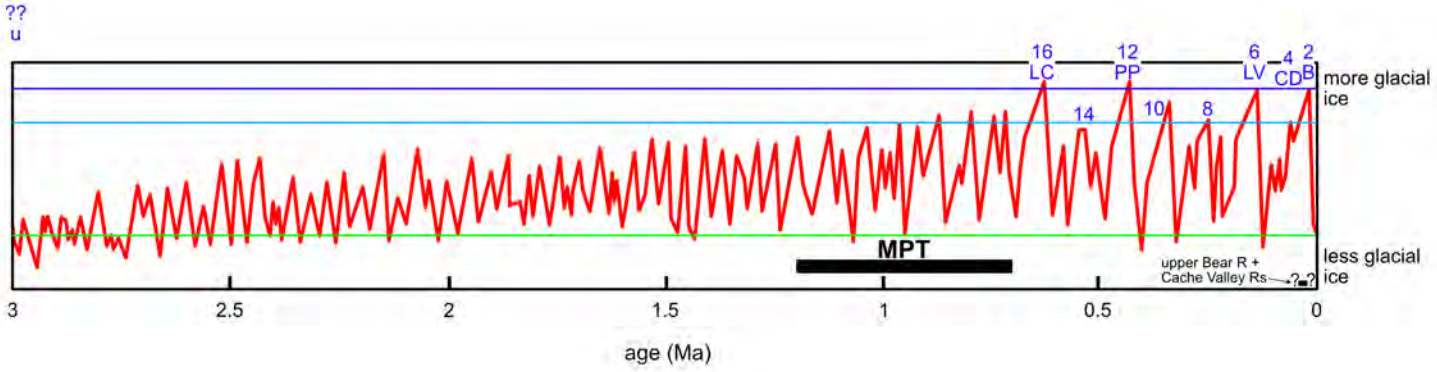

Figure 5. *Marine oxygen-isotope (MIS) record, which can be interpreted as representing the relative volume of global glacial ice (simplified from Lisiecki and Raymo, 2005), and known deep-lake cycles in the GSL-BB during the past 3 Ma. The red line is a stacked record of $\delta^{18}O$ in foraminifera fossils from 57 sites around the world where deep-sea cores have been taken (Lisiecki and Raymo, 2005; values of $\delta^{18}O$ in ocean water were relatively high at times when glacial ice attained large volumes on Earth's surface, and relatively low when ice sheets melted and the water flowed back to ocean basins; values of $\delta^{18}O$ are also correlated with water-temperature changes). Deep-lake cycles in the GSL-BB are shown in blue with their presumed correlative MIS stage numbers—B (Bonneville) ≈ MIS 2; CD (Cutler Dam) ≈ MIS 4; PP (Pokes Point) ≈ MIS 12; LC (Lava Creek) ≈ MIS 16 (Oviatt and others, 1999); the MIS stage number possibly correlative with the unnamed lake cycle ("u") about 3 Ma is unknown. Three other even-numbered stages are marked on the figure that are likely to have been correlative with deep lakes in the GSL-BB, but deposits of those hypothetical lakes have not been found. A possible age (very approximately 30 ka) of the diversion of the upper Bear River and Cache Valley rivers into the GSL-BB, is plotted. For reference, the green line is plotted at the level on the isotope curve approximately coincident with MIS 1 (the Holocene); the pale blue line is plotted at the level on the isotope curve approximately coincident with the CD lake cycle (MIS 4); the darker blue line is plotted at the level on the MIS curve approximately coincident with the LB cycle (MIS 2). The approximate duration of the middle Pleistocene transition (MPT; Clark and others, 2006) is shown.*

probably did not rise higher than the CD lake cycle; deep-lake cycles account for less than 1% of that period. Therefore, for over 90% of the past ~3 Ma lakes in the GSL-BB were shallow.

Of course, if further evidence is found for deep lakes other than the ones that have so-far been described for the past 3 Ma, the percentage of time during which deep lakes occupied the GSL-BB would be greater than 9 %. However, environmental conditions like what we see now (not including human influences) apparently were the rule rather than the exception for at least the past 3 Ma, and probably for a longer period (based on the MIS record of Lisiecki and Raymo [2005, their Figure 4], which extends back beyond 5 Ma). The domination of shallow lakes in the GSL-BB is not surprising considering that the upper Bear River and the Cache Valley rivers did not enter the GSL-BB until just a few tens of thousands of years ago (Figure 5).

As shown in Figure 5, very deep lakes in the GSL -BB were uncommon prior to the Middle Pleistocene transition (MPT; between about 1.2 Ma and 700 ka), which marked a change in the magnitude and frequency of Pleistocene glaciations (Clark and others, 2006; Clark, 2012). After the MPT, global climate varied with high-amplitude 100-ka cyclicity (as seen in MIS curves; Figure 5), and prior to the MPT, global climate varied with lower amplitude 41-ka cyclicity. After the MPT large Northern Hemisphere ice sheets began to attain great elevations and had larger volumes than earlier ice sheets (Clark, 2012). Very thick Northern Hemisphere ice sheets probably affected global atmospheric circulation patterns and may have been important in the growth of large lakes in the Great Basin (Antevs, 1948), although it's likely that the influence of ice sheets on global circulation was more complicated than that portrayed by Antevs (Oster and others, 2015).

The CD lake cycle and the post-LB Gilbert-episode lake are not represented by deposits in the Burmester core (or in any of the Eardley cores, except possibly in the Knolls core — Figure 3), but independently those lakes are known to have covered the Burmester core site and all other Eardley-core sites. Perhaps those lake cycles were quick (fast up, fast down), and little sediment was available at the core sites; or perhaps sediment from those lakes was present immediately after the lake cycles but was not preserved. If sediments of those lake cycles do not exist in the Eardley cores, maybe other major lake cycles occurred in the basin but have not yet been detected. Balch and others (2005) in a study of core GSL00-4 from GSL, including lake sediments that ranged in age from the present to as old as ~280 ka (Table 1), did not report evidence of those short-lived lake cycles. However, the spacing of the samples they

examined averaged about 1 m (this represents an average of about 2400 years in that core). Even if sedimentation was continuous in some depressions on the floor of GSL (as at the site of GSL00-4), sampling at ~2400 years spacing may not have been close enough to intercept lake cycles that may have lasted only centuries or less. Clearly much remains to be learned about pre-LB lakes in the GSL-BB.

Based on what we know now, it is safe to say that the long-term appearance of the GSL-BB has been close to what we see today, with a shallow saline lake on the floor of the basin. LB was an anomaly, as were other deep-lake cycles in the basin. Our historic view of GSL (the past 170+ years) is occurring during a drop in the ocean of geologic time. From a perspective grounded in geologic time, GSL should be viewed as typical rather than as a "remnant" of LB.

ACKNOWLEDGMENTS

I am grateful to many people who have helped me with thoughts and principles, data, and various kinds of inspiration. Andy Roberts (Australian National University, Canberra) consulted with me about the age of the Brunhes/Matuyama geomagnetic boundary. Genevieve Atwood (Earth Science Education, Salt Lake City), read an earlier draft of this paper and made good suggestions for improvement. Don Clark (Utah Geological Survey) has been an able and thoughtful colleague in many phases of the work summarized here. I am grateful to the reviewers for helpful comments, and to Rick Ford and Mike Vanden Berg for encouragement.

REFERENCES

Abbott, B.W., Baxter, B.K., Busche, K., de Freitas, L., Frei, R., Gormez, T., Karren, M.A., Buck, R.L., Price, J., Frutos, S., Sowby, R.B., Brahney, J., Hopkins, B.G., Bekker, M.F., Bekker, J.S., Rader, R., Brown, B., Proteau, M., Carling, G.T., Conner, L., Cox, P.A., McQuhae, E., Oscarson, D., Nelson, D.T., Davis, R.J., Horns, D., Dove, H., Bishop, T., Johnson, A., Nelson, K., Bennion, J., and Belmmont, P., 2023, Emergency measures needed to rescue Great Salt Lake from ongoing collapse: https://pws.byu.edu/great-salt-lake, 34 p.

Antevs, E., 1948, The Great Basin, with emphasis on glacial and post-glacial times: Climatic changes and pre-white man: Bulletin of the University of Utah Biological Series, v. 38, p. 168-191.

Arnow, T., and Stephens, D., 1990, Hydrologic characteristics of the Great Salt Lake, Utah: 1847-1986: U.S. Geological Survey Water-Supply Paper 2332, 32 p., map scale 1:125,000

Atwood, G., Wambeam, T.J., and Anderson, N.J., 2016, The present as a key to the past: Paleoshoreline correlation insights from Great Salt Lake, *in* Oviatt, C.G., and Shroder, J.F., Jr., editors, Lake Bonneville — A scientific update: Developments in Earth Surface Processes 20. Elsevier. p. 1-27.

Balch, D.P., Cohen, A.S., Schnurrenberger, D.W., Haskell, B.J., Valero Garces, B.L., Beck, J.W., Cheng, H., Edwards, R.L., 2005, Ecosystem and paleohydrological response to Quaternary climate change in the Bonneville basin, Utah: Palaeogeography, Palaeoclimatology, Palaeoecology, v. 221, p. 99-122.

Bekker, M.F., DeRose, R.J., Buckley. B.M., Kjelgren, R.K., and Gill, N.G., 2014, A 576-year Weber river streamflow reconstruction from tree rings for water resource risk assessment in the Wasatch front, Utah: Journal of the American Water Resources Association (JAWRA), DOI: 10.1111/jawr.12191, p. 1-11.

Bernau, J.A., 2022, Spatial and temporal scales of water and salt movement at the Bonneville Salt Flats: Salt Lake City, University of Utah, Ph.D. dissertation, 195 p.

Bernau, J.A., Bowen, B.B., Oviatt, C., and Clark, D., 2024, Great Salt Lake Desert landscape change over multiple temporal scales: A field trip covering the Bonneville Salt Flats and Knolls sand dunes: Utah Geological Association 51.

Bohacs, K.M., Carroll, A.R., Neal, J.E., and Mankiewicz, P.J., 2000, Lake-basin type, source potential, and hydrocarbon character: An integrated-sequence-stratigraphic– geochemical framework, *in* Gierlowski-Kordesch, E.H. and Kelts, K.R., editors, Lake basins through space and time: American Association of Petroleum Geologists Studies in Geology 46, p. 3-34.

Bortz, L.C., 2002, Heavy-oil deposit, Great Salt Lake, UT, *in* Gwynn, J.W., editor, Great Salt Lake-- A scientific, historical, and economic overview: Utah Geological and Mineral Survey Bulletin, v. 116, p. 243-250.

Bright, R.C., 1963, Pleistocene lakes Thatcher and Bonneville, southeastern Idaho: Minneapolis, University of Minnesota, Ph.D. dissertation, 292 p.

Bright, J., Kaufman, D.S., Oviatt, C.G., and Clark, D.L., 2022, Amino acid racemization geochronology results from the Wendover core in the Salduro Quadrangle, Utah: Utah Geological Survey Open-File Report 741, variously paginated, https://doi.org/10.34191/OFR-741.

Channell, J.E.T., Hodell, D.A., Singer, B.S., and Xuan, C., 2010, Reconciling astrochronological and $^{40}Ar/^{39}Ar$ ages for the Matuyama-Brunhes boundary and late Matuyama Chron: Geochemistry, Geophysics, Geosystems (G^3), v. 11, p. 1-21. Q0AA12, doi:10.1029/2029/2010GC003203

Clark, D.L., Oviatt, C.G., Miller, D.M., Felger, T.J., Hardwick, C.L., Langenheim., V.E. Bowen, B.B., Bernau, J.A., and Page, D., in preparation 2023. Geologic map of the Bonneville Salt Flats and east part of the Wendover 30' X 60' quadrangles, Tooele County, Utah. Utah Geological Survey, scale 1:62,500.

Clark, P.U., 2012, Ice sheets in transition: Science, v. 337, p. 656-658.

Clark, P.U., Archer, D., Pollard, D., Blum, J.D., Rial, V.B., Mix, A.C., Pisias, N.G., and Roy, M., 2006, The middle Pleistocene transition: Characteristics, mechanisms, and implications for long-term changes in atmospheric pCO_2: Quaternary Science Reviews, v. 25, p. 3150-3184.

Davis, O.K., 2002, Late Neogene environmental history of the northern Bonneville basin-- A review of palynological studies, *in* Hershler, R., Madsen, D.B., and Currey, D.R., editors, Great Basin aquatic systems history: Smithsonian contributions to the earth sciences number 33, Smithsonian Institution Press, p. 295-307.

Davis, O.K., and Moutoux, T.E., 1998, Tertiary and Quaternary vegetation history of the Great Salt Lake, Utah, USA: Journal of Paleolimnology, v. 19, p. 417-427.

Delorme, L.D., 1969, Ostracodes as Quaternary paleoecological indicators: Canadian Journal of Earth Sciences, v. 6, p. 1471-1476.

Eardley, A. J., 1938, Sediments of Great Salt Lake, Utah: American Association of Petroleum Geologists Bulletin, v. 22, p. 1305-1411.

Eardley, A.J., 1962, Glauber's salt bed west of Promontory Point, Great Salt Lake. Utah Geological and Mineralogical Survey, Special Studies 1, 12 p.

Eardley, A.J., and Gvosdetsky, V., 1960, Analysis of Pleistocene core from Great Salt Lake, Utah: Geological Society of America Bulletin, v. 71, p. 1323 -1344.

Eardley, A.J., Gvosdetsky, V., Marsell, R.E., 1957, Hydrology of Lake Bonneville and sediments and soils of its basin: Geological Society of America Bulletin, v. 68, p. 1141-1202.

Eardley, A.J., Shuey, R.T., Gvosdetsky, V., Nash, W.P., Picard, M.D., Grey, D.C, and Kukla, G.J., 1973, Lake cycles in the Bonneville Basin, Utah: Geological Society of America Bulletin, V. 84, p. 211-216.

Fitzmayer, J., Larsen, D., Braxton, D., and Staes, E., 2004, Hydrogeology of Government Creek Basin, Dugway, Utah, with a recommended practical approach to ground-water management in arid, saline regions of the Great Basin-- in Ground Water in Utah-- Resource, Protection, and Remediation: Utah Geological Association Publication 31, p. 161-178.

Forester, R.M., 1987, Late Quaternary paleoclimate records from lacustrine ostracodes, *in* Ruddiman, W. F. and H. E. Wright Jr., editors, North America and adjacent oceans during the last deglaciation: Geology of North America K-3, Geological Society of America, Boulder, p. 261-276.

Gilbert, G. K., 1890, Lake Bonneville: U.S. Geological Survey Monograph 1, 438 p.

Hardie, L.A., and Eugster, H.P., 1970, The evolution of closed-basin lakes: Mineralogical Society of America Special Paper 3, p. 273-290.

Hart, W.S., Quade, J., Madsen, D.B., Kaufman, D.S., and Oviatt, C.G., 2004, The $^{87}Sr/^{86}Sr$ ratios of lacustrine carbonates and lake-level history of the Bonneville paleolake system: Geological Society of America Bulletin, v. 116, p. 1107-1119.

Hintze, L.F., and Kowallis, B.J., 2021, Geologic history of Utah-- A field guide to Utah's rocks: Special Publication #10, Department of Geological Sciences, Brigham Young University, 266 p.

Hunt, C.B., 1982, The anomalous transverse canyons of the Wasatch Range, *in* Nielson, D.L., editor, 1982 Symposium and Field Conference, Overthrust belt of Utah: Utah Geological Association Publication 10, p. 81-90.

Hutchinson, G.E., 1957, A treatise on limnology--Volume 1, geography, physics, and chemistry: New York, John Wiley & Sons, Inc., 1015 p.

Janecke, S.U., Carney, S.M., Perkins, M.E., Evans, J.C., Link, P.K., Oaks, R.Q., Jr., and Nash, B.P., 2003, Late Miocene-Pliocene detachment faulting and Pliocene-recent Basin-and-Range extension inferred from dismembered rift basins of the Salt Lake Formation, SE Idaho: *in* Rocky Mountain Section (SEPM), Cenozoic Systems of the Rocky Mountain Region, p. 369-406.

Kaufman, D.S., Forman, S.L., and Bright, J., 2001, Age of the Cutler Dam Alloformation (Late Pleistocene), Bonneville Basin, Utah: Quaternary Research, v. 56, p. 322-334.

Kowalewska, A., and Cohen, A.S., 1998, Reconstruction of paleoenvironments of the Great Salt Lake Basin during late Cenozoic: Journal of Paleontology, v. 20, p. 381-407.

Lisiecki, L.E., and Raymo, M.E., 2005, A Pliocene-Pleistocene stack of 57 globally distributed benthic $\delta^{18}O$ records: Paleoceanography, v. 20, PA1003, doi:10.1029/2004PA1071, 1-17.

Lister, K.H., 1975, Quaternary freshwater ostracoda from the Great Salt Lake Basin, Utah: The University of Kansas, Paleontological Contributions, Paper 78, 34 p., 5 plates.

Long, S.P., Link, P.K., Janecke, S.U., Perkins, M.E., and Fanning, C.M., 2006, Multiple phases of Tertiary extension and synextensional deposition of the Miocene-Pliocene Salt Lake Formation in an evolving supradetachment basin, Malad Range, southeastern Idaho, U.S.A.: Rocky Mountain Geology, v. 41, no. 1, 27 p.

Maw, G.G., 1968, Lake Bonneville history in Cutler Dam quadrangle, Cache and Box Elder Counties, Utah: Logan, Utah State University, M.S thesis, 58 p.

McClellan, P.H. and Smith, G.R., 2020, Late Miocene fishes of the Cache Valley Member of the Salt Lake Formation, Utah and Idaho: Miscellaneous Publications, Museum of Zoology, University of Michigan, No. 208, 54 p.

Miller, D.M., Oviatt, C.G., and Nash, B.P., 2008, Late Pleistocene Hansel Valley basaltic ash, northern Lake Bonneville, Utah, USA: Quaternary International, v. 178, p. 238-245.

Moutoux, T.E., 1995, Palynological and tephra correlations among deep wells in the modern Great Salt Lake, Utah, USA -- Implications for a Neogene through Pleistocene climatic reconstruction: Tucson, University of Arizona, M.S. thesis, 30 p.

Moutoux, T.E., and Davis, O.K., 1995, Neogene through Pleistocene paleoclimate of the Great Salt Lake region, northeastern Great Basin, USA: Proceedings of the Eleventh Annual Pacific Climate (PACLIM) Workshop, Asilomar, California, April 19-22, p. 127-135.

Oaks, R.Q., Jr., Smith, K.A., Janecke, S.U., Perkins, M.E., and Nash, W.P., 1999, Stratigraphy and tectonics of Tertiary strata of southern Cache Valley, northcentral Utah, *in* Spangler, L.E., editor: Utah Geological Association Publication 27, p. 71-110.

Oaks, R.Q, Jänecke, S.U., Rittenour, T.M., Erickson, T.L., and Nelson, M.S., 2018, OSL-IRSL ages of two, perhaps three, pre-Bonneville deep-water pluvial lakes in Cache Valley, Utah-Idaho: Implications of their unexpected high altitudes for excavation of Cutler Narrows from a level above 1494 m (4901 ft), down to the present level of 1314 m (4310 ft) mainly during the Bonneville lake cycle-- Proceedings Volume: 2018 Lake Bonneville Geologic Conference and Short Course, Utah Geological Survey MP-170, p. 90-153.

Oaks, R.Q. Jr., Janecke, S.U., Rittenour, T.M., Erickson, T.L., and Nelson, M.S., 2024, Implications and hydrographs for two pre-Bonneville pluvial lakes and double geosols from 14 OSL-IRSL ages in Cache Valley, NE arm of the Bonneville Basin, *in* Vanden Berg, M.D., Ford, R., Frantz, C. Hurlow, H., Gunderson, K., and Atwood, G. (eds.), Great Salt Lake and the Bonneville Basin: Geologic History and Anthropocene Issues: Utah Geological Association Publication 51.

Oster, J.L., Ibarra, D.E., Winnick, M.J., and Maher, K., 2015, Steering of westerly storms over western North America at the Last Glacial Maximum: Nature Geoscience, v. 8, p. 201-205, DOI: 10.1038/NGEO2365.

Oviatt, C.G., 2015, Chronology of Lake Bonneville, 30,000 to 10,000 yr B.P.: Quaternary Science Reviews, v. 110, p. 166-171.

Oviatt, C.G., McCoy, W.D., and Reider, R.G., 1987, Evidence for a shallow early or middle Wisconsin lake in the Bonneville Basin Utah: Quaternary Research, v. 27, p. 248-262.

Oviatt, C.G., Clark, D.L., Bernau, J.A., and Bowen, B.B., 2020, Data on the surficial deposits of the Great Salt Lake Desert, Bonneville Salt Flats and east part of the Wendover 30' x 60' quadrangles, Tooele County, Utah: Utah Geological Survey Open-File Report 724, 70 p.

Oviatt, C.G., Thompson, R.S., Kaufman, D.S., Bright, J., and Forester, R.M., 1999, Reinterpretation of the Burmester core, Bonneville Basin, Utah: Quaternary Research, v. 52, p. 180-184.

Palacios-Fest, M.R., Duke, D., Young, D.C., Kirk, J.D., and Oviatt, C.G., 2021, A paleo-lake and wetland paleoecology associated with human use of the distal Old River Bed delta at the Pleistocene-Holocene transition in the Bonneville Basin, Utah, USA: Quaternary Research, p. 1-19. doi:10.1017/qua.2021.49. Published online by Cambridge University Press 10 September 2021.

Patton, T.L., and Lent, R.L., 1980, Current hydrocarbon exploration activity in the Great Salt Lake, *in* Gwynn, J.W., editor, Great Salt Lake-- A scientific, historical, and economic overview: Utah Geological and Mineral Survey Bulletin, v. 116, p. 115-124.

Pederson, J.L., Janecke, S.U., Reheis, M.C., Kaufman, D.S., and Oaks, R.Q., Jr., 2016, The Bear River's history and diversion-- Constraints, unsolved problems, and implications for the Lake Bonneville record, *in* Oviatt, C.G., and Shroder, J.F., Jr., editors, Lake Bonneville-- A scientific update: Developments in Earth Surface Processes 20, Elsevier, p. 28-59.

Pederson, J.L., Rittenour, T.M., Jänecke, S.U., and Oaks, R.Q., Jr., 2018, The Bear River's diversion and the cutting of Oneida Narrows at ~55-50 ka and relations to the Lake Bonneville record-- Pro-

ceedings Volume: 2018 Lake Bonneville Geologic Conference and Short Course, Utah Geological Survey MP-170, p. 74-89.

Perkins, M.E., Nash, W.P., Brown, F.H., and Fleck, R.J., 1995, Fallout tuffs of Trapper Creek, Idaho -- A record of Miocene explosive volcanism in the Snake River Plain volcanic province: Geological Society of America Bulletin, v. 107, no. 12, p. 1484-1506.

Rhode, D., 2016, Quaternary vegetation changes in the Bonneville Basin, *in* Oviatt, C.G., and Shroder, J.F., Jr., editors, Lake Bonneville — A scientific update: Developments in Earth Surface Processes 20. Elsevier. p. 420-441.

Shuey, R. T., 1971, Paleomagnetic chronology and correlation of Great Salt Lake Basin sediments: National Science Foundation, Final technical report for grant GA-16134, 15 p.

Schnurrenberger, D., and Haskell, B., editors, 2001, Initial reports of the global lakes drilling program. Volume 1. GLAD 1—Great Salt Lake, Utah, and Bear Lake, Utah/Idaho. Covering Expedition GLAD1 of the Drilling Barge Kerry Kelts and the GLAD800 Drilling System, 10 August, 2000 to 4 September, 2000: Limnological Research Center, Minneapolis, University of Minnesota, 315 p.

Spencer, R.J., Baedecker, M.J., Eugster, H.P., Forester, R.M., Goldhaber, M.B., Jones, B.F., Kelts, K., McKenzie, J., Madsen, D.B., Rettig, S.L., Rubin, M., and Bowser, C.J., 1984, Great Salt Lake and precursors, Utah-- The last 30,000 years: Contributions to Mineralogy and Petrology, v. 86, p. 321 -334.

Stephens, J.C., 1974, Hydrologic reconnaissance of the northern Great Salt Lake Desert and summary hydrologic reconnaissance of northwestern Utah: Utah Department of Natural Resources Technical Publication 42, 55 p.

Taylor, D.W., and Bright, R.D., 1987, Drainage history of the Bonneville Basin: *in* Cenozoic geology of western Utah -- Sites for precious metals and hydrocarbon accumulation-- Utah Geological Association Publication 16, p. 239-256.

Thompson, R.S., Toolin, L.J., Forester, R.M., and Spencer, R.J., 1990, Accelerator-mass spectrometer (AMS) radiocarbon dating of Pleistocene lake sediments in the Great Basin: Palaeogeography, Palaeoclimatology, Palaeoecology, v. 78, p. 301-313.

Thompson, R.S., Oviatt, C.G., Honke, J.S., McGeehin, J.P., 2016. Late Quaternary changes in lakes, vegetation, and climate in the Bonneville Basin reconstructed from sediment cores from Great Salt Lake. *in* Oviatt, C.G., and Shroder, J.F., Jr., editors, Lake Bonneville-- A scientific update. Developments in Earth Surface Processes 20: Elsevier, p. 221-291.

Thompson, R.S., Oviatt, C.G., Roberts, A.P., Buchner, J., Kelsey, R., Bracht, C., Forester, R.M., and Bradbury, J.P., 1995, Stratigraphy, sedimentology, paleontology, and paleomagnetism of Pliocene-early Pleistocene lacustrine deposits in two cores from western Utah: U.S. Geological Survey Open-File Report 95-1.

Utah Geological Survey, 2023, Utah geologic hazards portal: https://geology.utah.gov/apps/hazards/

Walker, J.D., Geissman, J.W., Bowring, S.A., and Babcock, L.E., compilers, 2018, Geologic Time Scale v. 5.0: Geological Society of America.

Wambeam, T.J., 2001, Modeling Lake Bonneville Basin morphometry using digital elevation models: Salt Lake City, University of Utah, M.S. thesis, 60 p.

Williams, J.S., 1958, Geologic atlas of Utah, Cache County: Utah Geological and Mineral Survey Bulletin 64, 104 p.

Williams, S.K., 1994, Late Cenozoic tephrochronology of deep sediment cores from the Bonneville Basin, northwest Utah: Geological Society of America Bulletin, v. 105, p. 1517-1530.

WGUEP [Working Group on Utah Earthquake Probabilities], 2016, Earthquake probabilities for the Wasatch Front region in Utah, Idaho, and Wyoming: Utah Geological Survey Miscellaneous Publication 16-3.

Evolution of Great Salt Lake's Exposed Lakebed (1984-2023): Variations in Sediment Composition, Water, and Vegetation from Landsat OLI and Sentinel MSI Satellite Reflectance Data

Mark H. Radwin and Brenda B. Bowen
University of Utah, Salt Lake City, Utah, markradwin@gmail.com

10.31711/ugap.v51i.134

ABSTRACT

The Great Salt Lake has been rapidly shrinking since the highstand of the mid-1980s, creating cause for concern in recent decades as the lake has reached historic lows. Many investigators have assessed the evolution of lake elevation, geochemistry, anthropogenic impacts, and links to climate and atmospheric processes; however, the use of remote sensing to study the evolution of the lake has been significantly limited. Harnessing recent advancements in cloud-processing, specifically Google Earth Engine cloud computing, this study utilizes over 600 Landsat TM/OLI and Sentinel MSI satellite images from 1984-2023 to present time-series analyses of remotely sensed Great Salt Lake water area, exposed lakebed area, surface cover types, and chlorophyll-a analyses paired with modelled estimates for water and exposed lakebed area. Results show that since the highstand of 1986-1987, the water area has declined by 45% (~3,000 km^2) and the exposed lakebed area has increased to ~3,500 km^2 from ~500 km^2. The area of unconsolidated sediments not protected by vegetation or halite crusts has risen to ~2,400 km^2. Significant halite crusts are observed in the North Arm, having a max extent of ~150 km^2 between 2002 and 2003, while only small extents of halite crusts are observed for the South Arm. Vegetation is more prevalent in the Bear River Bay and South Arm, with surface area increases over 400% since 1990. Gypsum is widely observed independent of halite crusts. The results highlight multiple instances of land-use/water-management that led to observable changes in water/exposed lakebed area and halite crust extent. This study demonstrates the important benefits of maintaining a lake elevation above ~4,194 ft to maximize lake and halite crust area, which would help mitigate possible dust events and maintain a broad lake extent.

INTRODUCTION

In recent years the Great Salt Lake in northern Utah has attracted the attention of local legislators and a global audience as the lake reached historic lows and caused concerns for public health and the health of the overall Great Salt Lake ecosystem. Once part of the vast Pleistocene Lake Bonneville, the Great Salt Lake has shrunk to the modern state from an evaporative evolution in a closed basin with natural inputs from three major rivers (Bear, Jordan, and Weber rivers). However, in recent centuries, anthropogenic activity has considerably affected the Great Salt Lake. This influence extends to direct physical alterations of the lake's landscape, modifications to its hydrology that alter water flow and distribution, the introduction of invasive plant species, and extensive resource extraction. In 1959 a railroad causeway was completed, separating the lake into a North and South Arm, which has been modified over the years with various breaches, culverts, and berms to control flow between the flow between the two arms (Figure 1). Additionally, the railroad causeway, mineral operator evaporation ponds, and other various impoundments have significantly separated and controlled the flow from Bear River Bay to the South Arm. With the North Arm largely cut-off from major river inputs, it has evolved to be much more saline and commonly surpasses halite saturation, leading to precipitation of lake-bottom and shoreline halite crusts as well as a different color of water due to halophilic microorganisms. The lake has been used by wildlife as a crucial bird migratory location and anthropogenically for resource extraction. In the 1980s the lake rose nearly 8 ft due to an unusually heavy period of precipitation between 1982 and 1987, but has been steadily shrinking since, reaching a historic low in 2022. With the ongoing reduction in the lake's size, there is an escalating risk of moderate-to-severe dust storms associated with lakebed exposure and substantial changes in the ecosystem, which could adversely impact bird migrations. Additionally, the overall stability of the regional ecosystem is becoming increasingly compromised.

Many aspects of the Great Salt Lake's evolution are well documented. Since the mid-1800s the US Geological Survey has been recording lake elevations and water quality metrics, and since the mid-1900s

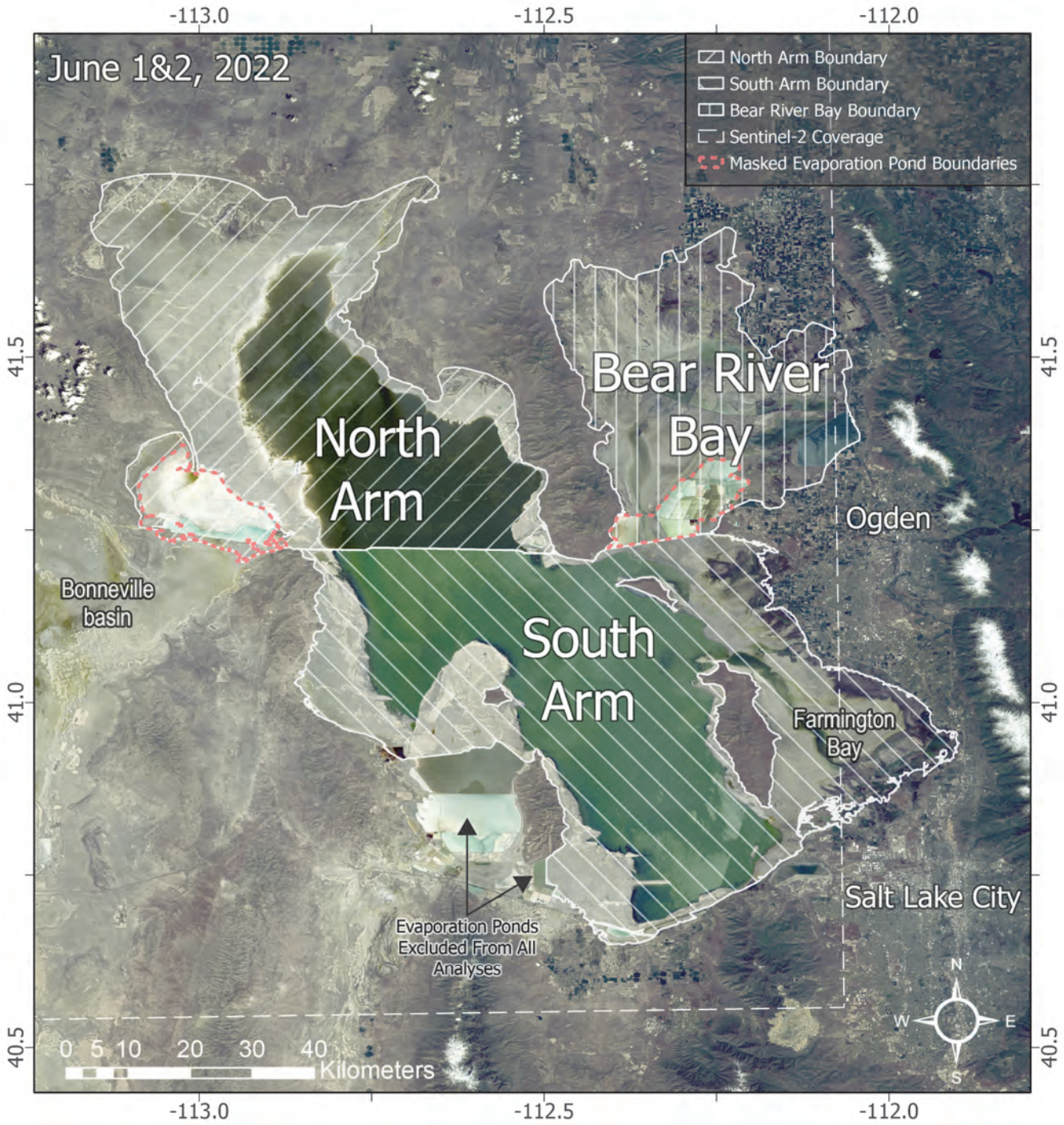

Figure 1. *Map of the Great Salt Lake system and surrounding localities, including boundaries for the North Arm, South Arm, and Bear River Bay. Also defined are the boundaries of the North Arm mineral operator evaporation pools included in analyses between 1984-1994 and the evaporation pool masked for halite analyses in the Bear River Bay. The dashed rectangular line indicates the area captured by the Sentinel-2 MSI satellite and the base-map is Landsat 8 OLI imagery from June 1st (south image) and 2nd (north image).*

the Utah Geological Survey has been recording geochemical measurements (Arnow, 1984; Gwynn, 2007; Rupke and McDonald, 2012; Naftz and others, 2013). In recent decades investigators have started assessing the contributing factors to the decline of the Great Salt Lake through water balance models, finding anthropogenic reduction of inflow and drought conditions (precipitation/inflow) to be the leading drivers of lake decline, with climate (evaporation) being a secondary factor (Mohammed and Tarboton, 2012; Wurtsbaugh and others, 2016; Wurtsbaugh and others, 2017; Wine and others, 2019; Null and Wurtsbaugh, 2020; Wurtsbaugh and Sima, 2022). More recent reports have constrained the impact of natural and human consumptive use to be responsible for 67-73% of the Great Salt Lake water loss

(Ahmadi and others, 2023). Other studies have observed relationships between atmospheric oscillations in the Pacific and multidecadal drought conditions which directly affect Great Salt Lake levels, and determined that although climate change will lower lake levels through higher temperatures, evaporation, and changes in the snowmelt cycle, those impacts will be overshadowed by anthropogenic water withdrawal and drought conditions (Wang and others, 2012; Mohammed and Tarboton, 2012; Wine and others, 2019; Hall and others, 2021; Ahmadi and others, 2023). Further, climate models suggest there will be an increase in precipitation with a warmer climate, but increases in precipitation will be negated by a greater increase in evaporation (Ahmadi and others, 2023).

Related to the impacts of a shrinking Great Salt Lake, others have investigated dust sources around the shoreline, impacts from dust events and dust-on-snow, pollutant contamination of dust-derived-sediments, regional land cover changes, and the atmospheric characteristics of dust events, all finding Great Salt Lake sediments to be a significant dust source in northern Utah (Hahnenberger and Nicoll, 2012; Hahnenberger and Nicoll, 2014; Skiles and others, 2018; Perry and others, 2019; Nicoll and others, 2020; Carling and others, 2020). Although these aspects of the lake are well documented, the use of remote sensing to document the changing Great Salt Lake system is only limited to water-surface-temperature, algal blooms, outdated classification maps, and the common use of side-by-side true-color satellite image comparisons (Hung and Wu, 2005; Bradt and others, 2006; Crosman and Horel, 2009; Hansen and others, 2016).

Here, multispectral remote sensing data of the Great Salt Lake from 1984 to 2023 are used to assess the evolution of sediment types and sediment area, vegetation area, water area, and relative chlorophyll-a concentrations between the North Arm, South Arm (including the Farmington Bay), and Bear River Bay. The NASA/USGS Landsat 5 Thematic Mapper (TM), Landsat 8 Operational Land Imager (OLI), and Landsat 9 OLI, as well as the ESA Sentinel 2 A&B Multi-Spectral Instrument (MSI) satellite platforms are chosen for this study, where the Landsat imagery extends back to the 1980's while the Sentinel imagery extends back to 2019 for this region. Combining these datasets results in over 600 near-cloud-free satellite scenes of the region from 1984 to 2023. Historically, this volume of data prevented analyses due to the sheer amount of work and processing power involved, but has recently become feasible through automation and cloud-processing platforms. The results will help to understand the evolution of exposed sediments, halite crust formation, changes in vegetation, and the relationships between land-use, climate, and increasing sediment area. This work builds off of recent remote sensing studies in the Bonneville basin which utilized Landsat 5 TM and 8 OLI multispectral imagery to map halite, gypsum, and carbonate-muds (lacustrine detritus; Bowen et al., 2017; Radwin & Bowen, 2021).

METHODS

Data Sources and Cloud Processing

The Landsat TM/OLI and Sentinel MSI platforms were used for this analysis as these sensors can capture the entire extent of either arm of the Great Salt Lake and Bear River Bay during a single swath path, have suitable spatial and spectral band wavelengths for investigating surface features and types, theoretically allow for at least one image acquisition per month, and have longevity with multispectral data extending back to the 1980s. The Landsat 5 TM, 8 OLI, and 9 OLI platforms have a spatial resolution of 30 m/pixel and seven bands (six for TM) ranging the VSWIR spectrum (~350-2500 nm), with a revisit time of 16 days (Table 1). The Landsat 5 platform was operational from 1984 to 2012, and the Landsat 8 and 9 platforms have been operational since 2013 and 2021, respectively. The Sentinel-2 MSI platform, operational since 2015, has a spatial resolution that ranges from 10-60 m/pixel (max 20 m/pixel used in this study) and 12 bands ranging the VSWIR spectrum (Table 1), with a revisit time of 10 days (5-days including both A&B satellites).

Although the Sentinel-2 platform has been active since 2015, images for Utah were not acquired until very late 2018. Additionally, the extent of the Sentinel swath fails to image the entirety of the Farmington Bay region (Figure 1 - dashed white line), but this is accounted for when comparing to Landsat observations by cropping the Landsat observations for vegetation to the extent of Sentinel 2 tiles. Image acquisition and processing is done in the cloud with Google Earth Engine (GEE), implemented via the GEE Python 3 API in conjunction with the geemap python package for interactive mapping and data export (Amani and others, 2020; Tamiminia and others, 2020; Wu, 2020). Pre-processed, atmospherically corrected Landsat Level 2 (Tier 1, Collection 2) and Sentinel-2 Level-2A (harmonized) reflectance image collections are defined from the base GEE collections, which are then filtered to near-cloud-free images covering the Great Salt Lake region. Landsat 5 TM bands are renamed to match Landsat 8 & 9 OLI specifications, and all the Landsat images are merged into the

Table 1. *Spectral band specifications for Landsat TM, OLI, and Sentinel MSI multispectral sensors.*

Landsat 5 TM				Landsat 8 & 9 OLI				Sentinel 2 MSI			
Band Number	**Band Name**	**Spectral Range (nm)**	**Resolution (m)**	**Band Number**	**Band Name**	**Spectral Range (nm)**	**Resolution (m)**	**Band Number**	**Band Name**	**Spectral Range (nm)**	**Resolution (m)**
1	Blue	450-520	30	1	Coastal Aerosol	433–453	30	1	Coastal Aerosol	433-453	60
2	Green	520-600	30	2	Blue	450–515	30	2	Blue	458-523	10
3	Red	630-690	30	3	Green	525–600	30	3	Green	543-578	10
4	NIR	760-900	30	4	Red	630–680	30	4	Red	650-680	10
5	SWIR 1	1550-1750	30	5	NIR	845–885	30	5	Vegetation Red Edge	698-713	20
6	TIRS	10400-12500	120 (30)	6	SWIR 1	1560–1660	30	6	Vegetation Red Edge	733-748	20
7	SWIR 2	2080-2350	30	7	SWIR 2	2100–2300	30	7	Vegetation Red Edge	773-793	20
				8	Panchro-matic	500–680	15	8	NIR	785-900	10
				9	Cirrus	1360–1390	30	8a	Narrow NIR	855-875	20
				10	TIRS 1	10600-11200	100	9	Water Vapor	935-955	60
				11	TIRS 2	11500-12500	100	10	SWIR – Cirrus	1360-1390	60
								11	SWIR	1565-1655	20
								12	SWIR	2100-2280	20

same collection. Cloudy image filtering is accomplished using image cloud percentage metadata provided by the USGS and ESA (Drusch and others, 2012; Foga and others, 2017; Tiede and others, 2021), where images with less than 10% of the scene covered by clouds are chosen to process for both Landsat and Sentinel imagery. For Sentinel-2, many images were found to have a significant percentage of bad-pixels (no data), thus a bad-pixel filter was applied to remove those images.

The size and swath path of Landsat imagery results in only one complete arm of the lake being imaged for each swath, meaning each arm of the lake is observed on different dates. However, Sentinel-2 can image both arms on the same date. For this reason, all imagery results are split between North and South Arm. The Landsat tile specifications are rows 31 and 32, and paths 38 and 39, while the Sentinel tile specifications are 12TUM and 12TUL. Images with the same date are combined to a single image, but images without a paired same-date southern or northern swath image are discarded as that indicates the other scene isn't suitable and the entire area couldn't be observed. Landsat 1 true-color images from 1972, 1974, and 1979 are used for manual delineation of lake extent to provide a reference prior to the wet 1980's. Landsat 5 images from 1984 are used for manually delineating the extent of the entire Great Salt Lake system, also referencing recent imagery, to be used for masking the data to a boundary and for exposed lakebed area calculations (Figure 1). The exposed lakebed is here defined as the area extending from the shoreline to the imposed Great Salt Lake system boundary (Figure 1) that encompasses lacustrine derived sediments, evaporites, and vegetation.

Select mineral operator evaporation ponds within the project-defined boundary of the Great Salt Lake system are not included in the analyses. These areas include the evaporation ponds to the southwest, west and south of Stansbury Island, and to northeast in the Bear River Bay, which were established prior to 1984, in addition to evaporation ponds to the north-

west. However, the area of the evaporation pond to the northwest, in the North Arm, is included in analyses up until the evaporation pond was constructed in 1994. Similarly, the evaporation ponds situated in the southern region of Bear River Bay are employed for satellite monitoring, with the exception of halite detections. This is to circumvent any false readings caused by halite linked with mining activities. Other evaporation ponds that exist within the study area are not masked-out and are included in analyses, albeit the remaining ponds are small in comparison to the evaporation ponds removed from analyses. The size of the North Arm evaporation pond accounts for ~7.6% of the area within the North Arm boundary (Figure 1).

Spectral Indices

The general mineralogy of the Great Salt Lake exposed lakebed sediments are similar to the sediments in the proximal Bonneville basin (A.K.A., Great Salt Lake Desert) as both landscapes share a provenance (Lake Bonneville) and are connected by a spillway. The general mineralogical suite can be simplified to carbonate-rich lacustrine sediments, that comprise the majority of the sediments, which are overlain or interfingered with gypsum ($CaSO_4 \cdot 2H_2O$) and halite (NaCl) evaporite deposits that vary spatiotemporally. The carbonate-rich lacustrine sediments are subsequently referred to as carbonate-muds, as they are typically an intimate mixture of carbonates (including authigenic coatings/cements/nodules, oolitic sands, skeletal fragments, and intraclasts of calcite or aragonite; $CaCO_3$), quartz grains (SiO_2), and phyllosilicates (clays/muds), but also may contain magnesite ($MgCO_3$), mirabilite ($Na_2SO_4 \cdot 10H_2O$), and other lesser-occurring but still prevalent minerals (Lines, 1979; Pace and others, 2016; Newell and others, 2017; Perry and others, 2019; Dunham and others, 2020; Ingalls and others, 2020; Smith and others, 2020; Jagniecki and others, 2021; Homewood and others, 2022). The grain size distribution as well as proportion of mineralogical components varies spatially for exposed carbonate-muds, but only the surface mineralogy type is considered here (Perry and others, 2019). Gypsum deposits are found precipitating from springs found within the Great Salt Lake system, but much of the gypsum within the system is likely redistributed rather than actively precipitating, as the Great Salt Lake chemistry is calcium limited and now an $MgSO_4$ system (Hardie and Eugster, 1970; Jagniecki and others, 2021). To map these three sediment type classes, each satellite image is processed to mask out other landcover, leaving only surficial sediments, and then each sediment type is differentiated using multi-spectral indices adapted from work in the Bonneville basin mapping similar surface types (Radwin and Bowen, 2021). To map the extent of water and vegetation, which is used to isolate surficial sediments, the Normalized Difference Water Index (NDWI) and Normalized Difference Vegetation Index (NDVI) are utilized (McFeeters, 1996; Gandhi and others, 2015; Huang and others, 2021). For this study, the halite index takes the form of RED – SWIR1 / RED + SWIR1 and the index for gypsum and carbonate-muds takes the form of SWIR1 – SWIR2 / SWIR1 + SWIR2. The halite index exploits a significant drop in reflectance from the RED (~650 nm) to the SWIR1 (~1600 nm) bands observed in local halite spectra, which is not observed for the other sediment types (Radwin and Bowen, 2021). Likewise, the gypsum index exploits a slight decrease in reflectance between the SWIR1 (~1600 nm) and SWIR2 (~2200 nm) bands observed for local gypsum spectra, which is not typically observed for the local intimate-mixture of carbonates, quartz, or phyllosilicates (carbonate-muds).

All resulting images from surface type indices are masked to the surface type of interest using image histogram thresholds. For Landsat NDWI results, the threshold is sensitive to sensor-type as well as radiometric differences between scenes, and is determined for each image using an adapted Otsu image segmentation technique, which is then offset by +0.15, +0.175, and +0.175 for the North Arm, South Arm, and Bear River Bay, respectively (Otsu, 1979; Ji and others, 2009). The dynamic thresholding is noted to drastically help the accuracy of water detection for Landsat imagery, particularly at the water-shore interface. Other index results use a static threshold for all images, with differing values for Landsat and Sentinel to account for differences between sensors. All static thresholds are determined through incrementally assessing how thresholds perform delineation of surface type boundaries, with the goal of having the threshold provide the greatest separation from background values without including background values in the results. For Landsat indices, the thresholds chosen are: ≥ 0.345 for halite, ≥ 0.153 for gypsum, < 0.153 for carbonate-muds, and ≥ 0.105 for NDVI. For Sentinel, the thresholds chosen are: ≥ 0.58 for halite, ≥ 0.3 for gypsum, < 0.3 for carbonate-muds, ≥ 0.185 for NDVI, and ≥ 0.06 for NDWI. Rather than employ a separate index to map carbonate muds, the gypsum index is also used where all unmasked sediments below the threshold used for gypsum are classified as carbonate-muds or other by process-of-elimination. Dynamic thresholding for Sentinel NDWI images is not applied as there are data-issues associated with bad/no-data pixels that hinder the dynamic threshold

processing for dozens of images with no apparent fix. However, the NDWI threshold for Sentinel appears to be less sensitive compared to Landsat results. For Sentinel-2 MSI gypsum, carbonates, and chlorophyll-a indices, the 10 m/pixel input bands are resampled to 20 m/pixel to match the resolution of the SWIR bands.

To assess relative chlorophyll-a concentrations, the KIVU and 2BDA indices are used for Landsat and Sentinel imagery, respectively (Gitelson and others, 2003; Buma and Lee, 2020). Different indices are chosen as the Sentinel MSI sensor is better suited for chlorophyll detection having red-edge bands. The KIVU index takes the form of BLUE – RED / GREEN while 2BDA takes the form of RED-EDGE-1 / RED.

Processing Workflow

All images are masked to the correct arm of the lake system prior to processing spectral indices. A systematic workflow is implemented to process each surface type index, where the order of processing follows: 1) water (NDWI), 2) vegetation (NDVI), 3) halite, 4) gypsum, and 5) carbonate-muds/other (Figure 2). It is important to note that the results of each index are used to mask the image of the following index, to ensure no pixels are classified twice. For example, the input image for the halite index is masked to be absent of water (NDWI) or vegetation (NDVI) pixels and is theoretically just surficial sediments. The order of processing is chosen as NDWI and NDVI are more standard and broadly applicable spectral techniques that can be used regardless of the surrounding geolog-

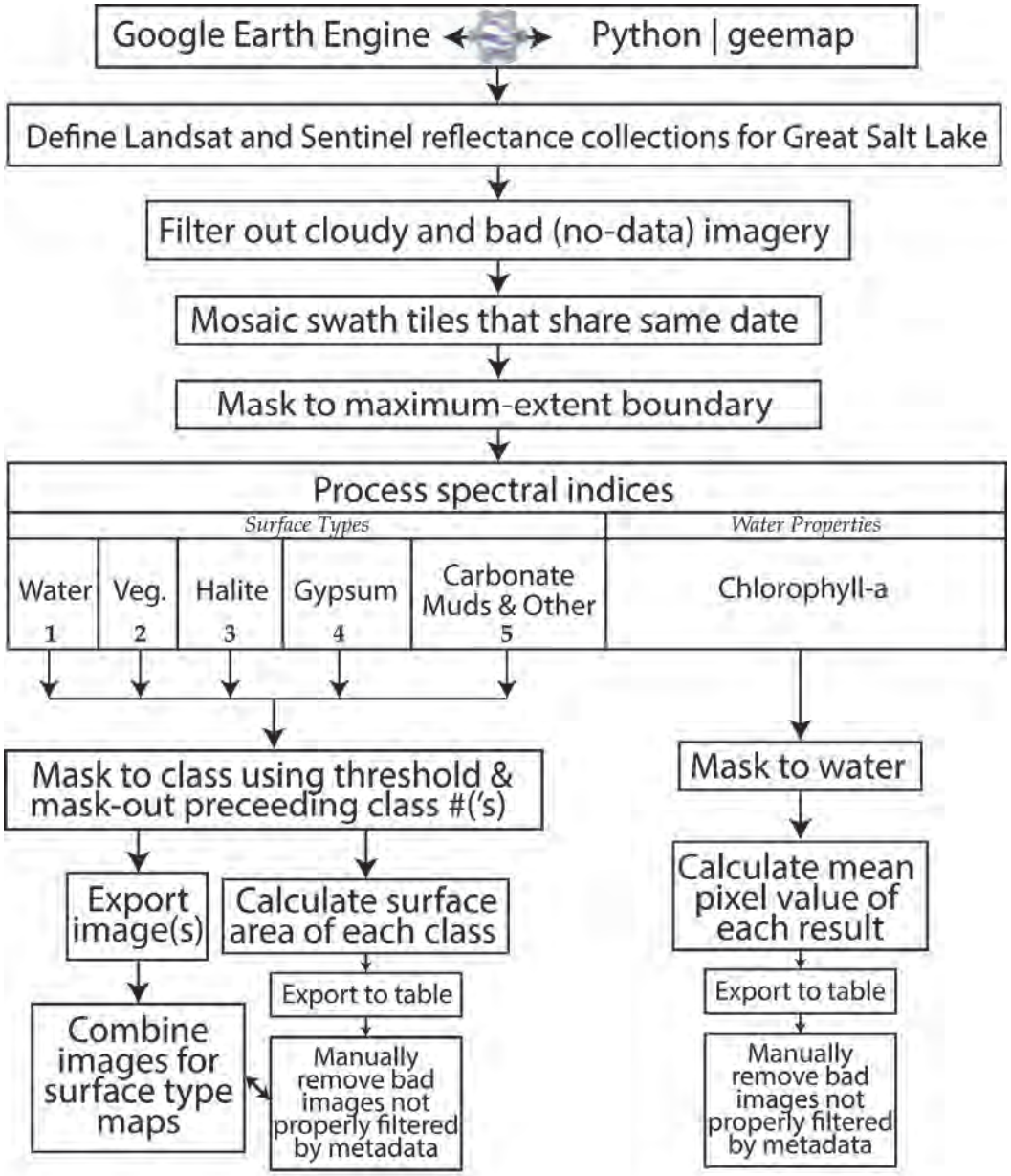

Figure 2. *Workflow chart of methods used to define and process satellite imagery using Google Earth Engine Python API.*

ical/mineralogical context, while the sediment indices rely on the isolation of surficial sediments with the mineralogical framework found in the Great Salt Lake and Lake Bonneville system for the intended performance. The halite index is processed as the first sediment index as it exploits a significant spectral characteristic not found in the other sediments and is believed to be the most sensitive of the mineralogical indices used here. Thus, the order of index calculation and image masking follows the most broad-to-limited applicability for the chosen spectral indices and mitigates water or vegetation false-positives for mineralogical differentiations. Changing the order of NDWI and NDVI should not have much impact, but the order of the sediment indices matters as the gypsum index can wrongly detect halite pixels as gypsum. For the chlorophyll-a sensitive indices, the NDWI results are used to isolate the data to water pixels prior to processing.

All final index results are exported as single-band images and all of the unmasked/output pixels are used to determine the surface area extent of each class. Area calculation of each class result requires the use of GEE specific area functions to account for the projection of each pixel and calculate the geodesic area of each unmasked pixel. Area calculations without accounting for projection are greatly overestimated. All pixel-areas of unmasked pixels for each index result are summed together to estimate the total area of the class. These results are stored and exported as tables for analysis. In contrast, for the KIVU and 2BDA chlorophyll-a indices, the mean value of all unmasked pixels is calculated for each arm to represent the relative chlorophyll-a concentrations.

Other Data, Issues, and Error

From the index results, the exposed lakebed area is estimated by summing the area of vegetation, halite, gypsum, and carbonate-muds/other, while the calculated exposed lakebed area is estimated by subtracting the water area from the total area of the respective arm of the lake. A calculated exposed lakebed area is also presented for true-color images before 1984, where the water area is manually delineated and subsequently subtracted from the total area. The modelled exposed lakebed area is calculated by subtracting the modelled water area from the total area for each region. Erodable exposed lakebed area is calculated by summing the area of the gypsum and carbonate-muds/other classes, as these sediment types are unconsolidated and potentially susceptible to eolian transport. It is assumed that halite and vegetation around the rest of the exposed lakebed aids in retraining sediments from eolian transport by adding a protective surface (Reynolds and others, 2007). However, it has been observed that salt crusts may also contribute to dust events if enough desiccation and/or wind occurs (Bucher and Stein, 2016).

Additional products presented derived from spectral results are lake area extent boundaries (shapefiles) from select images, as well as a historical halite classification map derived from summing all halite index results for the North Arm. Lake area extent shapefiles are produced using the output NDWI rasters in ArcGIS Pro, where the rasters are converted to shapefiles, boundaries are dissolved, and all features except the main water body are removed. The historical halite classification map is also produced in ArcGIS Pro by summing all pixel-cell values for all North Arm halite images, which effectively produces a historical occurrence map of halite crusts across the lakebed since 1984. The halite values were then classified by value to ten quantiles to form a decile classification map to better assess distribution patterns. Daily precipitation data are acquired from NOAA station USW00024127 at the Salt Lake City International Airport, which is situated proximal to the southern end of the lake. River discharge data for the Bear, Jordan – West, Jordan – East, and Weber rivers are taken from USGS stations 10126000, 10171000, 10170500, and 10141000, respectively. Each station is proximal to the lake and roughly represents the river-water influx into the lake system. Yearly-running-averages of Palmer Drought Severity Index (PDSI) data, a relative dryness/drought indicator using temperature and precipitation data, is acquired for the Great Salt Lake region from 1982-2020 from Climate Engine using the gridMET Drought (4km resolution) dataset. A polygon is used to define the general area of the Great Salt Lake system in Climate Engine and the mean PDSI value of all gridded pixels within the polygon is calculated then exported.

Although official cloud percentage metadata are used to filter out cloudy scenes, it is noted that over 30 scenes show excessive amounts of clouds and are removed from analyses. This poor performance of the cloud detection algorithm is shared between both Landsat and Sentinel products but is infrequent as it occurs in only about five percent of the total amount of images. Other issues such as snow, smoke, and surficial-cyanobacteria-growth are observed for a handful of images and those are also excluded from analyses. However, over 15 other Landsat images were excluded from analyses due to strange image artifacts, encompassing much of the water body, resulting in a plethora of missing pixels for some or all of the spectral bands. In total, the observations from 80 images are excluded from analyses.

Given the constraints and limits of manually being able to differentiate surface types from multispec-

tral satellite imagery, as well as the vast spatial and temporal scope of the study area, one of the only error assessments available is to assess the performance of water-body detection with manually derived comparisons. Three locations around the lake are chosen for two separate Landsat scenes, and for each region the waterbody is manually delineated and the area is calculated and compared to the area reported by NDWI for the same locations. The magnitude of difference between the results is used as a rough error metric, indicating a difference of <1% for deep waters and difference of ~4% for shallow waters such as the Farmington Bay. It is observed in many resulting images that when the water in Farmington Bay is shallow, NDWI has difficulty and typically underestimates the water area. The performance of the vegetation and halite results appear to be very robust in that there is clear separation from background values when assessing the resulting images. Additionally, it is worth noting that both indices use a conservative threshold and thus may slightly underestimate the total area of these classes, as it is observed for many images that there is a slight halo around regions of classified pixels with values that could be also included in the class-of-interest as they are well-separated from background values.

A temporal model of Great Salt Lake water area is also included as a comparator for water-body detection performance and as an additional source of data. The model is based on a univariate spline interpolation of published values for area vs elevation of the lake, and estimates area via lake elevation data from USGS water-station sites 10010000 and 10010100 (Robert, 2005; Robert, 2006). The modelled values are a rough estimate as the initial resolution of the lake area data is for every 0.5 ft of lake elevation. However, the interpolation strongly matches the USGS curve as the interpolation utilizes 15 breakpoints (4169, 4171, 4173, 4178, 4183, 4188, 4194, 4200, 4201, 4203, 4205, 4207, 4209, 4211, and 4214 ft; Figure S1). Sources of differences between the modelled and observed area values primarily stem from differences in the boundaries utilized. The USGS North Arm area data does not include the evaporation pond to the west, which is included in this study in analyses until 1994, and the USGS South Arm area data includes the large evaporation pond west of Stansbury island, which is not included in analyses from this study and accounts for significant differences between the model and NDWI up until the year 2000 (when the water elevation dropped below the level which would naturally inundate the evaporation ponds). Nonetheless, the model provides a useful comparison and shows robust agreement with the NDWI results.

RESULTS & DISCUSSION

Water and Exposed Lakebed Area Evolution

The resulting time series data show a stark evolution in the surface area of the lake that closely follows the trends from lake elevation data as well as the modelled surface area (Figure 3). Annual oscillations in lake level are observable for years with more than about three images, as confirmed by the lake elevation and modelled data (Figure 3a). Sentinel imagery have a much higher temporal resolution and capture annual oscillations in greater detail. After the year 2000, the image-derived and modelled water areas have strong agreement, where the weaker agreement is due to the modelled area including a portion of the South Arm salt pool areas for years prior to 2000. The observations between the Landsat and Sentinel platforms appear to agree well and show relatively little difference.

The water surface area for both arms of the lake increase drastically from the 1970's into the mid 1980's where the lake filled due to significant precipitation, then slowly decreases in time with only a handful of wet years to follow. For the Bear River Bay, the water surface area decreased alongside falling lake levels until the early 2000's when the modelled and observed water area began to diverge. The modelled water area suggests the Bear River Bay should have been absent of standing water Around 2005, but the observed area indicates an anthropogenically maintained water surface area between 200 and 500 km^2, with an average of 300 km^2. After 2005 the Bear River Bay water surface area no longer followed trends in lake elevation change. Since the maximum extent of 1986-1987, which closely resembles the estimated mean lake area in the absence of anthropogenic consumption (Wurtsbaugh and others, 2017), the total observed lake area has decreased from ~5,700 km^2 to ~2,590 km^2 during the summer months, a loss of ~45%. When considering just the North and South Arms, the observed lake area has decreased ~30% from ~3,400 km^2 to ~2,380 km^2 since 1979. The South Arm water area has responded greater to lake elevation change, losing >250 km^2 more than the North Arm since 1986, with the drying up of the shallow Farmington Bay being partly responsible. During lowstands the South Arm water area is seen to oscillate in greater amplitude compared to the North Arm water area, which is coincident with the South Arm being directly influenced by seasonal fluxes in river input and association with more shallow lakebed. However, during highstands, when the lake arms are closer to equilibrium in elevation, the water areas fluctuate similarly. In contrast, the water area

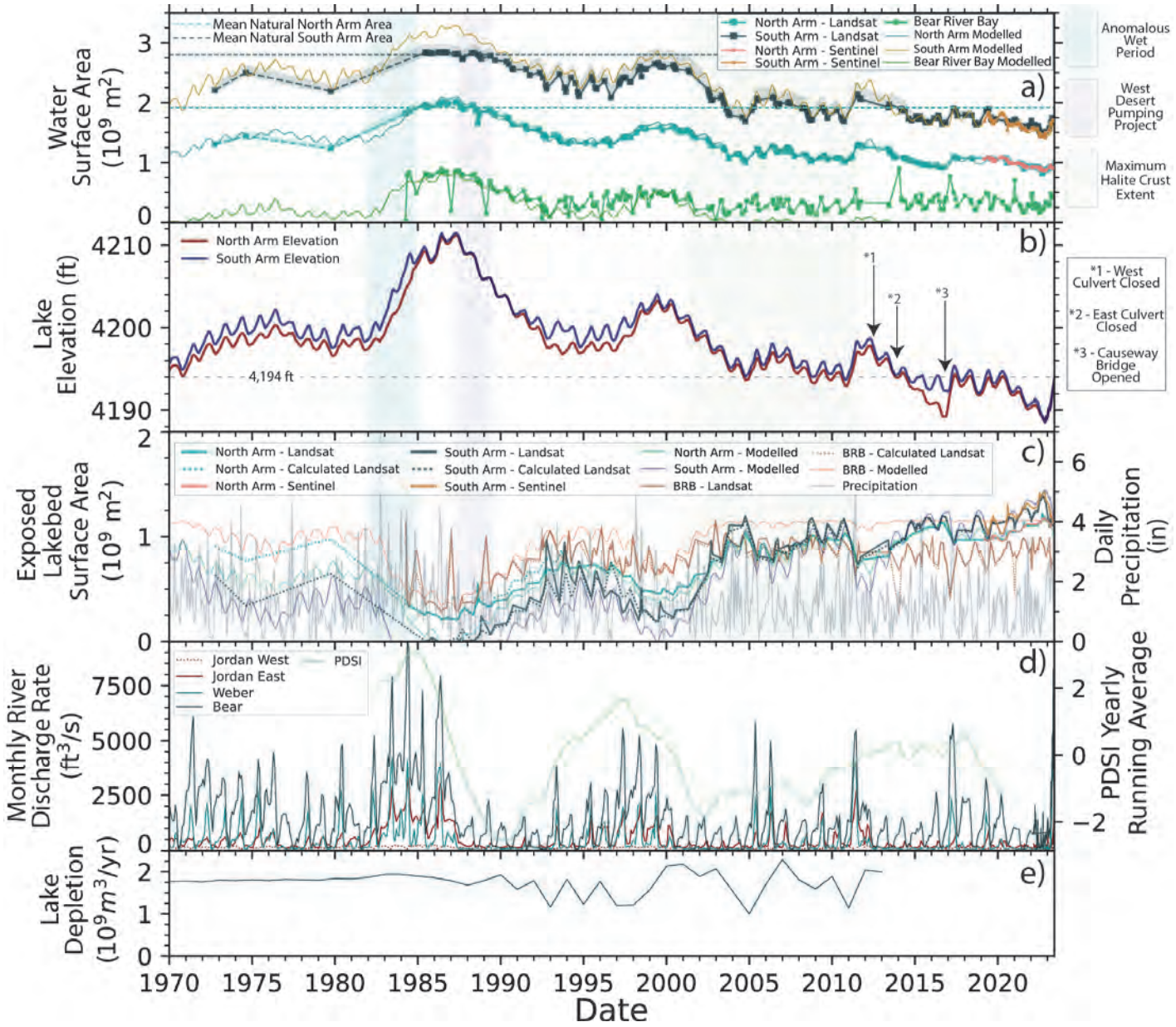

Figure 3. *Evolution of lake surface area (a), lake elevation (b), exposed lakebed surface area and daily precipitation (c), monthly river discharge rate and Palmer Drought Severity Index (PDSI) (d), and lake-input depletion data (e) (from Wurtsbaugh and others, 2017). The dashed horizontal lines on panel a) indicate the estimated natural mean area of each arm of the lake (corresponding to ~4,207 ft lake elevation) in the absence of anthropogenic consumption (Wurtsbaugh and others, 2017). The dashed horizontal line on panel b) indicates the 4,194 ft topographic threshold. Also included are color bars indicating times of the anomalous wet period (light blue), west desert pumping project (light purple), and maximum halite crust extents (light green). Error bars of -2.5% and +5% are used for lake surface area measurements, as it is more likely to underestimate the observation than overestimate. For the South Arm, between 1995 and 2015, the error bars show -2.5% and +10% due to the shallow Farmington Bay waters. The analyses do not include the North Arm salt pool after 1994. Arrows indicate specific events in time. The lake and exposed lakebed surface area panels (a, c) include remotely sensed area estimates and the modelled area derived from published surface area vs elevation calculations (Robert, 2005; Robert, 2006). Lake elevation data are from USGS water-stations 10010000 and 10010100. Daily precipitation data are from NOAA station USW00024127 at the Salt Lake City International Airport. Monthly river discharge rate data for the Bear, Jordan – West, Jordan – East, and Weber rivers are from USGS water-stations 10126000, 10171000, 10170500, and 10141000, respectively. PDSI data acquired from Climate Engine for the Great Salt Lake region.*

fluctuations within the Bear River Bay appear to follow greater seasonal and inter-seasonal variations, associated with seasonal flow variations for the Bear River and water-management actions.

For years with significant rains (Figure 3c), where the water elevation has been able to rebound multiple feet, the water area can be seen to dramatically increase, typically by 500-750 km^2, between the North and South Arms. For example, the wet year of 2011 increased the lake elevation by ~4 ft and North + South Arm area by ~670 km^2 (Figure 4). As the topography of the lake-bottom becomes significantly steeper below ~4,194 ft, water elevation changes below this elevation have significantly less impact to water area (Figure S1; Robert, 2005; Robert, 2006). Starting in 2003 the mean lake elevation began to fluctuate near 4,194 ft, which lasted until about 2020, and whenever lake elevation is seen to drop below ~4,194 ft there are noticeably less significant changes in water surface area. Knowing that the lake area is

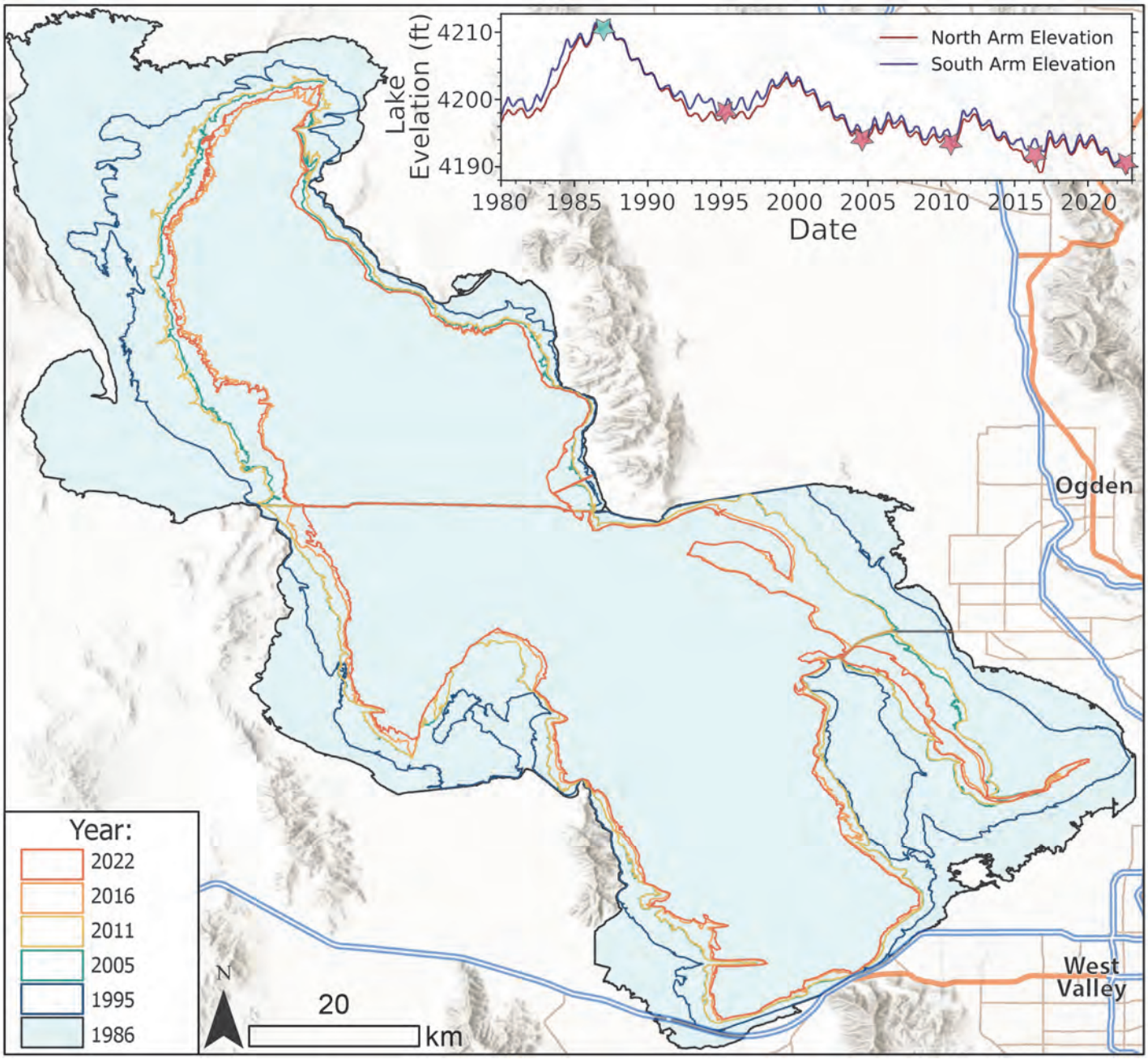

Figure 4. *Water boundaries of both the North and South Arms for all the major lowstands since 1986 (1995, 2005, 2011, 2016, and 2022) compared to the highstand boundary of 1986. The boundaries show the outermost boundary and do not include interior boundaries such as the boundaries along island perimeters. The southwestern North Arm evaporation pool is only included for the 1986 boundary and the Bear River Bay is not included. A lake elevation plot is inset in the upper right as reference, with the data being from USGS water-stations 10010000 and 10010100. The basemap is the ESRI World Hillshade map with an ESRI highway layer. The 2005 and 2011 boundaries are close to the ~4,194 ft threshold.*

more sensitive to lake elevation above ~4,194 ft indicates that lake managing efforts should aim to keep the lake at least above ~4,194 ft to maximize the area of the lake and sediment coverage. Ideally, when considering maximizing water area (sediment coverage), the water elevation should be kept above ~4,200 ft so fluctuations don't drop near the ~4,194 ft threshold. Maximizing sediment coverage will be increasingly important in the future to mitigate more-significant dust events. A recent report for policymakers determined the optimal range of lake elevation is between 4198 and 4205 ft, with a transitionary zone between 4195 and 4198 ft, based on impacts to air quality, ecosystem, mineral production, recreation, and brine shrimp viability (Ahmadi and others, 2023). These proposed elevations align with the presented minimum threshold of ~4194 ft, and if implemented would result in a North + South Arm lake area of ~3,100 to ~4,700 km^2, roughly 700 to 2,300 km^2 greater than the lake area in 2022.

Associated with the lake surface area change, the total observed exposed lakebed area has increased ~2,985 km^2, from ~504 km^2 to ~3,489 km^2 over 36 years (Figure 3c). Assessed as a simple trend, this suggests the rate of exposed lakebed area growth has been roughly 80 km^2 per year. Compared to 1979, before the significantly wet period, the exposed lakebed area for the North and South Arms has increased ~1,000 km^2, from ~1,600 km^2 to ~2,600 km^2. Since 1986-1987 the South Arm has exposed nearly 50% more exposed lakebed compared to the North Arm, as the South Arm has had a stronger response to water level dropping. However, much of this additional exposed lakebed, particularly in Farmington Bay, has been altered from a saline mudflat to a vegetated wetlands ecosystem with the rapid encroachment of phragmites. Erodable exposed lakebed, exposed lakebed without vegetation or halite crusts to entrain the sediments, has increased from ~330 km^2 to ~2,750 km^2 since 1986-1987 for the total lake system. Erodable exposed lakebed increased by ~900, ~1,110, and ~390 km^2 for the North Arm, South Arm, and Bear River Bay, respectively, since 1986-1987. The Bear River Bay has had much less of an increase in erodable exposed lakebed due to anthropogenic maintenance of surface waters and the smaller size of the subsystem area. Although vegetation and halite help to protect a sizable portion of the exposed lakebed surface, erodable exposed lakebed has consistently dominated more than 80% of the exposed lakebed surface, except for Bear River Bay where the average proportion of erodable lakebed surface has been roughly 60%. A caveat associated with vegetation growth protecting the surface is that much of the vegetation in the South Arm is due to invasive Phragmites, which consume significant amounts of water compared to native vegetation (Kulmatiski and others, 2011).

Precipitation and river discharge data (Figure 3c-d) help explain major changes to water and exposed lakebed area, where years with significant rains typically result in a much greater river discharge which significantly increase water area and decrease exposed lakebed area. However, years with higher amounts of precipitation but no increase in river discharge (i.e., 2002, 2003, and 2015), associated with river diversion/extraction for agricultural and other uses (Figure 3e), are seen to have little effect on the lake/exposed lakebed area (Wurtsbaugh and others, 2017; Ahmadi and others, 2023). Thus, although precipitation directly impacts river discharge, if consumption of the river waters is too great there may be no increase in water/exposed lakebed area and perhaps a decrease. Utilizing a yearly-running-mean of the Palmer Drought Severity Index (PDSI) emphasizes wetter and drier periods, effectively separating periods with low and high river discharge connected to climatic cycles (Figure 3d). The PDSI values of the mid-1980's and late 1990's are indicative of wetter periods (>1), which is clear from precipitation and river discharge data, but the mid-2010's are indicated to be transitional (~0) although discharge into the lake was relatively low. In general, trends from PDSI follow trends from lake elevation and area well up until ~2013, where infrequent but significant precipitation caused the PDSI to slightly rise but the lake elevation and area continued to decline.

Exposed Lakebed Evolution

Results from the spectral indices for vegetation, halite, gypsum, and carbonate-muds highlight key similarities and differences between the North Arm, South Arm, and Bear River Bay (Figure 5). Sentinel and Landsat surface classifications agree well, although there are noticeable differences during 2022 where Sentinel appears to underestimate the vegetation and evaporite extent. The most significant difference between the sediments shared between the lake regions is that the extent of evaporite formation is magnitudes greater in the North Arm (Figure 5a-e). Carbonate-muds comprise the majority (>75%) of the exposed lakebed for all lake regions and vegetation is typically the second most prevalent land cover type. Through the temporal evolution of exposed lakebed area, the percentage of each surface type appears to stay relatively consistent through time, in that there haven't been any significant changes to the proportion of sediment types as the lake has rapidly

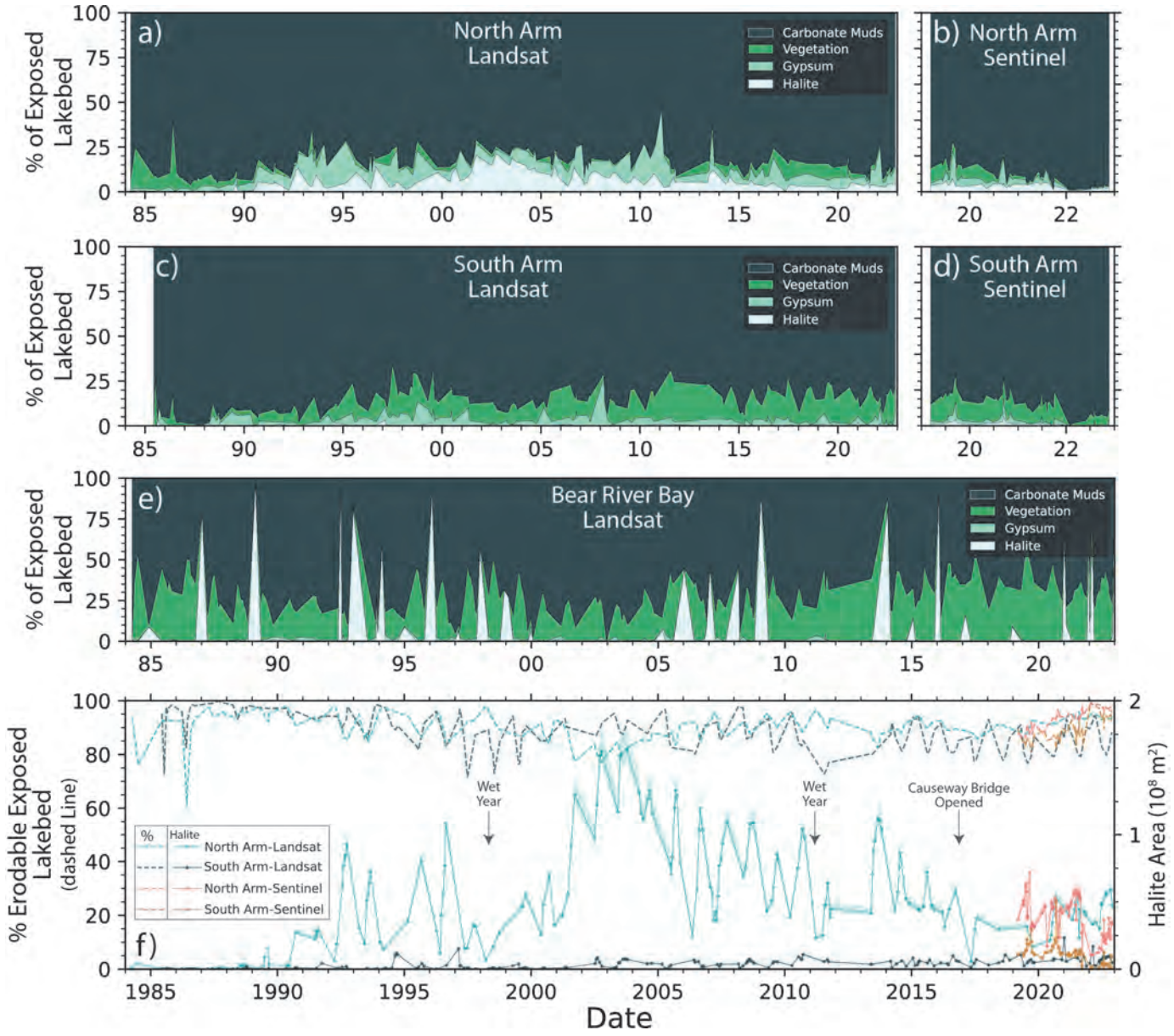

***Figure 5**. Percentage of each surface type for the North Arm (a-b), South Arm (c-d), and Bear River Bay (e) exposed lakebed areas, split between Landsat (a, c, e) and Sentinel (b, d) observations, as well as the percentage of erodable exposed lakebed area and detected halite area for the North and South Arms (f). The dashed line on f) indicates the percentage of erodable exposed lakebed.*

dropped. This is also observed through temporally assessing the percentage of erodable exposed lakebed (Figure 5f – dashed line) which consistently oscillates between ~75-95% of the exposed lakebed area for the North and South Arms. Seasonal oscillations in extent for vegetation and evaporites coincide with wet/cold and dry/warm seasons, as seen by the annual fluctuations of exposed lakebed land cover proportions by ~5-20%. Seasonal variation in halite extent appears to be greatest for the Bear River Bay, as there are spikes of halite detection during the winter months when the surface waters are at a minimum extent (Figure 5e). However, the halite variations in the Bear River Bay are likely overestimated by the sensor as the values appear unreasonably high. Overall, evaporites appear to be lesser occurring in Bear River Bay as compared to the North and South Arms, and minimally contributes to the Bear River Bay lakebed outside of winter months.

Halite crust formation has been a significant part of the evolution of the North Arm exposed lakebed area (Figure 5a,f). Halite crust in the North Arm is formed from either evapoconcentrating pore-waters of surficially saturated sediments or by precipitation of halite in the supersaturated lake waters and accumulation on the lake-bottom. Spanning much of the North Arm lake-bottom is a robust and thick (>1 ft) halite crust, which becomes partially exposed around the perimeter of the water when the lake recedes (Rupke and others, 2016; Rupke and Boden, 2020). Additionally, during the warmer months the waters and saturated sediments on and/or near the fringe of

the water-sediment-interface commonly reach halite supersaturation through evapoconcentration, or are already supersaturated, and form halite crusts that vary in extent depending on a variety of factors (Jagniecki and others, 2021). From the satellite observations, the greatest observed extent of halite in the North Arm is roughly 150 km^2, in contrast to the greatest observed extent of halite in South Arm of roughly 30 km^2. However, the temporal evolution of halite crust extent in the North Arm is complex and the average extent of halite since 1990 is ~78 km^2. Seasonal fluctuations in halite crust area can vary in magnitude but it is common to see changes greater than 50 km^2 during the wet and cold months when halite crusts dissolve and/or when sediments wash in and mask the crust surface.

Gypsum extent appears to be independent of halite formation, as gypsum extent is observed to vary regardless of halite. However, gypsum extent follows seasonal variations where the greatest extent is during the colder and wetter months, and is most prevalent in the North Arm, despite that active gypsum precipitation of significant amounts is unlikely to occur from lake waters. These observations may be attributed to seasonal coverage/reworking by loose sediments or halite crusts, detecting other hydrated sulfate rich minerals (such as mirabilite), or annual cycles of gypsum precipitation from springs or interstitial brines (Jagniecki and others, 2021). Significant aggregates of mirabilite, if present, are likely classified as gypsum, as their mineralogy and spectral characteristics are similar (Kokaly and others, 2017). As gypsum observations are greatest in winter when mirabilite is known to form in the Great Salt Lake system, it is reasonable to interpret that the observations are indeed incorporating detections of mirabilite, which suggests the variations are less in part due to variations in gypsum distribution but rather variations in the combined distributions of gypsum and mirabilite. It is likely a significant portion of the surficial gypsum at a given time is retained from previous years due to redistribution to drier, more protected zones. Redistributed gypsum may also be a by-product of evaporative mining in the system. Although the South Arm forms few halite crusts, gypsum spatiotemporally accounts for an appreciable portion of the exposed lakebed surface, which may be a valid observation or indicate the gypsum threshold is too low as the reported amounts of gypsum are unexpectedly significant. Observations from Bear River Bay indicate a minimal presence of gypsum, a finding that is consistent with the bay's fresher water qualities but may also be associated with local geology, biological mediation, and/or hydrologic processes.

Vegetation in the Great Salt Lake system spread dramatically starting in the early 1990s, where vegetation in the South Arm and Bear River Bay started growing with rates of ~9 and ~11 km^2 per year, respectively (Figure 6a). The areas of greatest vegetation growth are associated with the Farmington and Bear River bays, with the Bear River Bay hosting the most vegetation. The Bear River Bay hosts a variety of agricultural, wetland, and floodplain vegetation types while the Farmington Bay mainly hosts wetland vegetation types. The greatest seasonal variations in vegetation area are attributed to Bear River Bay, which can vary over 300 km^2 (up to >90%) from summer to winter, with the South Arm also showing significant seasonal variations. In 2020 the area of vegetation in the Bear River Bay spiked over 500 km^2, 340+ km^2 (>300%) greater than pre-1995 observations of vegetation area. The area of vegetation in 2022 is ~400+% greater than the area of vegetation between 1984-1994. Vegetation in the North Arm shows no significant growth up until around 2010, when vegetation started growing rapidly and quadrupled in area in about 6 years. However, since 2019 the extent of vegetation in the North Arm has dropped dramatically. NDVI comparisons between Landsat and Sentinel agree extremely well, possibly better than any of the other indices used in this study. Overall, satellite observations suggest vegetation is rapidly encroaching on the exposed lakebed of the Bear River Bay and Farmington Bay.

Chlorophyll-a analyses represent the mean relative chlorophyll-a concentration for each arm of the lake and shows much different temporal results for both arms of the lake (Figure 6b-c). Although the microbiology of both arms is greatly different and that many of the organisms don't produce chlorophyll-a but produce carotenoids (a different biotic pigment), it is expected the chlorophyll-a indices should still capture changes in pigment (Weimer and others, 2009; Roney and others, 2009; Baxter, 2018). The North Arm shows a continual decrease in relative chlorophyll-a concentrations through time, having the greatest decreases between ~1992-1995 and ~2012-2013 (Figure 6b). In contrast, the South Arm shows a relatively consistent average chlorophyll-a concentration that fluctuates seasonally with variations in temperature, nutrient flux, and turbidity (Figure 6c).

Sentinel 2BDA results, which are likely more sensitive to true chlorophyll-a changes due to the inclusion of a red-edge band, capture large seasonal chlorophyll-a fluctuations in the South Arm that are much greater in amplitude than changes in the North Arm. Given that the salinity of the North Arm is much greater than the South Arm due to a lack of inputs, and that turbidity is much lower in the South Arm, the biotic regime is known to be much different and ex-

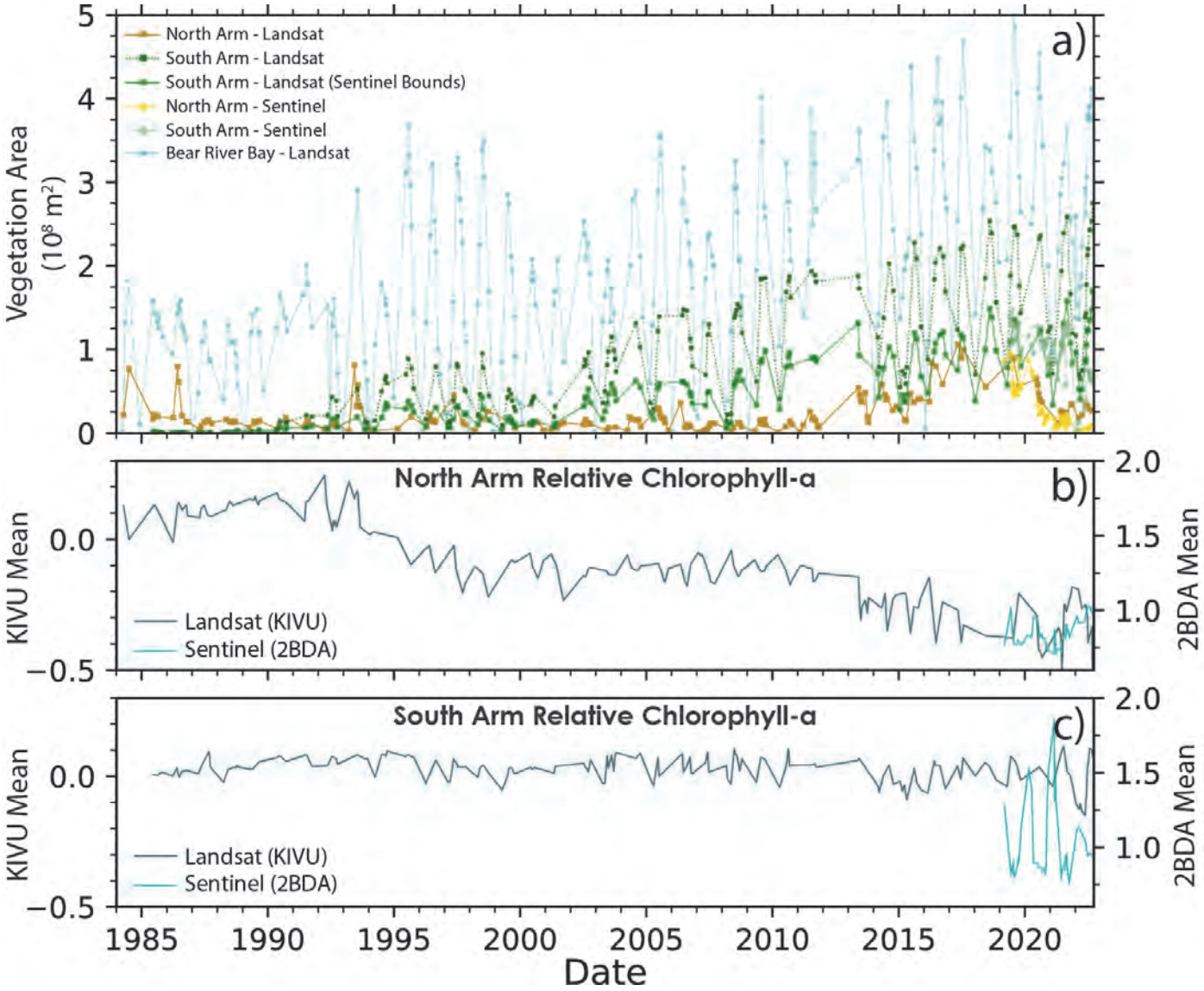

Figure 6. *Evolution of vegetation area (a) for each region of the Great Salt Lake and mean relative chlorophyll-a concentrations for the North (b) and South (c) Arms from both Landsat and Sentinel data. The dark green line of panel a), labeled "South Arm – Landsat (Sentinel Bounds)" shows the area of vegetation in the South Arm for Landsat data that are clipped to the extent/boundary of the Sentinel-2 imagery for direct comparison.*

plains the differences between the lake arms. Reasoning to explain the continual decline of chlorophyll-a in the North Arm is that in the 1980s when the lake filled the salinity dropped drastically, nutrient flux increased, and turbidity increased all leading to conditions favorable for microorganism growth. As the North Arm has evolved to be more saline, the microorganism community transitioned to saline-favorable organisms and subsequently the less halotolerant microorganisms died (Almeida-Dalmet and others, 2015; Baxter, 2018). Additionally, it has been observed that the modern community of microorganisms in the North Arm is more resistant to changes in salinity and temperature than in the South Arm (Almeida-Dalmet and others, 2015), which may explain the slower rate of observed changes between 1995 and 2013 as well as the smaller magnitude of seasonal changes in the North Arm. The Landsat and Sentinel results agree well for changes in chlorophyll-a concentration in the North Arm but appear inversed for the South Arm, which may be due to environmental noise or the limitations of the Landsat TM and OLI sensors to observe changes in chlorophyll-a response of the microorganisms present in the South Arm.

Evolution of Halite Crusts

Exposed halite crusts in the North Arm were nonexistent during the highstand following the mid-1980s but started forming or becoming exposed in the early 1990s (Figure 5f). Overall, it appears halite crusts grow in extent as lake levels recede to lowstands (1995, 2004, 2010, 2015, and 2022) and when there is moderate-to-significant annual variations in water surface area (annual redistribution of saline waters to

sediment-pore-spaces). In contrast, the halite crusts appear to shrink during periods of wet seasons or extended exposure. Following a wet season that dissolved most of the halite crusts in 1998, the lake reached a highstand in 2000 then slowly receded where halite crusts subsequently reached a maximum extent of ~163 km^2 in October 2002 and 2003. Following 2003 the extent of halite crusts slowly dropped until another wet year during 2011, which quickly diminished halite extent and was followed by receding lake levels through 2016. Halite crusts grew again in 2013 to extents similar between 2005-2010 but then started shrinking to the lowest extent in roughly 20 years in 2017. Since 2017 halite crusts have been slowly growing again, increasing in size leading up to the lowstand of 2022, but are roughly half the size of crusts observed between 2005-2010 and a quarter of the maximum extent.

Changes in halite crust extent are observed to partially correspond to significant water management changes. In 2012 the western culvert allowing for flow between the South and North Arm was closed and similarly in 2013 the eastern culvert was closed (Figure 3b and 5f). The closure of both culverts led to a drop in lake elevation for the North Arm of greater than 5 ft as the North Arm no longer had any major water input. The rapid drop in lake elevation would have led to exposure of nearshore salt crusts that were previously under water, which is likely responsible for the increase in halite crust area in 2013. Subsequent rain and sheetflow events would have progressively dissolved the exposed lake-bottom halite crust, as seen from 2013 to 2016. In late 2016 a causeway bridge was opened to resume flow into the North Arm, which resulted in a rapid increase in water elevation and dilution of the North Arm water salinity (Jagniecki and others, 2021). The significant decrease in halite extent during the early summer of 2017 is likely due to the mixed contribution of rapid water level increase and the influx of fresher waters. Rapid water level rise, where the lake rose several feet over the course of a few months, would have inundated and/or dissolved nearshore halite crusts, and fresher water influx undersaturated the water with respect to halite leading to halite dissolution. Waters appear to have reached halite saturation by late 2017 into early 2018 as halite crusts reappear (Figure 5e). These observations indicate that water management, specifically managing the flow from the South Arm to the North Arm, has a large impact on halite crust formation processes.

Aside from direct precipitation (meteoric rain and snow), inundation, and water management, mirabilite formation driven by cold temperatures may be partly responsible for the decreases in halite crust extent, specifically for years where the winter months provided little precipitation but the halite extent dropped significantly. Reports have identified that during the colder months mirabilite precipitates from the North Arm water column and effectively lowers the salinity of the water to the point where the water becomes undersaturated with respect to halite (Jagniecki and others, 2021). This process may cause the lake water and sediment-pore-water to dissolve halite crusts along the shoreline during the winter months, even in the absence of precipitation.

Spatial Distribution of Surface Types

Although the time series results provide valuable information regarding the overall evolution of the lake system, the classification map results help understand the distribution of the surface types, which is useful for interpreting the processes responsible for shifts in exposed lakebed composition and cover. The classification results for the North Arm show that during the highstand of the 1980s when lake levels were very high there is little exposed lakebed exposed, but what lakebed is exposed is associated with a significant amount of vegetation (Figure 7a). Following this time, the lake declined rapidly into the 1990s where significant exposed lakebed area appears with sizable halite crusts focused on the northwest sector of the exposed lakebed and much less vegetation (Figure 7b). The halite crusts during this period extend roughly 1-4 km from the shoreline and show a close association to proximal gypsum deposits that are likely underlying much of the halite. Gypsum appears most prevalent in the North Arm during the 1990s but also reappears in similar extent in later years (Figure 7b,c,h). The classification maps from 2002 and 2006 show some of the greatest extents of halite, where the map from 2002 shows halite at its near-maximum extent with crusts on average extending 5 km from the shoreline on the western side (Figure 7d). Additionally, during this period sizable crusts are observed on the eastern side near the location of the Spiral Jetty. Although the lake area in 2011 rebounded to near the 2002 extent, the distribution of halite crusts during and after 2011 is dramatically less and is limited to about 1-2 km from the shoreline (Figure 7f). This suggests that the majority of exposed halite crusts in the North Arm are formed as part of the lake-bottom crust rather than evapoconcentration of saturated sediment-pore-water, and that the lake-bottom crust didn't have suitable time or conditions to grow near the 2002 extent during the highstand of 2011. In 2017 the vegetation in the North Arm is seen to grow dramatically and the water area decreased, along with a thin

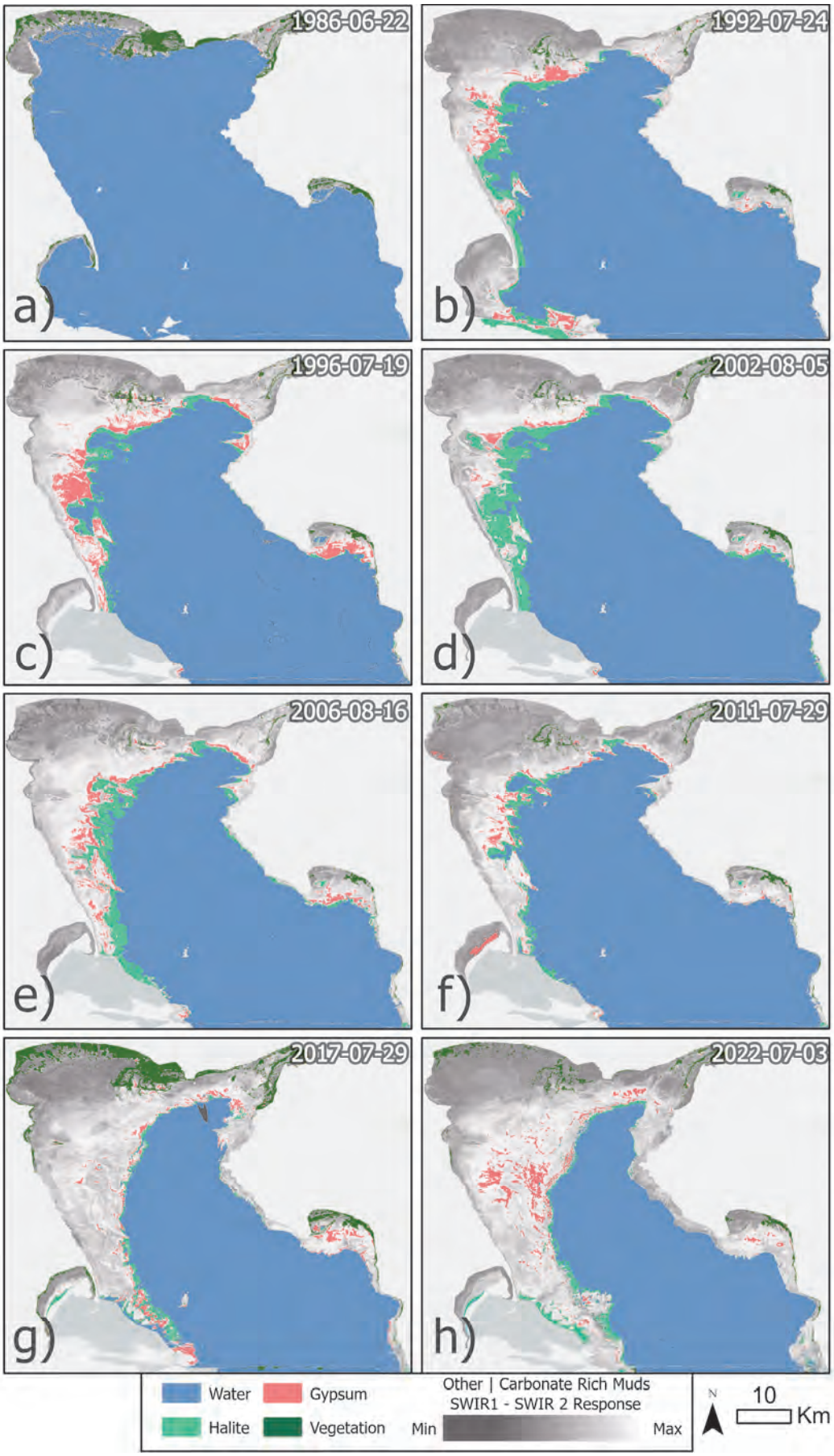

Figure 7. *North Arm classification maps illustrating surface type distributions during 1986 (a), 1992 (b), 1996 (c), 2002 (d), 2006 (e), 2011 (f), 2017 (g), and 2022 (h).*

extent of halite along the western perimeter of the shoreline (Figure 7g). The 2022 classification is similar, with a further decline in water extent but perhaps somewhat more halite distributed about the shoreline as well as on the outside perimeter of the salt ponds to the southwest (Figure 7h). However, the vegetation growth observed in 2017 is absent in 2022 and there is significantly more distributed gypsum to the northwest.

In general, as the water elevation and water area decreased, the halite has been focused around the western side of the North Arm shoreline and crusts have slowly fallen in elevation and extent alongside the lake. It is likely that the shallow slope of the lakebed on the western side of the North Arm has contributed to the greater observed extents of halite crust. A historical halite distribution map, produced by summing all halite images in the North Arm and classifying the image using deciles (ten quantiles), emphasizes the lateral migration of halite crusts through time as the areas where halite crusts repeatedly formed on the western side have much greater values (recurrence of detections) than the surrounding landscape but extend nearly 10-15 km from the modern shoreline (Figure 8). Recent crusts, which rim the water boundary, show up within the lower decile classes, reflecting less recurrent observations of halite in those areas since 1984. Spherical-to-ellipse shaped zones with high pixel values ($\geq 80^{th}$ decile) on the western side may be local lows that promoted halite crust formation through ponding. Although the western side has been the predominant location for halite crust formation, the map shows that halite crusts have formed along the entire shoreline since initial exposure in 1990. Years with the most halite appear to correspond to years where there has been a sustained drop from higher-to-lower water elevations exposing the robust lake-bottom crust and/or where the water elevation is above ~4,194 ft such that the exposed lakebed slope is shallower. When the water levels seasonally fluctuate above ~4,194 ft a broader area of sediments can become saturated with saline waters, which should result in more expansive halite crust formation during the summer months when evapoconcentration of sediment-pore-water can form a thin halite crust on the surface. This effect may explain why recent halite crusts have been much smaller than the crusts observed between ~1995-2013, as the water elevations have been on average below ~4,194 ft and the seasonal water area fluctuations are much less. Alternatively, the opening of the new causeway breach in 2016, which allows for much greater south-to-north flow, could be responsible for the smaller recent crusts, as the waters significantly dropped in salinity and have been slowly recovering. Both seem reasonable explanations that can occur in conjunction, however, it appears lake-bottom crust temporally composes the majority of exposed North Arm halite crust. Thus, the new causeway has likely had a greater impact on recent halite crust formation/exposure than changes to seasonal redistribution of saline waters to sediment-pore-spaces.

In contrast to the North Arm, classification results for the South Arm show a much different distribution of sediment types and vegetation. In 1986 the South Arm was very full (Figure 9a) but decreased significantly into the 1990s, leading to lakebed exposure and the start of vegetation growth in the Farmington Bay region (Figure 9b-c). Relatively little halite is observed in the South Arm during the 1990s except for a small crust and associated gypsum to the south. The 2002 and 2006 classification maps (Figure 9d-e) show the initial decline of Farmington Bay waters and indicate some small halite crusts to the south. In 2006 there is a significant increase in gypsum extent that appears to be linked to the gypsum distributions through 2017 (Figure 9e-g). The 2011 map shows a significant increase in water and vegetation area, but also highlights water detection issues in the shallow and turbid Farmington Bay as some of the water area is classified as carbonate-muds and vegetation (Figure 9f). The maps from 2017 and 2022 (Figure 9g-h) show drastic reductions in water area for the Farmington Bay alongside slight vegetative growth and a somewhat significant halite crust to the south that is roughly 5 km long and 2 km wide. The water elevation and area during 2022 was the lowest ever recorded. The 2022 classification map also shows errors for shallow and turbid water detection as the outer lateral sides of the water in the Farmington Bay (now in a channel) are detected as carbonate-muds (Figure 9h).

CONCLUSIONS

This study processed over 600 reflectance satellite images to better understand the evolution of the water, vegetation, halite, gypsum, and carbonate-mud land cover types in the Great Salt Lake system from 1984 to 2023. The results highlight the magnitude and pace of changes in the system, showing that the exposed lakebed area and halite crust area has responded significantly to lake elevation changes through time. Since 1986-1987 the total lake area has decreased by ~45%, from ~5,700 km^2 to ~2,590 km^2 during the summer months, where the South Arm has decreased in greater extent than the North Arm. Likewise, the exposed lakebed area has increased by ~2,985 km^2 over 36 years and reached an area of over ~3,489 km^2 in 2022. The Bear River Bay followed a natural decline in water area up until ~2000, when the

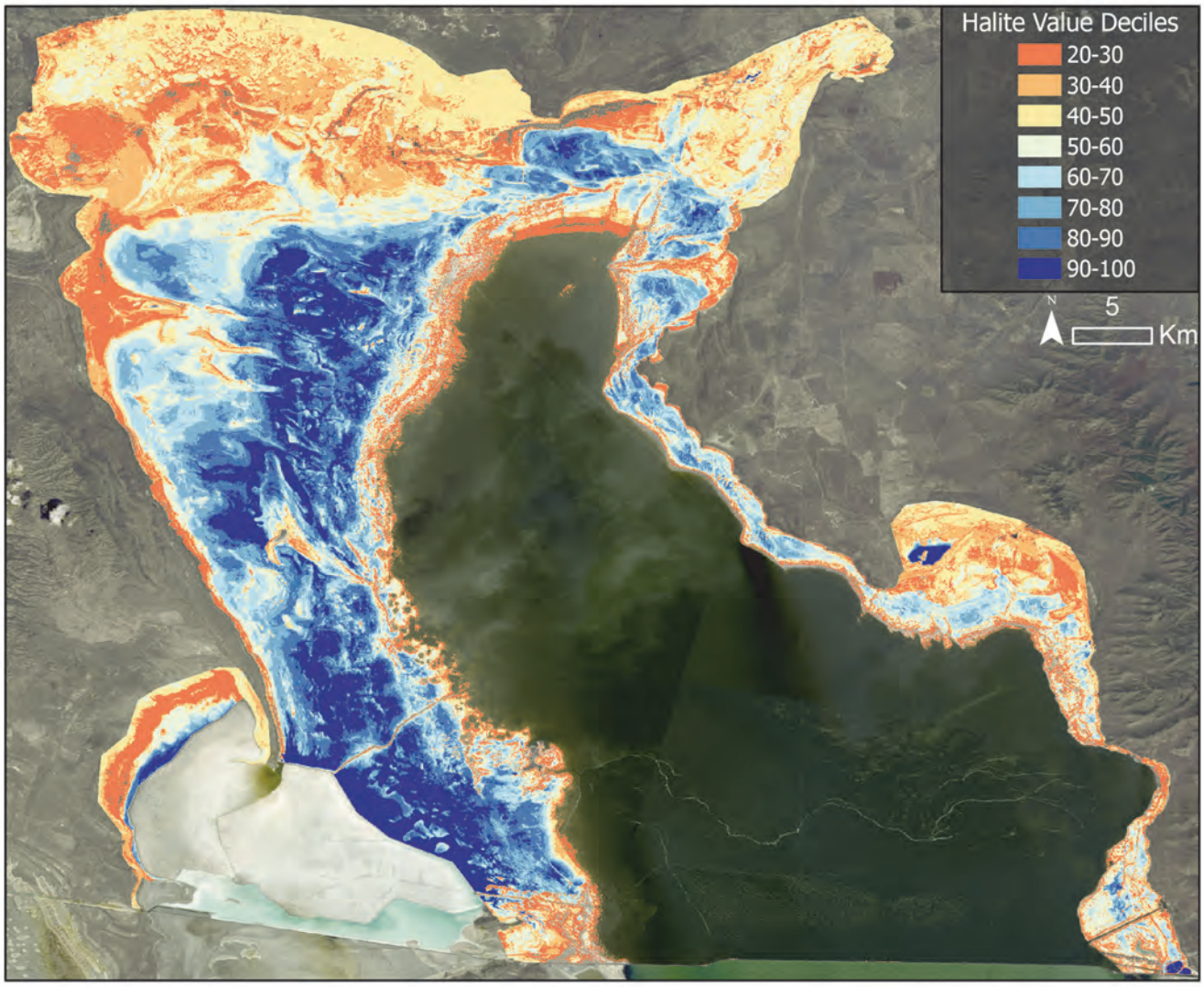

Figure 8. *Decile classification raster produced from the summation of all North Arm halite pixel cells between 1984 and 2023, showing the historical halite distribution and areas with most-or-least recurrent halite crusts. Values are separated into ten quantiles (deciles), where the largest decile indicates the greatest summation of halite values and the most common historical sites of halite formation. Modern halite crust locations, confined near the water boundary, have had significantly fewer recurring observations and are classified in lower deciles. The basemap is Landsat 8 OLI imagery from June 1st (south image) and 2nd (north image).*

water area diverged from the natural evolution to be anthropogenically maintained near an average surface area of ~300 km^2.

The critical elevation of ~4,194 ft, where there is a shift in the topographic slope of the lake-bottom, has a sizable impact on the magnitude of water/exposed lakebed area changes and should be of importance to land-managers and law makers associated with the management of the Great Salt Lake. Above ~4,194 ft the lake responds much more significantly to changes in elevation, such that the water area increases significantly even for small changes in water elevation. This is not only important to maintain a healthy size of the lake but to promote evapoconentrative halite formation in saturated sediment-porewaters, as it appears halite crusts have formed in more distributed amounts when the lake fluctuates in elevation above ~4,194 ft and effectively saturates more sediments with a saline brine. Furthermore, a greater extent of lake waters promotes expanded lake-bottom halite crust formation, which would be exposed when lake levels recede. Years with significant river discharge into the South Arm, which can sometimes be associated to years with lower river water consumption rather than higher amounts of precipitation, are observed to rapidly and significantly increase the water surface area, typically by 500-750 km^2. This suggests that water conservation efforts, that would lead to a greater annual river discharge into the Great Salt Lake, have the potential to significantly increase the surface area of the lake.

Halite crusts are predominantly observed in the North Arm, where the extent of crusts has undergone a complex evolution since the 1980's. The maximum extent of halite occurred between 2002 and 2003 in the North Arm, with crusts extending over 150 km^2.

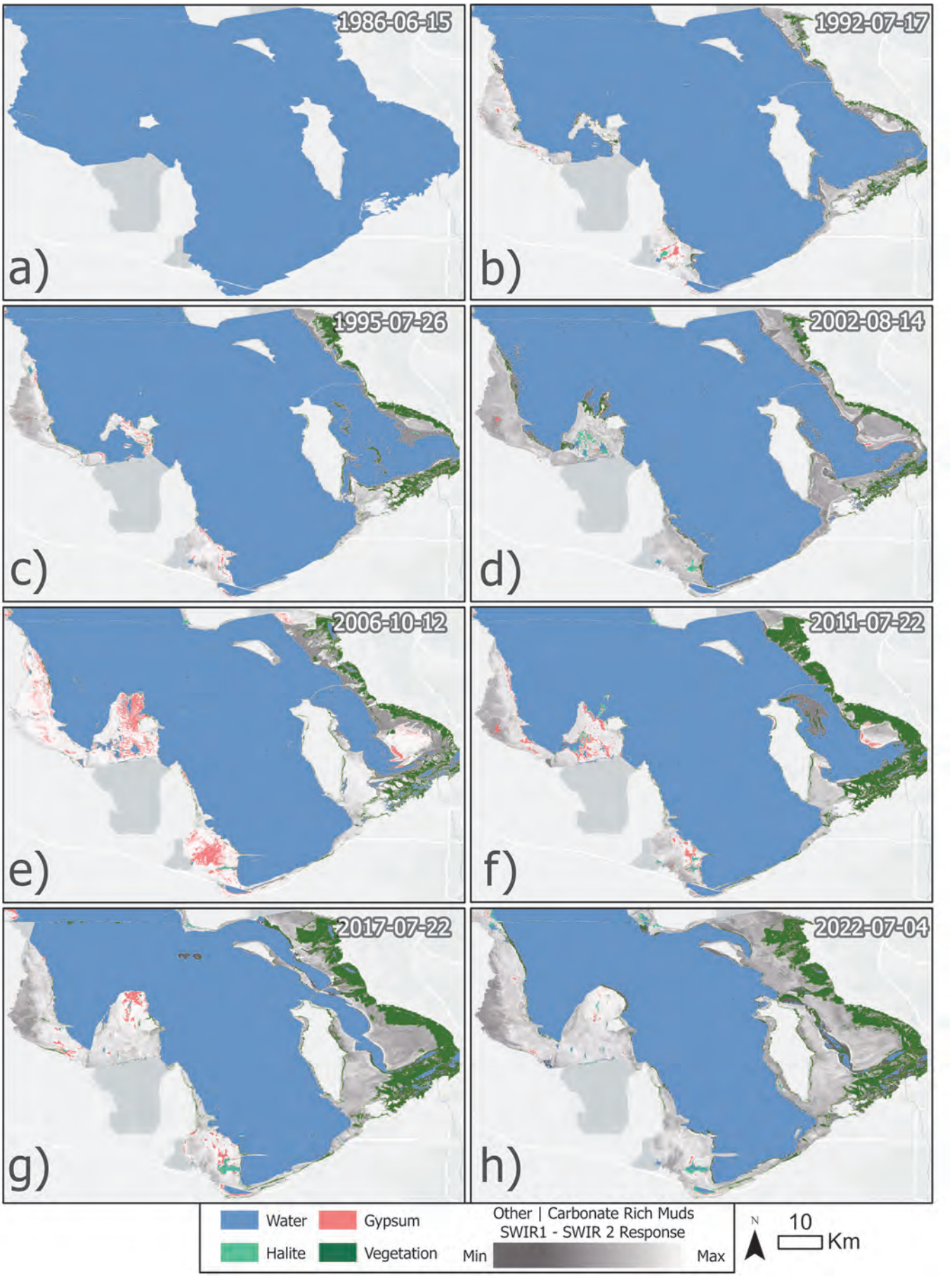

Figure 9. *South Arm classification maps illustrating surface type distributions during 1986 (a), 1992 (b), 1995 (c), 2002 (d), 2006 (e), 2011 (f), 2017 (g), and 2022 (h).*

Since the peak extent halite crusts have significantly shrunk, related to changes in land-use, lake elevation, and annual fluctuations. The most important control over halite extent appears to be associated with the lake-bottom crust formation/accumulation, topography, and magnitude of seasonal fluctuations. Periods of elevated water levels facilitate the restoration and expansion of the lake-bottom halite crust. Subsequent receding water levels then enable the exposure of these crusts. Greater seasonal elevation fluctuations and shallower topography leads to broader sediment saturation and evapoconcentrative halite crust formation. Other important controls that may have impacted the extent and distribution of halite crusts is management of the causeway, where management has affected the salinity and water levels of the North Arm waters. Additionally, results from this study are consistent with recent findings in the North Arm of forced halite dissolution by mirabilite precipitation in cold temperatures, such that there are significant seasonal variations of halite extent even for winters with relatively little precipitation to dissolve the expansive halite crusts.

Overall, remote sensing techniques to monitor the Great Salt Lake system have been established in this study and provide valuable observations that should be used in conjunction with other monitoring campaigns in the future. Future studies should utilize ground truth missions using spectroradiometers and drone surveys to quantify errors using these spectral techniques as well as provide further information on the modern land cover types. Similarly, the use of multispectral and active-radar satellites in future studies may help differentiate vegetation types in the Great Salt Lake system.

SUPPLEMENTAL DATA

The results of the analyses, including supplemental data such as a list of outlier images not used for analyses and the NDWI thresholds for each Landsat image, as well as satellite imagery based videos animating the evolution of the lake, are stored on an online database: https://doi.org/10.5281/zenodo.7996314 or https://zenodo.org/record/7996314

Code utilized in this study for data retrieval and modelling can be found on GitHub: https://github.com/radwinskis/Great-Salt-Lake-2023-Study-Code

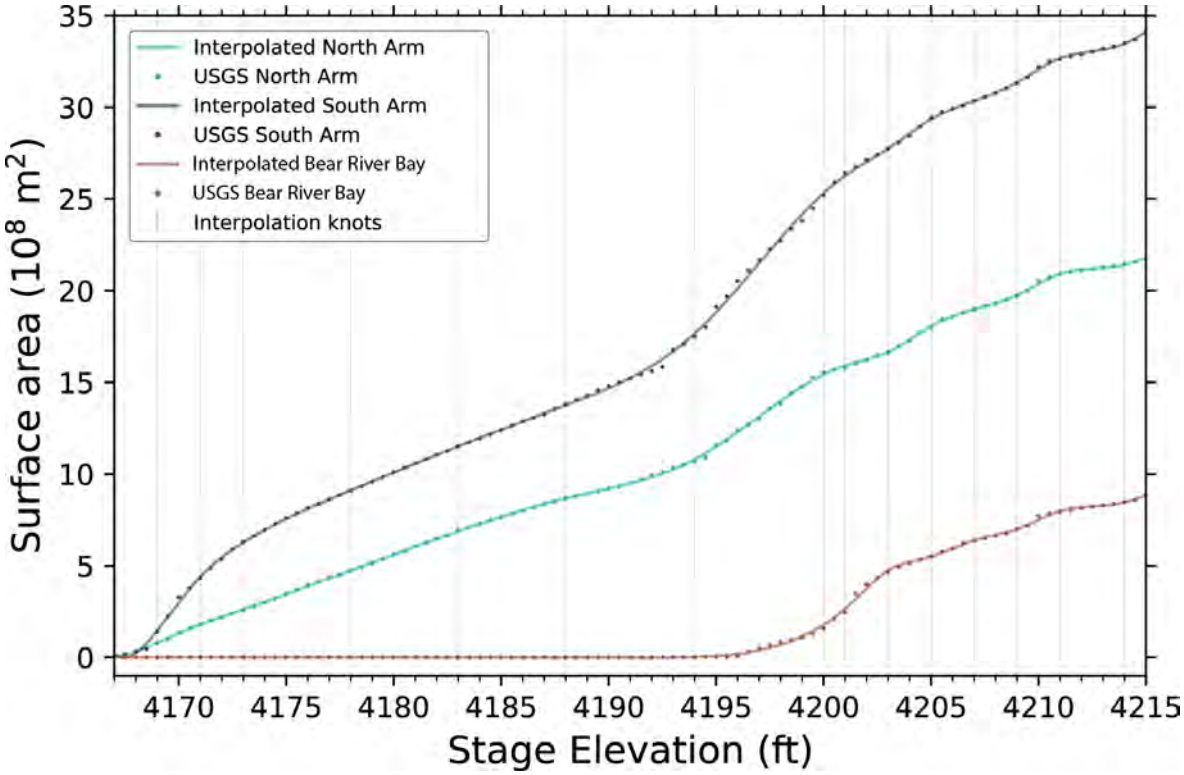

Figure S1. *Hypsometric data and curves for the North Arm, South Arm, and Bear River Bay as shown by published USGS data (dots) and interpolations of the USGS data (solid lines), illustrating the changes in surface area compared to changes in elevation, which is related to the topography of the lake-bottom. The ~4,194 ft threshold is easily seen where the slope of the lines change between 4190 and 4200 ft. From ~4,195 to ~4,201 ft the slope is much steeper, which indicates between these elevations the topography is much shallower. The interpolated lines are formed using 15 breakpoints shown as gray vertical lines. The data and interpolations show to fit very well, supporting the use of interpolation to model lake surface area.*

REFERENCES

Ahmadi, L., Albers, E., Bingham, B., Brooks, P., Endter-Wada, J., Hasenyager, C., Lin, J., McEntire, A., Neilson, B., Null, S., Perry, K., Stireman, B., Strong, C., Vernon, L., and others, 2023, Great Salt lake policy assessment – a synthesized resource document for the 2023 General Legislative Session: Great Salt Lake Strike Team Great Salt Lake Policy Assessment.

Almeida-Dalmet, S., Sikaroodi, M., Gillevet, P., Litchfield, C., and Baxter, B., 2015, Temporal study of the microbial diversity of the north arm of Great Salt Lake, Utah, U.S.: Microorganisms, v. 3, no. 3, p. 310–326 (doi: 10.3390/microorganisms3030310).

Amani, M., Ghorbanian, A., Ahmadi, S.A., Kakooei, M., Moghimi, A., Mirmazloumi, S.M., Moghaddam, S.H.A., Mahdavi, S., Ghahremanloo, M., Parsian, S., Wu, Q., and Brisco, B., 2020, Google Earth engine cloud computing platform for remote sensing big data applications – a comprehensive review: IEEE Journal of Selected Topics in Applied Earth Observations and Remote Sensing, v. 13, p. 5326–5350 (doi: 10.1109/JSTARS.2020.3021052).

Arnow, T., 1984, Water-level and water-quality changes in Great Salt Lake Utah, 1847-1983: U.S. Geological Survey Circular 913, 22 p.

Baskin, R.L., 2005, Calculation of area and volume for the south part of Great Salt Lake, Utah: U.S. Geological Survey Open-File Report 2005-1327.

Baskin, R.L., 2006, Calculation of area and volume for the north part of Great Salt Lake, Utah: U.S. Geological Survey Open-File Report 2006-1359.

Baxter, B.K., 2018, Great Salt Lake microbiology: a historical perspective: International Microbiology, v. 21, no. 3, p. 79–95 (doi: 10.1007/s10123-018-0008-z).

Bowen, B.B., Kipnis, E.L., and Raming, L.W., 2017, Temporal dynamics of flooding, evaporation, and desiccation cycles and observations of salt crust area change at the Bonneville Salt Flats, Utah: Geomorphology, v. 299, p. 1–11 (doi: 10.1016/j.geomorph.2017.09.036).

Bradt, S., Wurtsbaugh, W.A., Naftz, D., Moore, T., and Haney, J., 2006, Remote sensing as a tool to track algal blooms in the Great Salt Lake, Utah, USA [abs.]: American Geophysical Union Fall Meeting Abstracts, abstract H52A-04.

Bucher, E.H., and Stein, A.F., 2016, Large salt dust storms follow a 30-year rainfall cycle in the Mar Chiquita Lake (Córdoba, Argentina): PLOS ONE, v. 11, no. 6, p. e0156672 (doi: 10.1371/journal.pone.0156672).

Buma, W.G., and Lee, S.-I., 2020, Evaluation of Sentinel-2 and Landsat 8 images for estimating chlorophyll-a concentrations in Lake Chad, Africa: Remote Sensing, v. 12, no. 15, p. 2437 (doi: 10.3390/rs12152437).

Carling, G.T., Fernandez, D.P., Rey, K.A., Hale, C.A., Goodman, M.M., and Nelson, S.T., 2020, Using strontium isotopes to trace dust from a drying Great Salt Lake to adjacent urban areas and mountain snowpack: Environmental Research Letters, v. 15, no. 11, p. 114035 (doi: 10.1088/1748-9326/abbfc4).

Crosman, E.T., and Horel, J.D., 2009, MODIS-derived surface temperature of the Great Salt Lake: Remote Sensing of Environment, v. 113, no. 1, p. 73–81 (doi: 10.1016/j.rse.2008.08.013).

Drusch, M., Del Bello, U., Carlier, S., Colin, O., Fernandez, V., Gascon, F., Hoersch, B., Isola, C., Laberinti, P., Martimort, P., Meygret, A., Spoto, F., Sy, O., Marchese, F., and Bargellini, P., 2012, Sentinel-2 – ESA's optical high-resolution mission for GMES Operational Services: Remote Sensing of Environment, v. 120, p. 25–36 (doi: 10.1016/j.rse.2011.11.026).

Dunham, E.C., Fones, E.M., Fang, Y., Lindsay, M.R., Steuer, C., Fox, N., Willis, M., Walsh, A., Colman, D.R., Baxter, B.K., Lageson, D., Mogk, D., Rupke, A., Xu, H., and others, 2020, An ecological perspective on dolomite formation in Great Salt Lake, Utah: Frontiers in Earth Science, v. 8, p. 24 (doi: 10.3389/feart.2020.00024).

Foga, S., Scaramuzza, P.L., Guo, S., Zhu, Z., Dilley, R.D., Beckmann, T., Schmidt, G.L., Dwyer, J.L., Joseph Hughes, M., and Laue, B., 2017, Cloud detection algorithm comparison and validation for operational Landsat data products: Remote Sensing of Environment, v. 194, p. 379–390 (doi: 10.1016/j.rse.2017.03.026).

Gandhi, G.M., Parthiban, S., Thummalu, N., and Christy, A., 2015, Ndvi: Vegetation change detection using remote sensing and gis – a case study of Vellore District: Procedia Computer Science, v. 57, p. 1199–1210 (doi: 10.1016/j.procs.2015.07.415).

Gitelson, A.A., Gritz, Y., and Merzlyak, M.N., 2003, Relationships between leaf chlorophyll content and spectral reflectance and algorithms for non-destructive chlorophyll assessment in higher plant leaves: Journal of Plant Physiology, v. 160, no. 3, p. 271–282 (doi: 10.1078/0176-1617-00887).

Gwynn, J.W., 2007, Great Salt Lake brine chemistry databases and reports 1966-2006: Utah Geological Survey Open-File Report 485, 22p.

Hahnenberger, M., and Nicoll, K., 2012, Meteorological characteristics of dust storm events in the

eastern Great Basin of Utah, U.S.A.: Atmospheric Environment, v. 60, p. 601–612 (doi: 10.1016/j.atmosenv.2012.06.029).

Hahnenberger, M., and Nicoll, K., 2014, Geomorphic and land cover identification of dust sources in the eastern Great Basin of Utah, U.S.A.: Geomorphology, v. 204, p. 657–672 (doi: 10.1016/j.geomorph.2013.09.013).

Hall, D.K., O'Leary, D.S., DiGirolamo, N.E., Miller, W., and Kang, D.H., 2021, The role of declining snow cover in the desiccation of the Great Salt Lake, Utah, using MODIS data: Remote Sensing of Environment, v. 252, no. 4, p. 112106 (doi: 10.1016/j.rse.2020.112106).

Hansen, C.H., Dennison, P., Burian, S., Barber, M., and Williams, G., 2016, Hindcasting water quality in an optically complex system, *in* Proceedings of the 13th International Conference on Modelling, Monitoring and Management of Water Pollution (WP 2016), Venice, Italy, p. 35–44 (doi: 10.2495/WP160041).

Hardie, L.A., and Eugster, H.P., 1970, The evolution of closed-basin brines: Mineralogical Society of America Special Paper 3, p. 273–290.

Homewood, P., Mettraux, M., Vanden Berg, M., Foubert, A., Neumann, R., Newell, D., and Atwood, G., 2022, Onshore groundwater spring carbonate mounds to lacustrine microbialites, the perplexing record of a transitional Great Salt Lake carbonate shoreline at Lakeside, Utah: The Depositional Record, v. 8, no. 1, p. 9–38 (doi: 10.1002/dep2.148).

Huang, S., Tang, L., Hupy, J.P., Wang, Y., and Shao, G., 2021, A commentary review on the use of normalized difference vegetation index (NDVI) in the era of popular remote sensing: Journal of Forestry Research, v. 32, no. 1, p. 1–6 (doi: 10.1007/s11676-020-01155-1).

Hung, M.C., and Wu, Y.H., 2005, Mapping and visualizing the Great Salt Lake landscape dynamics using multi-temporal satellite images, 1972-1996: International Journal of Remote Sensing, v. 26, no. 9, p. 1815–1834 (doi: 10.1080/0143116042000298324).

Ingalls, M., Frantz, C.M., Snell, K.E., and Trower, E.J., 2020, Carbonate facies-specific stable isotope data record climate, hydrology, and microbial communities in Great Salt Lake, UT: Geobiology, v. 18, no. 5, p. 566–593 (doi: 10.1111/gbi.12386).

Jagniecki, E., Rupke, A., Kirby, S., and Inkenbrandt, P., 2021, Salt crust, brine, and marginal groundwater of Great Salt Lake's North Arm (2019 To 2021): Utah Geological Survey Report of Investigation 283, 40 p. (doi: 10.34191/RI-283).

Ji, L., Zhang, L., and Wylie, B., 2009, Analysis of dynamic thresholds for the normalized difference water index: Photogrammetric Engineering & Remote Sensing, no. 75, p. 1307–1317 (doi: 10.14358/PERS.75.11.1307).

Kokaly, R., Clark, R., Swayze, G., Livo, K.E., Hoefen, T., Pearson, N., Wise, R., Benzel, W., Lowers, H., Driscoll, R., and Klein, A., 2017, USGS Spectral Library Version 7: U.S. Geological Survey Data Series 1035, 61 p. (doi: 10.3133/ds1035).

Kulmatiski, A., Beard, K.H., Meyerson, L.A., Gibson, J.R., and Mock, K.E., 2011, Nonnative *Phragmites australis* invasion into Utah wetlands: Western North American Naturalist, v. 70, no. 4, p. 541-552 (doi: 10.3398/064.070.0414).

Lines, G.C., 1979, Hydrology and surface morphology of the Bonneville Salt Flats and Pilot Valley playa, Utah: U.S. Geological Survey Water-Supply Paper 2057, 107 p. (doi: 10.3133/wsp2057).

McFeeters, S.K., 1996, The use of the Normalized Difference Water Index (NDWI) in the delineation of open water features: International Journal of Remote Sensing, v. 17, no. 7, p. 1426–1432 (doi: 10.1080/01431169608948714).

Mohammed, I.N., and Tarboton, D.G., 2012, An examination of the sensitivity of the Great Salt Lake to changes in inputs: Water Resources Research, v. 48, no. 11, 17 p. (doi: 10.1029/2012WR011908).

Naftz, D., Angeroth, C., Freeman, M., Rowland, R., and Carling, G., 2013, Monitoring change in Great Salt Lake: Eos, Transactions American Geophysical Union, v. 94, no. 33, p. 289–290 (doi: 10.1002/2013EO330001).

Newell, D.L., Jensen, J.L., Frantz, C.M., and Vanden Berg, M.D., 2017, Great Salt Lake (Utah) microbialite $\delta^{13}C$, $\delta^{18}O$, and $\delta^{15}N$ record fluctuations in lake biogeochemistry since the Late Pleistocene: Geochemistry, Geophysics, Geosystems, v. 18, no. 10, p. 3631–3645 (doi: 10.1002/2017GC007078).

Nicoll, K., Hahnenberger, M., and Goldstein, H.L., 2020, 'Dust in the wind' from source-to-sink – analysis of the 14-15 April 2015 storm in Utah: Aeolian Research, v. 46, p. 100532 (doi: 10.1016/j.aeolia.2019.06.002).

Null, S.E., and Wurtsbaugh, W.A., 2020, Water development, consumptive water uses, and the Great Salt Lake *in* Baxter, B.K. and Butler, J.K., editors, Great Salt Lake biology: A terminal lake in a time of change: Cham, Switzerland, Springer, p. 1–21 (doi: https://doi.org/10.1007/978-3-030-40352-2).

Otsu, N., 1979, A threshold selection method from

gray-level histograms: IEEE Transactions on Systems, Man, and Cybernetics, v. 9, no. 1, p. 62–66.,

Pace, A., Bourillot, R., Bouton, A., Vennin, E., Galaup, S., Bundeleva, I., Patrier, P., Dupraz, C., Thomazo, C., Sansjofre, P., Yokoyama, Y., Franceschi, M., Anguy, Y., Pigot, L., Virgone, A, and Visscher, P.T., 2016, Microbial and diagenetic steps leading to the mineralisation of Great Salt Lake microbialites: Scientific Reports, v. 6, no. 1, p. 31495 (doi: 10.1038/srep31495).

Perry, K., Crosman, E.T., and Hoch, S., 2019, Results of the Great Salt Lake dust plume study (2016-2018): University of Utah, Department of Atmospheric Sciences, 305 p.

Radwin, M., and Bowen, B.B., 2021, Mapping mineralogy in evaporite basins through time using multispectral Landsat Data: examples from the Bonneville Basin, Utah, USA: Earth Surface Processes and Landforms., v. 46, no. 6, p. 1160-1176 (doi: 10.1002/esp.5089).

Reynolds, R.L., Yount, J.C., Reheis, M., Goldstein, H., Chavez, P., Fulton, R., Whitney, J., Fuller, C., and Forester, R.M., 2007, Dust emission from wet and dry playas in the Mojave Desert, USA: Earth Surface Processes and Landforms, v. 32, no. 12, p. 1811–1827 (doi: 10.1002/esp.1515).

Roney, H.C., Booth, G.M., and Cox, P.A., 2009, Competitive exclusion of cyanobacterial species in the Great Salt Lake: Extremophiles, v. 13, no. 2, p. 355–361 (doi: 10.1007/s00792-008-0223-1).

Rupke, A., and Boden, T., 2020, Great Salt Lake north arm salt crust monitoring, spring 2017 update: Utah Geological Survey Open-File Report 714, 13 p. (doi: 10.34191/OFR-714).

Rupke, A., Boden, T., and Nielsen, P., 2016, Great Salt Lake's north arm salt crust: Utah Geological Survey Report of Investigation 276, 40 p. (doi: 10.34191/RI-276).

Rupke, A., and McDonald, A., 2012, Great Salt Lake brine chemistry database, 1966-2011: Utah Geological Survey Open-File Report 596 (doi: 10.34191/OFR-596).

Skiles, S.M.K., Mallia, D.V., Hallar, A.G., Lin, J.C., Lambert, A., Petersen, R., and Clark, S., 2018, Implications of a shrinking Great Salt Lake for dust on snow deposition in the Wasatch Mountains, UT, as informed by a source to sink case study from the 13-14 April 2017 dust event: Environmental Research Letters, v. 13, no. 12 (doi: 10.1088/1748-9326/aaefd8).

Smith, B.P., Ingalls, M., Trower, E.J., Lingappa, U.F., Present, T.M., Magyar, J.S., and Fischer, W.W., 2020, Physical controls on carbonate intraclasts – modern flat pebbles from Great Salt Lake, Utah: Journal of Geophysical Research: Earth Surface, v. 125, no. 11 (doi: 10.1029/2020JF005733).

Tamiminia, H., Salehi, B., Mahdianpari, M., Quackenbush, L., Adeli, S., and Brisco, B., 2020, Google Earth Engine for geo-big data applications – a meta-analysis and systematic review: ISPRS Journal of Photogrammetry and Remote Sensing, v. 164, p. 152–170 (doi: 10.1016/j.isprsjprs.2020.04.001).

Tiede, D., Sudmanns, M., Augustin, H., and Baraldi, A., 2021, Investigating ESA Sentinel-2 products' systematic cloud cover overestimation in very high altitude areas: Remote Sensing of Environment, v. 252, p. 112163 (doi: 10.1016/j.rse.2020.112163).

Wang, S.-Y., Gillies, R.R., and Reichler, T., 2012, Multidecadal drought cycles in the Great Basin recorded by the Great Salt Lake – modulation from a transition-phase teleconnection: Journal of Climate, v. 25, no. 5, p. 1711–1721 (doi: 10.1175/2011JCLI4225.1).

Weimer, B.C., Rompato, G., Parnell, J., Gann, R., Ganesan, B., Navas, C., Gonzalez, M., Clavel, M., and Albee-Scott, S., 2009, Microbial biodiversity of Great Salt Lake, Utah: Natural Resources and Environmental Issues, v. 15, Article 3.

Wine, M.L., Null, S.E., DeRose, R.J., and Wurtsbaugh, W.A., 2019, Climatization—negligent attribution of Great Salt Lake desiccation – a comment on Meng (2019): Climate, v. 7, no. 5, p. 67 (doi: 10.3390/cli7050067).

Wu, Q., 2020, geemap: A Python package for interactive mapping with Google Earth Engine: Journal of Open Source Software, v. 5, no. 51, p. 2305 (doi: 10.21105/joss.02305).

Wurtsbaugh, W.A., Miller, C., Null, S.E., DeRose, R.J., Wilcock, P., Hahnenberger, M., Howe, F., and Moore, J., 2017, Decline of the world's saline lakes: Nature Geoscience, v. 10, no. 11, p. 816–821 (doi: 10.1038/ngeo3052).

Wurtsbaugh, W., Miller, C., Null, S., Wilcock, P., Hahnenberger, M., and Howe, F., 2016, Impacts of water development on Great Salt Lake an d the Wasatch Front: Utah State University, Watershed Sciences Faculty Publications, Paper 875, 9 p.

Wurtsbaugh, W.A., and Sima, S., 2022, Contrasting Management and Fates of Two Sister Lakes – Great Salt Lake (USA) and Lake Urmia (Iran): Water, v. 14, no. 19, p. 23 (doi: https://doi.org/10.3390/w14193005).

Record Low Water-Surface Elevations at Great Salt Lake, Utah, 2021–2022

Ryan C. Rowland and Mike L. Freeman
U.S. Geological Survey, Utah Water Science Center, West Valley City, Utah, rrowland@usgs.gov

10.31711/ugap.v51i.135

ABSTRACT

The United States Geological Survey (USGS) operates two long-term water-surface elevation (WSE) gages on Great Salt Lake, Utah, one north of the Union Pacific Railroad causeway in the historic Little Valley Boat Harbor (Saline gage), and one south of the causeway in the harbor at Great Salt Lake State Park (Saltair gage). From September 28 to December 15, 2022, lake levels were too low in the harbor for the Saltair gage to operate and WSE data was measured at the South Causeway gage, a relatively new gaging station (installed in 2020) located immediately south of the causeway. Data collected at the South Causeway gage were used to estimate the daily mean WSE record for the Saltair gage for the period it was shut down, preserving the continuity of the 175-year WSE record that is associated with this gage. The long-standing historic low daily mean WSE measured at the Saltair gage on October 15, 1963 (4,191.35 feet, relative to the National Geodetic Vertical Datum of 1929 (NGVD29)) was broken on July 21, 2021. Seasonal lake-level declines from July 2021 to October 2021 and April 2022 to early November 2022 resulted in a new historic low daily mean WSE of 4,188.5 feet NGVD29, measured during several days during November 2022 at the South Causeway gage. The same value is also the new historic low daily mean WSE for the Saline gage and was measured during several days in November and December 2022 (the previous historic low of 4,188.98 feet NGVD29 was measured in September and October 2016 and was related to closure of two railroad causeway culverts). USGS also operates streamgages on major surface-water inflows including the Bear River, Weber River, Jordan River, and Surplus Canal. The combined annual discharge measured at these gages in water years 2021 and 2022 was 0.704 and 0.743 million acre-feet, respectively, which is less than half of the combined median annual discharge (1.57 million acre-feet) based on the period of record for each gage.

INTRODUCTION

The United States Geological Survey (USGS), in cooperation with the Utah Department of Natural Resources, operates two long-term water-surface elevation (WSE) gages on Great Salt Lake (GSL), Utah (figure 1). USGS station 10010000 Great Salt Lake at Saltair Boat Harbor, UT (Saltair gage) (U.S. Geological Survey, 2023), is located about 35 miles south of the Union Pacific Railroad Causeway (referred to as the causeway in the rest of this document) in the harbor at GSL State Park. This gage is associated with a WSE data record dating back to 1847. The record from 1847 to 1874 was compiled by Grove Karl Gilbert, first Chief Geologist of the USGS, and is based on oral reports from stockmen who had ridden horses across sandbars to reach Antelope and Stansbury Islands (Gilbert, 1890; Arnow and Stephens, 1990). The accuracy of the early measurements does not compare to those made with modern methods (for example, Arnow and Stephens (1990) state that water levels from 1847 to 1874 should be considered accurate only to within 1 foot (ft)); however, this does not detract from the scientific value of those early observations.

Systematic lake level measurements at GSL began in 1875 as described by Gilbert (1890):

> *"In the year 1875, Dr. John R. Park, of Salt Lake City, at the suggestion of Prof. Joseph Henry of the Smithsonian Institution and with the cooperation of other citizens, instituted a series of observations. There was erected at the water's edge at Black Rock a granite block cut in the form of an obelisk and engraved on one side with a scale of feet and inches; and Mr. John T. Mitchell was engaged to observe the water-height at intervals of a few days."*

From 1875 to 1938, the lake level was measured at staff gages by many different individuals and organizations at variable intervals ranging from weekly to monthly. Since 1939, lake levels associated with the Saltair gage have been measured continuously with various recorder devices operated by the USGS. The Saltair gage has been moved several times within GSL State Park because of storm damage, rebuilding of the harbor dikes, high lake levels, and low lake levels. From September 28 to December 15, 2022, lake levels were too low in the harbor for the Saltair gage to operate. During this period, WSEs south of the causeway were obtained from USGS station

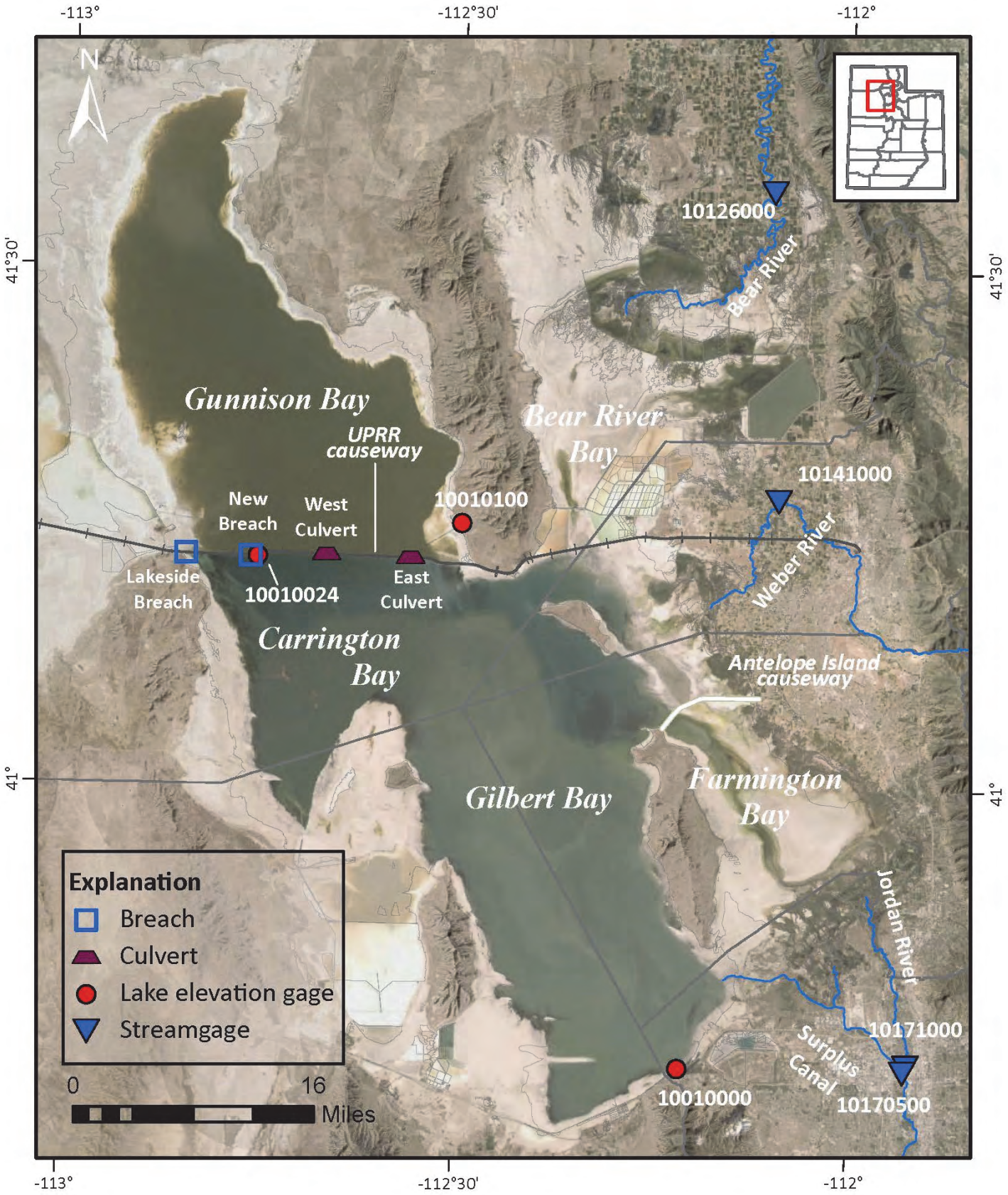

Figure 1. *Locations of selected United States Geological Survey gaging stations (U.S. Geological Survey, 2023) at and near Great Salt Lake, Utah. Base from Maxar Imagery digital data, various scales, 2019-2022. Universal Transverse Mercator projection, zone 12 N, North American Datum of 1983.*

10010024 GSL South Side of Causeway, 6 Miles East of Lakeside, Utah (referred to as the South Causeway gage in the rest of this document) (U.S. Geological Survey, 2023), a relatively new gage installed in 2020.

The second long-term WSE gage is USGS station 10010100 Great Salt Lake near Saline, UT (Saline gage) (U.S. Geological Survey, 2023), is in the historic Little Valley Boat Harbor on the west side of Promontory Point, about 2.7 miles north of the causeway. This gage was installed in 1966, about 7 years after the causeway was completed (figure 1). Water-surface elevations at this gage have been measured continuously with various recorder devices operated by the USGS. It has only been moved once within the harbor (in May 1996) so that the pier it was mounted to could be removed by the owner.

The USGS also operates four long-term streamgages on major surface-water inflow sources to the south part of GSL (collectively referred to as inflow gages in this document). While these gages do not measure all surface-water inflows to GSL (there are several unmeasured surface-water inflows), and also unmeasured losses or gains of water between the gages and GSL, they provide important insight into GSL WSE changes over time. These inflow gages are USGS stations 10126000 Bear River near Corinne, UT (Bear River gage); 10141000 Weber River near Plain City, UT (Weber River gage); 10171000 Jordan River at 1700 South at Salt Lake City, UT (Jordan River gage); and 10170500 Surplus Canal at Salt Lake City, UT (Surplus Canal gage) (U.S. Geological Survey. 2023) (figure 1). The Weber River gage is among the 10 oldest streamgages in Utah and has been active since October 1907, with some discrete-discharge measurements starting in 1904. The other inflow gages were installed in the 1940s.

The primary objective of this document is to summarize selected data from the locations listed above through November 2022, which includes the lowest daily mean WSE measured at GSL. This document 1) reports how record low WSEs at GSL were measured and validated; 2) summarizes extended periods of WSE and inflow gage data; 3) compares WSEs to inflow gage data; and 4) compares WSE and inflow gage data to a standardized measure of drought severity in Utah.

The locations of USGS monitoring stations discussed in this document are shown in figure 1 and a summary of parameters used in this document, including the period of record associated with each parameter, are summarized in table 1. Data summarized in table 1 are available via the USGS National Water Information System (NWIS) (U.S. Geological Survey, 2023).

Table 1. *U.S. Geological Survey (USGS) station name, number, and available period of record for data used in this report. Data are available via the USGS National Water Information System (U.S. Geological Survey, 2023).*

Station Name	Station Number	Parameter and units	Available Period of Record
Great Salt Lake at Saltair Boat Harbor, Utah	10010000	Daily and annual mean water-surface elevation above National Geodetic Vertical Datum of 1929, in feet	10/15/1847 to current
Great Salt Lake near Saline, Utah	10010100	Daily and annual mean water-surface elevation above National Geodetic Vertical Datum of 1929, in feet	4/15/1966 to current
Great Salt Lake South Side of Causeway, 6 Miles East of Lakeside, Utah	10010024	Daily mean water- surface elevation above National Geodetic Vertical Datum of 1929, in feet	2/25/2020 to current
Bear River near Corinne, Utah	10126000	Daily and monthly mean discharge, in cubic feet per second	10/1/1949 to 9/29/1957 and 10/1/1963 to current (No data 9/30/1957 to 9/30/1963)
Weber River near Plain City, Utah	10141000	Daily and monthly mean discharge, in cubic feet per second	10/1/1907 to current
Jordan River at 1700 South at Salt Lake City, Utah	10171000	Daily and monthly mean discharge, in cubic feet per second	12/1/1942 to current
Surplus Canal at Salt Lake City, Utah	10170500	Daily and monthly mean discharge, in cubic feet per second	12/1/1942 to current

DESCRIPTION OF STUDY AREA

Great Salt Lake is a closed-basin lake bordered on the west by desert and on the east by the Wasatch Range. Its abundant food and wetlands attract nearly 2 million shorebirds, including over 1.5 million grebes (Podiscipedidae) and several million migrating waterfowl (Wurstbaugh and others, 2017). Construction of a rock-fill causeway across GSL in 1959 created two separate but connected parts of the lake with different WSEs, salinities, and densities resulting from more than 95 percent of all freshwater surface inflow entering the lake south of the causeway (Loving and others, 2000). The differences between the WSEs and densities of the south and north parts of GSL provide the potential for water (GSL water is technically brine because it contains more than 35,000 milligrams per liter of dissolved solids; however, for simplicity, the term water is used in this document) to flow in both directions through the causeway conveyances. Generally, the less-dense water from the south part flows northward through the upper part of the causeway conveyances (breaches and causeway fill) and the more-dense water from the north part flows southward through the lower part of the causeway conveyances (Loving and others, 2000). Currently, the means of conveyance include the following: a 290 ft wide breach (often referred to as the Lakeside breach) near the west end of the causeway that was completed in 1984 with a bottom elevation of 4,200 ft that was lowered to 4,193 ft relative to the National Geodetic Vertical Datum of 1929 (NGVD29) in 2000; a relatively new 150 ft wide breach about 4.5 miles from the west end of the causeway that was opened on December 1, 2016, with an adjustable berm that has a current top elevation of 4,192 ft NGVD29; and the permeability of the rock-fill material used to construct the causeway. The 150 ft wide breach completed in 2016 replaced two culverts, referred to as the east and the west culverts, that were in service from causeway completion in 1959 until closure in November 2012 (east culvert) and December 2013 (west culvert).

METHODS

Measurement of Water-Surface Elevation

Gaging stations located on GSL are used to measure WSE. The measurement of WSE at GSL follows USGS protocols outlined in Sauer and Turnipseed (2010) which details the measurement of stage. In summary, each gaging station has a network of reference points and reference marks. These reference locations are surveyed, using a variety of techniques, to establish an elevation relative to an assigned datum. Once an elevation is assigned to these reference locations, a nonrecording reference gage can be established at the gaging station. The reference gage is used to physically measure the WSE of GSL. Once the WSE is measured using the reference gage, a recording water-level instrument can be set up to measure the WSE at a set interval relative to the reference gage WSE reading. Currently, WSE recorders for GSL are set up to measure every 15 minutes. Gaging stations are visited every 1–2 months to read the WSE from the reference gage and compare those readings with the WSE recorder. If a difference is observed between the reference and recorded values because of instrument drift, a correction is applied to the recorded data so that the WSE is accurately reported. Daily and annual mean WSEs discussed in this report are available via NWIS (U.S. Geological Survey, 2023).

Water-Surface Elevation Reported Datum

Reference marks, reference gages and recording gages are all referenced to NGVD29. NGVD29 is similar in elevation to dynamic heights reported by the National Geodetic Survey (NGS). Dynamic height values are defined by an equipotential surface allowing for accurate representation of hydrologic gradient when measuring WSEs over a large geographic area (Meyer and others, 2006). The reporting of vertical datums using dynamic heights to accurately measure water gradients is best documented in the establishment of the International Great Lakes Datum of 1985 (Meyer and others, 2006). The equipotential surface applied to dynamic heights provides a WSE that flows downhill as expected. Dynamic heights for the GSL region are most accurately reported when referencing WSE to NGVD29. In contrast, the more commonly used North American Vertical Datum 1988 (NAVD88) is influenced by gravitational models that can cause WSEs that suggest water flowing in an upstream direction when a downstream gradient is known and expected. Because of the causeway and the dividing of GSL, it is important to accurately represent hydraulic gradient across the causeway and, therefore, elevation should always be reported with respect to an equipotential surface so that hydraulic gradient can accurately be measured.

To accurately report WSEs of GSL, the stability of the gaging station's reference to NGVD29 is verified using a variety of survey methods. The survey method used to verify vertical datum is determined by the location of the three lake gaging stations. The Saltair and South Causeway gaging stations are located on earthen-fill material and have shown vertical

movement in previous years related to the rising and falling WSE of the GSL. As WSE of GSL increases, the earthen material rises with increasing water level, whereas when the WSE of the GSL decreases the earthen material subsides within the lake substrate. To maintain accurate reporting of WSE at these locations, the two sites are surveyed at the peak and the trough of the annual hydrograph. By surveying at the peak and the trough, WSE data are corrected based on the annual fluctuations of GSL. In contrast, the Saline gage has demonstrated vertical stability and is surveyed annually to ensure the gage is reporting WSE accurately. Because of the complex surveying techniques required to verify vertical datum at GSL gaging stations, WSE reported by the USGS GSL gages are considered to be accurate to within +/-0.10 ft of the datum in use (Loving, 2002).

USGS Station 10010000 Great Salt Lake at Saltair Boat Harbor, UT

To verify that this gaging station is reporting accurately to NGVD29, trigonometric and differential leveling techniques are used to carry vertical datum from NGS vertical control point C-174 (table 2) to the gaging station. Starting from NGS Reference Mark C-174, a double-run spur traverse (DRST) using trigonometric leveling techniques documented in Noll and Rydlund (2020) is used to carry datum approximately 0.5 miles from the reference mark near Kennecott Smelter to the harbor at Great Salt Lake State Park. The level line from the DRST establishes an elevation relative to NGVD29 to a reference mark closer to the Saltair gaging station where differential leveling techniques can be used to verify the datum of the reference gage (Kenney, 2010). If the reference gage has moved (+/-0.05 ft) a datum correction is applied to the WSE record of the gage to correct for movement of the reference gage.

USGS Station 10010024 GSL South Side of Causeway, 6 Miles East of Lakeside, UT

To verify that this gaging station is reporting accurately to NGVD29, Survey-Grade Global Navigational Satellite Systems (GNSS), trigonometric, and differential leveling techniques are used to verify vertical datum. To begin datum verification, GNSS static survey techniques outlined in Rydlund and others (2012) are performed on four independent benchmarks near the causeway. The four independent benchmarks, documented in table 2, are occupied for a minimum of 2 hours with all four static surveys overlapping in time for a minimum of 1 hour. Once the static survey is complete, a NGS Online Positioning User Service (OPUS) Project is performed to verify that the four independent benchmarks are stable and to determine the elevation of the reference mark (RM4) at the causeway bridge. Once the elevation of RM4 is verified, the NAVD88 elevation from the OPUS Project is converted to NGVD29 using NGS Vertcon (National Oceanic and Atmospheric Administration, 2023a). A DRST is then performed to carry the datum approximately 0.3 miles to an established reference mark near the South Causeway gaging station. The level line from the DRST establishes an elevation relative to NGVD29 to a reference mark closer to the South Causeway gaging station where differential leveling techniques can be used to verify the datum of the reference gage. If the reference gage has moved (+/-0.05 ft) a datum correction is applied to the WSE record of the gage to correct for movement of the reference gage.

USGS Station 10010100 Great Salt Lake near Saline, UT

In 2009, differential leveling techniques were used to carry NGVD29 vertical datum from NGS Benchmark FMK-77 (table 2) to this gaging station. The level loop was approximately 1.0 mile long and predated the trigonometric leveling techniques used at other GSL gaging stations. Differential levels carried NGVD29 vertical datum to three independent benchmarks near the Saline gaging station which have remained stable as referenced in Kenney (2010). Differential levels are run annually to verify the reference gage at the Saline gaging station. If the reference gage has moved (+/-0.05 ft) a datum correction is applied to the WSE record of the gage to correct for movement of the reference gage.

Table 2. *Benchmarks used to maintain vertical datum at U.S. Geological Survey Great Salt Lake gaging stations (U.S. Geological Survey, 2023).*

Benchmark Name	Latitude	Longitude	NGVD29 (ft)	NAVD88 (ft)	USGS Gage
C-174	40° 43' 34.00"	112° 12' 19.00"	4230.63	4233.87	10010000
77-FMK	41° 14' 33.21"	112° 29' 28.95"	4231.16	4234.20	10010100 and 10010024
MOORE	41° 14' 50.06"	112° 15' 33.03"	4237.63	4240.60	10010024
120-FMK	41° 13' 10.04"	112° 51' 07.35"	4223.31	4226.23	10010024
RM4	41° 13' 15.49"	112° 45' 56.49"	4216.02	4218.95	10010024

Estimating Water-Surface Elevations for the Saltair Gage

From September 2022 to December 2022 the harbor at Great Salt Lake State Park was mostly dry and the USGS Saltair gaging station could not measure WSE of GSL. As a result, the elevation record was estimated for the Saltair gaging station by comparing hydrographs with the South Causeway gage. The two gaging stations have a nearly identical hydrograph during calm conditions. Because of the location of the gages in the south part of GSL, the two gages can exhibit inverse hydrographs during wind-driven lake seiches. With the South Causeway gage located on the north end of the south part, and the Saltair gage being located on the southern tip of the south part, when a lake seiche occurs, one gage will have an elevated WSE whereas the opposing gage will have a suppressed WSE. Figure 2 provides a time-series comparison of the two gages and the inverse WSE observed during higher lake levels in May 2021. Considering the inverted relationship, when estimating the WSE for the Saltair gage, the WSEs associated with seiche events were estimated to account for the high and low water levels that most likely occurred during the storm events.

Measurement of Discharge

A streamgage is a structure that contains equipment that measures and records the water level of a stream. The water level of a stream is often referred to as gage height or stage, reported in feet, and is measured using methods outlined in Sauer and Turnipseed (2010). Stage is typically recorded by an instrument at a set interval ranging from 5 to 15 minutes. The continuous record of stage is then used as a surrogate to compute discharge in cubic feet per second (cfs). To compute and report discharge at a given stage, discharge measurements are made at a variety of stages to cover low, medium, and high flow conditions. Discharge measurements at all stages follow methods outlined in Turnipseed and Sauer (2010). Once a range of stage and discharge measurements have been made, a stage-discharge rating curve can be developed. A rating curve is a graphical representation of the relationship between stage and discharge, with the assumption that for every stage, there is a unique discharge. Once a stage-discharge rating curve is established for a streamgage station, the continuously recorded stage at the streamgage can be used to compute a continuous discharge record. The stage-discharge method for computing discharge is applicable to gaging stations 10141000 (Weber River gage) and 10126000 (Bear River gage) (U.S. Geological Survey, 2023).

The stage-discharge relationship becomes inaccurate when backwater conditions occur. Backwater conditions cause the stage-discharge relationship to fail because the same discharge can occur at a range in stage values due to the backwater conditions. If backwater conditions exist at a streamgage, discharge can be computed using an index velocity method (Levesque and Oberg, 2012). Index velocity methods require that, in addition to continuously measured

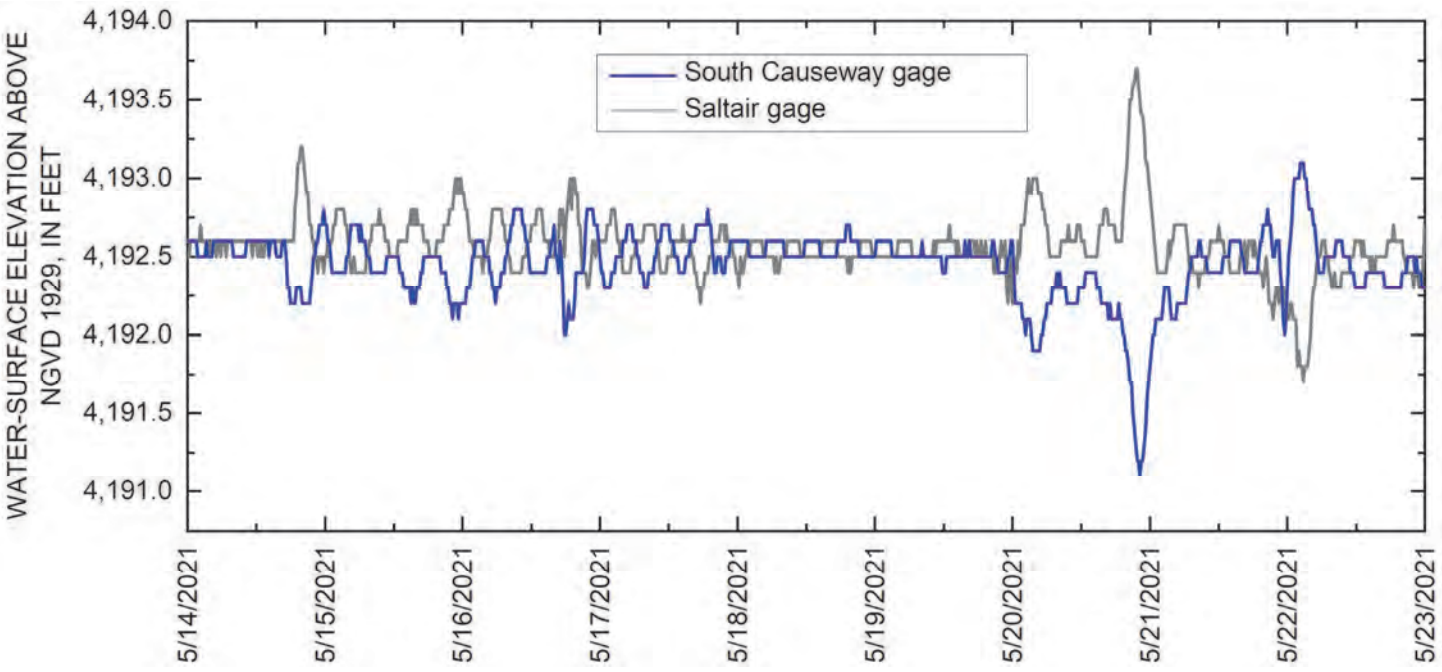

Figure 2. *Example of seiche event impact on 15-minute interval water-surface elevations measured at USGS station 10010000 Great Salt Lake at Saltair Boat Harbor, Utah (Saltair gage), and USGS station 10010024 GSL South Side of Causeway, 6 Miles East of Lakeside, Utah (South Causeway gage) (U.S. Geological Survey, 2023).*

stage, a velocity sensor is installed at the stream to continuously measure water velocity at the same measurement interval as the stage sensor (5 to 15 minutes). Discharge measurements are made over a range in stage and velocity to develop a mathematical relationship between measured indexed velocity and the mean channel velocity at the streamgage. Once this relationship is established, the measured index velocity is used to compute a mean velocity for the channel. The velocity is multiplied by a known cross-sectional area (computed from the stage value and documented channel geometry) to compute a continuous discharge at the streamgage. The index velocity method for continuous discharge is applicable to gaging stations 10171000 (Jordan River gage) and 10170500 (Surplus Canal gage) (U.S. Geological Survey, 2023).

Most streamgage stations are located on natural channels which are subject to changes over time. These changes can be seasonally influenced or occur over several years. Streamgage stations are visited routinely throughout the year to verify accurate stage data and to maintain an accurate stage-discharge or index velocity relationship.

Annual discharge values discussed in this report are in units millions of acre-feet (maf). These values were computed for each inflow gage by downloading daily mean discharge values, in cfs, from NWIS and converting these values to daily discharge, in acre-feet per day, followed by summing these values for each water year of interest. Monthly mean discharge values, in cfs, also are discussed in this report and are available via NWIS (U.S. Geological Survey, 2023).

DATA PRESENTATION AND DISCUSSION

Water-Surface Elevations

Figures 3 shows the complete period of record of daily mean WSE for the Saltair gage (a daily mean value is the average of the recorder values logged each day; periodic WSE observations made by individuals at GSL prior to installation of recorders are considered daily mean values). For detailed descriptions of the early record before June 1986, see Arnow (1984) and Arnow and Stephens (1990); it is briefly summarized below. The high stands in the 1870s and 1980s are prominent features of the early Saltair gage record along with a succession of low stands in the early 1900s, 1930s, and early 1960s. Seasonal variation, where lake levels increase from approximately late autumn to late spring and decrease from approximately early summer to mid-autumn, becomes more apparent in the record after systematic measurements began in 1875. Seasonal variation is driven by the balance between inflows and evaporation where lake levels increase when inflow exceeds evaporation and decrease when evaporation exceeds inflow (Arnow and Stephens, 1990). Until July 2021, the record low mean daily WSE was 4,191.35 ft, measured at the Saltair gage on October 15, 1963. At the time of the record low in 1963, many people thought the lake was going to become dry and roads, railroads, wildfowl management areas, recreational facilities, and industrial installations were established on the exposed

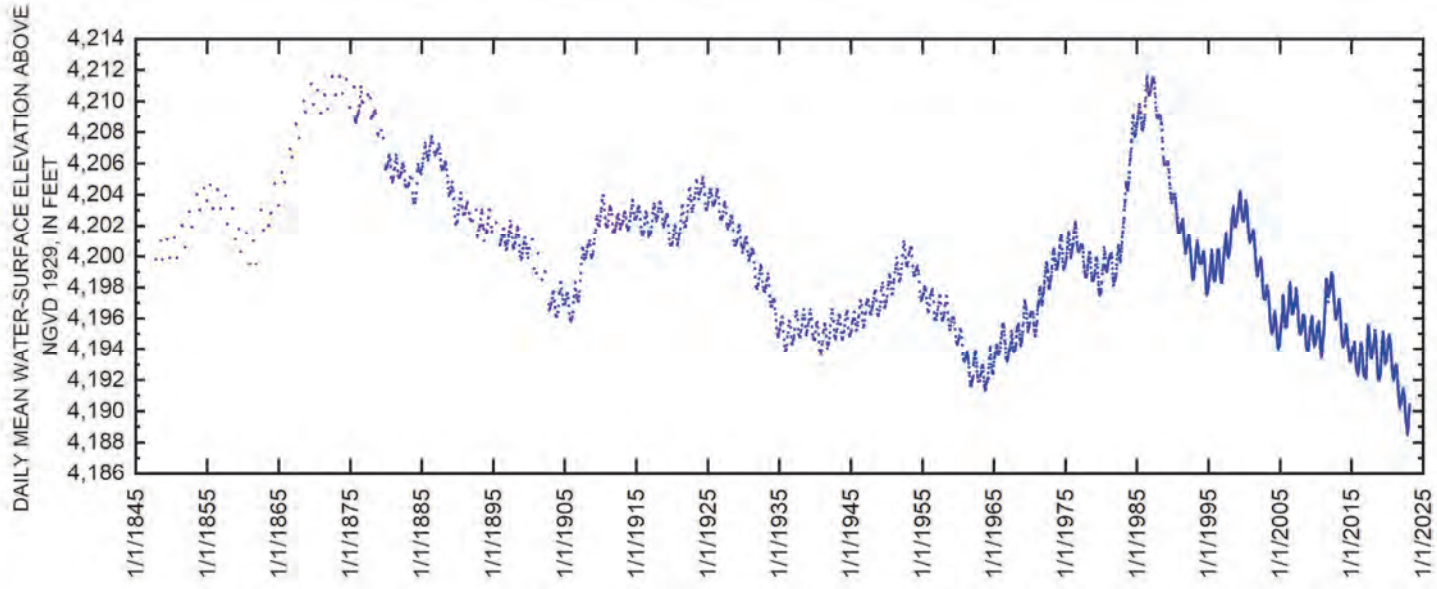

Figure 3. *Daily mean water-surface elevation at USGS station 10010000 Great Salt Lake at Saltair Boat Harbor, Utah (Saltair gage), 1847-2022 (U.S. Geological Survey, 2023).*

lakebed (Arnow, 1984). From the low in 1963 to 1976 lake levels increased about 11 ft leading to discussions about pumping water from the lake into the undeveloped desert west of GSL, but in 1977 lake levels began to decline ending concerns about high water (Arnow, 1984). From September 1982 to its historic peak on June 3, 1986 (4,211.60 ft NGVD29), lake levels had a net rise of about 12 ft. This period of rapid rise culminated in $240 million in flood damages and prompted completion of the Lakeside breach in the causeway in August 1984 to help decrease the approximate +3.5 ft WSE difference between the south and north parts of the lake. It also prompted completion of the West Desert Pumping Project in June 1987. The pumps associated with that project were shut down on June 30, 1989, after pumping 2.2 million acre-feet of water from GSL into the West Desert Pond, which reduced GSL's WSE by about 2.2 feet (Austin, 2002).

A plot of daily mean WSEs for the Saltair and Saline gages from June 1986 to November 2022 is shown in figure 4. The difference between the WSEs for the two gages depends on factors such as inflows, densities of the south and north parts of GSL (which provides the potential for GSL water to flow in both directions through the causeway conveyances), evaporation, and modifications to causeway conveyances. It is beyond the scope of this paper to discuss each of these factors in detail; however, modifications were made to the causeway conveyances during the periods that are associated with observed WSE differences (figure 4). Because almost all surface-water inflow is to the south part of the lake, WSEs at Saltair are usually higher than Saline (median value for period shown in plot is +0.7 ft). The increased difference in WSE between Saltair and Saline from November 1991 through January 1998 occurred during an extended period when the culverts were frequently plugged with debris (Loving, 2002). The effective depth of the Lakeside breach was deepened from about 4,200 ft to 4,198 ft NGVD29 in August 1996 (Loving, 2002), which likely contributed to the subsequent reduction in WSE difference between Saltair and Saline from 1996 to 1998. The increased WSE difference from September 2014 to February 2017 is associated with closure of the east (November 2012) and west (December 2013) culverts. The rapid decrease in WSE difference from December 2016 to June 2017 is associated with the opening of the new breach on December 1, 2016. This breach has an adjustable berm on the north side of the causeway. To help manage the salinity in the southern half of the lake the top of the berm was raised from 4,183 to 4,187 ft NGVD29 (completed July 27, 2022) and from 4,187 to 4,192 ft NGVD29 (completed February 9, 2023). The latter modification raised the top of the berm above the WSE of the south part of the lake at the time and contributed to the increased WSE difference after February 9, 2023.

The magnitude of seasonal fluctuations in the daily mean WSE record from 1986 to 2022 are shown in figure 5. At Saltair, the average seasonal increase is 1.8 ft and the average seasonal decrease is 2.4 ft. The largest seasonal lake level increase (5.1 ft) occurred from autumn 2010 to late spring 2011. The largest seasonal lake level decrease (3.2 ft) occurred during

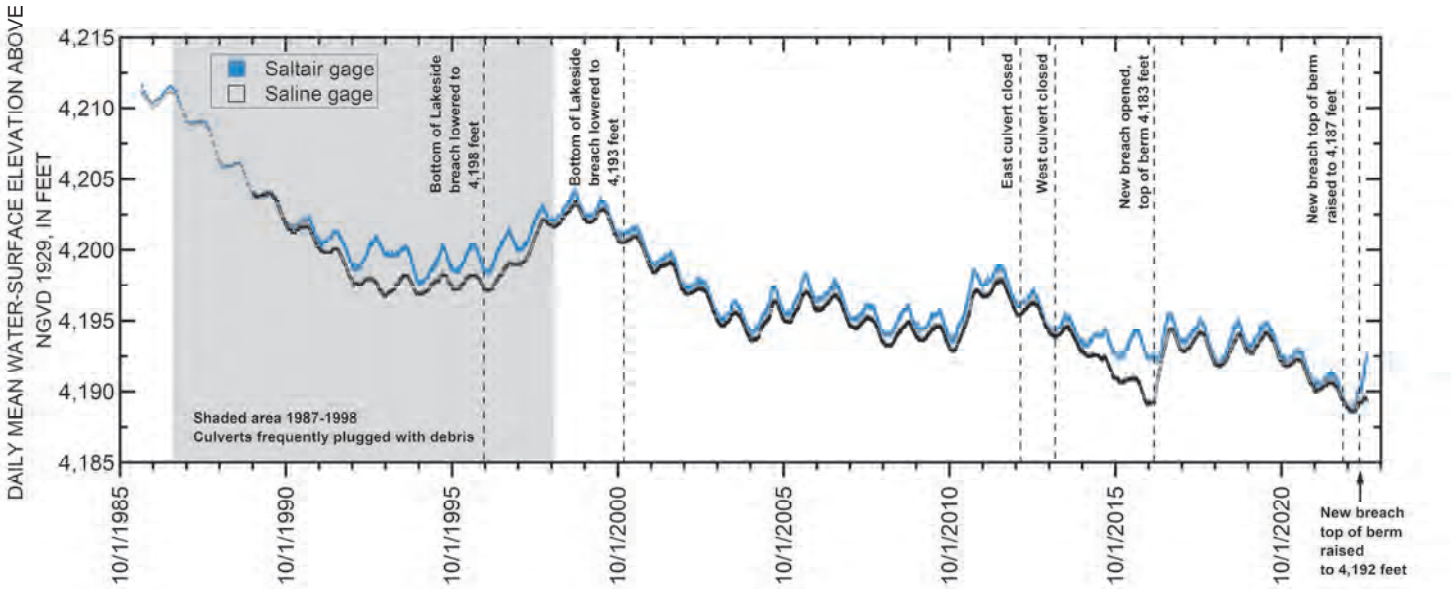

Figure 4. *Daily mean water-surface elevation at USGS station 10010000 Great Salt Lake at Saltair Boat Harbor, Utah (Saltair gage), and USGS station 10010100 Great Salt Lake near Saline, Utah (Saline gage), 1985-2022 (U.S. Geological Survey, 2023).*

spring and summer 1988 and 2018. Lake level decreases exceeded increases in 25 of the 36 seasonal cycles shown. At the Saline gage, the average seasonal increase is 1.5 ft and the average seasonal decrease is 2.1 ft. The largest seasonal lake level increase (5.5 ft) occurred from December 2016 to May 2017, after the new 150 ft wide breach was opened restoring open channel connection between the south and north parts of the lake that was previously associated with the east and west culverts. The largest seasonal lake level decrease (3.3 ft) occurred during spring and summer 1988. Lake level decreases exceeded increases in 22 of the 36 seasonal cycles shown in figure 5.

With seasonal decreases exceeding increases for most years following the record high WSE in June 1986, both the north and south parts of the lake had net WSE drops that resulted in record low WSEs in November 2022 (figure 4). The long-standing historic

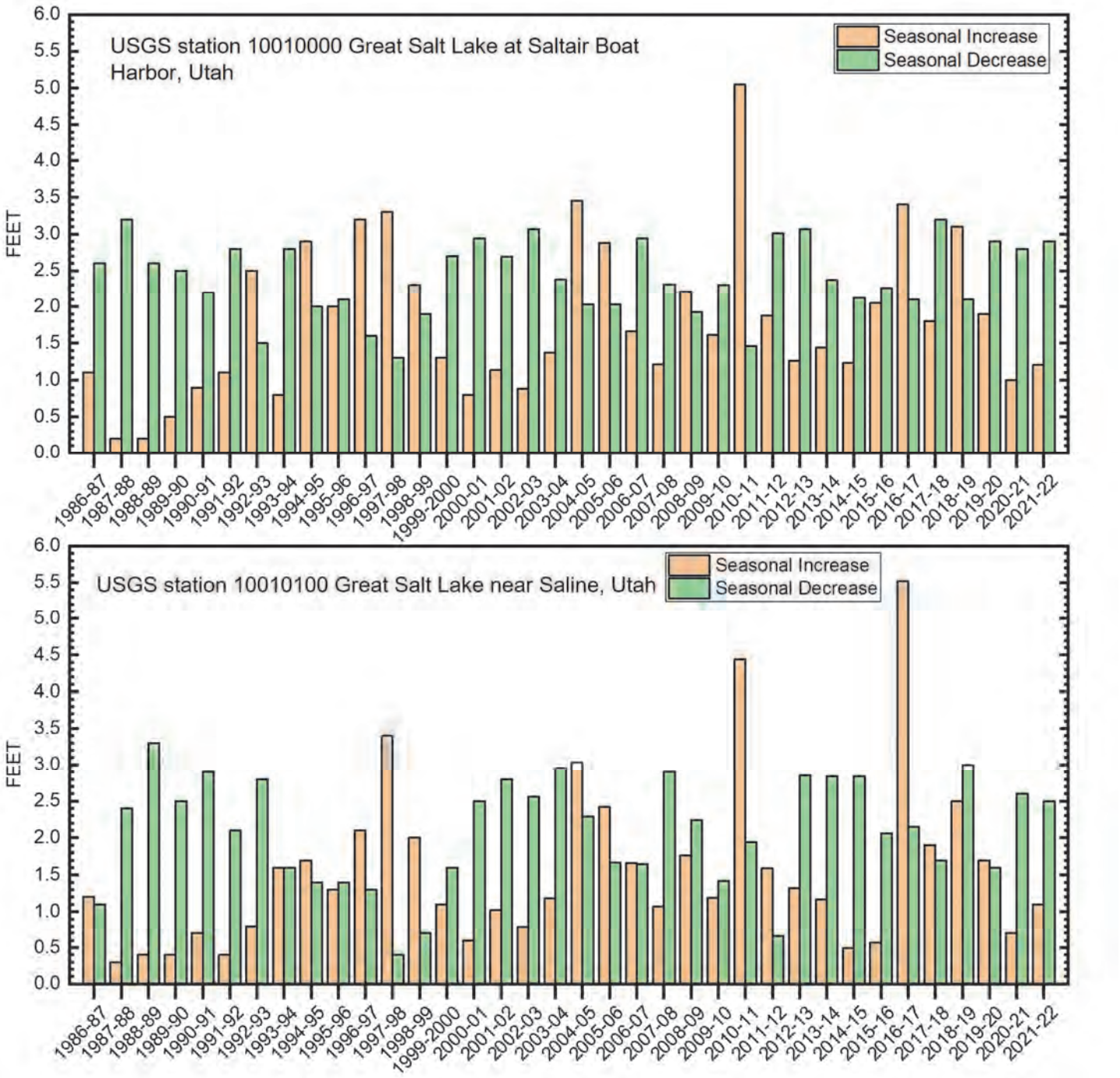

Figure 5. *Seasonal water-surface elevation increase and decrease at USGS station 10010000 Great Salt Lake at Saltair Boat Harbor, Utah (Saltair gage, top) and USGS station 10010100 Great Salt Lake near Saline, Utah (Saline gage, bottom), 1986 to 2022 (U.S. Geological Survey, 2023). Seasonal increases generally occur from late fall/early winter through the following spring/early summer. Seasonal decreases generally occur from late spring/early summer through mid fall/early winter.*

low daily mean WSE measured at the Saltair gage on October 16, 1963 (4,191.35 ft NGVD29) was broken on July 21, 2021. The WSE continued to decrease until October 18, 2021, when it reached a short-lived historic low of 4,190.2 ft NGVD29. The seasonal lake level increase from October 18, 2021, to early April 2022, was relatively low at 1.2 ft, and by July 3, 2022, the WSE dropped to 4,190.1 ft NGVD29, breaking the short-lived historic low set less than 9 months prior. By September 28, 2022, continued seasonal decrease resulted in too little water in the harbor at Great Salt Lake State Park for the Saltair gage to operate and it was shutdown. Water-surface elevation data for the south part of the lake continued to be measured at the relatively new (installed August 2020) South Causeway gage, maintaining continuity of the 175-year WSE record that is associated with the south part of GSL. Seasonal decreases continued until November 3, 2022, when the South Causeway gage recorded the new record low daily mean WSE for the south part of the lake of 4,188.5 ft NGVD29. Two days prior, on November 1, 2022, the Saline gage recorded 4,188.5 ft NGVD29, which also is the new historic low daily mean WSE for the north part of the lake (the previous historic low of 4,188.98 ft NGVD29 was measured in September and October 2016 and was related to closure of the two railroad causeway culverts). Net WSE decreases from June 1986 to November 2022 for the south and north parts of the lake were 23.1 ft and 22.7 ft, respectively.

By late November 2022, the south part of the lake began its seasonal increase (figure 4). The Saltair gage was restarted on December 15, 2022, and, as of May 4, 2023, the south part had risen to 4,192.6 ft NGVD29, a 4.1 ft increase. The north part of the lake did not start increasing until late December 2022 and, as of May 4, 2023, it had risen to 4,189.3 ft NGVD29, a 0.8 ft increase. The WSE of the south part of the lake reached 4,192.1 ft NGVD29 on April 17, 2023, exceeding the top of the berm at the new breach allowing for south to north flow (on May 3, 2023, USGS measured south to north discharge of 129 cfs). With a significant snowpack remaining in the Bear, Weber, and Jordan River basins, south to north flows were expected to continue until evaporation exceeds inflows and lake levels begin their seasonal decrease.

Streamflow and Great Salt Lake Water Surface Elevation

Annual discharge for water years 1985 to 2022 for each inflow gage are shown in figure 6. Also included in figure 6 are the median annual discharge values for each inflow gage. The median annual discharge values are based on the period or record associated with each gage (table 2). The Bear River gage has the highest median annual discharge (0.958 maf), followed by the Weber River gage (0.343 maf), Surplus Canal gage (0.170 maf), and Jordan River gage (0.101 maf). Relatively high flow years in the mid-1980s, late 1990s, 2011 and 2017; and relatively low flow years in the late 1980s, early 1990s, mid-2010s, and early 2020s are apparent in the data for the Bear River, Weber River, and Surplus Canal gages (note that a significant amount of flow in the Jordan River is diverted to the Surplus Canal). Of the 36 years of annual discharge record shown for each gage, the Bear River gage had 12 years where annual discharge exceeded its median annual discharge, the Weber River gage had 10 years, the Surplus Canal gage had 21 years, and the Jordan River gage had 12 years.

Annual discharge measured at the inflow gages and annual mean WSE measured at the Saltair gage for water years 1985 to 2022 are shown in figure 7. Annual mean WSE is related to annual discharge as consecutive years of relatively high flows from 1985-1987, 1995-1999, 2005–2006, and 2011–2012 contributed to annual mean WSE increases. Consecutive years of relatively low flows from 1988–1994, 2001–2004, 2013–2016, and 2021–2022 contributed to annual mean WSE decreases. During water years 2021 and 2022, when new record low WSEs were measured at GSL, combined annual discharge values were 0.704 and 0.743 maf, which are less than half of the median combined annual discharge of 1.57 maf (indicated by the horizontal dashed line in figure 7).

To put the WSE and discharge records into context with broader climatological conditions, monthly Palmer Drought Severity Index (PDSI) values for Utah (National Oceanic and Atmospheric Administration, 2023b), monthly mean WSE at Saltair, and combined monthly mean discharge for inflow gages, in cfs, are plotted in figure 8. The PDSI uses precipitation and temperature data to evaluate moisture supply and demand using a simple water balance model. A PDSI value of greater than 4 represents very wet conditions, while a PDSI less than -4 represents an extreme drought. Extended periods of negative PDSI values from November 1988 to November 1992, October 1999 to August 2004, November 2006 to November 2009, November 2011 to August 2016, and August 2019 to October 2022 correspond to net WSE declines and lower monthly mean discharge. These periods of extended negative PDSI are offset by relatively few periods of extended positive PDSI values and increased monthly mean WSE and higher combined monthly mean discharge.

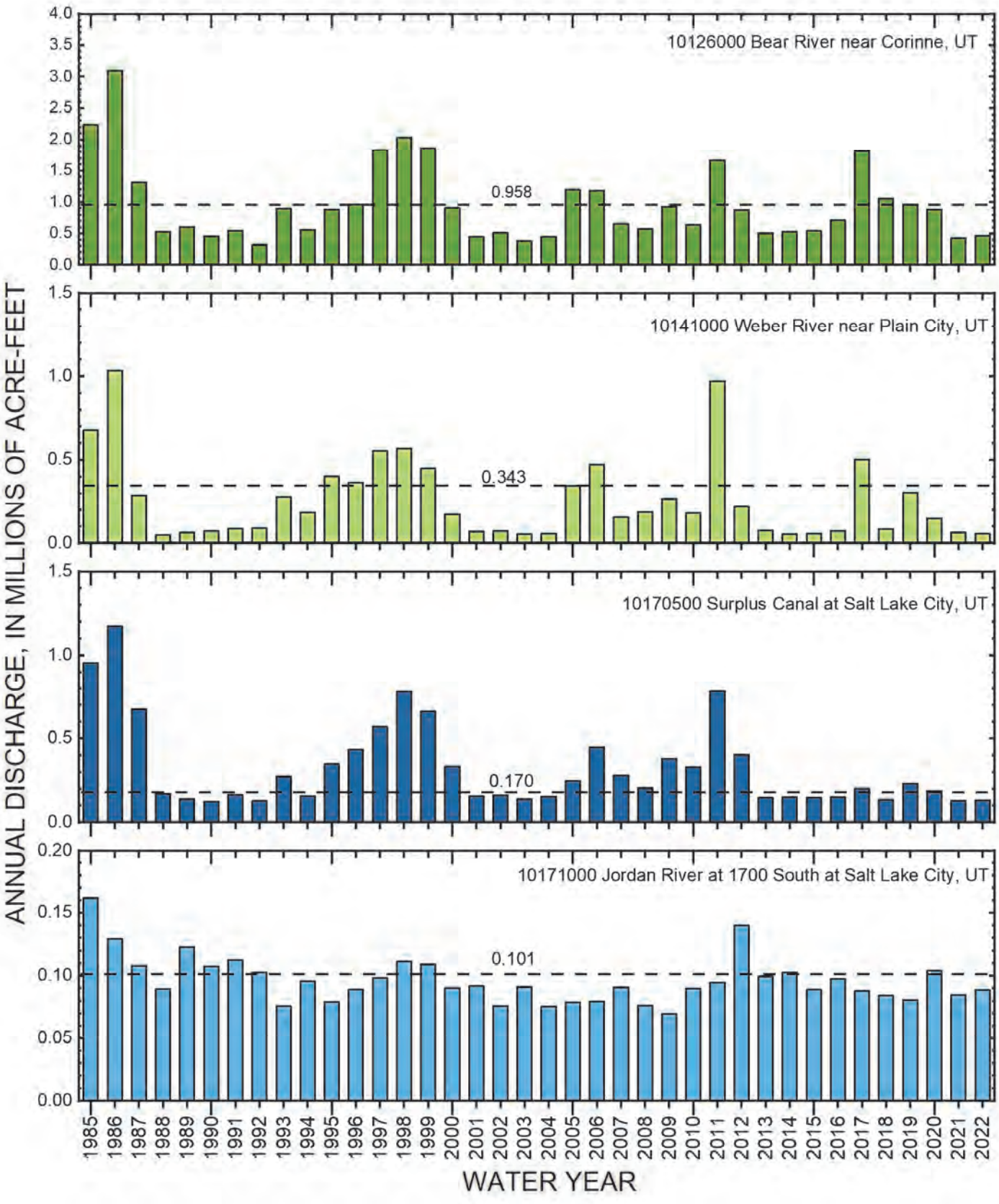

Figure 6. *Annual discharge measured at USGS inflow gages, water years 1985-2022 (U.S. Geological Survey, 2023). The median annual discharge for the period of record associated with each gage is indicated with a dashed line. The y-axis scale, discharge in millions of acre-feet, is customized for each gage.*

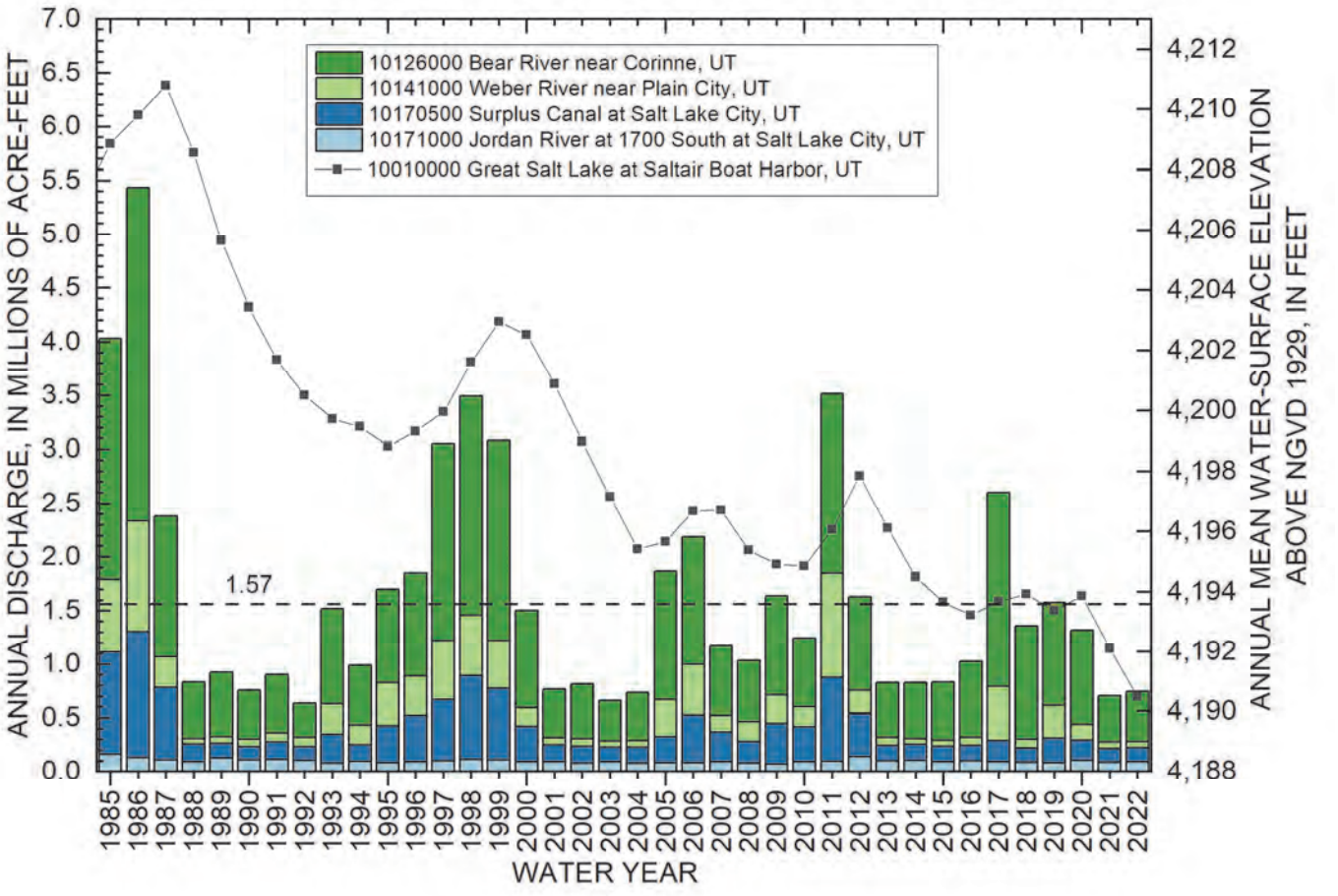

Figure 7. *Annual discharge for USGS inflow gages and annual mean water surface elevation at USGS station 10010000 Great Salt Lake at Saltair Boat Harbor, Utah (Saltair gage), water years 1985-2022 (U.S. Geological Survey, 2023). The combined median annual discharge for all four gages, based on the period of record for each gage, is indicated by the horizontal dashed line.*

CONCLUSIONS

A new historic low daily mean WSE of 4,188.5 ft NGVD29 was measured during November 2022 at gages north and south of the GSL causeway. From September 28 to December 15, 2022, there was too little water in the harbor at Great Salt Lake State Park for the Saltair gage to operate and the new historic low daily mean WSE for the south part of the lake was measured at a relatively new gage located just south of the causeway (South Causeway gage). Data collected at the South Causeway gage were used to estimate the daily mean WSE record for the Saltair gage for the period it was shut down, preserving the continuity of the 175-year WSE record that is associated with this gage.

Many factors, including direct precipitation, groundwater inflow, West Desert Pumping Project withdrawals (1987–1989), evaporation, and surface-water inflow contribute to the water balance and thus WSE of GSL. In this document, data were presented only for a portion of the surface-water inflow budget as measured by four long-term streamgages. For water years 1985 to 2022, trends in Saltair gage WSEs correspond to trends in combined annual discharge measured at the four streamgages, and both WSE and combined monthly mean discharge correspond to trends in PDSI values for Utah. This basic observation is true when the data records are examined back to 1950 when concurrent monitoring began at all sites (Cordova and Angeroth, 2012). For detailed analyses of GSL WSE variation and climate, see Wang and others (2010) and Mann and others (1995). The impact of upstream diversions from surface water inflow sources to GSL is beyond the scope of this document; however, Wurtsbaugh and others (2017) estimated that 11 ft of GSL WSE decrease from 1847 to 2016 can be attributed to consumptive use and related changes to evaporation. Detailed monitoring of GSL's water budget may support quantification of the complex interplay between drought cycles, consumptive use, and WSEs.

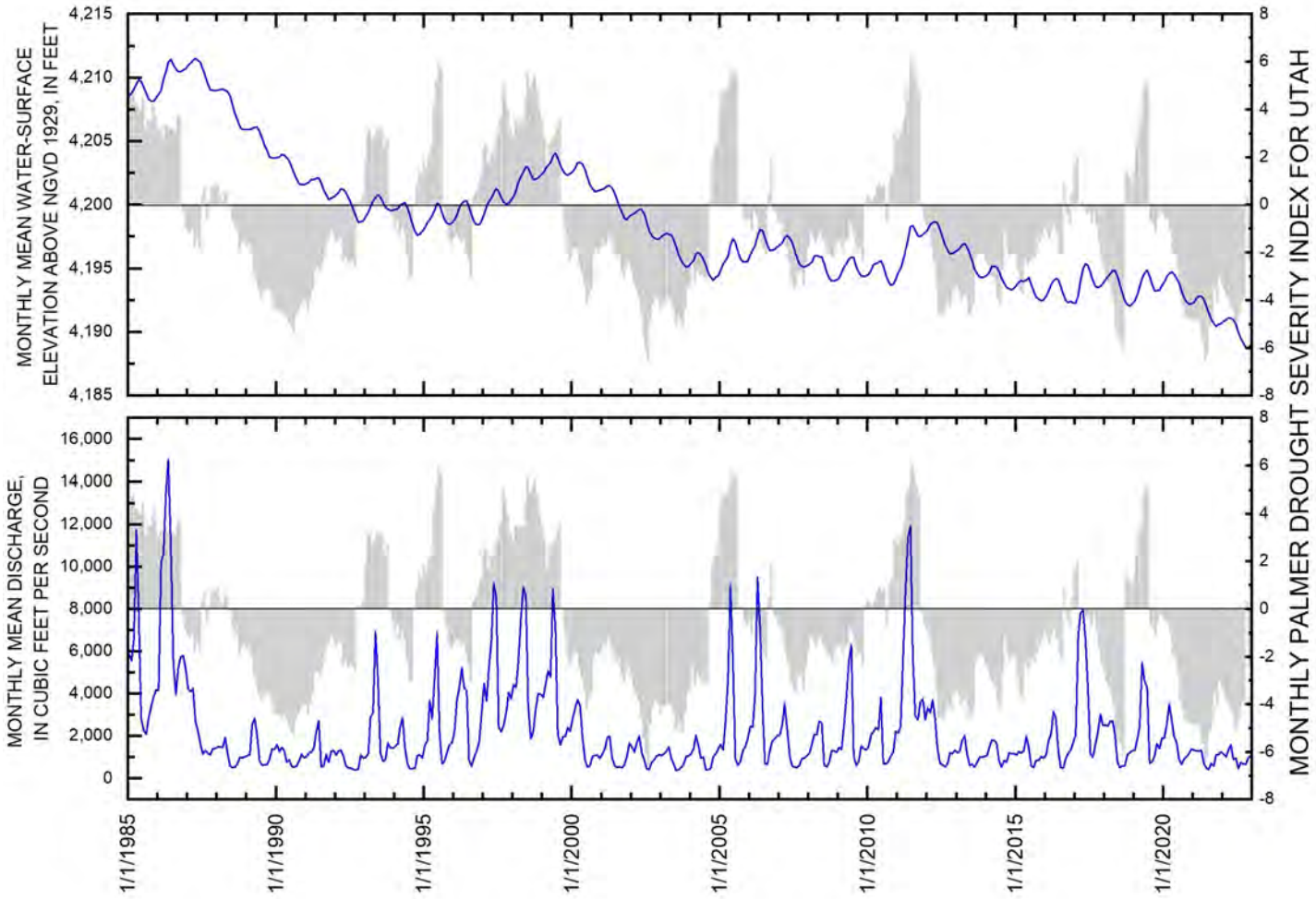

Figure 8. *Monthly mean water-surface elevation at USGS station 10010000 Great Salt Lake at Saltair Boat Harbor, Utah (Saltair gage, top), and combined monthly mean discharge for USGS inflow gages (bottom) (U.S. Geological Survey, 2023), compared to the monthly Palmer Drought Severity Index for Utah (indicated by light gray bars), January 1985 to December 2022 (National Oceanic and Atmospheric Administration, 2023b).*

Any use of trade, firm, or product names is for descriptive purposes only and does not imply endorsement by the U.S. Government.

REFERENCES

Austin, L.H., 2002, Problems and management alternatives related to the selection and construction of the West Desert Pumping Project, in Gwynn, J.W., editor, Great Salt Lake an overview of change, Special Publication of the Utah Department of Natural Resources, p. 303-312.

Arnow, T., 1984, Water-level and water-quality changes in Great Salt Lake, Utah, 1847-1983: U.S. Geological Survey Circular 913, 22p.

Arnow, T. and Stephens, D., 1990, Hydrologic characteristics of the Great Salt Lake, Utah, 1847-1986: United States Geological Survey Water-Supply Paper 2332, 32 p.

Cordova, J.T. and Angeroth, C.E., 2012, Runoff conditions in Utah for Water Year 2011. Available online: https://pubs.usgs.gov/fs/2012/3041/ (accessed February 1, 2023).

Gilbert, G.K., 1890, Lake Bonneville: U.S. Geological Survey Monograph I, 438 p.

Kenney, T.A., 2010, Levels at gaging stations: U.S. Geological Survey Techniques and Methods 3-A19, 60 p. Available online: https://pubs.usgs.gov/publication/tm3A19 (accessed February 1, 2023).

Levesque, V.A., and Oberg, K.A., 2012, Computing discharge using the index velocity method: U.S. Geological Survey Techniques and Methods 3–A23, 148 p. Available online: http://pubs.usgs.gov/tm/3a23/ (accessed February 1, 2023).

Loving, B.L., Waddell, K.M., Miller, C.W., 2000, Water and salt balance of Great Salt Lake, Utah,

and simulation of water and salt movement through the causeway, 1987-98: U.S. Geological Survey Water- Resources Investigations Report 00-4221, 32 p. Available online: https://pubs.usgs.gov/publication/wri004221 (accessed February 1, 2023).

Loving, B.L., 2002. Adjustments to 1966-2001 Great Salt Lake Water-Surface Elevation Records, due to Corrected Benchmark Elevations. Great Salt Lake: An Overview of Change. Special Publication of the Utah Department of Natural Resources, Salt Lake City, Utah, p. 167-170.

Mann, M.E., Lall, U., and Saltzman, B., 1995, Decadal and secular climate variability: understanding the rise and fall of the Great Salt Lake. Geophysical Research Letters, v. 22, p. 937-940.

Meyer, Thomas H.; Roman, Daniel R.; and Zilkoski, David B., 2006, What Does Height Really Mean? Part III: Height Systems: Department of Natural Resources and the Environment Articles. 2. Available online: https://opencommons.uconn.edu/nrme_articles/2 (accessed February 1, 2023).

Noll, M.L., and Rydlund, P.H., 2020, Procedures and best practices for trigonometric leveling in the U.S. Geological Survey: U.S. Geological Survey Techniques and Methods, book 11, chap. D3, 94 p. Available online: https://doi.org/10.3133/tm11D3 (accessed February 1, 2023).

National Oceanic and Atmospheric Administration, 2023a, VERTCON – North American Vertical Datum Conversion: National Geodetic Survey. Available online: https://geodesy.noaa.gov/TOOLS/Vertcon/vertcon.html (accessed July 1, 2023).

—2023b, National Centers for Environmental information, Climate at a Glance: Statewide Time Series. Available online: https://www.ncei.noaa.gov/access/monitoring/climate-at-a-glance/statewide/time-series (accessed May 5, 2023).

Rydlund, P.H., Jr., and Densmore, B.K., 2012, Methods of practice and guidelines for using survey-grade global navigation satellite systems (GNSS) to establish vertical datum in the United States Geological Survey: U.S. Geological Survey Techniques and Methods, book 11, chap. D1, 102 p. with appendixes.

Sauer, V.B., and Turnipseed, D.P., 2010, Stage measurement at gaging stations: U.S. Geological Survey Techniques and Methods book 3, chap. A7, 45 p. Available online: http://pubs.usgs.gov/tm/tm3-a7/ (accessed February 1, 2023).

Turnipseed, D.P., and Sauer, V.B., 2010, Discharge measurements at gaging stations: U.S. Geological Survey Techniques and Methods book 3, chap. A8, 87 p. Available online: http://pubs.usgs.gov/tm/tm3-a8/ (accessed February 1, 2023).

U.S. Geological Survey, 2023, USGS water data for the Nation: U.S. Geological Survey National Water Information System database. Available online: https://waterdata.usgs.gov/nwis (accessed July 1, 2023).

Wang, S., Gillies, R.R., Jin, J., and Hipps, L.E., 2010, Coherence between the Great Salt Lake Level and the Pacific Quasi-Decadal Oscillation. Journal of Climate, v. 23. no. 8, p. 2161-2177.

Wurtsbaugh, W.A., Miller, C., Null, S.A., DeRose, R.J., Wilcock, P., Hahnenberger, M., Howe, F., and Moore, J., 2017: Decline of world's saline lakes: Nature Geoscience v. 10. Available online: https://www.nature.com/articles/ngeo3052 (accessed February 1, 2023).

Use of Remote Imagery to Map Microbialite Distribution at Great Salt Lake, Utah: Implications for Microbialite Exposure

Laura Wilcock[1,2], Carie M. Frantz[1], and Michael D. Vanden Berg[3]

[1]*Department of Earth & Environmental Sciences, Weber State University, Ogden, Utah; Laura.wilcock@utah.edu*

[2]*Department of Geology and Geophysics, University of Utah, Salt Lake City, Utah*

[3]*Energy & Minerals Program, Utah Geological Survey, Salt Lake City, Utah*

10.31711/ugap.v51i.136

ABSTRACT

The elevation of Great Salt Lake has fallen to historic lows in recent years, exposing once submerged microbialites along the lake's shores. Although prior studies have attempted to map microbialite locations, this has proved challenging, with mapped microbialite areas limited to accessible shoreline locations or via indirect sonographic evidence. Meanwhile, the importance of Great Salt Lake's microbialites to the lake's food chain has made quantifying the extent of microbialites exposed versus submerged at different lake elevations critical to lake management decisions. Low lake levels combined with seasonal high-water clarity have enabled microbialite reefs to be spotted in aerial and satellite imagery, even in deeper areas of the lake. In this study, satellite images were used to identify and map microbialite reef areas in Great Salt Lake and along its dry shores. In the south arm, submerged microbialites were easily recognized as dark green reefs against a light-colored benthic background (primarily ooid sand). Stationary microbialite mounds were distinguished from rip-up clasts or other dark-colored mobile material by comparing potential microbialite regions across several high-visibility timepoints. In this way, we identified 649 km^2 (251 mi^2) of putative microbialite reef area: 288 km^2 (111 mi^2) in the north arm, 360 km^2 (139 mi^2) in the south arm, of which 375 km^2 (145 mi^2) was mapped at a high degree of confidence. We also produced geospatial shapefiles of these areas. This map, combined with currently available lake bathymetric data, permits the estimation of the extent of microbialite reef exposed vs. submerged in various parts of the lake at different lake elevations. At the end of fall 2022, when lake level dipped to 1276.7 masl (4188.5 ft-asl) in elevation, we estimate that ~40% of the south arm microbialite reef area was exposed.

INTRODUCTION

Microbialites cover substantial portions of the Great Salt Lake benthos, and host microbial communities are believed to be important to the Great Salt Lake ecosystem. Models of the lake's ecosystem, therefore, must necessarily incorporate estimates of microbialite extent (Belovsky and others, 2011; Barrett, 2020), which need refining, particularly in the face of recent lake level decline and microbialite exposure.

Microbialites in Modern Great Salt Lake

Great Salt Lake is the largest saline lake in the western hemisphere. Unlike other terminal lakes in the Basin and Range of the western United States, which tend to be alkaline, Great Salt Lake is a Na-Mg-Cl-SO_4-dominated system with relatively low levels of alkalinity (Domagalski and others, 1989; Jones and others, 2009). High rates of Ca^{2+} and HCO_3^- delivery, slightly alkaline surface waters, the lake's hypersalinity (which promotes CO_2 degassing), and high levels of microbial activity produce conditions that approach or exceed aragonite saturation in much of the lake, despite relatively low lake water concentrations of Ca^{2+} and CO_3^- (Pace and others, 2016; Ingalls and others, 2020; Bouton and others, 2020). These factors have made Great Salt Lake (as well as its predecessors) a "carbonate factory," with carbonates making up a major portion of lake sediments, especially since the draining of Pleistocene Lake Bonneville (Jones and others, 2009; Vennin and others, 2019). Carbonate deposits blanket the modern bed of the lake, and include organic-rich carbonate mud, oolitic sand, and microbialite reefs (Eardley, 1938; Chidsey and others, 2015; Vanden Berg, 2019; Ingalls and others, 2020; Bouton and others, 2020; Baskin and others, 2022).

Microbialites are "organosedimentary deposits formed from interaction between benthic microbial communities…and detrital or chemical sediment" (Burne and Moore, 1987). They are typically formed by processes of trapping and binding by microbial mats (for example, Frantz and others, 2015),

induction of mineral precipitation via metabolic activities of microbial communities (for example, Dupraz and others, 2009), and/or inorganic calcification (for example, Shen and others, 2022). An aside on terminology: the term "bioherm," ostensibly coined by Cumings and Shrock (1928), broadly refers to any reeflike mound built by living organisms. "Microbialite," meanwhile, refers to a sedimentary rock built at least in part by the activities of microorganisms (Burne and Moore, 1987). Thus, "microbialite reef" is subtly different from "bioherm," indicating that microorganisms are involved in the construction of the reefs, but also acknowledging potential abiogenic contributions.

Great Salt Lake's microbialites were first documented by Eardley (1938) in his seminal tome describing the lake's chemistry and sediments, describing in detail the "extensive calcareous bioherms" that were visible during a period of relatively low lake elevation in the mid-1930s (Figure 1). He noted their dense mats (periphyton), dominated by the cyanobacterium *Aphanothece packardii* (now identified as *Eu-*

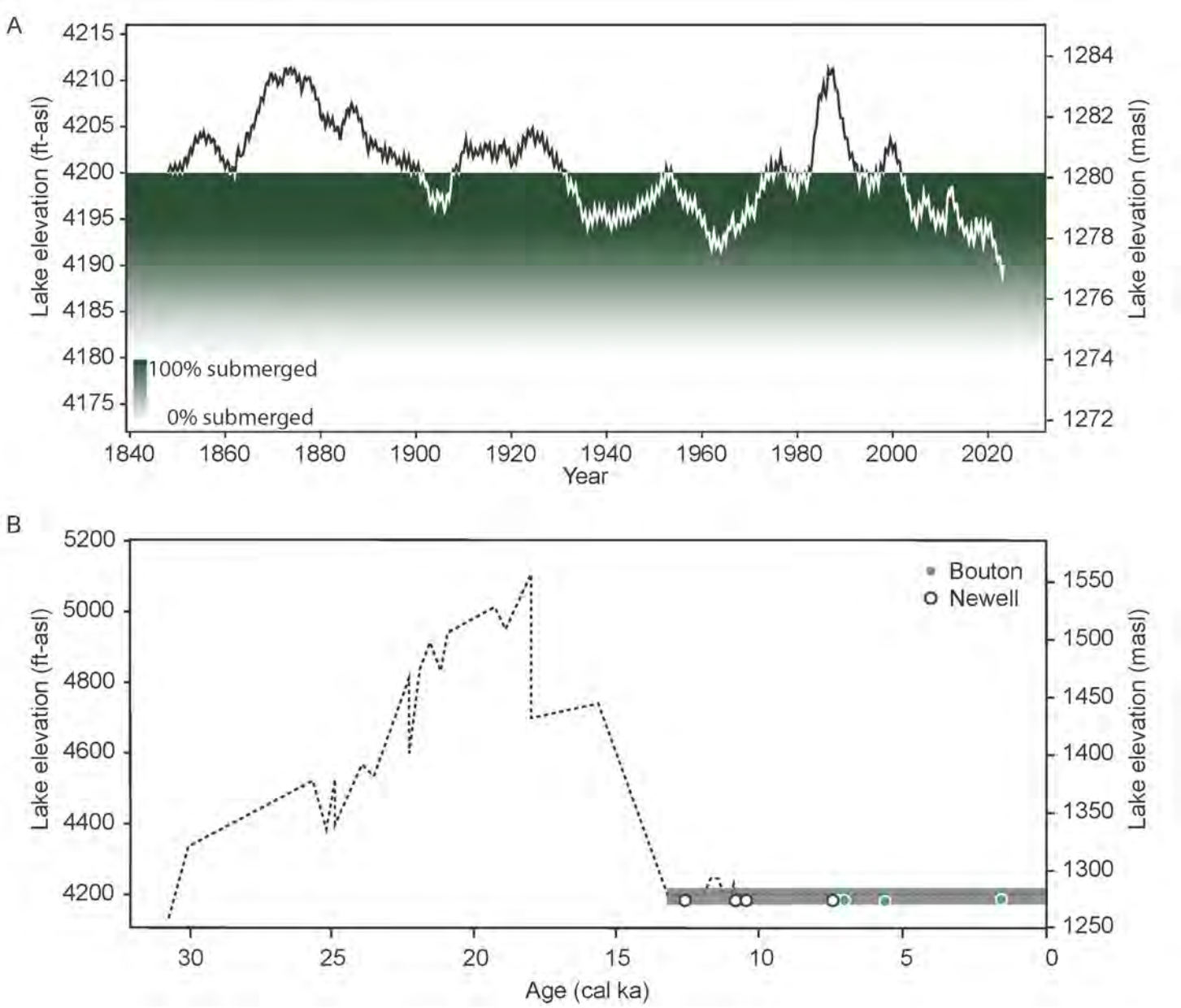

Figure 1. *A) Modern Great Salt Lake south arm surface elevations as measured at USGS water monitoring locations 1001000 and 10010024. Green shaded areas indicate 1 ft elevation bands below 4200 ft-asl where microbialites were mapped (this study), with shade indicating the total percentage of microbialites that would be submerged at that lake elevation. B) Lake Bonneville-Great Salt Lake hydrograph (black line) showing ages and elevations of dated microbialite materials from Bouton and others, 2016a (light green circles) and Newell and others, 2017 (dark green circles). Hydrograph prior to 13 ka modeled after Oviatt, 2015. Hydrograph after 13 ka modeled after Oviatt and others, 2021, with the dark gray horizontal bar indicating the uncertainty in lake elevation during the Great Salt Lake phase.*

halothece spp.; Lindsay and others, 2019; Frantz and others, 2023), and attributed their formation to microbially-mediated carbonate precipitation.

Even lower lake elevations in the early 1960s afforded a second look at the lake's microbialites. Carozzi (1962) examined their morphological variability and spatial distribution and linked their occurrence to underlying topographic highs. Halley (1976) described in detail the high variability in their internal structure, with laminated and unlaminated microfabrics existing within different portions of single microbialites (hence, "microbialite" vs. a more descriptive term such as thrombolite or stromatolites). He also noted a general lack of relationship between the living periphyton and observed calcified microstructure and microfossils, notably remarking that, "the organisms on the surface of the Great Salt Lake algal mounds are probably not those which are responsible for the internal structure."

By the late 1960s, the lake's microbialites were once again submerged by a rise in lake level and all but forgotten until they reappeared in the early 2010s during the period of prolonged lake level fall after the 1986–1987 lake highstand. This ushered in a new era of Great Salt Lake microbialite research in which the microbialites were investigated as contributors to the lake ecosystem (Wurtsbaugh, 2009; Belovsky and others, 2011; Wurtsbaugh and others, 2011) and as geobiologic curiosities (Pedone and Folk, 1996; Baskin, 2014; Pace and others, 2016; Lindsay and others, 2017). Interest in the structures was further enhanced by the discovery of the microbialite-associated pre-salt petroleum deposits of offshore Brazil in the mid-2000s, with interest in Great Salt Lake as a potential modern analog environment (Chidsey and others, 2015; Vanden Berg, 2019). Recent studies utilized new techniques and technology, including advanced microscopy (Pace and others, 2016), molecular biology (Lindsay and others, 2017), geospatial and marine acoustic technology (Baskin, 2014; Baskin and others, 2022), and drone imagery (Vanden Berg, 2019).

While the bulk of academic focus on the lake's microbialites (including that of this paper) has been on the extensive reefs that are submerged during "normal" levels of the modern lake, i.e., those below about 1280 meters above sea level (masl; 4200 feet above sea level, or ft-asl), microbialites and other putative microbial carbonates are also found in discrete locations at higher elevations, associated with earlier phases of the lake system (Chidsey and others, 2015; Vennin and others, 2019; Homewood and others, 2022). However, in the remainder of this paper, we use "microbialites" to refer only to the reef-forming deposits below 1280 masl (4200 ft-asl) in Great Salt Lake and its recently exposed shores.

The mega- and macrostructure (Shapiro, 2000) of Great Salt Lake's microbialites includes roughly circular domes ranging in size from ~15–300 cm in diameter, rings of the same scale with collapsed interiors, linear ridges up to several meters long, and mounds that outline the cracks of 30–75 m desiccation polygons at the lake margin (Vanden Berg, 2019) (Figure 2). The morphological diversity of the microbialites is presumably influenced by physical factors including substrate, bathymetry, tectonics, and hydrodynamics. Correlations between these physical factors and microbialite growth suggest that microbialites tend to grow on underlying raised substrate (Eardley, 1938; Chidsey and others, 2015; Bouton and others, 2016b; Bouton and others, 2016a; Vennin and others, 2019; Vanden Berg, 2019; Kanik and others, 2020; Baskin and others, 2022). At the mesoscale, the interior composition of the microbialites includes primarily clotted aragonite (posited to be of direct microbial origin (Pace et al, 2016; Vanden Berg, 2019), as well as trapped and cemented ooids, *Artemia* (brine shrimp) pellets, and some allochthonous grains (Chidsey and others, 2015). Many microbialites also include poorly-defined, laminated stromatolitic fabrics as a minor interior component. Thus, the term microbialite since the structures comprise a mix of fabric types, instead of using more specific terms such as stromatolite, thrombolite, or leolite.

Radiocarbon (^{14}C) dating of both solid carbonate and trapped organic material has yielded ages for microbialite material of 12.7–2.7 ka (Figure 1A) (Bouton and others, 2016b; Bouton and others, 2016a; Newell and others, 2017). The reservoir effect in the modern lake appears to be on the order of several hundred years (Bowen and others, 2019; Paradis and others, 2023), however, it may have been greater in the past (Bowen and others, 2019), and carbonate formation in close association with groundwater may incorporate a reservoir effect of over 5000 years (Homewood and others, 2022). Thus, there is a rather high degree of uncertainty in microbialite radiocarbon ages. Notwithstanding, to date, no modern ages have been measured from microbialite material, although dating is limited to only six microbialites from two locations at the northwest shore of Antelope Island, and none targeted periphyton-rich outer zones where modern carbonate precipitation appears to be happening (for example, Pace and others, 2016). It also appears that microbialites form over thousands of years, with a range from 7.6–12.7 cal ka measured from organic material extracted from four zones within a single microbialite (Newell and others, 2017). This covers a period when the surface elevation of Great Salt Lake is poorly constrained within a rough range of

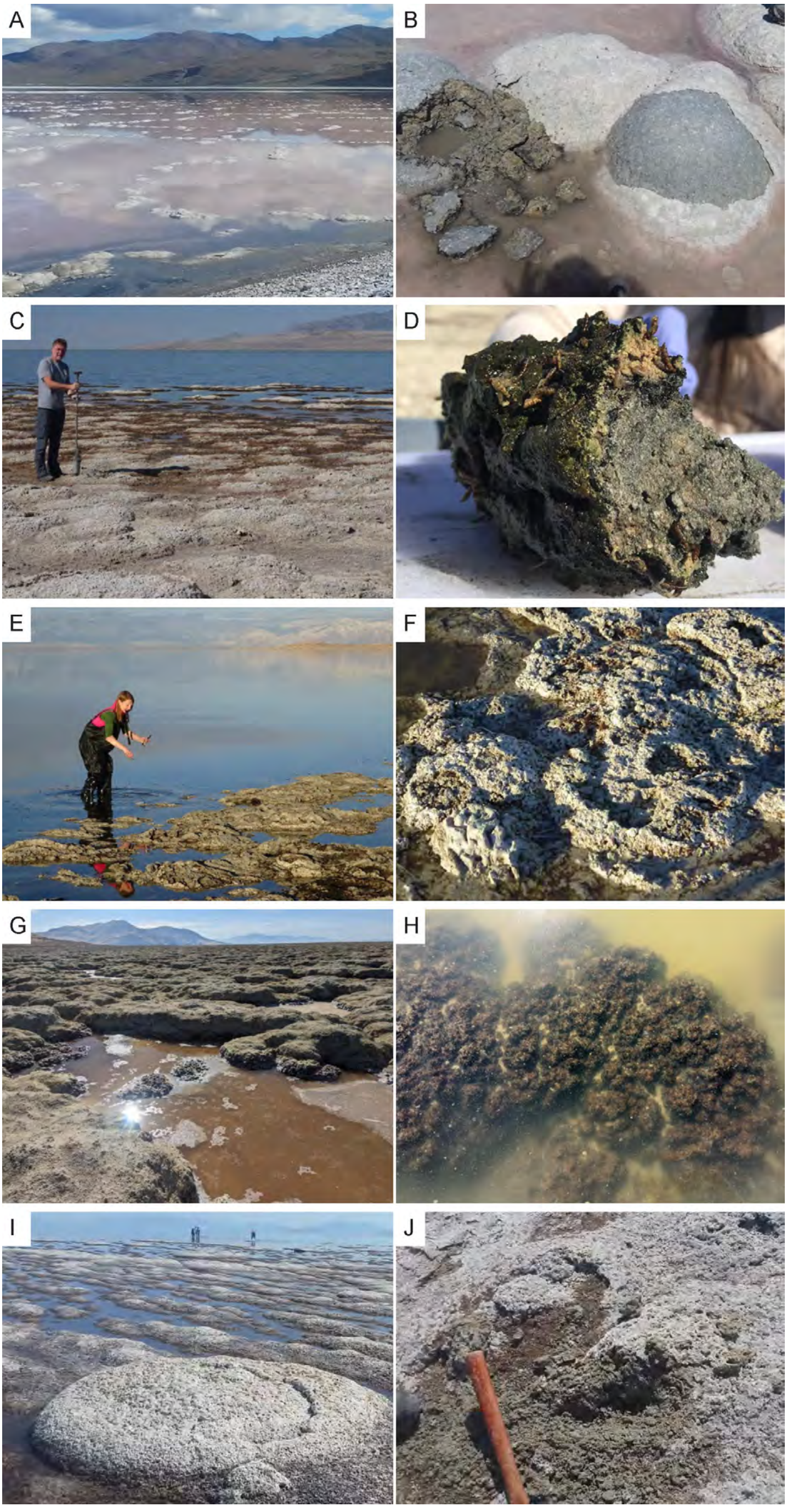

Figure 2. *Photographs of microbialites in and around Great Salt Lake. (A–B) Microbialites that grew at the boundaries of desiccation polygons at Promontory Point, north arm. Note the bright/light surface color (photosynthetic microbial mats are absent) of partially submerged microbialites in halite-saturated north arm water. (C–D) Microbialite reef at Ladyfinger Point on Antelope Island, showing transition from living periphyton to desiccated bright forms, (D) healthy mat and brine fly pupae visible on the surface of a collected microbialite sample; sample is roughly 14 cm across. (E–F) Microbialites at Bridger Bay off Antelope Island, showing (F) collapsed centers; area shown is roughly 1 m across. (G–H) Microbialite reef at Buffalo Point on Antelope Island, showing both exposed and partially-eroded structures, as well as (H) submerged structures with a dark, photosynthetic periphyton; area shown is roughly 0.8 m across. (I–J) Large and elongate microbialites off of Stansbury Island, with thrombolitic crust. Partially eroded crust visible in (J); area shown is roughly 1 m across. Locations where each set of photographs were taken are shown as markers on the map in Fig. 8.*

1271–1285 masl (4170–4216 ft-asl) (Oviatt and others, 2021) (Figure 1A).

Regardless of their age and origin, microbialites play an important role in the modern Great Salt Lake. The exposure of vast expanses of microbialites with historically low lake elevation levels is threatening their preservation and keystone function in the Great Salt Lake ecosystem. Great Salt Lake comprises distinct habitat types ranging from fresh– to brackish-water estuaries and wetlands where rivers enter the lake, to expansive mudflats and playas, to the hypersaline open water of Gunnison Bay (the north arm) and the south arm of Great Salt Lake. Great Salt Lake has historically supported a simple but hemispherically important ecosystem (Figure 3). Ten million birds rely on the lake, including 90% of the world's Eared Grebes (*Podiceps nigricollis*), two species of Phalaropes (*Phalaropus lobatus* and *Phalaropus tricolor*), and large nesting colonies of American White Pelicans (*Pelecanus erythrorhynchos*) and California Gulls (*Larus californicus*) (Conover and Bell, 2020). The lake also supports an economically important brine shrimp cyst-harvesting industry, which supports global aquaculture (Marden and others, 2020). Great Salt Lake's microbialites are a critical feature that supports this extreme ecosystem. Microbialites, the lithified structures, are distinct from microbialite periphyton communities, which, in Great Salt Lake, are robust, productive, and diverse microbial communities that blanket microbialite surfaces (Pace and others, 2016; Lindsay and others, 2017; Kanik and others, 2020; Ingalls and others, 2020). Microbialite periphyton communities are conservatively estimated to be responsible for 30% of the lake's primary productivity (Wurtsbaugh and others, 2011; Anderson and others, 2020; unpublished data by B. Baxter and others, 2023), the remainder is attributed to planktonic algae. The significance of microbialites is as anchored, solid substrates with substantial relief above the surrounding sediment in the Great Salt Lake benthos, providing islands of stability in otherwise mobile sediment where robust mats of photosynthetic microbes can develop. Microbialites can contribute biomass to pelagic zones via sloughing, wave action,

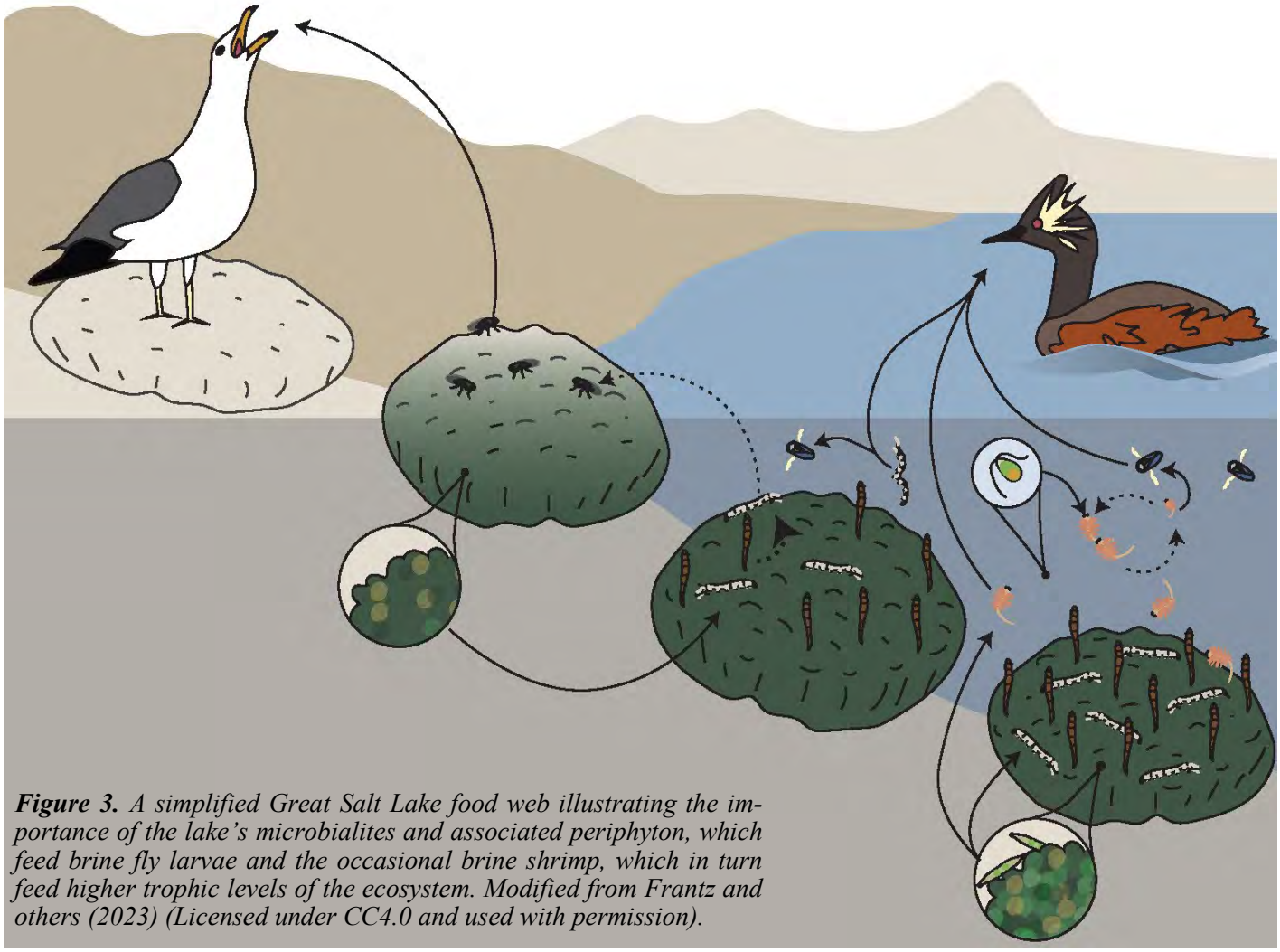

Figure 3. *A simplified Great Salt Lake food web illustrating the importance of the lake's microbialites and associated periphyton, which feed brine fly larvae and the occasional brine shrimp, which in turn feed higher trophic levels of the ecosystem. Modified from Frantz and others (2023) (Licensed under CC4.0 and used with permission).*

and/or bioturbation (MacIntyre and Melack, 1995; Barrett, 2020; Marden and others, 2020). Brine shrimp (*Artemia franciscana*) are filter feeders that prefer pelagic microalgae for nutrition, however, they will also graze on microbialite periphyton in shallow waters (Caudell and Conover, 2006; Lindsay and others, 2019; Brown and others, 2022). Indeed, stable isotope and gut content DNA evidence suggests that brine shrimp feed on microbialite surface communities during summer months (Barrett, 2020; Marden and others, 2020), presumably because the shrimp reduce the planktonic phytoplankton concentrations below the level at which they can efficiently feed (Belovsky and others, 2011), necessitating a supplementary food source.

Microbialites are also a critical part of the brine fly (*Ephydra* spp.) lifecycle, which depend on microbialites for habitat and food (Collins, 1980; Caudell and Conover, 2006; Belovsky and others, 2011; Wurtsbaugh and others, 2011; Conover and Bell, 2020; Brown and others, 2022), and are a critical nutritional source for both shorebirds and pelagic birds at Great Salt Lake (Conover and Bell, 2020; Sorensen and others, 2020). The overwhelming majority of brine flies appear to pupate on submerged microbialites (Collins, 1980; Wurtsbaugh, 2009), again, because they offer a stable benthic substrate. Hatched brine fly larvae then feed primarily on microbialite periphyton communities (Collins, 1980; Barrett, 2020). In shore areas where submerged microbialites are nearby and salinity levels do not exceed 20% (which may be an upper survival limit for microbialite primary producers; Lindsay and others, 2019), the dense clouds of hatched brine flies in late summer are remarkable; walking through a microbialite reef disturbs innumerable thousands of flies that rise from the surface of microbialites and ponded water in swarms.

Lake ecosystem models (for example, those described by Belovsky and others, 2011; Barrett, 2020) require accurate estimates of microbialite extent and relationships between lake elevation and the proportion of submerged vs. exposed microbialites.

Lake Level Fall and Exposure of the Lake's Microbialites

Great Salt Lake elevation levels have dropped to historic lows in recent years, the result of megadrought and overuse of water in the upstream watershed (Null and Wurtsbaugh, 2020), with profound consequences to the lake ecosystem. Avian nesting grounds that were previously protected from predation as islands have become connected to outer lake shores, disrupting bird populations (Kijowski and others, 2020; Sorensen and others, 2020). Increases in lake salinity have produced conditions that exceed levels at which keystone members of the ecosystem optimally survive and reproduce (Baxter and Butler, 2020; Great Salt Lake Salinity Advisory Committee, 2021). In addition, low elevation and consequent shoreline shift has exposed hundreds of kilometers of microbialite reefs, subjecting them—and their ecologically-important periphyton communities—to desiccation, negating their ecosystem function.

Recent work by Frantz and others (2023) provided some hope in the face of current mass microbialite exposure, showing that exposed and desiccated microbialites can regain some of their periphyton community in relatively short order once re-submerged in healthy lake water. However, their study was limited to a brief period of recovery, well before thick, carbonate-rich mats began to reappear (which could take years to decades). Their results also indicated that recovery is limited as lake level continues to fall and salinity continues to rise. In addition, they noted results that hint that individual microbialite areas harbor distinct strains of *Euhalothece*, the primary microbialite phototroph; losing areas of reef may therefore disrupt natural microbial diversity and could make the lake's microbialite-supported ecosystem less resilient to future change. Furthermore, they showed that subaerially exposed microbialites are rapidly weathered. Extended periods of exposure could reduce the height of microbialite reefs (and raise the surrounding sediment), diminishing their value as habitat for periphyton and brine fly larvae, even if lake levels rebound.

Mapping Great Salt Lake's Microbialites

The current threat to the lake's microbialites with lake level fall, and consequent long-term impacts on the lake ecosystem, mean that management of Great Salt Lake and its watershed requires a quantitative understanding of how different lake elevations affect microbialite exposure. This in turn depends on accurate maps of microbialite reef extent in Great Salt Lake, as well as refined relationships between lake bathymetry and microbialite exposure. Additionally, low lake levels and the exposure of the lake's microbialites has presented new hazards for navigation of watercraft on the lake. Accurate mapping of microbialite extent also has scientific value, as illustrated by several recent publications that have linked microbialite locations and extent to topographic features, faults, tectonics, wave energy, depth bands, and groundwater availability (Bouton and others, 2016b; Bouton and others, 2016a; Vanden Berg, 2019; Baskin and others, 2022).

The first map of microbialite extent was from Eardley (1938), who took advantage of a period of relatively low lake level in the mid-1930s to map them roughly from shore, as well as observing them at depths up to 1 m during "considerable travel" via a boat, the appropriately named *Hydrographer*, near the shores of the lake and in transects between the lake's islands. His paper includes both site and aerial photographs at various locations around the lake shore. Importantly, he also noted that cores from previously conducted engineering studies indicated prior periods of microbialite formation in the lake in areas different from where he had observed them. He used a planimeter and his map to determine a rough microbialite reef area of 398 km^2 (154 mi^2) within the lake (Figure 4). Due to limited mapping technology and limited field observations, Eardley's map largely missed microbialite reefs on the western side of the lake, as well as deeper-water areas, whereas extents on the east side of the north arm are overestimated. Overall, Eardley underestimated the extent of Great Salt Lake microbialites.

For his 2014 Ph.D. dissertation, Baskin (Baskin, 2014) produced the first major update to Eardley's map, utilizing single-beam sound-velocity soundings obtained during his work producing digital bathymetric surveys of the lake with the United States Geological Survey (USGS) (Baskin and Allen, 2005; Baskin and Turner, 2006). His method for identifying microbialites involved a calculation of rugosity from the sounding data that was truthed in select high-rugosity areas using dual-frequency 2D side scan sonar, swept-frequency Chirp sub bottom profiles, and videography (when lake visibility permitted), as well as *in situ* sampling in known microbialite locations. The extents identified in his dissertation were then updated and refined with the publication of Baskin and others (2022). This newer publication identified an area of ~1000 km^2 (~390 mi^2) of putative microbialite reef, with >700 km^2 (270 mi^2) in the south arm and >300 km^2 (~120 mi^2) in the north arm (Figure 4), nearly tripling the extent mapped by Eardley (1938). In his thesis, Baskin also noted the effect of the railroad causeway, completed in 1959, that bisected the lake and cut off the north arm from most of the lake's freshwater input, causing it to become rapidly salt-saturated and killing off the *Euhalothece*-based periphyton on north arm microbialites (this was also noted by Post, 1977, and verified with DNA sequencing by Lindsay and others, 2017). Although extensive, Baskin's map was largely based on indirect data; due to time and resource constraints he was only able to verify the presence of benthic microbialites in limited areas of his reported mapped extent.

Vanden Berg (2019) produced an alternative map of microbialite extent using Google Earth imagery and limited field mapping, yielding a microbialite reef aerial extent of 680 km^2. However, the map and extent estimates were limited by the availability of clear-water imagery and stated the need for further field verification.

Bouton and others (2020) further amended microbialite extent estimates by merging the Eardley (1938) and Baskin (2014) maps and adding additional refinement based on limited remote imagery of western Antelope Island from Bouton and others (2016a), yielding an expanded (and overestimated) microbialite reef aerial extent of 1261 km^2 (487 mi^2). In sum, maps of microbialite reef extent in the literature to date have given conflicting and highly variable results (Figure 4).

Recent low lake elevations and increasing resolution of satellite and aerial imagery have made microbialite mapping via remote imaging more powerful and accurate than ever before. Water column visibility in the lake varies greatly with season, biological activity, and weather, however, during clear-water periods the Secchi disk depth typically exceeds 3 m (10 ft), making the lake bottom visible from aerial view in all but the deepest portions of the lake (Belovsky and others, 2011). Microbialites are visible to depths in excess of 4 m (13 ft) in some high-visibility images, a fact that several studies have utilized to identify extents of microbialites against the lake bed (Bouton and others, 2016a; Vanden Berg, 2019). Advantages of using remote imagery over field-based mapping include the ability to quickly map large regions across the full extent of the lake (vs. transects or areas only accessible from shore), and that dry, shallow-water, and deep microbialites can all be mapped using the same method.

The varied estimates of microbialite extent from prior literature (Table 1) adds a large element of uncertainty to estimates of overall microbialite productivity, microbialite exposure, and other factors influencing the management of Great Salt Lake. Thus, our study attempted to improve on previous estimates by (1) mapping microbialites using satellite imagery, taking advantage of historic low lake level and improved spatial and temporal resolution of available images, (2) confirming (or refuting) the presence of suspected microbialite areas from prior mapping efforts via aerial imagery and field checks, and (3) generating shapefiles of microbialite reef extent that can be used in quantitative estimates of microbialite extent and exposure. Here, we present our results, which include the most detailed map of Great Salt Lake microbialite extent to date and a model of microbialite exposure at different lake elevations.

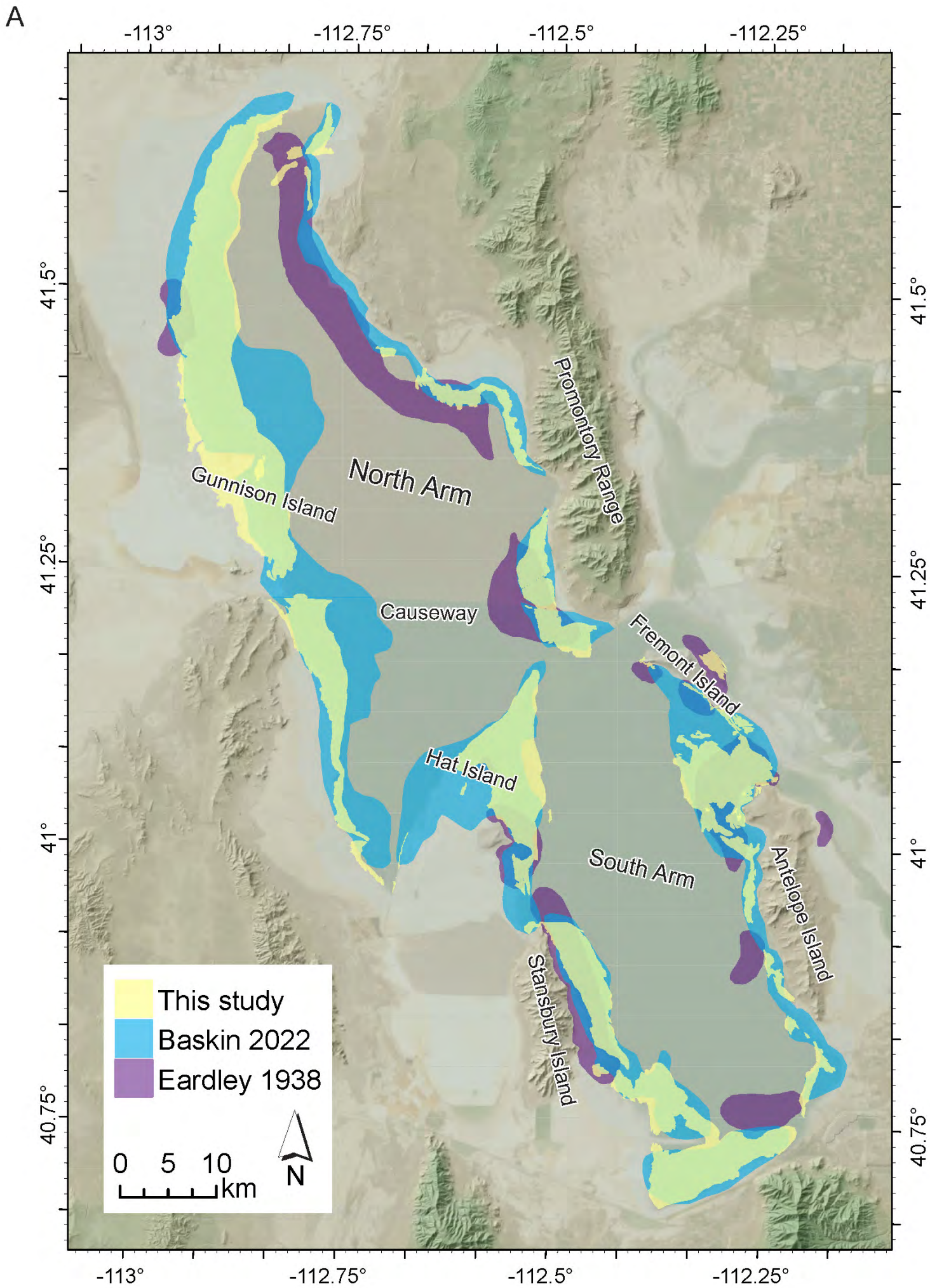

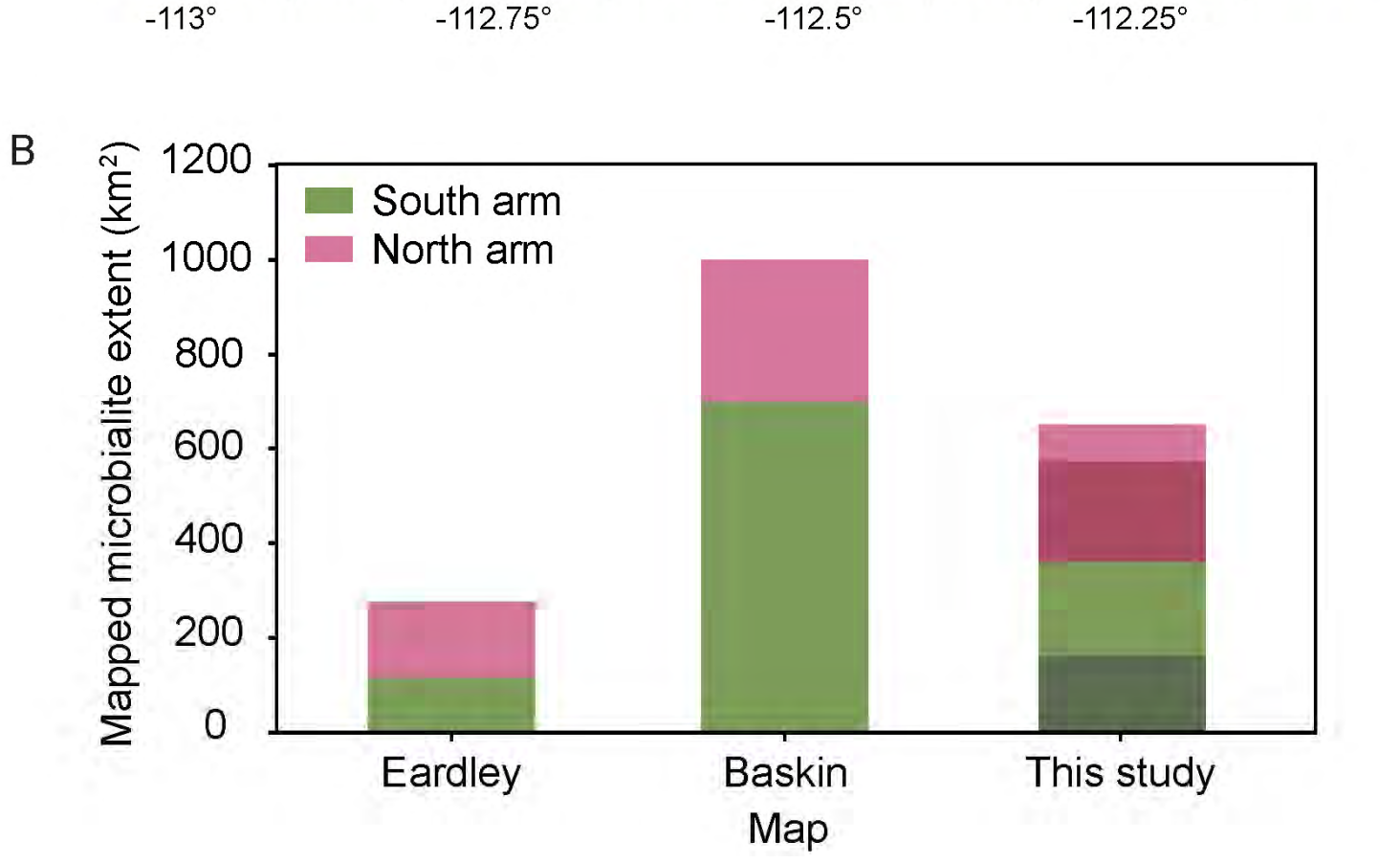

Figure 4. *Comparison of previously published microbialite reef extent maps for Great Salt Lake with our mapped reef extent. (A) Microbialite reef areas mapped by Eardley (1938; in purple), Baskin and others (2022; in blue), and this study (yellow), highlighting areas of overlap and major differences. (B) Quantified comparison of mapped reef areas in the three studies. Darker vs. lighter colors in the plot for this study indicate regions of high vs. low confidence.*

Table 1. *Summary of prior attempts to map lakebed microbialites in Great Salt Lake. Where given, reported values are non-italicized while values inferred from traced shapefiles are italicized.*

Reference	Method	Shortcomings and uncertainties	Mapped microbialite extent (km^2)		
			South Arm	North Arm	Total
Eardley, 1938	Field verification from shore and by boat	Limited to primarily nearshore areas confirmed in the field, missed areas of deeper microbialite reef and areas in the western portions of the lake	*117*	*160*	*277* 260
Baskin and others, 2022	Rugosity from acoustic soundings during bathymetric surveys, partially confirmed in the field	Indirect measure with limited field confirmation	700 *654*	300 *446*	1000 *1099*
Vanden Berg, 2019	Remote imagery	Limited image availability, limited field verification	*56*	*92*	*147*
Bouton and others, 2020	Merged prior maps with additional areas from remote imagery reported in Bouton and others, 2016a	Inherited uncertainties from prior work, assumed variable regions were due to burial vs. rip-up clasts			1261
This study (high confidence)	Remote imagery	Limited field verification, some deep-water areas could not be mapped	288	360	648

METHODS

Mapping Microbialites Using Satellite Imagery

Data Acquisition

Positive identification of microbialites through the application of remote sensing required high-resolution imagery with sufficient temporal resolution to permit analysis of areas of interest during favorable periods (i.e., periods without obscuring cloud cover, with low lake elevations, and with good water clarity). Imagery was collected through Esri's World Imagery Wayback (EWIW) archive. EWIW is a digital archive of published world imagery since 2014 that is stored as layer files that can be downloaded or viewed online through ArcGIS's living atlas. The current extent of the Great Salt Lake covers over 4000 km^2 within the Great Salt Lake basin (within the quad 40.6 –41.8°N, 111.8–113.2°W). Imagery for the region is collected via multiple satellite constellations at different temporal sequences that are location-dependent. North and south arms of Great Salt Lake required sets of time series imagery that often come from different capture dates (Table 2). EWIW acquires imagery via Landsat, USDA NAIP, TerraColor, Digital Globe, GeoEye IKONOS and AeroGRID at 0.6–15 m spatial resolution depending on location and provider.

Dates were selected to provide optimal below-water visibility, with favorable atmospheric conditions (especially low cloud cover), clear water periods (during the absence of water turbulence or algal blooms), and relatively low lake levels (permitting visibility in deeper areas of the lake), allowing good visual records of changing microbialite reef exposure (Figure 5). The analysis over multiple time points was vital for distinguishing loose debris from true reef, as illustrated in Figure 6. Google Earth Pro (GEP) was also utilized to compare and contrast visible reef zones with EWIW imagery. GEP utilizes Landsat and Copernicus satellite constellations for imagery collection. Dates of available archival GEP imagery vary; imagery from 2016–2022 provided the best clarity for positive or negative identification of microbialites. Imagery in GEP varies based on location and scale, with each view of lake locations utilizing several remote sensing sources and acquisition dates.

High-resolution historical imagery was collected from EWIW and downloaded as layer files. Once imported into ArcGIS Pro, each layer file was used for side-by-side comparison of microbialite structures. This side-by-side analysis of archived EWIW and GEP imagery was used to digitize areas that could be positively identified as reef zones via remote sensing.

Identification and Mapping

To develop criteria for microbialite reef identification, we first compared characteristics of known reef zones (from field studies by the authors) to our remote sensing imagery (Figure 7). We identified three reliable patterns for identifying microbialites in remote imagery.

Table 2. *Summary of remote imagery utilized for this study. Image Capture Date is the date satellite images were captured, while World Imagery Date is a date of availability in ArcGIS for the set of images.*

Image Capture Date	World Imagery Date	Location	Provider	Resolution (m)	Accuracy (m)
2014-06-29	2015-07-08	South Arm	NAIP	1	6
2014-08-31	2015-07-08	North Arm	NAIP	1	6
2016-06-26	2017-05-03	South Arm	NAIP	1	6
2016-07-15	2017-05-03	North Arm	NAIP	1	6
2016-05-07	2018-01-08	North Arm	Digital Globe	0.5	10.2
2013-08-29	2018-01-08	South Arm	Digital Globe	0.5	10.2
2022-05-07	2022-11-02	South Arm	Maxar (GEO1)	0.46	5
2021-10-15	2022-11-02	North Arm	Maxar (WV02)	0.5	5
2021-04-08	2022-12-14	South Arm	Maxar (GEO1)	0.46	5
2021-10-15	2022-12-14	North Arm	Maxar (WV02)	0.5	5

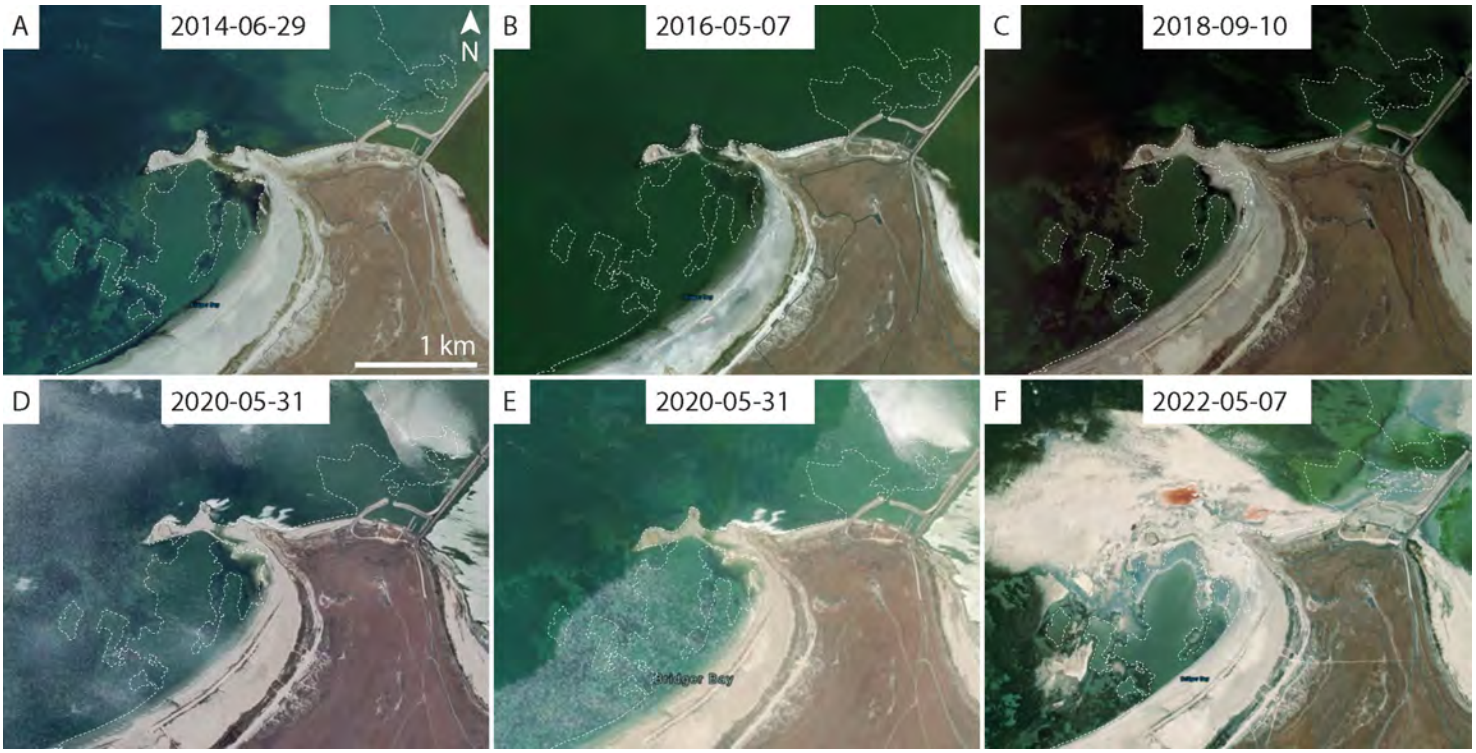

Figure 5. *Comparison of satellite images of a specific location at northern Antelope Island (41.06°, -112.26°) using different image dates. In all images, the thin, white dashed line shows the area outlined as microbialite reef in this study. (A) Microbialite reef can be seen as a dark green submerged region in June 2014 (Esri World Imagery Wayback). (B) In May 2016, visibility of the reef was limited due to poor water clarity and higher lake elevation (Esri World Imagery Wayback). (C) In September 2018, part of the visible reef was obscured due to image distortion and resolution issues (Google Earth Pro). (D) Waves on the lake in May 2020 obscure the reef (Google Earth Pro). (E) Waves and light reflection again obscure parts of the reef, with image stitching artifacts obscuring other portions (Esri World Imagery Wayback). (F) Exposed microbialite reef appear as bright/light regions during low lake level in May 2022 (Esri World Imagery Wayback).*

First, "healthy," submerged microbialites appear dark green in remote imagery and stand out against the brighter carbonate sediment background (Figs. 7A & 7D). In some instances of dark green submerged substrate, microbialite reefs were indistinguishable from loose microbialite debris (Figure 6) in single images; for such regions, we compared images from at least three different dates to look for evidence of mobility, with only stationary features mapped as reef.

Second, as lake levels fall, microbialites become exposed and "bleach" (Frantz and others, 2023), causing exposed reef areas to appear bright in partially-exposed reef areas. Our second identified pattern was that of white reef areas (bleached microbialites) with patterned high-relief mounds (for example, Figs. 7C & D).

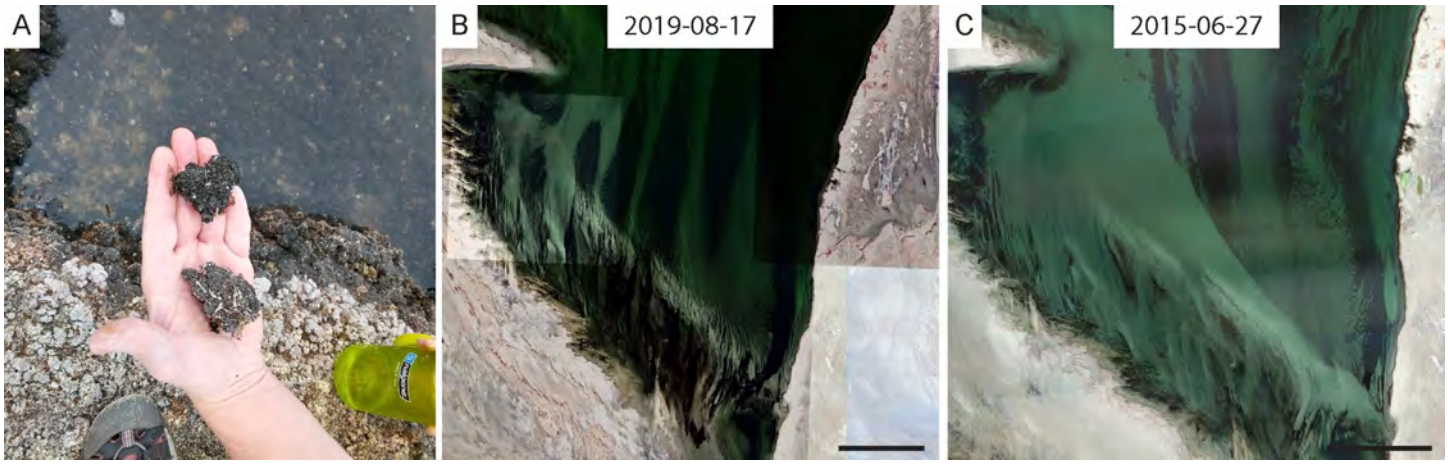

Figure 6. *Examples of mobile debris. (A) Field photograph of loose carbonaceous microbial mat debris between actual microbialite mounds at Buffalo Point in August 2021. (B) Google Earth Pro remote image showing a dark green region of potential microbialite reef in the southwest arm of the lake (40.983°, -112.709°) on 2019-08-17, and (C) Google Earth Pro remote image of the same location on 2015-06-27 showing shifted mobile debris. Scale bars in (B) and (C) are both 1 km.*

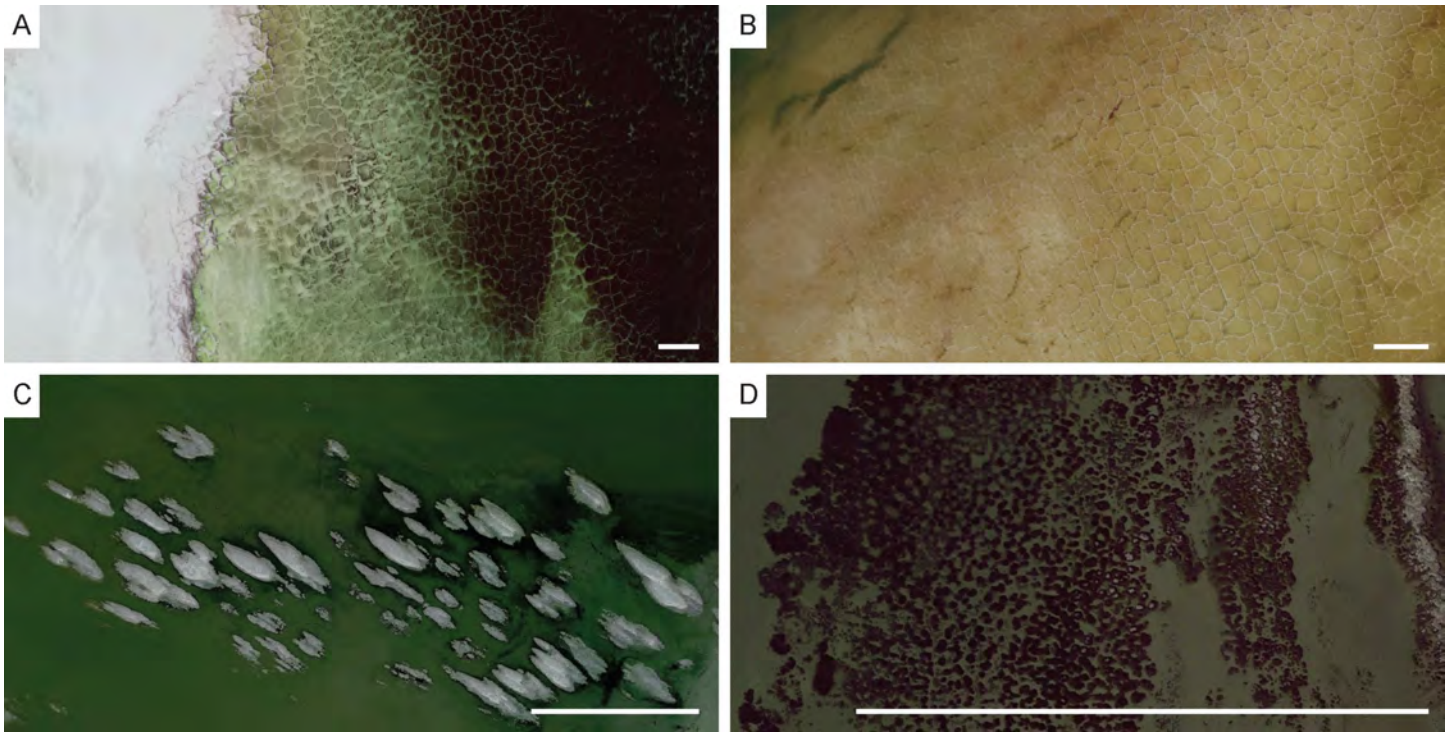

Figure 7. *Examples of field-verified microbialite reef areas identified from remote imagery in the south arm of Great Salt Lake. (A) Dark green submerged microbialites and bright bleached megapolygons indicate the presence of microbialites in a nearshore area in the south arm of the lake (41.073°, -112.573°). (B) Submerged desiccated microbialite-edged polygons in the north arm of the lake (41.249°, -112.533°). (C) Bright exposed and desiccated microbialites stand out against green lake water at a site near the Antelope Island marina (41.064°, -112.237°). (D) Partially submerged microbialites between Buffalo Point and White Rock Bay (41.033°, -112.275°). Scale bar in all images is 100 m. Image locations are shown as markers on the map in Fig. 8. Images from Google Earth Pro.*

Finally, microbialites tend to form on the perimeters of "megapolygons"—polygonal structures roughly 30–75 meters in diameter (Vanden Berg, 2019) (Figs. 7A & 7B). Thus, megapolygons are our third identified pattern. In contrast, zones of smaller desiccation–related polygons, averaging only 4–9 meters, are present along shoreline areas at higher elevation and are not associated with microbialites (Vanden Berg, 2019). These smaller polygons can be ephemeral, appearing and disappearing with changes in lake level.

In some areas, particularly north and northwest of Hat Island (112.586°W 41.071°N), we identified broad regions of megapolygons (some quite faint) at elevations above 4195 ft-asl, however, we excluded these from our map due to lack of field verification and their anomalously high elevations; if microbialites are found associated with these megapolygons, they might belong to an older generation.

Regions positively identified as containing micro-

bialite reefs were mapped in ESRI's ArcGIS Pro. Separate feature classes were created for the north and south arms and were digitized using ArcGIS Pro by tracing shapes over downloaded imagery. Feature classes as well as bathymetric layers were imported and projected as UTM NAD83 zone 12N to minimize distortion and maximize location accuracy. Areas were initially digitized in large zones before being refined to greater resolution in a second stage of processing.

Comparison to Prior Work

Areas mapped by prior studies were given extra attention in our analysis, with maps by Eardley (1938), Vanden Berg (2019), Bouton and others (2020), and Baskin and others (2022) providing a framework for the mapping efforts described in this study (Figure 4). Some regions identified as reef zones by Baskin and others (2022) were not able to be conclusively analyzed using remote imagery due to their occurrence in deeper areas of the lake. We included some of these regions from Baskin in our map as low-confidence regions.

Field Verification

Many identified reef sites were confirmed with field verification, particularly in accessible shoreline areas (Figure 8); these regions are denoted as high-confidence regions in our map. The western shores of the lake are difficult to access due in part to military restrictions and private land ownership, thus most sites on the west side of the lake have not been field verified. Identified reef sites not yet confirmed with field verification are denoted as low-confidence regions except for those associated with megapolygons, which were classified as high-confidence even in the absence of field verification.

Lake Elevation-Exposure Model

In order to develop a model of microbialite exposure at different lake elevations, we used shapefiles for the mapped microbialites and determined overlap with lake bathymetry shapefiles (1 ft intervals) imported from Baskin and Allen (2005) and Baskin and Turner (2006). However, caution should be exercised when using the historical bathymetry data, especially in the nearshore environment: modern observations during extreme low lake level indicate that these contours are significantly incorrect in several nearshore environments around the lake. Inaccuracies in the bathymetric data will create inaccuracies in the exposure models presented in this study, but currently this is the only published bathymetric data available. Microbialite reef area shapes were combined in distinct layers for the north vs. south arm of the lake, since the two arms can have independent water surface elevation levels and can be managed separately for ecosystem function. Digitized microbialite reef zones were split based on bathymetric data. These clipped zones were used to identify areas of exposure as lake levels decline.

Areas of mapped microbialite reef at elevations above bathymetric lines were considered exposed at that lake elevation, whereas areas of microbialite reef at or below bathymetric lines were considered submerged. The curve fit least-squares function in the scipy.optimize python package (Virtanen and others, 2020) was used to generate logistic regression models parameterized to fit the area vs. bathymetry elevation values for each arm of the lake using the least squares method.

RESULTS

Microbialite Reef Extent

Our remote imagery-based mapping of microbialite extent indicates 360 km^2 (139 mi^2) of microbialite reef between 1271.6 and 1280.5 masl (4172–4201 ft-asl) in the south arm of Great Salt Lake, of which 45% are high-confidence regions. In the north arm of the lake, we mapped 288 km^2 (111 mi^2) of microbialite reef in the same elevation band, of which 74% are high-confidence regions confirmed with field observation (Figure 8). The distributions of mapped microbialites by elevation were similar in the north and south arms (Figure S1), although our mapped region in the north arm was limited by limited field verification, poor water visibility, and image resolution.

Our mapped extent was somewhat similar with the Baskin and others (2022) map, with several important differences. First, we were able to map microbialites in exposed shore environments that were inaccessible by boat and therefore unable to be mapped sonographically by Baskin, thus, our map extends to higher elevations than the Baskin and others (2022) map (for example, bottom left of Figure 9C). Second, in some regions, areas mapped by Baskin extended deeper into the lake than what we found, for example, on the western shore of the lake (Figure 9B–C). Third, our map is more spatially refined (Figure 9E). Also, some regions mapped by Baskin were exposed as dry shoreline in recent years, with no apparent microbialites present (for example, Figure 9D).

Most (95%) of the microbialites that we mapped lie in an elevation band between 1274.0 and 1278.6

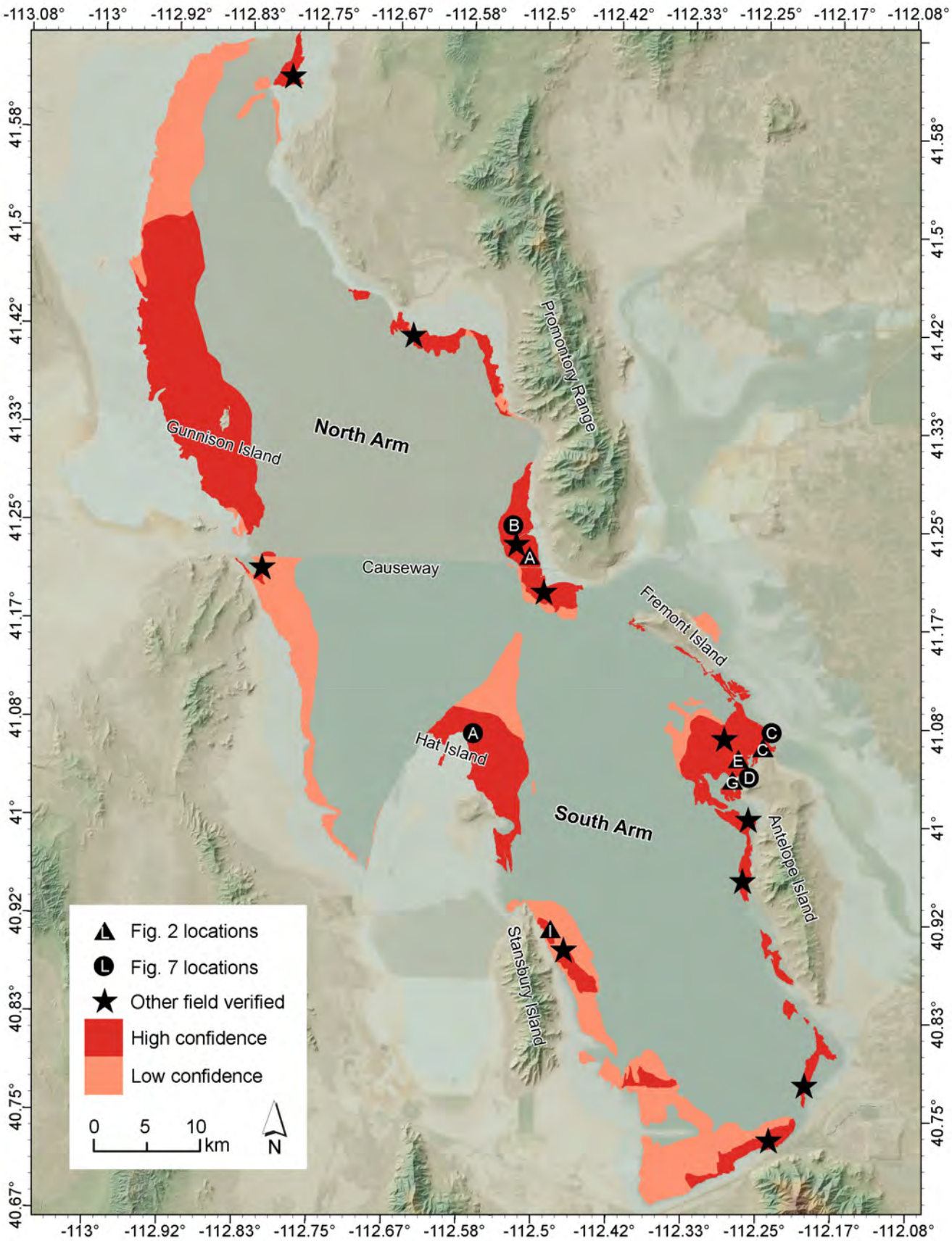

Figure 8. *Mapped extent of microbialites in Great Salt Lake (this study) showing regions of high confidence of microbialite occurrence (areas confirmed with field verification or presence of megapolygons) and regions mapped at low confidence of microbialite occurrence (areas of apparent microbialite reef in remote imagery). Stars indicate areas where field verification of microbialite reef existence (or non-existence) was verified. Triangles mark the approximate locations of photograph sets shown in Fig. 2. Circles mark the locations of remote imagery shown in Fig. 7. Basemap imagery provided by Earthstar Geographics.*

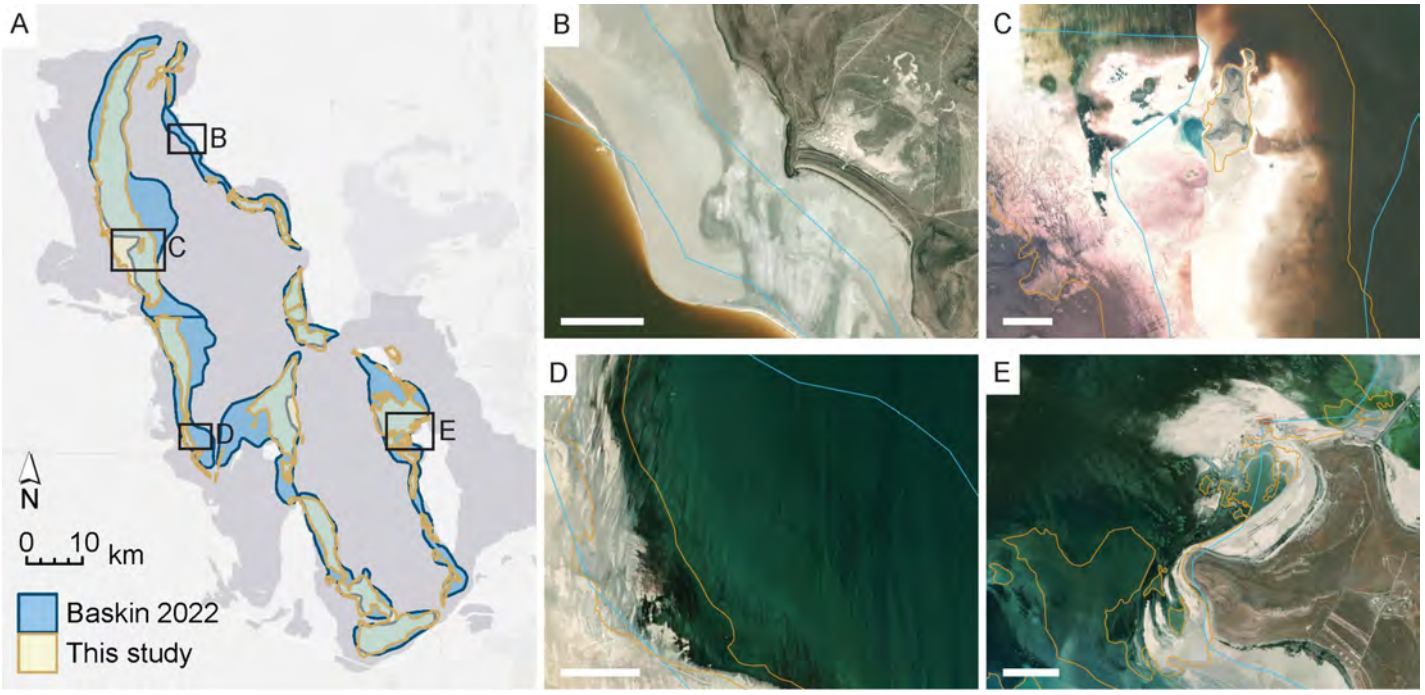

Figure 9. *Example detail areas where mapped microbialite extents in this study differed significantly from Baskin and others (2022). (A) Mapped microbialite extents in Baskin (blue) vs. this study (yellow) showing areas of detail (B–E). (B) Region along the northeastern lakeshore mapped as having microbialites by Baskin where we were unable to find evidence of microbialites in remote imagery or via field checks. Base image from Maxar 2015-07-08. (C) Area along the western shore of the lake where we identified a region of higher elevation microbialites visible in remote imagery but unmapped by Baskin. The Baskin map also extends into deeper water than we were able to confirm. Base image from Maxar 2015-04-27; mid-image color changes is an imagery artifact. (D) Area at the southwestern shore of the lake where the Baskin map includes microbialites where we only observed regions of mobile clasts. Base image from Maxar 2021-10-16. (E) Region off the northwest shore of Antelope Island where high-resolution imagery from Esri World Imagery Wayback and Google Earth Pro allowed for more precise mapping of microbialite reef zones in our study relative to the Baskin map. Base image from Maxar/Earthstar Geographics 2022-05-08. White scale bars in areas of detail (B–E) are all 1 km.*

masl (4180–4195 ft-asl) (Figure 10). Several notable deeper-water outlier areas are bounded by active Quaternary fault zones (Figure S2).

Elevation-Exposure Model

Our findings for microbialite exposure at different lake elevations are summarized in Table 3 and Figs. 11–12.

Fitting a logistic regression line (Equation 1) using the least-squares method to the lake elevation (*elev*, in masl or ft-asl) vs. microbialite exposure data (in km^2 or mi^2) gave r^2 values ≥ 0.995 for all models (Figure 12).

Equation 1: $$A_{exposed} = \frac{L}{1+e^{-k\cdot(x_0-elev)}} + b$$

In Equation 1, $A_{exposed}$ is the area (in km^2 or mi^2) of microbialites exposed at a given lake elevation (*elev*, in masl), where L, k, x_0, and b are model parameters defined in Table 4.

DISCUSSION

Refined Map of Microbialite Reef Extent for Great Salt Lake

Our remote imagery-based map of microbialite extent yielded an extent of microbialites between the lower and upper bounds of prior work (Figure 4): at both low and high confidence levels, we mapped significantly more microbialite area than Eardley (1938), but substantially less than what was mapped by Baskin and others (2022).

Because it relied on limited field observation and rough mapping tools available at the time, the Eardley (1938) map represents an understandable underestimate of microbialite extent. Meanwhile, the Baskin and others (2022) map covered the entire lakebed in relatively high resolution, however, by relying on indirect measurements of lake-bottom rugosity, it could have overestimated true microbialite extent. In general, our map refines the spatial extent of reefs identified by Baskin: 86% of our mapped regions were also mapped by Baskin, for both our high and low confi-

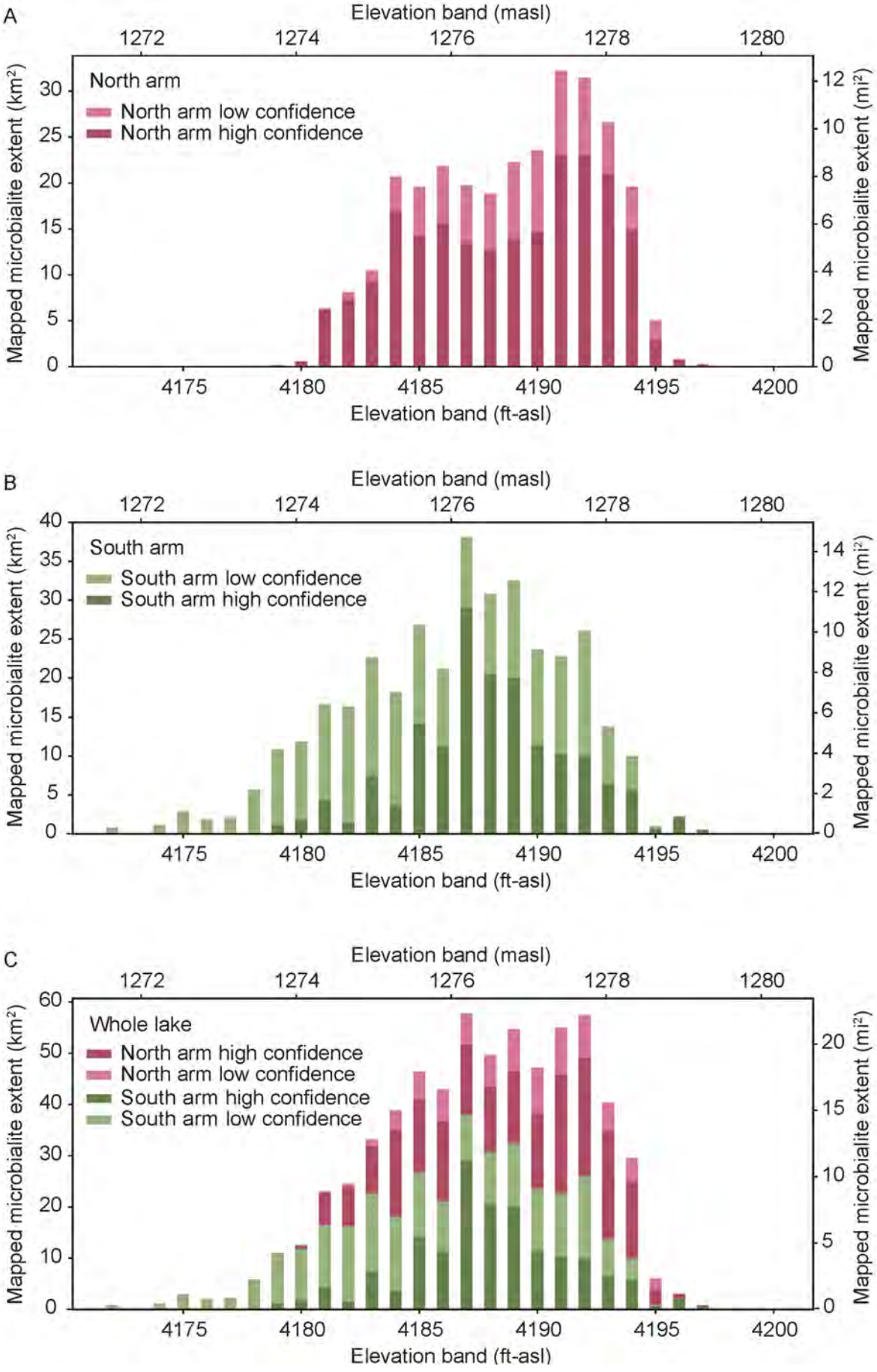

Figure 10. *Histograms of microbialite reef area identified at high and low confidence in different 1 ft elevation bands (labels show the lower bound of the band). (A) North arm (NA). (B) South arm (SA). (C) Both arms.*

Table 3. *Mapped microbialite reef area in different elevation bands, and area of microbialite exposure when lake level reaches the lower elevation bound.*

	Area of mapped microbialite reef (km2)				Total area exposed at lower elevation bound (km2)					
Elevation band	High confidence		Low confidence		High confidence		All mapped (high + low conf.)			
(ft-asl)	North Arm	South Arm	North Arm	South Arm	North Arm	South Arm	Whole lake	North Arm	South Arm	Whole lake
4172 – 4173	0.00	0.01	0.00	0.79	212.0	162.6	374.6	288.45	360.4	648.8
4173 – 4174	0.00	0.00	0.00	0.03	212.0	162.6	374.6	288.45	359.6	648.0
4174 – 4175	0.00	0.02	0.00	1.06	212.0	162.6	374.6	288.45	359.5	648.0
4175 – 4176	0.01	0.01	0.00	2.90	212.0	162.5	374.6	288.45	358.4	646.9
4176 – 4177	0.04	0.06	0.00	1.80	212.0	162.5	374.5	288.43	355.5	644.0
4177 – 4178	0.09	0.08	0.00	2.04	212.0	162.5	374.4	288.39	353.7	642.1
4178 – 4179	0.09	0.15	0.00	5.55	211.9	162.4	374.3	288.30	351.6	639.9
4179 – 4180	0.15	1.17	0.00	9.65	211.8	162.2	374.0	288.21	345.9	634.1
4180 – 4181	0.59	1.81	0.01	10.07	211.6	161.1	372.7	288.07	335.0	623.1
4181 – 4182	6.33	4.35	0.01	12.28	211.1	159.3	370.3	287.47	323.2	610.6
4182 – 4183	7.30	1.45	0.82	14.94	204.7	154.9	359.6	281.12	306.5	587.6
4183 – 4184	9.36	7.41	1.16	15.21	197.4	153.5	350.9	273.00	290.1	563.1
4184 – 4185	16.90	3.66	3.78	14.49	188.1	146.0	334.1	262.48	267.5	530.0
4185 – 4186	14.32	14.12	5.30	12.67	171.2	142.4	313.5	241.80	249.4	491.2
4186 – 4187	15.62	11.27	6.19	9.90	156.8	128.3	285.1	222.18	222.6	444.8
4187 – 4188	13.67	29.04	6.05	9.06	141.2	117.0	258.2	200.37	201.4	401.8
4188 – 4189	12.73	20.46	6.09	10.36	127.5	88.0	215.5	180.64	163.3	344.0
4189 – 4190	13.99	20.04	8.26	12.43	114.8	67.5	182.3	161.82	132.5	294.3
4190 – 4191	14.65	11.45	8.91	12.21	100.8	47.5	148.3	139.58	100.0	239.6
4191 – 4192	23.07	10.32	9.15	12.43	86.2	36.0	122.2	116.02	76.4	192.4
4192 – 4193	23.11	10.01	8.31	16.06	63.1	25.7	88.8	83.80	53.6	137.4
4193 – 4194	21.04	6.50	5.52	7.30	40.0	15.7	55.7	52.38	27.5	79.9
4194 – 4195	14.96	5.71	4.63	4.28	19.0	9.2	28.1	25.82	13.7	39.5
4195 – 4196	2.91	0.71	2.15	0.24	4.0	3.5	7.5	6.22	3.7	10.0
4196 – 4197	0.77	2.19	0.07	0.03	1.1	2.8	3.8	1.16	2.8	4.0
4197 – 4198	0.25	0.54	0.00	0.00	0.3	0.6	0.9	0.32	0.6	0.9
4198 – 4199	0.07	0.00	0.00	0.00	0.1	0.0	0.1	0.07	0.0	0.1
4199 – 4200	0.00	0.01	0.00	0.00	0.0	0.0	0.0	0.00	0.0	0.0
4200 – 4201	0.00	0.01	0.00	0.00	0.0	0.0	0.0	0.00	0.0	0.0

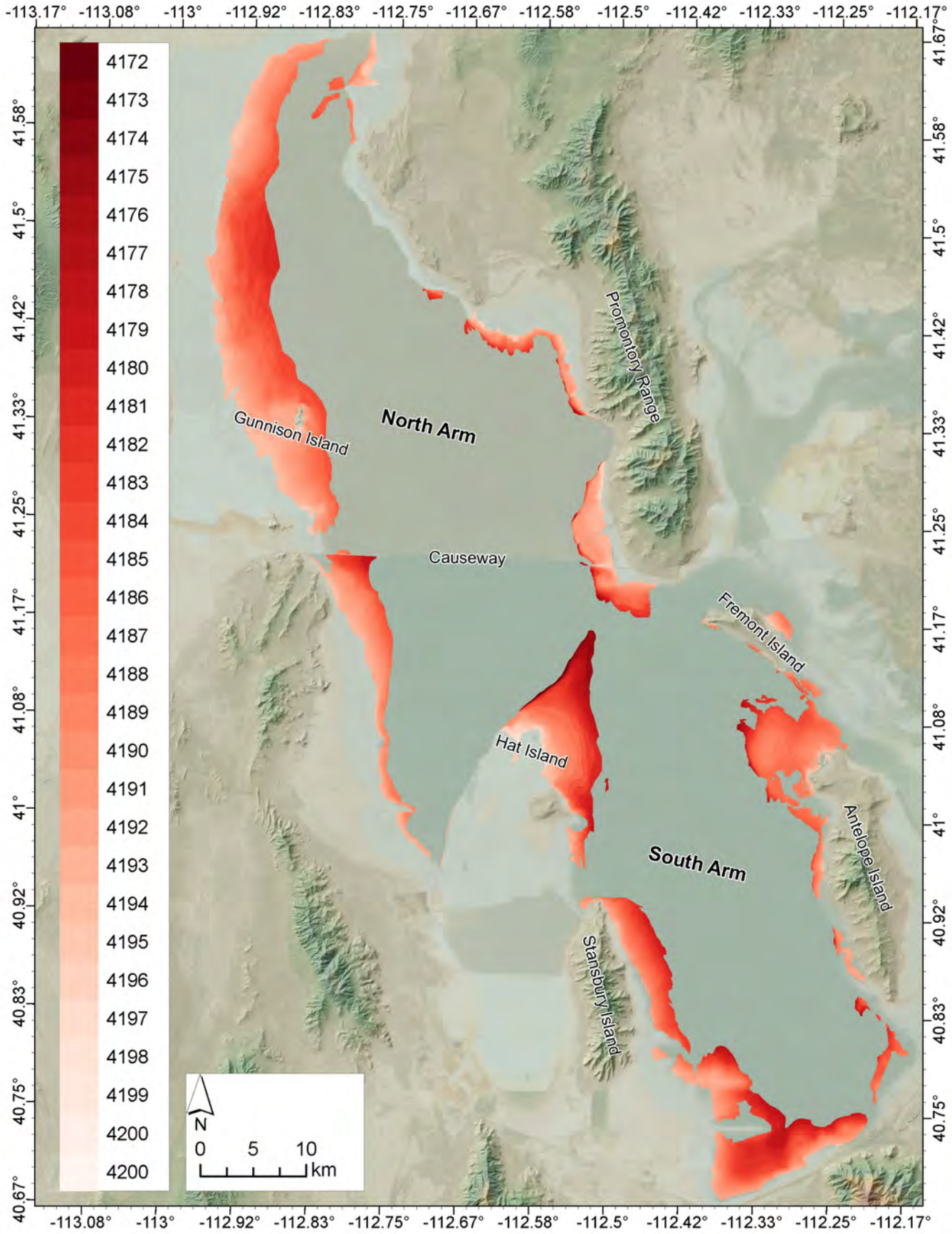

Figure 11. *Map of microbialite reef areas (this study) correlated with lake bathymetry, highlighting the areas of microbialite reef exposed at different lake surface elevations (in ft-asl). Basemap imagery provided by Earthstar Geographics.*

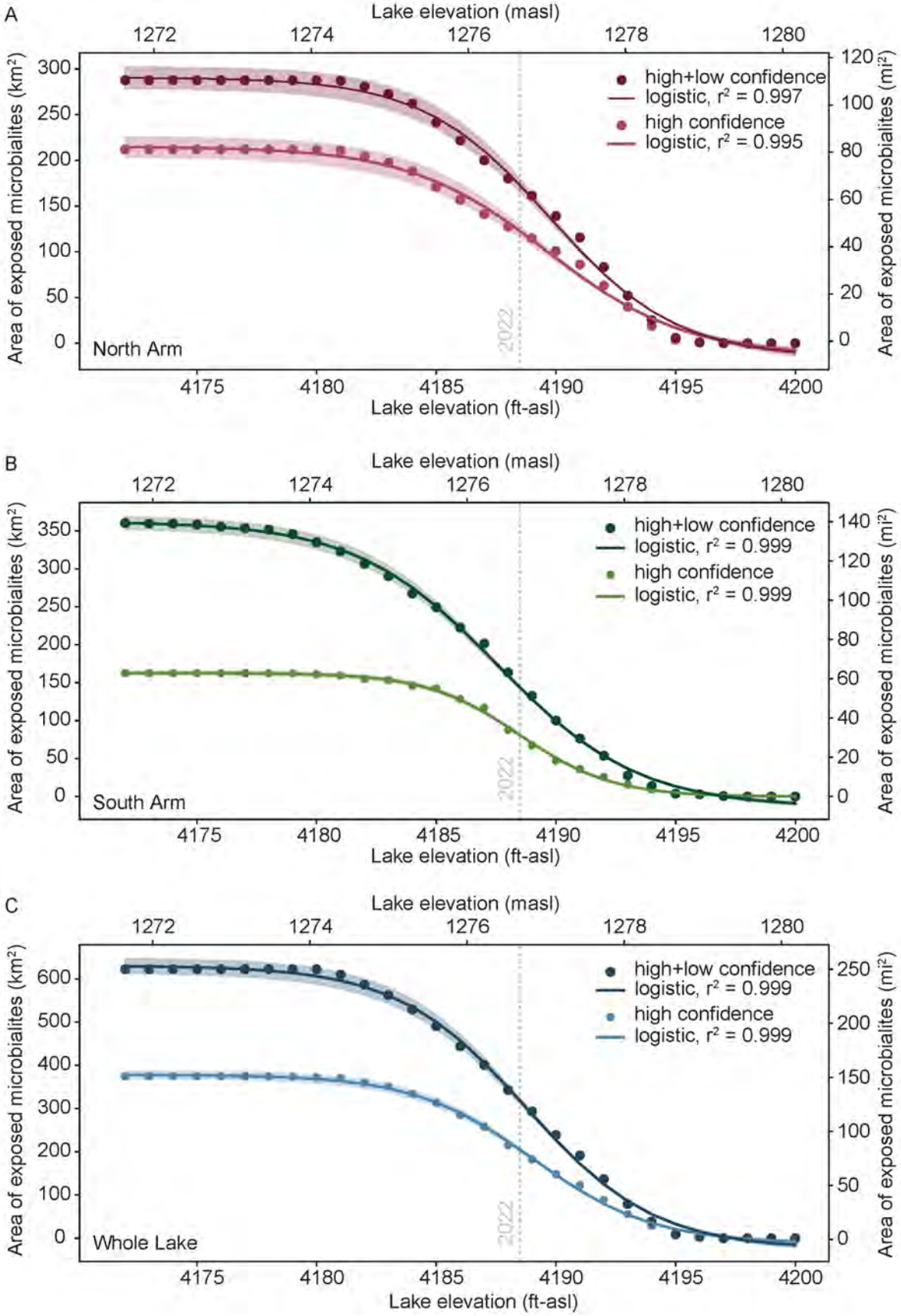

Figure 12. *Relationship between lake elevation and total cumulative microbialite exposure in Great Salt Lake. Data points for each elevation band that we mapped are shown as points along with corresponding logistic regression best-fit lines. Shaded areas represent the range of standard error for the regression models. The dashed vertical line marks the lake elevation at the autumn 2022 minimum (4188.5 ft-asl). (A) Microbialites mapped in the north arm of Great Salt Lake at high (light) and high+low (dark) confidence. (B) Microbialites mapped in the south arm of Great Salt Lake at high (light) and high+low (dark) confidence. (C) Values for the whole lake, with mapped microbialites at high (light) and high+low (dark) confidence.*

Table 4. *Logistic regression model results for microbialite exposure area at different lake elevations. To aid in the use of models for management, values are presented for use of both metric units (masl for lake elevation, km² for area of exposed microbialites) and imperial units (ft-asl for lake elevation, mi² for area of exposed microbialites).*

			Logistic regression model parameters - metric units (masl, km²)				**Logistic regression model parameters - imperial units** (ft-asl, mi²)			
Arm	**Confidence**	**r^2**	**L**	**k**	**x_o**	**b**	**L**	**k**	**x_o**	**b**
North Arm	high	0.9954	229 ± 6	1.14 ± 0.07	1277.0 ± 0.1	-14 ± 5	88 ± 2	0.35 ± 0.02	4189.6 ± 0.2	-5.4 ± 1.8
North Arm	high+low	0.9967	308 ± 6	1.23 ± 0.06	1277.0 ± 0.1	-16 ± 5	119 ± 2	0.38 ± 0.02	4189.8 ± 0.2	-6.3 ± 1.9
South Arm	high	0.9992	163 ± 1	1.71 ± 0.04	1276.7 ± 0.0	0 ± 1	63 ± 0	0.52 ± 0.01	4188.5 ± 0.1	-0.1 ± 0.4
South Arm	high+low	0.9988	376 ± 5	1.12 ± 0.04	1276.4 ± 0.0	-14 ± 3	145 ± 2	0.34 ± 0.01	4187.5 ± 0.1	-5.5 ± 1.2
Whole lake	high	0.9988	390 ± 4	1.32 ± 0.04	1276.8 ± 0.0	-12 ± 3	151 ± 2	0.40 ± 0.01	4189.1 ± 0.1	-4.7 ± 1.3
Whole lake	high+low	0.9986	684 ± 9	1.14 ± 0.04	1276.7 ± 0.0	-31 ± 7	264 ± 4	0.35 ± 0.01	4188.6 ± 0.1	-12.0 ± 2.6

dence maps. However, Baskin mapped ~350 km² (135 mi²) more microbialite areas than we could confirm, largely in deep-water areas of the lake. There are several key differences between our map and the Baskin map that warrant future field verification. First, our technique allowed for mapping of microbialites in shore environments that were not navigable and therefore unmapped by Baskin, for example, in an area north of Lakeside where we identified desiccation megapolygons (Figure 9B). Second, areas mapped by Baskin frequently extended deeper into the lake than our remote imagery-based approach permitted, for example, on the western shore of the lake, and in the area between Antelope Island and Fremont Island (Figs. 4, 9B–C). We did not include these deeper-area regions of putative reef mapped by Baskin in our map or elevation-exposure model, however, we cannot rule out that they exist. Also, our map only accounts for consistently unburied microbialites, which are more likely to contribute to lake productivity than intermittently buried microbialites, which could have been included in the Baskin and others (2022) map. Heavily eroded microbialites may also have been missed by our map.

Lake Elevation and Microbialite Exposure

During the autumn 2022 historic lake lowstand of 1276.7 masl (4188.5 ft-asl), we estimate (from microbialites mapped at both high and low confidence in this study) that >294 km² (114 mi², or >45%) of the lake's microbialites were exposed, >133 km² (51 mi²) in the south arm (>37% exposure), and 162 km² (63 mi²) in the north arm (>56% exposure). Microbialites in the lake's north arm no longer support a robust microbialite surface community because of the arm's high salinity levels (Lindsay and others, 2019), thus, their exposure or submergence likely does not have much influence on the support of higher tropic levels in the Great Salt Lake food web. In the south arm, recent evidence suggests that microbialite photosynthetic (periphyton) communities can survive months of subaerial exposure, and that re-submerged microbialites appear to be rapidly recolonized by lake water microorganisms (Frantz and others, 2023). However, subaerially exposed microbialites cannot contribute to the benthic or planktonic food chains in the lake. Additionally, areas of microbialites that experienced frequent exposure in the past half century never fully redeveloped a healthy periphyton (marked by thick gelatinous mats) even when re-submerged for periods of several seasons to years, indicating that the damage caused by prolonged exposure is long-lasting. It is also important to note that microbialites in the hypersaline north arm of the lake also lack the robust mats of primary producers that are present in "healthy" microbialites (Lindsay and others, 2017); this is one of the reasons we clearly separate our maps of north vs. south arm microbialites. Finally, exposed microbialites are subjected to rapid weathering, and it could take decades or even centuries for the raised mounds that represent stable oases in an otherwise shifting lake benthos to re-form. Thus, the consequences of long-term subaerial exposure of the lake's microbialites are profoundly concerning for the lake ecosystem.

Even in the short term, there are ecosystem consequences of microbialite exposure. If microbialite periphyton communities conservatively represent 30% of primary production in Great Salt Lake, the expo-

sure of ~ 40% of them in the lake's south arm may have equated to a > 10% reduction in overall lake primary production in summer 2022 compared to "healthy" lake elevations (when microbialites are fully submerged). If one assumes that the bulk of microbialite-supported primary productivity occurs in relatively shallow water (i.e., the year-round photic zone), it is possible that the relative aerial extent of microbialites that occupy this zone has been relatively stable over the past several years of lake level fall, however, further lake level decline would substantially decrease the area of productive microbialites. Also significant to the ecosystem is the substantial decrease in *Ephydra* pupa anchor sites that occurs when microbialites become subaerially exposed.

The greatest change in submerged microbialites occurs between 1275.6 and 1278.0 masl (4185–4193 ft-asl; Figure 12) because of the large expanses and high density of microbialites in this zone (Figure 10). The lower bound for the lake elevation target range for management of 1279.5 masl (4198 ft-asl) (Utah DNR Forestry, 2013) ensures that nearly all of the lake's microbialites are submerged. At 1278 masl (4193 ft-asl), 88% are submerged, while at 1275.6 masl (4185 ft-asl), only 24% remain submerged. Additionally, at lake elevation levels below ~1277 masl (4190 ft-asl), microbialite community health becomes threatened not only by exposure, but by salinity. At salinity levels above 15%, the primary productivity of *Euhalothece*—and, thus, microbialite-associated productivity—declines (Lindsay and others, 2019); this corresponds to a lake elevation of roughly 1277 masl (4191 ft-asl). Thus, due both to microbialite exposure and high salinity levels, elevations above 1277 masl (4191 ft-asl) should be a minimum for lake management with respect to microbialite-supported ecosystem survival, whereas elevations above 1278.6 masl (4195 ft-asl) keep nearly all of the lake's microbialites submerged.

Limitations of this Study

Although we believe our map is a significant improvement over previously published maps of microbialite extent, it has several limitations and caveats.

First, our map is limited to visible reef areas. In regions where remote imagery is low resolution, we were unable to confidently map microbialites. We were also unable to conclusively confirm or refute microbialite reef areas in deep-water portions of the lake (generally, below 1275 masl, or 4183 ft-asl, although this varied somewhat by remote imagery available), where water obscures reflected light. These deep-water portions of the lake represent an area of 1800 km^2 (~700 mi^2) and include 232 km^2 (90 mi^2) of microbialite reef mapped by Baskin and others (2022); we cannot rule out the existence of microbialites above surrounding lake sediment at depths below 1275 masl (4183 ft-asl), but we were only able to confirm the probable existence of microbialites in 53 km^2 (20 mi^2) of that area based on remote imagery and the methods of our study. This could account for some, but not all discrepancies between the Baskin map and ours. This caveat to our study could be remedied with a comprehensive field verification campaign. Deep-water areas may need to be verified by divers. Our study could also be used to help refine Baskin's benthic rugosity-based mapping algorithm (Baskin, 2005).

Second, we excluded regions of reef that were not consistently visible in remote imagery. We did this to exclude areas of shifting microbialite debris/rip-up clasts. However, the change in visibility could also be due to shifting ooid sands covering up and then re-exposing areas of active reef (as noted by Bouton and others, 2016). These regions of reef could still, when exposed, contribute to primary production in the lake. Roughly 59 km^2 (23 mi^2) of the lakebed we analyzed in this study comprised regions of variable brightness, i.e., either mobile clasts or varied exposure/covering by surrounding sediment, and it was not possible to distinguish mobile clasts from shifting sediment obscuring true reef areas.

Third, our model of microbialite exposure vs. lake elevation is based on the bathymetry of Baskin and Allen (2005) and Baskin and Turner (2006), which was limited spatially to 1-km transects in the navigable portions of the lake (Baskin, 2005; Baskin, 2006). Thus, the bathymetry, especially in the elevation band of 1276.5–1278.6 masl (4188–4195 ft-asl), which corresponds to one of the greatest expanses of microbialite reef (Figure 10), is poorly constrained, limiting the accuracy of our model. Bathymetry in this band can be improved with detailed lidar mapping, work that is currently being explored and, we hope, done more extensively in the near future.

Finally, prolonged subaerial exposure of the lake's microbialites results in their rapid weathering (Frantz and others, 2023), thus, microbialite extents at higher elevation bands are subject to change (decrease) during periods of low lake elevation. Additional research is required to quantify and model rates of microbialite weathering.

SUMMARY

We mapped 649 km^2 (251 mi^2) of microbialite reef in Great Salt Lake by leveraging low lake levels and recent availability of high-resolution remote imagery. Of that, 375 km^2 (145 mi^2) were either field-

verified or were identified as megapolygons, which are linked to microbialites in Great Salt Lake (Vanden Berg, 2019). We believe that our map of microbialite extents refines previously published maps. We have also produced shapefiles of microbialite extent at different lake elevations (Supplemental Materials). Our model of microbialite exposure vs. lake elevation can be used to inform Great Salt Lake management: 1278.6 masl (4195 ft-asl) should be considered as a critical minimum lake elevation (with the understanding that higher lake levels provide greater protection) with respect to microbialites; at this depth, 98% of the lake's microbialites are submerged. During the historic lowstand in autumn 2022 of 1276.7 masl (4188.5 ft -asl), we estimate that >37% of the microbialites in the south arm of the lake were subaerially exposed, representing substantial damage to benthic primary productivity (which was likely already threatened by high salinity levels) and *Ephydra* larva habitat.

ACKNOWLEDGEMENTS

LW was supported by NSF RISE #1801760 to Elizabeth Balgord. CF was supported by NSF EAR #1826869. MVB was supported by the Utah Geological Survey.

We thank Ryan Frazier and Michael Hernandez for their extensive help with GIS aspects of this project, and several reviewers for detailed and helpful comments on a prior version of this manuscript.

REFERENCES

Anderson, N.L., Barrett, K.L., Jones, S.E., and Belovsky, G.E., 2020, Impact of abiotic factors on microbialite growth (Great Salt Lake, Utah, USA): a tank experiment: Hydrobiologia, v. 847, no. 9, p. 2113–2122, doi: 10.1007/s10750-020-04235-9.

Barrett, K.L., 2020, Microbialite communities and food web linkages in Great Salt Lake: Notre Dame, University of Notre Dame, Ph.D. Dissertation, 195 p.

Baskin, R., 2005, Calculation of area and volume for the south part of Great Salt Lake, Utah: USGS Open-File Report 2005–1327, 7 p.

Baskin, R.L., 2006, Calculation of area and volume for the north part of Great Salt Lake, Utah: USGS Open-File Report 2006–1359, 6 p.

Baskin, R.L., 2014, Occurrence and Spatial Distribution of Microbial Bioherms in Great Salt Lake, Utah: Salt Lake City, University of Utah, Ph.D. Dissertation, 203 p.

Baskin, R.L., and Allen, D.V., 2005, Bathymetric map of the south part of Great Salt Lake, Utah, 2005: U.S. Geological Survey Scientific Investigations map 2894, scale 1:24,000.

Baskin, R.L., Della Porta, G., and Wright, V.P., 2022, Characteristics and controls on the distribution of sublittoral microbial bioherms in Great Salt Lake, Utah: Implications for understanding microbialite development: The Depositional Record, v. 8, no. 1, p. 39–66, doi: 10.1002/dep2.159.

Baskin, R.L., and Turner, J., 2006, Bathymetric Map of the North Part of Great Salt Lake, Utah, 2006: U.S. Geological Survey Scientific Investigations Map 2954, scale 1:24,000.

Baxter, B.K., and Butler, J.K. (Eds.), 2020, Great Salt Lake Biology: A Terminal Lake in a Time of Change: Cham, Springer International Publishing, 527 p., doi: 10.1007/978-3-030-40352-2.

Belovsky, G.E., Stephens, D., Perschon, C., Birdsey, P., Paul, D., Naftz, D., Baskin, R., Larson, C., Mellison, C., Luft, J., Mosley, R., Mahon, H., Van Leeuwen, J., and Allen, D.V., 2011, The Great Salt Lake Ecosystem (Utah, USA): long term data and a structural equation approach: Ecosphere, v. 2, no. 3, p. 1–40, doi: 10.1890/ES10-00091.1.

Bouton, A., Vennin, E., Amiotte-Suchet, P., Thomazo, C., Sizun, J., Virgone, A., Gaucher, E.C., and Visscher, P.T., 2020, Prediction of the calcium carbonate budget in a sedimentary basin: A "source-to-sink" approach applied to Great Salt Lake, Utah, USA: Basin Research, v. 32, no. 5, p. 1005–1034, doi: 10.1111/bre.12412.

Bouton, A., Vennin, E., Boulle, J., Pace, A., Bourillot, R., Thomazo, C., Brayard, A., Désaubliaux, G., Goslar, T., Yokoyama, Y., Dupraz, C., and Visscher, P.T., 2016a, Linking the distribution of microbial deposits from the Great Salt Lake (Utah, USA) to tectonic and climatic processes: Biogeosciences, v. 13, p. 5511–5526, doi: 10.5194/bg-13-5511-2016.

Bouton, A., Vennin, E., Mulder, T., Pace, A., Bourillot, R., Thomazo, C., Brayard, A., Goslar, T., Buoncristiani, J.-F., Désaubliaux, G., and Visscher, P.T., 2016b, Enhanced development of lacustrine microbialites on gravity flow deposits, Great Salt Lake, Utah, USA: Sedimentary Geology, v. 341, p. 1–12, doi: 10.1016/j.sedgeo.2016.05.004.

Bowen, G.J., Nielson, K.E., and Eglinton, T.I., 2019, Multi-Substrate Radiocarbon Data Constrain Detrital and Reservoir Effects in Holocene Sediments of the Great Salt Lake, Utah: Radiocarbon, v. 61, no. 4, p. 905–926, doi: 10.1017/RDC.2019.62.

Brown, P.D., Craine, J.M., Richards, D., Chapman, A., and Marden, B., 2022, DNA metabarcoding of the phytoplankton of Great Salt Lake's Gilbert

Bay: Spatiotemporal assemblage changes and comparisons to microscopy: Journal of Great Lakes Research, v. 48, no. 1, p. 110–124, doi: 10.1016/j.jglr.2021.10.016.

Burne, R.V., and Moore, L.S., 1987, Microbialites: Organosedimentary Deposits of Benthic Microbial Communities: PALAIOS, v. 2, no. 3, p. 241–254., doi: 10.2307/3514674.

Carozzi, A.V., 1962, Observations on Algal Biostromes in the Great Salt Lake, Utah: The Journal of Geology, v. 70, no. 2, p. 246–252, doi: 10.1086/626814.

Caudell, J.N., and Conover, M.R., 2006, Energy content and digestibility of brine shrimp (*Artemia franciscana*) and other prey items of eared grebes (*Podiceps nigricollis*) on the Great Salt Lake, Utah: Biological Conservation, v. 130, no. 2, p. 251–254, doi: 10.1016/j.biocon.2005.12.018.

Chidsey, T.C., Vanden Berg, M.D., and Eby, D.E., 2015, Petrography and characterization of microbial carbonates and associated facies from modern Great Salt Lake and Uinta Basin's Eocene Green River Formation in Utah, USA: Geological Society, London, Special Publications, v. 418, no. 1, p. 261–286, doi: 10.1144/SP418.6.

Collins, N., 1980, Population ecology of Ephydra cinerea Jones (Diptera: Ephydridae), the only benthic metazoan of the Great Salt Lake, U.S.A.: Hydrobiologia, v. 68, no. 2, p. 99–112, doi: 10.1007/BF00019696.

Conover, M.R., and Bell, M.E., 2020, Importance of Great Salt Lake to Pelagic Birds: Eared Grebes, Phalaropes, Gulls, Ducks, and White Pelicans, *in* Baxter, B.K., and Butler, J.K., editors, Great Salt Lake Biology: A Terminal Lake in a Time of Change: Cham, Springer International Publishing, p. 239–262, doi: 10.1007/978-3-030-40352-2_8.

Cumings, E.R., and Shrock, R.R., 1928, Niagaran Coral Reefs of Indiana and Adjacent States and Their Stratigraphic Relations: GSA Bulletin, v. 39, no. 2, p. 579–620, doi: 10.1130/GSAB-39-579.

Domagalski, J.L., Orem, W.H., and Eugster, H.P., 1989, Organic geochemistry and brine composition in Great Salt, Mono, and Walker Lakes: Geochimica et Cosmochimica Acta, v. 53, no. 11, p. 2857–2872.

Dupraz, C., Reid, R.P., Braissant, O., Decho, A.W., Norman, R.S., and Visscher, P.T., 2009, Processes of carbonate precipitation in modern microbial mats: Earth-Science Reviews, v. 96, no. 3, p. 141–162, doi: 10.1016/j.earscirev.2008.10.005.

Eardley, A.J., 1938, Sediments of Great Salt Lake, Utah: AAPG Bulletin, v. 22, no. 10, p. 1305–1411.

Frantz, C.M., Gibby, C., Nilson, R., Stern, C.J., Nguyen, M., Ellsworth, C., Dolan, H., Sihapanya, A., Aeschlimann, J., and Baxter, B.K., 2023, Desiccation of ecosystem-critical microbialites in the shrinking Great Salt Lake, Utah (USA): PLOS Water, v. 2, no. 9, e1000100, doi: 10.1371/journal.pwat.0000100.

Frantz, C.M., Petryshyn, V.A., and Corsetti, F.A., 2015, Grain trapping by filamentous cyanobacterial and algal mats: implications for stromatolite microfabrics through time: Geobiology, v. 13, no. 5, p. 409–423, doi: 10.1111/gbi.12145.

Great Salt Lake Salinity Advisory Committee, 2021, Great Salt Lake Salinity Matrix 2021: Utah Division of Forestry, Fire & State Lands, 1 p.

Halley, R.B., 1976, Textural variation within Great Salt Lake algal mounds, *in* Walter, M.R., editor, Stromatolites: Elsevier Developments in Sedimentology, p. 435–445.

Hart, I., Jones, K.B., Brunelle, A., DeGraffenried, J., Oviatt, C.G.J., Nash, B., Duke, D., and Young, D.C., 2022, Building a master chronology for the western lake Bonneville basin with stratigraphic and elemental data from multiple sites, USA: Radiocarbon, v. 64, no. 1, p. 69–85, doi: 10.1017/RDC.2022.3.

Homewood, P., Mettraux, M., Vanden Berg, M., Foubert, A., Neumann, R., Newell, D., and Atwood, G., 2022, Onshore groundwater spring carbonate mounds to lacustrine microbialites, the perplexing record of a transitional Great Salt Lake carbonate shoreline at Lakeside, Utah: The Depositional Record, v. 8, no. 1, p. 9–38, doi: 10.1002/dep2.148.

Ingalls, M., Frantz, C.M., Snell, K.E., and Trower, E.J., 2020, Carbonate facies-specific stable isotope data record climate, hydrology, and microbial communities in Great Salt Lake, UT: Geobiology, v. 18, no. 5, p. 566–593, doi: 10.1111/gbi.12386.

Jones, B.F., Naftz, D.L., Spencer, R.J., and Oviatt, C.G., 2009, Geochemical Evolution of Great Salt Lake, Utah, USA: Aquatic Geochemistry, v. 15, no. 1–2, p. 95–121, doi: 10.1007/s10498-008-9047-y.

Kanik, M., Munro-Ehrlich, M., Fernandes-Martins, M.C., Payne, D., Gianoulias, K., Keller, L., Kubacki, A., Lindsay, M.R., Baxter, B.K., Vanden Berg, M.D., Colman, D.R., and Boyd, E.S., 2020, Unexpected Abundance and Diversity of Phototrophs in Mats from Morphologically Variable Microbialites in Great Salt Lake, Utah (H. Atomi, Ed.): Applied and Environmental Microbiology, v. 86, no. 10, p. e00165-20, doi: 10.1128/AEM.00165-20.

Kijowski, A.M., Neill, J., Wickline, A., Swift, J., Butler, J.K., Kimberly, D.A., Van Leeuwen, J., Luft, J., and Stone, K., 2020, American white pelicans of Gunnison Island, Great Salt Lake, Utah, *in* Baxter, B.K., and Butler, J.K., editors, Great Salt Lake Biology: A Terminal Lake in a Time of Change: Cham, Springer International Publishing, p. 311–344, doi: 10.1007/978-3-030-40352-2_10.

Lindsay, M.R., Anderson, C., Fox, N., Scofield, G., Allen, J., Anderson, E., Bueter, L., Poudel, S., Sutherland, K., Munson-McGee, J.H., Van Nostrand, J.D., Zhou, J., Spear, J.R., Baxter, B.K., and others, 2017, Microbialite response to an anthropogenic salinity gradient in Great Salt Lake, Utah: Geobiology, v. 15, no. 1, p. 131–145, doi: 10.1111/gbi.12201.

Lindsay, M.R., Johnston, R.E., Baxter, B.K., and Boyd, E.S., 2019, Effects of salinity on microbialite-associated production in Great Salt Lake, Utah: Ecology, v. 100, no. 3, doi: 10.1002/ecy.2611.

MacIntyre, S., and Melack, J.M., 1995, Vertical and horizontal transport in lakes: Linking littoral, benthic, and pelagic habitats: Journal of the North American Benthological Society, v. 14, no. 4, p. 599–615, doi: 10.2307/1467544.

Marden, B., Brown, P., and Bosteels, T., 2020, Great Salt Lake Artemia: Ecosystem functions and services with a global reach, *in* Baxter, B.K., and Butler, J.K., editors, Great Salt Lake Biology: A Terminal Lake in a Time of Change: Cham, Springer International Publishing, p. 175–237, doi: 10.1007/978-3-030-40352-2_7.

Newell, D.L., Jensen, J.L., Frantz, C.M., and Vanden Berg, M.D., 2017, Great Salt Lake (Utah) Microbialite δ^{13}C, δ^{18}O, and δ^{15}N Record Fluctuations in Lake Biogeochemistry Since the Late Pleistocene: Geochemistry, Geophysics, Geosystems, v. 18, no. 10, p. 3631–3645, doi: 10.1002/2017GC007078.

Null, S.E., and Wurtsbaugh, W.A., 2020, Water development, consumptive water uses, and Great Salt Lake, *in* Baxter, B.K., and Butler, J.K., editors, Great Salt Lake Biology: A Terminal Lake in a Time of Change: Cham, Springer International Publishing, p. 1–21, doi: 10.1007/978-3-030-40352-2_1.

Oviatt, C.G., 2015, Chronology of Lake Bonneville, 30,000 to 10,000 yr B.P.: Quaternary Science Reviews, v. 110, p. 166–171, doi: http://linkinghub.elsevier.com/retrieve/pii/0277379114005071.

Oviatt, C.G., Atwood, G., and Thompson, R.S., 2021, History of Great Salt Lake, Utah, USA: since the termination of lake Bonneville, *in* Rosen, M.R., Finkelstein, D.B., Park Boush, L., and Pla-Pueyo, S., editors, Limnogeology: Progress, Challenges and Opportunities : A Tribute to Elizabeth Gierlowski-Kordesch: Cham, Springer International Publishing Syntheses in Limnogeology, p. 233–271, doi: 10.1007/978-3-030-66576-0_8.

Pace, A., Bourillot, R., Bouton, A., Vennin, E., Galaup, S., Bundeleva, I., Patrier, P., Dupraz, C., Thomazo, C., Sansjofre, P., Yokoyama, Y., Franceschi, M., Anguy, Y., Pigot, L., and others, 2016, Microbial and diagenetic steps leading to the mineralisation of Great Salt Lake microbialites: Scientific Reports, v. 6, no. 1, p. 31495, doi: 10.1038/srep31495.

Paradis, O.P., Corsetti, F.A., Bardsley, A., Hammond, D.E., Berelson, W., Xu, X., Walker, J., and Celestian, A., 2023, Radiocarbon chronology/growth rates of ooids from Great Salt Lake, Utah, *in* Vanden Berg, M.D., Ford, R., Frantz, C., Hurlow, H., Gunderson, K., and Atwood, G. (eds.), Great Salt Lake and the Bonneville Basin: Geologic History and Anthropocene Issues: Utah Geological Association Publication 51, p. [PLACEHOLDER PENDING INFO FROM VOLUME].

Pedone, V.A., and Folk, R.L., 1996, Formation of aragonite cement by nannobacteria in the Great Salt Lake, Utah: Geology, v. 24, no. 8, p. 763-765, doi: 10.1130/0091-7613(1996)024<0763:FOACBN>2.3.CO;2.

Post, F.J., 1977, The microbial ecology of the Great Salt Lake: Microbial Ecology, v. 3, no. 2, p. 143–165, doi: 10.1007/BF02010403.

Shapiro, R.S., 2000, A comment on the systematic confusion of thrombolites: Palaios, v. 15, p. 166–169.

Shen, Y., Suarez-Gonzalez, P., and Reitner, J., 2022, Contrasting modes of carbonate precipitation in a hypersaline microbial mat and their influence on biomarker preservation (Kiritimati, Central Pacific): Minerals, v. 12, no. 2, p. 267-297, doi: 10.3390/min12020267.

Sorensen, E.D., Hoven, H.M., and Neill, J., 2020, Great Salt Lake Shorebirds,their habitats, and food base, *in* Baxter, B.K., and Butler, J.K., editors, Great Salt Lake Biology: A Terminal Lake in a Time of Change: Cham, Springer International Publishing, p. 263–309, doi: 10.1007/978-3-030-40352-2_9.

Utah DNR Forestry, 2013, Great Salt Lake comprehensive management plan: Utah Department of Natural Resources Division of Forestry, Fire & State Lands Record of Decision 13-0315–1, 391 p.

Vanden Berg, M.D., 2019, Domes, Rings, Ridges,

and Polygons: Characteristics of microbialites from Utah's Great Salt Lake (L. Birgenheier & H. Harper, Eds.): The Sedimentary Record, v. 17, no. 1, p. 4–10, doi: 10.2110/sedred.2019.1.4.

Vennin, E., Bouton, A., Bourillot, R., Pace, A., Roche, A., Brayard, A., Thomazo, C., Virgone, A., Gaucher, E.C., Desaubliaux, G., and Visscher, P.T., 2019, The lacustrine microbial carbonate factory of the successive Lake Bonneville and Great Salt Lake, Utah, USA (A. Brasier, Ed.): Sedimentology, v. 66, no. 1, p. 165–204, doi: 10.1111/sed.12499.

Virtanen, P., Gommers, R., Oliphant, T.E., Haberland, M., Reddy, T., Cournapeau, D., Burovski, E., Peterson, P., Weckesser, W., Bright, J., van der Walt, S. J., Brett, M., Wilson, J., Millman, K. J., Mayorov, N., Nelson, A. R. J., Jones, E., Kern, R., Larson, E., Carey, C. J., Polat, I., Feng, Y., Moore, E. W., VanderPlas, J., Laxalde, D., Perktold, J., Cimrman, R., Henriksen, I., Quintero, E. A., Harris, C. R., Archibald, A. M., Ribeiro, A. H., Pedregosa, F., van Mulbregt, P., and SciPy 1.0 Contributors, 2020, SciPy 1.0: Fundamental Algorithms for Scientific Computing in Python: Nature Methods, v. 17, no. 3, p. 261-272.

Wurtsbaugh, W.A., 2009, Biostromes, brine flies, birds, and the bioaccumulation of selenium in Great Salt Lake, Utah: Saline lakes around the world: unique systems with unique values. Natural Resources and Environmental Issues, vol XV, v. 15, p. 1–15.

Wurtsbaugh, W.A., Gardberg, J., and Izdepski, C., 2011, Biostrome communities and mercury and selenium bioaccumulation in the Great Salt Lake (Utah, USA): Science of The Total Environment, v. 409, no. 20, p. 4425–4434, doi: 10.1016/j.scitotenv.2011.07.027.

SUPPLEMENTARY INFORMATION

.

Mapped microbialite area shapefiles, data tables, Python code used for analysis, and supplemental figures are available at Open Science Framework: https://osf.io/uf9yg/.

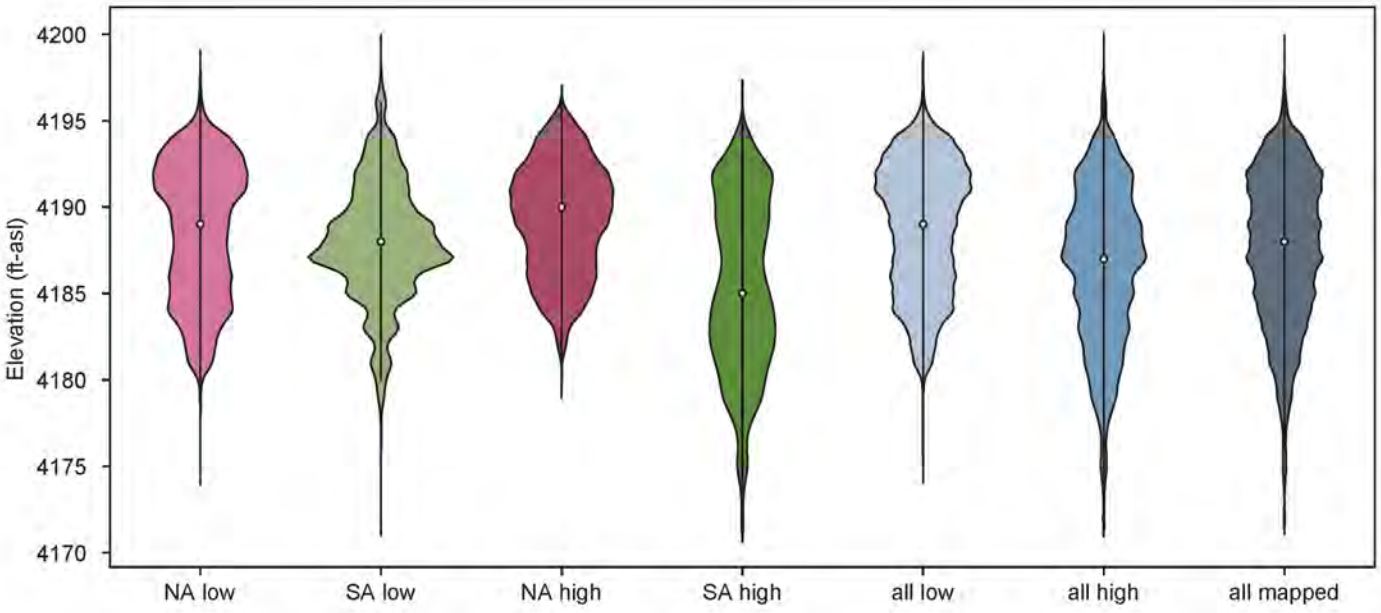

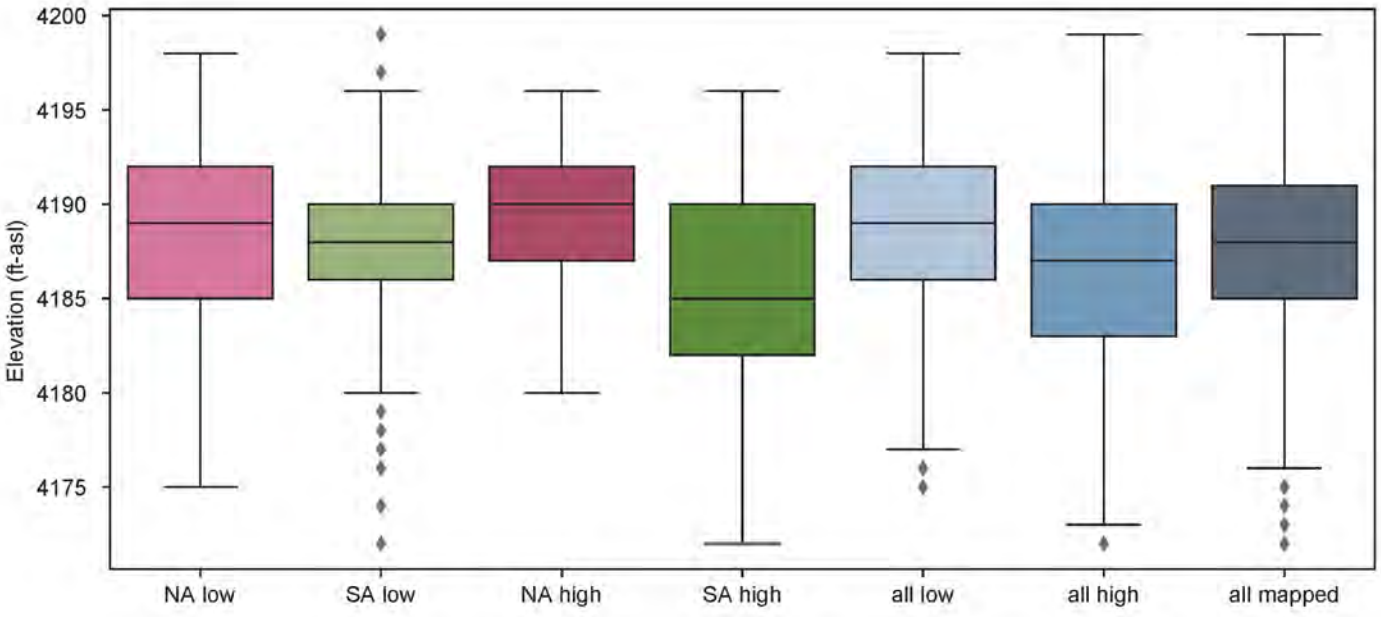

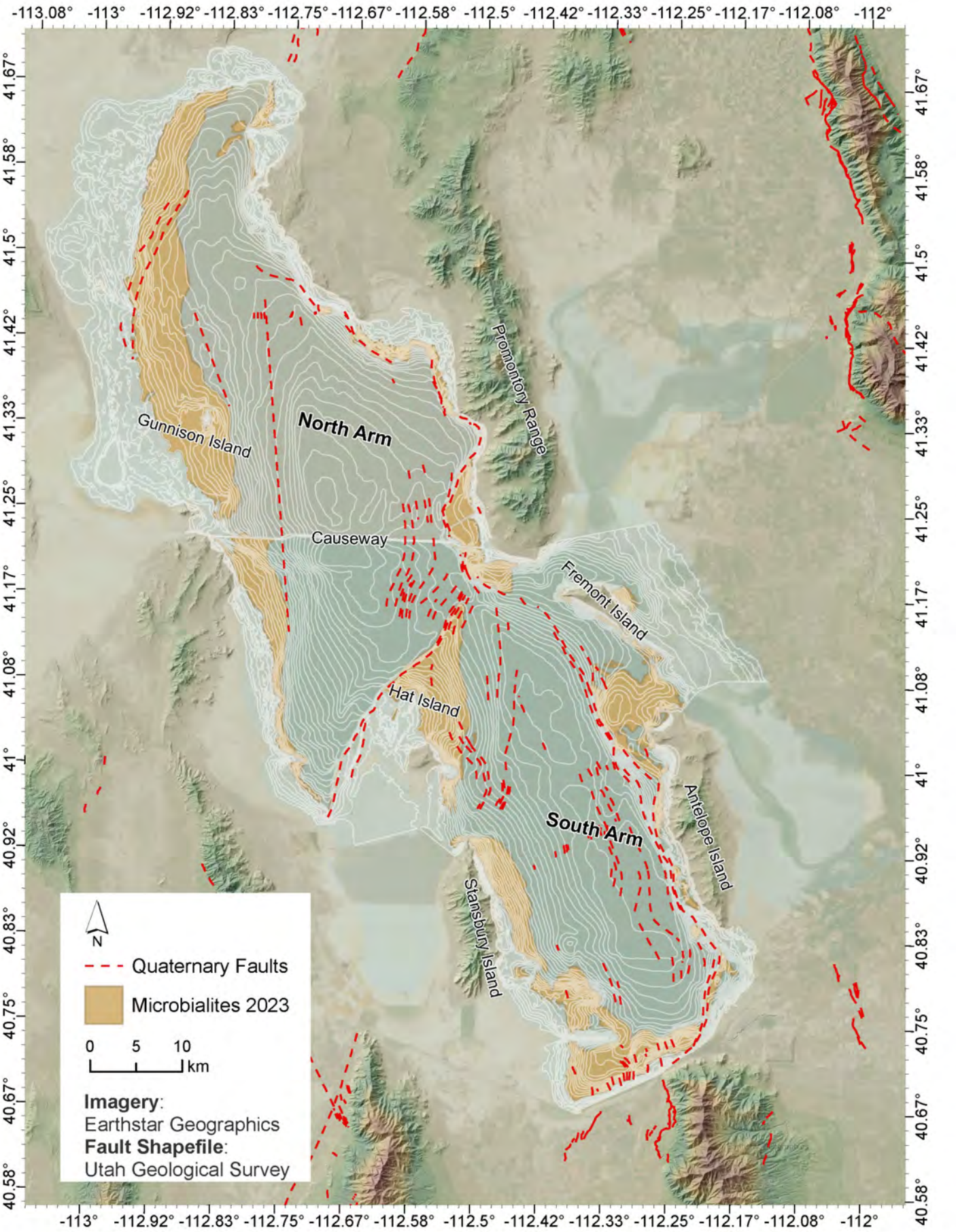
-113.08° -113° -112.92° -112.83° -112.75° -112.67° -112.58° -112.5° -112.42° -112.33° -112.25° -112.17° -112.08° -112°
41.67° 41.58° 41.5° 41.42° 41.33° 41.25° 41.17° 41.08° 41° 40.92° 40.83° 40.75° 40.67° 40.58°
Gunnison Island
North Arm
Promontory Range
Causeway
Fremont Island
Hat Island
South Arm
Antelope Island
Stansbury Island
N
Quaternary Faults
Microbialites 2023
0 5 10
km
Imagery:
Earthstar Geographics
Fault Shapefile:
Utah Geological Survey

Radiocarbon Chronology/Growth Rates of Ooids from Great Salt Lake, Utah

Olivia P. Paradis[1], Frank A. Corsetti[1], Audra Bardsley[2], Douglas E. Hammond[1], William Berelson[1], Xiaomei Xu[3], Jennifer Walker[3], and Aaron Celestian[4]

[1]*Department of Earth Sciences, University of Southern California, Los Angeles, Calirforia; opiazza@usc.edu*
[2]*Environmental Studies Program, University of Southern California, Los Angeles, California*
[3]*Department of Earth System Science, University of California, Irvine, California*
[4]*Department of Mineral Sciences, Natural History Museum of Los Angeles County, Los Angeles, California*

10.31711/ugap.v51i.137

ABSTRACT

Ooids (calcium carbonate coated grains) are common in carbonate environments throughout geologic time, but the mechanism by which they form remains unclear. In particular, the rate of ooid growth remains elusive in all but a few modern marine environments. In order to investigate the rate of ooid growth in a non-marine setting, we used ^{14}C to date ooids from Great Salt Lake, Utah, a well-known site of aragonitic ooids. Bulk ooids obtained from the northern shore of Antelope Island and the northeast shore of Great Salt Lake near Spiral Jetty were sieved into different size fractions and produced mean ages ranging between 2728±15 and 4373±20 ^{14}C yr BP. Larger ooids were older than smaller ooids, implying that larger ooids grew in the environment for a longer duration, with the caveat that bulk age dating integrates the growth history of an ooid. To better resolve growth history, ooids from the coarse fraction were sequentially dissolved, and ^{14}C ages were obtained for each dissolution step to create a time series of ooid growth. The results of the sequential dating indicate that the coarse Great Salt Lake ooid growth began between 5800-6600 ± 60 ^{14}C yr BP while their outer cortices are nearly modern. Sequentially dated ooids from the South Arm of Great Salt Lake at Antelope Island record a nearly linear growth history (~ 10-15 μm/kyr), whereas ooids from Spiral Jetty record somewhat faster growth between ~6000 and 4000 years ago (0.03 – 0.06 μm/yr) followed by a 10x slower growth history for the remainder of their lifespan (0.003 – 0.008 μm/yr). The lifespan of Great Salt Lake aragonitic ooids is two to six times longer than those from modern marine environments, and thus provides a unique end member for understanding the mechanisms behind ooid formation. The ooid age range indicates that geochemical parameters measured from bulk ooid dissolution integrates over ~6000 years and thus does not represent a geochemical snapshot in time, as some previous studies have suggested.

INTRODUCTION

Ooids are small (generally <2 mm) laminated, coated grains, with a calcium carbonate cortex surrounding a nucleus. Ooids are ubiquitous in the geologic record in marine and lacustrine settings, and as accretionary structures, may serve as repositories of high resolution aqueous evolution, preserving both biogeochemical (Diaz and others, 2015, 2013; Summons and others, 2013) and isotopic (Duguid and others, 2010) information. Despite their ubiquity, ooid formation remains enigmatic. Both abiogenic and biogenic modes of formation have been proposed (Diaz and others, 2013, 2015, 2017; O'Reilly and others, 2017; Pacton and others, 2012; Summons and others, 2013), and the rate of ooid accretion remains elusive for the majority of ooid occurrences. Without a better understanding of how rapidly ooids form, their utility as paleoenvironmental indicators is hindered and the question of biogenicity remains unclear.

Radiocarbon (^{14}C; half-life = 5730 ± 40 yr) has been successfully used for the step-wise dating of marine ooids from the Bahamas (Beaupré and others, 2015; Duguid and others, 2010), Australia (Beaupré and others, 2015; James and others, 2004), and Hawaii (Hearty and others, 2010). Regardless of location, ^{14}C ages decrease from the ooid nuclei toward their outer surfaces with the exception of a ^{14}C anomaly of unknown origin in ooids from Highborne Cay, Bahamas (Beaupré and others, 2015). Using the radiocarbon chronology, Beaupré and others (2015) argued "modern" marine ooid net growth rates were slow and relatively constant, with mean lifespans ranging from 800 ± 135 to 1470 ± 280 ^{14}C years and growth rates ranging from 0.36 ± 0.03 to 2.2 ± 0.3 ng C-$CaCO_3$/ooid-year. However, calculated net growth rates from these radiocarbon dating experiments on ooids are likely underestimating gross carbonate precipitation due to abrasion, as lab experiments have shown growth can be four orders of magnitude faster than radiocarbon net growth rates (Trower and others, 2017).

The Great Salt Lake (GSL) in Utah provides a

unique opportunity to assess the net growth rate of radial aragonitic ooids that texturally resemble many ancient ooids, both marine and lacustrine (Figure 1). In addition to their utility in understanding radial ooid formation, GSL ooids may be targets for understanding the history of GSL, which as a terminal lake with no outflow, is particularly sensitive to climatic shifts. The GSL has also been subjected to environmental alteration by human activity. Especially notable is the partitioning of the lake by a railroad causeway constructed in 1959, which created a northern and southern salinity contrast. However, like marine ooids, the utility of lacustrine ooids in reconstructing paleoenvironmental changes is dependent on their placement within a proper temporal framework. The aim of this study is to use ^{14}C as a chronometer to sequentially date ooids from Great Salt Lake, and thus constrain modern ooid formation in this setting and provide necessary chronological context so that their potential as paleoenvironmental indicators may be explored.

Great Salt Lake

Great Salt Lake Environmental Setting

Great Salt Lake (GSL) is a terminal lake in northern Utah with circumneutral pH. GSL represents the present phase (since 11.5 ka BP) that resulted from

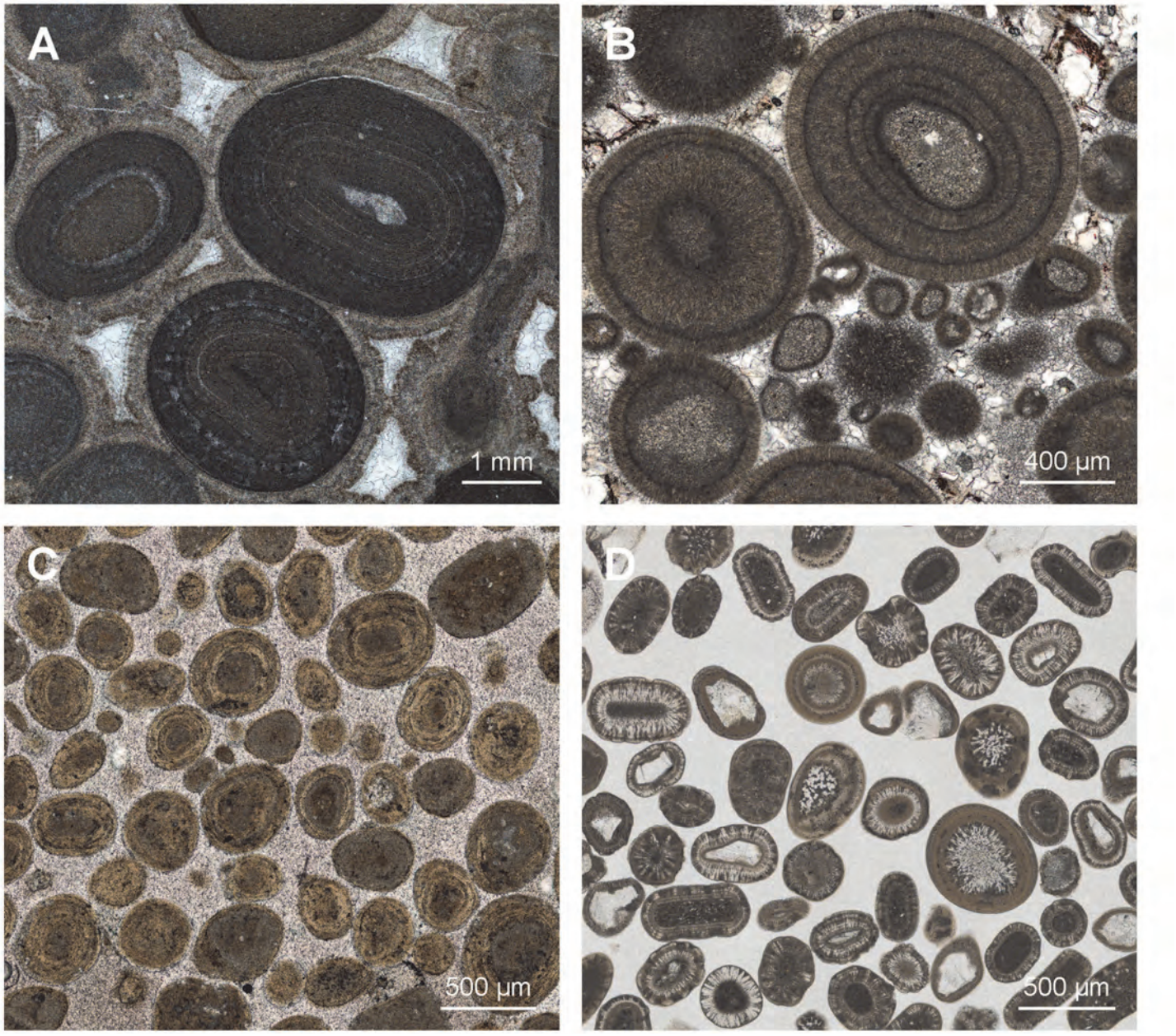

Figure 1. *Examples of ancient and modern ooid microfabrics. A) Neoproterozoic tangential ooids from the Beck Springs formation. B) Radial ooids from the Neoproterozoic Johnnie formation. C) Modern ooids from Joulter's Cay, Bahamas display tangential concentric laminae that are characteristic of many modern marine ooids. D) Modern ooids from Great Salt Lake, Utah have a primary radial crystal orientation.*

the transition of the larger and deeper Lake Bonneville (30-11.5 ka BP) to a shallow, hypersaline lake (Oviatt and others, 1992; Oviatt and others, 2015). The Holocene shallow lake interval of Great Salt Lake is accompanied by a shift to aragonite precipitation, which is in agreement with the Mg^{2+}/Ca^{2+} ratios of the lake water (Spencer 1985). The north arm of GSL is currently separated from the south arm by a rock-fill railroad causeway that was constructed in 1959. Because the three rivers that feed the lake (Bear, Jordan, and Weber rivers) enter the south arm, the north arm water is more saline (28%, at or above saturation for halite) than the south arm, which has a salinity of approximately 15% (Rupke and Macdonald, 2012; Stephens, 1990; USGS, 2023). The causeway was breached in 2016 to restore the flow between the north and south arms, but the berm in the bottom of the breach was raised by 4 feet in July 2022 help reduce north-to-south water flow but still allow water to flow from south to north. (Utah DNR, 2022).

Great Salt Lake Ooids

Ooids are found as shoreline deposits around the entirety of GSL (Baskin, 2014; Eardley, 1938). Eardley (1938) described the predominantly radial texture of the GSL ooid cortices, inferred ooid cortices were calcitic, and suggested that their radial texture was the result of recrystallization. The assumption of calcitic mineralogy in GSL ooids prevailed until Kahle (1974) demonstrated that GSL ooids are in fact aragonite and their cortical fabric is depositional. However, Kahle (1974) concluded aragonite-aragonite inversion had taken place. Sandberg (1975) confirmed the aragonitic mineralogy of GSL ooids, demonstrated that the radial aragonite fabric is depositional, and found no evidence that aragonite-aragonite inversion had taken place. Subsequently, Reitner (1999) suggested that organic matrices on the surface of GSL ooids could be important in the mineralization of the aragonite, and Lincoln et al. (2022) implicated sulfate reducing bacteria in the precipitation of Mg-silicates associated with some GSL ooids, and hypothesized some of the aragonite could be secondary vs. primary. Trower and others (2020) developed an approach to understand the unique cortical history of Great Salt Lake ooids, noting that the grains within the same deposit likely record similar histories, but found differences between populations of ooids across various localities in GSL. With respect to the age of the GSL ooids, (Mcguire, 2014) attempted serial dissolution of unsorted ooids from 15 cm water depth in the modern south arm of GSL that resulted in ^{14}C ages from 2024±36 yr BP (outermost composite sample) to 8144±29 yr BP (innermost composite sample), indicating that the ooids were quite old relative to modern marine examples, but the coarse sampling resolution could not discern whether modern precipitation took place. As part of a large-scale survey of the tufa-like carbonate mounds that many refer to as "microbialites", Bouton and others (2016) measured the bulk ^{14}C age of unsorted GSL ooids from the shoreline of the south arm of the lake. Their results yielded a composite ooid ^{14}C age of 3300 yr BP. Thus, while some constraints regarding the age of the ooids exist, many questions remain.

METHODS

Sample Collection

Ooids were collected at the sediment-water interface in less than 10 cm water depth from Bridger Bay on Antelope Island and near Spiral Jetty in March 2014 (Figure 2). Samples were rinsed with deionized water, dried in an oven at 50°C, and sieved to partition the ooids into discrete size fractions (125-250 µm, 250-355 µm, 355-500 µm). Ooid masses from each size fraction were normalized by mass to establish a grain size distribution (Figure 3). Unfiltered lake water was sampled from the shore of the northern tip of Antelope Island in the south arm of GSL and the beach at Spiral Jetty in the north arm of GSL in September 2016 for dissolved inorganic carbon ^{14}C analysis. Unfiltered river and well water were sampled in May 2017 from Bear, Jordan, and Weber rivers as well as a well in Ogden, Utah (Weber State University). At each site, one liter of water was collected in 1000ml size glass bottles (Fisher #06-414-8) which had been previously rinsed three times with deionized water, soaked in 10% HCl, and rinsed three more times with deionized water. The bottles were field rinsed three times before water was sampled with no head space and immediately poisoned with 100 µl of saturated $HgCl_2$ in the field to preclude later biologic activity.

Raman Spectroscopy

Raman spectra of GSL ooids were obtained using a Horiba XploRa+ micro-Raman spectrometer. Specimens were measured using an incident wavelength of 532 nm, laser slits of 200 µm, 1800 gr/mm diffraction grating, a 100x (0.9 NA) objective. Laser spot size was approximately 2 micrometers in diameter, and the laser power measured at the sample was approximately 87 (+/- 3) µW. Data were collected on individual grain mount ooids that were polished and thin-sectioned. Hyperspectral mapping was collected with

Figure 2. *Map of Great Salt Lake, modified from Currey and others, 1984. Ooid samples were collected from the sediment water interface from: Spiral Jetty in the north arm of GSL, and Bridger Bay on Antelope Island in the south arm of GSL. Scale bar equals 8km.*

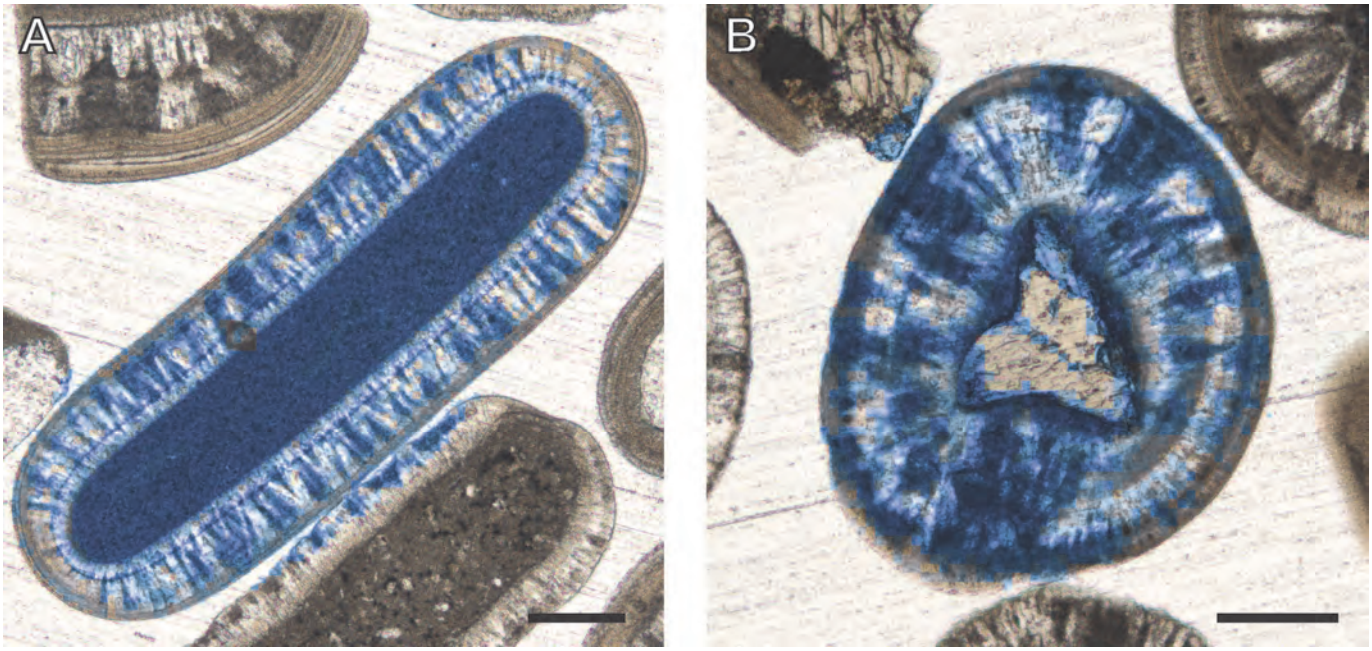

Figure 3. *Presence of organic matter (blue) within an ooid from the north arm (A) and south arm (B) of Great Salt Lake acquired from Raman spectroscopy. Only the central grain was scanned in each image. A survey of 30 ooids was carried out to confirm the distribution of organic matter within ooid cortices (SI Table 2). Scale bars equal 100 µm. Organic matter is distributed within peloidal nucleus (A) and throughout carbonate cortex (A and B).*

0.1-sec exposure averaged over three acquisitions using an 8 µm x 8 µm mapping grid. These spectral acquisition parameters were determined by trial and error to maximize signal-to-noise and keep acquisition time to less than 24 hours for most maps. After collecting hyperspectral maps, principal component analysis was performed to find those unique spectra representing the total variability within each ooid. The total number of components found for all ooids was aragonite, organic material, burned organic material (burned by the laser), pigment (carotenoid), quartz, K -feldspar, and epoxy (SI Figure 1). Microplastics were found but were exceedingly rare within the ooids. Once components were identified for each ooid, heat maps were generated by least squares fitting to every spectrum in the map (in some cases, these were >80,000 spectra per map). The least squares fitting does provide an approximate percentage of each component in the spectra; however, these values often have very high errors. Therefore, the heat maps were treated as the presence or absence of each component and were not used for absolute abundances.

Massive organic material has a characteristic Raman signal and strong luminescence with the 532 nm laser. These patterns were compared to known organic materials from pigmented crustacea after digestion by red-ear slider turtles (Clause 2021). The result is intense luminescence from the organic-rich parts of the sample, and therefore no individual organic molecule could be identified except for the carotenoids. The carotenoids were all found in spectra with organic luminescence. Attempts to collect data with a 785 nm laser resulted in very poor signal-to-noise ratio, and it was determined that large maps could not be collected in a reasonable time frame (< 24 hrs), even though the background luminescence intensity was lower. Burned organic material has characteristic D and G bands common for soot, char, and organic materials with high thermal maturity.

Dissolved Inorganic Carbon ^{14}C Age

Lake, river, and well water samples were prepared using the headspace-extraction method (Gao and others, 2014). All radiocarbon results have been corrected for isotopic fractionation according to the conventions of Stuiver and Polach (1977), with $\delta^{13}C$ values measured on prepared graphite using the AMS spectrometer. These may differ from $\delta^{13}C$ of the original material, if fractionation occurred during sample graphitization of the AMS measurement, and thus, the d13C values reported herein were measured on water dissolved inorganic carbon (DIC) directly using Gas Bench coupled with IRMS (Finnigan Delta Plus).

Bulk Inorganic and Organic Carbon Ooid ^{14}C Ages

Total organic and inorganic C was extracted from each sieved ooid sample (125-250 µm, 250-355 µm, 355-500 µm) and an unsorted ooid sample. The extracted organic and inorganic carbon was analyzed for ^{14}C at the Keck Carbon Cycle Accelerator Mass Spectrometer (KCCAMS) facility at the University of California, Irvine (Beverly and others, 2010; Southon and others, 2004). Details regarding methodology for the bulk organic and inorganic carbon extractions may be found in the supplementary information (SI Table 1).

Sequential Ooid Acidification

To assemble an ooid chronology, we measured the ^{14}C ages of fractions of CO_2 collected during sequential acid addition to sieved ooids (355-500 µm) from Spiral Jetty and Antelope Island. Ooids (~50g) and 150ml of deionized water (DIW) were placed in a reaction vessel constructed from a 500ml graduated round media storage bottle (VWR cat. # 89000-238) and a suspended magnetic stir rod (SI, Figure 2). The reaction vessel was purged with N_2 that was scrubbed with Ascarite-II while a stir bar spun at 700 rpm to drive off any dissolved CO_2 in the water for a total of 30 minutes. The sample was acidified by injecting 60 ml of 3.3M HCl at a flow rate (acid) of 10ml/min. Gas was shunted for the first 5 seconds of acidification to off-gas any residual N_2 before collecting the sample in Tedlar bags which had been rinsed with ultra-high purity (UHP) helium scrubbed with Ascarite-II. Gas was collected in 3 Tedlar bags per each acidi-

Table 1. *14C and δ13C composition of Weber, Bear, and Jordan rivers as well as well water sampled in Ogden, Utah. Dissolved inorganic carbon (DIC) is reported in millimolar (mM). Water was treated with HgCl2.*

Water Source	Latitude	Longitude	$\delta^{13}C$(‰)	±	fraction Modern	±	$\Delta^{14}C$(‰)	±	^{14}C age (yr BP)	±	DIC (mM)
Well	41.192175	-111.93894	-15.5	0.1	0.8377	0.0014	-169.1	1.4	1425	15	6.6
Weber River	41.218295	-111.987708	-10.2	0.1	0.9332	0.0015	-74.3	1.5	555	15	3.2
Bear River	41.545895	-112.095349	-8.4	0.1	0.8348	0.0016	-171.9	1.6	1450	20	4.1
Jordan River	40.771568	-111.975878	-9.7	0.1	0.8416	0.0014	-165.2	1.4	1385	15	4.1

fication step. The first Tedlar bag collected gas for the first 30 ml of acid added, the second Tedlar bag collected gas during the second 30 ml acid addition, while the third Tedlar bag collected remaining CO_2 that evolved after all 60 ml acid had been added and was left to sit for 3 minutes before pulling it off the vessel. Four discrete acidification steps were performed, with a subsample of 5-10 ooids removed from the acidification vessel between each. The subsample of ooids was examined using a Hitachi TM-1000 environmental scanning electron microscope (SEM) to confirm dissolution was occurring from the outside to the inside (SI, Figure 3). Between acidifications, ooids were rinsed three times with deionized water (DIW) and dried overnight. The reaction vessel and its components were rinsed in 10% HCl and dried between each acidification. The DIW in the reaction vessel was replaced, and the reaction vessel was purged for 30 minutes with ascarite-scrubbed N_2 to remove any atmospheric carbon. The acidification procedure, using 60 ml of 3.3 M HCl, DIW rinse, acid wash, and 30-minute purge, was repeated for each acidification (four times total). Following the final acidification, the remaining nuclei were rinsed three times with DIW, dried overnight, and reserved for ^{14}C analysis of the organic carbon fraction. Some calcium carbonate remained on the oolitic nuclei at the end of the experiment to ensure ancient carbonate nuclei were not dissolved which might skew the oldest inorganic carbon age.

^{14}C Analysis

For ^{14}C analysis, gas samples from the sequential leach were cryogenically purified through a dry ice/ethanol trap and collected in a liquid nitrogen trap. Residuals from ooid dissolution of bulk ooids and from the sequential leach were combusted at 900°C for 3 hours to obtain CO_2. All purified CO_2 samples were graphitized using a sealed-tube zinc reduction method (Xu and others, 2007). Graphite was pressed into aluminum target holders and analyzed for ^{14}C at the Keck Carbon Cycle Accelerator Mass Spectrometer (KCCAMS) facility at the University of California, Irvine (Beverly and others, 2010; Southon and others, 2004). Data were normalized to oxalic acid standard OX1 and background corrected using radiocarbon-dead reference carbonates acidified in the same reaction vessel. A modern CSTD standard (an in-house coral standard from Ellen Druffel, with a fraction modern value of 0.9445 ± 0.0018 (1σ stdev, n=262) was also processed by the acidification and measured for quality control (Gao and others, 2014). ^{14}C data are presented according to the conventions presented in Stuiver and Polach, 1977. Non-calibrated ages (given in year before present, or YBP) are presented in this paper to be consistent with ages reported in the literature.

RESULTS

^{14}C Analyses in the Great Salt Lake

The radiocarbon ages of the surface water that enters Great Salt Lake (Bear, Jordan, and Weber Rivers) and water from a groundwater well in Ogden, Utah were measured in May 2017. The ^{14}C ages of the Weber River, Bear River, and Jordan River are 555±15 yr BP, 1450±20 yr BP, and 1385±15 yr BP, respectively (Table 1). Water sampled from a groundwater well on Weber State University campus in Ogden, UT produced a ^{14}C age of 1425±15 yr BP.

Bulk Ooid ^{14}C Results

Bulk unsorted and sieved ooids from each site yield inorganic and organic ^{14}C ages that represent the average of a mix of older and younger carbon in the samples, and thus do not represent a unique age for the ooids. However, bulk ages can help bracket the general age of the ooids and provide some indication of their antiquity. In general, bulk ooid carbonate analyses produced ages that ranged from 2728±15 (Spiral Jetty) to 4373±20 yr BP (Spiral Jetty), whereas bulk organics produced slightly younger ages, between 1935±15 (Antelope Island) and 4200±15 yr BP (Spiral Jetty) (Table 2). Smaller ooids have younger average ^{14}C ages, which is reflected in both inorganic and organic carbon. Total organic carbon of bulk ooids from both sites varies from 0.43% to 1.34%; however, ooids from the north arm of GSL have more than double the organic carbon of south arm ooids (Table 2). Raman spectroscopy of ooid cross sections

Table 2. *Inorganic and organic ^{14}C ages from bulk ooids.*

Locality	Grain Size (µm)	Inorganic C Age (^{14}C yr BP)	Organic C Age (^{14}C yr BP)	% Total Organic Carbon
Spiral Jetty - North Arm				
	Unsorted	3872±15	3490±15	**1.34**
	355-500	4373±20	4200±15	1.3
	250-355	3759±15	3520±20	0.97
	125-250	2728±15	2335±15	1.19
Antelope Isl -- South Arm				
	Unsorted	3556±15	2175±20	**0.46**
	355-500	3947±15	2680±20	0.43
	250-355	3834±15	2250±15	0.48
	125-250	3158±15	1935±15	0.55

shows that organic matter is distributed both in the micritic nuclei of ooids (when the nuclei are peloids) and incorporated throughout the carbonate cortices (Figure 3, SI Figure 1). Grain size analysis reveals both north and south arm ooids are skewed toward finer grain sizes which contain more organic C in the nuclei proportionally, between 63 and 355 µm. North arm ooids are less dominated by the 63 – 355 µm size class (45%), than southern arm ooids (73%) (Figure 4).

Serial ^{14}C Ooid Record

^{14}C ages of CO_2 that was released during acidification of 355 – 500 µm diameter ooids from Spiral Jetty increased in a non-linear manner from an age of 660±15 yr BP in the first layer dissolved to 5830±60 yr BP in the last layer dissolved. The ^{14}C ages of ooids from Antelope Island increased linearly from 460±20 yr to 6600±60 yr BP (SI Table 1) (uncorrected for reservoir effect). ^{14}C ages of organic matter combusted from the nuclei remaining at the end of the experiment were 5975±15 and 6210±20 yr BP for Spiral Jetty and Antelope Island ooids, respectively.

As dissolution progresses and ooids become smaller, each successive sample taken represents a thicker width of ooid cortex dissolved (assuming the mass dissolved from each acid addition is constant), thus homogenizing the ^{14}C over a larger range of radial cortex depths. To account for this, ages were integrated over ooid cortices ranging from 355 – 500 µm in diameter assuming they had a spherical geometry and constant net growth (precipitation - abrasion) (Figure 5A, 5B) using $V = 4/3 * \pi r^3$, where V is volume and r is radius in micrometers. To summarize, our experiments indicate that 355-500 µm ooids from GSL began precipitating around 5830-6600 ± 60 ^{14}C years BP with a continuous chronology to near modern ages (when corrected for reservoir effect). Organic carbon extracted from the nuclei material left at the

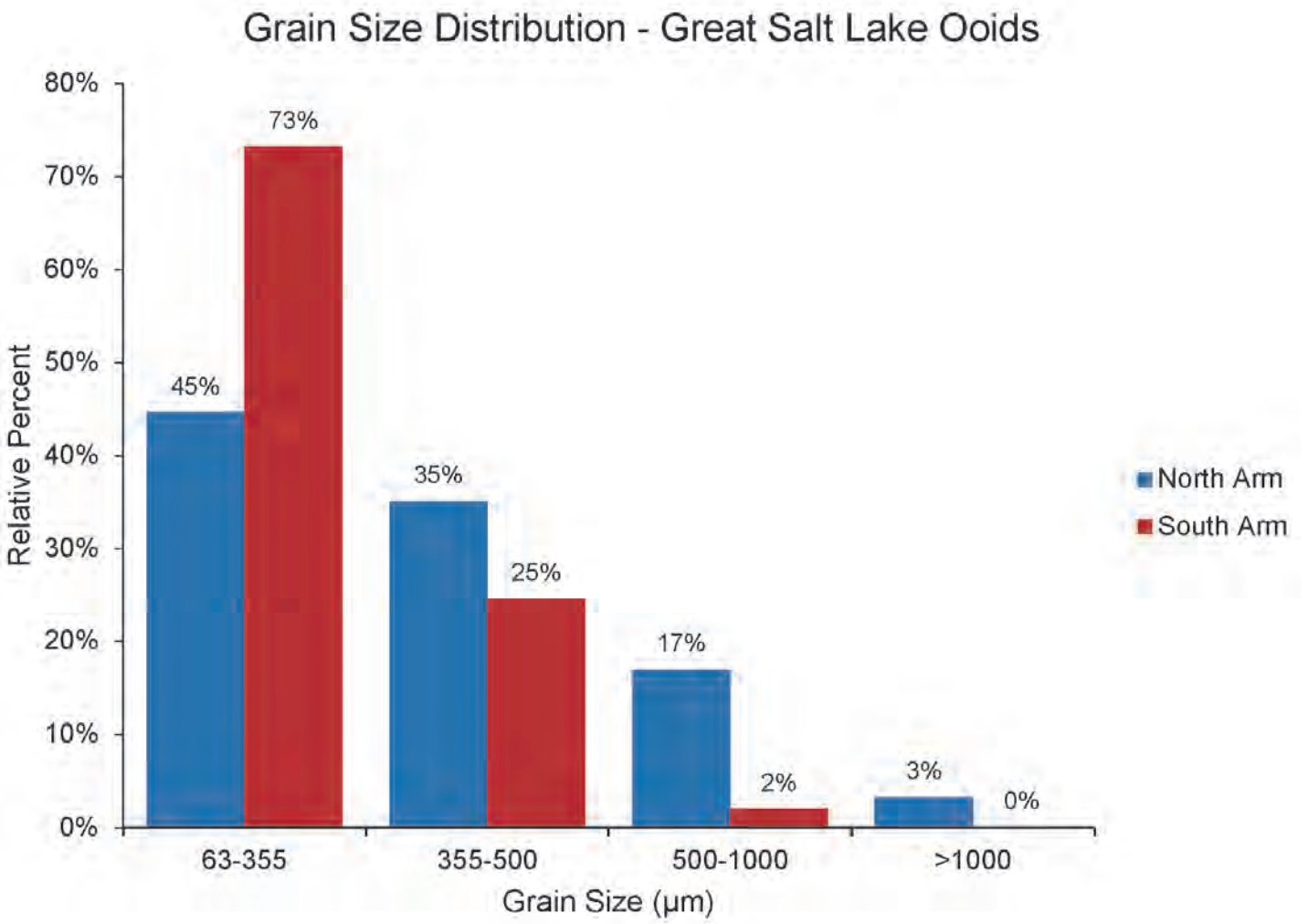

Figure 4. *Grain size distribution of Great Salt Lake ooids sampled from the north and south arms of the lake. Ooids from both arms of the lake are dominated by finer sized ooids (63 – 355 µm), though south arm ooids are more heavily skewed toward fine grain sizes.*

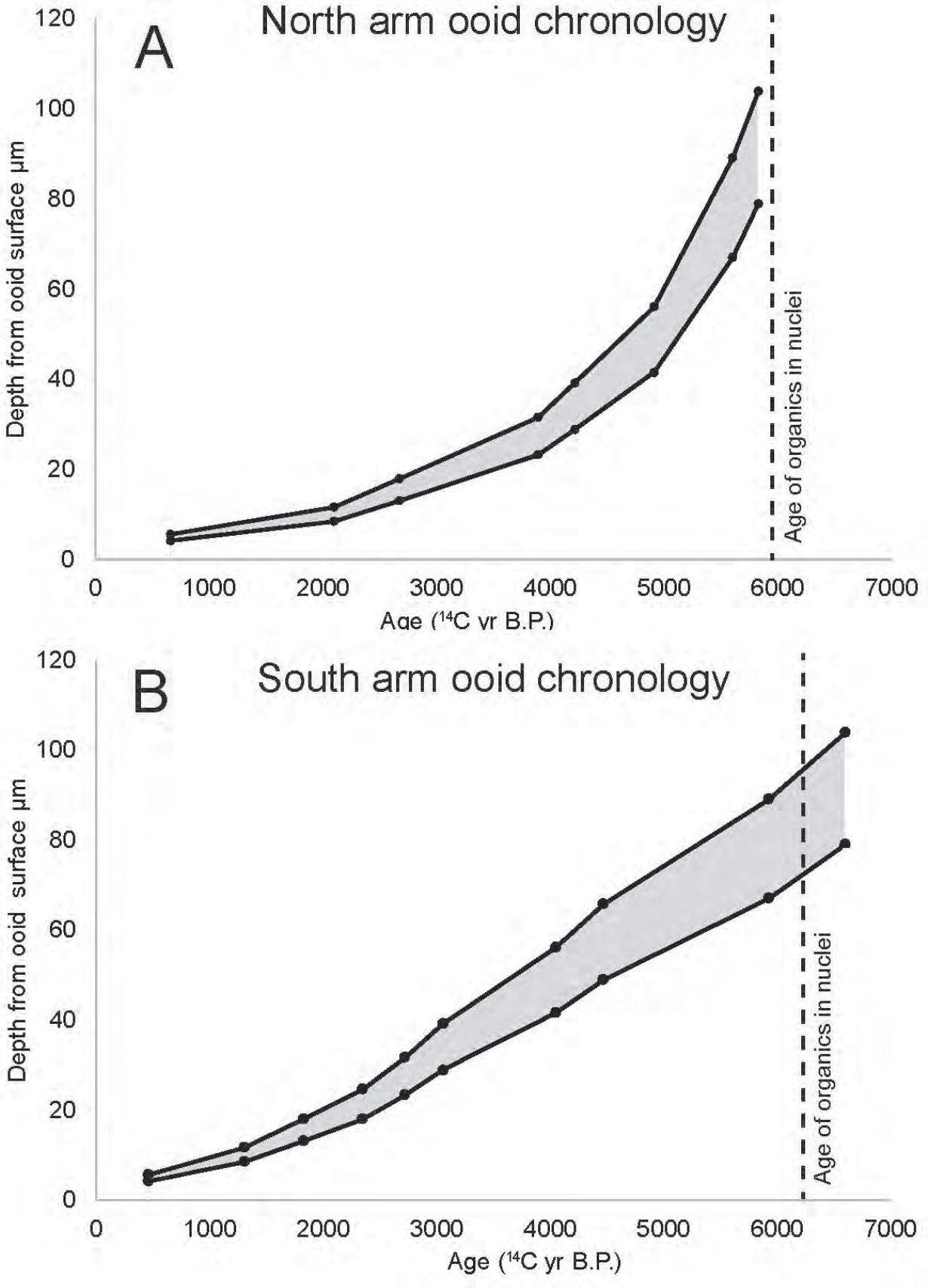

Figure 5. *Inorganic ^{14}C chronologies from north arm ooids (A) and south arm ooids (B) were integrated over ooid cortical ranges of 355-500 µm in diameter (represented by shaded region), assuming spherical geometry and constant net growth. ^{14}C ages from organic carbon (dotted line) from remaining ooid nuclei were 5975±15 and 6210±20 yr for north arm (A) and south arm (B) ooids respectively.*

end of the experiment yield nearly contemporaneous ages with the oldest inorganic carbon samples, lending credence to the presumed onset of ooid formation by our methods. The average ooid age extracted from the sequential dissolution yields mean ages of 3737 yr BP and 3277 yr BP for North and South arm ooids (355 – 500 µm diameter), respectively.

DISCUSSION

It is important to consider the behavior of ^{14}C in the GSL, as the ^{14}C age of lacustrine carbonates may be subject to a "reservoir effect", whereby lakes can accumulate old dissolved inorganic carbon over time. Lakes acquire some of this carbon from inflowing water that travels over ancient limestones that reside in their catchment, causing their dissolved inorganic carbon pool to have an apparent age that would be older than the atmospheric value. Any calcium carbonate that precipitates from that lake water would record an apparently older ^{14}C age than coeval atmospheric ^{14}C. Our analyses reveal that reservoir effects represent the largest source of uncertainty in our data. Surface water enters the lake via three rivers: Bear, Jordan, and Weber, all of which enter the south arm of GSL. Our results show that these river waters and water from a well in Ogden, Utah (representing groundwater) deliver ancient inorganic carbon to the lake. The continuous exchange of CO_2 between the lake water and the atmosphere reduces the age of the lake water reservoir, and thus the reservoir age at any given time is a reflection of the water balance of the inputs of ancient DIC, lake surface area (exchange of CO_2), DIC removal, and the existing reservoir age. Two anthropogenic changes may have influenced the lake reservoir age in contrasting ways. The causeway has reduced the north arm surface area by a factor of two, reducing the rate of atmospheric exchange in this region proportionally. However, bomb testing has increased $^{14}C/^{12}C$ in the atmosphere by an average of 50% during the past 50 years. Because those two effects may largely negate one another, we assume the modern south arm reservoir effect of 295± 20 yr BP is likely more representative of pre-causeway homogeneous lake conditions and therefore more applicable to this dataset. There remains uncertainty in how the reservoir age may have varied through the past 6000 years. Paired U-Th and ^{14}C ages from lacustrine cave carbonates suggest the reservoir effect for Lake Bonneville (from 25 to 13 ka) was 200 years or less (McGee and others, 2012), which agrees with previous estimates of Lake Bonneville's reservoir effect (Oviatt and others, 1992). However, Bowen and others (2019) suggest reservoir ages for much of the Holocene may exceed 1000 years, and they estimate that the reservoir age decreased substantially from >1200 years to <500 years during the late Holocene.

Bulk inorganic ^{14}C ages from sieved ooids reveal that smaller ooids are younger than larger ooids (Table 2). The younger average bulk ^{14}C ages of finer sized ooids may be attributed to a more recent onset in formation and implies that an ooid factory has been active in Great Salt Lake since ~6000 YBP. Therefore, ooid size in the GSL would appear to scale with age rather than some later physical sorting mechanism indicating that ooids have been growing in GSL over at least the past several thousand years at these localities. The grain size distribution is skewed toward finer grain sizes in both arms of the lake, which is also suggestive of an active ooid factory when combined with bulk ooid age data (Table 2, Figure 4). Bulk ooid ages also indicate that the Great Salt Lake ooids are significantly older than the modern marine ooids from Carbla Beach, Australia and the Bahamas (Beaupré and others, 2015; Duguid and others, 2010). However, some significant caveats require exploration while interpreting bulk ^{14}C ages. Bulk ooid ages do not allow for the differentiation between relic ooids that formed thousands of years ago versus modern ooid formation if the population of ooids in a size class is a mixture of material of different ages. In addition, Raman spectroscopy demonstrates that organic carbon is not exclusively found in peloidal nuclei but is also incorporated throughout the ooid cortex. Thus, bulk ooid organic carbon ages represent a mixture of organic carbon from *Artemia* pellet nuclei and younger organic carbon incorporated at various points in the growth of the aragonitic cortex. Ooids from the northern arm of GSL have older bulk organic carbon ages (Table 2) for each size fraction, including unsorted ooids. Because the total organic carbon content in north arm ooids is twice that of south arm ooids and the bulk organic carbon ages are older, we expect this age disparity is attributed to a higher occurrence of ooids with organic-rich brine shrimp pellet nuclei in the north arm of the lake. Petrographic investigation of 100 ooids in thin section from the northern and southern arm of GSL confirm this hypothesis, with 83% pellet nuclei in the north compared to 56% pellet nuclei in the south (SI Figure 4). The distribution of organic matter throughout ooid cortices coupled with the need to resolve a chronology from the carbonate fraction, highlight both the problems with interpreting bulk age data from ooids and the need for serial dissolution.

Our serial dissolution experiments present a chronology from modern lacustrine ooids that demonstrate the ancient onset of ooid formation over ~6,000 years ago. Once corrected for reservoir effect, the youngest inorganic carbon ages suggest ooids continued to form, apparently up to the present. We hypothesize

ooid formation may still be occurring, as any modern ^{14}C would be homogenized with slightly older ^{14}C in our youngest sample. The $^{14}C_{org}$ from Antelope Island ooids is slightly younger than the oldest inorganic carbon sample, and this may be attributed to 1) residual organics of younger origin, 2) partial leaching of ancient carbonate material in the center of the ooids, and/or 3) a reservoir effect yielding inorganic carbon which is apparently older by hundreds of years.

The age of the onset of ooid growth from the north and south arm of GSL is similar, as indicated by the oldest inorganic and organic carbon ages of ooids, but the growth curve of their chronologies varies. For example, the south arm ooids appear to have a near-constant growth rate (between ~0.01 – 0.015 μm/yr) within the resolution of the data and assumptions. In contrast, the growth of the north arm ooids appears to have been initially more rapid (~0.03 – 0.06 μm/yr) and then slowed somewhat throughout their growth history (0.003 – 0.008 μm/yr). The differences in slope (Figure 5) may be attributed to local site-specific variations affecting carbonate precipitation or abrasion in each part of the lake, or assumptions made when calculating dissolution depth (i.e., constant net growth rate, spherical geometry). To determine whether the assumption of spherical geometry in age integration is responsible for the difference in the slope of the ooid growth curves, we integrated the ages over assumed ellipsoidal ooid geometries. The resulting slope differences were exacerbated when we assumed 100% ellipsoidal geometry (SI Figure 5), suggesting that there are likely other effects (environmental, geochemical, or physical) during the ooid growth history causing their differences in slope. It is intriguing that the north arm ooids fit the prediction that ooid growth should be rapid at first and then slow as they reach hydrologic equilibrium and spend more time as bedload versus suspended load (Trower and others, 2017) but coevally, the south arm ooids display a linear growth trend. The prevailing wind direction at GSL is from the SE (Western Regional Climate Center, 2023). Because of the locations of the samples (Figure 1), the north arm site should receive stronger wave action than the south arm site, resulting in greater abrasion and slower growth as the grain grows in size. The grain size data (Fig. 4), seem to support this, as coarse grained ooids may have been selectively concentrated by stronger wave energy at the northern site.

Comparison to Marine Ooid Chronologies

The GSL ooid growth histories raise some unexpected questions with respect to how ooids form in the GSL and thus how ooids grow in general. The lifespan of 355-500 μm radial ooids from Great Salt Lake is between two and six times longer than most modern marine ooids from the Bahamas Archipelago and Australia (Beaupré and others, 2015; Duguid and others, 2010). The ooids are very old compared to modern marine examples, yet sequential dating reveals they experienced continuous net growth for over 6000 years while existing within the GSL environment. Trower and others (2017) note that the balance of precipitation versus abrasion are key components in the formation of ooids. On the one hand, the GSL has a very different chemical environment versus the marine settings. For example, in marine settings where ooids grow, the seasonal water temperature variations are low, whereas the Great Salt Lake experiences comparatively large temperature fluctuations (SI Figure 6). Paradis 2019 showed that the solubility of aragonite decreases as temperature increases and CO_2 escapes to the atmosphere, thus the favorable window for aragonite precipitation in the GSL may only exist over a short window in the summer when the lake water is significantly warmer, whereas marine settings are likely to be supersaturated with respect to aragonite year-round. Additionally, we expect abrasion is less intense in the GSL than in marine systems as GSL is a significantly lower energy environment than marine examples. Finally, the much lower Ca^{+2}/Mg^{+2} in GSL (0.03, Jones and others, 2009) compared to the ocean (0.2) may slow growth rates.

It is unclear how the balance between abrasion and precipitation should be reconciled given how slowly net ooid growth appears to be in the GSL system. Do they experience rapid growth then significant abrasion on a yearly basis, thus accounting for such a slow net growth rate, or do they simply grow very slowly? Growth could also be episodic in response to variations in salinity driven by rainfall variations on decadal (or longer) time scales. Petrographic investigation reveals what appear to be relatively delicate aragonite crystals that we speculate would not survive intense abrasion, supporting the premise that that perhaps the GSL ooids simply grow very slowly. Furthermore, how might the radial fabric affect or indicate growth rate versus the tangential fabric in modern marine ooids? Could the low Ca^{+2}/Mg^{+2} in GSL facilitate growth at the tips of crystals extending into the solution? Interestingly, Lincoln et al. (2022) hypothesized that the large ray-like aragonite crystals common in GSL ooid cortices may represent a replacement of a precursor Mg-silicate (that is, not a primary phase, but one formed later vs. adjacent, subjacent, or superjacent aragonite). We note that the ^{14}C chronologies of all sampled ooids are coherent (inside/older-outside/younger from initiation of growth to termination for the sequentially dated ooids, with the ^{14}C organic dates of the nuclei corroborating the initiation of ooid growth, as well as larg-

older-smaller/younger for the bulk dated ooid). While our work cannot comment on the paragenetic sequence of the ooid fabrics, the coherence of ^{14}C ages is unexpected if secondary replacement of aragonite was widespread. Future work, including finer scale sequential dating, may help resolve the unanswered questions surrounding the GSL ooids.

Ooids and the History of the Great Salt Lake

During ooid growth, the north and south arms of Great Salt Lake would have been in communication with one another as part of one large body of water (rather than two arms separated by a railway), thus the generally similar chronologies for onset of ooid growth from each arm of the lake ~6000 years ago agrees with the lake's history. Furthermore, 10,000 ^{14}C yr BP marks the end of the Gilbert episode of Great Salt Lake, where the lake experienced a brief 15m transgression during which the lake had freshened enough to support ostracods and possibly fish (Broughton and others, 2000; Oviatt and others, 2015). After the Gilbert episode, GSL regressed to average historic GSL levels (near 1280 m) and brine shrimp cysts and pellets appeared in lake sediment cores (Oviatt and others, 2015). It is thought that Great Salt Lake did not transgress higher than modern lake levels during early parts of the Holocene (11.5-10.2 cal ka BP; 10-9 ^{14}C ka BP), but little is known about the remainder of Holocene lake level because Holocene sediments on the floor of GSL have been largely reworked (Oviatt and others, 2015). On one hand, a bulk chemical analysis of ooids would represent an homogenized signal over ~6000 years and provides one outlook for the duration of aquatic history that ooids may represent, with relevance to other systems where ooids are analyzed as paleoenvironmental indicators. On the other hand, sequential dissolution of the ooids preserved in GSL ooids has the potential to resolve some of the finer scale lake level variations in GSL during the last ~6,000 years and potentially longer given that $\delta^{13}C$ and $\delta^{18}O$ are coupled in this closed-basin system, and $\delta^{18}O$ can correlate with lake level (e.g., Talbot 1990).

CONCLUSIONS

The high-resolution ^{14}C chronology of GSL ooids demonstrates that: ^{14}C is a robust tool for dating ooids in GSL, and GSL ooids have a lifespan between two and six times longer than modern marine ooids. The long ooid lifespan confirms the need to temporally resolve accretionary structures like ooids before interpreting bulk geochemical data. The ^{14}C ages obtained from organics in ooid nuclei corroborate the timeframe of onset of aragonite precipitation. Additionally, Raman spectroscopy coupled with ^{14}C ages from bulk unsorted and sieved ooids shed light on the importance of sequentially derived chronologies due to the fact that bulk ages underestimate the maximum age of ooids by thousands of ^{14}C years. This study highlights the disparity in net growth rate, lifespan, and seasonality in precipitation between radial ooids from Great Salt Lake and modern marine ooids. Ooids from different parts of the lake show differing growth histories, perhaps reflecting localized variations in wave energy due to prevailing wind direction or other local environmental conditions. Lastly, the >6000 year chronology captured in GSL ooids highlights the caution needed in utilizing these accretionary sediments in a bulk geochemical analysis as ooids are repositories of thousands of years of environmental change.

ACKNOWLEDGEMENTS

We thank Bonnie Baxter and Jaimi Butler for their support in organizing field sampling. We also thank Dr. Carie Frantz, Dr. Victoria Petryshyn, Dr. Dylan Wilmeth, Dr. Scott Perl, Dr. John Spear and Dr. Joyce Yager for their helpful assistance in the field and Nick Rollins for help in the lab. This work was supported in part by the SEPM student research award.

REFERENCES

Baskin, R. 2014. *Occurrance and Spatial Distribution of Microbial Bioherms in Great Salt Lake, Utah*. University of Utah.

Beaupré, S. R., Roberts, M. L., Burton, J. R., & Summons, R. E. 2015. Rapid, high-resolution ^{14}C chronology of ooids. *Geochimica et Cosmochimica Acta*, *159*, 126–138. https://doi.org/10.1016/j.gca.2015.03.009

Beverly, R. K., Beaumont, W., Tauz, D., Kaelyn, M. O., Karl, F. V. R., Guaciara, M. S., & Southon, J. R. 2010. The Keck Carbon Cycle AMS Laboratory, University of California, Irvine: Status Report. *RADIOCARBON*, *52*, 301–309. Retrieved from https://www.ess.uci.edu/researchgrp/ams/files/beverly_et_al_2010_52_2.pdf

Bouton, A., Vennin, E., Boulle, J., Pace, A., Bourillot, R., Thomazo, C., … Visscher, P. T. 2016. Linking the distribution of microbial deposits from the Great Salt Lake (Utah, USA) to tectonic and climatic processes. *Biogeosciences*, *13*(19), 5511–5526. https://doi.org/10.5194/bg-13-5511-2016

Bouton, A., Vennin, E., Mulder, T., Pace, A., Bourillot, R., Thomazo, C., … Visscher, P. T. 2016. Enhanced development of lacustrine microbialites on gravity flow deposits, Great Salt Lake, Utah, USA. *Sedimentary Geology*, *341*, 1–12. https://doi.org/10.1016/j.sedgeo.2016.05.004

Bowen, G., Nielson, K., & Eglinton, T. 2019. Multi-Substrate Radiocarbon Data Constrain Detrital and Reservoir Effects in Holocene Sediments of the Great Salt Lake, Utah. Radiocarbon, 61(4), 905-926. doi:10.1017/RDC.2019.62

Broughton, J. M., Madsen, D. B., & Quade, J. 2000. Fish Remains from Homestead Cave and Lake Levels of the Past 13,000 Years in the Bonneville Basin. *Quaternary Research*, *53*(3), 392–401. https://doi.org/10.1006/QRES.2000.2133

Clause, A. G., Celestian, A. J., & Pauly, G. B. (2021). Plastic ingestion by freshwater turtles: a review and call to action. Scientific Reports, 11(1), 1-10.

Currey, D. R., Atwood, G., & Mabey, D. R. 1984. Major levels of Great Salt Lake and Lake Bonneville. *Utah Geological and Mineral Survey Map 73*.

Diaz, M., Eberli, G., Blackwelder, P., Phillips, B., & Swart, P. 2017. Microbially mediated organomineralization in the formation of ooids. *Geology*, *45*(9). https://doi.org/10.1130/G39159.1

Diaz, M., Piggot, A., Eberli, G., & Klaus, J. 2013. Bacterial community of oolitic carbonate sediments of the Bahamas Archipelago. *Marine Ecology Progress Series*, *485*, 9–24. https://doi.org/10.3354/meps10359

Diaz, M., Swart, P., Eberli, G., Oehlert, A., Devlin, Q., Saeid, A., & Altabet, M. 2015. Geochemical evidence of microbial activity within ooids. *Sedimentology*, *62*(7), 2090–2112. https://doi.org/10.1111/sed.12218

Duguid, S. M. A., Kyser, T. K., James, N. P., & Rankey, E. C. 2010. Microbes and Ooids. *Journal of Sedimentary Research*, *80*(3), 236–251. https://doi.org/10.2110/jsr.2010.027

Eardley, A. J. 1938. the American Association of Petroleum Geologists. *Bulletin of the American Association of Petroleum Geologists*, *22*(10), 1305–1363. https://doi.org/10.1126/science.58.1489.27

Gao, P., Xu, X., Zhou, L., Pack, M. A., Griffin, S., Santos, G. M., … Liu, K. 2014. Rapid sample preparation of dissolved inorganic carbon in natural waters using a headspace-extraction approach for radiocarbon analysis by accelerator mass spectrometry. *Limnology and Oceanography: Methods*, *12*(APR), 174–190. https://doi.org/10.4319/lom.2014.12.174

"Great Salt Lake Causeway Berm Raised 4 Feet to Protect Salinity Levels." Utah Division of Forestry, Fire & State Lands, Utah DNR, https://ffsl.utah.gov/uncategorized/dnr-modifies-great-salt-lake-causeway-breach-in-response-to-salinity-issues/.

Hearty, P. J., Webster, J. M., Clague, D. A., Kaufman, D. S., Bright, J., Southon, J., & Renema, W. 2010. A pulse of ooid formation in Maui Nui (Hawaiian Islands) during Termination I. *Marine Geology*, *268*, 152–162. https://doi.org/10.1016/j.margeo.2009.11.007

James, N. P., Bone, Y., Kyser, T. K., Dix, G. R., & Collins, L. B. 2004. The importance of changing oceanography in controlling late Quaternary carbonate sedimentation on a high-energy, tropical, oceanic ramp: north-western Australia. *Sedimentology*, *51*(6), 1179–1205. https://doi.org/10.1111/j.1365-3091.2004.00666.x

Jones, B., Naftz, D., Spencer, R., & Oviatt, C. 2009. Geochemical Evolution of Great Salt Lake, Utah, USA. *Aquatic Geochemistry*, *15*(1), 95–121. https://doi.org/10.1007/s10498-008-9047-y

Kahle, C. F. 1974. Ooids from Great Salt Lake, Utah, as an analogue for the genesis and diagenesis of ooids in marine limestones. *Journal of Sedimentary Petrology*, *44*(1), 30–39.

Mcdonald, D., Price, M., Goodrich, J., Nawrocki, E., Desantis, T., Probst, A., … Hugenholtz, P. 2012. An improved Greengenes taxonomy with explicit ranks for ecological and evolutionary analyses of bacteria and archaea. *The ISME Journal*, *6*(3), 610–618. https://doi.org/10.1038/ismej.2011.139

Mcgee, D., Quade, J., Lawrence Edwards, R., Broecker, W. S., Cheng, H., Reiners, P. W., & Evenson, N. 2012. Lacustrine cave carbonates: Novel archives of paleohydrologic change in the Bonneville Basin (Utah, USA). *Earth and Planetary Science Letters*, *351–352*, 182–194. https://doi.org/10.1016/j.epsl.2012.07.019

Mcguire, K. M. 2014. Comparative Sedimentology of Lake Bonneville and the Great Salt Lake, 34.

National Water Information System data available on the World Wide Web (USGS Water Data for the Nation). 2023. Retrieved from http://waterdata.usgs.gov/nwis/

O'Reilly, S. S., Mariotti, G., Winter, A. R., Newman, S. A., Matys, E. D., McDermott, F., … Klepac-Ceraj, V. 2017. Molecular biosignatures reveal common benthic microbial sources of organic matter in ooids and grapestones from Pigeon Cay, The Bahamas. *Geobiology*, *15*(1), 112–130. https://doi.org/10.1111/gbi.12196

Oviatt, C. G., Currey, D. R., & Sack, D. 1992. Radiocarbon chronology of Lake Bonneville, Eastern Great Basin, USA. *Palaeogeography, Palaeoclimatology, Palaeoecology*, *99*(3–4), 225–241. https://doi.org/10.1016/0031-0182(92)90017-Y

Oviatt, C. G., Madsen, D. B., Miller, D. M., Thompson, R. S., & McGeehin, J. P. 2015. Early Holocene Great Salt Lake, USA. *Quaternary Research*, *84*(1), 57–68. https://doi.org/10.1016/j.yqres.2015.05.001

Pacton, M., Ariztegui, D., Wacey, D., Kilburn, M. R., Rollion-Bard, C., Farah, R., & Vasconcelos, C. 2012. Going nano: A new step toward understanding the processes governing freshwater ooid formation. *Geology*, *40*(6), 547–550. https://doi.org/10.1130/G32846.1

Prevailing Wind Direction., Western Regional Climate Center, 2023. Web. 22 August 2023. http://wrcc.dri.edu/Climate/comp_table_show.php?stype=wind_dir_avg

Reitner, J. and others. 1997. *Organic matter in Great Salt Lake ooids (Utah, USA) - First approaches to a formation via organic matrices*. *Facies* (Vol. 36).

Rupke, A., & Mcdonald, A. 2012. *Great Salt Lake brine chemistry database, 1966-2011: Utah Geological Survey Open-File Report 596*. Retrieved from http://ugspub.nr.utah.gov/publications/open_file_reports/ofr-596/appa.xls

Sandberg, P. 1975. New interpretations of Great Salt Lake ooids and of ancient non-skeletal carbonate mineralogy. *Sedimentology*, *22*(4), 497–537. https://doi.org/10.1111/j.1365-3091.1975.tb00244.x

Southon, A., Santos, J. R., Druffel-Rodriguez, G. M., Southon, J., Guaciara Santos, B., Kevin Druffel-Rodriguez, B., … Maya Mazon, B. 2004. The Keck Carbon Cycle AMS Laboratory, University of California, Irvine: Initial Operation and a Background Surprise. *Radiocarbon*, *46*(46), 41–49. Retrieved from https://escholarship.org/uc/item/4522n2x6

Spencer, R.J., Eugster, H.P., and Jones, B.F. 1985. Geochemistry of Great Salt Lake, Utah II: Pleistocene-Holocene Evolution. *Geochemica et Cosmicha Acta*, *49(3)*, 739-747. https://doi.org/10.1016/0016-7037(85)90168-1.

Stephens, D. W. 1990. Changes in lake levels, salinity and the biological community of Great Salt Lake (Utah, USA), 1847-1987. *Hydrobiologia*, *197*(1), 139–146. https://doi.org/10.1007/BF00026946

Stuiver, M., & Polach, H. A. 1977. Discussion: reporting of 14 C data. *Radiocarbon*, *19*(3), 355–363. https://doi.org/10.1021/ac100494m

Stuiver, M., & Reimer, P. J. 1993. Extended ^{14}C data base and revised CALIB 3.0 ^{14}C age calibration program. *Radiocarbon*, *35*(1), 215–230.

Summons, R. E., Bird, L. R., Gillespie, A. L., Pruss, S. B., Roberts, M., & Sessions, A. L. 2013. Lipid biomarkers in ooids from different locations and ages: Evidence for a common bacterial flora. *Geobiology*, *11*(5), 420–436. https://doi.org/10.1111/gbi.12047

Talbot, M. R. 1990. A review of the palaeohydrological interpretation of carbon and oxygen isotopic ratios in primary lacustrine carbonates. Chemical Geology: Isotope Geoscience Section, 80(4), 261–279. https://doi.org/10.1016/0168-9622(90)90009-2

Trower, E. J., Lamb, M. P., & Fischer, W. W. 2017. Experimental evidence that ooid size reflects a dynamic equilibrium between rapid precipitation and abrasion rates. *Earth and Planetary Science Letters*, *468*, 112–118. https://doi.org/10.1016/j.epsl.2017.04.004

Trower, E. J., Bridgers, S. L., Lamb, M. P., & Fischer, W. W. 2020. Ooid cortical stratigraphy reveals common histories of individual co-occurring sedimentary grains. Journal of Geophysical Research: Earth Surface, 125, e2019JF005452. https://doi.org/10.1029/2019JF005452

Xu, X., Trumbore, S. E., Zheng, S., Southon, J. R., McDuffee, K. E., Luttgen, M., & Liu, J. C. 2007. Modifying a sealed tube zinc reduction method for preparation of AMS graphite targets: Reducing background and attaining high precision. *Nuclear Instruments and Methods in Physics Research Section B: Beam Interactions with Materials and Atoms*, *259*(1), 320–329. https://doi.org/10.1016/J.NIMB.2007.01.175

SUPPLEMENTARY INFORMATION

.

Methods for bulk organic and inorganic carbon extractions on sieved ooids

To obtain bulk inorganic carbon ages on sieved and unsieved ooids, ooids were dissolved in 3 extractions, and the results of those extractions were weighted and reported herein. The first CO_2 extraction occurred after 0.8 ml H_2PO_4 acid was added at 70°C and left to react for 1-2 hours. The second CO_2 extraction occurred after an additional 0.8 ml H_2PO_4 was added and left to react for 2 more hours at 70°C. The third CO_2 extraction occurred after 2 hours at 70°C after the second extraction, but no extra acid was added to the samples. All purified CO_2 samples were graphitized using a sealed-tube zinc reduction method (Xu and others, 2007). Graphite was pressed into aluminum target holders and analyzed for ^{14}C at the Keck Carbon Cycle Accelerator Mass Spectrometer (KCCAMS) facility at the University of California, Irvine (Southon and others, 2004; Beverly and others, 2010). Data were normalized and background corrected using both modern coral and radiocarbon-dead reference carbonates acidified in the same reaction vessel. Resulting fractions of modern (FM) carbon were weighted according to yield to calculate bulk inorganic carbon age, and ^{14}C data are presented according to the conventions presented in Stuiver and Polach (1977).

To measure bulk organic carbon content and radiocarbon age from the acid insoluble fraction, 1M HCl was added to 10g of ooids at 70°C for 24 hours until pH maintained at 1 for 2 hours. During acidification, the solution containing the sample was centrifuged and the solution was decanted, then a new aliquot of 1M HCl was added. This process was repeated until the pH maintained at 1 for 2 hours. The residuals were then rinsed with Milli-Q until the pH became neutral.

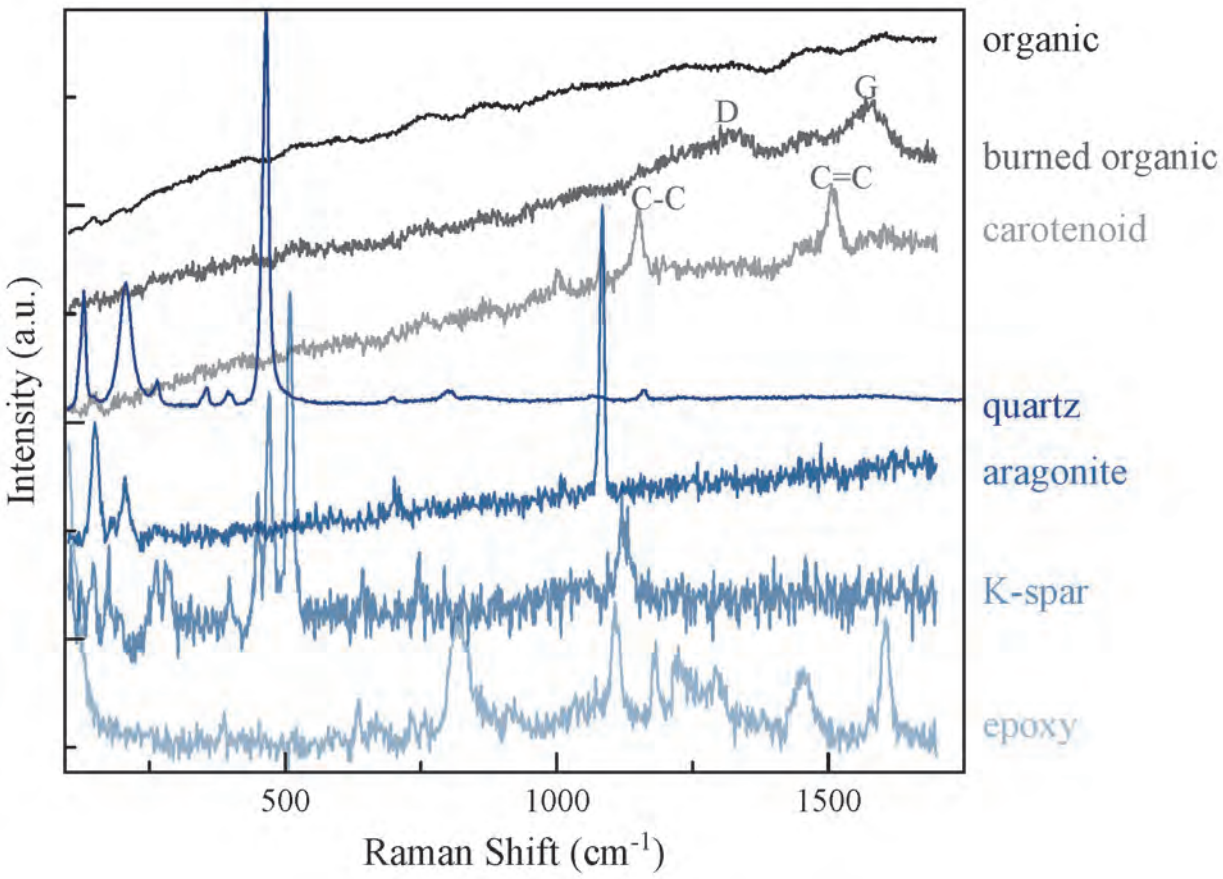

Figure 1. *Example of spectra obtained from Raman spectroscopy on one ooid demonstrating the materials identified.*

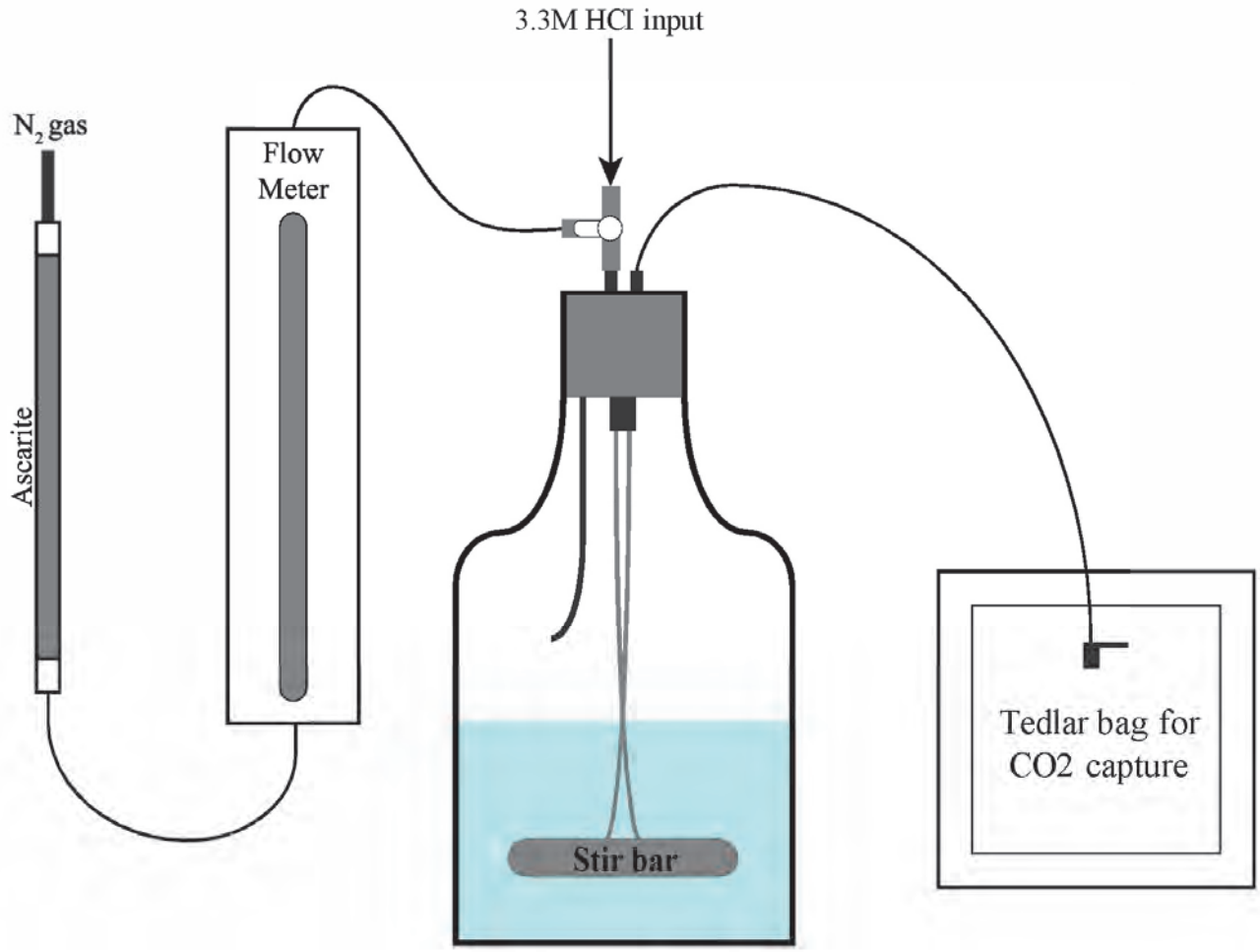

Figure 2. *Ooid dissolution reaction vessel. 50g of size-sieved ooids were added to the reaction vessel with 150cc of deionized water. Ascarite-scrubbed N2 flowed through while the stir bar spun at 600 rpm for 30 min. This step ensured no atmospheric carbon remains in the reaction vessel or water. Next, the outflow and gas inflow stopcocks were closed. For each dissolution step, 60cc of 3.3M HCl were added to the reaction vessel at a rate of 10cc/min. Tedlar bags were filled with the resulting gas every ~3min. The gas was then moved into He-rinsed and evacuated 25cc serum vials that were submitted to UC Irvine for radiocarbon analysis.*

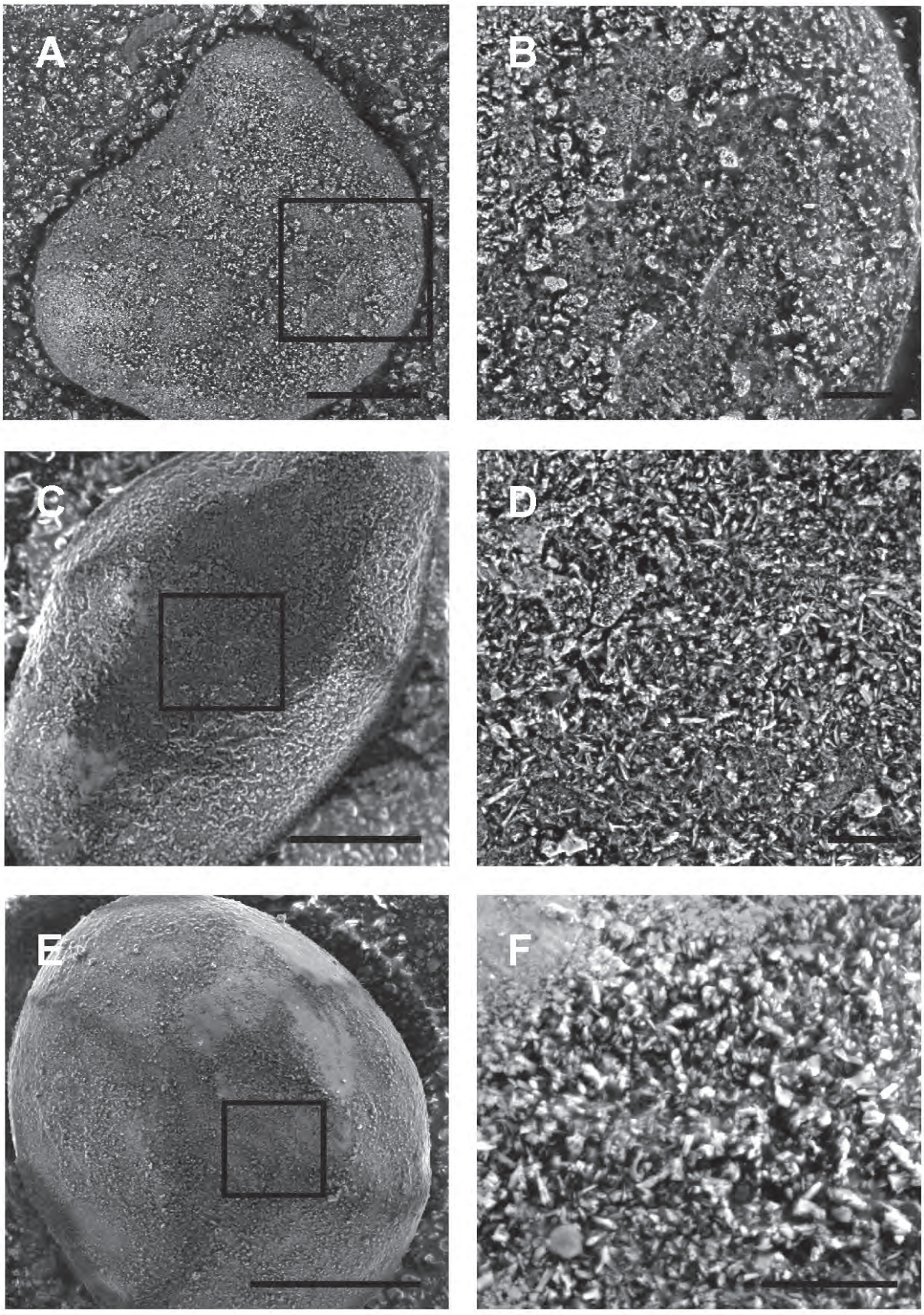

Figure 3. *Scanning electron microscope images of individual ooids with close-up inset after 60ml (A – B), 120ml (C – D), and 180ml (E – F) of 3.3M HCl was added to reaction vessel. Ooids maintain general shape post-acidification confirming dissolution occurred fairly uniformly from exterior to interior.*

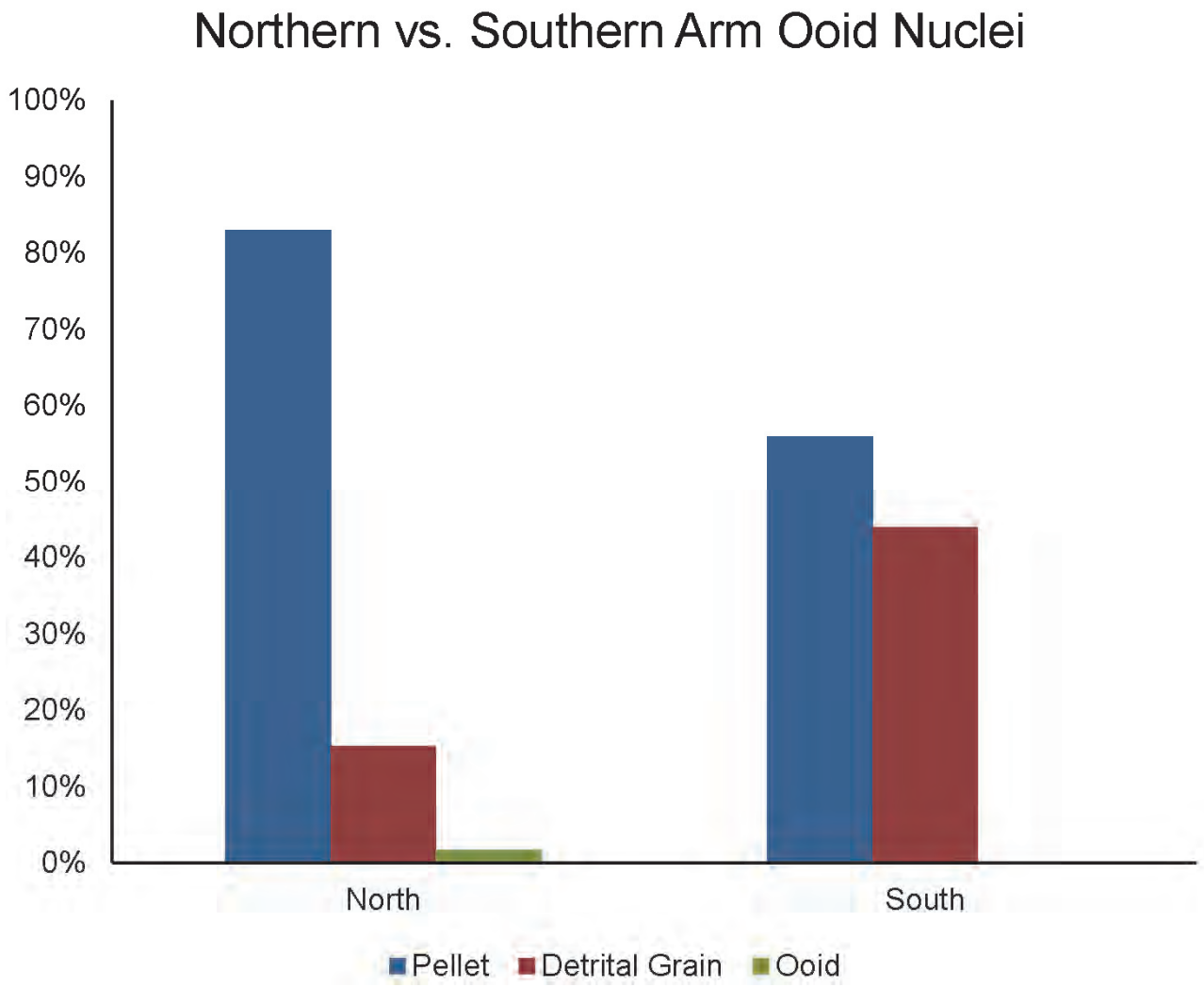

Figure 4. *Nuclei composition in north vs south arm GSL ooids as observed in thin section. North arm ooids have 83% brine shrimp pellet nuclei, 15% detrital grains such as quartz and feldspar, and 2% other ooids as nuclei. Southern arm ooids have 56% brine shrimp pellet nuclei and 44% detrital grain nuclei.*

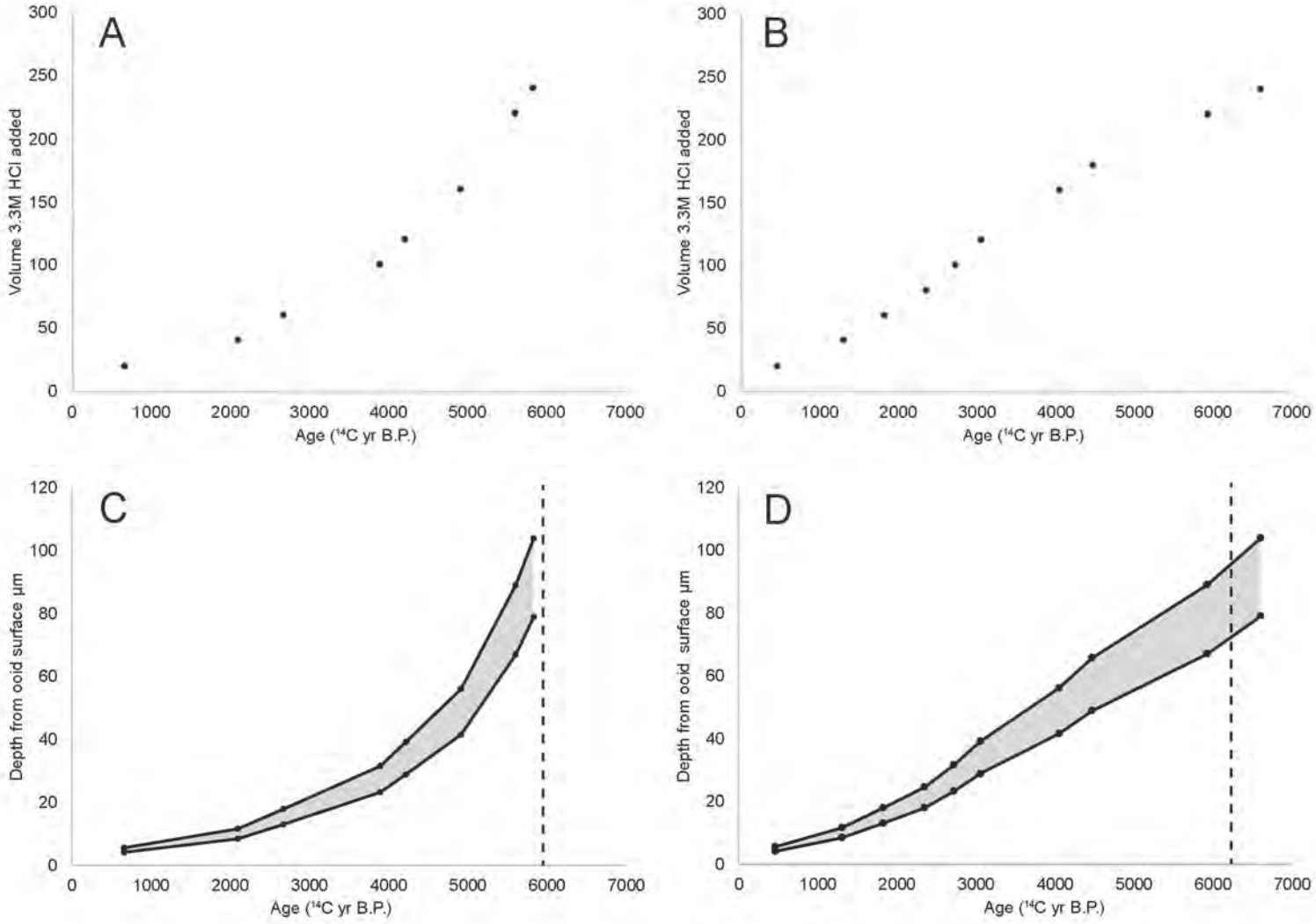

Figure 5. *Comparison of ooid chronologies from the northern arm of GSL (7B, 7D) to the southern arm of GSL (7A, 7C). Figures 7A and 7B use the radiocarbon chronology and integrate the ages assuming spherical geometry of ooids (using mean ooid radius of 213 µm). The resulting slope of the north arm ooid growth curve (B) is steeper (more rapid growth) during the first several thousand years of ooid growth and slows down during the last several thousand years, while the southern arm ooid growth curve (A) is more linear. Because north arm ooids have a larger occurrence of ooids with peloidal nuclei (roughly cylindrical geometry), the radiocarbon chronology was also integrated over an assumed cylindrical geometry using* $V = L * \pi r^2$*, where V is volume, L is length (6 * radius), and r is radius (213 µm) in micrometers. The slope of the north arm ooid growth curve remains highly non-linear even after assuming cylindrical geometry, suggesting there are other factors (environmental or otherwise) accounting for the difference in slope. The error bars represent the relations for ooids at 355 and 500 µm.*

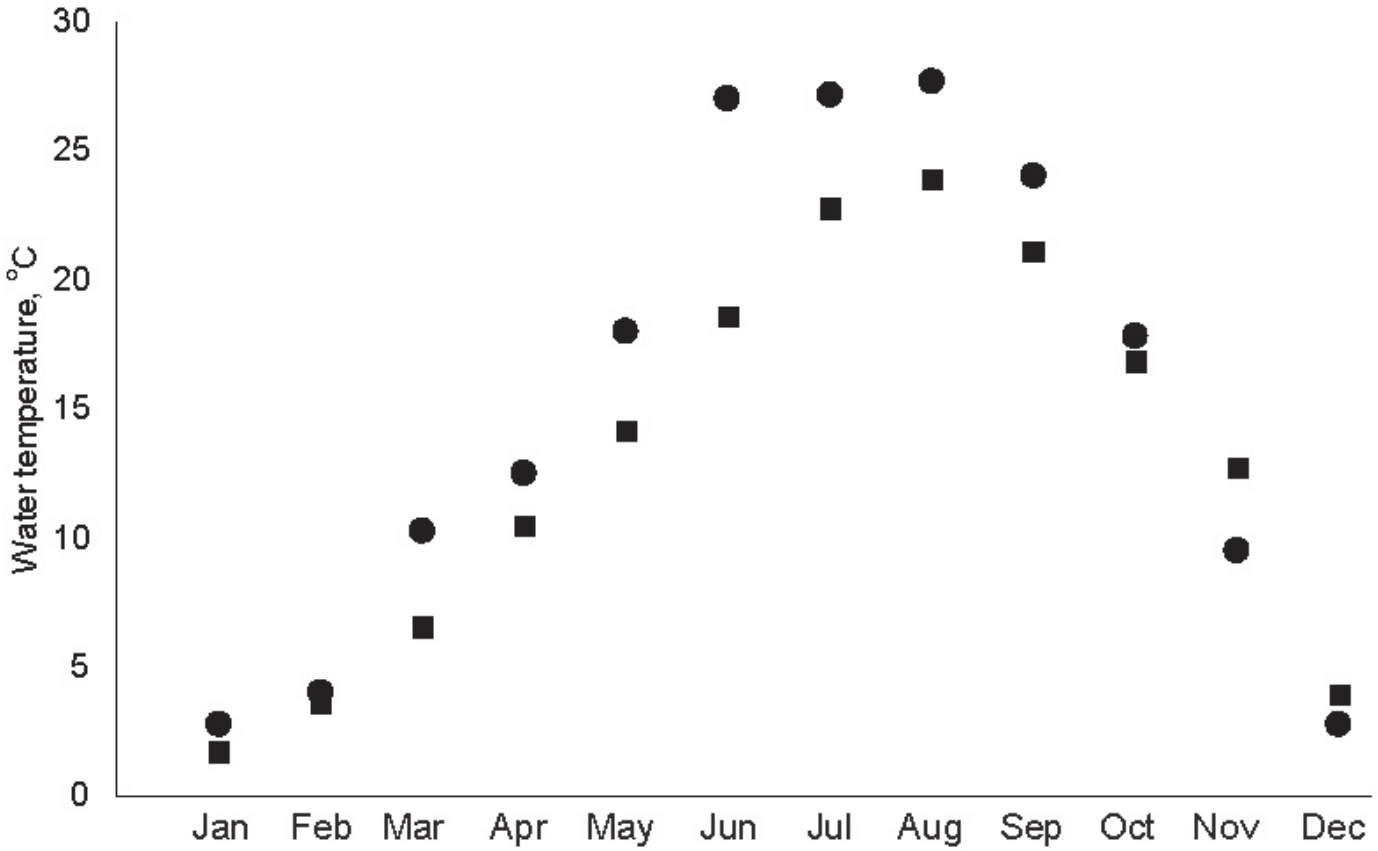

Figure 6. *Monthly average water temperature in north (circle) and south (square) arms of Great Salt Lake as measured by USGS from 2010-2016. (U.S. Geological Survey, 2016).*

Table 1. *Bulk inorganic carbon extractions for sieved and unsorted ooids. The ^{14}C ages from each extraction were pooled to calculate a bulk age for each sample.*

Grain Size (µm)	Extraction	Yield (mgC, Inorg)	Inorg C Fraction	F_m	Bulk F_m	Bulk ^{14}C Age (yr BP)
Unsorted	1	2.29	0.6844	0.7097 ± 0.0012	0.6423 ± 0.0012	3556 ± 15
	2	0.97	0.2904	0.4952 ± 0.0010		
	3	0.08	0.0252	0.5086 ± 0.0021		
355-500	1	2.36	0.6706	0.6676 ± 0.0012	0.6118 ± 0.0011	3947 ± 15
	2	0.98	0.2792	0.4977 ± 0.0009		
	3	0.18	0.0501	0.5004 ± 0.0011		
250-355	1	2.22	0.6584	0.6838 ±0.0012	0.6204 ± 0.0011	3834 ± 15
	2	1.04	0.3092	0.5024 ± 0.0009		
	3	0.11	0.0324	0.4599 ± 0.0018		
125-250	1	2.42	0.7559	0.7222 ± 0.0013	0.6749 ± 0.0012	3158 ± 15
	2	0.72	0.2257	0.5254 ± 0.0009		
	3	0.06	0.0184	0.5659 ± 0.0027		
Unsorted	1	3.29	0.7682	0.6482 ± 0.0011	0.6175 ± 0.0011	3872 ± 15
	2	0.84	0.1965	0.5202 ± 0.0010		
	3	0.15	0.0354	0.4924 ± 0.0015		
355-500	1	2.99	0.7542	0.6030 ± 0.0011	0.5802 ± 0.0011	4373 ± 20
	2	0.82	0.2055	0.5217 ± 0.0010		
	3	0.16	0.0403	0.5020 ± 0.0012		
250-355	1	2.89	0.8339	0.6491 ± 0.0011	0.6263 ± 0.0011	3759 ± 15
	2	0.52	0.1503	0.5133 ± 0.0011		
	3	0.05	0.0158	0.5010 ± 0.0031		
125-250	1	3.00	0.8602	0.7359 ± 0.0013	0.7120 ± 0.0013	2728 ± 15
	2	0.44	0.1253	0.5646 ± 0.0011		
	3	0.05	0.0145	0.5685 ± 0.0032		

Table 2. *Thin sections of individual ooids (A) analyzed with Raman spectroscopy (B) to map the presence of organic matter (blue) within the ooid cortex. A Raman spectrum with a strong noise signal suggesting the presence of organic material was selected from a GSL ooid and established as the "organic material reference spectrum". Each point on the thin section was analyzed using Raman spectroscopy and compared to the reference spectrum. The similarity of the measured spectra to the reference organic matter spectrum was mapped on thin sections with a blue overlay, with blue indicating presence of organic material.*

p.	Thin Section Label	Site	Grain Size (µm)	Ooid Number
1	AI-oc	Antelope Island – S. Arm	355 – 500	1
2	AI-oc	Antelope Island – S. Arm	355 – 500	2
3	AI-oc	Antelope Island – S. Arm	355 – 500	3
4	AI-oc	Antelope Island – S. Arm	355 – 500	4
5	AI-oc	Antelope Island – S. Arm	355 – 500	5
6	AI-om	Antelope Island – S. Arm	250 – 355	1
7	AI-om	Antelope Island – S. Arm	250 – 355	2
8	AI-om	Antelope Island – S. Arm	250 – 355	3
9	AI-om	Antelope Island – S. Arm	250 – 355	4
10	AI-om	Antelope Island – S. Arm	250 – 355	5
11	AI-of	Antelope Island – S. Arm	125 – 250	1
12	AI-of	Antelope Island – S. Arm	125 – 250	2
13	AI-of	Antelope Island – S. Arm	125 – 250	3
14	AI-of	Antelope Island – S. Arm	125 – 250	4
15	AI-of	Antelope Island – S. Arm	125 – 250	5
16	SJ-oc	Spiral Jetty – N. Arm	355 – 500	1
17	SJ-oc	Spiral Jetty – N. Arm	355 – 500	2
18	SJ-oc	Spiral Jetty – N. Arm	355 – 500	3
19	SJ-oc	Spiral Jetty – N. Arm	355 – 500	4
20	SJ-oc	Spiral Jetty – N. Arm	355 – 500	5
21	SJ-om	Spiral Jetty – N. Arm	250 – 355	1
22	SJ-om	Spiral Jetty – N. Arm	250 – 355	2
23	SJ-om	Spiral Jetty – N. Arm	250 – 355	3
24	SJ-om	Spiral Jetty – N. Arm	250 – 355	4
25	SJ-om	Spiral Jetty – N. Arm	250 – 355	5
26	SJ-of	Spiral Jetty – N. Arm	125 – 250	1
27	SJ-of	Spiral Jetty – N. Arm	125 – 250	2
28	SJ-of	Spiral Jetty – N. Arm	125 – 250	3
29	SJ-of	Spiral Jetty – N. Arm	125 – 250	4

Shoreline Superelevation, Clues to Coastal Processes of Great Salt Lake

Genevieve Atwood[1], Tamara J. Wambeam[2], and Charles G. Oviatt[3]
[1]*Earth Science Education, Salt Lake City, Utah, genevieveatwood@comcast.net*
[2]*Salt Lake City, Utah*
[3]*Department of Geology, Kansas State University, Manhattan, Kansas*

10.31711/ugap.v51i.138

ABSTRACT

Coastal processes create the shoreline evidence of Great Salt Lake. Shoreline superelevation is the difference in elevation between still water lake level and the shoreline evidence produced by the lake at that level. Processes of formation include effects of wind strength, fetch, beach attributes, coastline aspect, and coast morphology. A series of field studies from 1986 through 2000 concluded strong storm winds from the northwest contribute to the patterns and magnitude of shoreline superelevation. Weather data for 2020-2023 for Gunnison Island and Hat Island document strong storm winds from the north and northwest for Gunnison Bay and with more complexity for Gilbert Bay. The strongest wind patterns are consistent with the geologic evidence of shoreline superelevation produced by the high lake stands of 1986-1987.

Wind strength, fetch, and storm duration cause Great Salt Lake wave regimes. The wave-regimes of Great Salt Lake are fetch-limited due to the size and morphology of the water body. In contrast, the long fetch of large lakes such as Lake Bonneville (the enlarged manifestation of the Great Salt Lake lacustrine system), determines the magnitude and patterns of their shoreline superelevation. Geologic evidence of shoreline superelevation of modern- and paleo- fetch-limited lakes similar to Great Salt Lake may be durable evidence of storm wind direction.

INTRODUCTION

Great Salt Lake (GSL) is a closed-basin lake located in the lowest region of the GSL drainage basin, and it has no surface outlet (Figure 1). Its shorelines and lake bottom sediments record lake conditions. GSL shoreline elevation fluctuates as the lake's volume fluctuates in response to the balance of water entering the lake by direct precipitation and runoff, and water leaving the lake by evapotranspiration. Therefore, patterns of shoreline elevations are interpreted as patterns of climate. Understanding the chronology of lake fluctuations underpins interpretations of changed climate over time. However, the details of the history of climate changes have not yet been deciphered for post-Lake Bonneville time from the geomorphic and stratigraphic records (Oviatt and others, 2021).

Shoreline materials also contribute to the understanding of lake processes (Gilbert, 1890). Terrigenous materials deposited by waves become the geologic record. If a paleoshoreline defines a horizontal plane, it can be used to distinguish post-depositional change. Examples of the use of this assumption include studies of isostatic rebound, tectonic displacements, and effects of wind and waves (Gilbert, 1890; Tackman, 1993; Adams and Wesnousky, 1998; Tackman and others, 1998; Adams and others, 1999; Adams and Bills, 2016; and Chen and Maloof, 2017). However, should initial shoreline conditions not define a horizontal plane, the original non-horizontality introduces uncertainty to interpretations (Gilbert, 1890, Currey, 1982).

This paper summarizes a series of field studies documenting the shoreline left by Utah's 1980s wet cycle (1982-1987). In 1986 and again in 1987, GSL reached its historic highstand elevation, 4212.15 ft (Arnow and Stephens, 1990). It left pristine, undisturbed, continuous evidence around the perimeter of Antelope Island as lines of organic and inorganic debris. This paper explores the coastal processes that caused the original non-horizontality of the 1986-1987 shoreline. Wind waves that are higher and more energetic in some places than others cause patterns of shoreline superelevation. The following definitions contribute to understanding "superelevation" (Figure 2). Lake setup is "elevated lake surface caused by any process whether or not storm-related." Wind setup is "the component of lake setup caused by wind" and is accompanied by lake setdown, a lowered lake level. Lake seiche is "the oscillation of the lake's surface initiated by lake setup." Wave runup is "the rush of water with entrained sediment landward and upward to

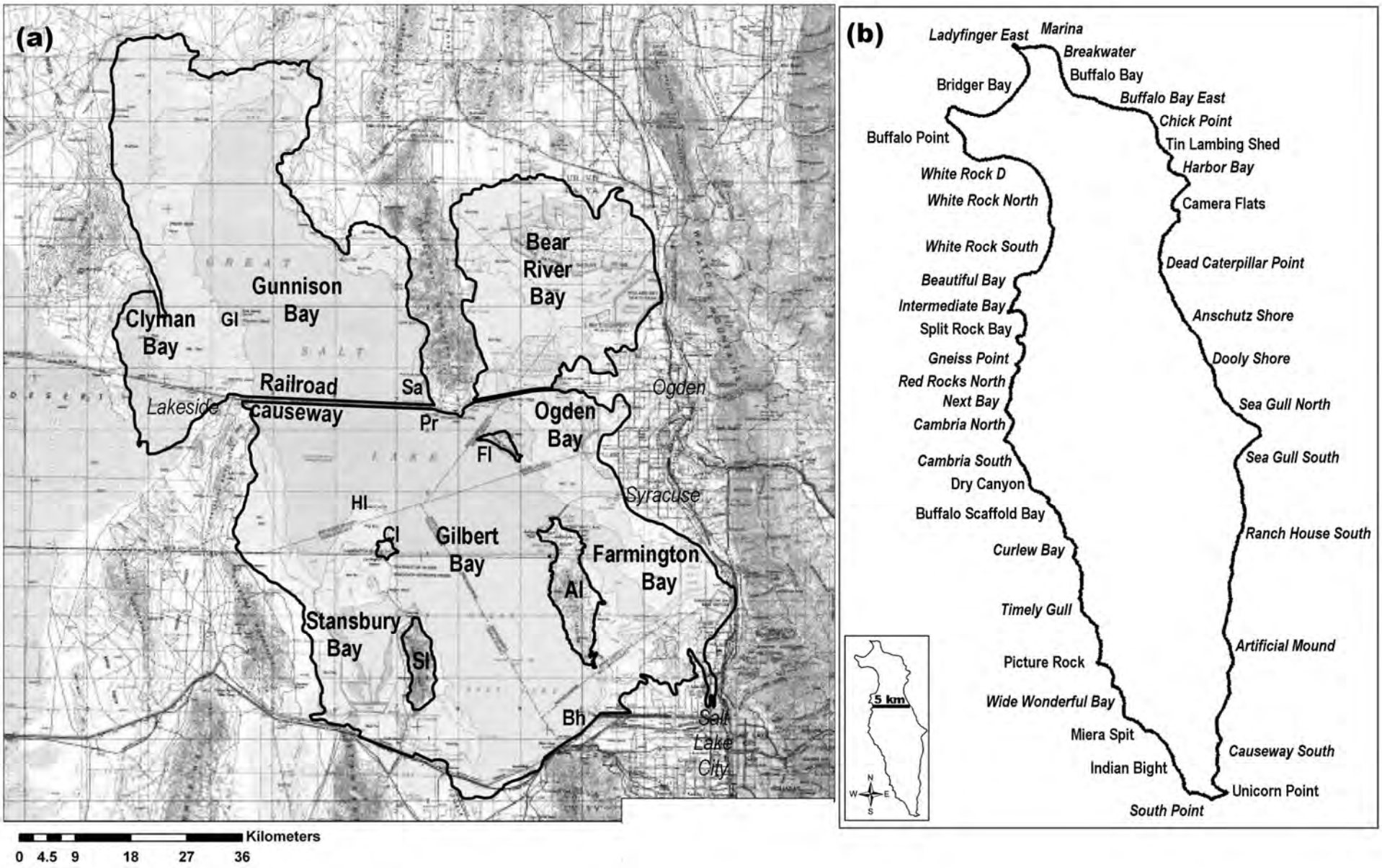

Figure 1. *Location Maps for Great Salt Lake and Antelope Island. Adapted from Atwood (2006) (a). Great Salt Lake: Place names include bays of Great Salt Lake and major islands: Antelope Island (AI), Carrington Island (CI), Fremont Island (FI), Gunnison Island (GI), Hat Island (HI), and Stansbury Island (SI). Lake-level monitoring gages are Saltair Marina Boat Harbor (Bh), Promontory (Pr), and Saline (Sa). Names of communities are shown in italics. The dark line indicates the extent of 1986-1987 highstand flooding. (b). Antelope Island: Formal and informal names (in italics) for locations of shoreline superelevation surveyed during 1997-1998.*

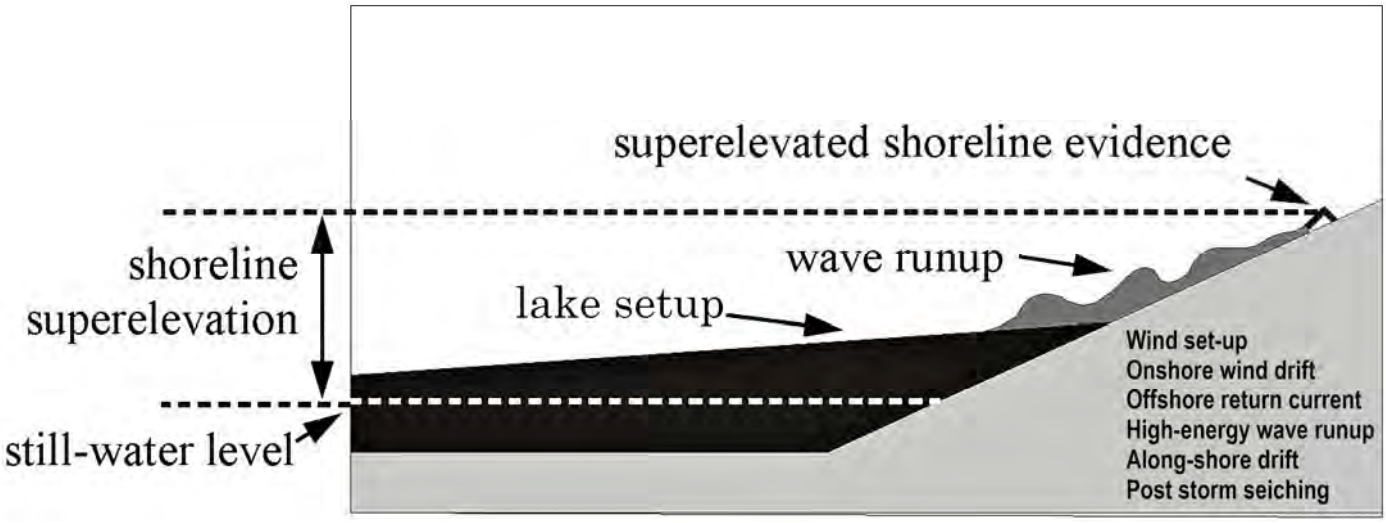

Figure 2. *Shoreline superelevation, evidence of interactions of Earth systems. The schematic simplifies and summarizes diverse conditions and processes that result in shoreline superelevation. Under strong winds or as storms progress, waves develop, and lake water is pushed up against windward shores. Winds blow across the surface causing waves, and the waves deposit the terrigenous debris that becomes the durable geologic evidence of lake elevation. Patterns of shoreline superelevation include interactions among the atmosphere, the hydrosphere, the geosphere, and the biosphere.*

its highest shoreline expression." Wave runup is the highest elevation reached by waves, and the entrained sediment deposited by the waves provides a record of shoreline superelevation. Shoreline superelevation is the difference in elevation between the shoreline evidence and the independently monitored still water elevation. (Atwood 2006).

Earlier field studies documented patterns of shoreline superelevation and suggested that the patterns were the effects of wind strength and direction as well as of fetch (distance across open water). This paper reports how present-day meteorological data supplement the findings of field surveys of 1986-2000 (Atwood, 2006), which did not have the advantage of 2020-2023 records from weather stations on Hat and Gunnison Islands. The strongest winds across GSL blow from the north and west, corroborating the geomorphic evidence. Patterns of shoreline superelevation document the effects of wind strength and direction because GSL is fetch-limited. "Fetch-limited" refers to water bodies where the size of the wave generation area limits wave height and energy.

METHODS AND DATA

Purpose and Methods of the Field Surveys, 1986-2000

Several surveys conducted between 1986 and 2000 by D.R. Currey, D.R. Mabey and G. Atwood provide field-based data for the present paper. A summary of methods, data, and results is given below and is set out fully in Atwood (2006). Shoreline features were observed, described, and their elevations were measured directly in the field during, immediately after, and in the decades following the 1986-1987 GSL highstand. Unmistakable floated debris (e.g., wood, plastic, and windrows of organic matter), as well as fresh gravel ridges, identified 1986-1987 shoreline evidence that persisted for over a decade (Figure 3). Surveyed shoreline debris defined shoreline superelevation patterns. Over the past four decades, some of that evidence has degraded, but gravel ridges remain in many places where they can be spotted by their vegetation (sunflowers).

1986 Survey - Currey and Mabey on the Eastern Shore of Antelope Island

The purpose of the 1986 survey was to repeat G.K. Gilbert's survey in 1877 of the evidence of the 1870s highstand shoreline (Gilbert, 1890). Mabey and Currey (Mabey, 1986), concerned that the rising lake would rework and destroy the 1870s evidence, repeated Gilbert's survey on the east shore of Antelope Island using hand-held equipment similar to Gilbert's era. They identified three places on aerial photographs and surveyed them on the ground using the United States Geological Survey (USGS)-monitored still water level for vertical control. In the century between Gilbert's survey in 1877, and the work of Currey and Mabey in 1986, the shoreline evidence had become difficult to recognize, except as patterns on aerial photographs and patches of gravel.

According to Mabey (1986), "In the spring of 1986 when the lake was at a level of 4211.85 ft, a storm line was formed on the east side of Antelope Is-

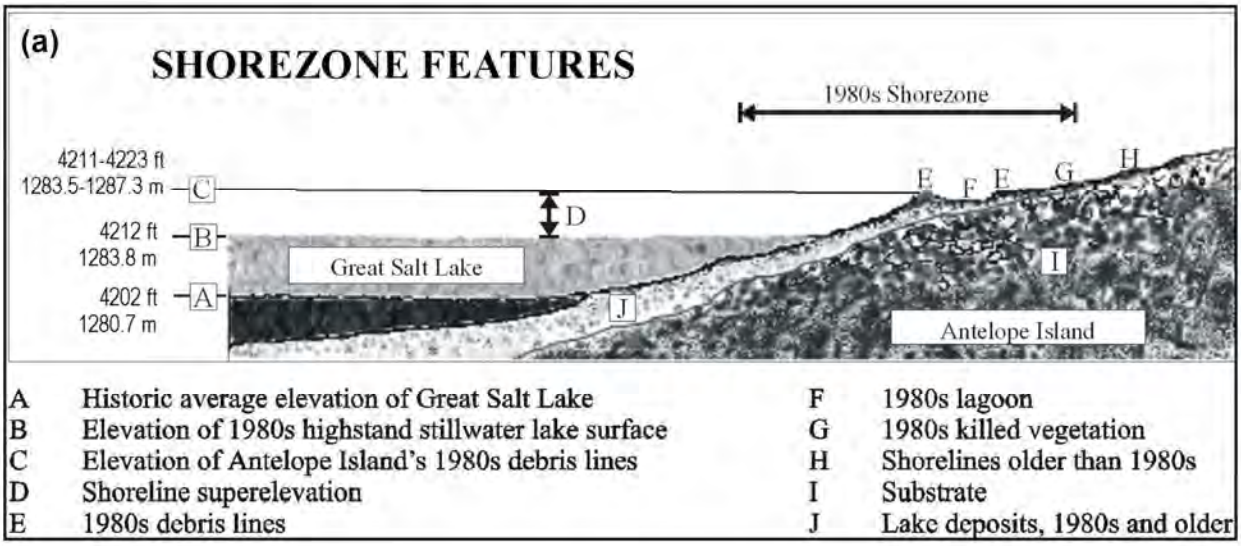

Figure 3. *Evidence of shoreline superelevation. Adapted from Atwood (2006). (a). The sketch illustrates the shorezone features relative to shoreline superelevation. The difference between the 1986 and 1987 USGS-monitored still water elevation (4212 ft) and the 1986-1987 highstand debris lines on Antelope Island is shoreline superelevation. Shore features include lagoons, killed vegetation, and higher and older shorelines. (b). The photograph taken in 1998 looks east along the northern exposure of Ladyfinger East. The 1986-1987 shoreline expression, foreground, includes terrigenous debris of cobbles, gravel, and sand. Contrasts in vegetation patterns, the upper center of the photograph, and lumber and timber in the beach zone are evident a decade after the 1986-1987 flooding. (c). The photograph taken in 1998 looks northeast toward the intersection of the northern and southern expressions of the spit at Unicorn Point. The man with the rod stands on the northern, northeast-facing, lower expression, and the younger man stands on a southeast-facing expression. (d). The photograph taken in 1998 looks north from Timely Gull Bay toward Curlew Bay along the west side of Antelope Island. Note the stacked timber and lumber at the south of the bay indicating transport by wind waves from the northwest. (e). The photograph taken in 1986, during the highstand years, looks north along the eastern exposure of Tin Lambing Shed, south of Harbor Bay. Note the terrigenous wash-over deposits of sand and 20th-century evidence of lumber.*

land at 4213.5 ft, the same elevation measured by Gilbert for the storm line formed in the 1870s." The shoreline evidence of both surveys was superelevated compared to the USGS-monitored still water elevations (Gilbert, 1890; Mabey, 1986). Based on records of the elevation of the highstand taken along the south shore of GSL, Gilbert estimated shoreline superelevation of one foot on the eastern side of Antelope Island.

1986 Survey by Atwood and Mabey

In 1986 G. Atwood and D.R. Mabey conducted a survey to compute the frequency of Holocene flooding of GSL (Atwood and Mabey, 2000). The idea was to survey the 1986 shoreline evidence and to count the shorelines between the historic highstands (1870s and 1980s) and Murchison's (1989) "Holocene high" of approximately 4217 ft. For the 1986 survey, we used an electronic measuring device (EDM) to measure elevations. Initially, we expected that the 1986-1987 highstand evidence would provide the horizontal datum from which to survey the higher, older shoreline elevations. However, the 1986-1987 shoreline evidence did not define a horizontal plane. Therefore, we used only the USGS-monitored still water lake level as vertical control for the survey.

The evidence of the 1986-1987 highstand was unmistakable and included debris lines of floated debris, gravel ridges and beaches, erosional steps, and vegetation lines (salt-kill zones). Floated debris included 20th-century wood and anthropogenic material (such as plastic). Terrigenous evidence included well-sorted cobbles, coarse and fine gravel, and sand. Shoreline evidence of 1986-1987 had no observable surface staining in contrast to older shorelines. In places, erosional steps had been cut into poorly consolidated, sandy sediments.

The evidence of Murchison's (1989) "Holocene high" at an elevation between 4217 and 4222 ft was discontinuous, subtle, and subject to interpretation, consisting of widely scattered gravel and cobble patches and subtle breaks in slope. For detailed discussion of Holocene lake fluctuations, see Oviatt and others (2021).

A summary of the findings of the 1986 survey on Antelope Island is as follows (Atwood and Mabey, 2000):

(a) The plot of shoreline elevations (Figure 4) indicated at least three highstand shorelines between the 1986-1987 highstand and 4226 ft. Counting the two historic excursions to 4212 ft in 1986 and 1987, GSL had risen a minimum of five times to elevations equal to or higher than 4212 ft.

(b) The 1986-1987 shoreline debris did not define a horizontal plane from which to measure relative elevations of Holocene shorelines. Evidence of the 1986-1987 GSL highstand was consistently superelevated, well-above the USGS-monitored still water lake level. The elevations of the higher, older shorelines appeared to have trends of superelevation resembling those of 1986-1987.

1997-1998 Atwood and Mabey Survey of 1986-1987 Highstand Evidence on Antelope Island

The 1997-98 survey aimed to document the character of the 1986-1987 highstand shoreline in detail before ephemeral evidence became unrecognizable (Atwood, 2006). We documented elevations of the 1986-1987 highstand evidence and recorded shorezone characteristics around the island's perimeter using a Sokia total station to survey elevations and Global Positioning System (GPS) data loggers to record horizontal positions of observations of shorezone characteristics. The USGS-monitored still water lake level provided vertical control. Throughout the day, we used a survey staff to measure water-level changes for the purpose of maintaining accurate vertical control. We also corroborated our elevations with Davis County Public Works' road elevations. Elevations were surveyed on the upper surface of the most-inland terrigenous deposits at 1,228 locations along the 64 km shoreline of Antelope Island. The data were downloaded into a geographic information system database, projected to a single route using ESRI Arc/Info linear referencing, and analyzed with simple spatial statistics (Atwood, 2006).

A decade after the 1986-1987 GSL highstand, much of the 1986-1987 flotsam (windrows of brine-fly carapaces, vegetative evidence, and automobile tires) was lost to disintegration, fire, and trash collection. Large debris, which included lumber and timber, became reliable evidence and it persisted long after deposition. Some smaller debris persisted included plastic and other 20th-century debris. Gravel ridges and sand beaches were intact. Erosional steps were evident but no longer had the angular shape of 1986-1987. Vegetation, specifically sunflowers, grew on the 1986-1987 gravels.

Patterns of shoreline superelevation along the 1986-1987 shoreline were consistent with observations of the 1986 survey. Patterns of shoreline superelevation were not random. They did not define a horizontal plane from which post-depositional change could be measured with confidence.

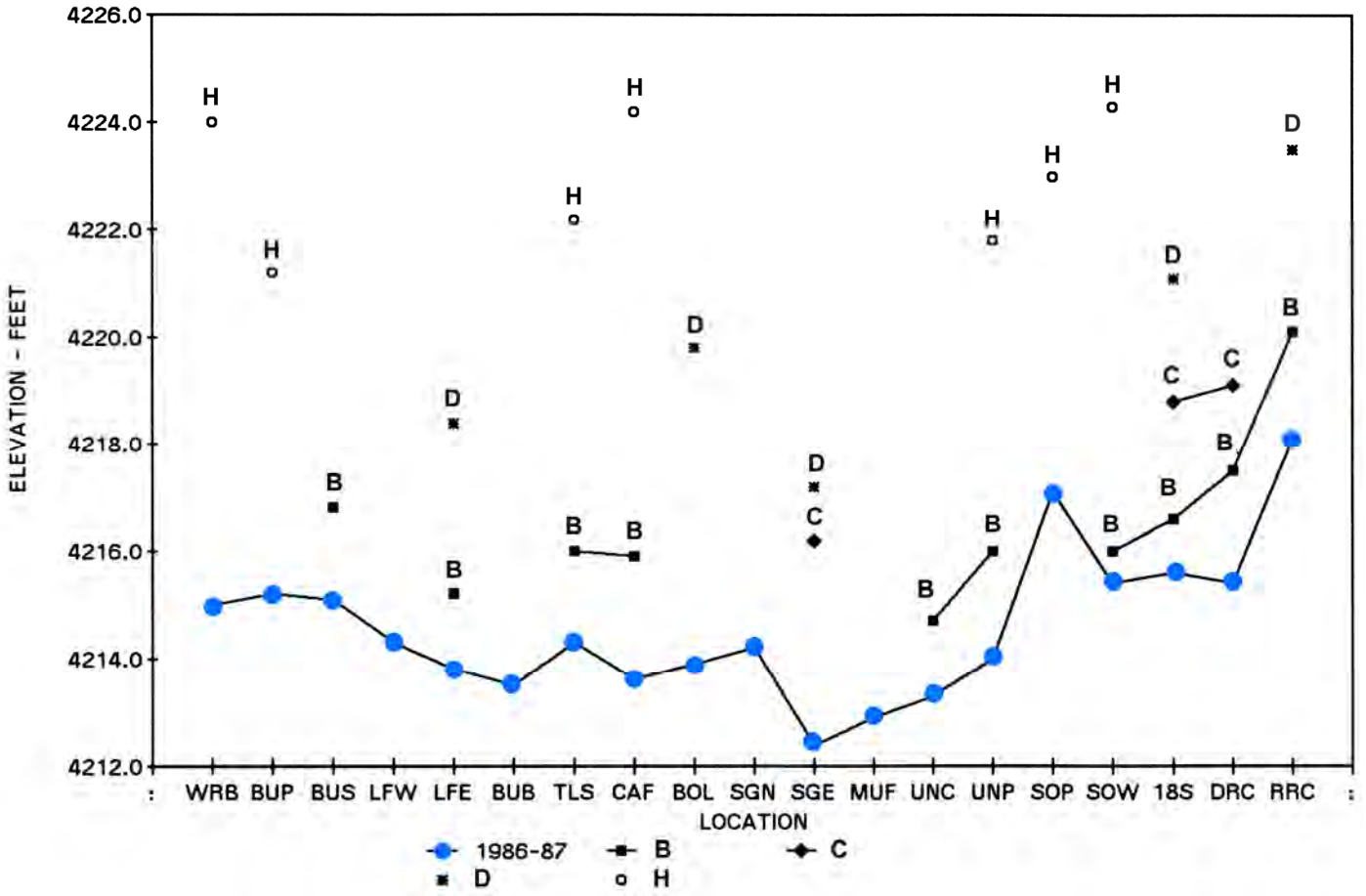

Figure 4. *Great Salt Lake shoreline elevation data of the 1987-1988 survey on Antelope Island. Plot of elevation (ft) at a progression of surveyed locations clockwise around Antelope Island beginning at White Rock Bay (WRB), continuing to Lady Finger Point (LFW, LFE), to Seagull Point (SGN, SGE), to Unicorn Point (UNC, UNP), to Dry Canyon (DRC) (refer to Fig. 1(b) for locations. Blue dots show surveyed elevations of shoreline debris of the 1986-1987 high-stand. Black dots show surveyed elevations of older, higher shoreline evidence around Antelope Island. Lines between locations indicate lateral correlation of shorelines. The blue dots, surveyed locations of 1986-1987 debris, consistently lie above 4212 ft, the elevation of the USGS-monitored still water level and documented flooding hazards above still water lake level. The lettered points (B, C, D, H) were grouped based on trends and position relative to the 1986-1987 shoreline evidence at each location. Adapted from Atwood and Mabey, 2000.*

Patterns of shoreline superelevation were compared with patterns of shorezone characteristics (Figures 5 and 6). Variations of shoreline superelevation from place-to-place record relative wave energy modified by diverse factors. Shoreline evidence was found consistently above still water lake level because, when there is no wind, there are no waves to rework materials and deposit evidence.

Wind waves are the most significant agents of coastal processes that affect lake shorelines (Komar, 1998). Waves erode and deposit the shoreline evidence. Wave height and wave energy largely determine shoreline superelevation.

However, other factors affect coastal dynamics. Wind setup and wind setdown due to atmospheric conditions lead to lake seiche (Wang, 1978). Seiche alone has little effect on shoreline erosion and deposition but may affect the magnitude of shoreline superelevation due to wind setup. Interference and harmonics of normal “gravity waves” create widely spaced infra-gravity waves (Bertin and others, 2020). Offshore and on-shore currents affect wind wave processes and wave heights. These factors make the initial, generally higher lake levels from which waves run up the shore.

Shoreline superelevation records the net effect of wave energy and shorezone conditions, including aspect, fetch, steepness, and materials. Aspect (the direction that the beach faces) was used as a proxy for wind direction. Figures 7, 8, and 9 show contrasts of Antelope Island shores. High shoreline superelevation correlates with long fetch and with north and northwest aspect. Low shoreline superelevation correlates with short fetch and geomorphic shielding. This observation implied that wind might be a recognizable contributing factor to shoreline superelevation of GSL in addition to the effects of fetch (Figure 10).

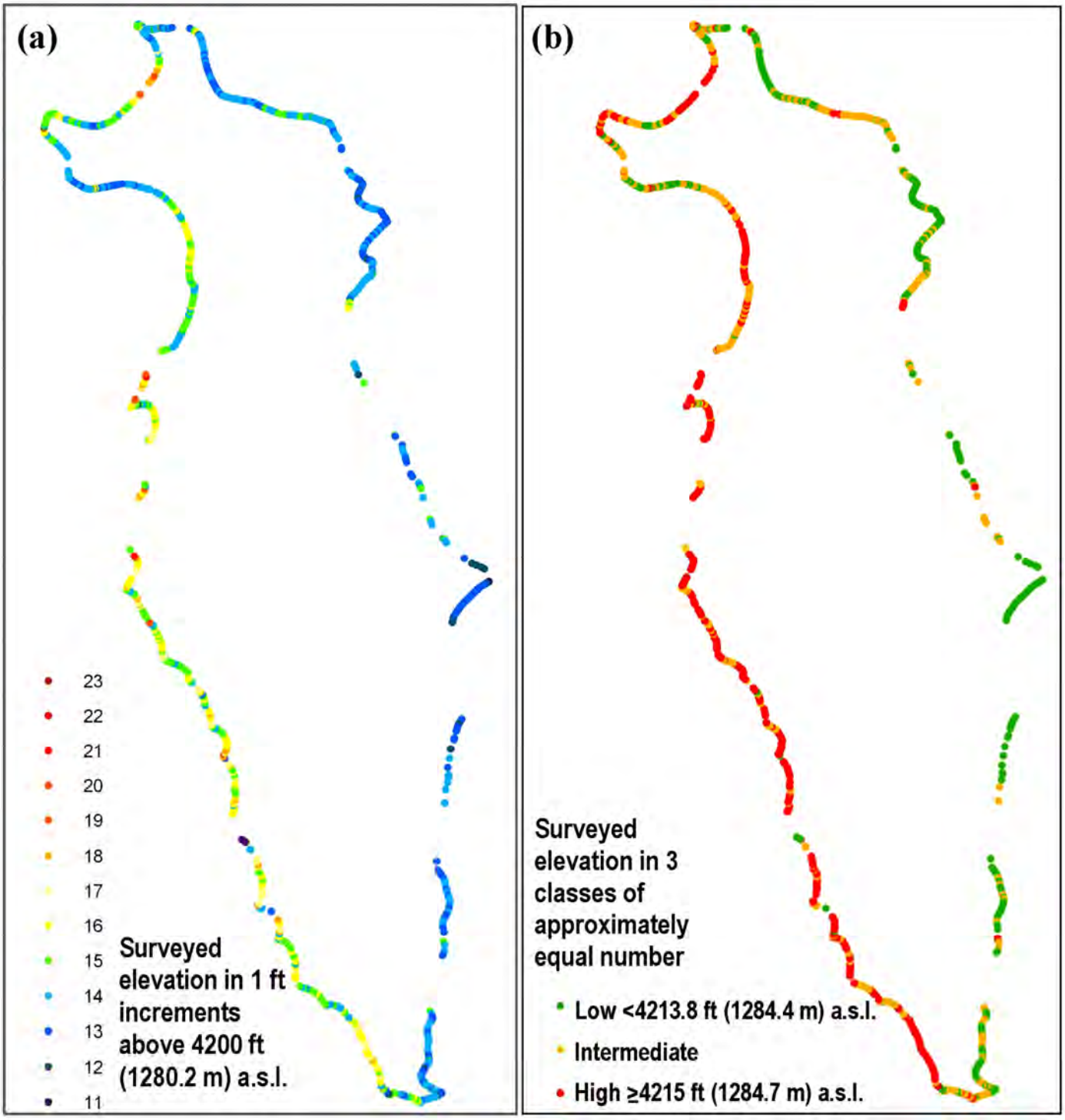

Figure 5. *Superelevation of shoreline evidence of Antelope Island, surveyed in 1998-1999. Adapted from Atwood (2006). Two maps of surveyed locations on Antelope Island showing shoreline superelevation in equal increments versus shoreline superelevation classes. (a). Shoreline superelevation displayed in equal 1-ft increments above the 4200 ft datum of the field study. Shoreline evidence ranged from 4211 ft to 4223 ft (11 to 23 on the key). Shoreline superelevation elevations ranged from at or slightly below USGS-monitored still water level along vegetated shore stretches to the highest levels, 11 ft above still water lake level, on bedrock outcrops bordering pocket beaches. (b). Shoreline superelevation classified in approximately equal populations. High superelevation is superelevation equal to or greater than 3.4 feet. Intermediate superelevation is superelevation between 2.2 and 3.4 feet. Low superelevation is superelevation less than 2.2 feet. Each of the three classes consists of approximately 400 surveyed elevations.*

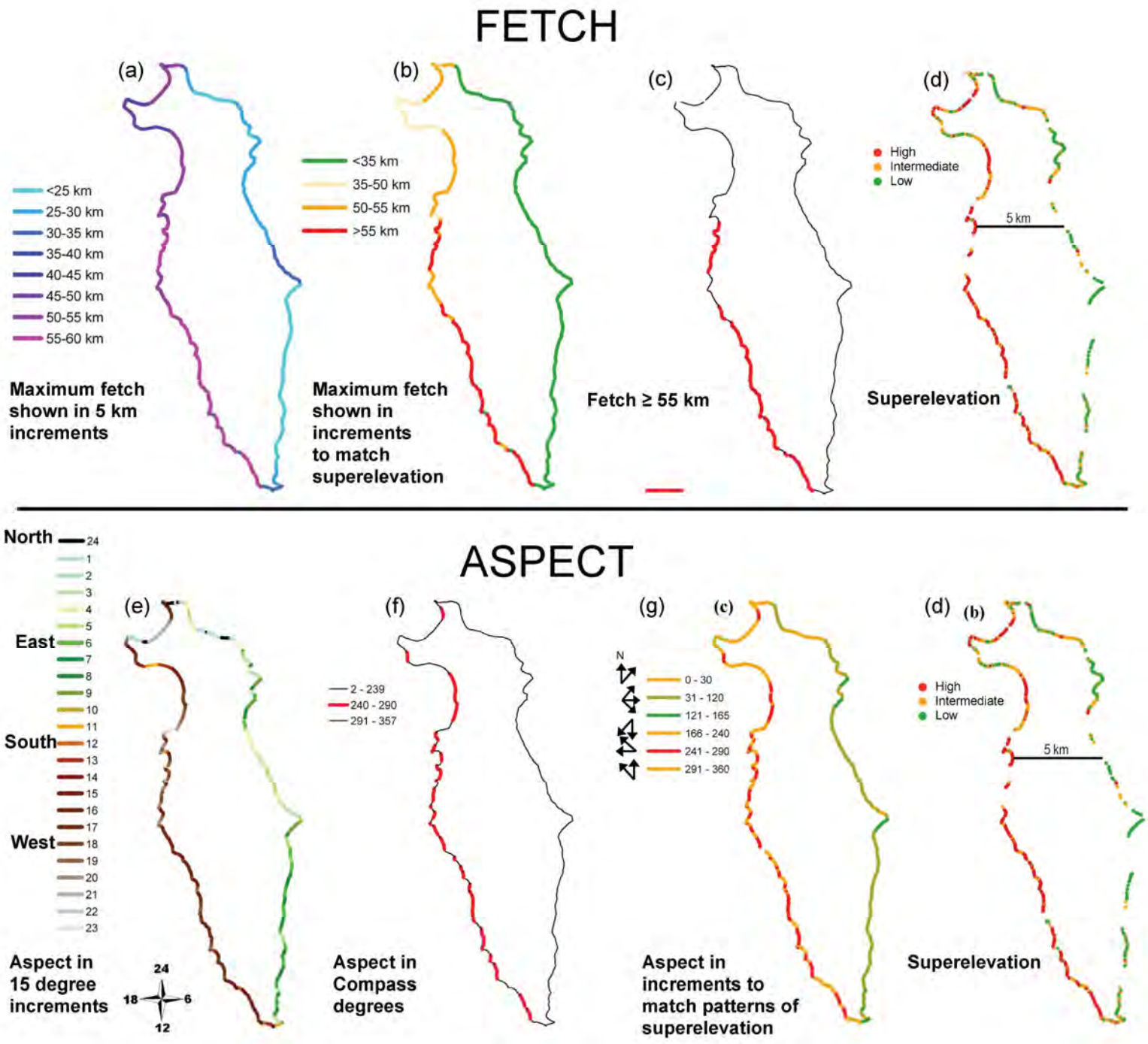

Figure 6. *Associations of shoreline superelevation with fetch and aspect. The two sets of maps show associations of maximum fetch, aspect in 15-degree increments, and shoreline superelevation. Visual inspection indicated correlations among shoreline superelevation, fetch, and aspect. Adapted from Atwood (2006).*

Lady Finger Point, Antelope Island, Utah. Image from 1987 USDA NAPP_354_139.

South Point, Antelope Island, Utah. Image from 1987 USDA NAPP_356_196.

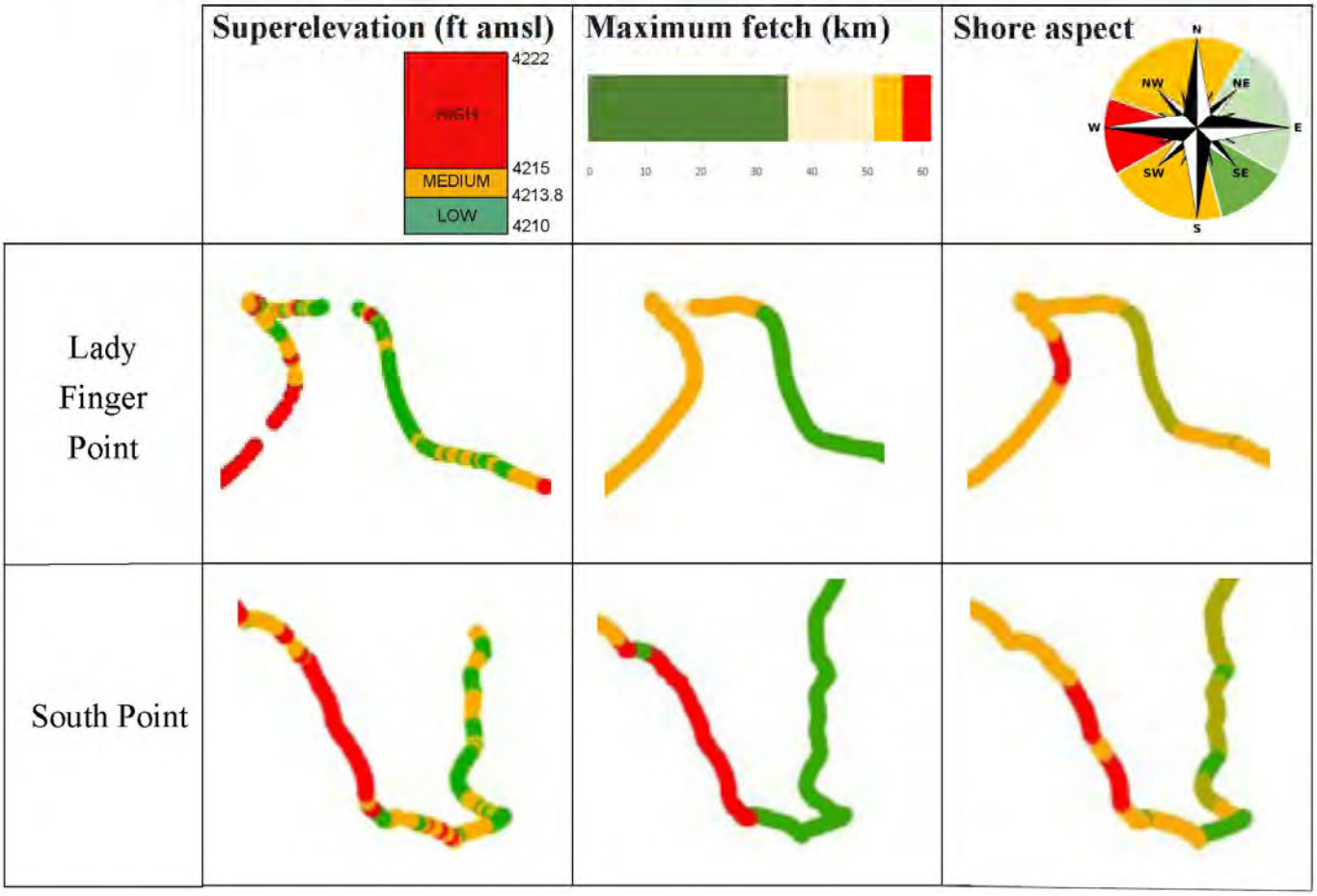

Figure 7. *Lady Finger Point and South Point patterns: superelevation, maximum fetch, and shore aspect. The orthophotos show Great Salt Lake near its highstand at the two red-circled locations on the map. Lady Finger Point juts into Gilbert Bay as a bedrock headland. Unicorn Point immediately to the east of South Point is named for the "unicorn" described by its 1986-1987 lagoons and spits. The table relates high shoreline superelevation, at a detailed scale with maximum fetch and shore aspect. The dots of the table entries indicate locations surveyed in the 1997-1998 Antelope Island survey. Shoreline superelevation was surveyed, whereas maximum fetch and aspect were interpreted from maps. The patterns show west-east contrasts. At Lady Finger Point, high shoreline superelevation correlates visually with medium fetch and western aspect. At South Point, high shoreline superelevation correlates visually with maximum fetch and shore aspects facing west and southwest.*

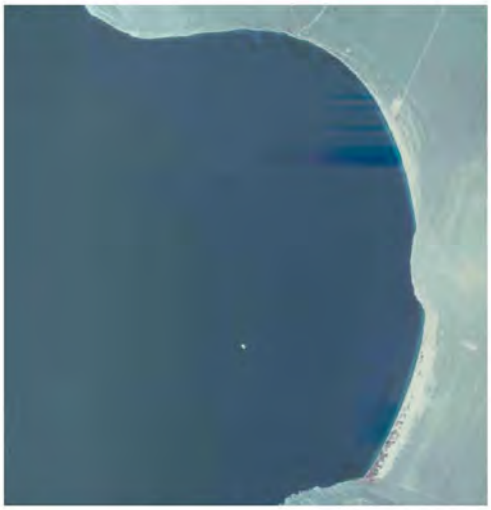

White Rock Bay, Antelope Island, Utah. Image from 1987 USDA NAPP_354_141.

Harbor Bay area, Antelope Island, Utah. Image from 1987 USDA NAPP_354_163.

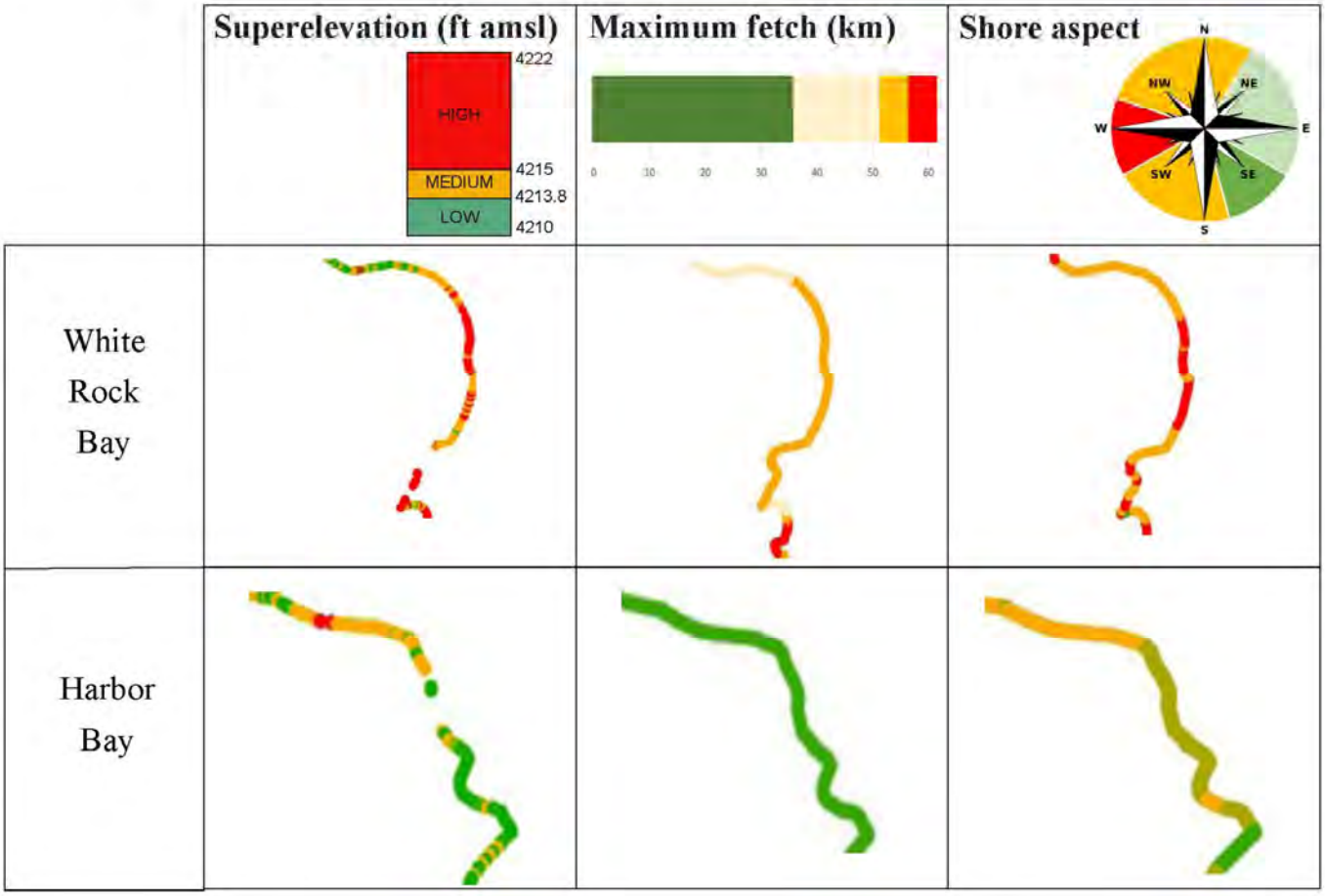

Figure 8. *White Rock Bay and Harbor Bay patterns: superelevation, maximum fetch, and shore aspect. The orthophotos show Great Salt Lake near its highstand at the two red-circled locations on the map. White Rock Bay, a broad, shallow bay opens to the west. Harbor Bay, a complex bay opens to the north and east. The dots of the table entries indicate locations surveyed in the 1997-1998 Antelope Island survey. Shoreline superelevation was surveyed, whereas maximum fetch and aspect were interpreted from maps. The patterns show west-east contrasts. At White Rock Bay, high shoreline superelevation correlates visually with medium fetch and western aspect, while low shoreline superelevation does not appear to correlate with fetch or aspect and may result from sheltering by geomorphic features. Harbor Bay has limited high shoreline superelevation with low shoreline superelevation correlating visually with low fetch and aspects facing southeast.*

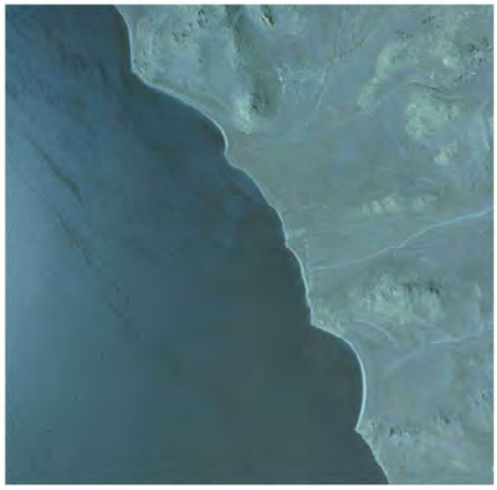

Buffalo Scaffold and Curlew Bays, Antelope Island, Utah. Image from 1987 USDA NAPP_354_161.

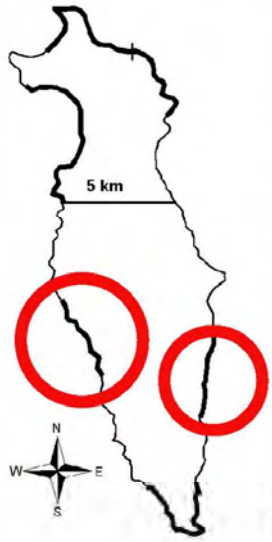

Ranch House South, Antelope Island, Utah. Image from 1987 USDA NAPP_356_196.

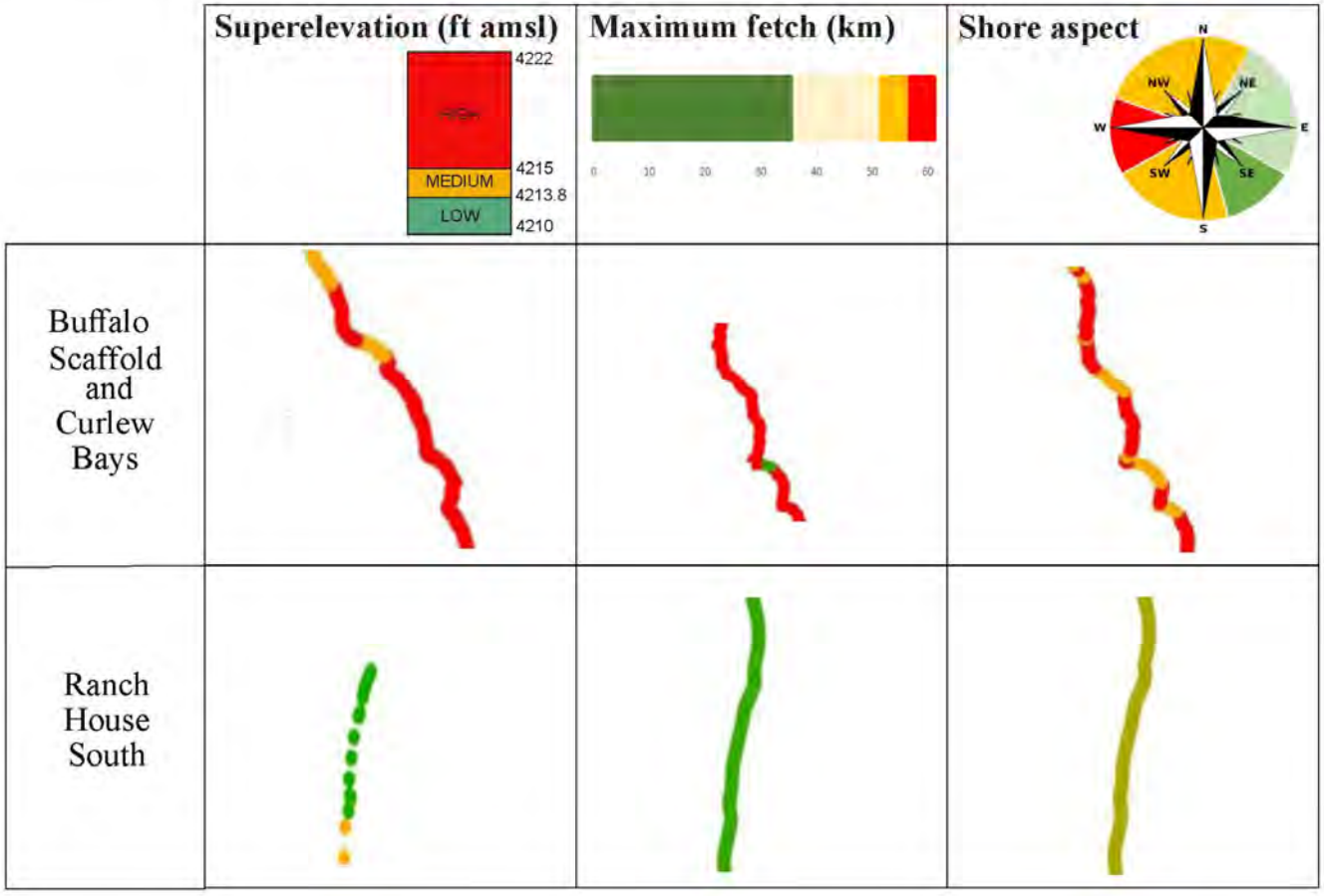

Figure 9. *Buffalo Scaffold - Curlew Bays and Ranch House South patterns: superelevation, maximum fetch, and shore aspect. The orthophotos show Great Salt Lake near its highstand at the two red-circled locations on the map. The bays and headlands of Buffalo Scaffold - Curlew Bay on the southwestern shore of the island contrast with the straight shore of Ranch House South. The dots of the table entries indicate locations surveyed in the 1997-1998 Antelope Island survey. Shoreline superelevation was surveyed, whereas maximum fetch and aspect were interpreted from maps. The patterns show west-east contrasts. At Buffalo Scaffold and Curlew Bays, high shoreline superelevation correlates visually with maximum fetch and with western aspects. At Ranch House South, low shoreline superelevation correlates visually with low fetch and eastern aspect.*

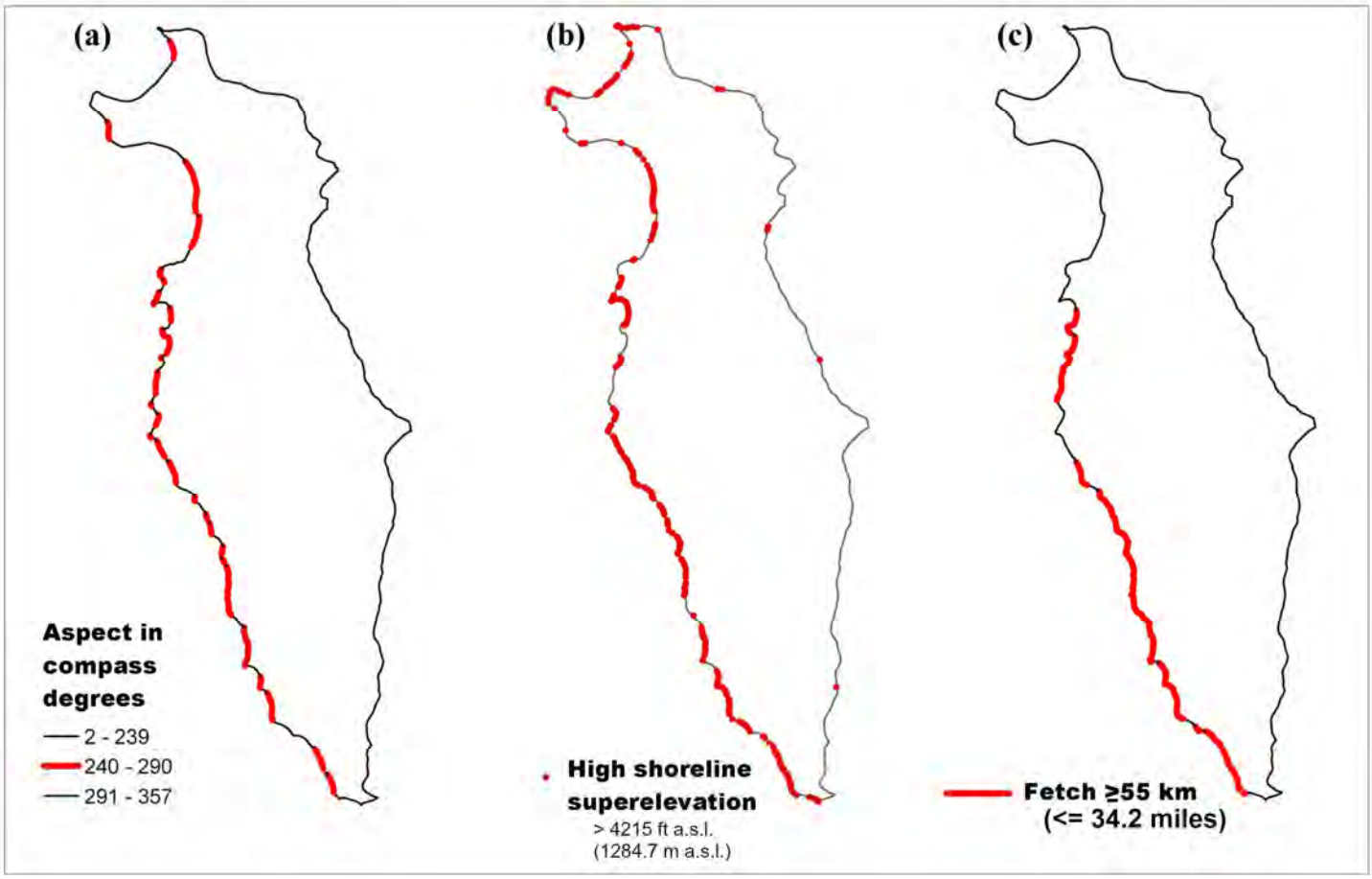

Figure 10. *Associations of high superelevation, long fetch, and aspects facing north and west. Series of three maps showing aspect, superelevation, and fetch. Patterns of (a) west-facing shores; (b) high shoreline superelevation; and (c) longest fetch are similar. Of the 400 surveyed locations with high superelevation, 86 percent have fetch ≥ 50 km; 55 percent have fetch ≥ 55 km; and 50 percent have aspect 240-290°. Of the 200 surveyed locations with both high superelevation and aspect 240-290°, 199 have fetch ≥ 50 km and 140 have fetch ≥ 55 km. On Antelope Island, because the patterns of fetch and aspect so closely resemble each other, it is difficult, if not impossible, to distinguish the relative importance of wind from fetch on shoreline superelevation. Adapted from Atwood (2006).*

As with previous surveys, elevations of shoreline evidence were not at the USGS 1986-1987 monitored still water lake level. Patterns of shoreline superelevation were not random and could be quantified. For example, highest shoreline superelevation was associated with fetch greater than 55 km and on shores facing north, northwest, and west. Shoreline superelevation ranged from as low as 4211.1 ft to 4223.4 ft. with a mean of 4214.5 ft. The shoreline superelevation of the west side of the island was generally higher and more variable than of the east side of the island.

The patterns of shoreline superelevation of the 1986-1987 shorelines on Antelope Island provide evidence of the geomorphic effects of wind waves. But because both the longest fetch and the strongest winds were from the northwest, patterns of shoreline superelevation on Antelope Island could not clarify the relative contributions of fetch and aspect to wave energy.

G.K. Gilbert observed shoreline superelevation on the southern shores of Lake Bonneville and cautioned that fetch, not wind strength or wind direction, caused the superelevation of Lake Bonneville shores. Gilbert (1890, p.107) expressed his recognition of the effects of long fetch in the following quote, which conveys his surprise, humility, and acceptance that long fetch, regardless of wind strength and direction, accounted for the high shoreline superelevation of Lake Bonneville's shores.

> At an early stage of the investigation, the writer thought that the coasts facing in certain directions gave evidence of exceptional amounts of wave work, and imagined that he had discovered therein the record of prevalent westerly winds or westerly storms in ancient times. This belief was dissipated by further study; and he discovered, as students of modern shores long ago discovered, that there is a close sympathy between the magnitude of the shore features and the "fetch" of the efficient waves. The greater the distance through which waves travel to reach a given coast, the greater

the work accomplished by them. The highest cliffs, the broadest terraces, and the largest embankments are those wrought by the unobstructed waves of the main body; and opposite coasts appear to have been equally affected.

Might processes of a fetch-limited lake such as GSL at its highstand level leave long-lasting evidence of wind strength and direction and therefore lasting geomorphic clues to storm conditions and weather patterns?

Atwood and Mabey 1999-2000 Survey at Places Around Gilbert and Gunnison Bays

The 1999-2000 survey (Atwood 2006) aimed to confirm whether patterns of shoreline evidence along the shores of Gilbert and Gunnison Bays resembled those along the shores of Antelope Island. We explored relationships among fetch, aspect, and shoreline superelevation. Disturbance of 1986-1987 shoreline evidence, accessibility, and inadequate vertical survey control limited the choice of locations with which to compare diverse conditions of fetch and aspect (Figure 11).

For the 1999-2000 survey, we followed the same procedures as for Antelope Island in 1997-1998. We used the same equipment, including the Sokia total station and the GPS data loggers. Vertical control was carried from first-order survey markers and/or from USGS-monitored still water lake level. We interpreted factors of fetch such as length and direction of the longest fetch, length of fetch north and northwest, the distance from the bay axis, shorezone aspect, shorezone slope, elevation of the lake shore bed, and bedrock outcrops between 4200 and 4220 ft a.s.l. from maps.

Much of the non-terrigenous evidence of the 1986 -1987 shoreline had been lost to natural disintegration, land cultivation, and development onto the lakebed as GSL retreated. Orthophotos documented shore features of 1986-1987. That evidence and 20th-century debris, such as large logs and railroad ties, confirmed field identification of the 1986-1987 highstand in contrast to higher, older shorelines.

The survey data were plotted on orthophotos and checked against geomorphic features. Figure 12 shows contrasts of patterns of shoreline superelevation at Strongs Knob near the southwestern shore of Gunnison Bay with those of Rozel Point along Gunnison Bay's eastern shore. The classifications of high, medium and low superelevation are those of the Antelope Island survey.

Patterns of shoreline superelevation of Gilbert and Gunnison Bays shores resembled those of Antelope Island. They confirmed that shoreline superelevation was a lake-wide phenomenon. As with the findings on Antelope Island, patterns of shoreline superelevation were not random and were quantifiable. Differences in elevation from place to place were easily detected. The 1986-1987 shoreline around Gilbert and Gunnison Bays, just as around Antelope Island, did not define a horizontal plane.

Coastal processes of GSL cause shoreline superelevation. We used a series of steps to explore whether fetch alone caused spatial variations in shoreline superelevation of Gunnison and Gilbert Bays (Figures 13 and 14). We assumed that equal fetch causes patterns of equal shoreline superelevation. Fetch lengths between surveyed locations on opposite sides of the lake were plotted on a diagram with midpoints placed on a center point.

If fetch alone, as Gilbert noted for Lake Bonneville (a fetch-dominated, much-larger version of the lake system), controlled the magnitude of shoreline superelevation for GSL, then the magnitude of shoreline superelevation would be similarly high at both ends of GSL in the direction of the longest fetch. In the direction of the shortest fetch, superelevation would be low at both ends of GSL. In addition, if fetch were the dominant control on superelevation, the midpoint patterns would resemble a bullseye. However, a pattern of the midpoint diagrams that showed trends of low to high superelevation could indicate that wind strength, in addition to fetch, caused the differences in shoreline superelevation. The patterns shown in Figure 14 indicate strong storm winds from the northwest (Atwood, 2006). Wind data for Gunnison and Gilbert Bays were not available in 2006 to corroborate or refute these conclusions.

2023 – Analysis of Patterns of Shoreline Superelevation and 2020-2023 Wind Data

In 2023, wind data from weather stations on Hat Island in Gilbert Bay and Gunnison Island in Gunnison Bay was analyzed to corroborate or refute interpretations of the earlier studies. Atwood (2006) suggested that patterns of shoreline superelevation were influenced by wind direction and strength, not simply by fetch. In 1990-2000, regional meteorological data, other than for Salt Lake International Airport, were unavailable, and the Salt Lake International Airport records were considered possibly non-representative of the open-lake conditions of Gilbert and Gunnison Bays. Instead, Atwood (2006) used estimates of wind parameters by W. Alder, Utah State Meteorologist, as

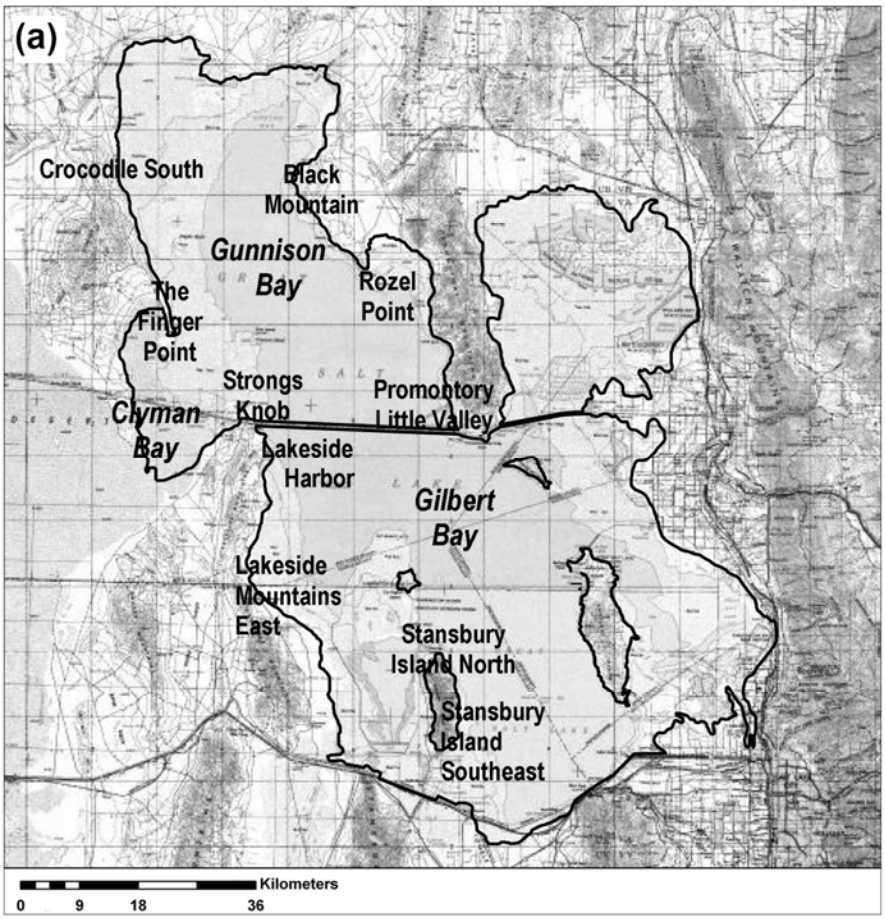

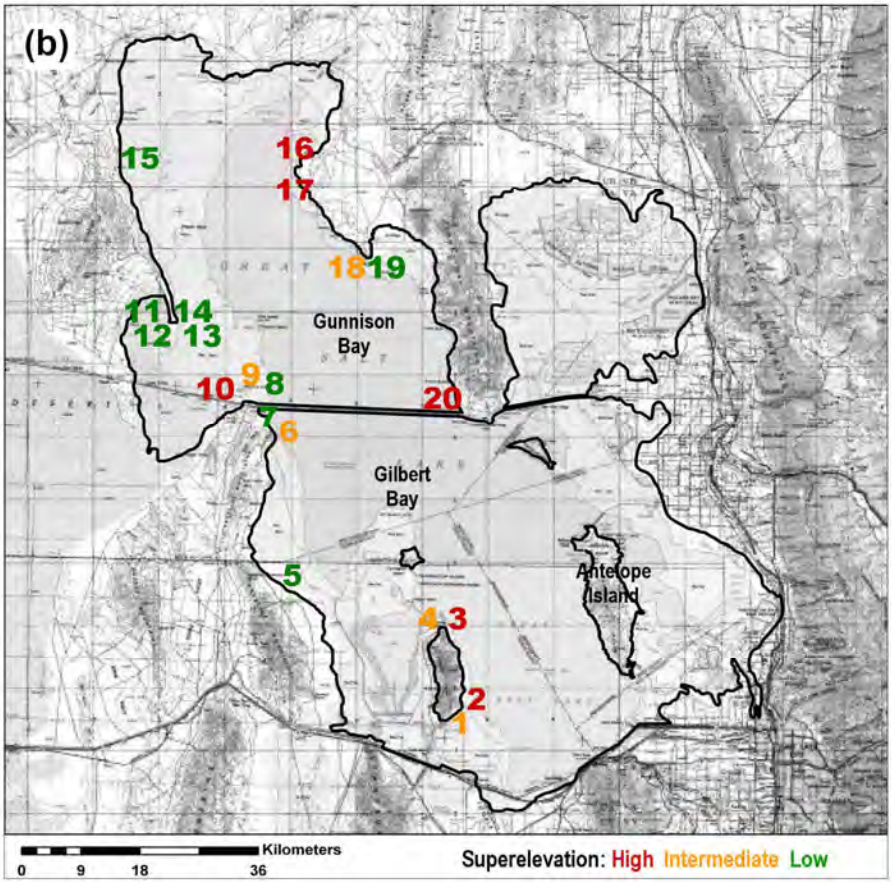

Figure 11. *Maps of the Great Salt Lake perimeter surveys 1999-2000. Adapted from Atwood (2006). (a). The map shows the names of the ten places along the perimeter of Great Salt Lake selected to test the findings of the 1997-1998 Antelope Island field surveys and explore relationships among aspect, fetch, and shoreline superelevation. (b). The numbers identify surveyed stretches at places along the perimeter of Gilbert and Gunnison Bays. They indicate the 20 contrasting shores of the field survey, classified as generally high (red), intermediate (orange), or low (green) shoreline superelevation using the criteria of the 1997-1998 Antelope Island survey.*

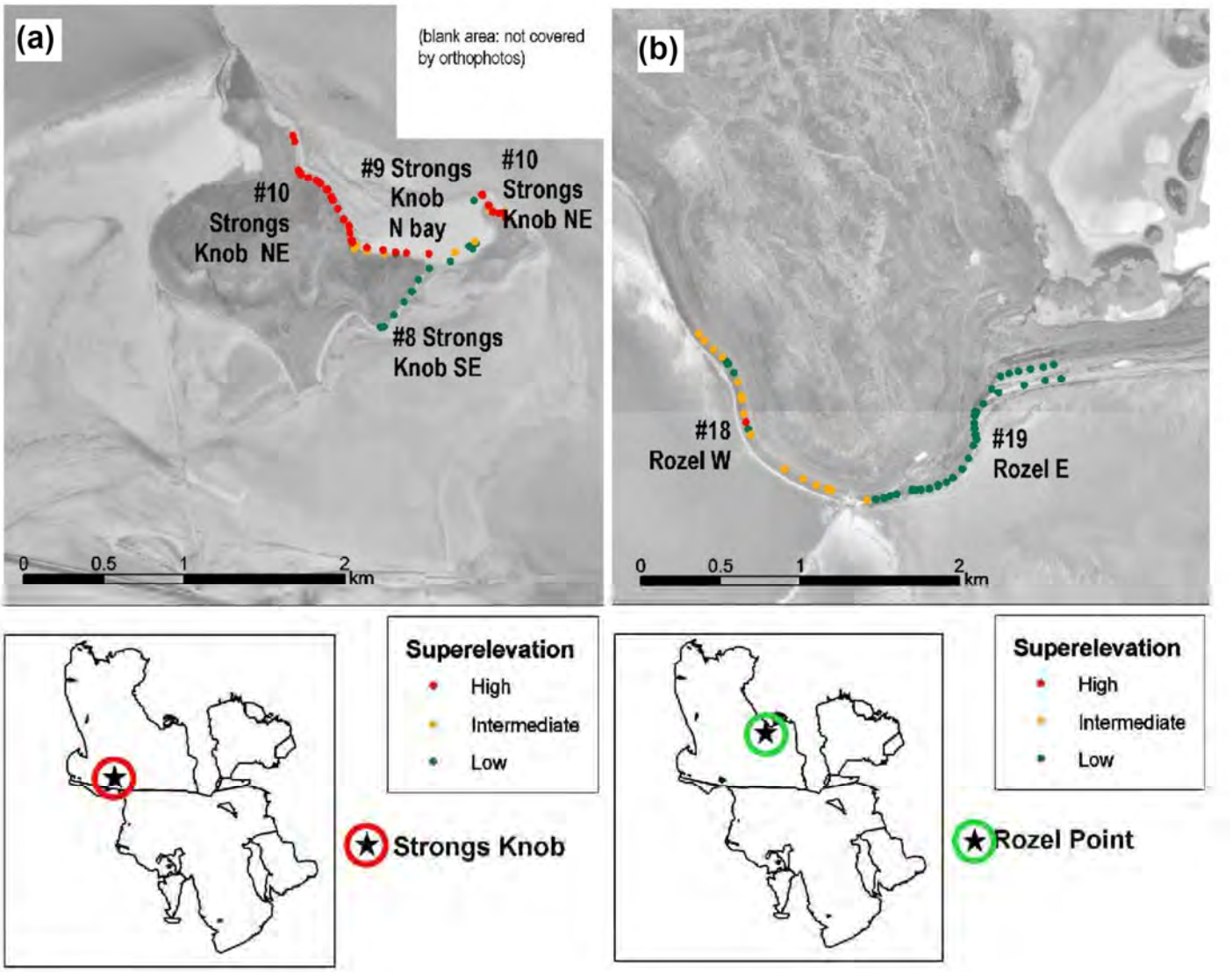

Figure 12. *Patterns of shoreline superelevation at Strongs Knob and at Rozel Point. Two location maps with two orthophotos showing survey locations in contrasting areas of Gunnison Bay. (a). Plot of surveyed places on the three shorezone stretches (8, 9, 10) of Strongs Knob. Strongs Knob, an island during 1986-1987, is located in southwestern Gunnison Bay immediately north of the railroad causeway. During the 1986-1987 highstand, Location #8 with southeast aspect and long fetch, had low shoreline superelevation. Location #9, a bay, had two northerly aspects. The northeast aspect had long fetch and high shoreline superelevation. The north-facing shore had long fetch and low shoreline superelevation. Location #10, two separate shores with east-facing aspect had long fetch and high shoreline superelevation. (b). Plot of surveyed places on the two shorezone stretches (18, 19) of Rozel Point. Rozel Point is located mid-bay on the east shore of Gunnison Bay. The rise of Great Salt Lake flooded the Spiral Jetty immediately offshore. Location 18 had a southwest aspect, intermediate fetch, and intermediate shoreline superelevation. Location 19 had south and southeast aspects, short fetch, and low shoreline superelevation.*

the empirical basis for definitions of wave environments for 1986-1987 (personal communication, reported in Atwood, 2006; Alder, 1986, 1987). University of Utah MesoWest weather stations on Gunnison and Gilbert Bays (www.mesowest.utah.edu) now provide real-time wind data for GSL. J.D. Horel (Atmospheric Sciences, University of Utah, personal communication, 2023) provided the wind roses shown in Figure 15. Figure 16 displays the wind rose patterns combined with patterns of shoreline superelevation. Downwind patterns explain patterns of GSL's physical evidence of shoreline superelevation. They corroborate interpretations that the strongest winds that form the waves that cause shoreline superelevation come from the north, northeast and northwest.

The cartoon sketches of Figure 17 show the progression of a low-pressure system from offshore the Pacific Northwest, across California and Nevada to Utah and GSL (Shafer and Steenburgh, 2008). South winds precede the front's arrival, followed by strong northerly winds during and after the front's passage. This substantiates the field surveys' findings that the durable geologic evidence of shoreline superelevation in GSL documents strong storm winds from the northwest.

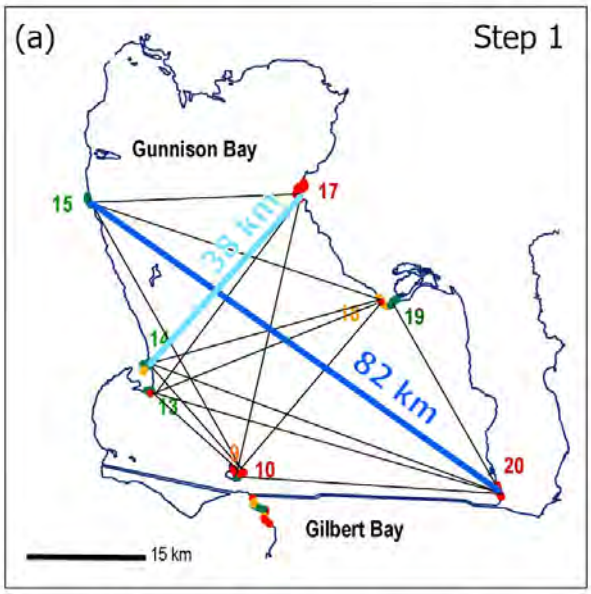

Map of Gunnison Bay displaying pairs of equal fetch with 2 digitized lines highlighted with total length between locations.

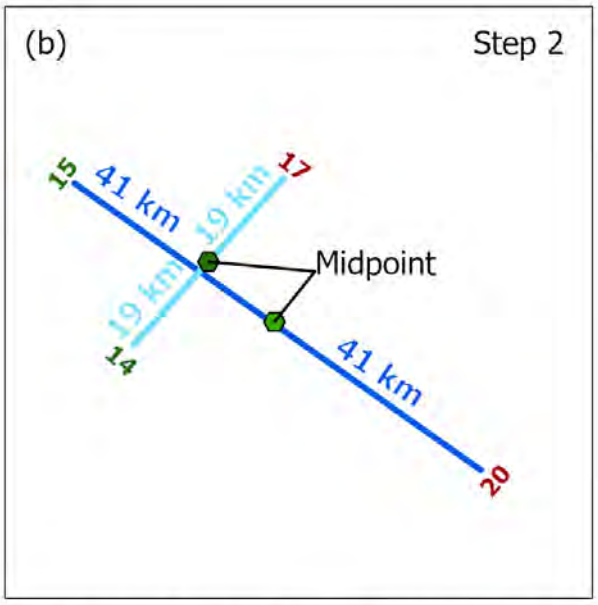

Highlighted pairs showing midpoint of the digitized line.

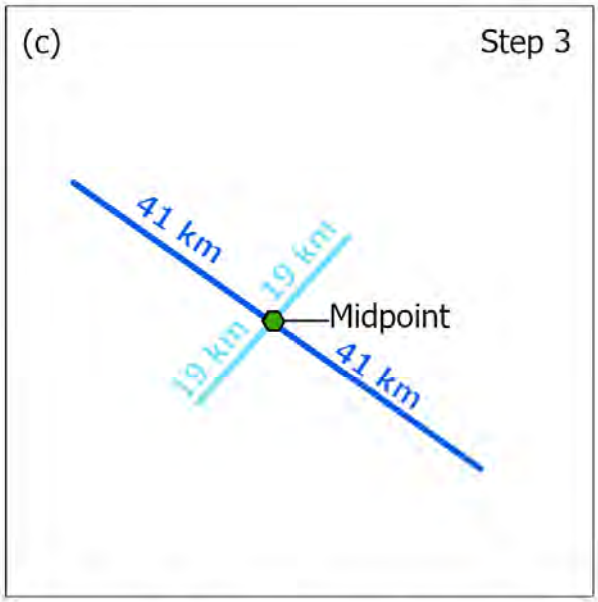

Directional orientation of highlighted lines with midpoints snapped to the same location

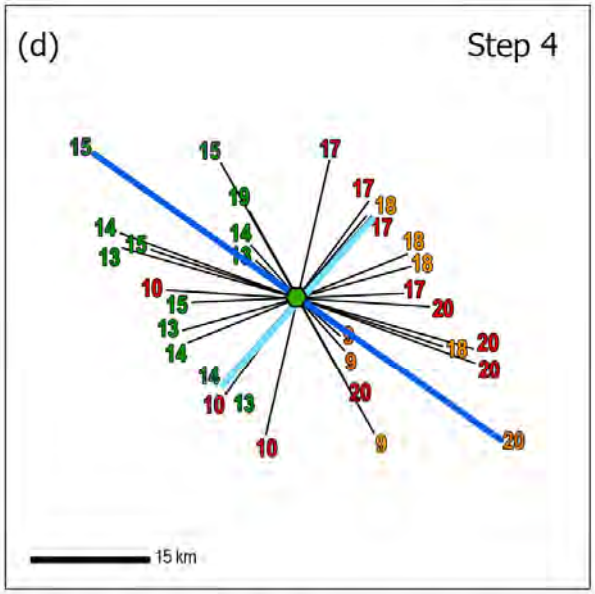

Final diagram displaying all pairs of equal fetch with midpoints snapped but directional orientation maintained.

Figure 13. *Pairings of surveyed locations. Adapted from Atwood (2006). The four figures represent four steps to display fetch vectors at a center point. (a). Step 1. Locate places of surveyed shoreline superelevation. The numbers represent the surveyed places in Gunnison Bay on Figure 12 with the number's color indicating the generalized superelevation. Draw lines representing fetch digitally between all pairs of places. Obviously, the distance, for example, from place 15 to place 20 (82 km) is the same as from place 20 to place 15. The lines represent distance and direction both ways. (b). Step 2. Locate the midpoint of each line. (c). Step 3. Copy each line digitally. Snap the lines across each other at their midpoints. (d). Step 4. Create the diagram that compares the effects of wind direction for places of fetch of equal length. The snapped diagram shows equal fetch to both ends. The color dot of the endpoints indicates relative shoreline superelevation, high (red), intermediate (yellow), and low (green).*

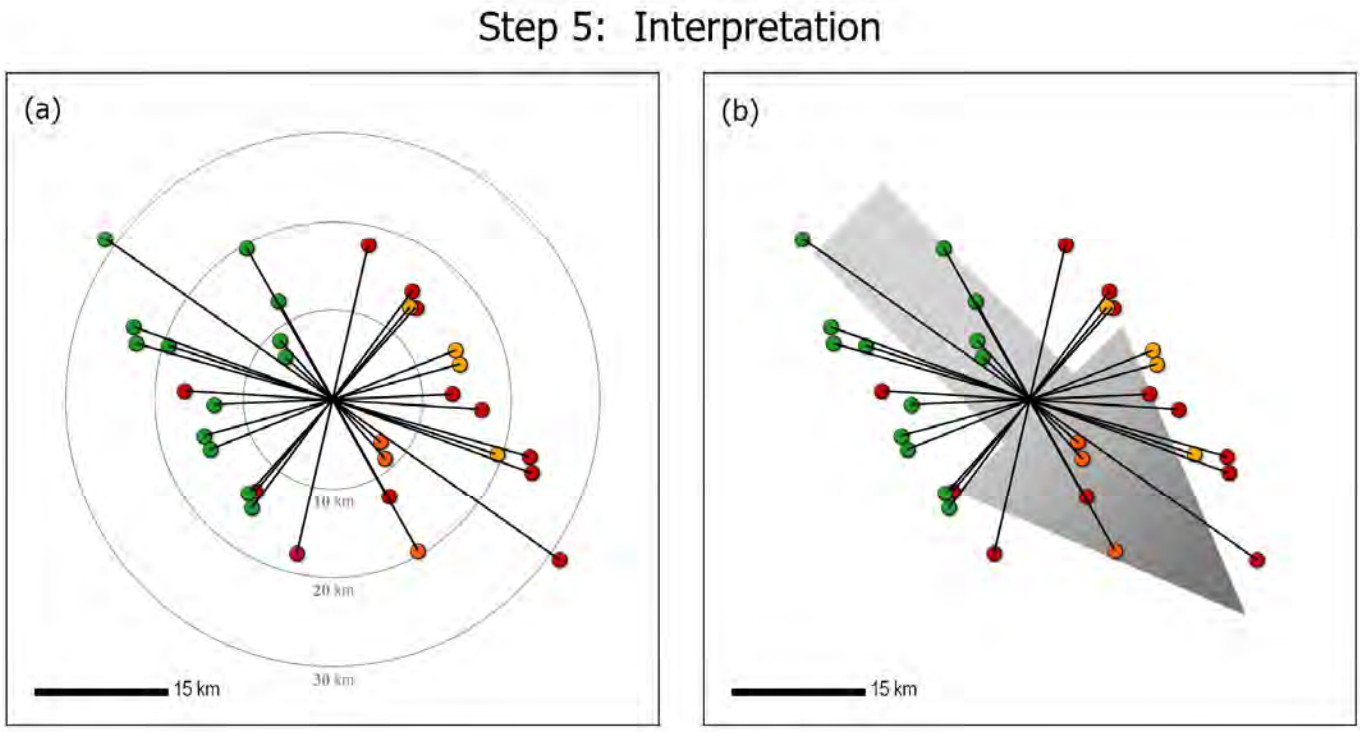

Figure 14. *Visual analysis of the fetch vector diagram. Adapted from Atwood (2006). (a). If fetch alone accounted for shoreline superelevation, the pattern of the colored endpoints would resemble a bull's eye. The green dots representing low superelevation would cluster closer to the center and red dots representing high superelevation away from the center. The color dots on the bullseye diagram do not have a bullseye pattern. (b). The pattern of the dots indicates generally lower shoreline superelevation for northwestern, upwind locations and higher shoreline superelevation for southeastern, downwind locations. This trend implies that strong storm winds from the northwest contribute to patterns of shoreline superelevation of Great Salt Lake, and both wind strength and fetch contribute to shoreline superelevation.*

DISCUSSION

Wave theory and wave dynamics, including the interaction of waves with coastlines and beaches, have generated extensive literature. Scientific aspects have been discussed, for instance, by Munk (1951), Wright and Short (1984), Komar (1998), and WMO (2018). Bertin and others (2020) recently reviewed infra-gravity waves. Coastal landforms, morphodynamics, and processes of fetch-limited shorelines have been documented and discussed by Cooper and others (2007) and Freire and others (2009). Fiedler and others (2020) provide a numerical modeling approach to beach erosion, wave overtopping, and street flooding from storm wave runup and superelevation where historical data are scarce or lacking. In contrast to the shoreline features of GSL, Theuerkauf and others (2021) present the patterns and processes of geomorphic change caused by coastal storms on the shorelines of longer-fetch Lake Michigan. Applequist (2013) presents a framework for assessing hazards in coastal environments linked to climate change, increasingly recognized as a factor in the evolution of weather patterns and storm intensity. From Gilbert (1890) to Schofield and others (2004) and Jewell (2007) fetch has been a subject of shore processes of Lake Bonneville, a lake with wave environments not limited by fetch.

Wind transfers energy from the atmosphere into the water, creating wind waves (Fontaine, 2013). The stronger and longer the wind blows, the higher and more energetic the wind waves. The transfer generates a chaos of wave heights and wave trajectories in a storm zone. The waves interact. As waves travel from a storm zone across a large open lake, the lake surface becomes progressively organized into a "fully arisen sea" of swell. Swell transfers energy with negligible energy loss toward shore. The "sea" becomes more organized with longer fetch. Wave energies and wind waves do not become fully organized if a lake is not big enough. Wave development may be cut off during regime growth by lack of fetch, and this defines fetch-limited conditions (Komar, 1998).

Under strong winds and as storms progress, waves develop, and lake water is pushed up against windward shores (wind setup). Waves lose energy as they encounter the shoreface and then break. More energetic waves run farther up the shore, depositing their entrained and floated debris above the still water level. The entrained and floated debris becomes the su-

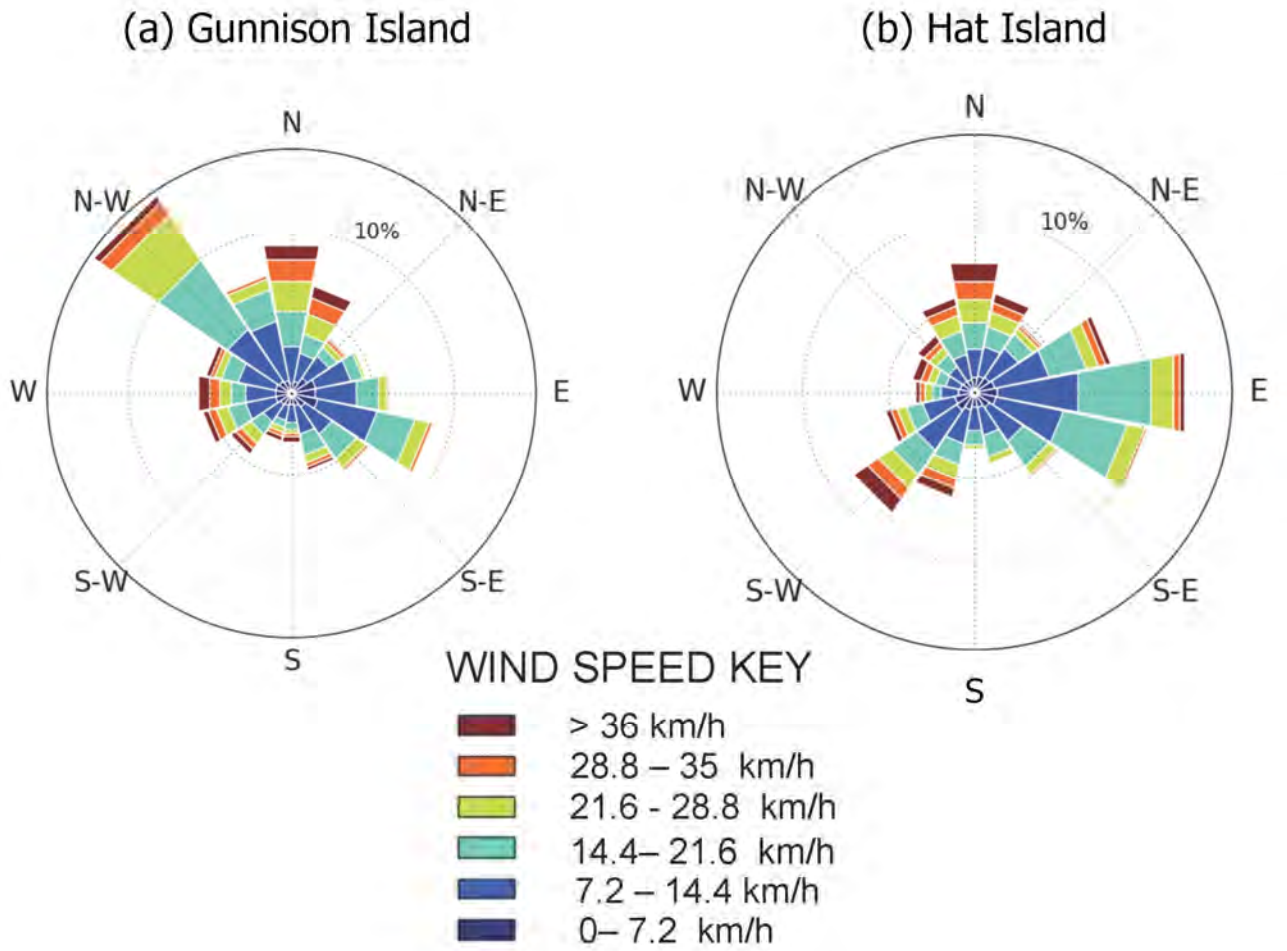

Figure 15. *Wind data for Gunnison and Gilbert Bays. The wind roses show wind direction and wind strength from over 300,000 total observations per location by MesoWest for 2020 to 2023 (J.D. Horel, Atmospheric Sciences, University of Utah, personal communication, 2023). Each wedge represents one of 16 cardinal directions. The length of the wedge represents the percent of the total observations for that site. The colors of the wedge represent the observations that fall in each of the speed classifications. (a) The wind rose for Gunnison Island in Gunnison Bay shows about 14% of the winds come from the northwest. Most of the strong winds come from the north and west and not from the south and east. (b) The wind rose for Hat Island in Gilbert Bay shows about 13% of the winds come from the east, about 8% from the north and 9% from the southwest. Most of the strong winds come from the north and southwest with fewer from the east.*

perelevated shoreline evidence of still water lake level. Winds directed straight at the shoreline inevitably produce greater superelevation than those of oblique incidence. Storm duration, wind strength, and fetch determine the energy input into wind waves. Complicating factors that affect wave runup and therefore shoreline superelevation, include wave setup, wind setup, wind-driven currents, the slope of the shore, shoreline morphology, lakebed and shoreline materials, and geographic features such as headlands that create sheltered zones. For example, Antelope Island shelters its eastern shore from most winds coming from the northwest. Shoreline superelevation at any one location, although dominated by the triad of wave energy, wind setup, and wave setup, is the cumulative effect of all contributing factors.

The US Army Shore Protection Manual (CERC 1984) treats the subject of coastal protection comprehensively and provides the empirical SMB-84 nomograph developed by Sverdrup and Munk (1947) and modified by Bretschneider (1952). The SMB-84 chart is a simple graphical method to identify fetch-limited wave regimes such as GSL. Figure 18, and Figure 19 its key present a nomogram for GSL modified from CERC (1984). It indicates that wave regimes of GSL are fetch-limited. Lo Re and others (2016) found that simple empirical wind-wave models, such as SMB-84, give reliable results, and they remain popular among coastal engineers.

The dark green line of the nomogram of Figure 18 indicates that neither Gunnison nor Gilbert Bay has sufficient fetch to develop a fully developed wave regime in response to storm winds. Strong winds across bays of GSL transfer energy into the waves that cause shoreline superelevation under fetch-limited conditions. Although maximum fetch across any direction of either Gunnison or Gilbert Bay (Figure 6) is too short for the wave environment to become fully developed during storm conditions, gentle winds over a long period of time can produce a fully developed re-

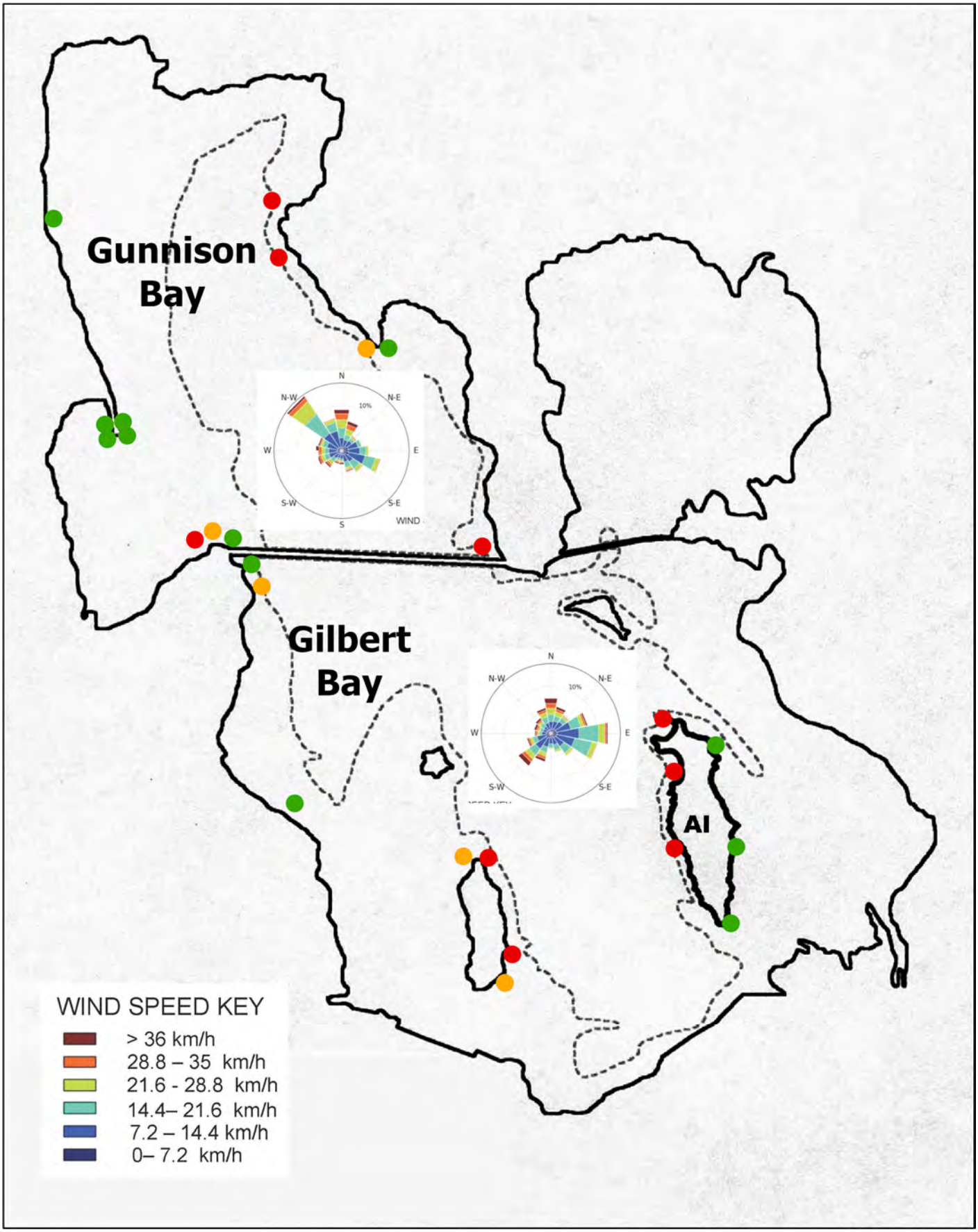

Figure 16. *Gunnison and Gilbert Bays: wind patterns and patterns of shoreline superelevation. Map of Great Salt Lake overlaid with the data from Figure 12 and wind roses from Figure 16. The dark line indicates the extent of the 1986-1987 highstand. The wind rose diagrams of wind direction and strength appear to explain some of the patterns of shoreline superelevation of Gunnison Bay. Patterns are more complex for Gilbert Bay.*

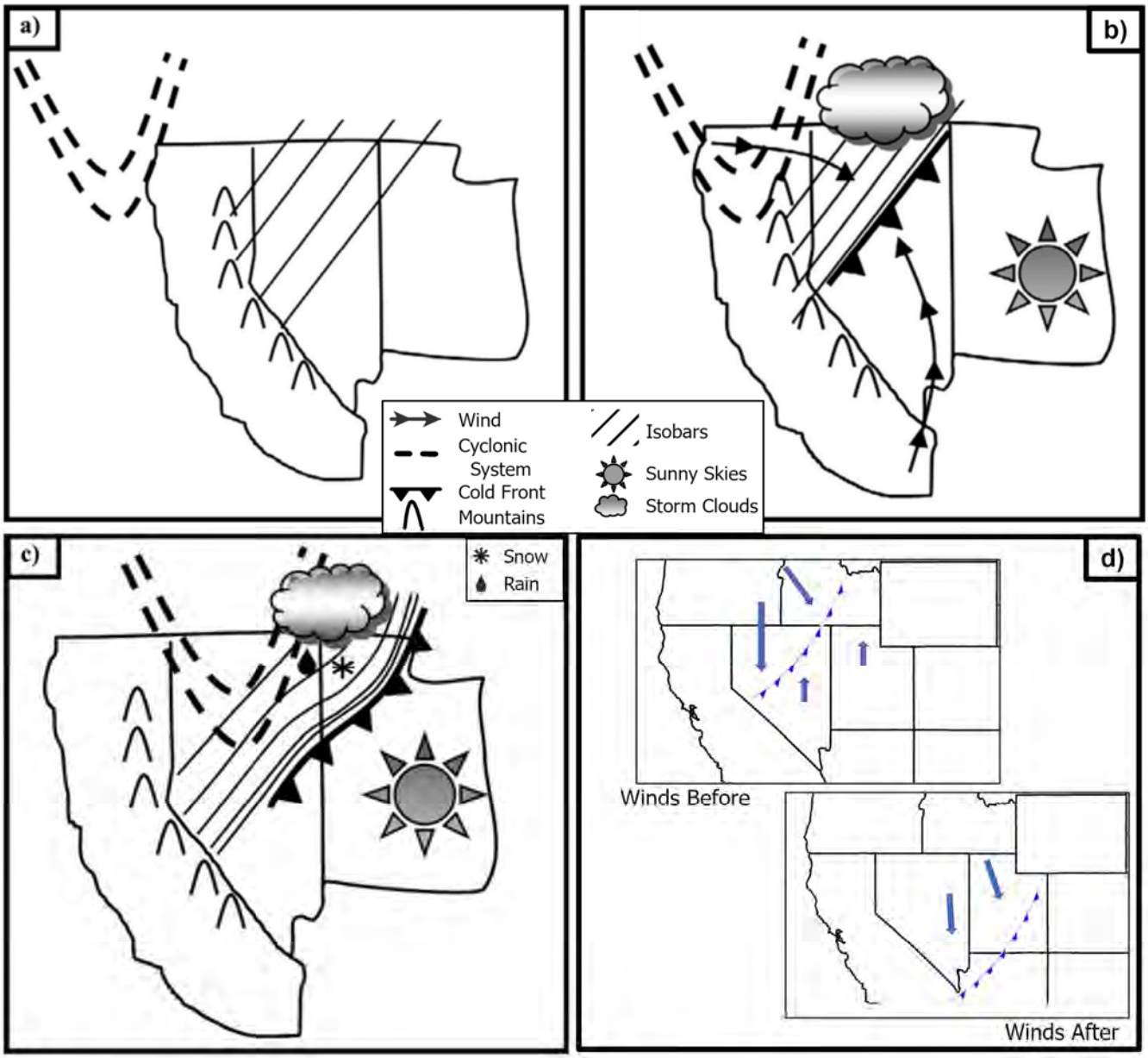

Figure 17. *Cartoon of the progress of a low-pressure storm system. Source: Figure a), b), c) adapted from Shafer and Steenburgh (2008). Key added. Figure d), from J.D. Horel, personal communication (2023). The low-pressure system progresses from offshore the Pacific Northwest coast to Great Salt Lake, where its winds create wind waves that leave evidence of shoreline superelevation. a). A cyclonic system arrives at the Pacific Northwest coast. b). The system digs in and progresses across the Great Basin. c). The cold front arrives and crosses Great Salt Lake. d). The two maps show wind direction and strength before and after a cold front crosses Great Salt Lake. Strong winds from the south precede the front's passage. Strong winds from the north and northwest follow. Strong winds transfer energy into the lake surface and create the wave regime that results in the superelevation of shoreline evidence.*

gime (wind energy at equilibrium with wave energy that arrives on GSL shores), as indicated by the small yellow triangle in Figure 18. Rowers and sailors commonly observe swell less than 1-2 ft on GSL (G. Atwood and T. Wambeam, personal observations). Those conditions may affect currents and sedimentation patterns but are not the wave environments that leave evidence of storm wind direction.

Wind speeds recorded for Hat Island and Gunnison Island, from 2020 through 2023 (J.D. Horel, Atmospheric Sciences, University of Utah, personal communication, 2023), together with limits of fetch, provide constraints on wave regimes represented by the green rectangle on Figure 18. A possible path of wave regime development over time under storm winds is plotted on the chart as a succession of three green stars (1, 2, 3). The blue star representing the empirical evidence of 1986-1987 conditions lies on the trajectory.

The values given by the blue polygon on Figure 18 for Gilbert Bay wave environments, for the lake at its 1986-1987 highest historic level, were based on in-

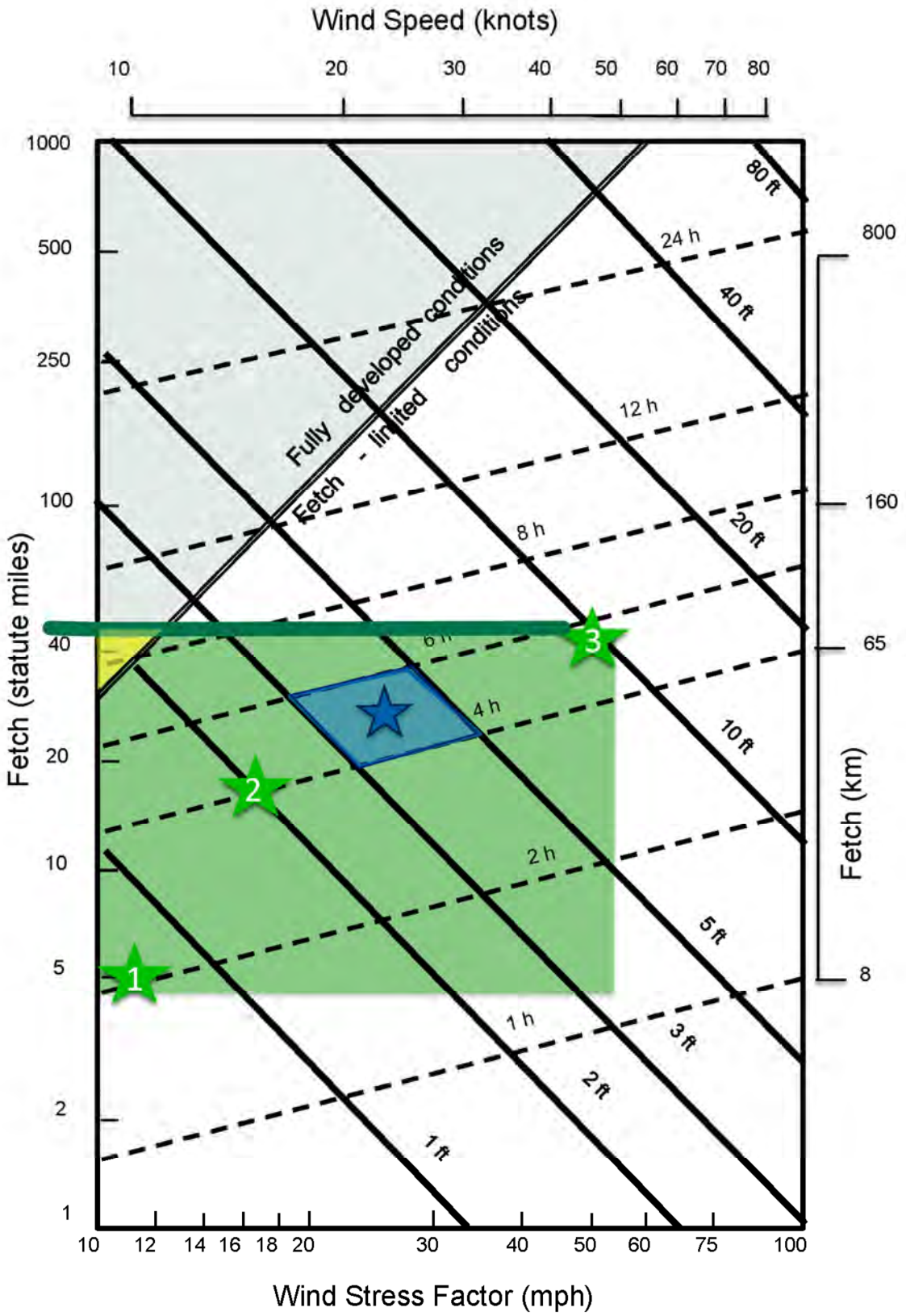

Figure 18. *Wave regime chart for Gilbert Bay. The wave regime chart (see key next page) has four variables: a) wind stress in miles per hour and knots; b) fetch in miles and kilometers; c) duration of strongest winds in hours; and d) significant wave height in feet (the average height of the tallest one-third of waves). This chart (adapted from the SMB-84 nomograph in CERC, 1984) summarizes the complex wave environment for given conditions. It shows a plot (blue polygon) for the conditions for Gilbert Bay reported in 1986-1987 (Atwood, 2006). The wind speeds of Figure 15 together with fetch suggest constraints on the limits of wave regime development in Gilbert Bay at that time (green rectangle). See the key and text for an explanation of the stars.*

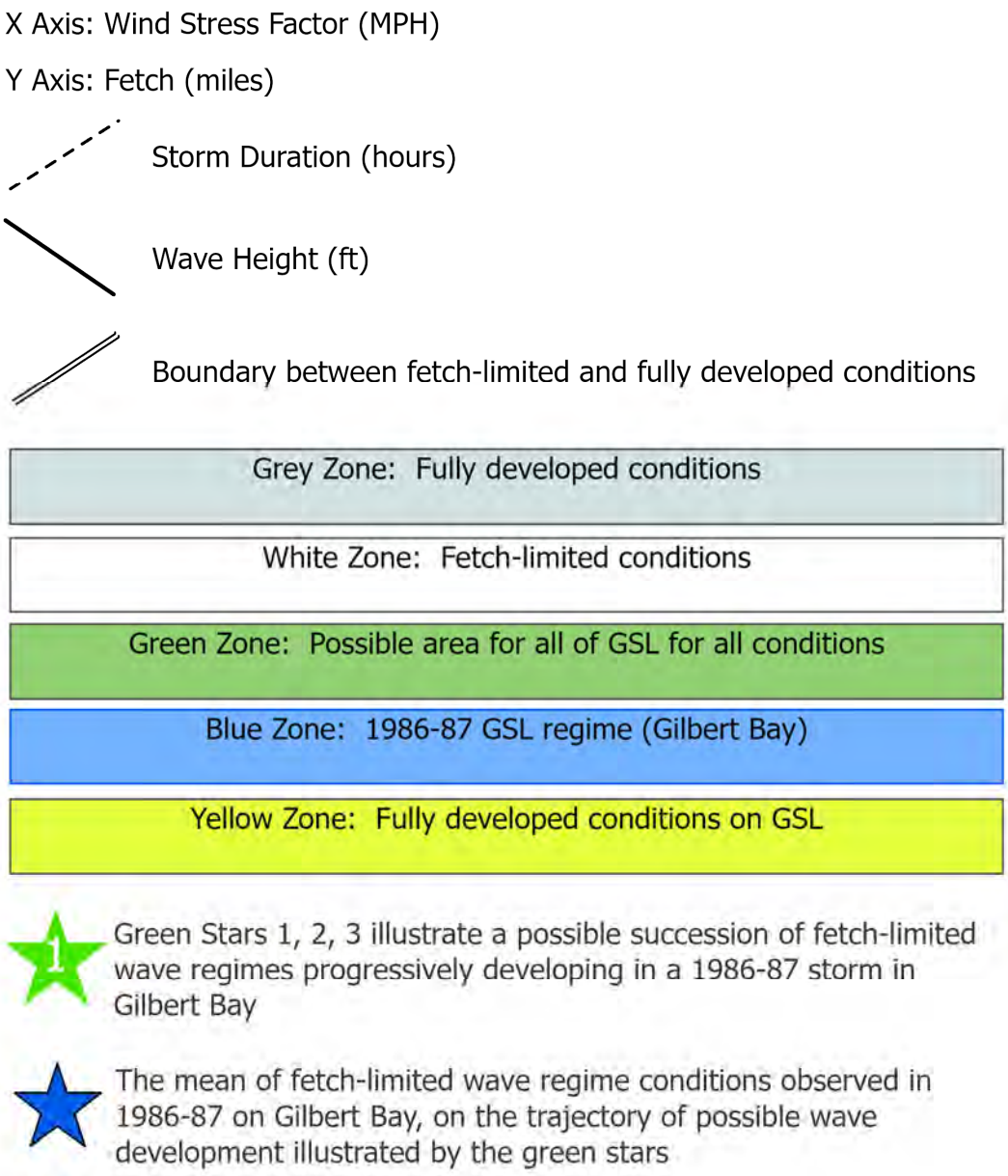

Figure 19. *Key to Figure 18*

terviews with W. Alder, Utah State Meteorologist, who estimated the duration of strongest storms and wind speeds and David Shearer, harbormaster of GSL Saltair Boat Harbor Marina, who estimated significant wave height and wind stress (Atwood, 2006). Fetch was measured from maps. The values for these four parameters define the blue polygon of Figure 18, lying well within fetch-limited conditions (the white region of the chart).

Summary of GSL Lake Processes

Shoreline superelevation is evidence of the lake processes of GSL. Wind develops waves and transfers energy into them. Under strong winds, lake water stacks up against windward shorelines (wind setup). Waves dissipate energy as they encounter the shoreface, run up, break, and deposit their entrained materials well above the static still water level monitored by the USGS.

Storm duration, wind strength, and fetch determine the energy input for the waves that leave the superelevated shoreline evidence. Factors affecting wave run-up on shorelines include wave setup, wind setup, wind-driven currents, the slope of the shore, shoreline morphology, from convex to straight to concave, lakebed and shoreline materials, and geographic features that block winds or create sheltered zones. The cumulative effect of these diverse contributing factors is that shoreline superelevation may at any one location, although dominated by wave energy, includes wind set up and wave set up. The patterns of

shoreline superelevation of Antelope Island 1986-1987 shoreline were caused by differences in the energy of wind waves arriving on shore. Those energy differences, although primarily due to differences in fetch, were noticeably affected by wind strength.

Insights from documentation of shoreline superelevation on Antelope Island, corroborated by the recent analysis of winds across Gunnison Bay, suggest that geomorphic patterns of shoreline superelevation of fetch-limited paleolakes can provide evidence of strongest wind direction and clues to regional paleoclimate and weather.

CONCLUSIONS

Previous papers by the authors defined and presented evidence to quantify shoreline superelevation of the 1986-1987 highstand on GSL, documenting that geomorphic shoreline evidence is not at the still water level of the lake and does not define a horizontal plane from which to measure post-depositional change with confidence. This paper extends the findings of earlier work with empirical evidence of wind patterns across Gilbert and Gunnison Bays from wind records from weather stations at Hat and Gunnison Islands. We further explore the processes of shoreline superelevation. Because GSL is fetch-limited, its geomorphic evidence at the highstand has a signal of wind direction and strength. Wind records of weather stations on GSL indicate the strongest winds across GSL are from the north and northwest and correlate with geomorphic evidence. Patterns of shoreline superelevation of gravel ridges and other geomorphic features along the shores of GSL are durable evidence of the direction of the strongest storm winds as well as effects of fetch. Examination of shoreline superelevation of additional modern- and paleo- fetch-limited lakes will lead to better understanding of their regional wind direction and strength and perhaps regional climate.

ACKNOWLEDGMENTS

We gratefully acknowledge Robert Baskin for his knowledge of GSL and his assistance with figures. We appreciate how William Alder, David Shearer, and John Horel shared knowledge via personal communications. This paper was completed with the knowledge and encouragement of Peter W. Homewood and Monique Mettraux, Geosolutions, Trd. Cameron Scharrer assisted with figures 13 and 14. We appreciate the 1986-2000 collaboration of the Utah Geological Survey, the University of Utah, and U.S. Geological Survey colleagues who worked together to better understand GSL 1986-1987 shorelines as evidence of lake processes. We are grateful to Ian Schofield and Daren Nelson, whose reviews improved this paper.

REFERENCES

Adams, K.D. and Wesnousky, G.G., 1998, Shoreline processes and the age of the Lake Lahontan highstand in the Jessup embayment, Nevada: Geological Society of America Bulletin, v.110 (10), p 1318-1332.

Adams, K.D., Wesnousky, G.G., and Bills, B.G., 1999, Isostatic rebound, active faulting, and potential geomorphic effects in the Lake Lahontan basin, Nevada and California: Geological Society of America Bulletin, v. 111, issue 12, p. 1739-1756.

Adams, K.D., and Bills, B.G., 2016, Isostatic rebound and palinspastic restoration of the Bonneville and Provo shorelines in the Bonneville basin, UT, NV, and ID, in Oviatt, C.G., Shroder, J.F., Jr., editors, Lake Bonneville: A scientific update. Developments in Earth Surface Processes 20: Elsevier, p. 145-164.

Alder W., 1986, 1987, daily journal entries: unpublished: Salt Lake City UT.

Applequist L.R., 2013, Generic framework for mesoscale assessment of climate change hazards in coastal environments: Journal of Coastal Conservation, v. 17, p. 59–74.

Arnow, T., and Stephens, D., 1990, Hydrologic characteristics of the Great Salt Lake, Utah: 1847-1986: U.S. Geological Survey Water-Supply Paper 2332, 32 p., map scale 1:125,000

Atwood, G., 2006, Shoreline Superelevation, evidence of coastal processes of Great Salt Lake, Utah Geological Survey, Miscellaneous Publication 06-9, 231 pp.

Atwood, G., and Mabey, D.R., 2000, Shorelines of Antelope Island as evidence of fluctuations of the level of Great Salt Lake, *in* King, J.K., and Willis, G.C., eds., Geology of Antelope Island, Davis County, Utah: Utah Geological Survey Miscellaneous Publication 00-1, p. 85-97.

Bertin, X., Martins, K., de Bakker, A., Chataigner, T., Guérin, T., Coulombier, T. and de Viron, O., 2020, Energy transfers and reflection of infragravity waves at a dissipative beach under storm waves: Journal of Geophysical Research: Oceans, v. 125, no. 5, e2019JC015714.

Bretschneider, C.L., 1952, The generation and decay of wind waves in deep water: Transactions American Geophysical Union, vol 33, p 381-389.

CERC (U.S. Army Coastal Engineering Research

Center), 1984, Shore protection manual, 4th edition: U.S. Government.

Chen, C.Y., and Maloof, A.C., 2017, Revisiting the deformed high shoreline of Lake Bonneville: Quaternary Science Reviews, v. 159, p. 169-189.

Cooper J.A.G., Lewis D.A., and Pilkey O., 2007, Fetch-limited barrier islands: Overlooked coastal landforms: Geological Society of America Geology, Geology Today, v. 17, no. 3, p. 4-9.

Currey, D.R., 1982, Lake Bonneville: selected features of relevance to neotectonic analysis of Great Salt Lake and vicinity, in Gwynn, J.W., ed., Great Salt Lake: a scientific, historical and economic overview; Bulletin 116: Salt Lake City, Utah Geological and Mineral Survey, p 69-82.

Fiedler, J.W., Young, A.P., Ludka, B.C., O'Reilly, W.C., Henderson, C. Merrifield, M.A. and Guza, R.T. 2020, Predicting site-specific storm wave run -up: Natural Hazards, v. 104, p. 493–517.

Fontaine, E., 2013, A theoretical explanation of the fetch- and duration-limited laws: Journal of Physical Oceanography, v.43, p. 233-247.

Freire, P., Ferreira, Ó., Taborda, R., Oliveira, F.S.B.F., Carrasco, A.R., Silva, A., Vargas, C., Capitão, R., Fortes, C.J., Coli, A.B., and Santos, J.A., 2009, Morphodynamics of fetch-limited beaches in contrasting environments: Journal of Coastal Research SI 56, Proceedings of the 10th International Coastal Symposium, p. 183-187.

Gilbert, G.K., 1890, Lake Bonneville: U.S. Geological Survey Monograph 1, 438 p.

Jewell, P.W., 2007, Morphology and paleoclimatic significance of Pleistocene Lake Bonneville spits, Quaternary Research v. 68, p. 421-30.

Komar, P.D., 1998, Beach processes and sedimentation (2nd edition): Prentice Hall, Upper Saddle River, New Jersey, 544 p.

Lo Re, C., Cannarozzo, M., and Ferreri, G.B., 2016, Present-day use of an empirical wave prediction method: Maritime Engineering, v. 169, issue MA1, 14 p.

Mabey, D.R., 1986, Notes on the historic high level of Great Salt Lake: Utah Geological and Mineral Survey, Survey Notes, v. 20, no. 2, p. 13-15.

MesoWest, www.mesowest.utah.edu

Munk, W.H., 1951, Origin and generation of waves: Proceedings of the 1st Coastal Engineering Conference, Long Beach, California, p. 1–4, doi: 10 .9753/ icce, v1 .1.

Murchison, S.B., 1989, Fluctuation history of Great Salt Lake, Utah, during the last 13,000 years: Salt Lake City, University of Utah, Ph.D. dissertation, 137 p.

Oviatt, C.G., Atwood, G., and Thompson, R.S., 2021, History of Great Salt Lake, Utah, USA, since the termination of Lake Bonneville, in Rosen, M.R., Finkelstein, D., Park-Boush, L., and Pla-Pueyo, S., editors, Limnogeology: Progress, Challenges and Opportunities: A tribute to Beth Gierlowski-Kordesch: Syntheses in Limnogeology no. 2, New York, Springer Nature AG, p. 233-271.

Schofield, I., Jewell, P.W., Chan, M., Currey, D.R., and Gregory, M., 2004, Shoreline development, longshore transport and surface wave dynamics, Pleistocene Lake Bonneville, Utah: Earth Surface Processes and Landforms, v. 29, p. 1675-1690.

Shafer, J.C., and Steenburgh, W.J., 2008, Climatology of strong Intermountain cold fronts: Monthly Weather Review, v 136, 784-807.

Sverdrup, H.U. and Munk, W.H., 1947, Wind, sea, and swell theory of relationships in forecasting: US Dept. of the Navy Hydrographic Office Publication, No 601.

Tackman, G.E., 1993, Middle and late Pleistocene hydrologic history of Diamond Valley, Eureka and Elko Counties, Nevada, with climatic and isostatic implications: Salt Lake City, University of Utah, Masters of Science thesis, 192 p.

Tackman, G.E., Currey, D.R., Bills, B.B., and James, T.S., 1998, Paleoshoreline evidence for postglacial tilting in Southern Manitoba: Journal of Paleolimnology, v. 19, 443-463.

Theuerkauf, E. J., Mattheus, C.R., Braun, K.N. and Bueno, J., 2021, Patterns and processes of beach and foredune geomorphic change along a Great Lakes shoreline: Insights from a year-long drone mapping study along Lake Michigan: Shore & Beach, v. 89, no. 2, p. 46-55.

WMO (World Meteorological Organization), 2018, Guide to wave analysis and forecasting. World Meteorological Organization report WMO No 702, 189 p.

Wang, P., 1978, Seiches in the Great Salt Lake: Salt Lake City, University of Utah, Ph.D. dissertation, 119 pp.

Wright, L.D., and Short, A.D., 1984, Morphodynamic variability of surf zones and beaches: a synthesis: Marine Geology, v. 56, p. 93–118.

Wave Dynamics and Sediment Transport in Great Salt Lake: A Model-Data Comparison

Benjamin Smith[1], Robert Mahon[2], Tyler Lincoln[3], Cedric J. Hagen[4], Juliana Olsen-Valdez[3], John Magyar[1], and Elizabeth Trower[3]

[1]*Division of Geological and Planetary Sciences, California Institute of Technology, Pasadena, California, bpsmith@caltech.edu*
[2]*Department of Earth and Environmental Sciences, University of New Orleans, New Orleans, Louisiana*
[3]*Department of Geological Sciences, University of Colorado Boulder, Boulder, Colorado, Lizzy.Trower@colorado.edu*
[4]*Department of Geosciences, Princeton University, Princeton, New Jersey*

10.31711/ugap.v51i.139

ABSTRACT

Great Salt Lake is a natural laboratory to test and refine ideas about the relationship between sediment transport by waves and the characteristics of shoreline carbonate sediments, in particular ooid sands and microbialite mounds. In this chapter, we present a year-long series of wave data collected from July 2021 through June 2022 and use these wave data to assess the performance of a US Army Corps of Engineers wave model previously used to estimate bed shear velocity and intermittency of sediment transport in Great Salt Lake (Smith and others, 2020). We use this model-data comparison to identify the strengths and weaknesses of the existing model for both geological and ecological applications, and areas of improvement for future model development. We also use shallow sediment cores and Unmanned Aerial Vehicle (UAV)-based orthomosaics collected from shorelines near each buoy to assess how the wave climate along two parts of the lake shore influences the stratigraphic record and the surface morphology of the lakebed.

INTRODUCTION

Great Salt Lake (GSL), UT is a critical ecological and economic resource—a key waypoint in the Pacific flyway (Paul & Manning, 2002) and a primary source of magnesium metal in North America (Tripp, 2009). GSL is also home to an exceptional modern geobiological archive of at least1000 km^2 of meter-scale microbialite mounds (Vanden Berg, 2019; Baskin and others, 2021) that play a key role in the GSL ecosystem (Wurtsbaugh and others, 2011). These mounds act as a food source and substrate critical for reproduction cycles for the brine fly, *Ephydra gracilis,* and the brine shrimp, *Artemia franciscana,* which in turn are key food sources for the millions of shorebirds and waterbirds that visit GSL each year (Collins, 1980; Wurtsbaugh, 2009; Belovsky and others, 2011). Radiocarbon dating, though complex, suggests that GSL microbialites have been accumulating for >10,000 years (Bouton and others, 2016a; Newell and others, 2017, 2020; Homewood and others, 2022). Previous authors have described gradients in microbialite morphology with distance from the shoreline and/or water depth (Eardley, 1938; Carozzi, 1962; Bouton and others, 2016a, 2016b; Vanden Berg, 2019), suggesting that hydrodynamics and sediment transport, in addition to geochemistry and microbial metabolic activity, play a role in microbialite construction. Previous workers have also observed that elongated microbialite mounds or domes tend to have preferred orientations relative to a shoreline and/or wave crests (Bouton and others, 2016a; Chidsey and others, 2015; Vanden Berg, 2019). These observations hint at a potential link between sediment transport and microbialite morphology and orientation. In theory, GSL microbialites are an ideal system in which to test ideas about the role of hydrodynamics and sediment transport on microbialite morphology because microbialites occur along shorelines with different orientations and therefore experience different wave conditions. However, this work first requires a more robust understanding of wave dynamics in the lake and an ability to accurately model past wave conditions (e.g., prior to causeway construction and at higher lake levels) along different shorelines.

Beyond microbialites, wave dynamics in the lake also affect other sedimentological and ecological characteristics of the lake. For example, the formation (including grain size and shape) of ooids is influenced by the frequency and energy of sediment transport (Trower and others, 2020). Wave dynamics can also influence mixing of the typically-stratified South Arm lake water, which in turn affects the ecosystem by varying the availability and mobility of nutrients (Belovsky and others, 2011) and delivery of toxins like mercury, selenium, and arsenic from the deep brine layer to the upper water column (Beisner and others, 2009; Jones and Wurtsbaugh, 2014). Furthermore,

given the historically low lake levels witnessed in 2021 and 2022 (Abbott and others, 2023), accurate models of wave climate are needed to better understand how different future lake levels (higher or lower) will influence the hydrodynamics of the ecosystem.

Previously, Trower and others (2020) and Smith and others (2020) applied a linear wave model (Rohweder and others, 2008) to calculate wave characteristics and bed shear stress using GSL bathymetry (Baskin and Allen, 2005; Baskin and Turner, 2006; Tarboton, 2017) and wind data from the University of Utah MesoWest database (Horel and others, 2002). However, this model was not necessarily designed to perform optimally for an environment like GSL, which includes very shallow and low sloping shorelines and the sharp changes in shoreline slope associated with the East Lake fault scarp off the western shore of Antelope Island (Colman and others, 2002). The purpose of this paper is to assess the performance of a linear wave model in GSL using data from two wave buoys in parts of the lake with contrasting shoreline orientations. -We evaluated the performance of this linear wave model using data from these wave buoys. We also present observations from sediment cores collected near each wave buoy and measurements of microbialite orientations adjacent to one wave buoy to assess how wave climate affects the composition and morphology of carbonate sediments along differently-oriented shorelines. Our ultimate goal is to assess whether the model performs sufficiently well to be more widely applied to predict future and/or reconstruct ancient wave hydrodynamics in GSL.

METHODS

Wind and Wave Measurements

SoFarOcean Spotter wave buoys were deployed at two locations along the South Arm of the lake from the period of July 13, 2021, through June 28, 2022 (Figure 1). The two sites were selected based on public interest and scientific importance. Buoy #1356 (Black Rock) was deployed near GSL State Park and buoy #1328 (Miera Spit) was deployed near the southern end of Antelope Island State Park. Previous work documented relationships between sedimentary facies and the physical environment near these locations, including Trower and others (2020) with ooids near Black Rock, and Smith and others (2020) with rip-up clasts and other storm features near Miera Spit. Both buoys were deployed in relatively shallow water, approximately 2.5 m for #1356 and 1.6 m for #1328. For each wave buoy, water depth was measured using HOBO U20L-04 water level loggers attached to anchors. Each logger recorded pressure and temperature every 30 minutes; pressure measurements from each logger were converted to water depth using a water density of 1100 kg/m^3 and corrected for atmospheric pressure using data from the KCC01 MesoWest weather station.

SoFarOcean buoys were chosen for deployment because they offer a lower-cost alternative to other wave monitoring techniques, and they transmit in real time through the use of onboard accelerometers and Iridium satellite communication capabilities. Buoys operated in six-hour cycles, alternating 5 hours of rest with one hour of active data collection. At the end of each cycle, buoys performed onboard processing of accelerometer data, converting it to spectral wave parameters—e.g., significant wave height, peak and mean direction, and spectral moments using open-source algorithms made available by SoFarOcean. At the end of the study, higher-frequency data were retrieved from the buoy's onboard memory and processed using SoFarOcean parsing and analysis scripts (parser_v1.12.0). The full dataset for both buoys is available in an online repository (Mahon and others, 2023), including additional wave data (e.g., directional spread, etc.) and metadata (e.g., temperature) not directly described in this chapter.

For each buoy, HOBO water depth time series data were examined to determine whether the anchors moved during the study period, as evidenced by substantial step changes in water depth. Water depths for #1356 (Black Rock) varied smoothly between 1.73-2.95 m, reaching a low point of 1.73 m in October 2021, corresponding to the new historical low of 4190.1 ft (Figure 2). Buoy #1356 (Black Rock) was retrieved in good working order with no evidence of anchor movement or onboard electronics failures, indicating that the buoy made reliable wave measurements over the full study period. In contrast, water depths for #1328 (Miera Spit) started at 1.78 m but dropped rapidly to 0.85m on July 15, 2021, and dropped further to 0.43m on August 17, 2021 (Figure 2). The timing of these rapid water depth changes matches the timing of buoy location changes when the anchor was dragged inshore by waves. When buoy #1328 (Miera Spit) was retrieved at the end of the study period, it was partially beached with its ballast chain touching the bed. We surmised that data quality was suspect after the second abrupt change in water depth on August 17, 2021, when the anchor was moved during a storm. A second consideration to buoy data quality was the detection limit of very low-amplitude waves. Under calm conditions, buoy sensors experience an internal electronic "ringing" which produces spurious derived wave data with unrelated

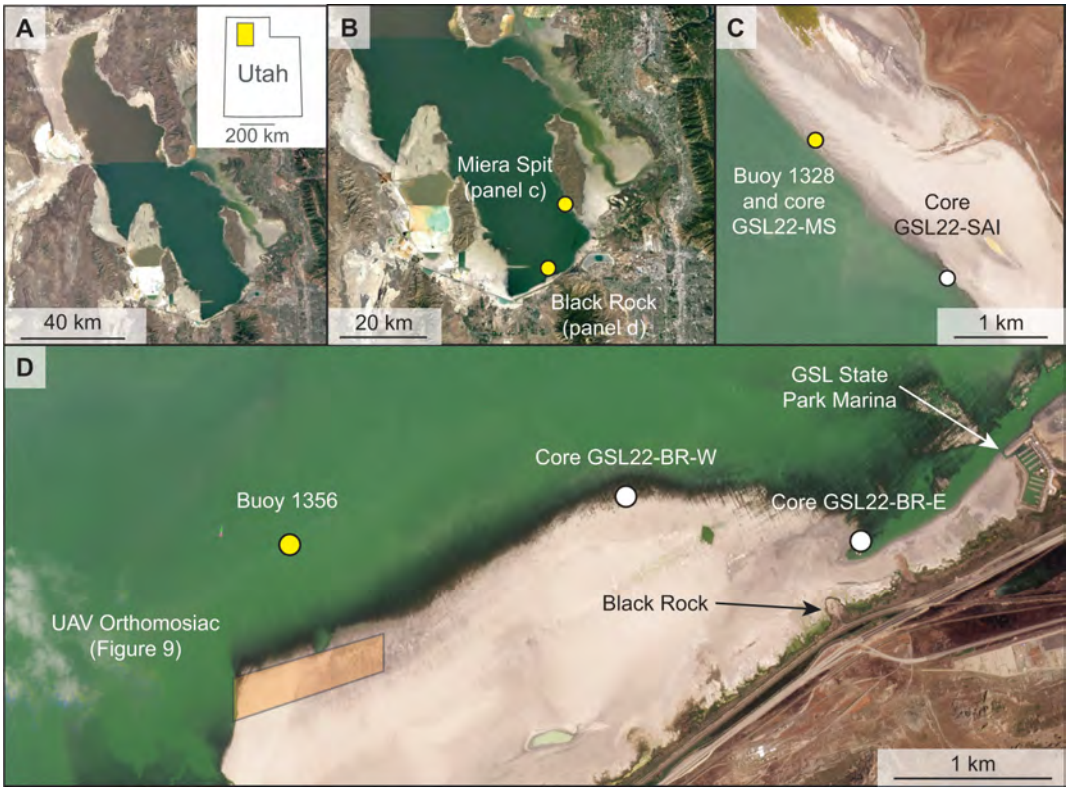

Figure 1. *The GSL-BB system. A. Location of GSL and Lake Bonneville in western Utah. B. Overview map of GSL showing the historic average elevation, and the new 2022 historic low (Figure from Clark and Baxter, 2023.) C. Corresponding Landsat satellite imagery of GSL elevations showing the record high of GSL in 1986 at left vs. historic low in 2022. AI = Antelope Island. Images (Images are public domain.) D. Known Bonneville basin lake cycles. The blue line labeled B in the main graph marks the Bonneville deep-lake cycle. Vertical black bars represent older deep-lake cycles. The base of the main graph is the elevation of modern GSL. Inset shows the shoreline history of Lake Bonneville (blue) and GSL (red) with named shorelines (also see Figure 3). (Inset figure from Oviatt and Shroder, 2016a).*

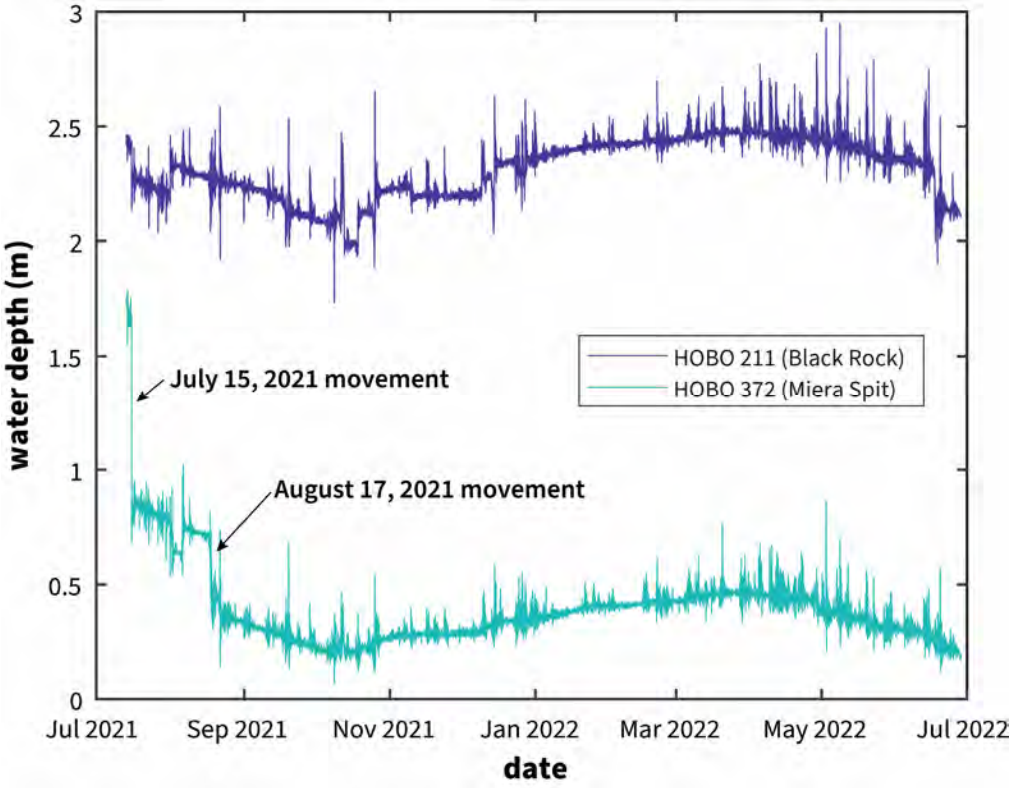

Figure 2. *Logs of water depth at each buoy location over the year-long deployment. Note abrupt drops in water depth at Miera Spit buoy on July 15, 2021 and August 17, 2021. These correspond with storm events and affect data quality after July 15th.*

directions and magnitudes. These data were distinguished by their long periods (up to 20s) which were unreasonable for waves in the lake. From the 1400 wave spectral records at buoy #1356 (Black Rock), 793 were deemed to accurately reflect present conditions based on their wave periods (<10s). For buoy #1328 (Miera Spit), 41 records were deemed suitable based on the abbreviated operation period and noise screening.

Wind speed and direction were obtained from several wind stations in the MesoWest database over a period coinciding with buoy deployment (7-13-2021 to 6-28-2022, Figure 3). For both wind/wave comparisons and fetch-limited calculations, stations were selected based on proximity to each buoy and completeness of wind data over the study period. Wind conditions near buoy #1356 (Black Rock) were taken from station KCC02, located in the marina of GSL State Park (Figure 3). Wind conditions near buoy #1328 (Miera Spit) were taken from the station at Hat Island (HATUT) because other, more proximal stations either had incomplete records or were not operational over the study period.

Comparing Estimated and Observed Wave Parameters

Wave parameters can be estimated using a combination of linear wave theory, empirically derived equations, and measurements for wind speed and fetch. Many studies use methods developed by the US Army Corps of Engineers as outlined in the Coastal Engineering Manual (U.S. Army Corps of Engineers, 2002) and the Shore Protection Manual (Coastal Engineering Research Center, 1984). In particular, this approach underlies recent work by Trower and others (2020) and Smith and others (2020) which used an ArcGIS plugin (Rohweder and others, 2008) to estimate wave parameters based on MesoWest wind data (Horel and others, 2002) and a digital elevation model (Tarboton, 2017). A comparison between observed and calculated wave parameters provides direct feedback on the appropriateness of commonly used approaches for GSL, as well as potential complications due to wave refractions/diffraction, interactions with lake bathymetry, and inaccuracy of the bathymetry model.

The model-data comparisons focused on significant wave heights, peak wave heights, and estimated shear velocities at the bed. Significant wave heights, defined as the average height of the upper one-third of wave crests, were calculated using a procedure used in the Coastal Engineering Manual for fetch-limited conditions (U.S. Army Corps of Engineers, 2002):

$$C_d = 0.001 * (1.1 + (0.035 * U_A) \quad (1)$$

$$U^* = (C_d)^{1/2} * U_A \quad (2)$$

$$\hat{x} = (g * x)/(U^*)^2 \quad (3)$$

$$\hat{H}_{m0} = \lambda_1 * (\hat{x})^{m1} \quad (4)$$

$$H_{m0} = \hat{H}_{m0} * (U^*)^2/g \quad (5)$$

where C_d is the drag coefficient, U_A is the wind speed (m/s) adjusted for height and whether the observations were collected over land or water, U^* is the friction velocity (m/s), x is the wind fetch, $\hat{x}$ is the non-dimensional wind fetch, $\hat{H}_{m0}$ is the non-dimensional significant wave height, H_{m0} is the significant wave height (m), λ_1 is a constant with a value of 0.0413, g is gravitational acceleration (9.81 m/s^2), and m_1 is a constant with a value of ½.

Peak wave periods under fetch-limited conditions were calculated using:

$$\hat{T}_p = \lambda_2 * (\hat{x})^{m2} \quad (6)$$

$$T_p = \hat{T}_p * U^*/g \quad (7)$$

where $\hat{T}_p$ is the non-dimensional peak wave period, λ_2 is a constant with a value of 0.751, m_2 is a constant with a value of ⅓, and T_p is the peak wave period.

Shear velocities were calculated using estimates of maximum orbital velocity and wavelength as intermediate steps. Wavelengths (L) were calculated as:

$$L = gT^2_p * 2\pi \quad (8)$$

and maximum orbital velocities, u_m, were calculated as:

$$u_m = \pi H_{m0}/(T_p \sinh(2\pi d_f/L)) \quad (9)$$

Shear velocities, u_*, were calculated as:

$$u_*^2 = 1/2\, f\, u_m \quad (10)$$

where f is the friction factor set to 0.032. Note that while significant wave height and wave period provide direct comparisons between model estimates and

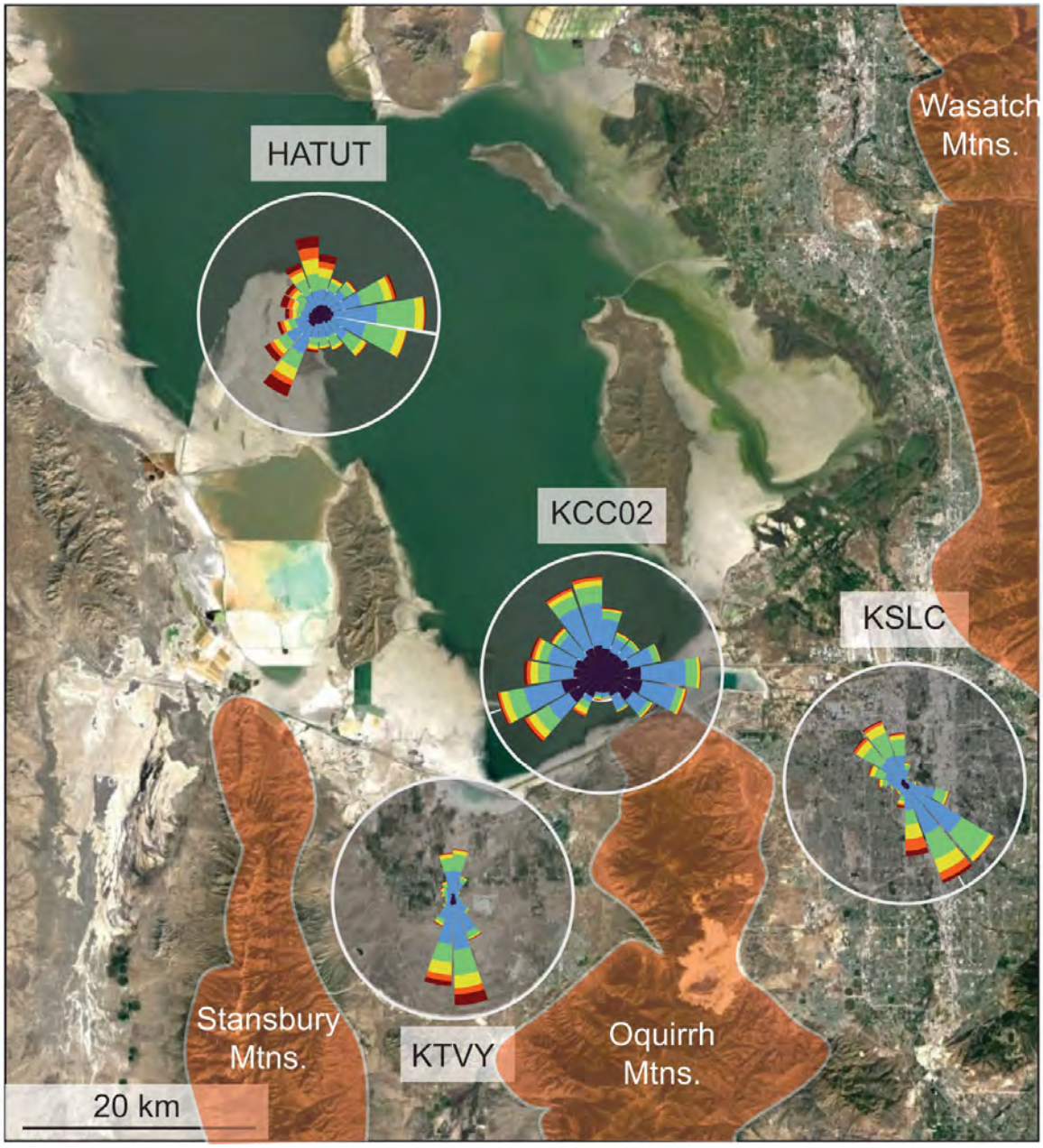

Figure 3. *Wind data for the study period from four stations in the MesoW est database. KTVY = Tooele Valley Airport, KSLC = Salt Lake City Airport, KCC02 = GSL State Park marina, HATUT = Hat Island.*

wave data, shear velocity is the most important variable for understanding sedimentary processes.

Unmanned Aerial Vehicle Photography

Ever since Eardley (1938) produced the first map of sediments in GSL, sedimentary studies in GSL have used multi-scale mapping to characterize shallow-water features such as bedforms and microbialites (Bouton and others, 2016a, 2016b; Vanden Berg, 2019; Smith and others, 2020; Baskin and others, 2021). Orthomosaic photos from unmanned aerial vehicles (UAVs) provide intermediate-scale maps that bridge field observations and satellite imagery. To facilitate comparisons with directional wave data, an orthomosaic was collected on June 29, 2022, from the Black Rock area using a DJI Mavic Air 2 at 200 ft standoff height via DroneLink mission planning software (Figure 1). A total of 877 orthophotos were collected and stitched together using PIX4Dcloud, covering an area of 0.278 km^2. Linear features within individual microbialites were measured using JmicroVision (Roduit, 2019) by tracing the long axes of 100 microbialite ridges from the mapped area as well as five lineations that crosscut the primary microbialite ridge orientation in the northwest corner of the mapped area.

Core Recovery and Grain Size Analysis

We collected three sediment cores using an SDI Vibecore Mini electric vibracore: one core from near Miera Spit (GSL22-MS) and two cores from near Black Rock (GSL22-BR-W and GSL22-BR-E) (Figure 1). We also collected an additional push core from a second location near Miera Spit (GSL22-SAI). We split each core using electric shears and collected ~15 mL sediment samples every 4 cm from one half of each core; the second half of each core was described and archived. Sediment samples were briefly rinsed with tap water to prevent grains from sticking together (due to salt precipitation from evaporating pore fluids) without dissolving minerals, then air dried. Grain size and shape of each sediment sample was analyzed using a Retsch Camsizer P4. Cores and subsamples of cores for analysis were registered with IGSNs (International Geo Sample Numbers) in the SESAR (System for Earth Sample Registration) database; parent core IGSNs are listed in the results section and subsamples from each core have unique IGSNs associated with their respective parent IGSN.

RESULTS

Observed Wind and Wave Conditions Near Black Rock and Miera Spit

Wind data over the study period were variable across MesoWest stations near Black Rock. South of Black Rock, wind stations have a predominantly N/S orientation. Data from Salt Lake City airport (station KSLC) are predominantly NW/SE while data from Bolinder-Tooele Valley Airport (station KTVY) are N/S. Wind orientations at both stations are consistent with previously observed lake breezes due to diurnal heating/cooling of the lake and land, as well as funneling of winds through the Salt Lake and Tooele Valleys, respectively (Ludwig and others, 2004). The station closest to Black Rock, KCC02, has strong N, E, and SW components. The near absence of strong and/or frequent winds from the south likely reflects obstruction from the nearby Oquirrh Mountains.

Overlapping time series of both wind and wave data suggested that wave orientations generally aligned with local wind orientations. Near Black Rock, wave observations, especially those with heights >15 cm, were oriented N/NNW (Figure 4). Less frequently, strong winds from the WSW produced waves arriving from this direction, most notably during late December of 2021 through early January 2022. Although wind data had multi-modal orientation, the rose diagram of wave directions had a strong modal peak oriented at 350°. In turn, the modal peak aligned with the long direction of the lake relative to the local shoreline. The largest wave heights were also observed in this direction, which was consistent with previous assumptions about fetch-limited wave conditions. In contrast, wave data from Miera Spit differed from those at Black Rock, even though they were collected over a relatively short interval (Figure 5). Significant wave events at Miera Spit were aligned with winds from the SW rather than the N/NNW.

Model-data Comparison for Black Rock

For model-data comparisons at Black Rock, we restricted our analysis to observations for which both wind and wave directions had an orientation of 350° +/- 10° based on the mode in wave directions (Figure 4). The estimated significant wave heights, peak wave periods, and shear velocities (red curves in Figure 6) were calculated as functions of wind speed along a fetch of 54 kilometers using Eqns. 1-7. Results show that the model slightly overestimates significant wave heights, and the effect is most pronounced at high wind speeds (Figure 6A). In contrast, model predictions for peak wave periods fall within the data (Figure 6B), although a normal Q-Q plot (Figure 6D) shows that the residuals are not normally distributed about the fit. Shear velocities predicted by model results also agree with those calculated with observed wave parameters (Figure 6C), although another Q-Q plot also shows some structure in the residuals (Figure 6F). No model-data comparison was performed for Miera Spit due to the shorter time interval and fewer wave measurements.

Core Sedimentology

Maximum depths of each core were 24 cm (GSL22-SAI; IGSN: 10.58052/IEEJT008B), 60 cm (GSL22-MS; IGSN: 10.58052/IEEJT008A), 77 cm (GSL22-BR-W; IGSN: 10.58052/IEEJT008C), and 74 cm (GSL22-BR-E; IGSN: 10.58052/IEEJT008D). For all cores, the maximum depth of coring represents the depth of a resistant hardground that we could not penetrate with our equipment. Sediments in cores from near Miera Spit (GSL22-MS and GSL22-SAI) were mainly composed of ooids with minor peloids (primarily *Artemia* fecal pellets), grapestones, and mica flakes; both cores lacked carbonate mud (Figure 7). Below 23 cm depth, ooid sands in the GSL22-MS core were roughly bimodal mixtures of fine and coarse ooids. Sediments in cores from near Black

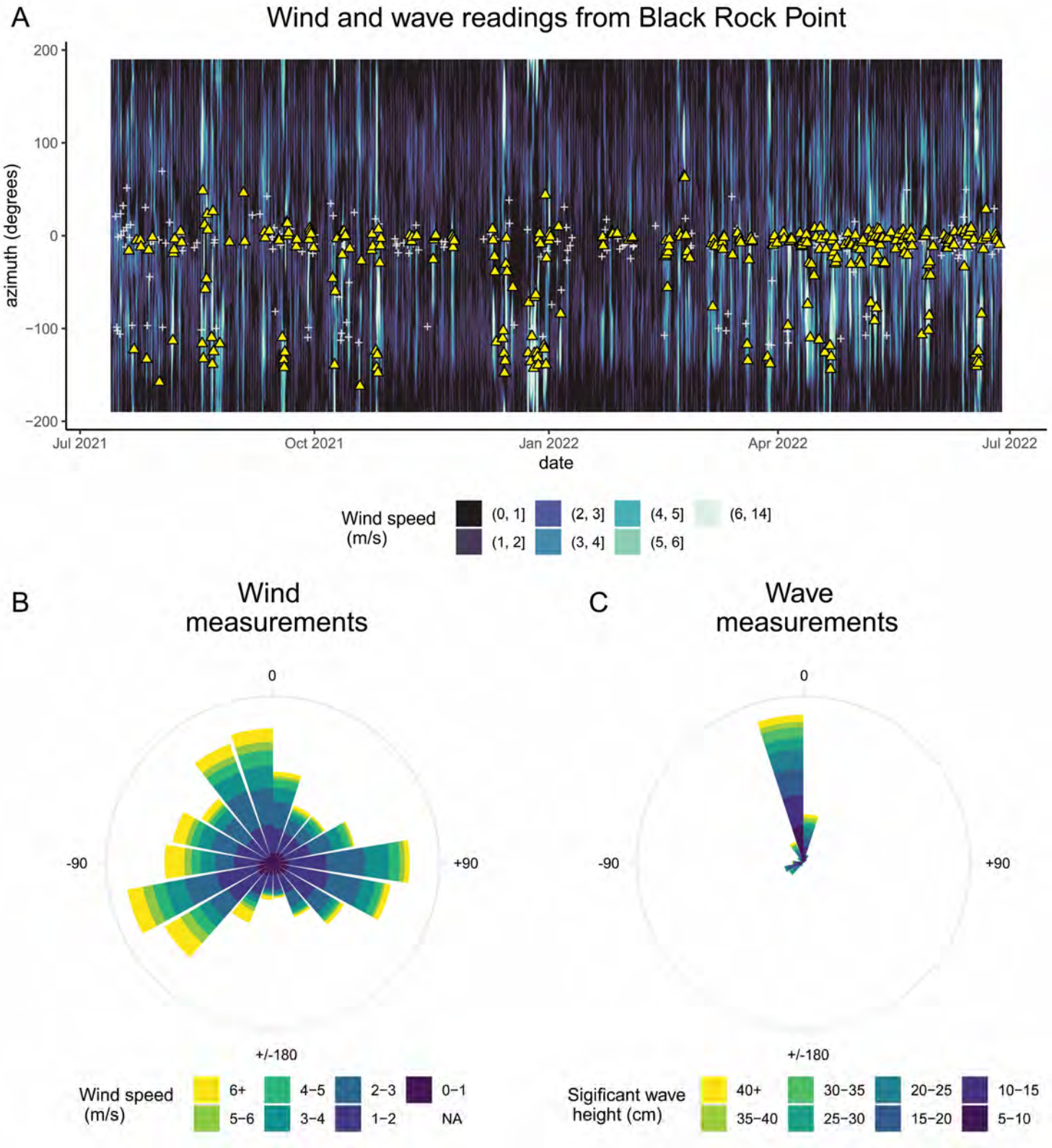

Figure 4. *Wind and wave observations near Black Rock collected from July 2021 to June 2022. A) Time series of wind speeds from a nearby wind station (KCCO2) plotted with significant wave heights from buoy #1356. The heatmap, which depicts wind speed and azimuth, shows that large wind events (light colors) are predominantly oriented N/NE with a secondary SW orientation. Significant wave heights >15 cm (yellow triangles) coincide with the timing and orientation of strong winds while wave heights <15 cm (grey crosses) have more variable orientations B) Rose diagram of wind measurements binned by 20° increments. Measurements are multimodal with W, S, and E peaks. C) Wave azimuths for significant wave heights. Wave directions were largely unimodal with an azimuth of 350° +/- 10°. Note that the dominant wave direction is both a frequent wind direction and a long fetch relative to the shoreline at Black Rock.*

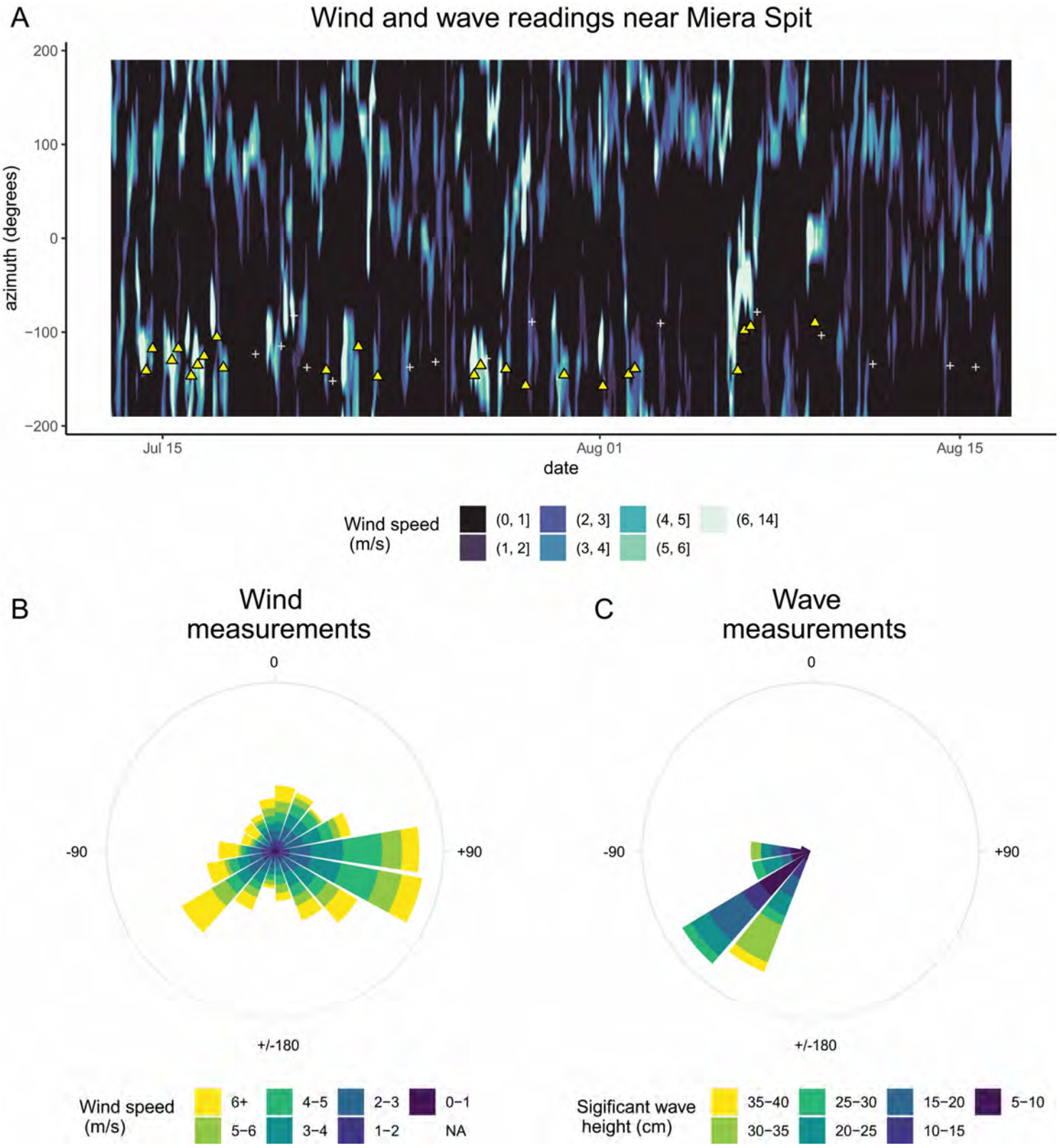

Figure 5*. Wind and wave observations near Miera Spit collected from July to August 2021. A) Time series of wind speeds from a nearby wind station (HATUT) plotted with significant wave heights from buoy #1328. The heatmap, which depicts wind speed and azimuth, shows that large wind events (light colors) are predominantly oriented E or SW. Significant wave heights >15 cm (yellow triangles) somewhat coincide with the timing and orientation of strong winds, although the match is weaker than at Black Rock. Wave heights <15 cm (grey crosses) have variable orientations. B) Rose diagram of wind measurements binned by 20° increments. Measurements are mostly bimodal with E and SW peaks. C) Wave azimuths for significant wave heights. Wave directions were largely unimodal with an azimuth of 210° +/- 10°. Note that the dominant wave direction differs from Black Rock (Figure 4), reflecting differences between wind and shoreline orientation between the two sites.*

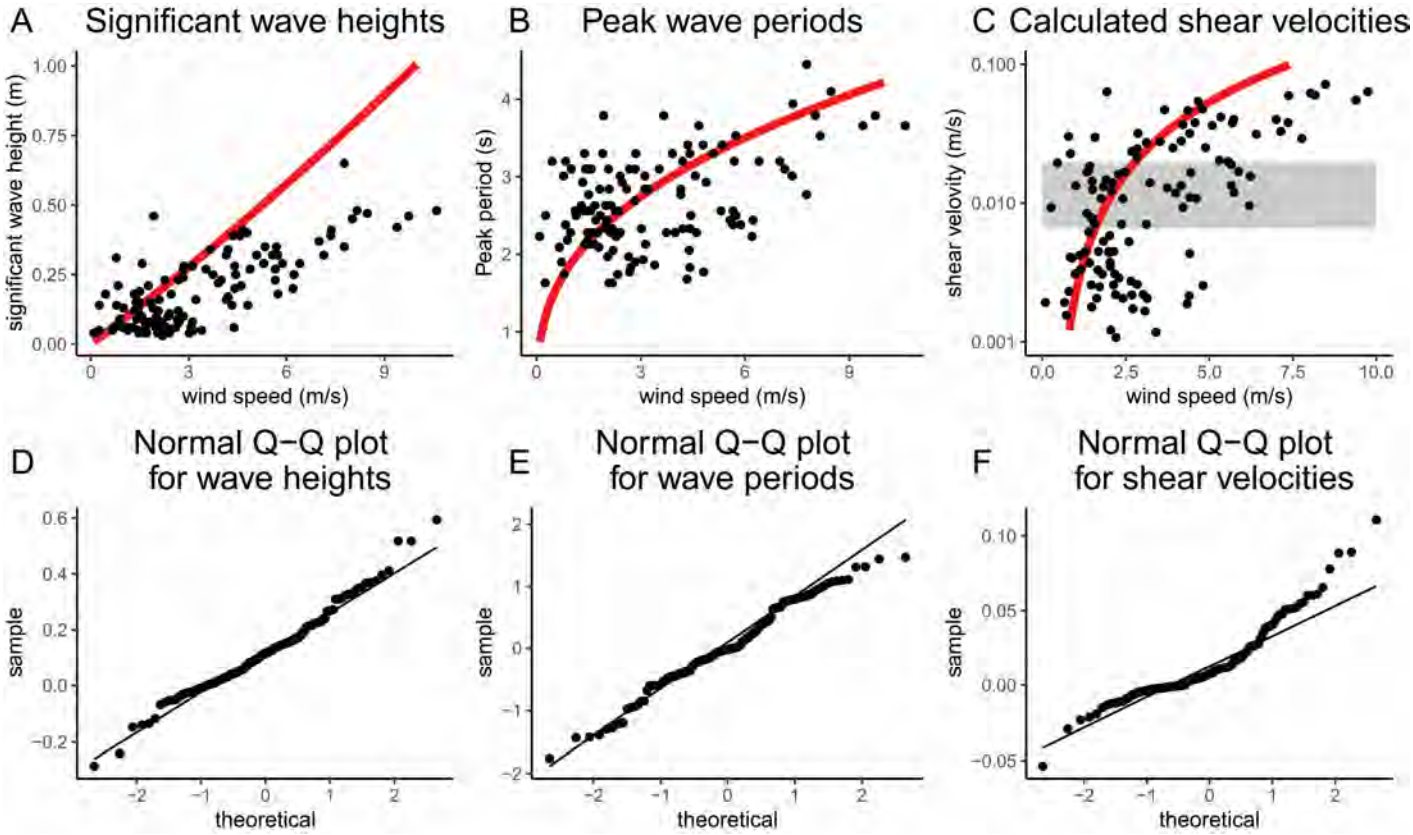

Figure 6. *Comparison of wind speed with significant wave heights (A), peak periods (B), and calculated shear velocities (C). Black circles represent simultaneous measurements of wind speed from station KCC02 matched with wave measurements at buoy #1356. Points represent a subset of wind and wave measurements with an azimuth of 350° +/- 10°. For A and B, red curves show wave parameters (vertical axes) as a function of wind speed as calculated by Eqns. 1-7 with a constant fetch of 54 km. For C, shear velocities were calculated using Eqns. 8-10. Black circles show shear velocities calculated using buoy observations of wave height and peak periods, while the red curve uses wave heights and peak wave periods calculated from Eqns. 1-7. The shaded gray bar shows the range of shear velocities most relevant to sediment transport near Black Rock: the lower and upper bounds represent thresholds for motion and suspension, respectively, for 370 μm sand.*

Rock (GSL22-BR-W and GSL22-BR-E) were composed of dark green- to dark orange-brown-pigmented, gravel-sized microbial mat or partially mineralized microbialite fragments (referred to as "pustular grains" and "microbial popcorn" by Chidsey and others (2015), grapestones, angular carbonate sand grains (not ooids), and peloids (also primarily *Artemia* fecal pellets) (Figure 7); with the exception of a few horizons, both cores lacked muddy matrix. Both Black Rock cores shared a similar sequence of ~20 cm of gravel-sized microbial mat and microbialite fragments overlying 40-50 cm of grapestone-dominated sediment. Core GSL22-BR-E had an additional 10.5-cm-thick layer of fine ooid sand overlying the microbialite fragment layer. Grapestone compositions included aggregates of ooids, peloids, and microbialite fragments.

The grain size and shape data are distinctly different between the Miera Spit and Black Rock sediment cores (Figure 8). Median grain diameters (D_{50}) in the Miera Spit cores range from 369-496 μm (GSL22-MS) and 332-434 μm (GSL22-SAI), with mean roundness in both cores ranging from 0.71-0.77. These values are similar to previously characterized GSL ooids (Trower and others, 2020), although the GSL22-MS core includes D_{50} values that are greater than reported in other areas. The grain size and roundness trends with depth are very similar between the two Miera Spit cores, showing little variability, although ooids in the GSL22-MS core are consistently larger than those in the GSL22-SAI core. In comparison, the Black Rock cores depict more variability, where the two Black Rock cores differ most in the upper 20 cm. These trends match the lithologic variability observed in the cores (Figure 8): samples in the upper 10.5 cm of GSL22-BR-E have median grain diameters (D_{50} = 281-322 μm) and mean roundness (0.72-0.78) characteristic of ooids, while the microbial mat and microbialite fragments were very coarse sand to very fine gravel sized (D_{50} = 1448-3528 μm) and angular (mean roundness = 0.32-0.37) and the grapestones were coarse to very coarse sand sized (D_{50} = 911-1839 μm) and angular (mean roundness = 0.36-0.43). Grapestones in the GSL22-BR-W core were consistently coarser than the GSL22-BR-E core.

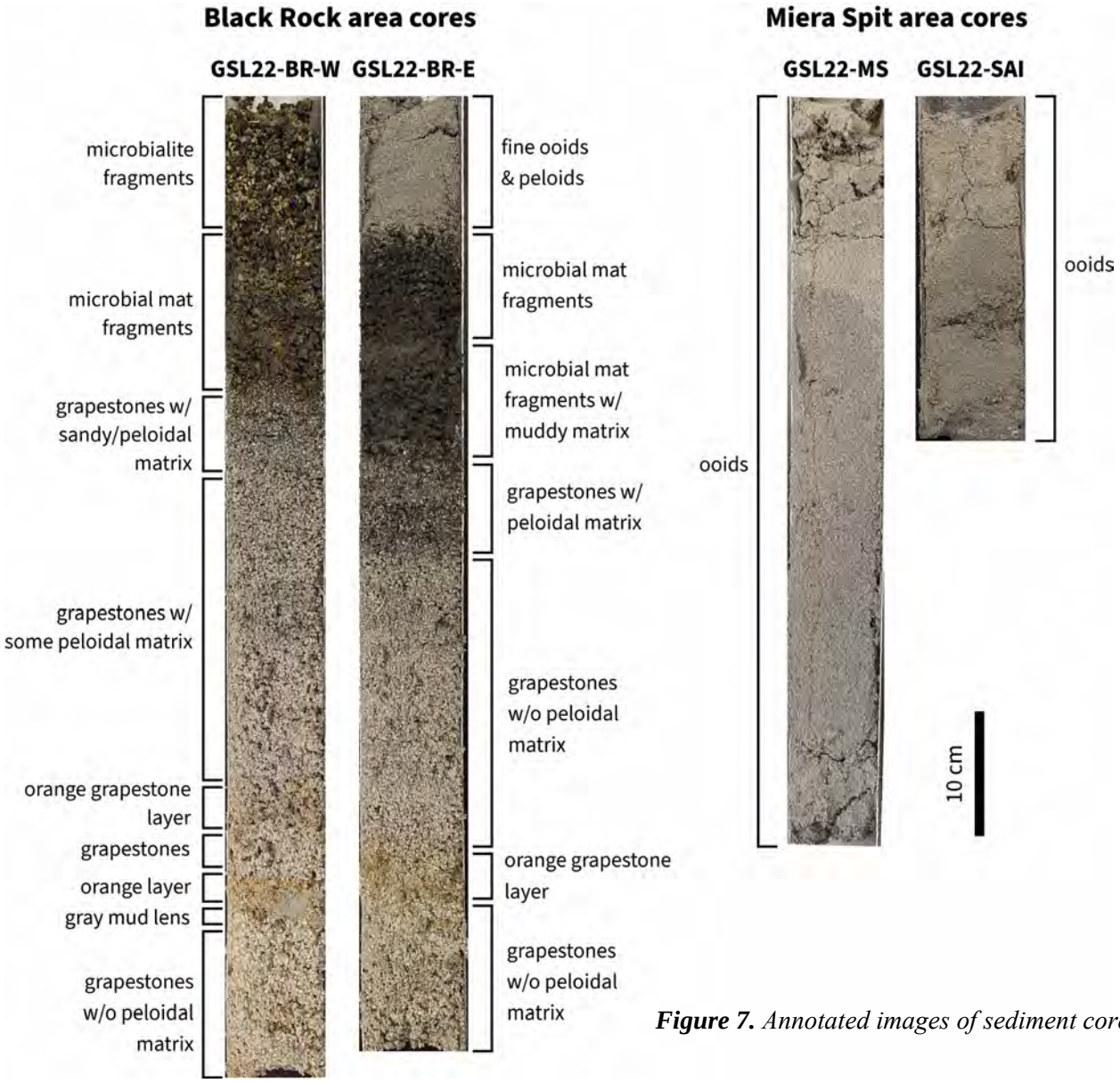

Figure 7. *Annotated images of sediment cores.*

Together, the core sedimentology data indicate that the Miera Spit area has historically been characterized almost exclusively by the production and deposition of ooid sand. In contrast, the Black Rock area was instead a grapestone factory prior to the more recent development of a continuous blanket of microbialites, overlain by a mobile and transient layer of ooid sand. Although the sets of Miera Spit and Black Rock cores were both significantly more similar amongst each set than between sets, both sets of cores displayed more subtle but systematic differences in grain size associated with their different locations along each shoreline.

UAV imagery of microbialite forms

UAV orthomosaic imagery at Black Rock reveals the orientations of exposed microbialite ridges (Figure 9). Individual microbialite ridges trend NNW/SSE along long axes. Multiple microbialites from the northwestern corner of the orthomosaic form an additional array of lineations roughly 20-25 m in length, trending NE/SW.

DISCUSSION

Wave Orientations Differ Between Sites

The differing wave orientations at the two sites reflect differences in the fetch between the two shorelines. At Black Rock, the predominant N/NNE wave orientation aligns with the long direction of the lake, and thus the longest available fetches. At a broader level, the regional geology provides an underlying factor linking basin orientation and diurnal wind patterns. Both the shape of the lake and the NNE/SSE wind directions follow the strong topography of nearby mountain ranges such as the Wasatch in the east

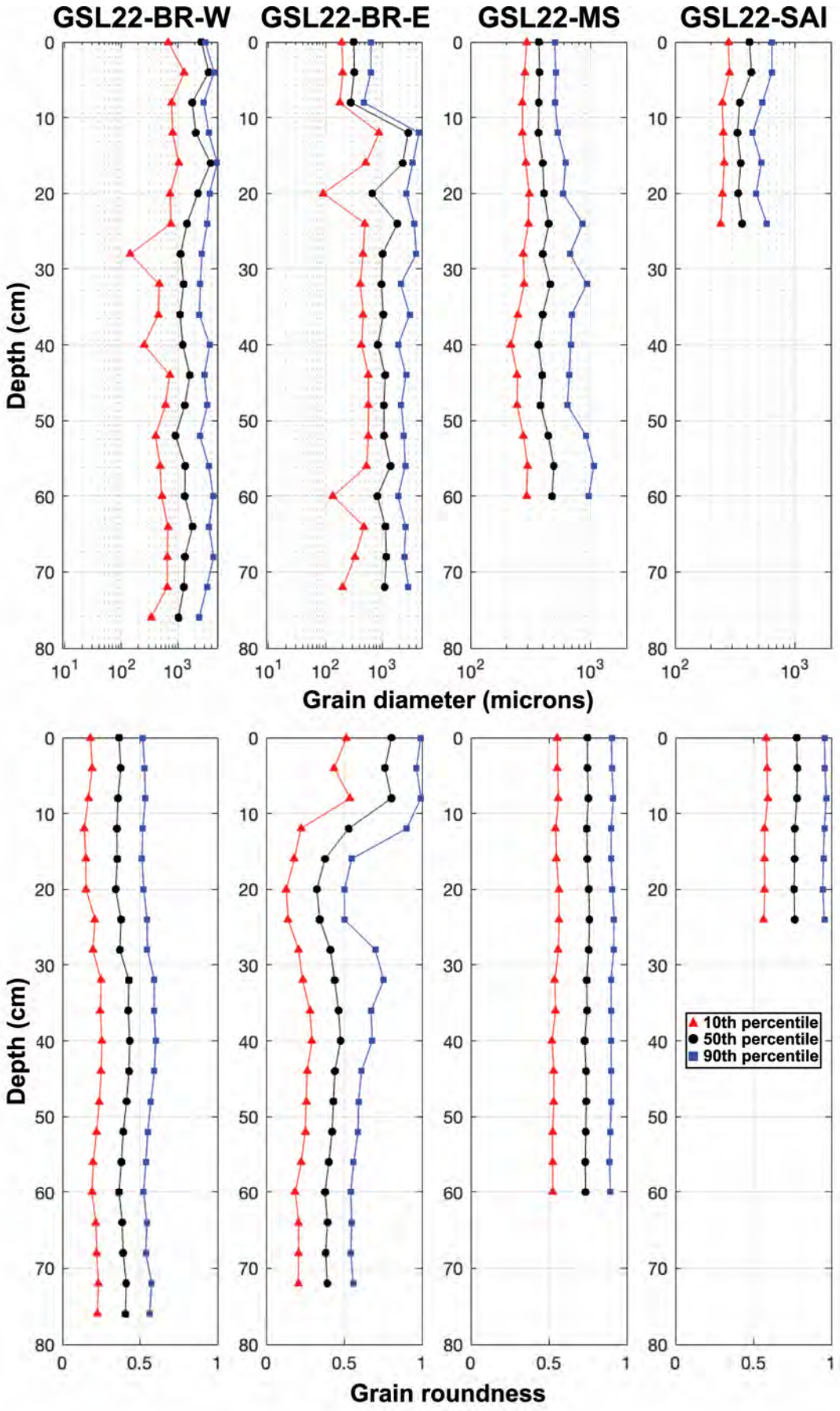

Figure 8. *Grain diameter and roundness from the four collected cores. Diameter and roundness metrics derived from Camsizer output data, where the red line indicates the 10th percentile (triangles), black indicates the 50th percentile (circles), and blue indicates the 90th percentile (squares).*

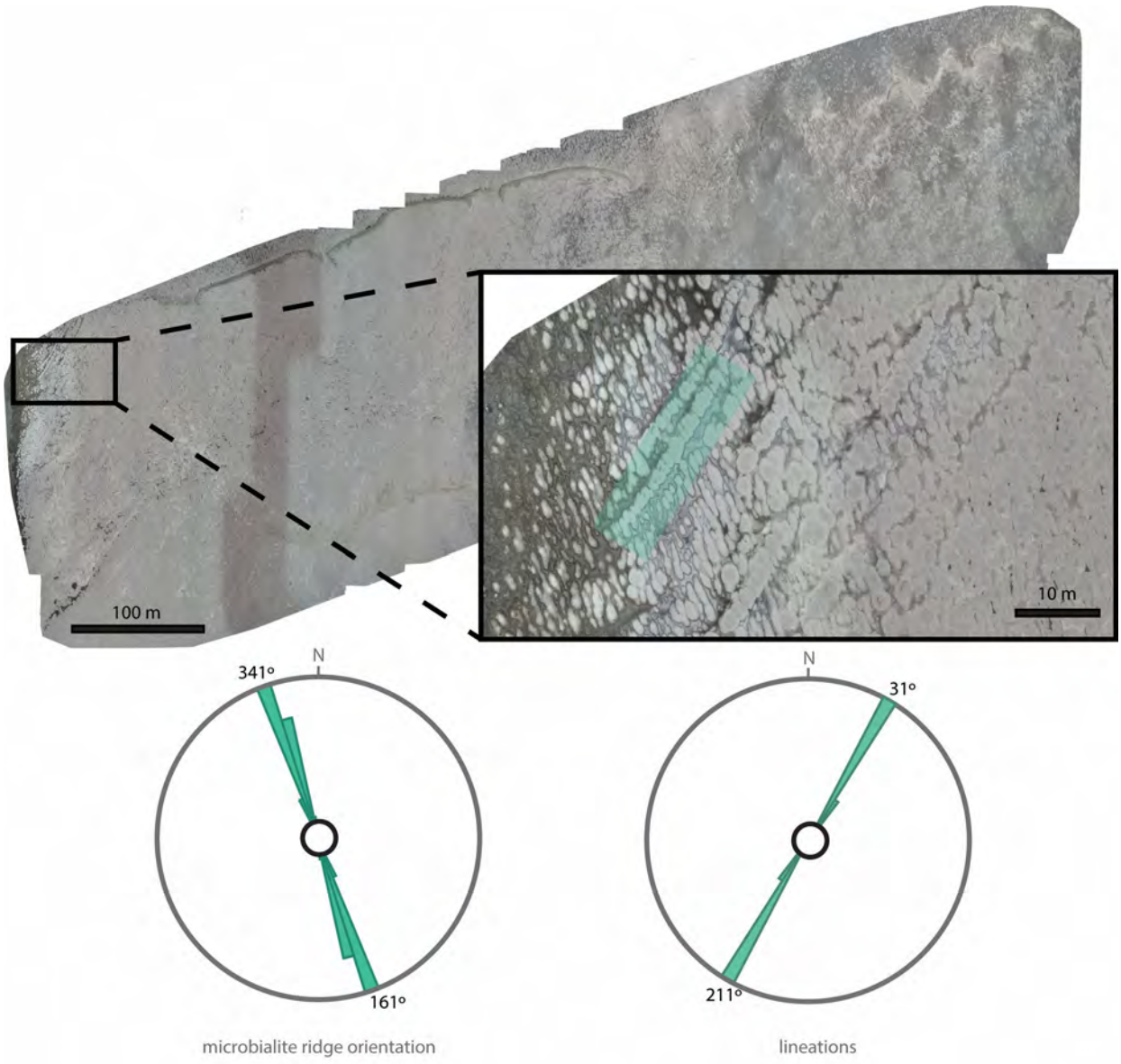

Figure 9. *UAV image of exposed microbialite ridges west of Black Rock, near buoy #1356. Individual microbialite ridges trend NNW/SSE along long axes. Multiple individual microbialite ridges group together to form arrays of lineations that trend NE/SW, highlighted in teal in image inset.*

(Figure 3). These effects are especially strong towards the south end of the lake where onshore/offshore lake breezes are funneled through the Tooele and Salt Lake valleys (Figure 3). Although the windrose for the marina (KCC02) is more complex than those in the valleys, the nearly unimodal wave directions from the north can be explained by short fetches for winds not aligned to the north.

In contrast, wave orientations at Miera Spit have a different alignment because the shoreline is nearly perpendicular to its counterpart near Black Rock. Winds from the N/NNW have short fetches obstructed by Antelope Island, Gunnison Island, and Promontory Point. Instead, most waves had a SW orientation, which is consistent with the analysis of nearby wave ripples and bar forms by Smith and others (2020). The regional wind patterns that generate these waves differ from the predominant NNW/SSE winds along the basin axis, but are aligned with the predominant southwesterly to southeasterly orientation of the strongest winds in the eastern and southern Bonneville basin from 1946–1993 compiled by Jewell (2007).

Waves, Microbialite Morphologies, and Paleoflow Indicators

At first glance, the near-unimodal orientation of waves at Black Rock provides a compelling test of microbialite ridge orientations as paleoflow indicators. However, even a first-order analysis precludes a 1:1 mapping of microbialite ridge orientation onto wave directions. First, there are at least two sets of su-

perimposed linear microbialite orientations in the area we analyzed near the Black Rock buoy, and the expected orientation of either set of linear features relative to the dominant wave direction likely depends on their origin. For example, Vanden Berg (2019) documented incipient microbialites forming on the crests of wave ripples. If some lineations in mature microbialites reflect underlying nucleation on bedforms, then the lineations should be perpendicular to the direction of the waves. In contrast, the long axes of microbialite ridges near the Black Rock buoy have a strong onshore/offshore orientation that is nearly parallel to measured wave directions. Thus, even when wave orientation reasonably influences microbialites, the orientation of lineations relative to wave features–and thus, their use as a paleoflow proxy–is complex. Additionally, other origins for strong lineations (e.g., underlying faults and fractures) must be accounted for.

A more complete understanding of potential paleoflow indicators has several spatial and temporal correlations. For example, why are the onshore-offshore lineations at Black Rock rotated with respect to measured wave orientations? One possibility is that waves observed at the buoy refract as they interact with steep and irregular bathymetry near the shoreline. Another possibility is that microbialites reflect a time-integrated signal of wave conditions, and that direct comparison to modern waves represents a recency bias. Addressing this issue requires more data on the absolute ages of microbialites and their underlying sediments from the vibracore recoveries (Figure 7). Sediments from Miera Spit and the Black Rock shoreline have not been previously dated with radiocarbon. However, radiocarbon dating of microbialites from the northern shores of Antelope Island (i.e., Bridger Bay, Buffalo Point, and White Rock Bay) and from the North Arm have suggested at least two pulses of microbialite formation from ~11.4 and 8 ka, and 3.8 and 1.7 ka (Bouton and others, 2016b; Newell and others, 2017, 2020). Furthermore, radiocarbon dating of GSL ooids from northern Antelope Island (Bridger Bay) and the North Arm (Spiral Jetty) suggest that ooids at the modern sediment surface have been slowly accumulating over the past ~6 ka (Paradis, 2019). Together, these data suggest that the microbialites on the Black Rock shoreline are likely at least 1.7 ka in age, and potentially thousands of years older. A dominant NNW orientation may therefore reflect basin orientation and tectonic effects on topography, which are stable over these time periods. The deviation from modern waves could be also explained by differences in wind patterns due to variations in Holocene climate, as well as differences in lake level and surface area. Nevertheless, because the Rohweder and others (2008) wave model performs relatively well at matching the modern wave data, we suggest that this model could be a useful tool to evaluate how different wind patterns and/or lake level in the past might better explain the microbialite ridge orientations.

Influences of Wave-driven Sediment Transport on Sedimentary Facies

Two notable sedimentological differences between the Miera Spit and Black Rock sites could be related to differences in transport mode and frequency: (1) the relatively large ooid diameters at Miera Spit (primarily upper medium sand sized, whereas most ooids elsewhere in the lake including at Black Rock are lower medium sand sized); and (2) the contrast between ooid-dominated sediments at Miera Spit and grapestone-dominated sediments (at depth in cores) at Black Rock. Here, we suggest hypotheses about how transport mode and frequency may influence the distinct sedimentology of these sites and use our data to provide an initial evaluation of these hypotheses.

Trower and others (2020) noted that the aragonite saturation state (Ω_{Ar}) of GSL water is lower than that characteristic of seawater in modern marine ooid-forming environments. This relatively low Ω_{Ar} value explains the relatively small sizes of GSL ooids because it results in relatively slow precipitation rates and therefore smaller equilibrium ooid sizes (Trower and others, 2017). Furthermore, GSL ooids are so small due to low lake water Ω_{Ar} that many of their sizes are close to the threshold below which impacts are completely viscously damped, resulting in no abrasion. Due to this effect, increasingly frequent transport events (i.e., increasing intermittency, f_{int}) cannot reduce ooid size beyond ~200 μm. Many GSL ooid sizes are close to this threshold (Figure 10). However, Miera Spit is unique in that ooids there have grown to larger sizes than observed in other locations. Within the equilibrium ooid size framework, we would therefore predict that the larger ooid sizes at Miera Spit must be associated with either less frequent transport (lower f_{int}), or more energetic transport (higher u_*) (Figure 10). Model-based estimates of intermittency of movement suggest similar values in the range of 1-2% (f_{int} = 0.01 - 0.02) at these two sites (Smith and others, 2020; Trower and others, 2020). Due to the limited size of the Miera Spit dataset, we are unable to make a robust comparison of shear velocities at the two sites to assess whether differences in u_* might be driving the larger ooid sizes at Miera Spit. An analysis of wind patterns along the eastern and southern margins of the Bonneville basin over a

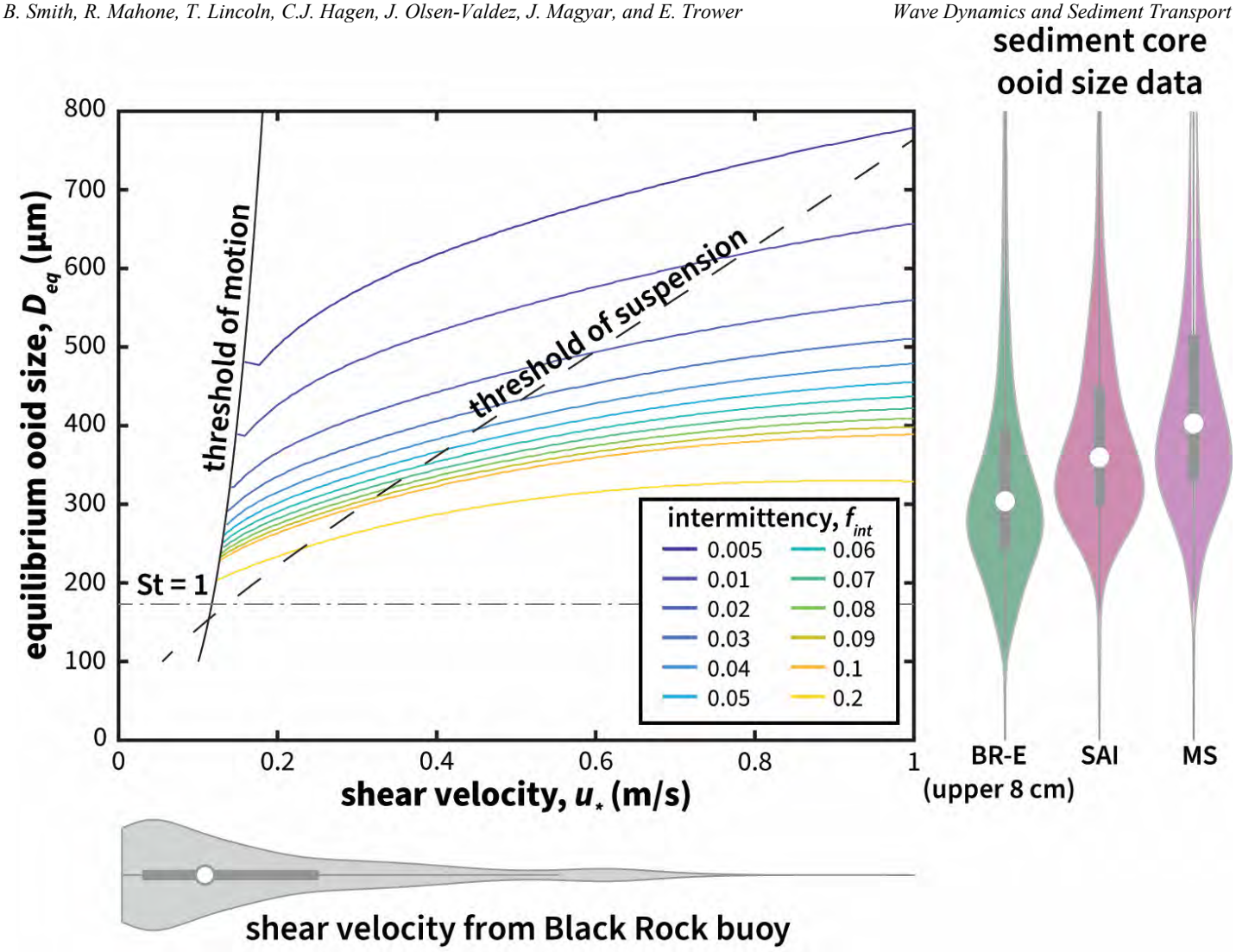

Figure 10. Plot of predicted equilibrium ooid sizes (D_{eq}) as a function of bed shear velocity (u_*) following Trower and others (2017) for a range of intermittencies (f_{int}), compared with violin plots of shear velocities from the Black Rock buoy (horizontal violin) and pooled ooid size data from the three cores that contained ooid-dominated layers (vertical violins). Solid black line shows threshold of motion, dashed black line shows threshold of suspension, and the dash-dot black line shows the viscous damping threshold (Stokes number, St = 1) below which grains cannot abrade. The larger ooids at Miera Spit could be explained by lower intermittency (less frequent transport) and/or higher shear velocity.

longer observation duration than our study indicated that the strongest modern winds were from the SW-SE over the period between 1946–1993 (Jewell, 2007). These southwesterly to southeasterly winds would have resulted in higher shear velocities at Miera Spit than at Black Rock due to the differences in fetch.

The dynamics of grapestone formation have been less thoroughly examined than those of ooids. Some workers have suggested that microbially-mediated carbonate mineral precipitation plays a key role in grapestone formation (Purdy, 1963; Winland and Matthews, 1974; Fabricius, 1977; Diaz and others, 2022). If this process is the key factor driving the formation of grapestones in GSL, we might expect to see microbial community differences between the Miera Spit and Black Rock areas. Although we did not collect microbial diversity data as part of this study, Ingalls and others (2020) did report some notable differences between ooid-dominated sediments from Bridger Bay (on the northern part of Antelope Island) and ooid-dominated sediments between Black Rock and GSL State Park. In particular, relative to samples from the GSL State Park/Black Rock site, samples from Bridger Bay lacked cyanobacteria (which are commonly implicated in driving carbonate precipitation) and had more abundant *Chloroflexi* and *Deinococcus-Thermus* sequences (Ingalls and others, 2020). However, there is no evidence directly linking this specific microbial community difference to sedimentary facies differences between those two sites. Further microbial community analyses of the Miera Spit area might help to better evaluate this hypothesis. However, it is not clear that the modern surface microbial community at each site would be representative of the community that was present when sediments at the base of each core were forming, particularly given that the modern lake microbial community

has already been influenced by the recent historically low lake levels (Frantz and others, 2022).

Alternatively, one could also speculate that physical, rather than biological, processes are responsible for the Black Rock grapestone factory. Grapestone formation is commonly thought to reflect very infrequent but very energetic transport, providing long rest periods for grains to be cemented together with transport events that can still entrain these relatively coarse compound grains. This explanation appears to conflict with the relatively similar estimates of intermittency between the two sites and our interpretation of higher shear velocities at Miera Spit based on differences in ooid size. The grapestones in the Black Rock cores could therefore reflect an older and deeper lake stage than that represented by ooids in either location. This idea is supported by our observation of grapestones in surface sediments (collected via dredge), which we only found in deeper waters (2.5-3 m water depth) off the southern Antelope Island shoreline (Figure 11). There, grapestones occurred in the troughs between microbialite mounds and ooids were rare. In contrast, we did not find any grapestones in microbialite troughs near Black Rock, suggesting that, currently, transport conditions are not as conducive to grapestone formation even in deeper

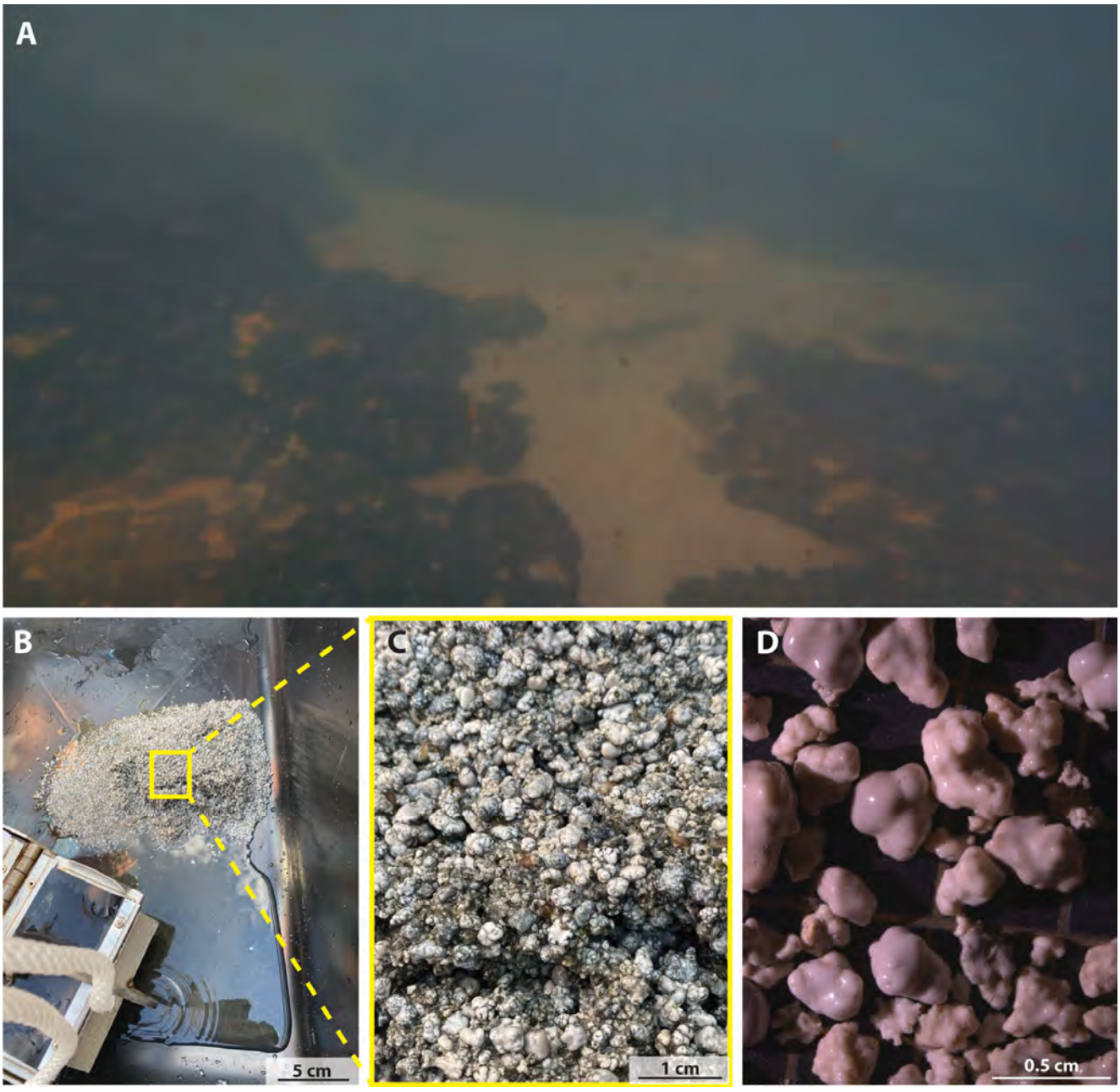

Figure 11. *Images of grapestones collected by dredge at the modern sediment surface in deeper water near the southern tip of Antelope Island. A) Grapestones occurred in patches of mobile sediment in troughs between microbialites, as illustrated in this image from a submersible remotely-operated vehicle (ROV). B-C) Grapestone-rich sediment collected by dredge (B) and zoomed-in field image of grapestone-rich sediment (C). D) Stereoscope image of grapestones from this location.*

water along that shoreline. Morphological analyses of spits associated with older Bonneville shorelines suggest that in the late Pleistocene (i.e., prior to the Gilbert episode (Oviatt, 2014)), wave transport in the lake was dominated by strong northerly to northwesterly storms (Schofield and others, 2004; Jewell, 2007). Infrequent but strong wave currents from these types of storms could be consistent with the optimal shoreline orientation and location for grapestone development in the past differing from that in the modern lake. Geochronological constraints and petrographic analysis of buried grapestone sediments at Black Rock are needed to further test this hypothesis and evaluate the roles of microbial community versus hydrodynamics on grapestone formation in GSL. Again, given the relatively good fit between the Rohweder and others (2008) model and the wave buoy data for the Black Rock area, we suggest that the model would be a useful tool to reconstruct historical wave conditions in this area.

Strengths, Weaknesses, and Potential Applications of Model

Cross-validation of wave models with buoy data provides several key takeaways for future studies of GSL across past, present, and future. In optimal cases (i.e., when high-quality, continuous wind data are available near the shoreline of interest), fetch-limited wave models yield reasonable results for key variables such as shear velocities. However, the plots of the residuals in Figures 6D-F suggest that there is unexplained structure in wave observations that are not captured by the model. A likely source of discrepancies is that some of the empirical constants in Eqns. 1 -7 were calibrated for seawater, which is less dense than GSL lake water. In particular, the drag coefficient in Eqn. 1 is sensitive to temperature and density variations of both air and water (Le Roux, 2009). A density effect could reasonably affect all three parameters in Figures 6A-C since they all involve the drag coefficient. Le Roux (2009) also notes that fluids denser than seawater—for example, those with high suspended sediment loads—produce waves that are smaller than those predicted by Eqns. 1-7. The overprediction of wave heights observed in Fig. 6A is thus consistent with a density effect.

The dependence on nearby wind stations is both a challenge and an opportunity. Even with limited results from Miera Spit and Black Rock, fetch-based wave models reasonably predict spatial differences in shear velocities and frequencies of motion that are crucial for further studies of how sedimentary facies are distributed across GSL. However, the variety of wind conditions observed at different MesoWest stations (Figure 3) strongly suggests that the quality of modeled wave parameters strongly depends on the proximity of relevant wind data. For example, onshore data from Salt Lake City (KSLC) and Tooele-Bolinder Airport differ considerably from stations on the shores of the lake itself, such as KCC02 and HATUT. At a more granular level, predicting conditions along specific shorelines requires local wind data. At present, the marina has two wind stations relevant to GSL State Park (AS768 and KCC02), but relevant wind data for Antelope Island State Park have been challenging to obtain since the loss of the Bridger Bay station in 2018. While data from other stations, such as Hat Island (HATUT), may be appropriate for sedimentary research, more proximal data is needed should these wave models become important for GSL conservation efforts and policymaking (Rohweder and others, 2008).

Even a rudimentary agreement between wave models and empirical data opens the door to using these models to study how past anthropogenic and climatic changes may have modulated the sedimentary facies we observe today. For example, construction of the causeway divided the lake into chemically distinct North and South Arms; did this causeway also change effective fetches, especially for shorelines near Black Rock? Since the causeway is recent within the context of the lake's Holocene inception, modeling pre-causeway conditions might prove instructive for interpreting both surficial and cored sediment data collected from near GSL State Park (Figure 7). For natural climatic variations, previous research has suggested that Lake Bonneville and other paleolake shorelines were associated not only with higher lake levels, but different prevailing winds (Schofield and others, 2004; Jewell, 2007). While linkages between lake level, paleoclimate, and lake chemistry strongly affect carbonate facies, fetch-limited wave models may provide a more holistic view of how paleolake levels related to sediment transport conditions beyond simple changes in water depth.

Finally, it is worth noting that the fetch-limited wave models used here and in previous work (Smith and others, 2020; Trower and others, 2020) have applications outside of sedimentary geology, such as for environmental forecasting and conservation. In fact, the Arc plugin used in these studies (Rohweder and others, 2008) was originally developed by the USGS for environmental conservation and management. While environmental forecasts and recommendations are beyond the scope of this work, we do point out that basic model-data comparisons–especially with respect to shear velocity and sediment mobility–are fundamental to future applications of lake modeling

with regards to GSL environmental conservation and policy making.

ACKNOWLEDGEMENTS

Permission to temporarily anchor buoys to the lakebed was granted by the State of Utah Department of Natural Resources under Right of Entry Permit No. 410-00698. Additional permission to access the lake shore at Miera Spit by land via Antelope Island State Park was provided by Utah Division of Parks and Recreation Special Use Permit P72-21.

REFERENCES

Abbott, B.W., Baxter, B.K., Busche, K., de Freitas, L., Frei, R., Gomez, T., et al., 2023, Emergency measures needed to rescue Great Salt Lake from ongoing collapse.

Baskin, R.L., and Allen, D.V., 2005, Bathymetric Map of the South Part of Great Salt Lake, Utah, 2005: USGS.

Baskin, R.L., and Turner, J., 2006, Bathymetric Map of the North Part of Great Salt Lake, Utah, 2006: USGS.

Baskin, R.L., Della Porta, G., and Wright, V.P., 2021, Characteristics and controls on the distribution of sublittoral microbial bioherms in Great Salt Lake, Utah: implications for understanding microbialite development: The Depositional Record, dep2.159, https://doi.org/10.1002/dep2.159

Beisner, K., Naftz, D.L., Johnson, W.P., and Diaz, X., 2009, Selenium and trace element mobility affected by periodic displacement of stratification in the Great Salt Lake, Utah: The Science of the Total Environment, 407(19), 5263–5273.

Belovsky, G.E., Stephens, D., Perschon, C., Birdsey, P., Paul, D., Naftz, D., et al., 2011, The Great Salt Lake Ecosystem (Utah, USA): long term data and a structural equation approach: Ecosphere, 2(3), art33.

Bouton, A., Vennin, E., Boulle, J., Pace, A., Bourillot, R., Thomazo, C., et al., 2016a, Linking the distribution of microbial deposits from the Great Salt Lake (Utah, USA) to tectonic and climatic processes: Biogeosciences, 13(19), 5511–5526.

Bouton, A., Vennin, E., Mulder, T., Pace, A., Bourillot, R., Thomazo, C., et al., 2016b, Enhanced development of lacustrine microbialites on gravity flow deposits, Great Salt Lake, Utah, USA: Sedimentary Geology, 341, 1–12.

Carozzi, A.V., 1962, Observations on Algal Biostromes in the Great Salt Lake, Utah: The Journal of Geology, 70(2), 246–252.

Chidsey, T.C., Vanden Berg, M.D., and Eby, D.E., 2015, Petrography and characterization of microbial carbonates and associated facies from modern Great Salt Lake and Uinta Basin's Eocene Green River Formation in Utah, USA: *In* Bosence, D.W.J., Gibbons, K.A., Heron, D.P.L, Morgan, W.A., Pritchard, T., and Vining, B.A. (eds.), Microbial Carbonates in Space and Time: Implications for Global Exploration and Production, London: The Geological Society of London. Vol. 418, 261–286.

Coastal Engineering Research Center, 1984, Shore Protection Manual. US Army Corps of Engineers. https://doi.org/10.5962/bhl.title.47829

Collins, N., 1980, Population ecology of Ephydra cinerea Jones (Diptera: Ephydridae), the only benthic metazoan of the Great Salt Lake, U.S.A: Hydrobiologia, 68(2), 99–112.

Colman, S.M., Kelts, K.R., and Dinter, D.A., 2002, Depositional history and neotectonics in Great Salt Lake, Utah, from high-resolution seismic stratigraphy: Sedimentary Geology, 148(1), 61–78.

Diaz, M.R., Eberli, G.P., and Weger, R.J., 2022, Indigenous microbial communities as catalysts for early marine cements: An in vitro study: The Depositional Record. https://doi.org/10.1002/dep2.202

Eardley, A.J., 1938, Sediments of Great Salt Lake, Utah: AAPG Bulletin, 22(10), 1305–1411.

Fabricius, F.H., 1977, Origin of marine oöids and grapestones. *In* Fuchtbauer, H., Lisitzyn, A. P., Milliman, J. D., and Seibold, E. (Eds.), Vol. 7, Schweizerbart.

Frantz, C., Gibby, C., Nilson, R., Aeschlimann, J., Athalye, R., Christensen, C., et al., 2022, Documenting a geobiological tragedy: The exposure of Great Salt Lake's microbialites and the undergraduate researchers at the vanguard: GSA Connects 2022, Denver, CO.

Homewood, P., Mettraux, M., Vanden Berg, M.D., Foubert, A., Neumann, R., Newell, D., and Atwood, G., 2022, Onshore groundwater spring carbonate mounds to lacustrine microbialites, the perplexing record of a transitional Great Salt Lake carbonate shoreline at Lakeside, Utah: The Depositional Record, 8(1), 9–38.

Horel, J., Splitt, M., Dunn, L., Pechmann, J., White, B., Ciliberti, C., et al., 2002, Mesowest: Cooperative Mesonets in the Western United States: Bulletin of the American Meteorological Society, 83 (2), 211–226.

Ingalls, M., Frantz, C.M., Snell, K.E., & Trower, E.J., 2020, Carbonate facies-specific stable isotope data record climate, hydrology, and microbial communities in Great Salt Lake, UT: Geobiology, 18

(5), 566–593.
Jewell, P.W., 2007, Morphology and paleoclimatic significance of Pleistocene Lake Bonneville spits: Quaternary Research, 68(3), 421–430.
Jones, E.F., and Wurtsbaugh, W.A., 2014, The Great Salt Lake's monimolimnion and its importance for mercury bioaccumulation in brine shrimp (*Artemia franciscana*): Limnology and Oceanography, 59(1), 141–155.
Le Roux, J.P., 2009, Characteristics of developing waves as a function of atmospheric conditions, water properties, fetch and duration: Coastal Engineering, 56(4), 479-483.
Ludwig, F.L., Horel, J., and Whiteman, C.D., 2004, Using EOF Analysis to Identify Important Surface Wind Patterns in Mountain Valleys: Journal of Applied Meteorology, 43(7), 969–983.
Mahon, R.C., Trower, E.J., Smith, B.P., Lincoln, T.A., Olsen-Valdez, J., Magyar, J.S., and Hagen, C.J., 2023, 2D Wave Spectral Data, South Arm, Great Salt Lake, Utah: DOI: https://doi.org/10.46428/sld
Newell, D.L., Jensen, J.L., Frantz, C.M., and Vanden Berg, M.D., 2017, Great Salt Lake (Utah) microbialite δ13 C, δ18 O, and δ15 N record fluctuations in lake biogeochemistry since the late Pleistocene: Geochemistry, Geophysics, Geosystems, 18(10), 3631–3645.
Newell, D.L., Vanden Berg, M.D., Fernandez, D.P., Frantz, C.M., and Jensen, J.L., 2020, Radiocarbon and u-Th double-dating and isotope geochemistry of great Salt Lake microbialites: Implications for the 14c reservoir and paleolake biogeochemical evolution: 72nd Annual GSA Rocky Mountain Section Meeting, Geological Society of America. https://doi.org/10.1130/abs/2020rm-346645
Oviatt, C.G., 2014, The Gilbert Episode in the Great Salt Lake Basin, Utah: Miscellaneous Publication 14-3, Utah Geological Survey.
Paradis, O.P., 2019, Great Salt Lake Ooids: Insights into Rate of Formation, Potential as Paleoenvironmental Archives, and Biogenicity: Ph.D. Dissertation, University of Southern California.
Paul, D.S., and Manning, A.E., 2002, Great Salt Lake Waterbird Survey Five-Year Report, 1997-2001: Utah Division of Wildlife Resources, No. 08-38.
Purdy, E.G., 1963, Recent Calcium Carbonate Facies of the Great Bahama Bank, Sedimentary Facies: The Journal of Geology, 71(4), 472–497.
Roduit, N., 2019, JMicroVision: Image analysis toolbox for measuring and quantifying components of high-definition images, Version 1.3.1. https://jmicrovision.github.io (accessed 5 April 2019).
Rohweder, J., Rogala, J.T., Johnson, B.L., Anderson, D., Clark, S., Chamberlin, F., and Runyon, K., 2008, Application of Wind Fetch and Wave Models for Habitat Rehabilitation and Enhancement Projects: Open-File Report 2008–1200, USGS.
Schofield, I., Jewell, P., Chan, M., Currey, D., and Gregory, M., 2004, Shoreline development, longshore transport and surface wave dynamics, Pleistocene Lake Bonneville, Utah: Earth Surface Processes and Landforms, 29(13), 1675–1690.
Smith, B.P., Ingalls, M., Trower, E.J., Lingappa, U.F., Present, T.M., Magyar, J.S., and Fischer, W.W., 2020, Physical controls on carbonate intraclasts: Modern flat pebbles from Great Salt Lake, Utah: Journal of Geophysical Research. Earth Surface, 125(11). https://doi.org/10.1029/2020jf005733
Tarboton, D., 2017, Great Salt Lake Bathymetry: Hydroshare.
Tripp, T.G., 2009, Production of magnesium from Great Salt Lake, Utah, USA: Natural Resources and Environmental Issues, 15, Article 10.
Trower, E.J., Lamb, M.P., and Fischer, W.W., 2017, Experimental evidence that ooid size reflects a dynamic equilibrium between rapid precipitation and abrasion rates: Earth and Planetary Science Letters, 468, 112–118.
Trower, E.J., Bridgers, S.L., Lamb, M.P., and Fischer, W.W., 2020, Ooid cortical stratigraphy reveals common histories of individual co-occurring sedimentary grains: Journal of Geophysical Research, Earth Surface, 125(7). https://doi.org/10.1029/2019jf005452
U.S. Army Corps of Engineers, 2002, Coastal Engineering Manual (No. EM-1110-2-1100).
Vanden Berg, M.D., 2019, Domes, rings, ridges, and polygons: Characteristics of microbialites from Utah's Great Salt Lake: The Sedimentary Record, 17(1), 4–10.
Winland, H.D., and Matthews, R.K., 1974, Origin and significance of grapestone, Bahama islands: Journal of Sedimentary Research, 44(3).
Wurtsbaugh, W.A., 2009, Biostromes, brine flies, birds and the bioaccumulation of selenium in Great Salt Lake, Utah: Natural Resources and Environmental Issues, 15(2), 1–13.
Wurtsbaugh, W.A., Gardberg, J., and Izdepski, C., 2011, Biostrome communities and mercury and selenium bioaccumulation in the Great Salt Lake (Utah, USA): The Science of the Total Environment, 409(20), 4425–4434.

Great Salt Lake Wetland Vegetation and What it Tells Us About Environmental Gradients and Disturbance

Becka Downard
Utah Geological Survey, Salt Lake City, Utah, beckad@utah.gov

10.31711/ugap.v51i.140

ABSTRACT

Great Salt Lake (GSL) wetlands support more than 300 species of migratory birds and provide many ecosystem functions, including flood and drought attenuation, dust mitigation, and water quality improvement. Wetland vegetation is a key factor in providing those functions and can also tell us about how healthy a wetland is. From 2013 to 2022, 135 GSL wetlands were surveyed to develop a multi-metric index of GSL wetland condition. That wetland condition data, along with environmental variables like soil and water chemistry and physical disturbance, are summarized here as 1) an ecological characterization of the three main types of GSL wetlands, 2) a description of how the plant community differs across environmental and anthropogenic disturbance gradients, and 3) assessment of the major risks to GSL wetland health. GSL wetland plant species are generally resistant to environmental disturbance because of the anatomical and physical adaptations that allow them to survive in dynamic wetland environments. However, land use conversion and the rapid expansion of invasive species, the major threats to GSL wetland health, have seriously degraded wetland condition around GSL. In addition to being useful in wetland monitoring and assessment, the results presented here can also identify wetlands in need of enhanced protection or those with restoration potential as well as setting realistic wetland restoration goals for the region.

INTRODUCTION: THE GREAT SALT LAKE ECOSYSTEM

Great Salt Lake (GSL) and its surrounding wetlands are often described in superlative terms: great, immense, critical, and essential. GSL is the largest saline lake in North America and eighth-largest in the world. More than 1,500 square kilometers of wetlands thrive on the margins of GSL where freshwater flows toward the lake (Figure 1). Millions of birds representing 338 species rely on GSL wetlands to power their migrations across the Western Hemisphere (Sorenson and others, 2020). Studying the plant community that thrives in GSL wetlands highlights significant features of natural history, the impacts of wetland management and human disturbances the GSL ecosystem experiences, and how to best protect and restore the wetlands in the future.

GSL Natural History

GSL is all that remains of historical Lake Bonneville which occupied much of northern and western Utah 15,000 years ago but shrank as the regional climate became much drier (Inkenbrandt, 2021). GSL is a terminal lake with no surface water outlets, water only leaves through evaporation. The solutes rivers bring to GSL have concentrated over time and currently the lake is more than three times saltier than ocean water, ranging in salinity between 125 and 185 g/L (U.S. Geological Survey, 2023). The Bear, Weber, and Jordan rivers provide approximately 90% of the water to GSL. The GSL watershed occupies a total of 91,908 square kilometers, an immense area within which changes in climate, water availability, and water quality can impact the GSL ecosystem (Zedler and Kercher, 2004; Ramsey and others, 2009). The rivers supplying GSL terminate in massive deltas composed of diverse wetland types, from sparsely vegetated saline playas to freshwater marshes and ponds.

Wetlands are defined by three characteristics: the presence of water for part of the year, soils with low oxygen (hydric soils), and plants adapted to flooding and low oxygen (Mitsch and Gosselink, 2015). Within that definition, a variety of environmental conditions create diverse wetland types with their own suite of ecosystem functions, from water quality improvement to hydrologic and climate regulation (Wetzel, 2006). The diversity of wetland types in GSL river deltas as well as their expansive size allows the ecosystem to support many species of birds, from tiny Snowy plovers to massive American white pelicans (Aldrich and Paul, 2002).

Though GSL wetlands are a reliable place for migratory birds to feed and nest, they are hardly static. Wetlands are dynamic habitats, shifting between

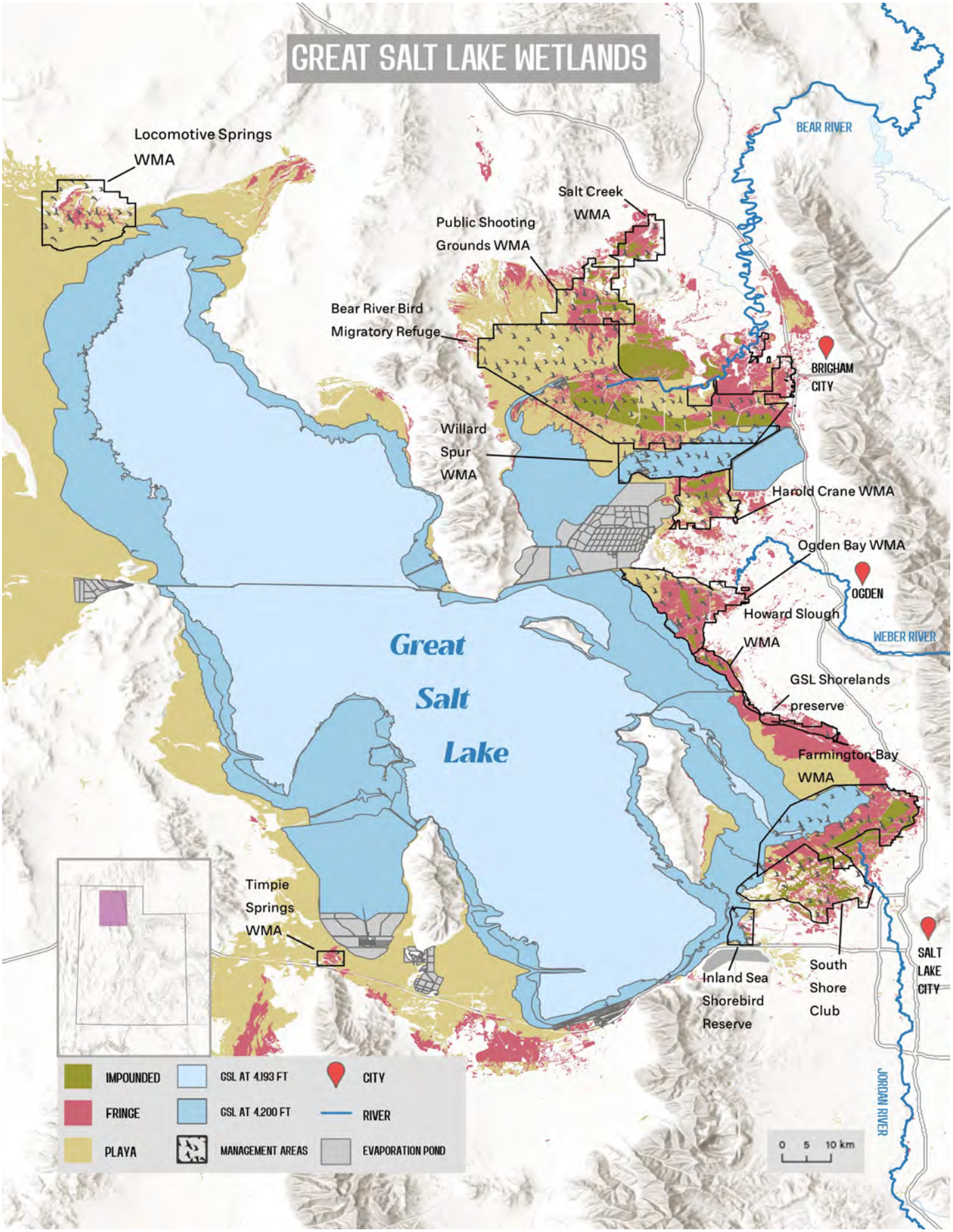

Figure 1. *Great Salt Lake ecosystem includes the lake and 1,500 sq. km of wetlands. Map by Grant Mauk. Wetlands layer (U.S. Fish and Wildlife Service, 2018), rivers and lakes layer (U.S. Geological Survey, 2020), Digital Elevation Model (Quantum Spatial, Inc, 2017)*

flooded and dry over the growing season and bridging the transition between aquatic and terrestrial environments; GSL wetlands are especially dynamic. Terminal lakes fluctuate in area much more than other lakes and this has big implications for GSL wetlands (U.S. Geological Survey, 2023). In high water conditions, the hypersaline waters of GSL can rise to inundate the wetlands, but as the lake retreats during drought, wetlands occupy the lakebed. These changes in area are significant; by one estimate, 180 square kilometers of lakebed are exposed for every foot in elevation that GSL falls (Aldrich and Paul, 2002). Within the wetland complexes, changes in water availability shift the boundaries between terrestrial, wetland, and fully aquatic environments.

GSL Human History

Peoples of the Ute, Paiute, Goshute, and Shoshone nations utilized GSL wetlands for centuries, but European settlers have left the most distinct marks on the system (Madsen, 2015). When John C. Fremont saw the Bear River delta in 1843, he described the sound of birds taking off as having "wings of thunder" because the birds were so numerous. European settlers arrived in the Salt Lake Valley in 1847 and immediately began diverting tributaries of the Jordan River to support agriculture. The Transcontinental Railroad was completed at the northern end of GSL in 1869 bringing industry and transportation of agricultural goods (Baxter and Butler, 2020). By the 1920s the Bear River delta had been dewatered so severely that avian botulism was leading to massive bird die-offs in the few locations migratory birds found habitat (Wilson and Carson, 1950). Local communities pressed Congress for the establishment of a federal wildlife refuge in the Bear River Delta and the first act of refuge building was the construction of a series of dikes to hold water in the river delta when it was available in the spring and manage drawdown more slowly during the irrigation season (Downard and Endter-Wada, 2013). This intense impounded wetland water management practice was successful in preserving migratory bird habitat and has been adopted by state waterfowl management areas, private hunting clubs, and conservation areas (Figure 1) (Downard and others, 2014).

According to both researchers and stakeholders, upstream consumptive water use and subsequent drought downstream is the primary threat to GSL wetlands and the lake itself (Wurtsbaugh and others, 2017; Utah Division of Water Quality, 2019). In the last century, the elevation of GSL has fallen approximately 11 feet due to diversion of surface water for human needs (Wurtsbaugh and others, 2016). In October 2022, GSL fell to a record low elevation of 4,188.7 feet which exposed thousands of square kilometers of lakebed (U.S. Geological Survey, 2023). Water quality threats, most notably legacy phosphorus bound to soils, also impact the GSL ecosystem and become more problematic as water availability decreases (Utah Division of Water Quality, 2014). Invasive species, especially *Phragmites australis*, complicate the water situation even further by changing how water flows across the very flat landscape and altering nutrient cycles in wetlands (Kettenring and others, 2020).

GSL Wetlands Ecology and Ecosystem Services

The path surface water follows through GSL wetlands from river to lake is a complex mix of deliberate management actions and unintended consequences of upstream water diversions and nearby water discharges. GSL wetlands are divided into three classes—impounded, fringe, and playa wetlands— that shift in area according to where water is available and how long and deep flooding is. Impounded wetlands are the most deeply flooded wetland class and are flooded for the longest part of the year. Fringe wetlands may be flooded nearly as deeply as impounded wetlands, but water depth often fluctuates between flooded and dry stages over the growing season. Playa wetlands are often not flooded, but saturated. The relatively permanent flow of water into impounded and fringe wetlands keeps them fresh to brackish, especially compared to the saline waters of playa wetlands and GSL.

Wetland vegetation is both a defining feature of wetlands and an indicator of the ecosystem functions wetlands perform and integrates the environmental stresses and anthropogenic disturbances a wetland faces over time (Moor and others, 2017). Differences in the growth form, life cycle, wetland indicator status, and habitat specificity of plant species present in wetlands vary over gradients of water regime, management history, and disturbance (Lytle and Poff, 2004). Wetlands present a suite of challenges to plant life and wetland species have a number of common adaptations that allow them to grow and reproduce. A wetland plant in this region must deal with unpredictable water regimes, soil anoxia when water is present and drought stress when water is absent, a range of salinities, and periodic catastrophic flooding. Wetland environmental gradients, especially water depth and salinity, act like a sieve, filtering the species that can occupy that space (Van Der Valk, 1981).

Water regime—the pattern of flooding and drying in a wetland— is largely considered the most im-

portant factor in determining the wetland plant community (Mitsch and Gosselink, 2015). In wetlands with relatively permanent flooding, perennial species with specialized adaptations to flooding like aerenchyma and floating seeds are dominant (Cronk and Fennessy, 2001). Wetlands that fluctuate between flooded and dry states more frequently (i.e., those with more seasonal hydroperiods) have a unique suite of species as well, often rapidly growing species with dense networks of rhizomes that allow clonal species to share gases when wetlands are flooded and water when wetlands are dry (Cronk and Fennessy, 2001). Temporarily or ephemerally flooded wetlands in turn tend to have communities dominated by annual species, those that can complete their lifecycle in a single growing season if conditions are right (Keddy, 2010).

In addition to the broad life history traits outlined above, botanists can also characterize how specific a species' ecological requirements are (i.e., how conservative their habitat is) and the complementary measure of how tolerant it is to ecological or anthropogenic disturbance. Highly conservative species with a Coefficient of Conservatism (CC score) of 10 are only found in a specific type of habitat and are sensitive to disturbance (Lopez and Fennessy, 2002). Species that occupy a wider range of habitat types and tolerate more disturbance have lower CC scores. The most successful and widespread invasive species tend to be disturbance specialists—species that can exploit a disturbance that leaves exposed soils and elevated water nutrients—and have a default CC score of zero (Hazelton and others, 2014).

Wetland condition is analogous to ecosystem health or biological integrity and is most often measured by the plant community because the species occupying a wetland integrate multiple impacts over time. Ecologically, wetland condition is the ability of a plant community to maintain its structure and function, compared to wetlands in undisturbed locations. A wetland in good condition looks and functions similarly to pristine wetlands, whereas wetlands in poor condition have experienced enough disturbance that they no longer support the same plant community or ecosystem functions (Davies and Jackson, 2006). Unlike birds or macroinvertebrates, plants cannot migrate when conditions get tough. Some plant species can abide in places with high levels of disturbance where other species will be eliminated, and a multimetric index (MMI) captures the ways disturbance tolerators or more sensitive species shape the wetland community (Magee and others, 2019). An MMI is a combination of multiple variables describing some aspect of the plant community that changes with increasing anthropogenic disturbance (i.e., it measures the overall health of a wetland).

A discussion of stress and disturbance terminology is merited before jumping into the methods and results. Stress, natural disturbance, and anthropogenic disturbance have similar effects on the wetland plant community but differ in origin and the time scale they operate at. In this paper, stress is a factor that limits a plant's ability to grow and reproduce, like living in an environment with limited oxygen, extreme temperatures, or low nutrient availability (Grime, 1989). Stress is a relatively constant feature of the environment, while disturbance is more episodic (Borics and others, 2013). Flooding and drought, fire, herbivore grazing, and plant species invasions are common natural disturbances in wetlands that can alter the plant community (Cronk and Fennessy, 2001). Anthropogenic disturbances include converting land uses from natural types to developed sites, diverting water from streams or adding points of discharge with water quality contaminants (Miller and Wardrop, 2006). Though it is possible to define those three terms separately on paper, it is difficult to distinguish between the three in the wetlands because anthropogenic disturbances like water diversion and climate change can increase the frequency of natural disturbances and lead to long-term stress. Further, plant communities respond similarly to stress and both types of disturbance, often becoming less diverse and dominated by fast-growing species (Cronk and Fennessy, 2001). This paper focuses on plant community adaptations to environmental stresses of the dominant species in each wetland class as well as the overall wetland response to anthropogenic disturbances.

Impounded wetlands form the heart of managed wetland complexes where dikes impound the terminus of a river or stream. Impounded wetlands are the only GSL wetland class that has firm boundaries because they are defined by the presence of dikes or berms that are designed to increase the depth and length of time this wetland class is flooded. Water depth is managed throughout the year with headgates. The primary goal of impounded wetland management is to grow submerged aquatic vegetation (SAV) that supports migrating waterfowl (ducks, geese, and swans) (Figure 2a), though emergent vegetation is also a component of the impounded wetland community (Aldrich and Paul, 2002).

Fringe wetlands are defined by emergent vegetation that forms deltas where water sources like streams, springs, and impounded wetland water control structures discharge onto the bed of GSL (Figure 2b) (Utah Division of Water Quality, 2016). The mix of short and tall emergent species provides critical nesting habitat for waterfowl and ample food for waterbirds like white-faced ibis and egrets. The extent of fringe wetlands changes based on freshwater availa-

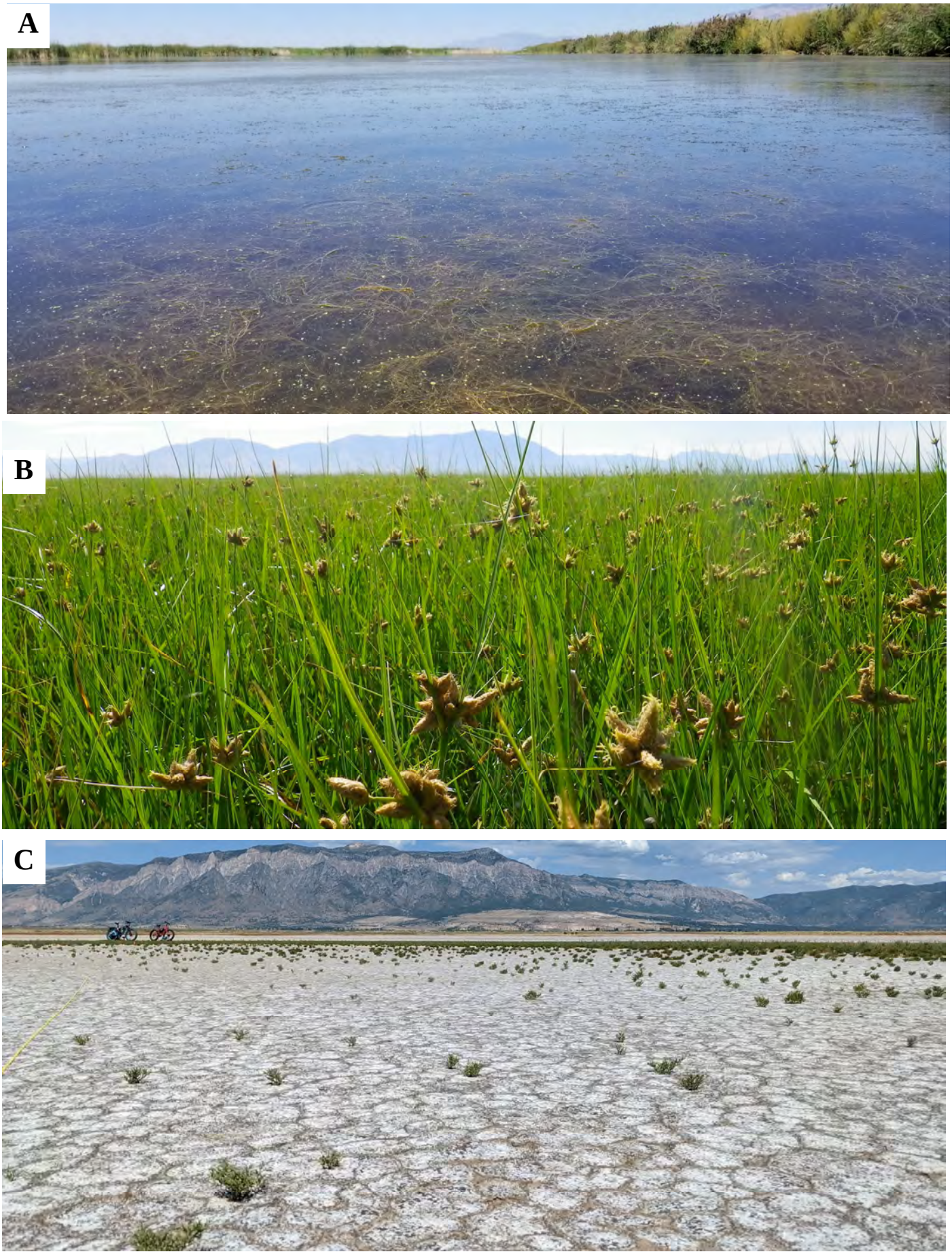

Figure 2. *Characteristic examples of A) impounded, B) fringe, and C) playa wetlands near GSL.*

bility, expanding where water is perennial and contracting when water is diverted elsewhere. Fringe wetlands are located outside the boundaries of impoundments and are commonly referred to as marshes and meadows.

Playa wetlands are ephemerally flooded or saturated, sparsely vegetated, often saline wetlands that support astounding populations of shorebirds, who probe the soils for macroinvertebrates (Figure 2c). This class contains two types of features, playas and mudflats. Playas are a geological feature that form in depressions often supported by shallow groundwater or precipitation (Oviatt, 2014). Mudflats are the exposed surfaces of drying lakes and wetlands. Though the processes that form playas and mudflats are different, they support the same vegetation communities and will be considered together here. As GSL has retreated over the last decade, playa wetlands have expanded to occupy the exposed lakebed. Depending on GSL elevation, playa wetlands account for as little as 40% or as much as 85% of the wetland acreage around GSL (U.S. Fish and Wildlife Service, 2018).

GSL WETLAND SURVEY METHODS AND ANALYSIS

The wetlands around GSL are a critical resource for Utahans and of great interest to many stakeholders, including the state agencies that pursued the projects described below. The data presented here are the result of more than ten years of vegetation monitoring in GSL wetlands with the overall objective of developing an MMI to measure wetland condition specific to this region. Altogether we have detailed vegetation data from five separate surveys that sampled 135 wetlands from all three GSL wetland classes. A summary of the site selection, field methods, and data analysis are presented below with citations to the supporting field protocols and detailed analysis documentation.

Site Selection

Survey sites were primarily selected via Generalized Random Tessellation Stratified (GRTS) samples. GRTS sample design creates spatially balanced samples that can be stratified by factors of interest and include factors that create unequal probabilities (Stevens and Olsen, 2004; Kincaid and others, 2019). Site selection for surveys conducted in 2019–2022 built on prior work with one key update: wetlands remained in the sample regardless of whether they had surface water during the time of sampling, in contrast to earlier surveys that required the presence of surface water to sample.

Forty impounded wetlands were surveyed in 2019, adapting protocols established in 2012. The GRTS samples were stratified so that an equal proportion of sites were drawn from the major watersheds of GSL (Bear, Weber, and Jordan) and an equal proportion of each size class (small, medium, and large) was represented (Utah Division of Water Quality, 2020) (Figure 3). The first fringe wetland surveys were conducted in 2013 and 2015 and gathered vegetation data from a targeted selection of sites. Rather than a random sample, project leaders selected sites they believed would represent the best and worst condition wetlands to capture the full range of condition possible (Utah Division of Water Quality, 2016). In 2020, 15 sites from a GRTS sample with no stratification were assessed to bring the collective number of fringe sites surveyed to 50. Finally, a 50-site GRTS sample of playa wetlands was surveyed in 2022. The playa sample was stratified by wetland system (palustrine or lacustrine) and an unequal probability factor was added to select more sites from HUC12 watersheds with higher percentage of riverine wetlands (Utah Division of Water Quality, 2022).

Field Methods

For all surveys, data were collected from 100 meter transects, though the placement and segmentation of those transects was adapted for each wetland class to capture the most representative vegetation (Utah Division of Water Quality 2020, 2022). Vegetation data was central to the analysis of each project, so each site visit was conducted during the index period that began on July 1 and ended on September 30, which captures the most representative and reliably identifiable vegetation. Impounded wetlands were visited twice during the survey, once during the early summer and later in the season. For all surveys, the identity and absolute cover of each species present along the 100-m transect was recorded as well as cover of bare ground, open water, and filamentous algae.

Water (surface water or pore water) and composite soil chemistry as well as on-site disturbance data were gathered in addition to vegetation data. Observations of physical disturbance within a 100-meter buffer surrounding the center point of each transect were recorded as well. Further details of laboratory analyses, data quality control, and individual project objectives are elaborated on in each survey's Sampling and Analysis Plan (Utah Division of Water Quality 2020, 2022).

Landscape disturbance data were gathered after field work from statewide geospatial layers. Small (100-meter) and large (1-kilometer) buffers were added to the center point of each wetland sampled and the prevalence of the following features were calcu-

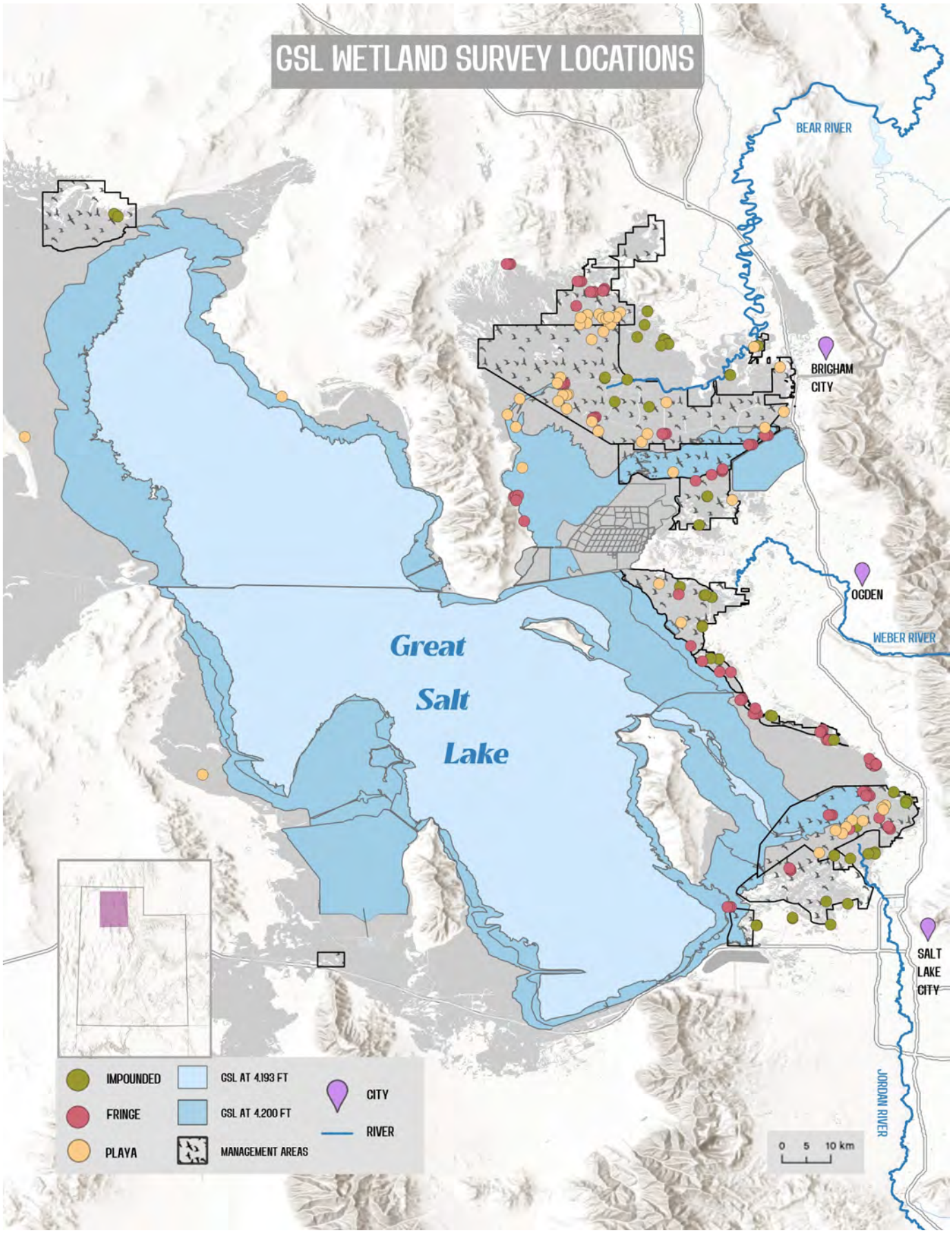

Figure 3. *Location of wetlands surveyed for this ecological characterization. Map by Grant Mauk. Wetlands layer (U.S. Fish and Wildlife Service, 2018), rivers and lakes layer (U.S. Geological Survey, 2020), Digital Elevation Model (Quantum Spatial, Inc, 2017).*

lated within those buffers: 1) agricultural and developed land uses; 2) impervious surface; 3) length of roadways; 4) water right points of diversion; 5) permitted point source and stormwater discharges; and 6) mineral mines and oil and gas wells (U.S. Geological Survey, 2019a and 2019b; Utah Geospatial Resource Center, 2020a, 2020b, 2020c, and 2020d).

Analysis

Data analysis occurred in three stages. First, a cumulative Disturbance Score was calculated for all GSL wetlands, which was in turn used to define reference condition for each wetland class. Second, a large group of vegetation metrics were calculated and then screened for their utility in measuring condition and built into MMI's. The third stage used the disturbance and condition indices to estimate the influence of individual anthropogenic disturbances on wetland condition. See Downard (2021) for further details of the analyses.

The Disturbance Score, modeled on the Anthropogenic Stress Indices developed for the National Wetland Condition Assessment (NWCA) is a cumulative measure of disturbance a wetland experiences based on nine measures (Lomnicky and others, 2019). The first four measures quantify land use impacts within the large one-kilometer site buffers: agricultural and developed land uses, extractive industry claims, and hydrologic modifications (impervious surface, roadways, diversions, and discharges). The fifth human disturbance metric is a standardized summary of the four large buffer metrics. Two disturbance measures are captured within the small 100-meter buffer: hydrologic modifications and vegetation removal by cattle grazing and herbicide use. The final two disturbance metrics that form the overall Disturbance Score were recorded from site visits—the number of heavy metals in soils that exceeded background concentrations and the relative cover of introduced species. Soil metal background concentrations were established specifically for GSL wetlands. Metals and metalloids selected for inclusion followed the recommendations of Nahlik and others (2019) and used a regression approach developed by Alfaro and others (2015).

Defining reference condition, the baseline against which wetland condition is compared to, is a critical step in any condition assessment. The simplest definition of reference condition is pristine, the state of a wetland that is not impacted by human activities (Stoddard and others, 2006). Wetland condition then measures how different a wetland is from reference (Davies and Jackson, 2006). However, un-impacted wetlands are nearly impossible to find, given the widespread nature of anthropogenic disturbance. Instead GSL wetland reference condition was defined as Least Disturbed Condition (LDC): the best available condition of wetlands is assumed to be those wetlands with the least amount of disturbance, accepting that human disturbance has impacted all wetlands to some degree. Defining LDC for each wetland class was an iterative process of determining the threshold of each type of disturbance included in the Disturbance Score that separated LDC from the more disturbed wetlands, following the lead of Herlihy and others (2019a). Choosing reference condition based on distributional approaches, as done here, is common and controversial. Assumptions about the impacts of disturbance, outliers and skewed data, and lack of minimally disturbed conditions can distort the results, thus the discussion of condition and risk should be interpreted with that knowledge in mind (Reynoldson and others, 1997).

To build an MMI of condition we calculated 211 potential vegetation metrics that captured some aspect of the plant community which were in turn sieved through a series of screens to test for applicability as a measure of wetland condition. Each vegetation metric fell into one of six categories: taxa composition, life history traits, hydrophytic status, sensitivity or tolerance to disturbance, vegetation structure, and floristic quality (Table 1). The PLANTS database lists the status of all plant species as native or introduced, life history and growth form traits, and their wetland indicator status (U.S. Department of Agriculture Natural Resource Conservation Service, 2020). Sensitivity and floristic quality measures of each species were retrieved from the NWCA database (U.S. Environmental Protection Agency, 2016). Differences in metrics between wetland classes were assessed using two univariate statistical methods. First, an Analysis of Variance (ANOVA) was conducted to determine if a metric varied by wetland class. If the ANOVA was significant ($p \leq 0.05$) then we conducted a pairwise t-test between combinations of wetland classes to determine which had significant differences.

Magee and others' (2019) NWCA data analysis provided guidance on sifting through potential MMI metrics by identifying those that span an appropriate range, are repeatable and responsive to disturbance. Skewed metrics or those observed over a very narrow range were removed as well as metrics that varied significantly over a single growing season (repeatability screen) or failed to distinguish between high and low disturbance sites (responsiveness screen). The 35 metrics that passed all three screens were equally scaled and standardized then assembled into unique MMI's of three, four, and five metrics. These candidate MMI's were screened through tests

Table 1. *Plant community attributes calculated based on wetland survey data.* Bold attributes are those selected in the final MMI.

Category	Metrics
Taxa Composition	Species Richness, Native Species [a], Introduced Species [a], Simpson's Diversity [b], Shannon-Wiener Diversity [b], Species Evenness
Life History [b]	Annual species, Perennial species, Forb species, Graminoid species, Monocot species, ***Dicot species***
Hydrophytic Status [b]	Obligate species, Obligate + Facultative Wetland species, ***Facultative Wetland Species***, Facultative Species, Facultative Upland + Upland Species
Sensitivity/Tolerance to Disturbance [b]	Sensitive Species, Intermediate + Insensitive Species, Tolerant Species, ***Highly Tolerant Species***
Vegetation Structure [b]	Emergent Species, Submerged Species, Floating Species, Algae, Bare Ground
Floristic Quality [c]	Mean Coefficient of Conservatism (CC), Total CC, Cover-weighted Mean CC, Floristic Quality Index, Cover-weighted Floristic Quality Index

a – metrics include total richness, relative richness, total cover, relative cover, mean cover, frequency, and importance
b – metrics calculated for all species present, native species only, and introduced species only
c – calculated for all species and native species only

of redundancy, sensitivity, and repeatability. The MMI described below has component metrics that are not highly correlated with one another (redundancy screen), distinguish between high and low condition wetlands (sensitivity screen), and remained consistent over the index period (repeatability) (Magee and others, 2019).

The final Great Salt Lake Vegetation-based Multi-Metric Index (GSL-VMMI) is a combination of three metrics: dicot species richness, cover of highly tolerant species, and cover of facultative wetland species. Each of those metrics increases with disturbance, thus wetlands in good condition have more monocot species than dicot species and higher cover of species that are less than highly tolerant of disturbance and obligate wetland species. Thresholds for good, fair, and poor condition were established individually for each wetland class based on the condition scores for sites that were in least disturbed reference condition (Magee and others, 2019). Setting condition thresholds based on a distribution is suboptimal because it creates a moving target with each new survey. However, it is the most realistic option for this dataset.

The final part of the analysis was to conduct a risk assessment calculating the influence of individual anthropogenic disturbances on wetland condition, measured as relative and attributable risk (Herlihy and others, 2019b). Relative risk is a ratio that expresses the likelihood that a wetland will be in poor condition when a particular disturbance is high. Attributable risk represents the proportion of wetlands in poor condition that could improve if a particular disturbance is removed. Thresholds for distinguishing between high and moderate levels of a particular disturbance were set by analyzing the distribution of a particular disturbance and setting "high" at a point that marked the 33rd percentile for disturbances with normal data distributions or the inflection point for disturbances with skewed distributions.

Risk estimates are calculated based on contingency tables that tabulate the number of wetlands in two condition categories— Not Poor Condition and Poor Condition— and two disturbance categories—High Disturbance and Not High Disturbance (Kincaid and others, 2019; R Core Team, 2020). The risk analysis assessed both the metrics that were part of the overall Disturbance Scores and individual parts of composite metrics (e.g., diversions were assessed separately from discharges) as well as potential sources of disturbance that are of particular interest to GSL stakeholders, like soil phosphorus and individual soil metals. Three significant assumptions go into the risk analysis: 1) there is causality between a disturbance and condition; 2) a disturbance is reversible; and 3) disturbances are independent (Herlihy and others, 2019b). Both risk calculations are bounded by 95% confidence intervals and require large datasets to detect statistically significant risks. Even with this relatively large dataset, the error bars on the risk estimates are quite large. Further, if any cell in the contingency table is empty (e.g., there are no sites in poor condition with high disturbance from mines) the estimate for both risk factors will be zero. The risk results should be taken with these grains of salt— big assumptions, big error bars, and missing estimates— in mind.

RESULTS: GSL WETLAND ECOLOGICAL CHARACTERIZATION

We used the data gathered in GSL wetlands to answer three questions. First, what plants characterize GSL wetlands and how are they similar or different between classes? Second, within a given wetland class, what factors drive variation in the plant community? Finally, over all GSL wetland classes, what disturbances represent the most significant risk to wetland condition?

What Plants Characterize GSL Wetlands?

Over the nine years of plant surveys, we found 123 unique species across three GSL wetland classes. Average species richness in GSL wetlands is five species per site, so even though we have a large species list, only 13 species were common, defined by being found in at least 10% of all GSL wetlands surveyed here, and most species were rare (Downard and others, 2018). The most common species varied according to the wetland class being surveyed (impounded, fringe, or playa wetlands), though species are not exclusive to wetland class and can be found in multiple wetland classes.

The first step in characterizing the community is to calculate and plot an ordination of the data, which summarizes complex patterns by visually highlighting species and sites that group together (McCune and Grace, 2002). Figure 4 is a non-metric multidimensional scaling (NMDS) output of GSL wetland plant communities calculated based on the relative cover of the most common GSL wetland species. Each color-coded point represents a wetland we sampled and the location along the vertical and horizontal axes show how similar or different the sampled plant communities are: points closer to each other have more similar communities and points farther from each other are more different. The text and grey points represent the center of a plant species' area and indicate the most important species in that part of the ordination.

Along the horizontal axis (NMDS 1), sites are

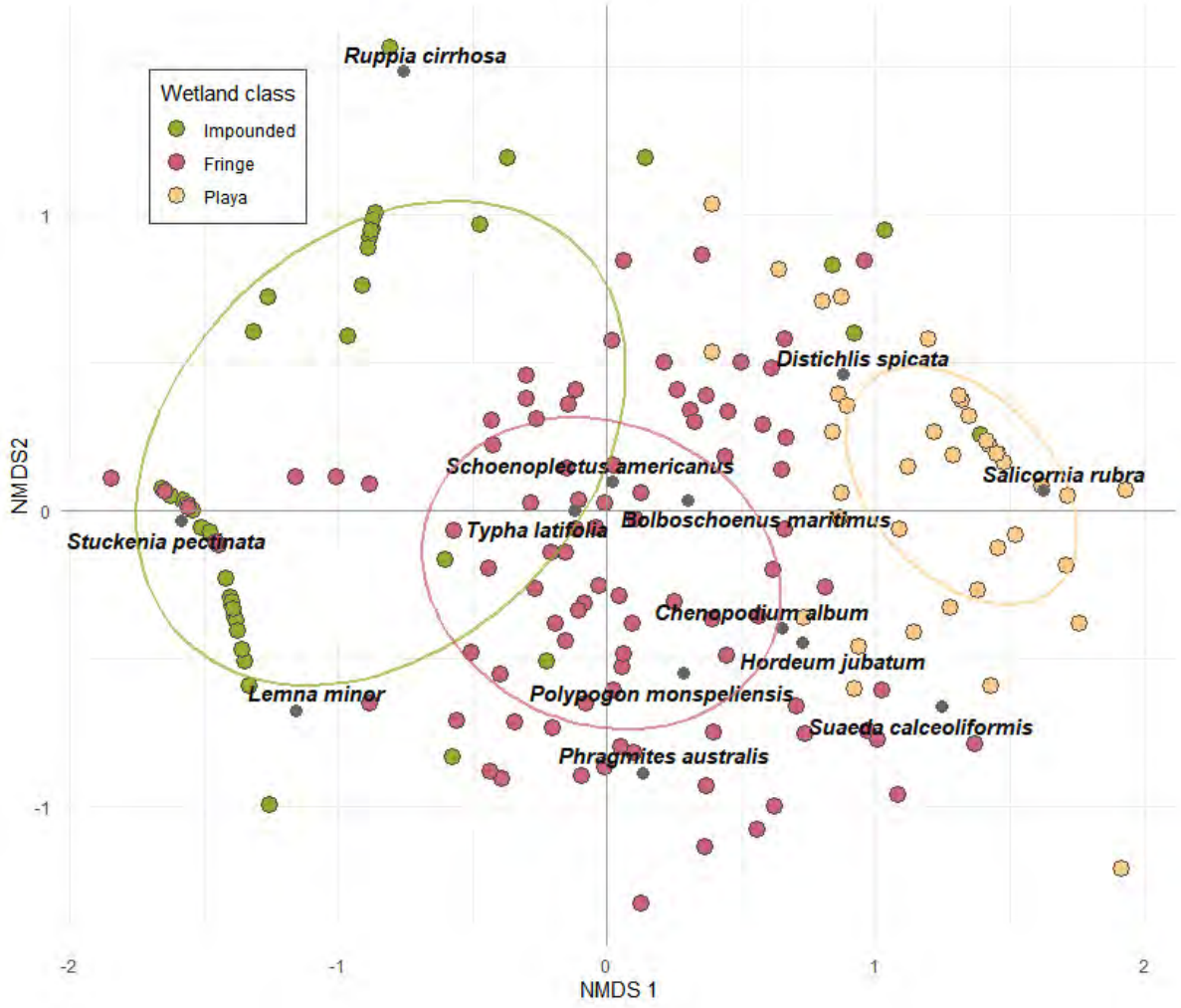

Figure 4. *Non-metric multidimensional scaling of GSL wetland plant community data. The ellipses represent a multivariate 95% confidence interval around the centroid of each wetland class.*

generally grouped according to wetland class. Impounded wetlands occupy the negative side of NMDS 1, fringe wetlands occupy the center, and playa wetlands are on the right side. This pattern also matches the differences in hydroperiod and salinity, with deepest flooding and freshest water on the left/impounded side and saturation with saline water on the right/playa side. Figure 5a shows the distribution of observed water depth measurements in each wetland class and Figure 5b shows the conductivity of surface water (impounded, fringe, and a minority of playa wetlands) or pore water (playa wetlands) recorded during field work. Impounded wetlands were flooded most deeply of the three wetland classes while playa wetlands rarely had recordable surface water. Salinity was similar between impounded and fringe wetlands, but significantly higher in playa wetlands.

Impounded wetlands are dominated by submerged aquatic vegetation (SAV) species (Table 2). For SAV to grow, these wetlands must be flooded for most or all of the growing season, which creates highly anoxic soil conditions that limits nutrient availability and drives the buildup of reduced forms of elements like selenium and mercury which can potentially be toxic (Cronk and Fennessy, 2001). Deep flooding also reduces light availability and gas exchange, which makes photosynthesis difficult (Mitsch and Gosselink, 2015). Adaptations to this challenging environment include being rootless (*Ceratophyllum demersem*, *Chara* spp), utilizing bicarbonate in photosynthesis cycles (*Stuckenia pectinata*, *C. demersem*), and having long, thin leaves that maximize surface area for light and gas exchange (all species in Table 2). Dense SAV growth drives many ecosystem functions; it provides structure for aquatic macroinvertebrates, sequesters metals and nutrients from soils temporarily, and oxygenates water through respiration (Cronk and Fennessy, 2001). All the plant and macroinvertebrate growth in impounded wetlands create critical feeding habitat for migratory birds, especially larger birds like waterfowl.

Emergent species of cattails (*Typha* spp), bulrushes (*Bolboschoenus* and *Schoenoplectus* spp), and grasses dominate in fringe wetlands (Table 3). Some emergent species can grow in water up to one meter deep (*Typha latifolia*), but really thrive in water that fluctuates between flooded and saturated or dry conditions that submerged species cannot tolerate (Larson, 1993). The species listed in Table 3 have life history strategies adapted to a variable water regime. The seeds of all four common fringe species require bare ground to germinate, though these species readily expand via clonal growth under flooded conditions. Clonal growth via adventitious rhizomes in combination with aerenchyma in their tissues allow patches of emergent species to share resources like oxygen and water across large distances, which supports the expanding margin of fringe wetlands (Cronk and Fennessy, 2001). Emergent marshes are some of the most productive habitats on Earth, enabling them to sequester soil metals and nutrients (Reddy and DeLaune, 2008). Dense vegetation also provides critical nesting habitat for migratory birds while vegetation that produces large seeds (e.g., bulrushes) also provides nutrient dense food (Sweetman and others, 2013, Marty and Kettenring, 2017).

Playa wetlands are largely defined by being mostly expanses of bare ground, but a couple species of halophytes—species that grow specifically in salty and alkaline locations—also thrive (Table 4). Most plant species cannot grow in saline environments because high salt concentration makes it difficult for plants to obtain water and acquire beneficial elements (Cronk and Fennessy, 2001). *Distichlis spicata* survives in saline wetlands through the ability to exude salt from specialized pores while *Salicornia rubra* has adopted succulence and the ability to concentrate salts in specialized cells (Welsh and others, 2004; Hauser, 2006). *S. rubra* is the only common annual species in GSL wetlands and reproduces strictly by seeds, allowing vegetation to appear seasonally based on water availability. *D. spicata*, on the other hand, most commonly reproduces through rhizomes, allowing it to share resources amongst clonal stems. While the plant species of playas do provide some food for migratory birds, the macroinvertebrates in the soils are the most crucial resource for shorebirds that can probe the soils (Sorensen and others, 2020). The isolated nature of playas also makes them critical nesting habitat for shorebirds because they are farther from infrastructure and predators than fringe or impounded wetlands.

How Do GSL Wetland Plant Communities Differ?

The simplest measure of a plant community is species richness, which is a count of how many species are present. Overall, species richness tends to be low in GSL wetlands but there are significant differences in richness between classes (Figure 6). Impounded wetlands have the lowest mean species richness (2.32), playa wetlands have intermediate richness (4.32), and fringe wetlands have the highest richness (7.92 species). Both high environmental stress and high disturbance environments tend to have low species richness (Cornk and Fennessy, 2001) and later analyses will try to parse the impacts of disturbance versus stress.

Whether plants present are native to the region or introduced from elsewhere is a clearer indicator of

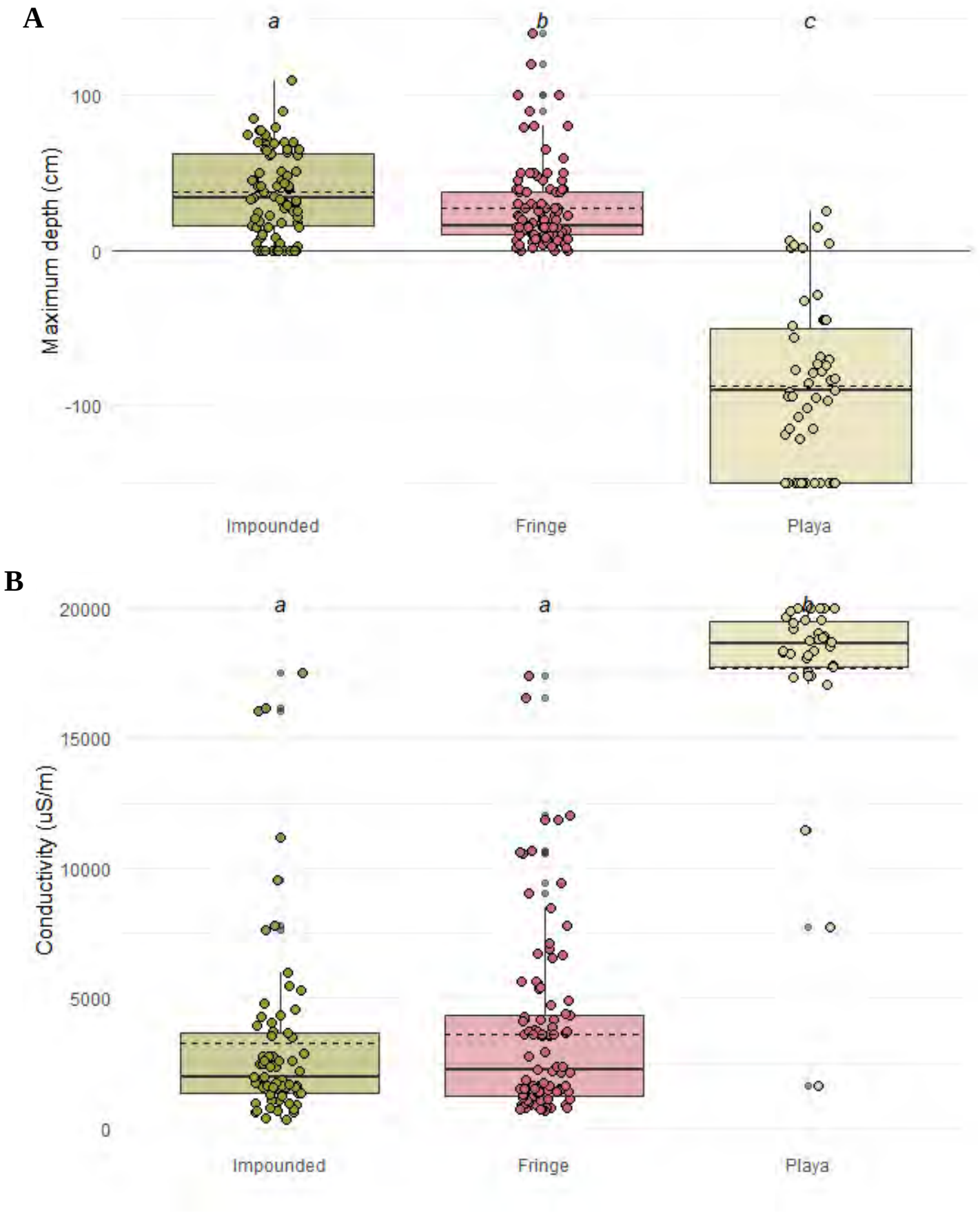

***Figure* 5.** *A) Median (solid line) and mean (dashed line) maximum water depth; and B) median (solid line) and mean (dashed line) water conductivity in three classes of GSL wetlands.*

Table 2. *Dominant plant species in impounded GSL wetlands.*

Species	Taxonomy	Growth form	Native	CC Score / Tolerance
Chara – Stinkweed	Algae – *Characeae*	Annual or perennial, macro-algae	Native, Obligate wetland	Undetermined
Ceratophyllum demersum – Coontail	Dicot – *Ceratophyllaceae*	Perennial, submerged aquatic forb	Native, Obligate wetland	3 - tolerant
Stuckenia pectinata – Sago pondweed	Monocot – *Potamogetonaceae*	Perennial, submerged aquatic forb	Native, Obligate wetland	3 – tolerant
Ruppia cirrhosa – Widgeongrass	Monocot – *Ruppiaceae*	Perennial, submerged aquatic forb	Native, Obligate wetland	6 – intermediate

Table 3. *Dominant plant species in fringe GSL wetlands.*

Species	Taxonomy	Growth form	Native	CC Score / Tolerance
Bolboschoenus maritimus – Alkali bulrush	Monocot – *Cyperaceae*	Perennial, emergent graminoid	Native, Obligate wetland	5 – intermediate
Schoenoplectus americanus – Threesquare bulrush	Monocot – *Cyperaceae*	Perennial, emergent graminoid	Native, Obligate wetland	5 – intermediate
Phragmites australis – Phragmites	Monocot – *Poaceae*	Perennial, emergent graminoid	Introduced, Facultative wetland	0 – highly tolerant
Typha latifolia – Broadleaf cattail	Monocot – *Typhaceae*	Perennial, emergent forb	Native, obligate wetland	2 – highly tolerant

Table 4. *Dominant plant species in playa GSL wetlands*

Species	Taxonomy	Growth form	Native	CC Score / Tolerance
Salicornia rubra – Pickleweed	Dicot – *Chenopodiaceae*	Annual forb	Native, Obligate wetland	4 – tolerant
Distichlis spicata – Saltgrass	Monocot – *Poaceae*	Perennial graminoid	Native, Facultative	4 – tolerant

how disturbed an environment is. Introduced species that can establish and expand in new wetland environment often have adaptations that take advantage of gaps in vegetation because they have wide ecological tolerances, grow rapidly, and reproduce prolifically (Zedler and Kercher, 2004). This is especially true for *Phragmites australis* (hereafter, phragmites), which occupies tens of thousands of acres of GSL wetlands (Kettenring and others, 2020). Introduced species relative cover (the proportion of all plant cover that is from introduced species) differs significantly in GSL wetland classes, matching patterns in species richness—highest in fringe wetlands and lowest in impounded wetlands (Figure 7). As we explore the sources and consequences of anthropogenic disturbance in wetland plant communities, fringe wetlands and introduced species will come up again.

Growth form of the dominant plant in a type of wetland (forb, grass, or shrub) is how wetlands are mapped in the National Wetland Inventory, a comprehensive dataset of nationwide wetland extent, and those nationwide patterns also distinguish between GSL wetland classes. Impounded wetlands tend to be aquatic bed features, fringe wetlands are predominantly emergent, and playa wetlands are those with less than 30% vegetation cover (U.S. Fish and Wildlife Service, 2019). GSL wetlands are almost entirely herbaceous which means that woody species are uncommon and a small part of the overall cover when present. Herbaceous plants can be further divided into graminoids—grasses, sedges, and other plants with grass-like growth patterns—and forbs—all the other species that tend to have broader leaves. Wetland plants can also be grouped based on the length of their life cycle. Annual species only live for one year whereas perennial species persist over multiple years,

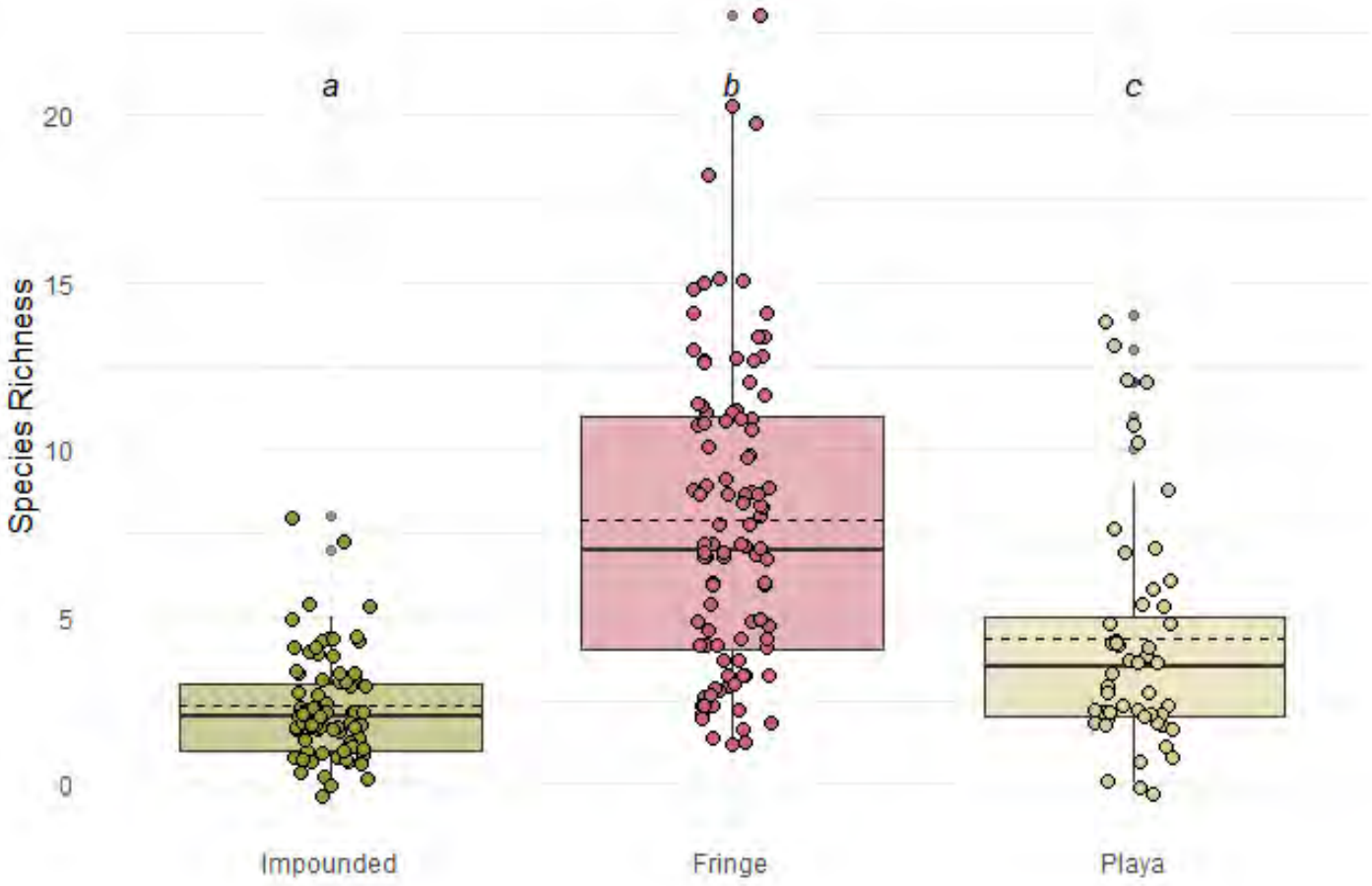

Figure 6. *Median (solid line) and mean (dashed line) species richness in three GSL wetland classes. Unique letters above boxplots indicate statistically different measures according to pairwise T-tests (α = 0.05).*

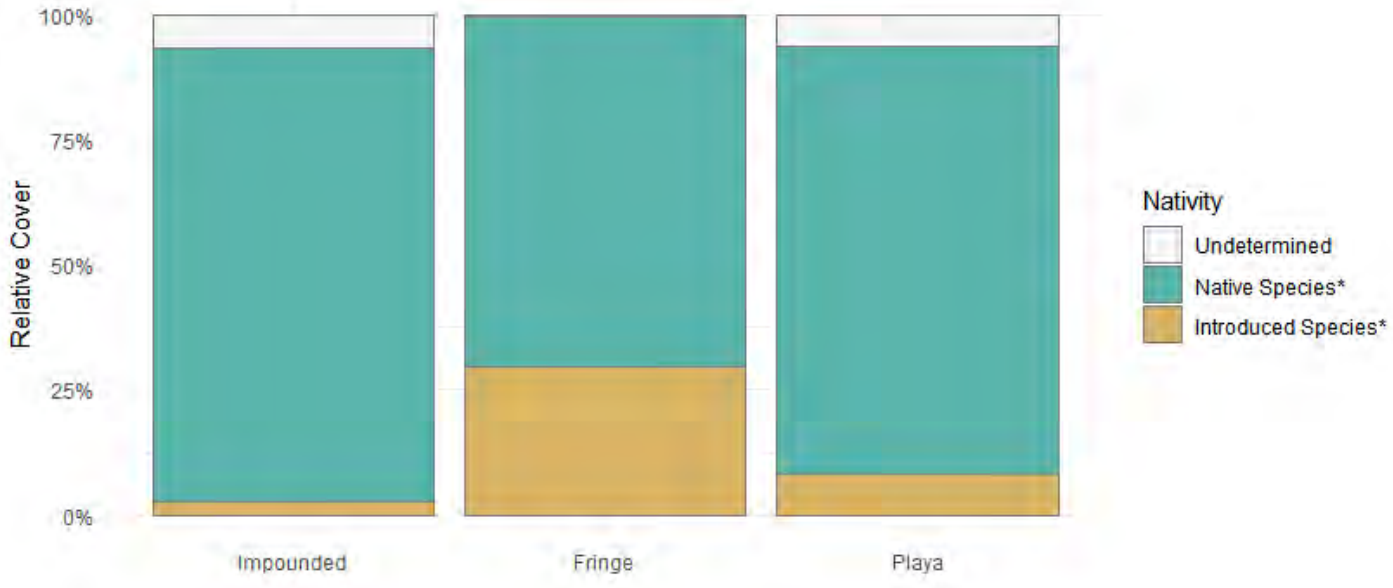

Figure 7. *Relative cover of native and introduced species in three wetland classes. Asterisks in legend indicate statistically different measures according to ANOVA (α = 0.05).*

growing back in subsequent seasons from perennating structures like rhizomes and tubers. The SAV that characterizes impounded wetlands are primarily perennial forbs, the emergent species that dominate fringe wetlands are perennial graminoids, and the most common halophytes in playa wetlands are annual forbs (Figure 8).

As discussed earlier, a limited group of species is adapted to life in wetlands. However, even with their adaptations, wetland species are not uniform in their ability to tolerate natural or anthropogenic disturbance. Sensitive plant species (as determined by U.S. Environmental Protection Agency, 2016) are a small component of cover across all GSL wetlands. Disturbance tolerant species cover the most area in GSL wetlands (Figure 9). Matching patterns reflected in introduced species cover by wetland class, the relative cover of highly tolerant species in fringe wetlands is significantly higher than in other wetland classes.

Coefficient of Conservatism (CC) scores, the continuous metric that compliments the categorical sensitivity/tolerance variable, can be built into simple or complex measures of the floristic quality of the community (Colorado Natural Heritage Program, 2022). Mean CC, the simplest of such measures, is nearly identical in impounded and playa wetlands, but significantly lower in fringe wetlands (Figure 10). The Floristic Quality Index (FQI) multiplies Mean CC by a coefficient of species richness, and in GSL wetlands that flips the floristic quality results: fringe wetlands

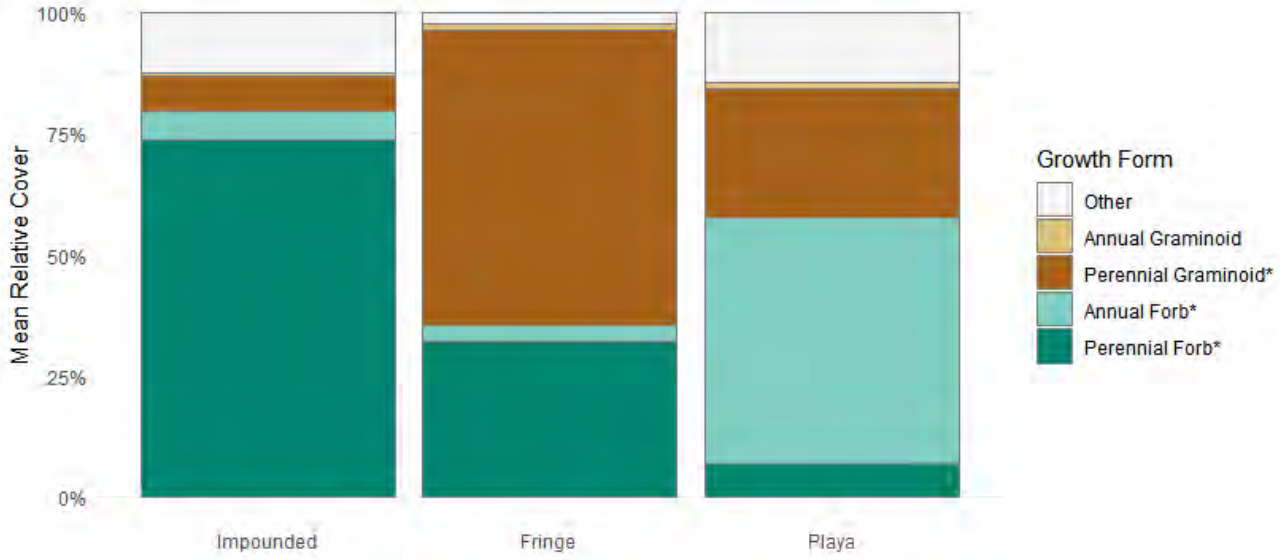

Figure 8. *Relative cover of annual and perennial forb and graminoid species in three GSL wetland classes. Asterisks in legend indicate statistically different measures according to ANOVA (α = 0.05). Other growth forms include shrubs, trees, and macroalgae.*

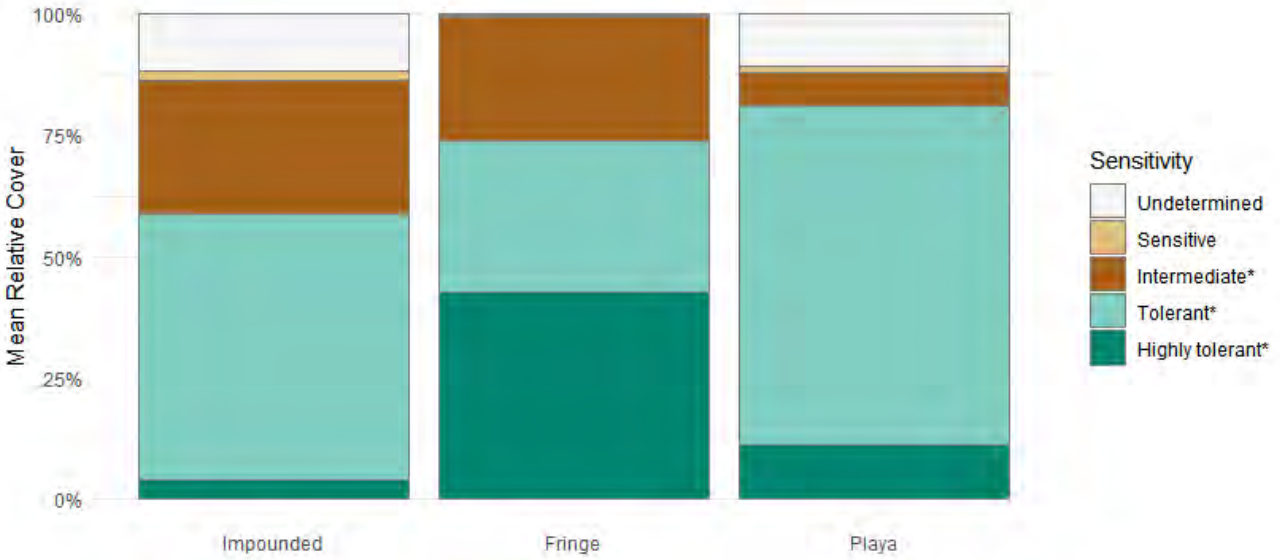

Figure 9. *Relative cover of sensitive, intermediate, tolerant, and highly tolerant species in all GSL wetlands and within three wetland classes. Asterisks in legend indicate statistically different measures according to ANOVA (α = 0.05).*

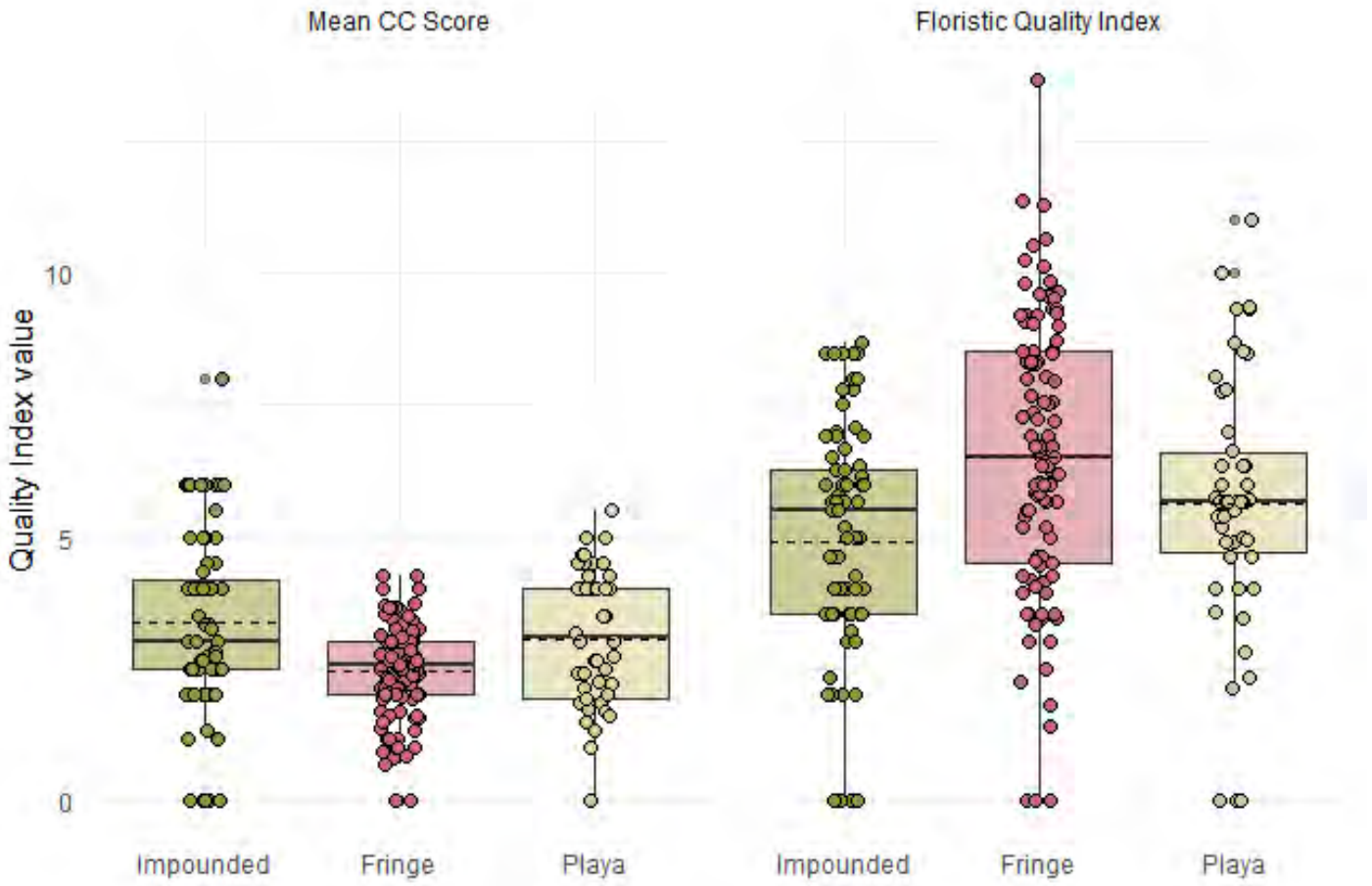

Figure 10. *Median (solid line) and mean (dashed line) Mean CC and Floristic Quality Index scores in three GSL wetland classes.*

have significantly higher FQI than the other wetland classes. The mechanisms for this switch in quality scores is clear, as fringe wetlands have higher species richness, but the implications are murky.

What Factors Are Associated with Differences in the Wetland Plant Community?

The differences in the plant community between wetland classes described above are the result of a complex mix of environmental gradients, management actions, and anthropogenic disturbance. These gradients may also drive variation with each wetland class. NMDS ordinations were generated using the most common species in each wetland class (those found in at least 10% of sites sampled for each class) and then overlaid with gradients of soil chemistry, water depth, and physical disturbances (Table 5) to visually assess important gradients to each community (Okansen and others, 2007). Only those factors with relatively high r^2 coefficients and p-values less than 0.05 were plotted because there was higher likelihood that those gradients are truly aligned with the plant community. However, measures of significance with ordinations do not hold the same rigor as in univariate data analysis and should be interpreted with that in mind (McCune and Grace, 2002).

Impounded wetland sites clustered in two distinct communities of submerged species along the horizontal NMDS1 axis and the vectors reflect common impounded wetland management practices (Figure 11a). *Stuckenia pectinata,* a highly valued habitat species for waterfowl, grows in deeper water than other SAV species (see water depth vector) which is often at the farthest downstream point of impoundments (see impervious surface vector). *Ruppia cirrhosa* favors more saline waters than other SAV species and the conductivity vector increases along the positive side of NMDS1. *Lemna minor* is an indicator of nutrient enrichment (Reddy and DeLaune, 2008) and the soil phosphorus and water quality discharge vectors both increase toward the upper left quadrant of the ordination that *L. minor* occupies. The divergent soil metal vectors are intriguing. Copper, zinc, and lead vectors increase on the negative range of NMDS 1 while selenium and barium follow the positive range of NMDS 1. Copper and zinc are both common in stormwater runoff from roads and it is possible *L. minor* and *C. demersum* could be indicators of contamination from roads (Ladislas and others, 2012).

The ordination of common species in fringe wet-

Table 5. *Environmental and anthropogenic gradients considered in NMDS and risk analysis and cutoffs that distinguish high from low stress for risk categorization.*

Gradient	High Disturbance Threshold
Environmental Factors	
Water depth	-
Conductivity – water	-
Conductivity – soil	-
Soil organic matter	-
Soil phosphorus	≥ 39.8 mg/kg
Aluminum – soil	-
Arsenic – soil	≥ 11.22 mg/kg
Barium – soil	-
Copper – soil	≥ 83.92 mg/kg
Lead – soil	-
Manganese – soil	-
Nickel – soil	-
Selenium – soil	≥ 0.17 mg/kg
Zinc – soil	-
Soil metal (exceedances of background for As, Ba, Cu, Pb, Mn, Ni, Se, and Zn)	≥ 5 exceedances
Physical Disturbances	
Water conductivity	-
Grazing severity	Severe
Herbicide severity	Severe
Impervious surface within 100m	>1
Roads within 100m	-
Discharges within 100m	-
Diversions within 100m	-
Impervious surface (%) within 1km	≥ 25%
Diversions within 1 km	≥ 3
Discharges within 1 km	≥ 1
Developed and agricultural land within 1 km	≥ 6%
Mines within 1 km	≥ 1
Introduced species cover	≥ 15% relative cover

lands does not have the clear clusters of sites that impounded wetlands displayed, but the centroids of species indicate associations of species (Figure 11b). Three factors associated with water management (diversions, water depth, and roads that are built on dikes) all increase toward the lower quadrant of the ordination occupied by two species of interest to wetland managers: *S. pectinata* and *Bolboschoneus maritimus*. It is possible the horizontal NMDS1 axis reflects the influence of or similar conditions to adjacent wetland classes—impounded wetlands on the right and playa wetlands represented by *Salicornia rubra* on the left. Two common species in fringe wetlands that are classified as highly tolerant, phragmites and *Typha latifolia*, occupy different sides of the vertical axis (NMDS 2) which suggests that multiple gradients are driving different types of highly tolerant communities, one dominated by *Typha* spp. and another by phragmites.

Based on the results of the NMDS, physical distance from infrastructure may isolate playa wetlands from anthropogenic disturbance, which is reflected in the fact that no physical disturbance factors were meaningfully aligned with the playa plant community (Figure 11c). Although playa wetland sites did not cluster in a clear pattern, the species centroids did show that the right side of the plot is dominated by the salt-loving species *S. rubra*, *Puccinellia nuttalliana*, and *D. spicata* along with a vector indicating higher soil salinity. The lack of clear vegetation patterns within playa wetlands may be due to the sparse vegetation present in this class of wetlands or the ephemeral nature of a community dominated by annual species.

What Condition Are GSL Wetlands in and Why?

While the previous sections detail the ways GSL wetlands are different between and within wetland classes, this final section will look at GSL wetlands collectively through the lens of wetland condition. Recall that GSL wetland condition is measured through the GSL-VMMI, a composite of three metrics: cover of highly tolerant species and facultative wetland species and dicot species richness. GSL wetlands that experience little anthropogenic disturbance tend to have more monocot species than dicot species and more cover of wetland obligate and less tolerant species. As condition decreases dicot species become more numerous and facultative wetland species and highly tolerant species occupy more wetland area. Through the process of selecting a VMMI explained in the analysis section, we know that condition is correlated with a cumulative measure of anthropogenic disturbance, but understanding the specific drivers of wetland condition requires a more robust analysis.

Risk analysis links the discrete measures of anthropogenic disturbance to poor wetland condition. Relative risk analysis identifies the individual factors that contribute to poor condition by estimating the likelihood of a wetland being in poor condition if it also experiences high levels of a particular disturbance. Ecological relative risk is analogous to heart disease risk: a human with high blood pressure (i.e., high stress or disturbance) is more likely to also have

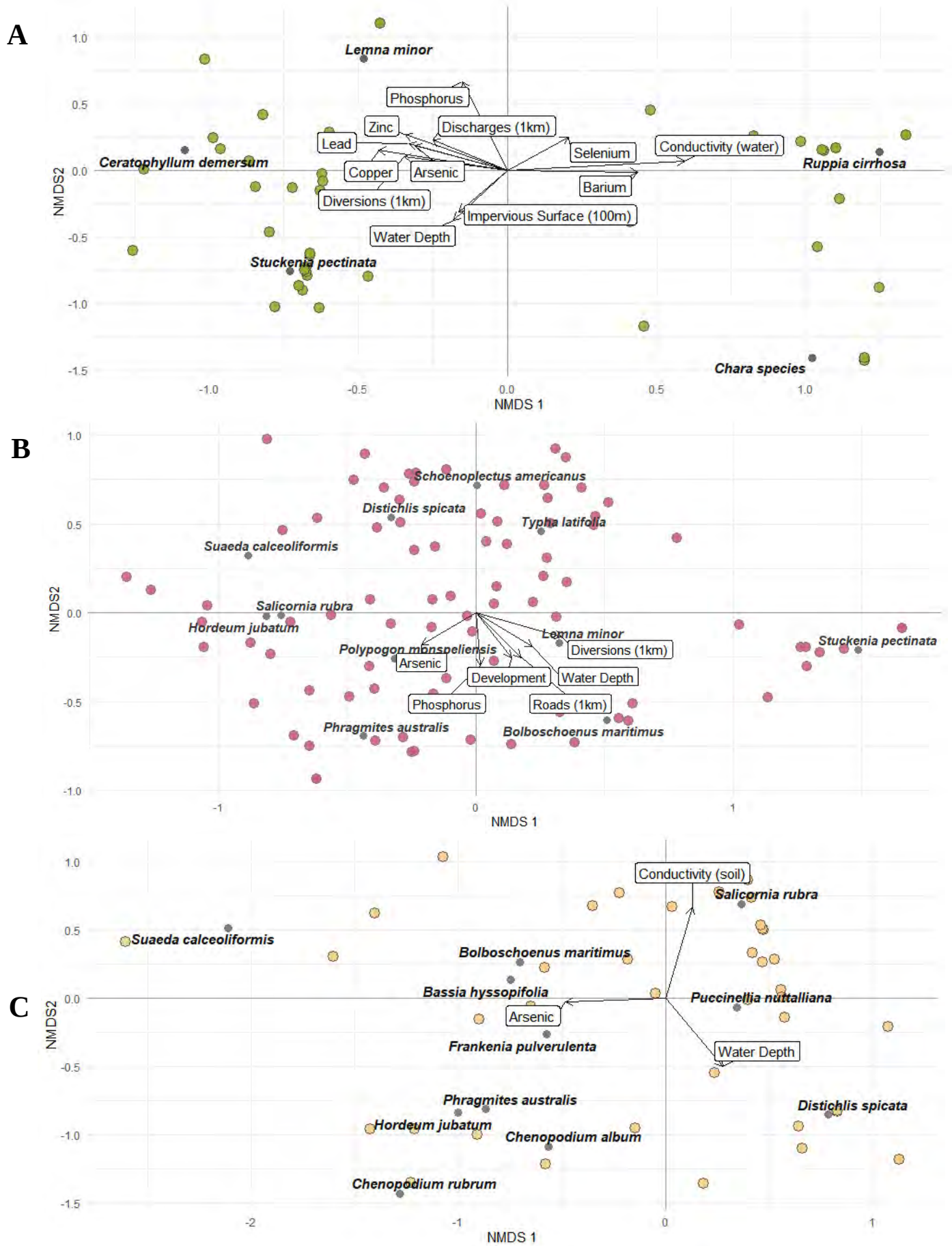

Figure 11. *Non-metric multidimensional scaling with significantly aligned environmental vectors in A) impounded, B) fringe, and C) playa wetlands.*

heart disease (i.e., poor condition) (Herlihy and others, 2019b). Attributable risk identifies the disturbances that, if removed, will result in improved condition. The estimate represents the proportion of poor condition sites that are likely to improve if a disturbance is removed. In the analogy of heart health, attributable risk is the improvement in heart health driven by decreasing blood pressure.

Risk estimates are interpreted with 95% confidence intervals; relative risk factors are considered significant if the lower confidence interval is greater than one and significant attributable risk factors have a lower confidence interval greater than zero (Van Sickle and Paulsen, 2008). Table 5 lists the disturbance factors included in the risk analysis and the threshold that separates high levels of disturbance from moderate to low disturbance.

When all wetland classes are considered together, introduced species and changes in land use near a wetland are both significant relative risks. Wetlands with more than 6% developed or agricultural land within one kilometer of the sample location are 2.6 times more likely to be in poor condition (Figure 12). When wetland class is considered, however, land use change is only a significant risk for fringe wetlands. High cover of introduced species (>15% relative cover) is a significant risk for all classes of wetlands but has especially high relative risk estimates in impounded and playa classes, 38.62 and 5.46 respectively (Table 6). The high relative risk of introduced species cover is likely driven by phragmites, which is widespread around GSL and has been a concern of wetland managers due to its propensity to crowd out native species and inability to support migratory bird use (Cranney, 2016; Long and others, 2017). Phragmites is a facultative wetland species and highly tolerant to disturbance, properties that correspond to two metrics in the GSL-VMMI, thus there is some circularity in the risk and condition estimates.

Higher soil arsenic and selenium concentrations are also a significant relative risk to all GSL wetlands (1.15), which is an interesting complement to existing concerns about selenium in the GSL open water ecosystem (Brix and others, 2004). Selenium bioaccumulates in the open water food web, from algae to brine shrimp to aquatic birds. The GSL-specific research into selenium did not look at soils or wetland macroinvertebrates but research elsewhere has found a

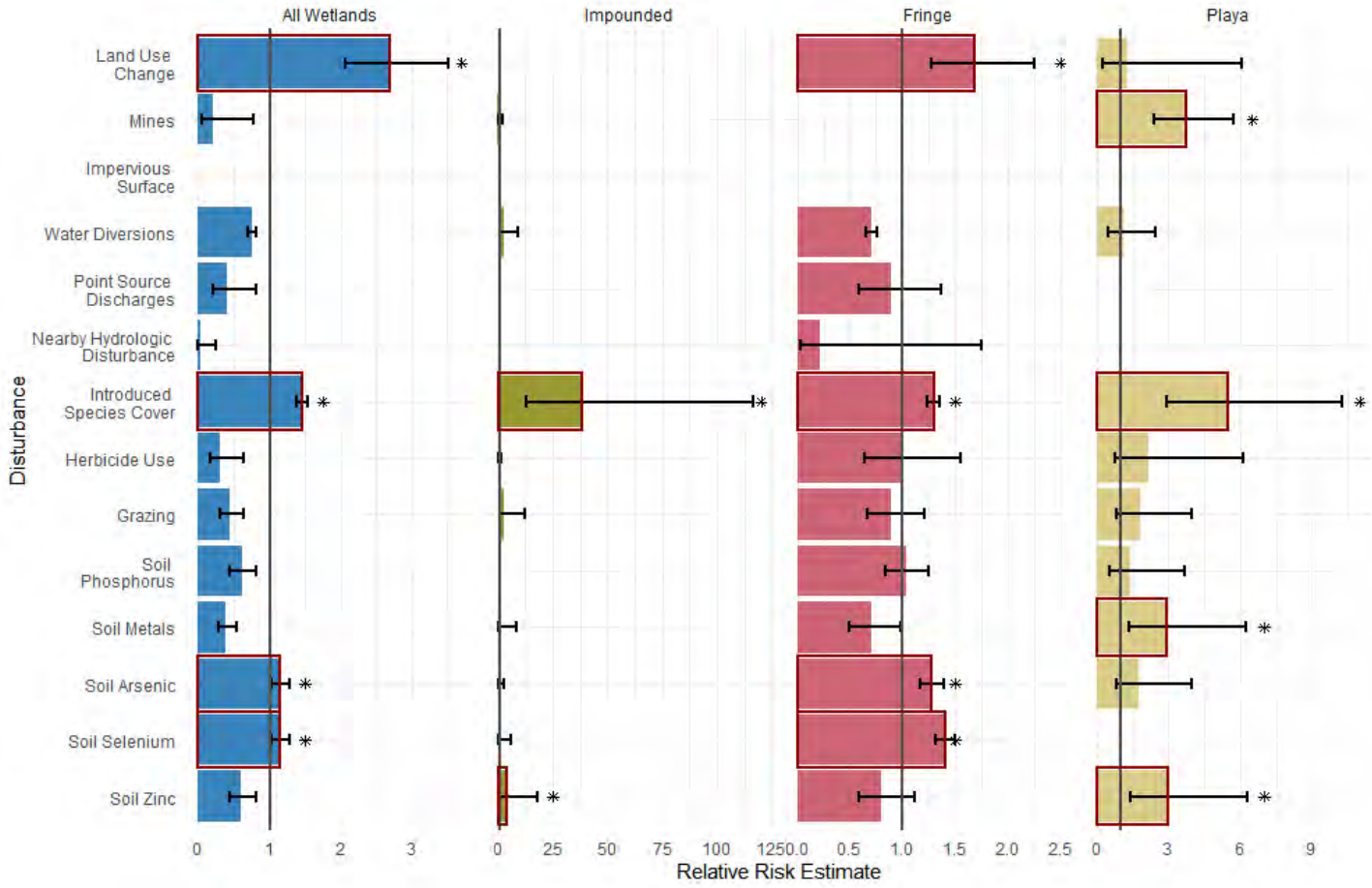

Figure 12. *Relative risk estimates for environmental and anthropogenic stressors in all GSL wetlands and in three wetland classes. Bold red boxes and asterisks indicate significant relative risk factors (estimate ± 95% confidence interval > 1).*

Table 6. *Significant relative and attributable risk estimates for disturbances in GSL wetlands.*

	Population	Disturbance	Risk Estimate	Lower CI	Upper CI
Relative Risk					
	All GSL	Land Use Change	2.70	2.07	3.51
	All GSL	Introduced Species Cover	1.45	1.38	1.53
	All GSL	Soil Arsenic	1.15	1.02	1.29
	All GSL	Soil Selenium	1.15	1.03	1.28
	Impounded	Introduced Species Cover	38.62	12.81	116.42
	Impounded	Soil Zinc	4.25	1.00	18.03
	Fringe	Land Use Change	1.69	1.27	2.25
	Fringe	Introduced Species Cover	1.30	1.24	1.36
	Fringe	Soil Arsenic	1.28	1.17	1.39
	Fringe	Soil Selenium	1.40	1.31	1.50
	Playa	Mines	3.71	2.41	5.69
	Playa	Introduced Species Cover	5.46	2.90	10.27
	Playa	Soil Metals	2.91	1.35	6.26
	Playa	Soil Zinc	2.97	1.39	6.32
Attributable Risk					
	All GSL	Land Use Change	0.59	0.48	0.09
	All GSL	Introduced Species	0.07	0.06	0.09
	All GSL	Soil Arsenic	0.02	<0.01	0.04
	All GSL	Soil Selenium	0.04	0.01	0.06
	Impounded	Introduced Species	0.63	0.13	0.84
	Fringe	Land Use Change	0.39	0.20	0.54
	Fringe	Introduced Species	0.05	0.04	0.06
	Fringe	Soil Arsenic	0.03	0.02	0.05
	Fringe	Soil Selenium	0.08	0.06	0.10
	Playa	Introduced Species	0.37	0.09	0.57

high potential for selenium accumulation in soils that are regularly flooded (Jones and others, 2017).

The most significant attributable risk factor for GSL wetlands is introduced species cover. When considered altogether, seven percent of poor condition wetlands would improve if the introduced species risk were removed (Figure 13). The attributable risk estimate is largest for impounded and playa wetlands (63% and 39% respectively). It is encouraging that introduced species removal may improve wetland condition because years of research and adaptive management directed at phragmites removal has made significant progress in alleviating pressure from that species (Rohal and others, 2017; Rohal, 2018). Though the circularity between condition metrics that reflect the presence of phragmites and risk estimates as well as the assumption of reversibility that is built into this analysis need to be remembered.

The two other significant attributable risk factors, land use changes and soil metals, are unlikely to be reversible, regardless of the impact of their removal. Land use change, a significant attributable risk for all GSL wetlands together and fringe wetlands in particular, are almost certainly permanent landscape features. Soil selenium and arsenic are also difficult to remediate, not only because soil remediation is challenging, but also because wetlands act as landscape sinks for both arsenic and selenium, continually capturing metals from across the watershed (Adams and others, 2015). However, decreasing soil metal concentrations would result in fewer poor condition fringe wetlands and have potential impacts for migratory bird populations, which can bioaccumulate both metals.

CONCLUSIONS

Characterizing the dominant plant communities and exploring the various environmental and anthropogenic gradients relevant to each class of GSL wetlands show the unique suite of factors that have filtered the plant community down to the species best adapted to each class. In impounded wetlands, deep freshwater flooding made possible by water management infrastructure supports predominantly native submerged aquatic plant species. The dynamic water regimes in fringe wetlands create an ideal environment for perennial emergent species. Playa wetlands

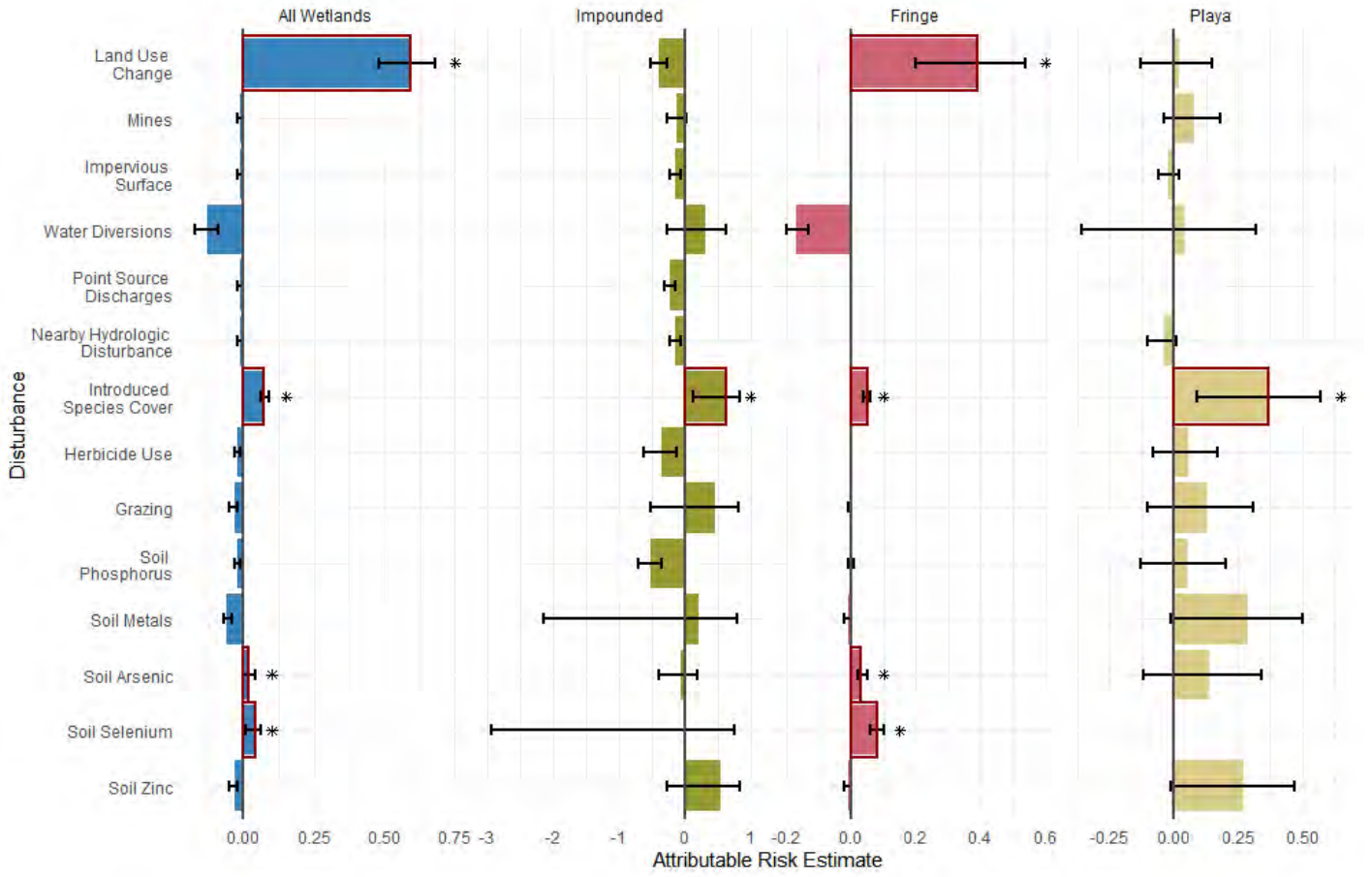

Figure 13. *Attributable risk estimates for environmental and anthropogenic stressors in all GSL wetlands and in three wetland classes. Bold red boxes and asterisks indicate significant attributable risk factors (estimate ± 95% confidence interval > 0).*

are dominated by species adapted to extremes in salinity. Water depth is associated with differences in community within each class according to ordination results. Finally, risk analysis identified land use change and introduced species as the greatest risks to condition and the greatest opportunity for restoration.

Restoration Implications

The ecological characterization presented here, the multi-metric index of wetland condition, and the risk analysis all have implications for restoration practices around GSL. Identifying the correct potential plant communities, which are specific to wetland class, is critical to any restoration project and should be carefully considered when selecting species to plant, water regimes that are possible, and ultimate restoration targets (Tarsa and others, 2022). The GSL -VMMI has a role both in identifying wetlands in need of restoration (those in poor condition) and in monitoring if a restored wetland is on a trajectory for better health over time. Finally, the results of the risk analysis should be considered when identifying appropriate sites for restoration efforts. Most especially, significant relative and attributable risk factors like introduced species should be minimized or eliminated prior to initiating restoration efforts.

Future Research Needs

GSL wetlands form vast complexes of intermingling classes, which is what drives much of the bird diversity the ecosystem supports. The entire Intermountain West region has experienced two decades of drought that pushed GSL to its lowest elevation and saltiest state. Even with the impact of climate change on precipitation patterns, humans diverting and using water to grow food and lawns has exacerbated the impacts of drought (Wurtsbaugh and others, 2016). As mentioned in the introduction, distinguishing between natural and anthropogenic disturbances is difficult and this is especially true for wetland water availability. The experience of the Bear River delta in the early 20th century provides a stark example of the impact that years of drought can have on the ability of wetland complexes to provide their ecosystems functions. However, we also know that many wetland species are adapted to periodic drying events. Future research into the natural range of hydrologic variability that GSL wetlands are adapted to and the nature of

disrupted hydrology would provide crucial insight to the roles of drought and water use in shaping existing wetland plant communities and critical thresholds to avoid.

REFERENCES

Adams, W., DeForest, D.K., and Brix, K.V., 2015, Longer-term monitoring or arsenic, copper, selenium, and other elements in Great Salt Lake (Utah, USA) surface water, brine shrimp, and brine flies: Environmental Monitoring and Assessment, v. 187, p. 188.

Aldrich, T.W., and Paul, D.S., 2002, Avian ecology of Great Salt Lake, *in* Gwynn, J.W., editor, Great Salt Lake: an overview of change: Salt Lake City, Utah, Utah Department of Natural Resources, p. 343–374.

Alfaro, M.R., Montero, A., Ugarte, O.M., do Nascimento, C.W A., de Aguiar Accioly, A.M., Biondi, C.M., and da Silva, Y.J.A.B., 2015, Background concentrations and reference values for heavy metals in soils of Cuba: Environmental Monitoring and Assessment, v. 187, no. 1, p. 1–10.

Baxter, B.K., and Butler, J.K., 2020, Climate change and Great Salt Lake, *in* Baxter, B.K., and Butler, editors, Great Salt Lake Biology: Cham, Switzerland, Springer Nature, p. 23–52.

Borics, G., Várbíró, G., and Padisák, J., 2013, Disturbance and stress: different meanings in ecological dynamics? Hydrobiologia v. 711, p. 1–7

Brix, K.V., Deforest, D.K., Cardwell, R.D., and Adams, W.J., 2004, Derivation of a chronic site-specific water quality standard for selenium in the Great Salt Lake, Utah, USA: Environmental Toxicology and Chemistry, v. 23, no. 3, p. 606–612.

Colorado Natural Heritage Program, 2022, Floristic Quality Assessment (FQA) Calculator for Colorado, Online resource: https://cnhp.colostate.edu/download/documents/cwic_docs/FQA_Calculator_Users_Guide_v2022.pdf, Accessed Dec 13, 2022.

Cranney, C.R., 2016, Control of large stands of Phragmites australis in Great Salt Lake, Utah wetlands, Logan, Utah State University, M.S. thesis, 100p.

Cronk, J.K., and Fennessy, M.S., 2001, Wetland plants—biology and ecology: Boca Raton, Florida, CRC Press LLC.

Davies, S.P., and Jackson, S.K, 2006, The biological condition gradient—a descriptive model for interpreting change in aquatic ecosystems: Ecological Applications, v. 16, no. 4, p. 1251–1266.

Downard , B., 2021, Improving Great Salt Lake wetland quality through monitoring of wetland uses, water quality, and condition: Utah Division of Water Quality contract deliverable to U.S. Environmental Protection Agency p. 162p.

Downard, R., and Endter-Wada, J., 2013, Keeping wetlands wet in the western United States—adaptations to drought in agriculture-dominated human-natural systems: Journal of Environmental Management, v. 131, p. 395–406.

Downard, R., Endter-Wada, J., and Kettenring, K.M., 2014, Adaptive management in an uncertain and changing arid environment: Ecology and Society, v. 19, no. 2, p. 23.

Downard, R., Frank, M., Perkins, J., Kettenring, K., and Larese-Casanova, M., 2018, Wetland plants of Great Salt Lake—a guide to identification, communities, and bird habitat, Logan, Utah: Utah State University Extension, 212p.

Grime, J.P., 1989, The stress debate—symptom of impending synthesis?: Biological Journal of the Linnean Society, v. 37, p. 3–17.

Hauser, A.S., 2006, Distichlis spicata, *in* Fire Effects Information Systems, Online: https://www.fs.usda.gov/database/feis/plants/graminoid/disspi/all.html, Accessed Dec. 17, 2022.

Hazelton, E.L., Mozdzer, T.J., Burdick, D.M., Kettenring, K.M. and Whigham, D.F., 2014, Phragmites australis management in the United States—40 years of methods and outcomes: AoB plants, v. 6.

Herlihy, A.T., Kentula, M.E., Magee, T.K., Lomnicky, G.A., Nahlik, A.M. and Serenbetz, G., 2019a, Striving for consistency in the National Wetland Condition Assessment—developing a reference condition approach for assessing wetlands at a continental scale: Environmental Monitoring and Assessment, v. 191, p. 1–20.

Herlihy, A.T., Paulsen, S.G., Kentula, M.E., Magee, T.K., Nahlik, A.M., and Lomnicky, G.A., 2019b, Assessing the relative and attributable risk of stressors to wetland condition across the conterminous United States: Environmental Monitoring and Assessment, v. 191, no. 320.

Inkenbrandt, P., 2021, Lake Bonneville: Online, https://storymaps.arcgis.com/stories/f5011189bdc94545b9231d56e4ffc1e4, accessed Feb. 24, 2023.

Jones, C.P., Grossl, P.R., Amacher, M.C., Boettinger, J.L, Jacobson, A.R., and Lawley, J.R., 2017, Selenium and salt mobilization in wetland and arid upland soils of Pariette Draw, Utah (USA): Geoderma v. 305, p. 363–373.

Keddy, P.A., 2010, Wetland Ecology—Principles and Conservation: Cambridge University Press, p. 497.

Kettenring, K.M., Cranney, C.R., Downard, R., Hambrecht, K.R., Tarsa, E.E., Menuz, D.R., and Rohal, C.B., 2020, Invasive plants of Great Salt Lake

wetlands: what, where, when, how, and why, *in* Baxter, B.K., and Butler, J.K, editors, Great Salt Lake Biology: Cham, Switzerland, Springer Nature, p. 397–435.

Kincaid, T.M., Olsen, A.R., & Weber, M.H., 2019, spsurvey—Spatial Survey Design and Analysis. R package version 4.1.0.

Ladislas, S., El-Mufleh, A., Gérente, C., Chazarenc, F., Andrès, Y., and Béchet, B., 2012, Potential of aquatic macrophytes as bioindicators of heavy metal pollution in urban stormwater runoff.: Water, Air, & Soil Pollution, v. 223, p. 877–888.

Larson, G.E., 1993, Aquatic and wetland plants of Northern Great Plains, Fort Collins, Colorado: Rocky Mountain Forest and Range Experiment Station, General Technical Report RM-238.

Lomnicky, G.A., Herlihy, A.T., and Kaufmann, P.R., 2019, Quantifying the extent of human disturbance activities and anthropogenic stressors in wetlands across the conterminous United States—results from the National Wetland Condition Assessment: Environmental Monitoring and Assessment, v. 191, p. 1–23.

Long, A., Kettenring, K., and Toth, R., 2017, Prioritizing management of the invasive grass Common reed (Phragmites australis) in Great Salt Lake wetlands, Invasive Plant Science and Management, v. 10, no. 2, p. 155–165.

Lopez, R.D., and Fennessy, M.S., 2002, Testing the floristic quality assessment index as an indicator of wetland condition: Ecological Applications, v. 12, no. 2, p. 487–497.

Lytle, D.A., and Poff, N.L, 2004, Adaptation to natural flow regimes: Trends in Ecology and Evolution, v. 19, no. 2, p. 94–100.

Madsen, D.B., 2015, A framework for the initial occupation of the Americas: PaleoAmerica v. 1, p. 217–250.

Magee, T.K., Blocksom, K.A., and Fennessy, M.S., 2019, A national-scale vegetation multimetric index (VMMI) as an indicator of wetland condition across the conterminous United States: Environmental Monitoring and Assessment, v. 191, p. 322.

Marty , J.E., and Kettenring, K.M., 2017, Seed dormancy break and germination for restoration of three globally important wetland bulrushes: Ecological Restoration, v. 35, no. 2, p. 138–147.

McCune, B., and Graces, J.B., 2002, Analysis of ecological communities, Gleneden Beach, Oregon: MjM Software.

Miller, S.J., and Wardrop, D.H., 2006, Adapting the floristic quality assessment index to indicate anthropogenic disturbance in central Pennsylvania wetlands: Ecological Indicators, v. 6, no. 2, p. 313–326.

Mitsch, W.J., and Gosselink, J.G., 2015, Wetlands: Hoboken, New Jersey, John Wiley and Sons, Inc.

Moor, H., Hydin, H, Hylands, K., Nilsson, M.B., Lindbord R, and Norberg, J., 2017, Towards a trait-based ecology of wetland vegetation: Journal of Ecology, v. 105, no. 6, p. 1623–1635.

Nahlik, A.M., Blocksom, K.A., Herlihy, A.T., Kentula, M.E., Magee, T.K., and Paulsen, S.G., 2019, Use of national-scale data to examine human-mediated additions of heavy metals to wetland soils of the US: Environmental Monitoring and Assessment, v. 191, p. 1–24.

Oksanen, J., Kindt, R., Legendre, P., O'Hara, B., Stevens, M.H.H., Oksanen, M.J., and Suggests, M.A.S.S, 2007, The vegan package: Community ecology package, v. 10, p. 631–637.

Oviatt, C.G., 2014, The Gilbert episode in the Great Salt Lake Basin, Utah: Utah Department of Natural Resources Miscellaneous publication 14-3, 24p.

Quantum Spatial, Inc, 2017. Utah 2016 LiDAR – Great Salt Lake AOIs, GIS layer: Online: https://gis.utah.gov/data/elevation-and-terrain/2016-lidar-gsl/, accessed Jan. 21, 2021.

R Core Team, 2020, R—a language and environment for statistical computing. Vienna, Austria: R Foundation for Statistical Computing (http://www.R-project.org).

Ramsey, R.D., Banner, R.E., and Leydsman McGinty, E.I., 2009, Watersheds of Utah, *in* Leydsman McGinty, E.I., compiler, Rangeland Resources of Utah: Logan, Utah State University Cooperative Extension , p. 29–38.

Reddy, K.R., and DeLaune, R.D., 2008, Biogeochemistry of wetlands—science and applications: Boca Raton, Florida, CRC Press LLC.

Reynoldson, T.B., Norris, R.H., Resh, V.H., Day, K.E., and Rosenberg, D.M., 1997, The reference condition—a comparison of multimetric and multivariate approaches to assess water-quality impairment using benthic macroinvertebrates: Journal of the North American Benthological Society, v. 16 no. 4, p. 833–852.

Rohal, C., Hambrecht, K., Cranney, C., and Kettenring, K., 2017, How to restore Phragmites-invaded wetlands: Utah Agricultural Experiment Station Research Report 224, Logan, Utah, 2p.

Rohal, C.B., 2018, Invasive phragmites australis management in Great Salt Lake wetlands—context dependency and scale effects on vegetation and seed banks: Logan, Utah State University, Ph.D. dissertation, 208p.

Sorensen, E.D., Hoven, H.M., and Neill, J., 2020, Great Salt Lake shorebirds, their habitats, and food base, *in* Baxter, B.K., and Butler, J.K, editors, Great Salt Lake Biology: Cham, Switzerland, Springer Nature, p. 263–310.

Stevens Jr., D.L., and Olsen, A.R., 2004, Spatially balanced sampling of natural resources: Journal of the American statistical Association, v. 99, no. 465, p. 262–278.

Stoddard, J.L., Larsen, D.P., Hawkins, C.P., Johnson, R.K., and Norris, R.H., 2006, Setting expectations for the ecological condition of streams—the concept of reference condition: Ecological Applications, v. 16, no. 4, p. 1267–1276.

Sweetman, A.C., Kettenring, K.M., & Mock, K.E., 2013, The pattern and structure of genetic diversity of Schoenoplectus maritimus—implications for wetland revegetation: Aquatic Botany, v. 104, p. 47–54.

Tarsa, E.E., Holdaway, B.M., and Kettenring, K.M., 2022, Tipping the balance—The role of seed density, abiotic filters, and priority effects in seed-based wetland restoration.: Ecological Applications v. 32, no. 8, p. e2706.

U.S. Department of Agriculture , National Resources Conservation Service, 2020, PLANTS Database: Plant List of Accepted Nomenclature, Taxonomy, and Symbols. Online: https://plants.usda.gov/home

U.S. Environmental Protection Agency, 2016, NWCA 2011 Plant CC and Native Status Values – Data, Online data: https://www.epa.gov/national-aquatic-resource-surveys/data-national-aquatic-resource-surveys, Accessed Nov. 21, 2021.

U.S. Fish and Wildlife Service, 2018, National Wetlands Inventory, GIS layer: Online, https://www.fws.gov/program/national-wetlands-inventory/wetlands-mapper, accessed Jan. 21, 2021.

U.S. Fish and Wildlife Service, 2019, Wetlands mapper documentation and instructions manual: Madison, WI, U.S. Fish and Wildlife Service Ecological Services.

U.S. Geological Survey, 2019a, National Land Cover Database (NLCD) 2016 Land Cover Conterminous United States. U.S. Geological Survey, Sioux Falls, SD. online: https://www.mrlc.gov/data

U.S. Geological Survey, 2019b, NLCD 2016 Impervious Surface Conterminous United States. U.S. Geological Survey, Sioux Falls, SD. online: https://www.mrlc.gov/data.

U.S. Geological Survey, 2020, National Hydrography Dataset, GIS layer: Online: https://www.usgs.gov/national-hydrography, accessed Jan. 21, 2021.

U.S. Geological Survey, 2023, Great Salt Lake Hydro Mapper: Online, https://webapps.usgs.gov/gsl/#salinity, accessed Feb. 24, 2023.

Utah Division of Water Quality, 2014, Wetlands *in* State of Utah's combined 2012/2014 Water Quality Integrated Report: Salt Lake City, Utah, Utah Department of Environmental Quality.

Utah Division of Water Quality, 2016, Ecological characteristics of Great Salt lake fringe wetlands: Grant deliverable, p. 77, Online: https://documents.deq.utah.gov/water-quality/standards-technical-services/gsl-website-docs/wetlands-program/wetland-monitoring-assessment/DWQ-2016-018241.pdf

Utah Division of Water Quality, 2019, Development of statewide water quality standards for Utah wetlands: Grant deliverable, p. 59, Online: https://documents.deq.utah.gov/water-quality/standards-technical-services/wetlands-program/wetland-water-quality-standards/DWQ-2019-021045.pdf

Utah Division of Water Quality, 2020, Great Salt Lake Wetland Monitoring 2019-2020 Sampling and Analysis Plan.

Utah Division of Water Quality, 2022, Great Salt Lake Wetland Monitoring 2022 Sampling and Analysis Plan. https://geodata.geology.utah.gov/pages/download.php?direct=1&noattach=true&ref=74881&ext=pdf&k=

Utah Geospatial Resource Center, 2020a, Roads, online: https://gis.utah.gov/data/transportation/roads-system/

Utah Geospatial Resource Center, 2020b, Utah Points of Diversion, online: https://services.arcgis.com/ZzrwjTRez6FJiOq4/arcgis/rest/services/PODView/FeatureServer

Utah Geospatial Resource Center, 2020c, Minerals, online: https://opendata.gis.utah.gov/datasets/utah-minerals

Utah Geospatial Resource Center, 2020d, Oil and Gas, online: https://gis.utah.gov/data/energy/oil-gas/

Van Der Valk, A.G., 1981, Succession in wetlands—a gleasonian approach: Ecology, v. 32, no. 3, p. 688–696.

Van Sickle, J., and Paulsen, S.G., 2008, Assessing the attributable risks, relative risks, and regional extents of aquatic stressors: Journal of the North American Benthological Society, v. 27, no. 4, p. 920–931.

Welsh, S.L., Crompton, C.W., and Clemants, S.E., 2004, Chenopodiaceae, *in* Flora of North American Volume 4, Online resource: http://www.efloras.org/florataxon.aspx?flora_id=1&taxon_id=10185

Wetzel, R.G., 2006, Wetland ecosystem processes, *in* Batzer, D.P, and Sharitz, R.R., editors, Ecology of freshwater and estuarine wetlands: Los Angeles, California, University of California Press, p. 285–312.

Wilson, V.T., and Carson, R., 1950, Bear River—a national wildlife refuge: Washington D.C., U.S. Fish and Wildlife Service.

Wurtsbaugh, W.A., Miller, C., Null, S.E., Wilcock, P., Hahnenberger, M., and Howe, F., 2016, Impacts of water development on Great Salt Lake and the Wasatch Front: Logan, Utah, Watershed Sciences Faculty Publications, Paper 875.

Wurtsbaugh , W.A., Miller, C., Null, S.E., DeRose, R.J., Wilcock, P., Hahnenberger, M., Howe, F., and Moore, J., 2017, Decline of the world's saline lakes: Nature Geoscience, v. 10, no. 11, p. 816–821.

Zedler, J.B., and Kercher, S., 2004, Causes and consequences of invasive plants in wetlands—opportunities, opportunists, and outcomes: Critical Reviews on Plant Sciences, v. 23, no. 5, p. 431–452.

Estimate of Groundwater Flow and Salinity Contribution to Great Salt Lake Using Groundwater Levels and Spatial Analysis

Hector A. Zamora and Paul Inkenbrandt
Utah Geological Survey, Salt Lake City, Utah, hector.zamora.hg@gmail.com, paulinkenbrandt@utah.gov

10.31711/ugap.v51i.141

ABSTRACT

Groundwater discharge to Great Salt Lake (GSL) is difficult to quantify but represents a potentially significant source of water and salinity to the lake's overall water budget and chemistry, respectively. Understanding groundwater and its role in the overall health of GSL is critical due to the current historically low lake levels. We compiled existing groundwater level data in wells in the basin-fill aquifer around GSL and used spatial analysis methods to 1) create potentiometric-surface maps in the areas adjoining GSL, 2) calculate groundwater contributions to GSL, and 3) estimate salinity inputs from groundwater to GSL. We observed groundwater-level declines in most of the basin-fill wells from the 1980s to 2010s. These declines are consistent with historical groundwater-level trends in the Salt Lake, Tooele, Curlew, and Weber Valleys and are a consequence of aquifer overdraft associated with less than average precipitation in the basin and increased groundwater withdrawals in the GSL watershed. Using the Darcy flux equation, we calculated a groundwater flux to GSL of 313,500 acre-feet per year, substantially greater than previous estimates derived from water balance studies but consistent with estimates derived from geochemical modeling of GSL water chemistry. We calculated a salt contribution from groundwater to GSL of 1.18 million metric tons per year, which represents about 10% of the solutes derived from surface flows to GSL in 2013.

INTRODUCTION

Background and Objectives

Groundwater discharge is an essential component in limnological systems' hydrologic and chemical balances (Healy and others, 2007; Rosenberry and Winter, 2009). Despite its importance in developing accurate hydrochemical balances in lakes, groundwater contribution is often neglected or underestimated because it is difficult to quantify (Rosenberry and others, 2015). Understanding the groundwater component and its associated solute input is imperative for managing the environmental and economic resources of lakes affected by extensive anthropogenic water use and drought, such as Great Salt Lake (GSL) in northern Utah. Potentiometric gradient and aquifer hydraulic conductivity are key inputs to calculate groundwater flow. This report focuses on the potentiometric data input for estimating groundwater flow. Future work will better constrain hydraulic conductivity and geochemistry at the lake interface to improve groundwater flow estimates.

GSL is a hypersaline terminal lake and a sink for surface and groundwater across a large part of the eastern Great Basin (Spencer and others, 1985; Duffy and Al-Hassan, 1988; Arnow and Stephens, 1990). Salinity inputs and evaporation impact GSL's ecosystems and mineral resources (Carling and others, 2013; Jagniecki and others, 2021). Surface-water flows to GSL and associated salt loading are well constrained (Shope and Angeroth, 2015). However, the quantity of groundwater discharge remains relatively unknown, and groundwater is a potentially significant source to GSL's overall salt load (Kirby and others, 2019; Bunce, 2022). The importance of understanding groundwater dynamics and its role in the overall health of GSL becomes prominant by the current, historically low lake levels. Groundwater inflows to GSL will become critically important as surface-water discharges decrease due to increasing water demands (Null and Wurtsbaugh, 2020), rising air temperatures, and changing snow cover conditions in the basin (Hall and others, 2021).

Given the significance and uncertainty of groundwater to GSL's system, the objectives of the present study are to 1) compile historical groundwater levels and use them to create generalized potentiometric-surface maps, 2) roughly estimate groundwater flow to GSL using a combination of spatial analysis techniques and Darcy's Law, and 3) combine the results from the previous objective with existing groundwater chemistry data to estimate salinity inputs to GSL derived from groundwater. Water and salt dynamics play a fundamental role in shaping not only GSL's

unique ecological, recreational, and mineral resources, but also the future development in the sprawling urban centers on the east shore of the lake. We provide the first systematic basin-wide assessment of groundwater levels in areas adjoining GSL to quantify groundwater contributions and their salt loading to the lake system. This information is required to constrain water and salt budgets needed by managing agencies to make informed decisions regarding the future health and productivity of ecosystems and industries in the lake. Our findings serve as a basis for future work to better define the role of groundwater in GSL's overall water volume and solutes budgets.

Study Area

The study area covers about 11,000 square miles in northern Utah and southern Idaho (figure 1). It is bounded on the east by the north-south-trending Wasatch Range and on the west by the Great Salt Lake Desert. Several mountain ranges (Hansel, Promontory, Oquirrh, Stansbury, Hogup, etc.) and associated valleys (Curlew, Hansel, Malald–Lower Bear River, Weber, Salt Lake, Tooele, Skull, etc.) bound the north and south flanks of the study area and drain into GSL (figure 1). GSL is the largest salt-water lake by area in the Western Hemisphere and the eighth largest in the world (Hammer, 1986). It is 75 miles long by 28 miles wide and covers approximately 1700 square miles with a maximum depth of 33 feet at the average water-surface elevation of 4200 feet above sea level (FASL). The Jordan, Bear, and Weber Rivers deliver on average 2.9 million acre-feet of water to GSL, approximately 95% of the total stream inflow (Stephens and Gardner, 2007; Mohammed and Tarboton, 2012). Previous studies (Arnow and Stephens, 1975; Waddell and Fields, 1976; Loving and others, 2000; Bunce, 2022) have estimated groundwater discharge to GSL ranges between 3% and 10% of the total inflow. The Jordan, Bear, and Weber Rivers also delivered an estimated 14.3 million metric tons of total dissolved solids (TDS) in 2013 (Shope and Angeroth, 2015). Groundwater potentially contributes a significant input to GSL's overall salt load (Hahl, 1968; Spencer and others, 1985; Loving and others, 2000), but the relationship between groundwater and GSL's salinity has not been well defined.

Salinity of the lake ranges from 5% to 29% and creates diverse opportunities for ecological, recreational, and mineral uses. GSL is part of the Pacific Flyway and provides important nesting and foraging habitat for over 250 species of birds as they travel between North and South America (The Nature Conservancy, 2022). Between 1.6 and 2.5 million metric tons of salt are commercially removed from the lake every year (Stephens and Gardner, 2007). Mineral extraction, brine shrimp cyst production, and recreation in GSL can generate an estimated economic value of $1.32 billion per year (Bioeconomics, 2012).

As a terminal lake, GSL loses water primarily through evaporation. Therefore, changes in streamflow conditions severely impact lake levels and salinity (Mohammed and Tarboton, 2012). Stream diversions for agricultural and municipal uses reduce the amount of water flowing into GSL by 39% (Null and Wurtsbaugh, 2020). These diversions and a warming climate led to the present-day lake-level decline (Wurtsbaugh and others, 2017; Wang and others, 2018). As of November 2022, the area covered by GSL was reduced to about 900 square miles at a historical low water-surface elevation of 4188.5 FASL. Consequently, salinity and the surface area covered by dry lakebed increased. Increased salinity levels stress microbialite, brine fly, and brine shrimp populations, jeopardizing the entire ecological community that depends on them. Dry lake beds are a major source of dust pollution and have the potential to accelerate snowmelt when dust is blown onto the snow (Reynolds and others, 2014; Skiles and others, 2018).

METHODS

Data Compilation

We compiled historical groundwater level data from various datasets including the U.S. Geological Survey (USGS) National Water Information System (NWIS, https://waterdata.usgs.gov/, U.S. Geological Survey, 2022a), the Utah Division of Water Rights (DWRi) well drilling records, the Utah Geological Survey (UGS) Geologic Hazards Program Subsurface Geotechnical Database, and the UGS Wetlands section field data. Data from the DWRi was derived from a combination of well information tables and the Water Rights points of diversion (WRPOD) feature class provided on the DWRi website (https://waterrights.utah.gov/). The WRPOD feature class only includes wells with a Well Identification Number (WIN) and excludes wells without an assigned WIN. The UGS Geologic Hazards Program Subsurface Geotechnical Database consists of 5141 boreholes in watersheds that contribute to the lake. The UGS Wetlands section field data consists of 362 shallow boreholes in the wetlands proximal to GSL. In addition to groundwater level data, well properties (latitude, longitude, surface elevation, screen depth, and well depth) were also gathered where available. Data compilation is limited to wells in the basin-fill aquifer and boreholes within the study area (figure 2).

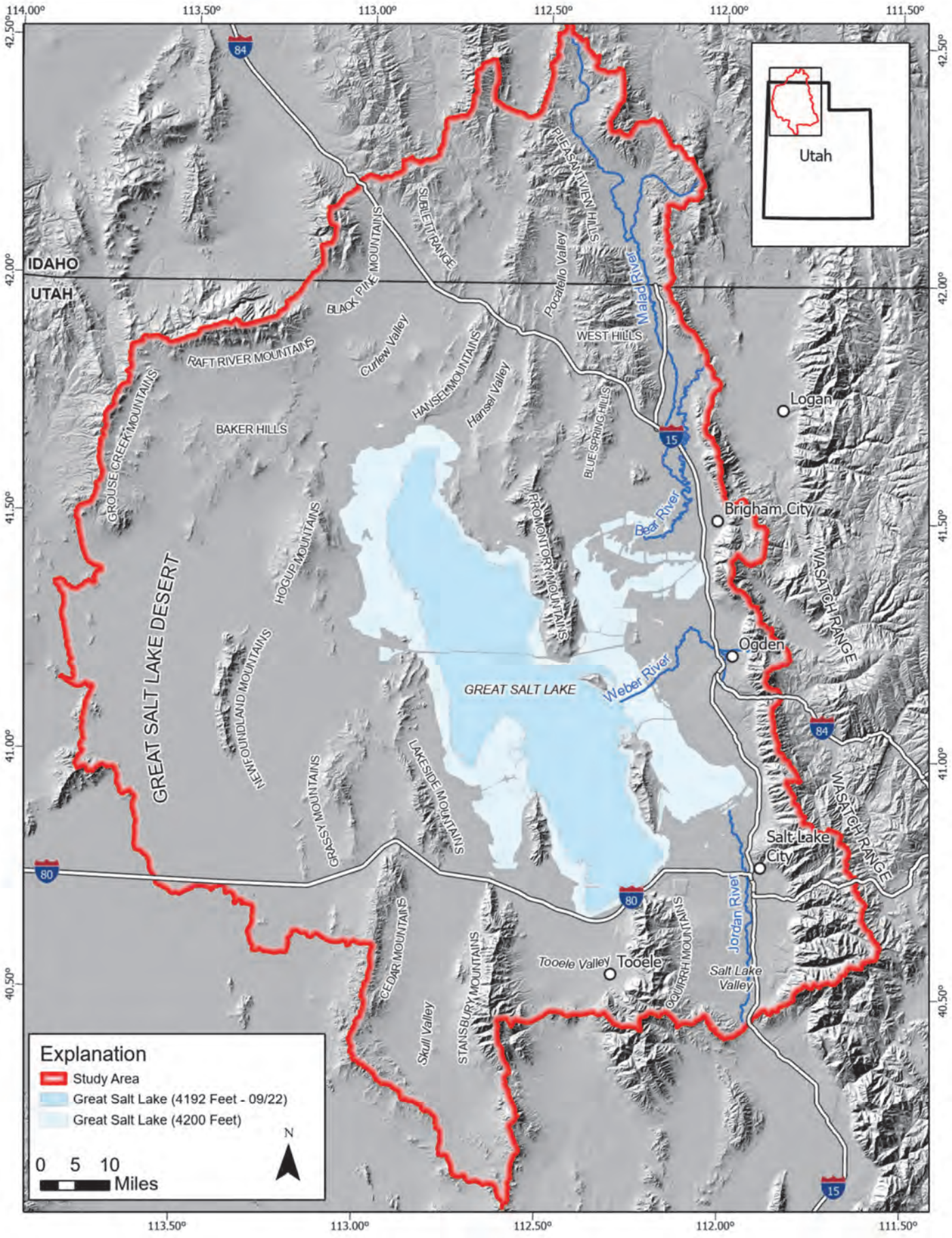

Figure 1. *Physiographic overview of GSL study area.*

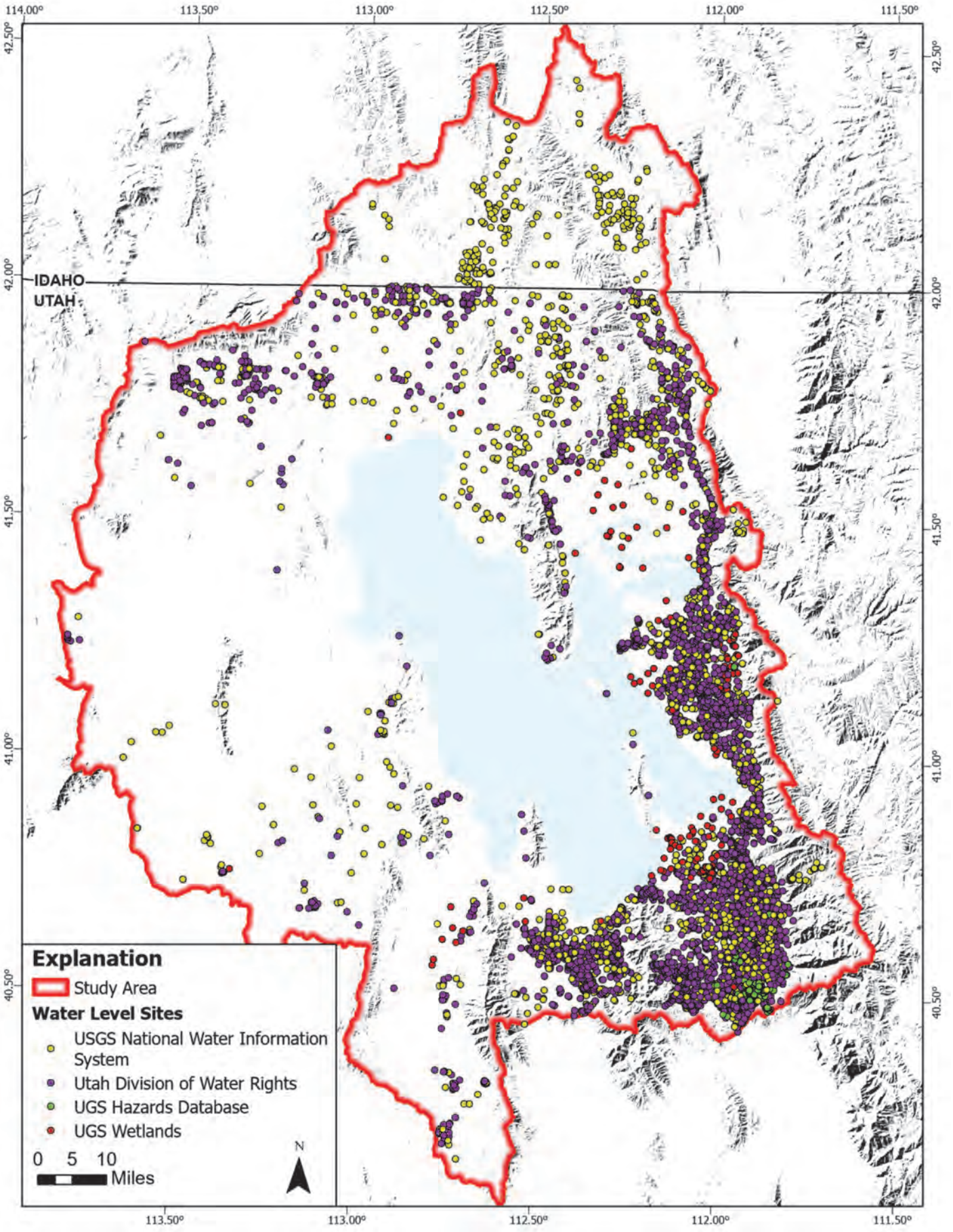

Figure 2. *Geographical location of historical groundwater-level sites.*

The compiled groundwater level data show spatial and temporal complexities within the study area. Groundwater level measurements began in the 1900s but were limited to only a few sites (33). The number of data collection sites increased over time to reach a maximum of 3136 during the 1990s but remained variable (figure 3). Furthermore, while many sites were visited regularly, others were visited less often, or only once in many cases. We reprojected, combined, and aggregated the data using Python 3 and created two different datasets to deal with these spatial and temporal intricacies. The two datasets (tables S1 and S2) are included as supplementary information in geodatabase format (contact authors for database).

The first dataset (table S1) contains data available from all sources (NWIS, DWRi, and UGS). Groundwater level data for each site were grouped by decade and a mean water level elevation value was calculated if more than a single measurement was recorded during the time frame. The second dataset (table S2) contains only USGS NWIS data for all wells available within the study area. Here, the groundwater elevation value is the mean of all available data for each site. This dataset also contains estimated aquifer properties including saturated thickness, hydraulic conductivity, and transmissivity for individual sites. Saturated thickness values were estimated by subtracting mean depth to water values from total well depth values. Hydraulic conductivity values were extracted from layer 2 of the USGS's groundwater model of the Great Basin carbonate and alluvial aquifer (Brooks, 2017). Finally, transmissivity values were calculated by multiplying saturated thickness times hydraulic conductivity.

We downloaded three high-resolution aerial photographs from the European Space Agency's Sentinel -2 satellites for August 25th, August 28th, and September 9th, 2022, using the USGS Global Visualization Viewer (GloVis, https://glovis.usgs.gov/). Sentinel-2 satellites carry an optical payload with visible, near infrared and shortwave infrared sensors encompassing 13 spectral bands: 4 bands at 10-meter, 6 bands at 20-meter, and 3 bands at 60-meter spatial resolution, with a swath width of 290 kilometers (European Space Agency, 2022). We created a single mosaicked image in ArcGIS Pro® and used it to trace the extent of the lake. We assigned a surface elevation of 4190 feet to this extent based on USGS lake stage observations at the Saltair boat harbor (USGS Site ID 10010000, https://webapps.usgs.gov/gsl/) on August 1st, 2022 (refer to figure 1 for location).

Lidar datasets are available for northern Utah but do not cover the entire study area. For consistency, we downloaded six digital elevation model (DEM) tiles from the Terra Advanced Spaceborne Thermal Emission and Reflection Radiometer (ASTER) Version 3 using the USGS Earth Explorer (https://earthexplorer.usgs.gov/). These DEM tiles have a one -third arc-second resolution (~10 meters) and are referenced to the North American Vertical Datum of 1988 (NAVD 88). We created a single mosaicked image in ArcGIS Pro® and used it to extract surface elevations in well sites where this information was missing. We also used the ASTER DEM as an explanatory variable input in the data interpolation process (discussed below).

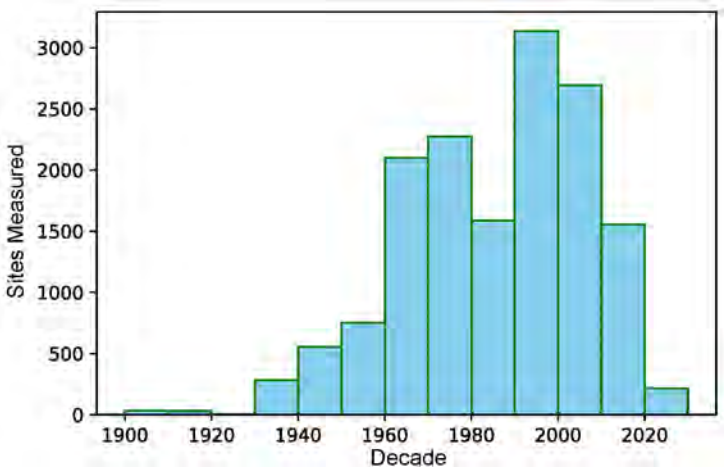

Figure 3. *Number of groundwater-level sites by decade.*

Potentiometric Surface Interpolation

We used the Empirical Bayesian Kriging Regression Prediction (EBK-RP) tool in ArcGIS Pro® to interpolate the water level elevation values in table S1. EBK-RP is a geostatistical interpolation method that uses EBK with explanatory variable rasters known to affect the value of the data being interpolated. The tool combines kriging with regression analysis to make predictions that are more accurate than either kriging or regression can achieve on their own (ESRI, 2022a). As the potentiometric surface generally follows topography, and because it is a component in the calculation of groundwater level elevation, we included the ASTER DEM as an explanatory variable. We created two generalized potentiometric-surface maps: one for the 1980s (figure 4) and one for the 2010s (figure 5). These two decades were chosen because 1) not enough information is available to create a potentiometric surface for the 2020s, thus the 2010s data represent the most recent groundwater conditions for the study area, 2) average decadal GSL surface levels were close to the historical average (4200 FASL) in the 1980s, and 3) both decades contain about the same number of sites available for interpolation (figure 3). We also used table S1 to create a water

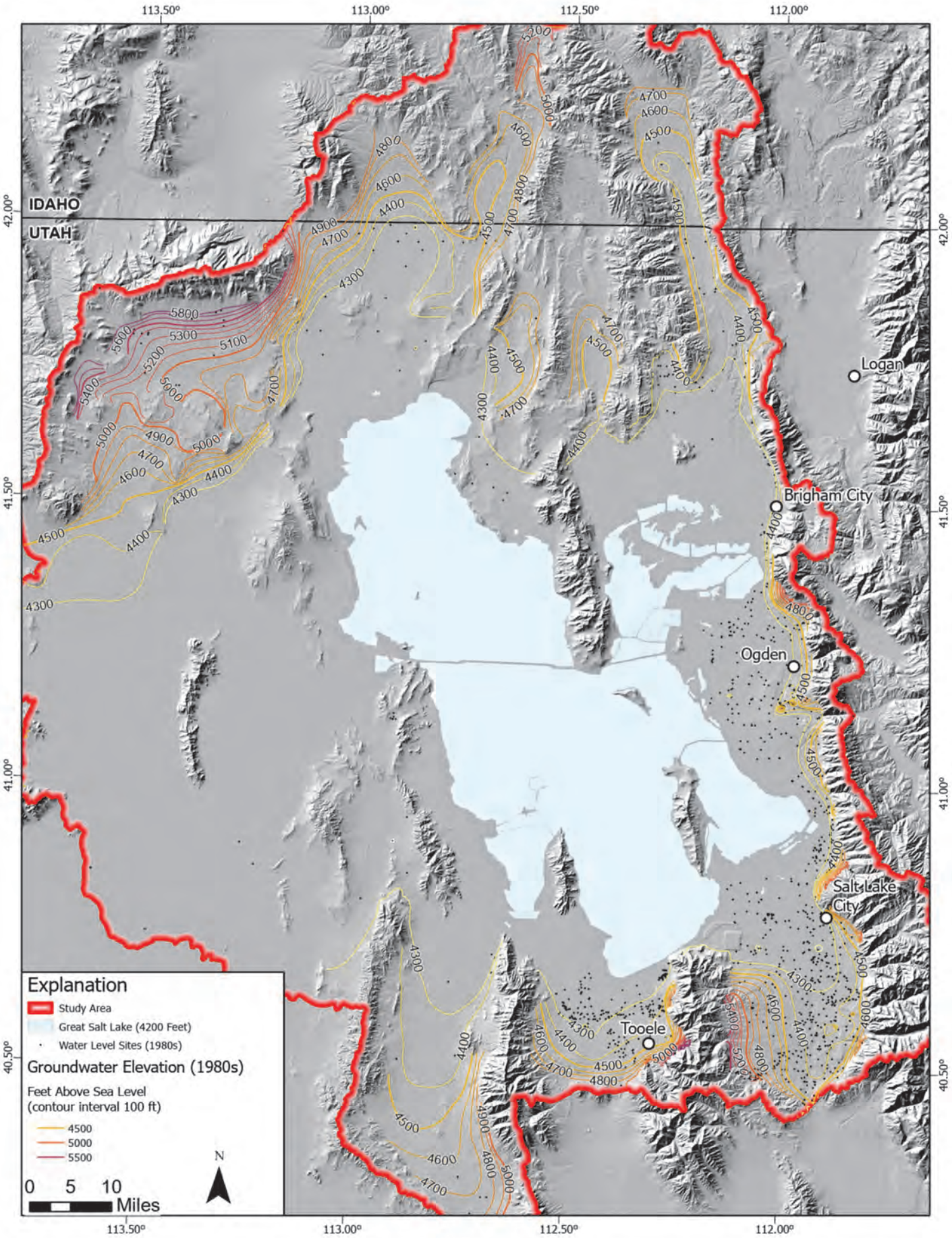

Figure 4. *Potentiometric surface elevation in study area for the 1980s.*

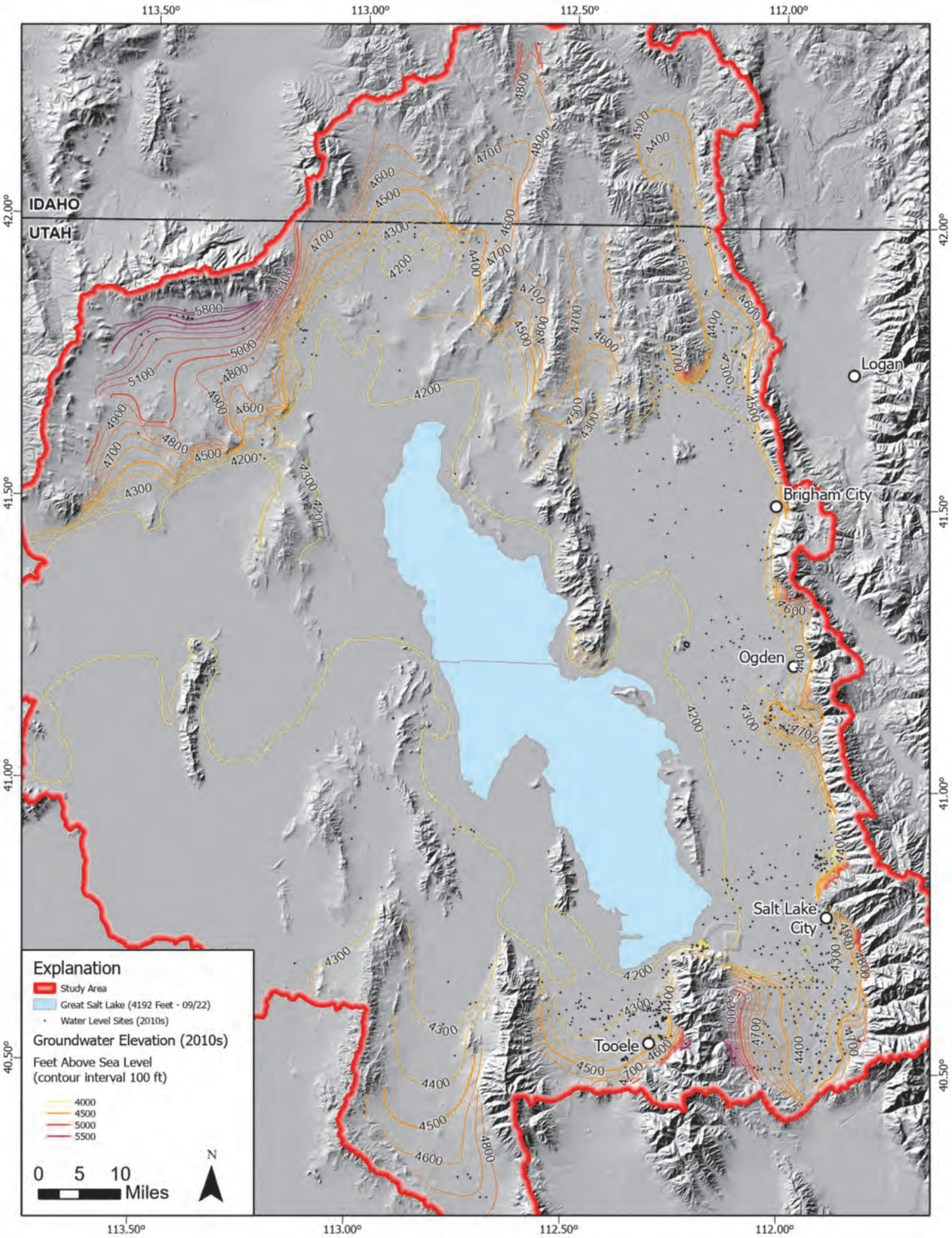

Figure 5. *Potentiometric surface elevation in study area for the 2010s.*

level difference map by subtracting water level elevation values (figure 6). This calculation was possible only for sites where data was available for both decades.

We used the Kriging tool in ArcGIS Pro® to interpolate the water elevation, saturated thickness, and transmissivity values in Table S2 (Figure 7). The three output rasters are floating point, have the same areal extent, and have a cell size of 100. Units are consistent for time (day) and length (feet) for all data. We used these rasters as input for the Darcy Flow tool in ArcGIS Pro® to estimate groundwater seepage velocity values around GSL (discussed below).

Groundwater Seepage Velocity and Darcy Flux

We applied two different approaches to estimate groundwater flow to Great Salt Lake. Both approaches are basic Darcy Flow estimates and should be considered rough approximations. The first approach used tools available in GIS software and the second approach used basic linear discretization of the valleys around the lake.

GIS-Based Calculations of Darcy Flow

For the first approach, we used the Darcy Flow tool in ArcGIS Pro® to estimate groundwater seepage velocity around the lake. This method uses Darcy's Law to model two-dimensional, vertically mixed, horizontal, and steady state flow, where groundwater head is independent of depth. Darcy's Law states that Darcy velocity in porous material is calculated from the hydraulic conductivity and the hydraulic gradient as:

$$q = -K\nabla i = -K\frac{\nabla H}{\nabla L} \quad (1)$$

where:

q = Darcy velocity, Darcy flux, or specific discharge (V/T/A or L/T)

K = hydraulic conductivity (L/T)

∇i = hydraulic gradient (dimensionless)

∇H = change in hydraulic head over length (L)

∇L = change in length (L)

Hydraulic conductivity (K) may be calculated from the transmissivity and thickness as:

$$K = T/b \quad (2)$$

where:

T = transmissivity (L^2/T)

b = aquifer thickness (L)

The specific discharge (q) is defined as the volume of water flow per unit time through a cross-sectional area normal to the direction of flow (Bear, 1979). Specific discharge is directly proportional to hydraulic conductivity. The aquifer flux is defined as:

$$U = -T\nabla i \quad (3)$$

where:

U = aquifer flux (V/T/L)

T = transmissivity (L2/T)

∇i = hydraulic gradient (dimensionless)

The aquifer flux (U) represents the discharge per unit width of the aquifer. The average fluid velocity within the pores, or seepage velocity, is the Darcy velocity (q) divided by the effective porosity of the medium:

$$V = \frac{q}{n} = -\frac{K\nabla i}{n} = -\frac{T\nabla i}{bn} \quad (4)$$

where:

V = groundwater seepage velocity (L/T)

q = Darcy velocity, Darcy flux, or specific discharge (V/T/A or L/T)

n = effective porosity (%)

The groundwater seepage velocity (V) is calculated on a cell-by-cell basis in the Darcy Flow procedure (ESRI, 2022b). For cell {i, j}, the aquifer flux (U) is calculated through each of the four cell walls, using the difference in heads between the two adjacent cells and the harmonic average of the transmissivities (Konikow and Bredehoeft, 1978), which are assumed to be isotropic (ESRI, 2022b).

The Darcy Flow tool requires four raster datasets as input: groundwater head elevation (FASL), saturated thickness (feet), formation transmissivity (square feet per day), and effective formation porosity. We created the first three datasets by interpolating the aquifer property data in table S2 (figure 7), and we assigned the effective formation porosity a value of 0.35 for the basin-fill aquifer. Two raster datasets result from this calculation: an output magnitude raster and an output direction raster. In the output magnitude raster, each cell value represents the magnitude of the seepage velocity vector (average linear velocity) at the center of the cell and is calculated as the average value of the seepage velocity through the four faces of the cell (ESRI, 2022b). In the output flow direction raster, each cell value represents the direction of the seepage velocity vector (ESRI, 2022b).

We extracted the mean groundwater seepage velocity around GSL from the output magnitude raster using the Zonal Statistics as Table tool in ArcGIS Pro® with the GSL perimeter shapefile (both 4190 and 4200 FASL, table 1) as the Feature Zone Data (dataset that defines zone of interest). We conducted zonal statistics using both polylines and polygons of GSL at both elevations to compare how the cells' statistics were aggregated. We also divided the 4190 FASL GSL perimeter shapefile into three different

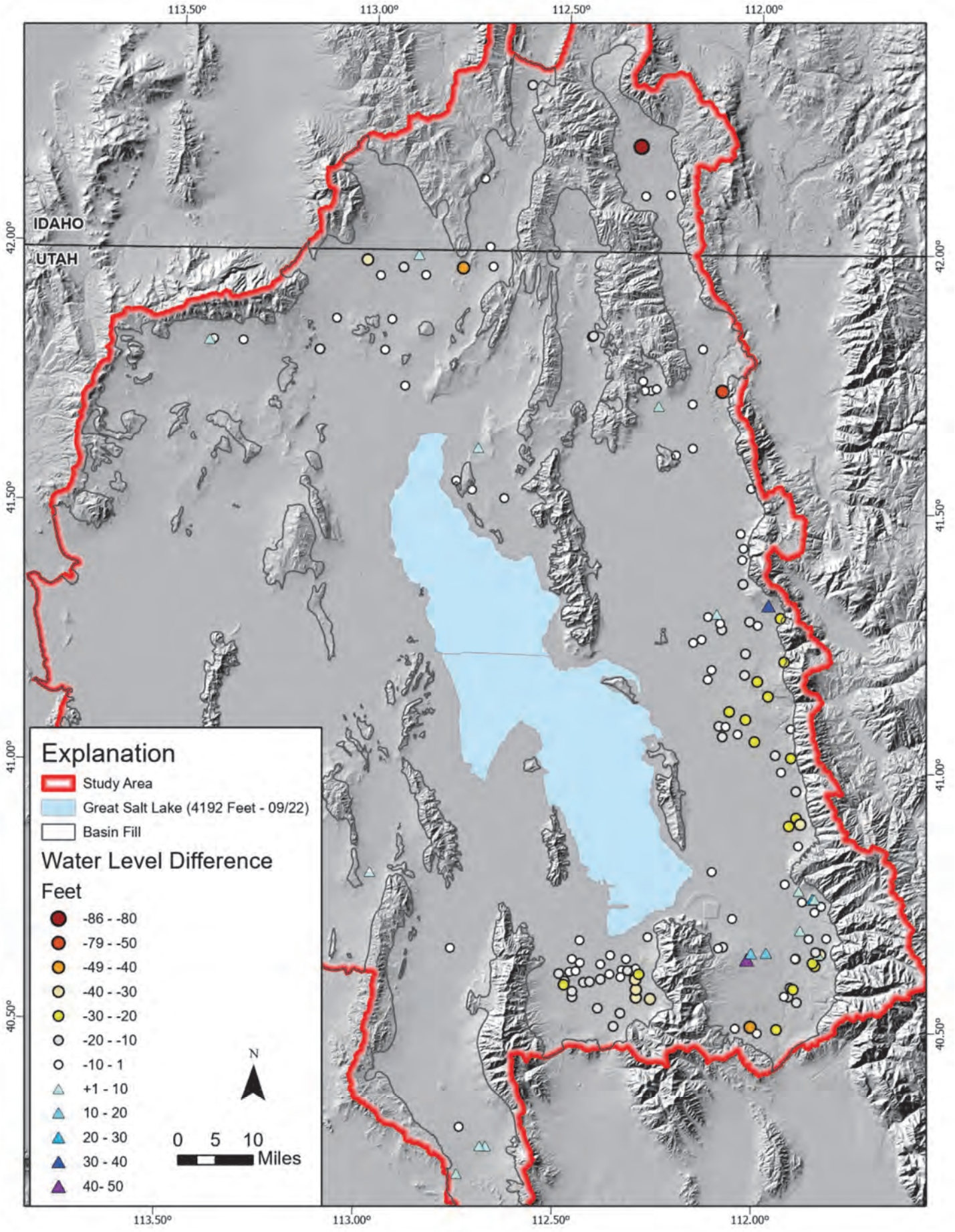

Figure 6. *Groundwater level difference between the 1980s and 2010s.*

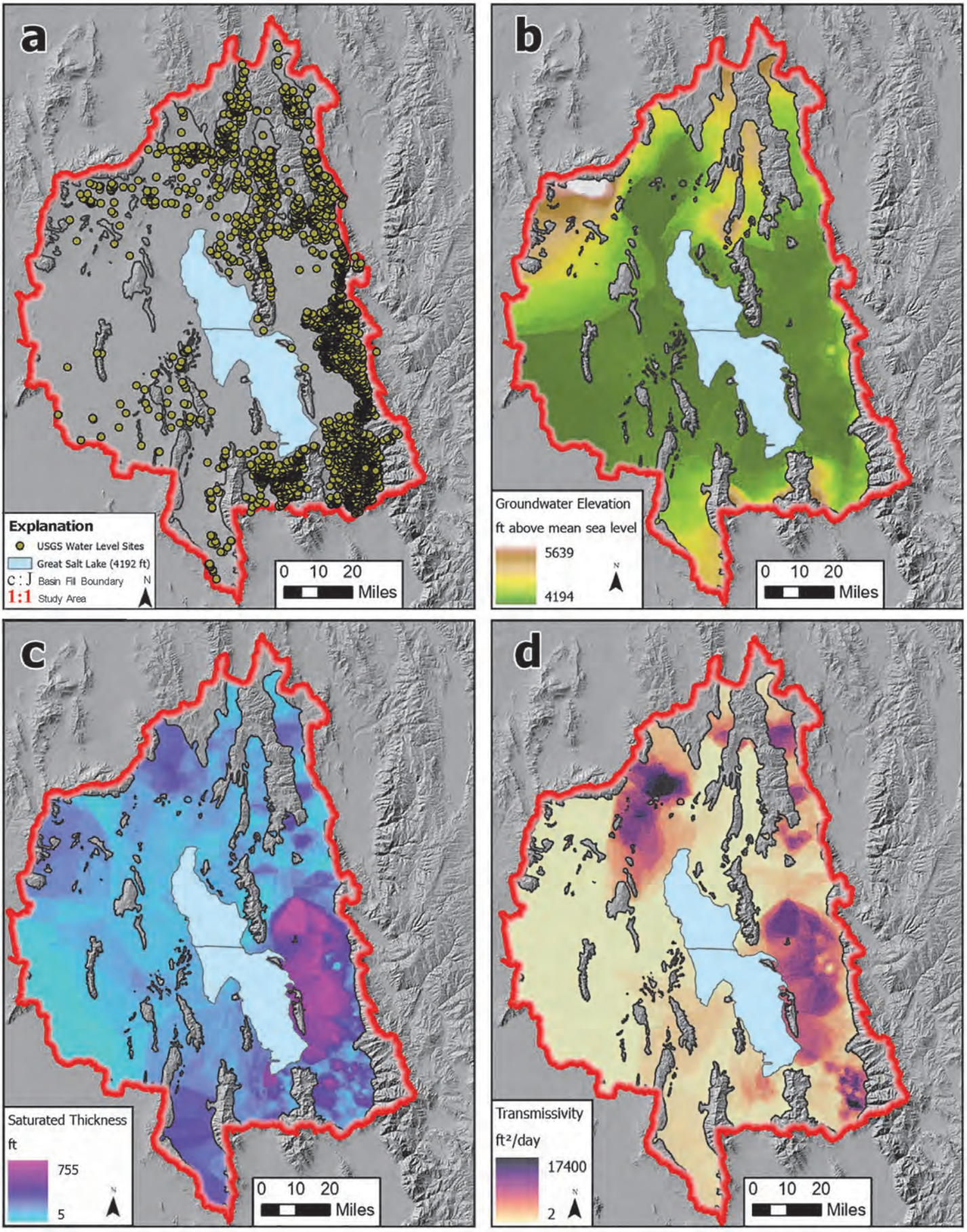

Figure 7. *Raster datasets used as input to calculate groundwater seepage velocity around GSL in ArcGIS Pro®: a) USGS water level sites, b) potentiometric surface, c) saturated thickness, and d) transmissivity. All data needed to create these raster datasets are available in table S2.*

Table 1. *Groundwater flux estimates for GSL in acre-feet per year.*

GSL Level (ft asl)	Length (ft)	Aquifer Thickness (ft)	Area (ft^2)	Mean Seepage Velocity (ft/day)	Q (af/year)
4190[a]	1,388,561	232	322,666,029	0.15	**411,000**
4190[b]	1,388,561	232	322,666,029	0.12	**324,000**
4200[a]	1,768,800	232	411,023,839	0.09	**310,000**
4200[b]	1,768,800	232	411,023,839	0.11	**379,000**

[a] Estimate made using GSL polyline

[b] Estimate made using GSL polygon

sections: west/south, north, and east (figure 8). We extracted the groundwater seepage velocities from these different sections (using the Zonal Statistics Tool as above) to estimate the potential groundwater contribution by area (table 2). Finally, we multiplied the groundwater seepage velocity by the mean aquifer thickness (232 feet, calculated from Table S2) and the perimeter length of GSL (obtained from the GSL perimeter shapefiles) to obtain an estimated groundwater contribution (Q) in acre-feet per year (tables 1 and 2).

Straight Line Calculations of Darcy Flow

For the second approach, we estimated the groundwater discharge from each adjoining basin-fill valley using Darcy's Law:

$$Q = -KA\nabla i = -KA\frac{\nabla H}{\nabla L} - KA\frac{H_2 - H_1}{L} \quad (5)$$

For this approximation, we used a mean K value of 12.43 feet per day (from table S2). We created several polygons to roughly constrain the areal extent of the basin fill in the valleys (figure 8). We calculated the cross-section area (A) for the flux calculations by multiplying the width of the polygon (perpendicular to the flow direction) by the mean aquifer thickness of 232 feet (from table S2). We calculated the hydraulic gradient (∇i) by extracting H1 and H2 values from the groundwater elevation raster, near the upper and lower ends of the polygons (figure 8) and dividing the difference between the two piezometric heads by the length of the polygon (parallel to groundwater flow). The geometrical properties and estimated groundwater discharge for each basin-fill area, (Q) in acre-feet per year, are presented in table 3.

Quantifying Error

To better understand the amount of variability that can be introduced by hydraulic conductivity, we iteratively calculated the groundwater flow for each area using the straight-line approach. We created a lognormal distribution of hydraulic conductivity, using 1.094 (log 10 of 12.43 ft/day) as the mean and 1.3 as the standard deviation, which is the standard deviation of the hydraulic conductivity of the upper basin-fill aquifer from the USGS groundwater model. We randomly sampled hydraulic conductivity 100,000 times from this distribution and used the resulting summary statistics to constrain variability of groundwater flow estimates from the calculations.

Salt Loading

We calculated mean TDS values around GSL using data available from previous studies in the area (Kirby and others, 2019). From Kirby and others' (2019) data, we obtained three different TDS values using 1) their calculated TDS values to compute a mean TDS for the whole study area, 2) their TDS raster and the Zonal Statistics as Table tool in ArcGIS Pro® to estimate the mean TDS value around GSL at 4190 FASL (polyline), and 3) their TDS raster and the Zonal Statistics as Table tool in ArcGIS Pro® to estimate the mean TDS value around GSL at 4200 FASL (polyline, table 4). We used the sectioned 4190 FASL GSL shapefile (west/south, north, and east) in figure 8 to extract mean TDS values by segment from the TDS raster using the Zonal Statistics as Table tool in ArcGIS Pro® (table 5). This approach helped to estimate the salt loading contribution by section. We combined the mean TDS values, in milligrams per liter (mg/L), with the groundwater discharge (Q, acre-feet) values in tables 1 and 2 to estimate a salt loading to the lake in metric tons per year (tables 4 and 5).

RESULTS

Generalized Potentiometric Surface

The generalized potentiometric surface maps for the 1980s and 2010s show that, at the scale of the study area, groundwater flow patterns are relatively constant over time (figures 4 and 5). Groundwater flows from the high-elevation mountains surrounding the study area towards the adjacent valleys and into

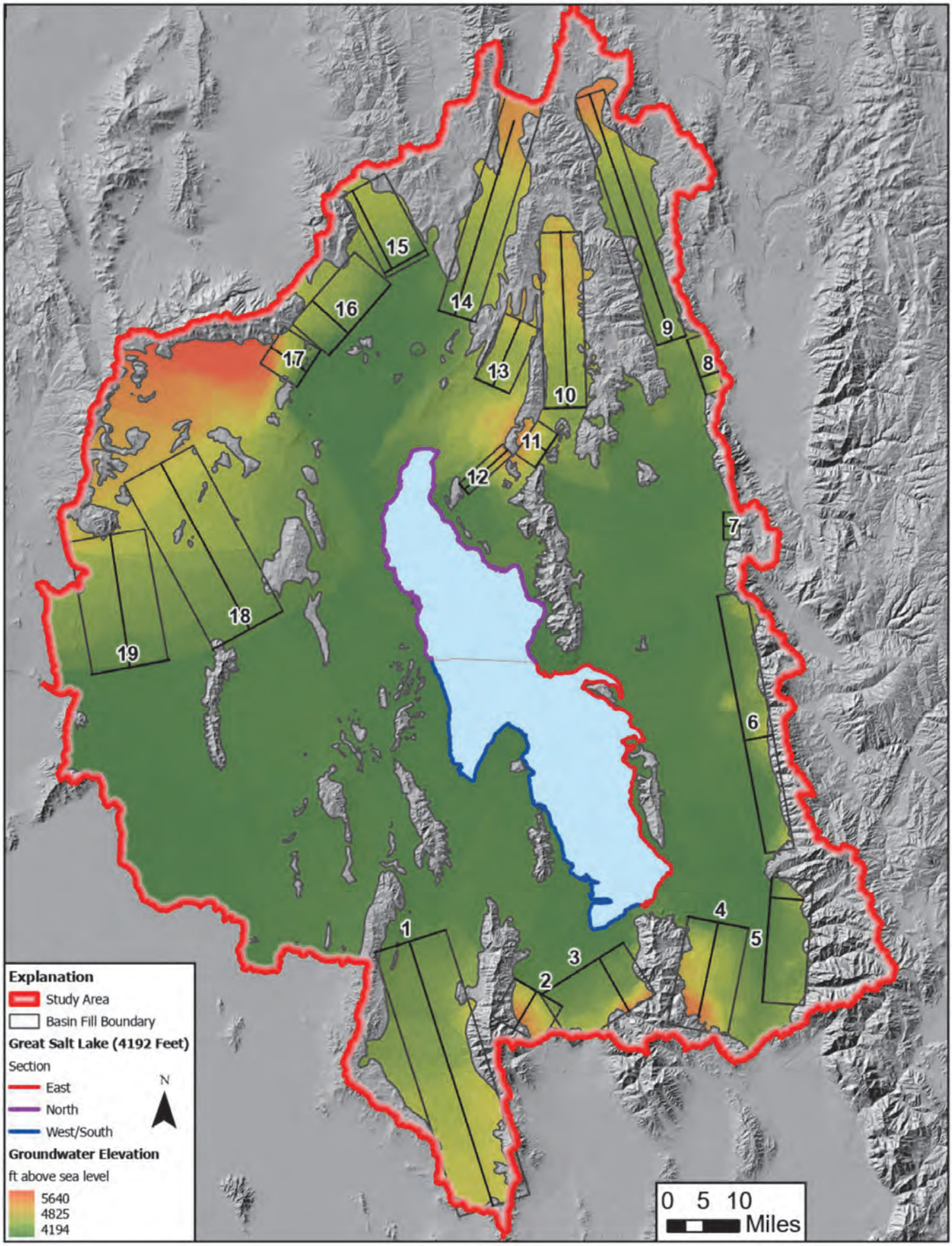

Figure 8. *Polygons used in Darcy's Law equation to estimate groundwater discharge from each basin-fill valley adjoining GSL. Colors around GSL show divisions used to estimate groundwater and salt contributions by section.*

Table 2. *Groundwater flux estimates for GSL by section at 4190 FASL in acre-feet per year.*

Section	Length (ft)	Thickness (ft)	Min Seepage Velocity (ft/day)	Max Seepage Velocity (ft/day)	Median Seepage Velocity (ft/day)	Mean Seepage Velocity (ft/day)	Min Q (af/year)	Median Q (af/year)	Mean Q (af/year)
West/South	485,343	232	0.0003	3.3	0.005	0.05	292	**4,900**	**50,000**
North	469,067	232	0.0004	16.8	0.016	0.30	332	**14,600**	**275,000**
East	434,151	232	0.0013	14.4	0.027	0.10	1,135	**23,000**	**86,000**
							1,759	**42,600**	**411,000**

GSL. For both decades, the steepest groundwater gradients occur in the vicinity of the Raft River Mountains, across the west flank of the Oquirrh Mountains (southeastern Tooele Valley), across the east flank of the Oquirrh Mountains (western Salt Lake Valley), and along the Wasatch Range (figures 4 and 5). There are noticeable changes in the potentiometric surface between the two decades. For example, in Salt Lake Valley, the 4300-foot contour has moved farther south (upstream), and we observed cones of depression north of the Oquirrh Mountains and in the Taylorsville and Bountiful areas (figures 9 and 10). We also observed some recovery in the Weber River delta area where groundwater recharge projects have been operating since the 2000s (Hurlow and others, 2011; figures 11 and 12). Figure 6 also shows groundwater-level recovery in some wells. However, groundwater-level recovery is an exception rather than the rule because 129 out of 147 wells having data available in both decades show a groundwater-level decline (figure 6). Groundwater-level declines are particularly high in localized areas of the north Malad River Valley in Idaho (-86 feet), Curlew Valley (-35 to -49 feet), near the Bear River (-51 feet), and Salt Lake Valley (-44 feet). The data in figure 6 show there has been a mean decrease in water levels of 10.14 feet from the 1980s to 2010s.

Seepage Velocity and Darcy Flux

Mean groundwater seepage velocities into GSL are 0.15 (polyline) and 0.12 (polygon) feet per day using the 4190 FASL shapefiles (table 1). Mean groundwater seepage velocities along the GSL perimeter are 0.09 (polyline) and 0.11 (polygon) feet per day using the 4200 FASL shapefiles (table 1). These mean seepage velocities result in groundwater fluxes ranging from 310,000 to 411,000 acre-feet per year (table 1). The average of these estimates is 356,000 acre-feet per year. The mean groundwater seepage velocities by section (4190 FASL) are 0.05 (west/south), 0.30 (north), and 0.10 (east) feet per day (table 2). These mean seepage velocities result in groundwater fluxes of 50,291 (west/south), 274,660 (north), and 85,829 (east) acre-feet per year for a total of 411,000 acre-feet per year (table 2).

Using the Darcy flux equation on the linear traverses in adjoining valleys (figure 8), groundwater contributions to GSL range from 3500 (Skull Valley) to 63,900 (Tooele Valley) acre-feet per year for a total of 313,500 acre-feet per year (table 3). The groundwater discharge from the Wasatch Range (sum of Salt Lake, Weber, and Malad Valley and Brigham City) is 146,400 acre-feet per year, 47% of the total groundwater contribution to the lake.

Salt Loading

The mean TDS values along GSL are 2116, 2538, and 3594 mg/L with an average value of 2749 mg/L using three different methods as explained in the "Methods" section (table 4). These TDS values and the calculated groundwater contributions in tables 1 and 3 result in yearly dissolved solid (salt) fluxes ranging from 810,000 to 1,820,000 metric tons, and an average of 1,060,000 metric tons, into GSL (table 4). Table 5 reports the mean TDS values by perimeter section as 4627 (west/south), 3055 (north), and 3023 (east) mg/L. These TDS values and the calculated groundwater contribution by section in table 3 result in yearly salt fluxes of 290,000 (west/south), 1,040,000 (north), and 320,000 (east) metric tons (table 5), resulting in 1,650,000 metric tons per year.

Error

The uncertainty of the Darcy flux calculations on the linear traverses through adjoining valleys is high. The 5th percentile for flow values is 2350 acre-feet/yr and the 95th percentile is 44.5 million ac-ft/yr. See table 3 for a complete list of variations associated with potential variability in hydraulic conductivity.

DISCUSSION

Generalized Potentiometric Surface

Groundwater levels declined in most of the basin-fill aquifer from the 1980s to the 2010s (figure 6). These declines are consistent with observed historical

Table 3. *Groundwater contribution from adjoining areas in acre-foot per year*

Polygon	Area	Avg K (ft/day)	Width (ft)	Thickness (ft)	H1 (ft)	H2 (ft)	Length (ft)	Gradient	Area (ft2)	Q (af/year)	5th %-tile (ac-ft/yr)	Median Q (ac-ft/yr)	95th %-tile (ac-ft/yr)
1	Skull Valley	12.43	54,454	232	4823	4289	203,975	0.0026	12,653,714	3,500	30	3,400	486,500
2	Tooele Valley	12.43	40,416	232	5179	4292	32,359	0.0274	9,391,642	26,800	200	26,600	3,780,500
3	Tooele Valley	12.43	71,767	232	5234	4282	44,598	0.0213	16,676,811	37,100	280	36,900	5,227,800
4	Salt Lake Valley	12.43	45,308	232	5255	4254	71,213	0.0141	10,528,418	15,400	110	15,300	2,173,300
5	Salt Lake Valley	12.43	92,678	232	4700	4277	24,740	0.0171	21,535,992	38,400	280	38,100	5,407,400
6	Weber Valley	12.43	191,539	232	4542	4267	21,629	0.0127	44,508,754	59,000	440	58,600	8,310,400
7	Brigham City	12.43	20,500	232	4686	4298	11,987	0.0324	4,763,675	16,100	120	16,000	2,264,400
8	Malad Valley	12.43	42,798	232	4600	4377	14,285	0.0156	9,945,158	16,200	120	16,100	2,279,900
9	Malad Valley	12.43	22,591	232	5224	4430	190,199	0.0042	5,249,569	2,300	20	2,300	321,800
10	Blue Creek	12.43	31,015	232	4950	4476	129,879	0.0036	7,207,091	2,700	20	2,700	386,300
11	N. Promontory	12.43	29,403	232	5069	4554	18,322	0.0281	6,832,504	20,000	150	19,900	2,820,300
12	N. Promontory	12.43	10,239	232	5090	4247	42,539	0.0198	2,379,281	4,900	40	4,900	692,400
13	Hansel Valley	12.43	27,543	232	4934	4495	53,115	0.0083	6,400,287	5,500	40	5,500	776,800
14	Curlew Valley	12.43	29,051	232	5107	4321	149,383	0.0053	6,750,708	3,700	30	3,700	521,600
15	Park Valley	12.43	34,923	232	4710	4266	64,256	0.0069	8,115,210	5,800	40	5,800	823,500
16	Park Valley	12.43	69,117	232	4658	4276	35,522	0.0108	16,061,019	18,000	130	17,900	2,536,400
17	Park Valley	12.43	32,002	232	5237	4212	32,206	0.0318	7,436,445	24,700	180	24,500	3,475,600
18	GSL Desert	12.43	58,076	232	4931	4292	138,707	0.0046	13,495,374	6,500	50	6,400	913,000
19	GSL Desert	12.43	58,197	232	4854	4223	99,404	0.0063	13,523,491	8,900	70	8,900	1,260,700
										315,500	2,350	**313,500**	44,458,600

Table 4. *Salt flux estimates for GSL in metric tons per year. Average values are in boldface.*

Q (af/year)	TDS (mg/L)		Dissolved load flux (metric ton/year)
313,500	2,116	a	820,000
313,500	2,538	b	980,000
313,500	3,594	c	1,390,000
411,000	2,116	a	1,070,000
411,000	2,538	b	1,290,000
411,000	3,594	c	1,820,000
324,000	**2,116**	a	850,000
324,000	**2,538**	b	1,010,000
324,000	3,594	c	1,440,000
309,966	2,116	a	810,000
309,966	2,538	b	970,000
309,966	3,594	c	1,370,000
379,000	2,116	a	990,000
379,000	2,538	b	1,190,000
379,000	3,594	c	1,680,000
347,493	**2,749**		**1,060,000**

[a]Average of calculated TDS values from available well data in the study area (Kirby and others, 2019)
[b]Estimate obtained using TDS raster from Kirby and others (2019) and GSL shapefile (polyline) at 4190 FASL
[c]Estimate obtained using TDS raster from Kirby and others (2019) and GSL shapefile (polyline) at 4200 FASL

Table 5. *Salt flux estimates for GSL by section at 4190 FASL in acre-feet per year*

Section	Q (af/year)	TDS (mg/L)	TDS (metric ton/year)
West/South	50,000	4627	290,000
North	275,000	3055	1,040,000
East	86,000	3023	320,000
			1,650,000

groundwater level trends in the Salt Lake, Tooele, and Curlew Valleys where levels dropped between 15 and 40 feet from 1975 to 2005 (Burden and others, 2005). Groundwater levels declined by an average of 27 feet from 1953 to 1985 in the Ogden area (Hurlow and others, 2011). Our data shows that, in general terms, this trend continued into the 2010s. These declines are a consequence of aquifer overdraft associated with less than average precipitation in the basin and increased withdrawals for municipal, industrial, and agricultural use (Burden and others, 2005). Young and others (2021) estimated that the GSL basin lost 8.8 ± 2.3 million acre-feet of groundwater storage whereas GSL lost 4.5 ± 0.8 million acre-feet of surface water during the 2012–2016 drought.

Overdraft conditions in basin-fill aquifers can cause several problems. Groundwater removal through pumping for anthropogenic use (and associated groundwater level declines) may lead to reduction of water in streams and lakes, land subsidence or ground failure due to soil compaction, increased costs for users due to higher pumping lifts, and deterioration of water quality from saltwater intrusion (U.S. Geological Survey, 2022b). Consumptive water uses in the GSL watershed have already depleted surface inflows to the lake by ~39% (Null and Wurtsbaugh, 2020). These inflow reductions are in part responsible for the recent ~10-foot drop in GSL's surface water level (figure 1; Null and Wurtsbaugh, 2020). The downward trend in water-surface elevation is expected to continue as human population and water consumption increase under changing climatic conditions in the state. Land subsidence and earth fissures due to long-term groundwater pumping in excess of recharge have been reported in Cedar Valley in southern Utah, where average basin-wide subsidence is estimated to continue at a rate of 0.04 to 2.4 inches per year under the current rates of groundwater decline (3 feet per year; Lund and others, 2011). Several instances of land subsidence have been reported in Woods Cross City (see figure 10 for location), but current subsidence rates are unknown. Several long-term monitoring sites on GSL's east shore show a significant increase in TDS over time (Clark and others, 1990), but saltwater intrusion into the freshwater aquifer has not been explicitly documented. However, groundwater-level declines on the east shore may create the conditions required to induce saltwater intrusion. Such phenomena have been observed in Lake Urmia, a terminal saline lake in Iran, where groundwater-level declines of 13 feet in the freshwater aquifer induced saltwater intrusion (Ahmadi and others, 2022).

The general trends in groundwater levels shown in figure 6 and the 100-foot contour intervals shown in figures 4 and 5 allow visualization of groundwater conditions in the study area. Unfortunately, 100-foot contours do not provide good spatial resolution on fine-scale responses to groundwater withdrawals in the basin-fill aquifers. Similarly, mean groundwater levels on a decadal timescale provide a glimpse of the hydrological conditions at specific sites, but do not offer a detailed temporal resolution of groundwater-level responses to withdrawal or recharge. Groundwater-level maps at finer spatial and temporal scales than presented here are needed for each individual valley adjoining GSL to track withdrawal responses on a yearly (or seasonal) basis. Thorough and more comprehensive groundwater-level maps are particularly needed along the east shore of GSL to monitor potential saltwater intrusion to the freshwater aquifer.

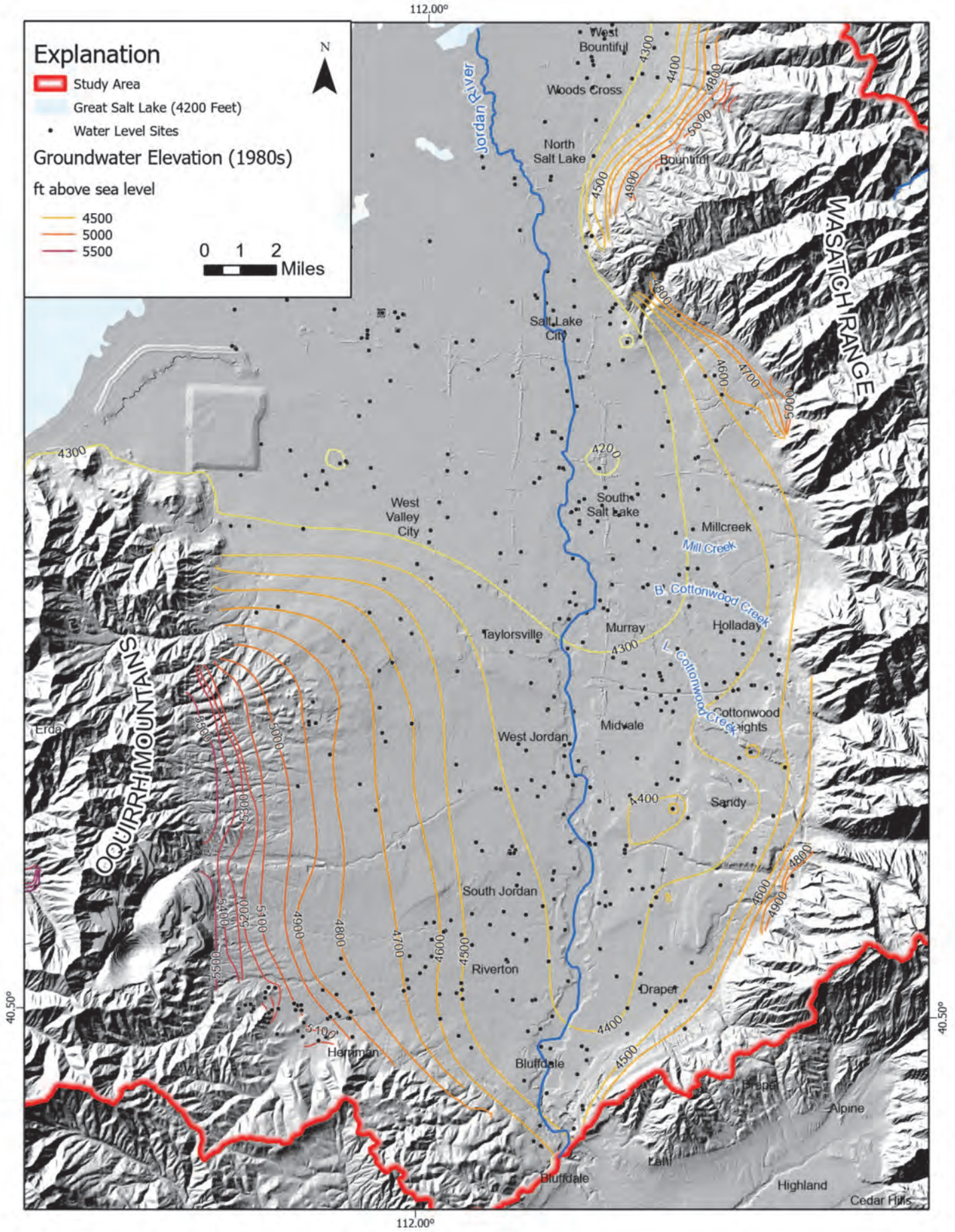

Figure 9. *Potentiometric surface elevation in the Salt Lake Valley area for the 1980s.*

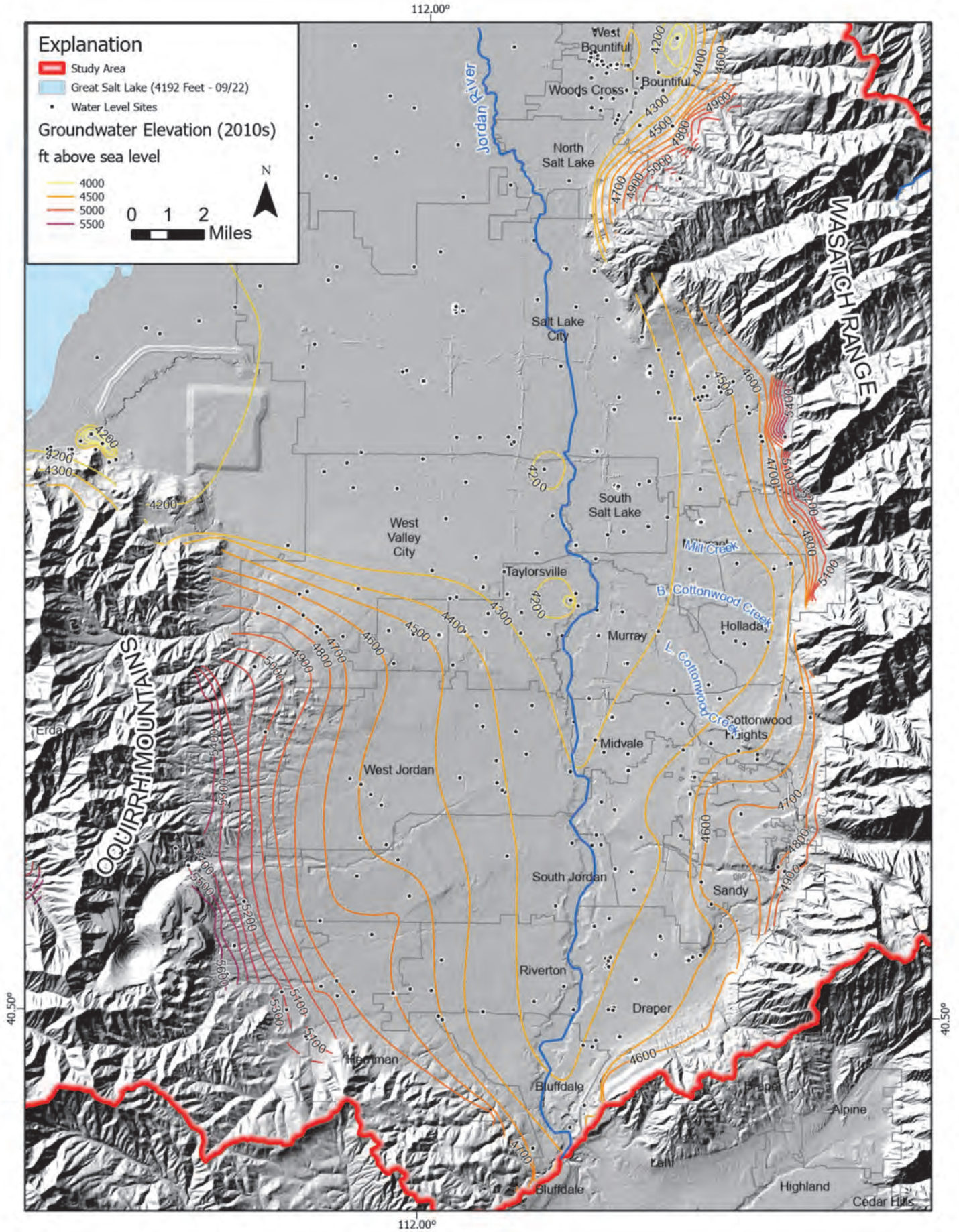

Figure 10. *Potentiometric surface elevation in the Salt Lake Valley area for the 2010s.*

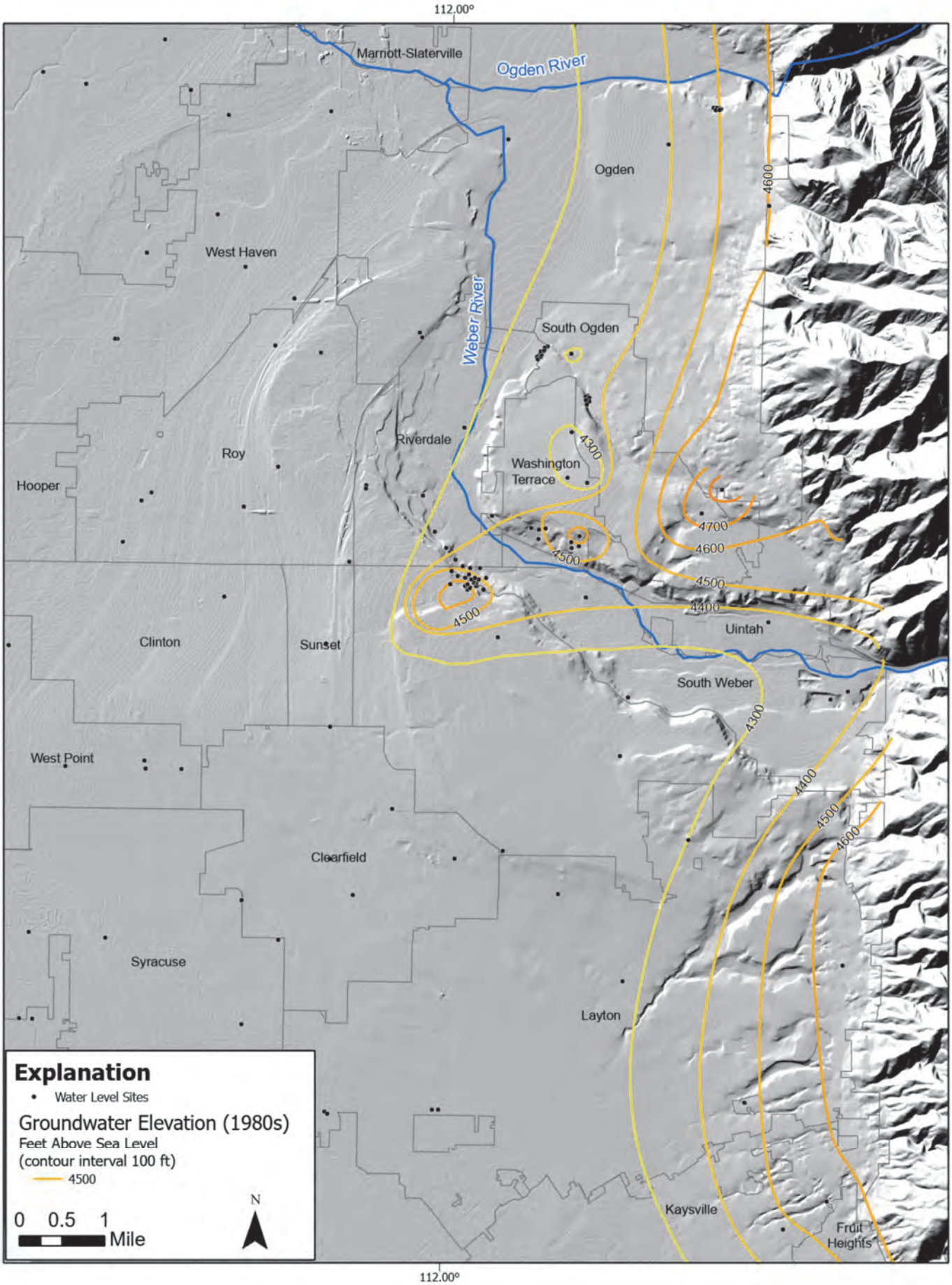

Figure 11. *Potentiometric surface elevation in the Weber Delta area for the 1980s.*

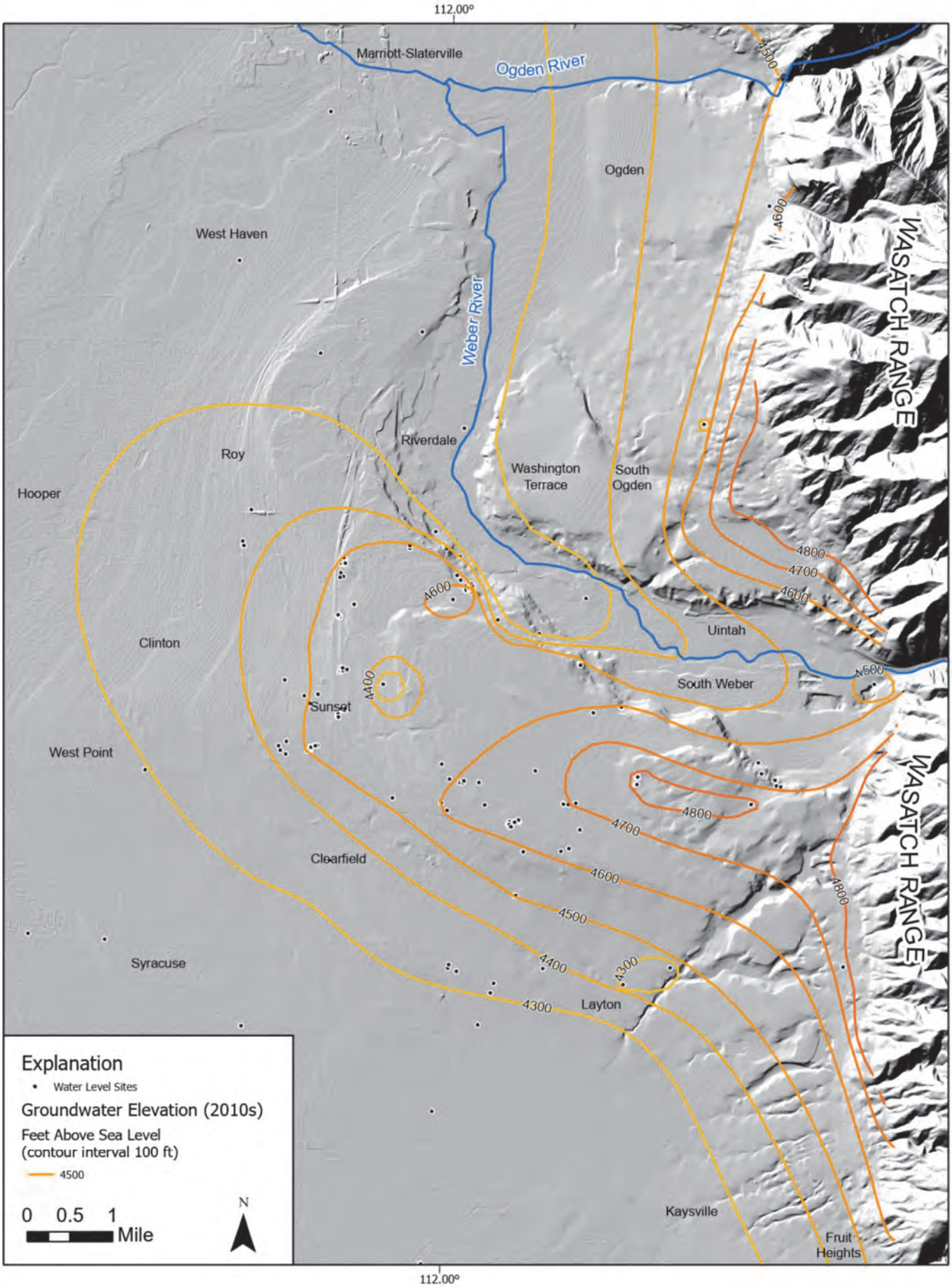

Figure 12. Potentiometric surface elevation in the Weber Valley area for the 2010s.

Groundwater Flow and Salt Loading

The total groundwater flux to GSL calculated in this study (an average of 356,000 acre-feet per year from the seepage calculations, 313,500 acre-feet per year from the Darcy flux calculations) is substantially higher than previous estimates derived from water balance studies (75,000 acre-feet per year; Waddell and Fields, 1976; Loving and others, 2000). Arnow and Stephens (1990) estimated that between 6250 and 100,000 acre-feet of groundwater enter the lake per year. However, our results are consistent with recent estimates derived from geochemical modeling of GSL water chemistry (10% of the total inflow or ~300,000 acre-feet per year), assuming surface water contributions of 2.9 million acre-feet per year to the system (Stephens and Gardner, 2007; Bunce, 2022). Estimates of groundwater seepage using seepage meters averaged 0.77 cm/day from July 8–15, 2010, (Anderson, 2012) at locations of suspected groundwater seepage. Extrapolating that rate to the entire lake at its current coverage area would suggest that about 560,000 acre-feet of groundwater seeps into the lake per year. However, the seepage estimates could vary spatially, seasonally, and temporally, and were likely biased towards higher seepage rates due to how the measurement sites were selected.

Based on our preliminary estimates, the largest groundwater contribution originates in the north and east sections of GSL (table 5) where steep hydraulic gradients occur (figures 4 and 5). The groundwater flow derived in the north section of GSL was unexpectedly high (table 2). This high number is likely explained by the high transmissivity values calculated for the areas around the Park and Curlew Valleys (figure 7d). Groundwater flow conditions in Park Valley are poorly known. Extensive groundwater pumping in Curlew Valley has substantially reduced groundwater levels and discharge from the Locomotive Springs complex during the past 40 years (Hurlow and Burk, 2008), therefore the groundwater flux from this valley to GSL has likely declined significantly.

The average salt contribution from groundwater to GSL calculated in this study (1.18 million metric tons per year) represents about 10% of the solutes delivered by the Jordan, Bear, and Weber Rivers to GSL in 2013 (14.3 million metric tons; Shope and Angeroth, 2015). The highest TDS concentrations are found in the west/south sections of GSL (table 5) where hydraulic gradients are shallow, evaporation rates are high, and recharge likely occurs at a slow rate.

Our new estimates of groundwater discharge and its salinity contribution will likely require revision of GSL's water and salt budgets. However, two important considerations limit how these should be evaluated and used.

1. Error on the estimates of groundwater flux is large. Based on sensitivity analyses from iterative calculations, the estimates are most sensitive to values of hydraulic conductivity. Hydraulic conductivity is lognormally distributed and can range by orders of magnitude over a study area as large as ours, resulting in estimates of flux that range over orders of magnitude. Of the iterative calculations conducted, 90% of resultant estimated flux fell between 2350 and 44,000,000 acre-ft/yr, indicating a need to better constrain aquifer properties.
2. Because we only considered wells completed in the basin-fill aquifer, our calculations do not include flow paths that are entirely within bedrock (but do include groundwater that discharges from bedrock to basin fill in the subsurface). Significant discharge from bedrock springs occurs in the southeastern part of the Malad–Lower Bear River Valley, along the margins of the Promontory Mountains, and in the northwest part of Tooele Valley. These springs contribute groundwater flow to the GSL playa and, perhaps, different salt loading having different compositions and concentrations than groundwater in the basin-fill aquifer.

Other aquifer properties, including porosity, saturated aquifer thickness, and cross-sectional area, also influence flux estimates. Further information is needed to constrain the differences in porosity values around GSL's shorelands and in the basin-fill aquifer. These data can potentially improve the seepage velocity estimates around GSL. Additionally, the aquifer thickness values we used (difference between depth to water and total well depth) have two sources of uncertainty. First, most of the wells in the basin fill only partially penetrate the saturated thickness of the aquifer. Thus, aquifer thickness values around GSL are likely larger than we estimated and could result in larger groundwater fluxes than presented here. Second, most of the wells used in this study were drilled to target the most productive aquifer depths. For some areas, this would result in larger groundwater and salinity contributions than expected due to bias toward higher aquifer-property values. Groundwater levels change over time due to natural and anthropogenic influences, resulting in variable hydraulic gradients and saturated thicknesses. Using previous work and ongoing groundwater-level observations, we can constrain these estimates fairly well. Cross-sectional area of groundwater flow paths is more complicated, especially if one assumes that the area matches that of the lake margin. The lake perimeter varies dramatically

depending on lake level. Increases in lake level will increase the lake perimeter length and the resultant cross-sectional area of estimation. Hypothetically, an increase in lake level would result in a decreased groundwater gradient, but due to lack of lake-margin groundwater data, we are unsure of this relationship.

Regarding salinity inputs from groundwater, the spring systems around GSL need further consideration. Springs in the area have been measured to reach TDS concentrations of up to ~76,000 mg/L (Bunce, 2022) and are point-sources of solutes to GSL. It is also possible that there are density differences in the groundwater system around and below GSL. These density variations have the potential to create flow boundaries that we did not account for (Rosen, 1994; Sheibani and others, 2020). Further studies are needed to understand spring dynamics and density-driven flows in order to provide further insight on their overall role in the water and salinity budgets in GSL.

CONCLUSIONS AND RECOMMENDATIONS

We provide the first systematic, basin-wide assessment of groundwater levels in areas adjoining GSL to quantify groundwater contributions and their salt loading to the lake system. We observed groundwater-level declines in most of the basin-fill aquifer from the 1980s to the 2010s (figure 6). These declines are consistent with historical groundwater level trends in the Salt Lake, Tooele, Curlew and Weber Valleys and result from aquifer overdraft associated with less than average precipitation in the basin and increased withdrawal for human consumption. We calculated a mean groundwater flux to GSL of 356,000 acre-feet per year using a seepage velocity method in ArcGIS and 313,500 acre-feet per year using the Darcy flux equation for linear traverses through adjoining valleys. Both estimates are substantially greater than previous estimates derived from water balance studies, but are consistent with estimates derived from previous in situ seepage measurements and geochemical modeling of GSL water chemistry. We calculated a salt contribution from groundwater to GSL of 1.06 million metric tons per year which represents about 10% of the solutes derived from surface flows to GSL in 2013. These estimates have very large uncertainty, and the input parameters need to be better understood and constrained. Groundwater monitoring wells and a formal groundwater model are recommended to constrain groundwater parameters.

The data presented here have the potential to improve current water and salt budgets for GSL's system. However, further work is needed to improve these estimates and better delineate surface/groundwater dynamics in the area. In order to do so, we recommend the following:

1. Estimates of the hydraulic properties of the basin-fill aquifer should be refined by compiling results from high-quality well tests and aquifer tests and, perhaps, conducting new aquifer tests.
2. A monitoring-well network should be established with local/state/federal participation within each valley adjoining GSL. This system of wells should be thorough and accessible to visit and measure water level fluctuations on a seasonal or, at least, yearly basis. This information could be used to create detailed, yearly potentiometric surface maps and track/compare changes in groundwater levels over the years.
3. Nested piezometers and/or monitoring wells should be installed along different sections of GSL. These piezometers at different depths could be used to calculate hydraulic gradients and to monitor water level/salinity trends in areas of the aquifer susceptible to brine intrusion. Core or cuttings recovered during the installation of these piezometers/monitoring wells could be used to estimate porosity values in the subsurface near GSL.
4. Sample springs around GSL and measure their flow. Geochemical and isotopic data on springs can provide information regarding sources, flow paths, residence time of groundwater and help to better understand their role in the water/salt budget of GSL.

ACKNOWLEDGMENTS

We would like to thank our sister-agency the Utah Division of Forestry, Fire and State Lands for funding this study. We also thank reviewers Marek Matyjasik and Craig Miller, and editor Carie Frantz for their contributions to this manuscript.

REFERENCES

Ahmadi, H., Hemmati, M., and Motallebian, M., 2022, Numerical modeling of saltwater wedge under intruding and receding conditions (Case Study: Kahriz Aquifer, Lake Urmia): Water Resources, v. 49, no. 2022, p. 249–258, doi: https://doi.org/10.1134/S0097807822020099.

Anderson, R.B., 2012, Quantity and quality of groundwater discharge in a hyper-saline lake environment, Great Salt Lake, Utah, USA: Salt Lake City, University of Utah, 85 p.

Arnow, T., and Stephens, J.C., 1975, Groundwater in-

flow to Great Salt Lake, Utah [abs]: Geological Society of America Abstracts with Programs, 1975 annual meeting, p. 81.

Arnow, T., and Stephens, D.W., 1990, Hydrologic characteristics of the Great Salt Lake, Utah, 1847-1986: U.S. Geological Survey Water Supply Paper 2332, 32 p., doi: https://doi.org/10.3133/wsp2332.

Bear, J., 1979, Hydraulics of groundwater: Mineola, Dover Publications, 595 p.

Bell, J.W., Amelung, F., Rameli, A.R., and Blewitt, G., 2002, Land subsidence in Las Vegas, Nevada, 1935-2000—New geodetic data show evolution, revised spatial patterns and reduced rates: Environmental and Engineering Geoscience, v. 8, no. 3, p. 155–174, doi: https://doi.org/10.2113/8.3.155.

Bioeconomics, Inc., 2012, Economic significance of the Great Salt Lake to the State of Utah: Missoula, Montana, consultant's report for State of Utah Great Salt Lake Advisory Council, p. 50.

Brooks, L.E., 2017, Groundwater model of the Great Basin carbonate and alluvial aquifer system version 3.0—Incorporating revisions in southwestern Utah and east central Nevada: U.S. Geological Survey Scientific Investigations Report 2017–5072, 77 p.

Brooks, L.E., Masbruch, M.D., Sweetkind, D.S., and Buto, S.G., 2014, Steady-state numerical groundwater flow model of the Great Basin carbonate and alluvial aquifer system: U.S. Geological Survey Scientific Investigations Report 2014-5213, 138 p., online: https://pubs.usgs.gov/sir/2014/5213/pdf/sir2014-5213.pdf.

Bunce, L.E., 2022, Significance of spring inflow to Great Salt Lake: Binghamton, Binghamton University, 64 p.

Burden, C.B., and others, 2005, Ground-water conditions in Utah, spring of 2005: Utah Department of Natural Resources and U.S. Geological Survey Cooperative Investigations Report No. 46, 138 p.

Carling, G.T., Richards, D.C., Hoven, H., Miller, T., Fernandez, D.P., Rudd, A., Pazmino, E., and Johnson, W.P., 2013, Relationships of surface water, pore water, and sediment chemistry in wetlands adjacent to Great Salt Lake, Utah, and potential impacts on plant community health: Science of The Total Environment, v. 443, p. 798–811, doi: 10.1016/j.scitotenv.2012.11.063.

Clark, D.W., Appel, C.L., Lambert, P.M., and Puryear, R.L., 1990, Ground-water resources and simulated effects of withdrawals in the east shore area of Great Salt Lake, Utah: Utah Department of Natural Resources, Division of Water Rights Technical Publication 93, 160 p.

Duffy, C.J., and Al-Hassan, S., 1988, Groundwater circulation in a closed desert basin—topographic scaling and climatic forcing: Water Resources Research, v. 24, no. 10, p. 1675–1688, doi: 10.1029/WR024i010p01675.

ESRI, 2022a, EBK regression prediction (Geostatistical Analyst): Online, https://pro.arcgis.com/en/pro-app/latest/tool-reference/geostatistical-analyst/ebk-regression-prediction.htm, accessed December 2022.

ESRI, 2022b, How Darcy Flow and Darcy Velocity work: Online, https://pro.arcgis.com/en/pro-app/latest/tool-reference/spatial-analyst/how-darcy-flow-and-darcy-velocity-work.htm, accessed December 2022.

European Space Agency, 2022, Applications—Sentinel-2 overview: Online, https://www.esa.int/Applications/Observing_the_Earth/Copernicus/Sentinel-2_overview/, accessed December 2022.

Hahl, D.C., 1968, Dissolved-mineral inflow to Great Salt Lake and chemical characteristics of the Salt Lake brine—Summary for water years 1960, 1961, and 1964: Utah Geological and Mineralogical Survey Water-Resources Bulletin 10, 37 p.

Hall, D.K., O'Leary, D.S., Girolamo, N.E., Miller, W., and Kang, D.H., 2021, The role of declining snow cover in the desiccation of the Great Salt Lake, Utah, using MODIS data: Remote Sensing of Environment, v. 252, no. 2021, p. 112,106, doi: https://doi.org/10.1016/j.rse.2020.112106.

Hammer, U.T., 1986, Saline lake ecosystems of the world: Boston, Dr. W. Junk, 616 p.

Healy, R.W., Winter, T.C., LaBaugh, J.W., and Franke, O.L., 2007, Water budgets—Foundations for effective water-resources and environmental management: U.S. Geological Survey Circular, v. 1308, p. 98.

Hurlow, H.A., and Burk, N., 2008, Geology and ground-water chemistry, Curlew Valley, northwestern Utah and south-central Idaho—Implications for hydrogeology: Utah Geological Survey Special Study 126, 185 p., 2 plates, https://doi.org/10.34191/SS-126.

Hurlow, H.A., Lowe, M., Matyjasik, M., and Gettings, P., 2011, The Weber River basin aquifer storage and recovery pilot project: Utah Geological Survey Special Study 136, 135 p., https://doi.org/10.34191/SS-136.

Jagniecki, E., Rupke, A., Kirby, S., and Inkenbrandt, P., 2021, Salt crust, brine, and marginal groundwater of Great Salt Lake's North Arm: Utah Geological Survey Report of Investigation 283, https://doi.org/10.34191/RI-283.

Kirby, S.M., Inkenbrandt, P.C., and Rupke, A., 2019, Mapping groundwater quality and chemistry adja-

cent to Great Salt Lake, Utah: Utah Geological Survey Open-file Report 699, 25 p., https://doi.org/10.34191/OFR-699.

Konikow, L.F., and Bredehoeft, J.D., 1978, Computer model of two-dimensional solute transport and dispersion in ground water: U.S. Geological Survey Techniques of Water-Resources Investigations 07-C2, 90 p.

Loving, B.L., Miller, C.W., and Waddell, K.M., 2000, Water and salt balance of Great Salt Lake, Utah, and simulation of water and salt movement through the causeway, 1987-98: U.S. Geological Survey USGS Numbered Series 2000–4221, 111 p.

Lund, W., Knudsen, T., Inkenbrandt, P.C., and Lowe, M., 2011, Land subsidence and earth fissures in Cedar Valley: Utah Geological Survey, Survey Notes, v. 43, no. 1, p. 1–3.

Mohammed, I.N., and Tarboton, D.G., 2012, An examination of the sensitivity of the Great Salt Lake to changes in inputs: Water Resources Research, v. 48, no. W11511, p. 17.

Null, S.E., and Wurtsbaugh, W.A., 2020, Water development, consumptive water uses, and the Great Salt Lake, in Baxter, B., and Butler, J. editors, Great Salt Lake Biology: Springer, Cham.

Reynolds, R.L., Goldstein, H.L., Moskowitz, B.M., Bryant, A.C., Skiles, S.M., Kokaly, R.F., Flagg, C.B., Yauk, K., Berquó, T., Breit, G., Ketterer, M., Fernandez, D., Miller, M.E., and Painter, T.H., 2014, Composition of dust deposited to snow cover in the Wasatch Range (Utah, USA)—controls on radiative properties of snow cover and comparison to some dust-source sediments: Aeolian Research, v. 15, p. 73–90, doi: https://doi.org/10.1016/j.aeolia.2013.08.001.

Rosen, M.R., 1994, The importance of groundwater in playas—A review of playa classifications and the sedimentology and hydrology of playas: Geological Society of America Special Papers, v. 289, p. 1–18, doi: 10.1130/SPE289-p1.

Rosenberry, D.O., Lewandowski, J., Meinikmann, K., and Nützmann, G., 2015, Groundwater—the disregarded component in lake water and nutrient budgets, Part 1—effects of groundwater on hydrology: Hydrological Processes, v. 29, no. 13, p. 2895–2921, doi: 10.1002/hyp.10403.

Rosenberry, D.O., and Winter, T.C., 2009, Hydrologic processes and the water budget, in Winter, T.C., and Likens, G.E., editors, Mirror Lake—Interactions among air, land, and water: Berkeley, University of California Press, p. 23–68.

Sheibani, S., Ataie-Ashtiani, B., Safaie, A., and Simmons, C.T., 2020, Influence of lakebed sediment deposit on the interaction of hypersaline lake and groundwater—A simplified case of lake Urmia, Iran: Journal of Hydrology, v. 588, p. 125110, doi: 10.1016/j.jhydrol.2020.125110.

Shope, C.L., and Angeroth, C.E., 2015, Calculating salt loads to Great Salt Lake and the associated uncertainties for water year 2013; updating a 48-year-old standard: Science of The Total Environment, v. 536, p. 391–405, doi: 10.1016/j.scitotenv.2015.07.015.

Skiles, S.M., Mallia, D.V., Hallar, A.G., Lin, J.C., Lambert, A., Petersen, R., and Clark, S., 2018, Implications of a shrinking Great Salt Lake for dust on snow deposition in the Wasatch Mountains, UT, as informed by a source to sink case study from the 13-14 April 2017 dust event: Environmental Research Letters, v. 13, no. 12, p. 124031, doi: https://doi.org/10.1088/1748- 9326/aaefd8.

Spencer, R.J., Eugster, H.P., Jones, B.F., and Rettig, S.L., 1985, Geochemistry of Great Salt Lake, Utah I—Hydrochemistry since 1850: Geochimica et Cosmochimica Acta, v. 49, no. 3, p. 727–737, doi: 10.1016/0016-7037(85)90167-X.

Stephens, D.W., and Gardner, J., 2007, Great Salt Lake, Utah: Water-Resources Investigations Report 99-4189, p. 4.

The Nature Conservancy, 2022, Great Salt Lake Shorelands Preserve: Online, https://www.nature.org/en-us/get-involved/how-to-help/places-we-protect/the-great-salt-lake-shorelands-preserve/, accessed December 2022.

U.S. Geological Survey, 2022a, National Water Information System data: Online, https://waterdata.usgs.gov/nwis/, accessed September 2022.

U.S. Geological Survey, 2022b, Groundwater decline and depletion: Online, https://www.usgs.gov/special-topics/water-science-school/science/groundwater-decline-and-depletion, accessed on December 2022.

Waddell, K.M., and Fields, F.K., 1976, Model for evaluating the effects of dikes on the water and salt balance of Great Salt Lake, Utah: U.S. Geological Survey, USGS Numbered Series 76–256, doi: 10.3133/ofr76256.

Wang, J., Song, C., Reager, J.T., Yao, F., Famiglietti, J.S., Sheng, Y., MacDonald, G.M., Brun, F., Schmied, H.M., Marston, R.A., and Wada, Y., 2018, Recent global decline in endorheic basin water storages: Nature Geoscience, v. 11, p. 926–932, doi: https://doi.org/10.1038/s41561-018-0265-7.

Wurtsbaugh, W.A., Miller, C., Null, S.E., DeRose, R.J., Wilcock, P., Hahnenberger, M., Howe, F., and Moore, J., 2017, Decline of the world's saline

lakes: Nature Geoscience, v. 10, p. 816–821, doi: https://doi.org/10.1038/ngeo3052.

Young, Z.M., Kreemer, C., and Blewitt, G., 2021, GPS constraints on drought-induced groundwater loss around Great Salt Lake, Utah, with implications for seismicity modulation: Journal of Geophysical Research: Solid Earth, v. 126, p. e2021JB022020, doi: https://doi.org/10.1029/2021JB022020.

Implications and Hydrographs for Two Pre-Bonneville Pluvial Lakes and Double Geosols from 14 OSL-IRSL Ages in Cache Valley, NE Bonneville Basin

Robert Q. Oaks, Jr., Susanne U. Jänecke, Tammy M. Rittenour, Thad L. Erickson, and Michelle S. Nelson
Geosciences Department, Utah State University, Logan, Utah, boboaks@comcast.net

10.31711/ugap.v51i.142

ABSTRACT

In the northeastern Great Basin, USA, thirteen new optically stimulated luminescence (OSL) ages and one infrared stimulated luminescence (IRSL) age show that two deep pluvial lakes preceded the Bonneville lake cycle in Cache Valley during marine oxygen-isotope stages (MIS) 6 (123-191 ka) and 4 (56-71 ka), respectively. Our new data define quantitative hydrographs of the Little Valley and Cutler Dam lake cycles in both Cache Valley and the main Bonneville basin. In western Cache Valley, excavation of a faulted, east-plunging spit has sequentially exposed these deposits and overlying MIS 3 Fielding humid-over-arid double geosols that end westward at a strand of the east-dipping Dayton-Oxford normal-fault zone. Lithologically identical double paleosols in eastern Cache Valley overlie a variety of deposits, including dated Little Valley lake beds, and persist above the Bonneville shoreline.

Six new ages show that the Little Valley lake cycle in Cache Valley began before 169 ka and ended after 143 ka, and its highest shoreline was above 1493 m. The >25 kyr duration of this pluvial lake cycle rivals the combined durations of the two subsequent lake cycles, during MIS 4 and MIS 2. The Cutler Dam lake rose at least to ~1450 m by ~67 ka in Cache Valley. In the type area in the main Bonneville basin, west of Cutler Narrows, four averaged IRSL dates from Cutler Dam lake beds show that the lake level there had dropped to ~1340 m by ~59 ka. The Little Valley lake rose at least 40 to 50 m above the local Provo shoreline whereas the Cutler Dam lake missed reaching the Provo shoreline by ~13 m.

Beneath central Cache Valley, southeast of the study area, there are two laterally extensive, confining layers of silty clay with an intervening sandy gravel layer, all overlying thick gravelly sediment. Both confining layers enclose additional thin and discontinuous gravel layers with adjacent oxidized clays. These alternating coarse and fine sediments are probably correlative with the exposed MIS 6 to MIS 1 deposits and, possibly, older lake cycles.

INTRODUCTION

Cache Valley is a narrow, elongate north-trending graben that straddles the Utah-Idaho border (Williams, 1948, 1958, 1962; Evans and Oaks, 1996; Janecke and Evans, 1999; Oaks, 2000; Janecke and others, 2003; Carney and Janecke, 2005). It is separated from the main Bonneville basin by a bedrock-cored horst upthrown between the Wasatch (west) and West Cache (east) fault zones. Cutler Narrows connects the two basins (Figure 1B). The Bear River fully entered Cache Valley through Oneida Narrows (Figure 1A) ~45 to 55 ka (Pederson and others, 2016) due to diversion by volcanic eruptions in Gem Valley in SE Idaho (Bright, 1963, 1967; Link and others, 1999; Janecke and Oaks, 2014; Utley, 2017).

PREVIOUS WORK

Pre-Bonneville Lakes in Cache Valley

The last three lake cycles of the Eastern Great Basin coincide with even-numbered marine-isotope stages (MIS) (Lisiecki and Raymo, 2005). These are the Little Valley (~123 to 191 ka, MIS 6), Cutler Dam (~ 56 to 71 ka, MIS 4), and Bonneville (~14 to 29 ka, MIS 2) lake cycles (Scott, 1988; Scott and others, 1982, 1983; McCoy, 1981, 1987; Oviatt and McCoy, 1988, 1992; Oviatt and others, 1987, 1992; Kaufman and others, 2001; Hart and others, 2004). Well- developed interglacial paleosols separate some but not all of the lake beds. A dated and formally defined paleosol is called a geosol.

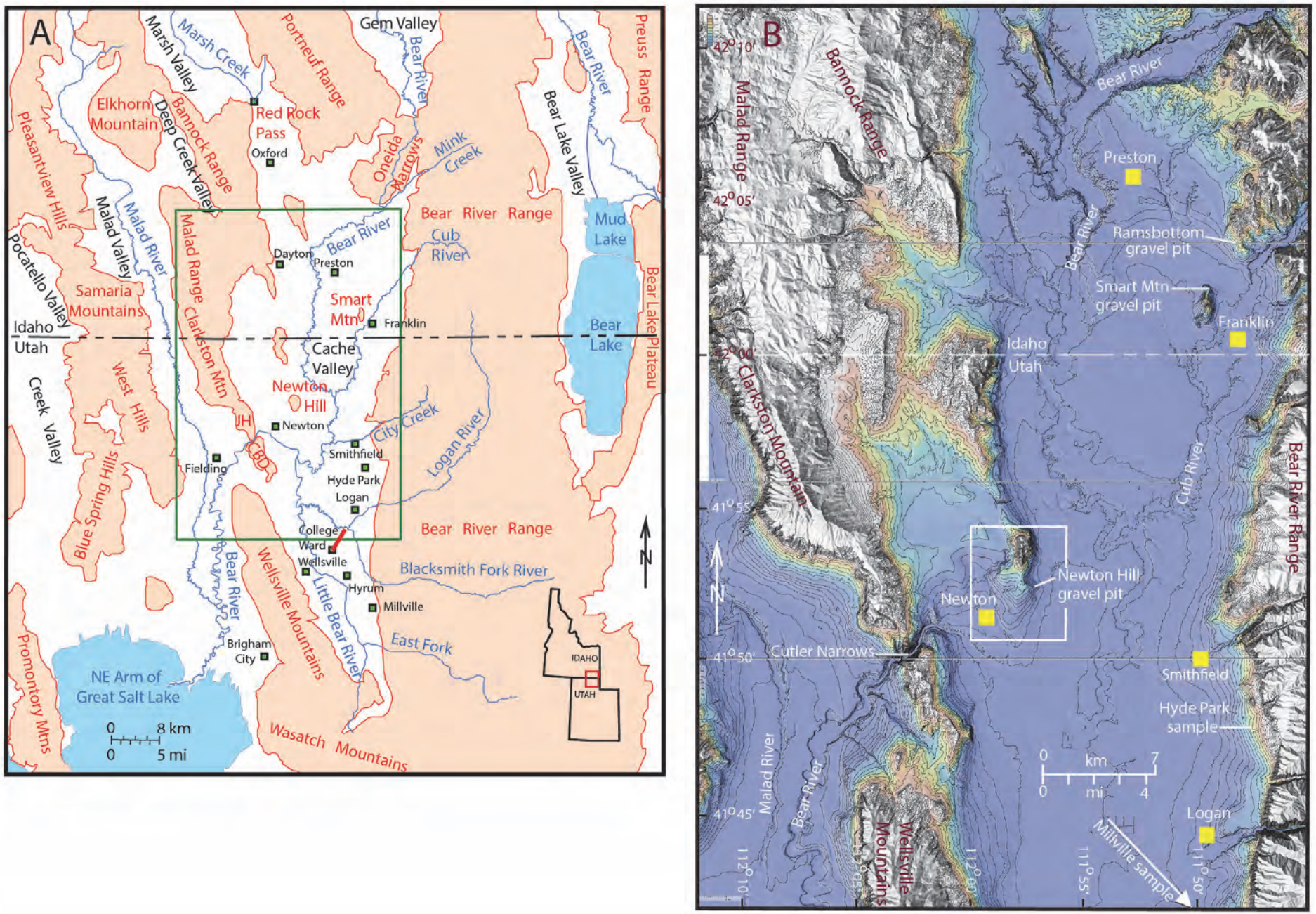

Figure 1. *A) Major features of the greater Cache Valley region, N-central Utah and SE Idaho. Green box outlines area in Figure 1 B. Red line NE from College Ward, south central Cache Valley, shows location of Figure 6. JH = Junction Hills; CBD = Cache Butte Divide. B) Landscape of Cache Valley area showing sites of pre- Bonneville deposits dated with AAR, OSL, and IRSL. Type area of Cutler Dam unit is along Bear River, SW of Cutler Narrows. Bonneville shoreline is lowest white; Provo shoreline is between blue and green shading. White box outlines area in Figure 2.*

Bright (1963, 1967) and McCoy (1981) identified lacustrine gravels below a paleosol beneath gravels of Lake Bonneville at the Ramsbottom gravel pit in Idaho, NE Cache Valley (Figure 1B). From that site and nearby Smart Mountain, Idaho, Scott and others (1982, 1983) derived amino-acid racemization (AAR) data from snail shells in the older lake beds beneath the paleosol that were correlative with AAR data from the Little Valley lake cycle in the main Bonneville basin.

Highest Altitudes of Pre-Bonneville Lakes

Oviatt and others (1987), Oviatt and McCoy (1988, 1992), and Kaufman and others (2001) concluded that the Cutler Dam unit, in exposures up to 15 m thick SW of Cutler Narrows, was deposited in marshy to shallow lacustrine conditions with ostracods indicative of fluctuating brackish conditions. The highest outcrop is at ~1340 m. The highest probable Little Valley gravels in the main Bonneville basin, which were not dated, are about half-way between the local Bonneville and Provo shorelines (Scott and others, 1982, 1983).

Incision of Cutler Narrows

The Bear River flows SW through Cutler Narrows, the deep and narrow canyon of the Bear River across the narrowest part of the Cache Butte Divide (Figure 1B). This canyon is cut into hard Paleozoic bedrock, is up to 392 m deep, and coincides with the highest bedrock along the Cache Butte Divide (Maw, 1968). Its bedrock channel is 1.8 km long.

Nearshore gravels of the Cutler Dam lake cycle in Cache Valley are ~110 m higher than somewhat younger marshy deposits in the main Bonneville basin. From that, Oaks and others (2019, 2020) concluded that most of the bedrock excavation of the lower part of Cutler Narrows, from an elevation between the highest levels attained by Cutler Dam and Little Valley pluvial lakes down to the present level near 1314 m, coincided with eastward flow during the Bonneville flood, ~17.4 ka (Marrero, 2009).

From their analysis of digital-elevation models (DEMs), Nelson (2012) and Chen and Maloof (2017) proposed that the Stansbury oscillation (~26 to 24 ka in Oviatt, 2015), may have reached into lower parts of Cache Valley through Cutler Narrows, across an area of ~300 km^2. If so, Cutler Narrows was already deeply incised to below the Stansbury level before Lake Bonneville existed, allowing Lake Bonneville to oscillate as a 5-10 m deep lake in lower Cache Valley.

METHODS

Introduction

Our study emphasizes a Staker-Parson gravel pit that we call the Newton Hill pit, in west-central Cache Valley (Figures 1, 2). Our emphasis is primarily on pre-Bonneville lakes, so the literature on Lake Bonneville is cited only where pertinent. All altitudes are above mean sea level. Those within the Newton Hill pit are tied to an altitude at a nearby section corner and based on electronic distance meter (EDM) and hand-level surveys. Altitudes of the original surface there and altitudes elsewhere are based on U.S Geological Survey 7.5-minute topographic maps, GPS readings, Caltopo Lidar, and Google Earth Pro. We report present altitudes without correction for post-Bonneville rebound or tectonics because Bonneville rebound is <10-20 m in our study area in Cache Valley and rebound of pre-Bonneville deposits cannot be computed without better pre-Bonneville hydrographs.

Age Control

We obtained 12 OSL (optically stimulated luminescence of quartz) and IRSL (infrared stimulated luminescence of feldspar) ages from the Newton Hill pit, one from the SE part of Hyde Park, Utah, and one from Muley Hill in Millville, Utah. The latter two are in the east side of Cache Valley (Figures 1A, 1B; Table 1). A metal tube was pounded horizontally into the sediment except at Muley Hill, where matrix sand was collected from gravel beds using double black plastic bags under red light at night. Surrounding sediment was obtained to establish both background data and moisture content for each sample. Lab analyses at the Utah State University OSL lab by Michelle Nelson were done under the supervision of Tammy Rittenour, with standard procedures outlined in the notes of Appendix 1.

Recalibration and new standards for OSL dating changed the OSL and IRSL dates reported earlier by us (Oaks and others, 2014, 2019, 2020). One previous pluvial lake bed dated at ~96 ka (N = 1; the Newton Hill beds), instead formed during the earlier Little Valley Lake cycle (sample USU-1083; Table 1; Appendix 1).

Construction of Map and Geologic Cross Sections

The evolving exposures of the pit walls were surveyed with a Leica model TC600 laser total station in

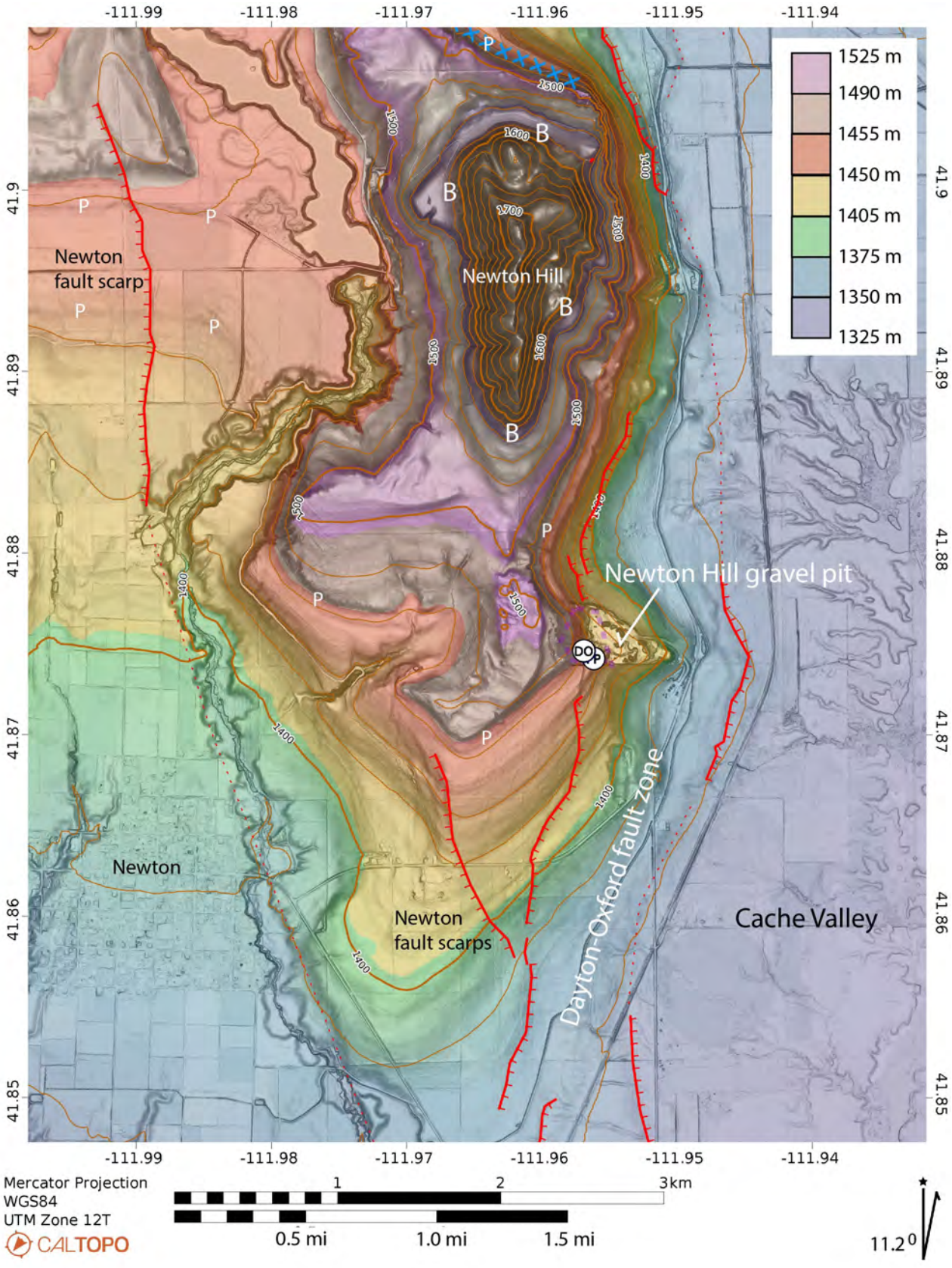

Figure 2. *Digital-elevation model of LIDAR data of the Newton Hill area. A western strand of the Dayton-Oxford fault zone intersects the pit (DO). Farther west, several Newton fault scarps are left unlabeled to show their clear topographic expression. B = Bonneville shoreline, P = Provo shoreline. Contour interval 20 m. Blue is lower, brighter colors higher.*

Table 1. *OSL & IRSL sample information and ages for Staker-Parson gravel pit (SE flank of Newton Hill), SE Hyde Park, and NE Millville, Cache County, Utah. See Appendix 1 for details for these samples.*

USU-Sample Number	Age in ka and Method	Hand-Level from EDM Control in Feet	EDM Altitude in Feet	Sample Altitude in Meters	Stratigraphic Unit	Location 1983 NAD	Comments; ~65 m W correction from 1983 GPS data to 1927 North American datum for USGS topographic maps in 1960s	Date and Collectors
859	15.42 ± 1.39 OSL	N.D. Map ~4790	4737 Depth ~53	1444	Late Qlbp	~ N 41° 52.614' ~W 111° 57.426'	NW edge of pit; silt & sand beds dip E; below ~4800' Qlbp highest shore	9-15-2010 TR & MN
3243 NE Millville, Utah	20.98 ± 3.04 OSL	GPS ~5083 Map ~5085 Google ~5087	N.D. Depth 3'	~1550	Early Qlbb	N 41° 41.2048' W 111° 48.2467'	3' below crest of Muley Hill, Millville, Utah; dissected older delta between Provo and Bonneville lake stands	11-19-2019 RO & TC & TR
1082	21.35 ± 3.48 OSL	~4665 Map ~4775	<4672 Depth ~115	~1422	Early Qlbb	N 41° 52.5244' W 111° 57.3198'	Center of pit; laminated silty sand over Qlv gravel; 10' above USU-1083	12-2-2011 RO & TE
854	21.72 ± 2.78 OSL	~4748 Map ~4785	N.D. Depth ~37	~1447	Early Qlbb	N 41° 52.4478' W 111° 57.3978'	Temporary road near S-center edge of pit; silty sand & clay above Qfg geosol, below Qlbp gravel	9-7-2010 TR & RO
855	39.28 ± 3.72 OSL	~4739 Map ~4810	N.D. Depth ~71	~1444	Qfg	N 41° 52.478' W 111° 57.393'	S-center of pit; red colluvium: sandy gravelly mud at top of loess geosol	9-7-2010 TR & RO
1084	53.51 ± 6.44 OSL	N.D. Map ~4875	4865 Depth ~10	1483	Qfg? Qcd?	N 41° 52.5045' W 111° 57.5009'	High W pit margin; white reworked ash and fine sand in NNW-SSE channel, under E-dipping gravel & soil, over 4° W-dipping Qlv gravel	12-5-2011 RO
856	66.82 ± 5.94 OSL	~4729 Map ~4810	N.D. Depth ~81	~1441	Qcd	N 41° 52.479' W 111° 57.388'	S-center of pit; gravel below Qfg red paleosol base; 9.8' below USU-855	9-7-2010 TR & RO
858	67.70 ± 6.46 OSL	~4709 Map ~4790	N.D. Depth ~81	~1435	Qcd	N 41° 52.473' W 111° 57.382'	S-center of pit; very fine to medium sand below gravel, ~25 ft below Qfg geosol base	9-15-2010 TR & MN
2895 SE Hyde Park, Utah	142.8 ± 13.1 OSL	N.D. Map ~4865 Google ~4898	N.D. Depth 9.25	~1493	Qlv	N 41° 47.8341' W 111° 47.8214'	N-S vertical wall; fine to coarse sand within pale green marl below Qfg white caliche geosol below Qlbb lag gravel under fine to very fine sand with snails	7-27-2018 RO
1083	144.3 ± 14.5 OSL	~4655 Map ~4780	<4673 Depth ~125	~1419	Qlv	N 41° 52.5243' W 111° 57.3310'	Center of pit; gravel 8.4' below base of Qlbb sand of USU-1082	12-2-2011 RO & TE
3202	150.0 ± 25.9 OSL	~4690' Map ~4885	N.D. Depth ~195	~1430	Qlv	N 41° 52.5570' W 111° 57.4022'	W-center of pit; pebbly sand 3.0' below base of Qfg red geosol, with thin Qcd between	10-28-2019 RO
2490	155.6 ± 21.4 IRSL	~4735 Map ~4840	N.D. Depth ~105	~1443	Qlv	N 41° 52.5203' W 111° 57.4165'	W-center of pit in WSW cut; sand and gravel in cobble gravel, 22' lower than base of overlying channel to W	9-26-2016 RO & TE
857	161.5 ± 16.8 OSL	N.D. GPS 4824 Map ~4865	N.D. . Depth ~44	~1470	Qlv	N 41° 52.492' W 111° 57.477'	SW pit in WSW cut; sand & pebble groundmass in cobble gravel; EDM 4821 later at graded site	9-15-2010 TR & MN
2491	169.4 ± 28.6 OSL	~4678 Map ~4805	N.D. Depth ~127	~1426	Qlv	N 41° 52.5548' W 111° 57.3882'	NW pit near S end of headwall; pebbly sand below Qcd calcareous sandy mud intertonguing upward with sandy pebbly cobble gravel clinoforms above	9-26-2016 RO & TE

OSL = optically stimulated luminescence on quartz sand; IRSL = infrared stimulated luminescence on feldspathic sand; ka = thousands of years ago; Google = Google Earth Pro; EDM = total station, electronic distance measurements with laser; GPS = global-positioning-system measurement; HL = hand level used from EDM base station; N.D. = no data; Map: original surface altitudes are interpolated from 1964 U.S. Geological Survey 7.5' Newton [C.I. = 5'] and Trenton [C.I. = 20'] topographic quadrangles; Qlbp = Provo highstand lake stage; Qlbb = Bonneville highstand lake stage; Qfg = Fielding emergent interval with multistory humid over arid geosols, and perhaps higher N-S channel; Qcd = Cutler Dam lake stage; Qlv = Little Valley lake stage; MN = Michelle S. Nelson; RO = Robert Q. Oaks, Jr.; TC = Tomas Capaldi; TE = Thad L. Erickson; TR = Tammy M. Rittenour. Note: Qcd and early Qlbb lakes in Cache Valley may have been separated at Cutler Narrows from lower coeval lakes in the main Bonneville basin.

2016. Thereafter, new contacts were surveyed with an Abney hand level from the EDM base station. These data, combined with our 12 OSL and IRSL ages from the central and western parts of the pit, were used to construct a map and four composite stratigraphic sections across much of the Newton Hill pit (Figures 3, 4). Correlations are tied to: (1) continuous and isolated exposures of the Fielding double geosols (Oviatt and McCoy, 1988) at the top of dated Cutler Dam lake beds in the central part of the pit, and westward atop dated Little Valley beds; (2) a thick green marl low within Bonneville deposits; and (3) an overlying pink marl.

Quantitative Hydrographs

Our new data (Table 1) and prior AAR data (Appendices 2, 3, 4) and thermoluminescence (TL) data, tied to altitudes (Appendix 5), constrain our quantitative hydrographs (Figure 5) of the Cutler Dam and Little Valley lake cycles in both Cache Valley and the main Bonneville basin. These hydrographs update schematic plots of Scott and others (1982, 1983), McCoy (1987), Oviatt and others (1987), and Hart and others (2004), for these two pre-Bonneville lake cycles. Our results align with far more detailed hydrographs of the Bonneville lake cycle in the main Bonneville basin of Currey and Oviatt (1985), Oviatt and others (1992), Nelson (2012), and Oviatt (2015, 2020). Our data also constrain the pre-Bonneville, post-Cutler Dam age of newly identified red-over-white double Fielding geosols in the Newton Hill pit and lithologically similar paleosols in eastern Cache Valley.

RESULTS

Overview of Newton Hill Gravel Pit

On the SE flank of Newton Hill, central Cache Valley, Utah (Figure 3), our ongoing studies have delineated the internal architecture of an east-plunging, nose-shaped compound spit deposited atop an east-sloping, eroded face of Little Valley gravel during the Cutler Dam and Bonneville lake cycles. The most continuous exposures lay between ~1408 m and ~1462 m, mostly below the prominent, higher Provo shoreline (Janecke and Oaks, 2011a, 2011b) at ~1463 m at this locality. Scattered exposures continued to ~1487 m. Exposures in the south-central part of the pit in 2006 were so extensive that the key stratigraphic relations and the overall architecture of the deposits were unambiguous (Figure 6).

The spit's original crest flattened uphill westward into a wave-cut and wave-built platform at the higher Provo shoreline of Lake Bonneville (Figure 2). The crest of the spit was parallel to and slightly north of the southern boundary of the gravel pit (Figure 6D). Pre-Bonneville sediment is mostly exposed in the central and western half of the gravel pit.

Little Valley Lake Beds

Stratigraphic Relationships

In the Newton Hill pit, Little Valley gravel is overlain by the upper red geosol at sample site USU-2490 (Figure 7A). At sample site USU-2491, there is no geosol between Little Valley pebbly sand and overlying Cutler Dam sandy mud (Figure 7B). At USU-1083 (Figures 4B, 4D) and at USU-857 (Figure 4A), Little Valley gravel is overlain by Bonneville deposits, with no geosol between. At USU-2895 Little Valley marl is overlain by a Fielding-like caliche paleosol beneath offshore Bonneville deposits. At USU-3202 Little Valley gravel is overlain by thin sediment of Cutler Dam lake cycle, then the upper Fielding geosol, beneath laminated fine-grained Bonneville deposits (Figures 4A, 4D). Although undated, at USU-1084 probable Little Valley gravel underlies a local channel with ashy sand under surficial gravels with modern soil. We did not find the base of the Little Valley deposits, nor identify pre-Little Valley units. Downward excavation ceased in the central part of the Newton Hill pit because of a noncommercial green marl 4 to 6 m thick according to two pit operators.

The Little Valley deposits are primarily pebble to cobble gravels and sandy gravels with low dips (Figure 7A). Discontinuous exposures west of the Dayton-Oxford fault strands reached at least 8 m thick. Locally there are thin marls and sand beds.

In Hyde Park, Utah, in eastern Cache Valley (Figure 1), at sample site USU-2895, a pale green Little Valley marl with a thin, calcareous, fine- to coarse sand lens is overlain by a white Bk paleosol 0.55 m thick, in turn overlain by a thin lag cobble gravel followed upward by 2.0 m of Bonneville light brown, thinly laminated, silty very fine sand with snails (cf. nearby exposure at Figure 8A). Elsewhere in eastern Cache Valley, weakly laminated to structureless marls and minor fine sands dominate probable Little Valley deposits. These undated older lake beds underlie the double Fielding geosols and Bonneville deposits, and persist at least up to ~1530 m, which is about 40 to 45 m below the local Bonneville shoreline (Figure 8B).

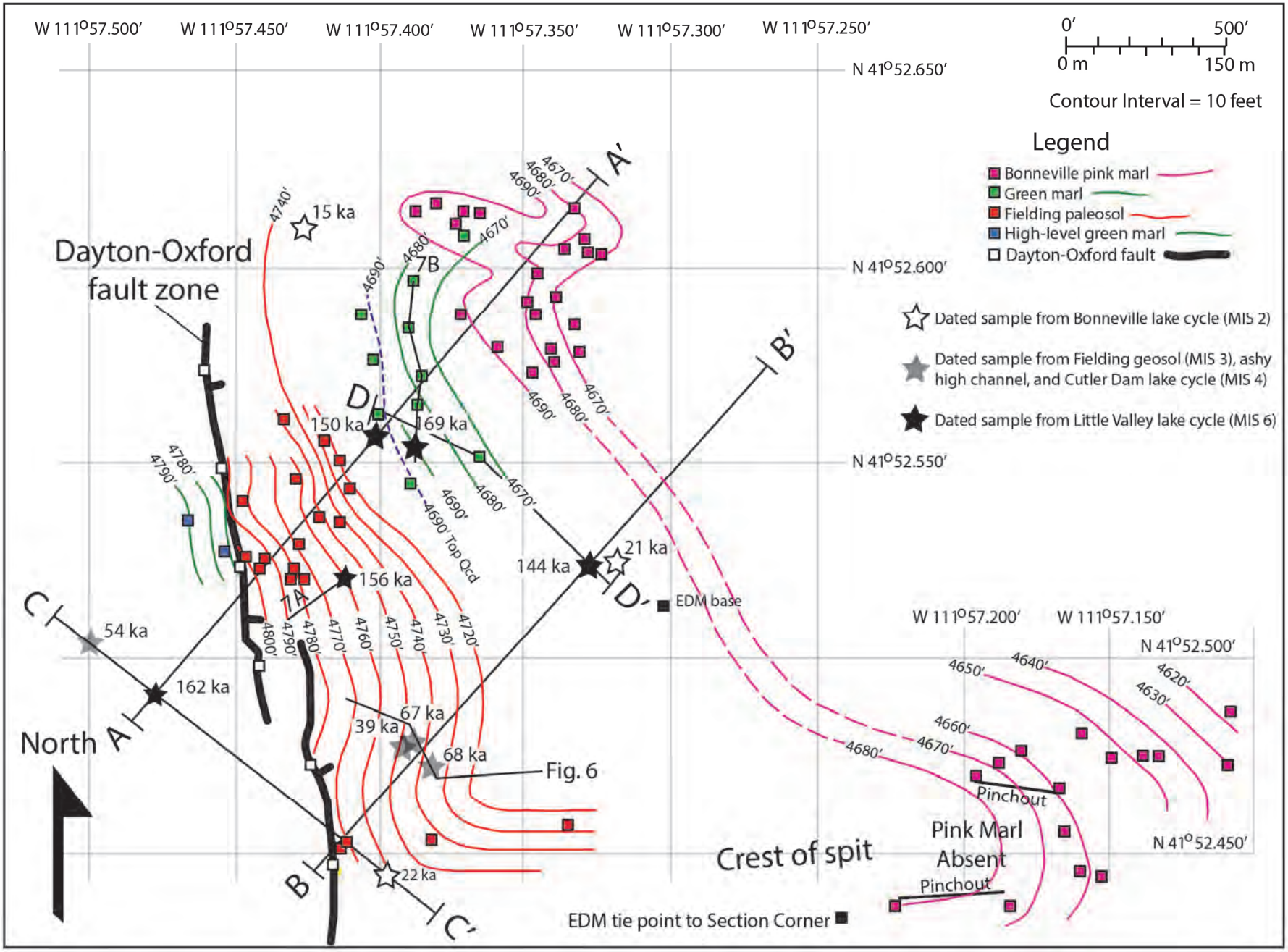

Figure 3. *Map of Staker-Parsons gravel pit SE of Newton Hill shows locations of OSL and ISRL age dates; contours of the tops of the extensive red Fielding geosol in the S and W, the pink/white/green shrinking marl in the N and SE, the laminated green clay between them; locations of geologic cross sections A - A′ to D - D′ in Figure 4, and locations of Figures 6A, B, C and 7A, B.*

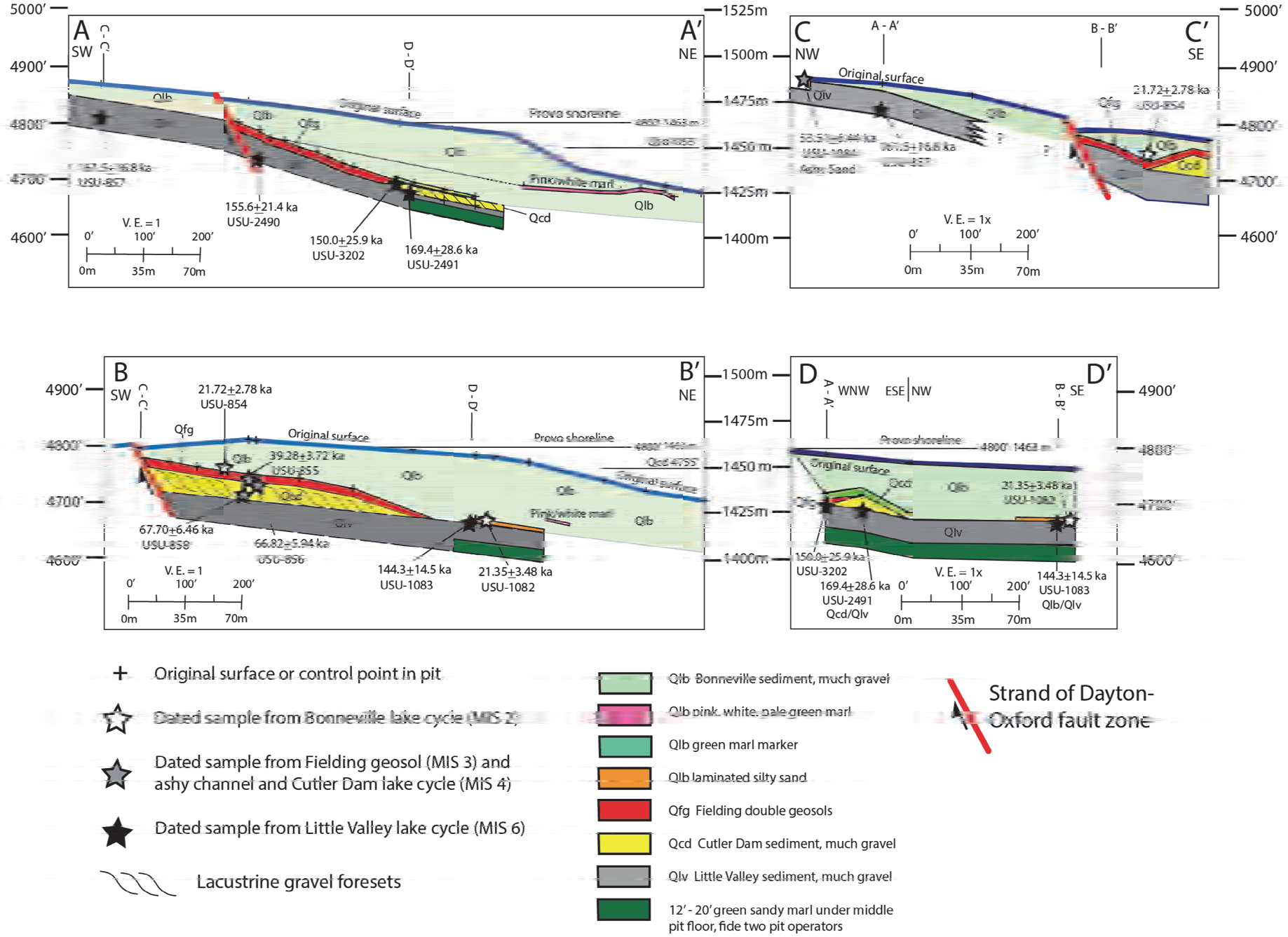

Figure 4. *Geologic cross sections A - A' to D -D' show extents of identified geologic units, original surface, OSL and IRSL age dates, pre-Bonneville lake deposits, and intersections with other geologic cross sections. See Figure 3 for locations.*

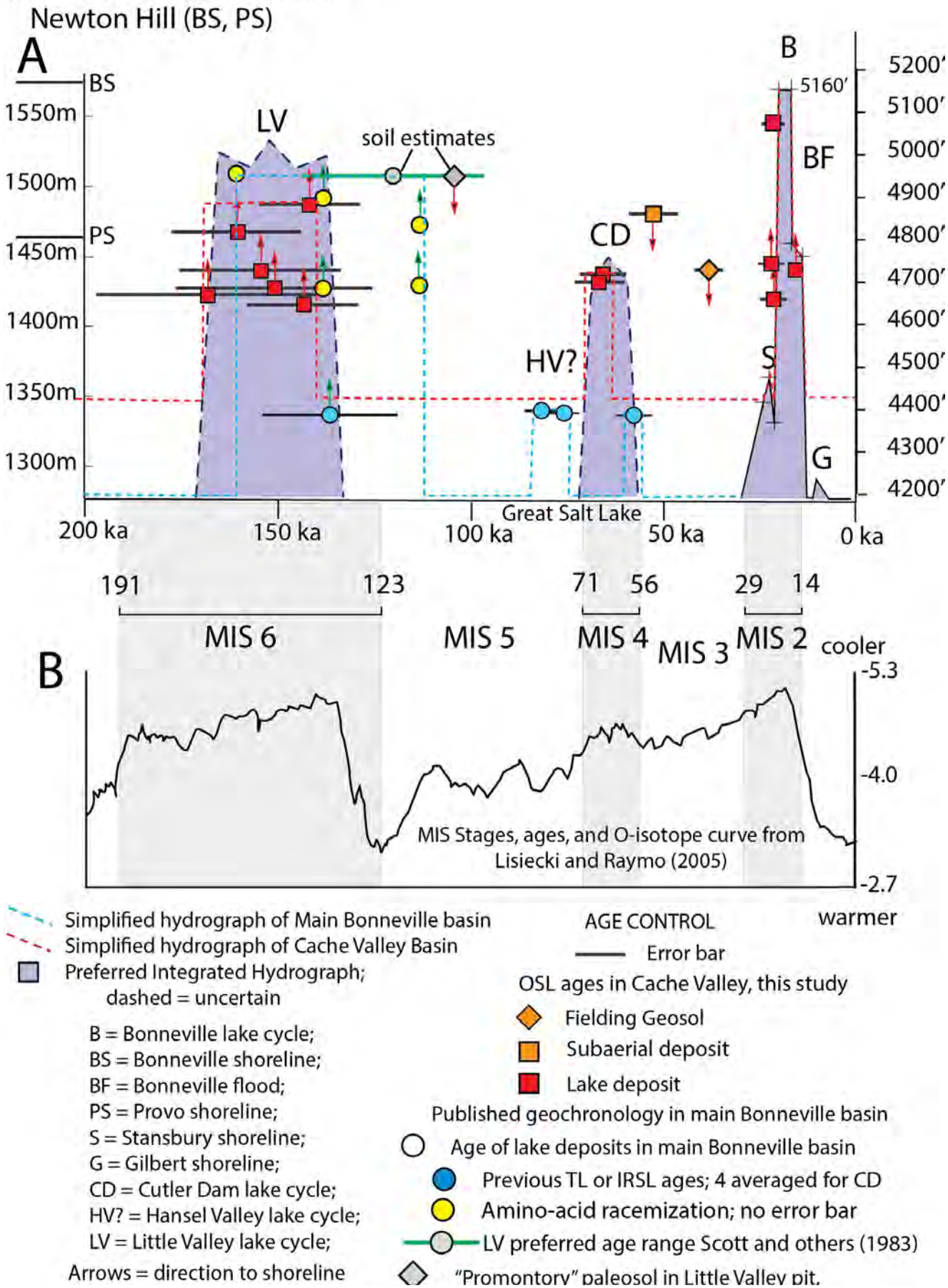

Figure 5. *Hydrographs showing changes in shoreline levels in the main Bonneville basin and Cache Valley since 200 ka compared with simultaneous climatic changes. Dates with error bars, ages of ashes and chrons, and sources are from Table 1 and Appendices 2 and were revised from Oaks and others (2019).*

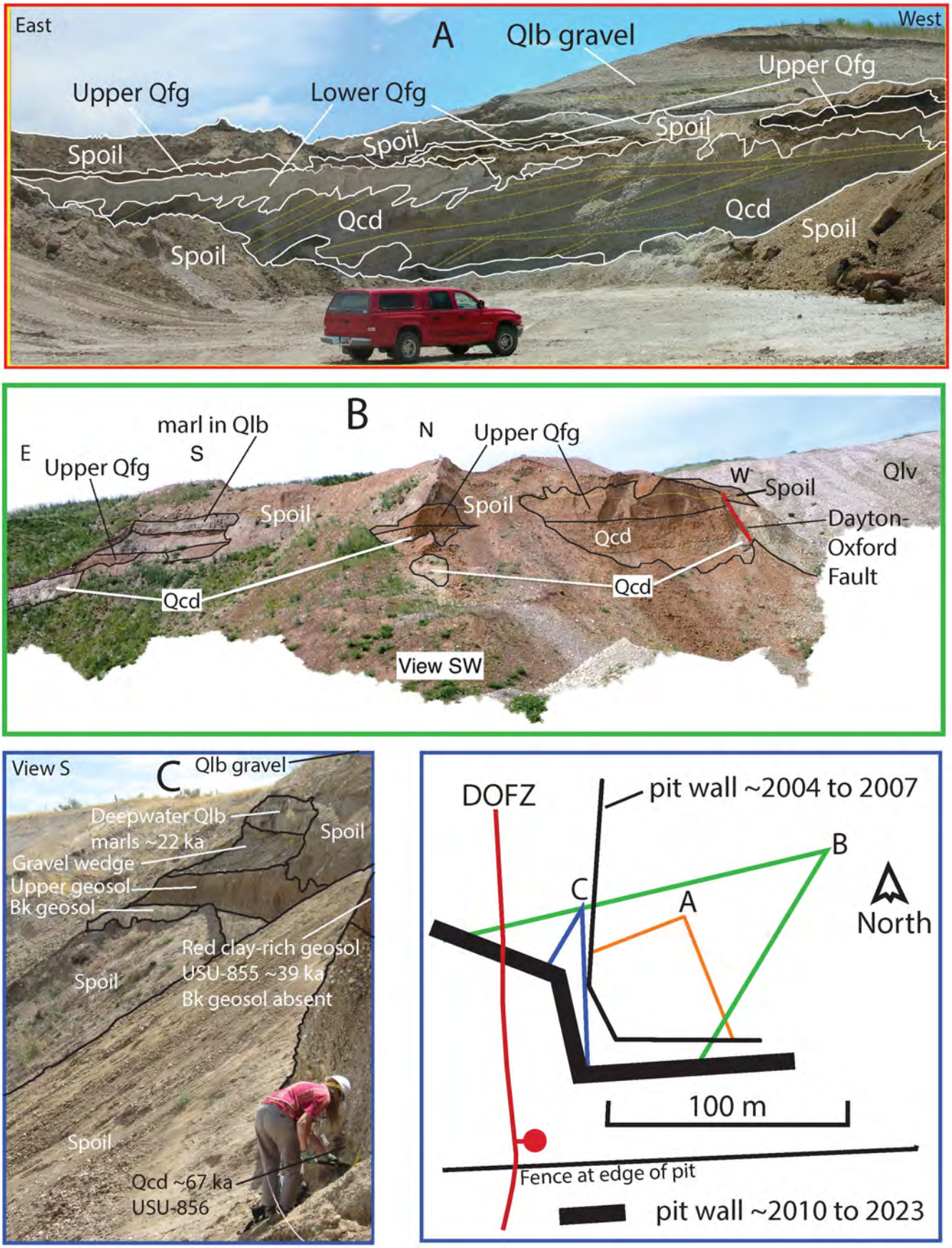

Figure 6. *A) Original exposure of Cutler Dam (Qcd) gravel overlain by the double Fielding geosols (Qfg), beneath deep-water Bonneville and younger Provo deposits (Qlb). B) Exposures W from the above site showed lateral continuity of this sequence in the hanging wall of the Dayton-Oxford fault. The fault dips toward viewer. Figure C) Details of Qcd, Qfg, and Qlb at sample site USU-856. D) Map showing camera positions of Figures 6A, B, C. Locations shown in Figure 3.*

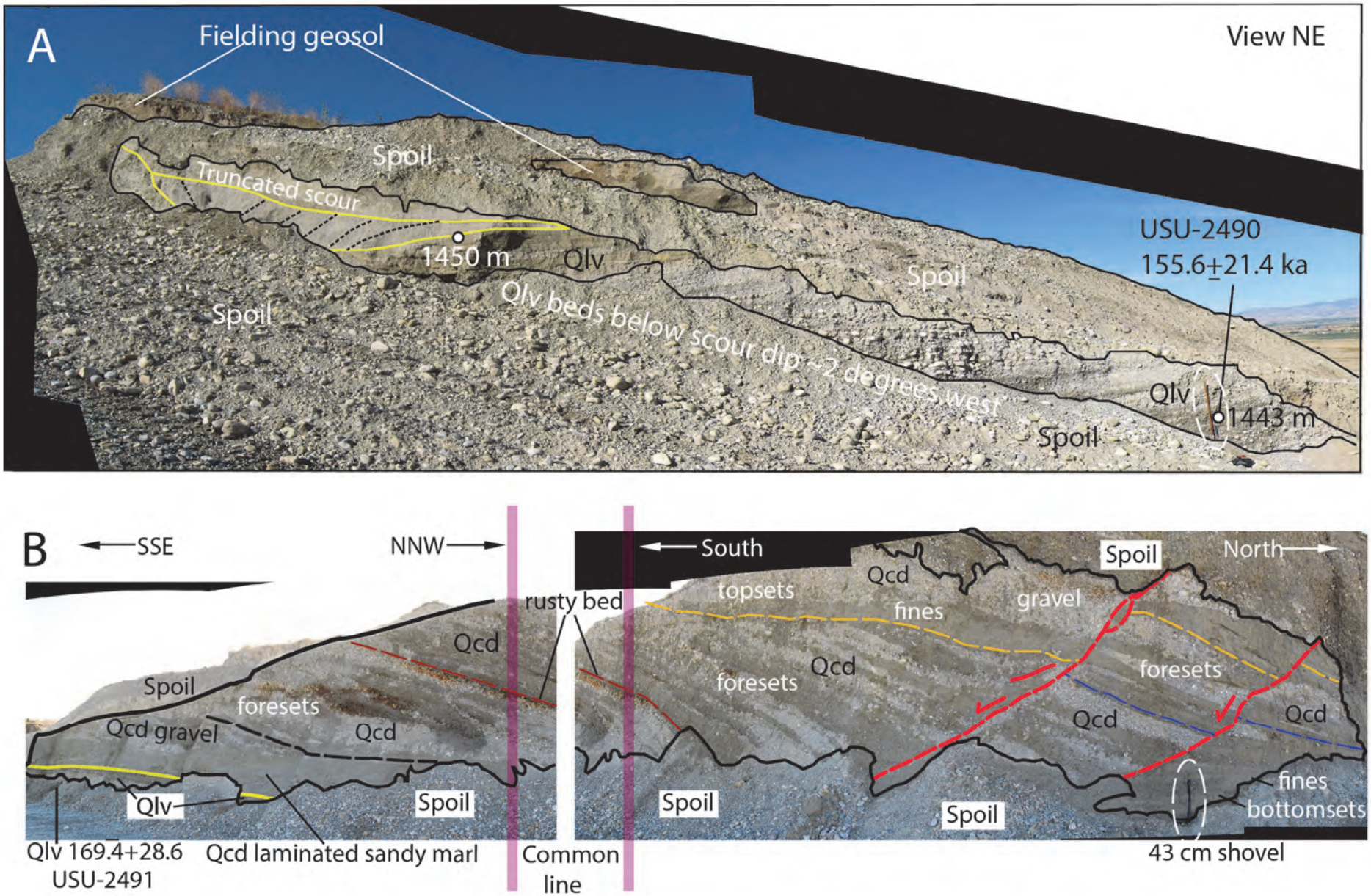

Figure 7. *A) Little Valley (Qlv) deposits. Truncated channel in upper left has curved sand laminae dipping toward the deepest part. Fielding red geosol here extended over Qlv. Staff = 1.50 m. Sample USU-2490 is the same altitude as the highest exposures of Cutler Dam (Qcd) deposits ~170 m SE, but below the highest (projected) Qcd ~1450 m ~120 m south B) Northwest edge of Newton Hill pit shows erosional unconformity (yellow) between Little Valley lake beds (Qlv) and overlying Cutler Dam beds (Qcd). There is no paleosol along this contact. Gravel and fines of the Cutler Dam lake cycle preserve bottomset, foreset, and topset beds (orange base) that formed in the east-plunging spit. Deposits are cut by two subsequent faults or slumps (red). Marker beds within the spit are color-coded. See Figure 3 for locations. Both photos 9-26-2016.*

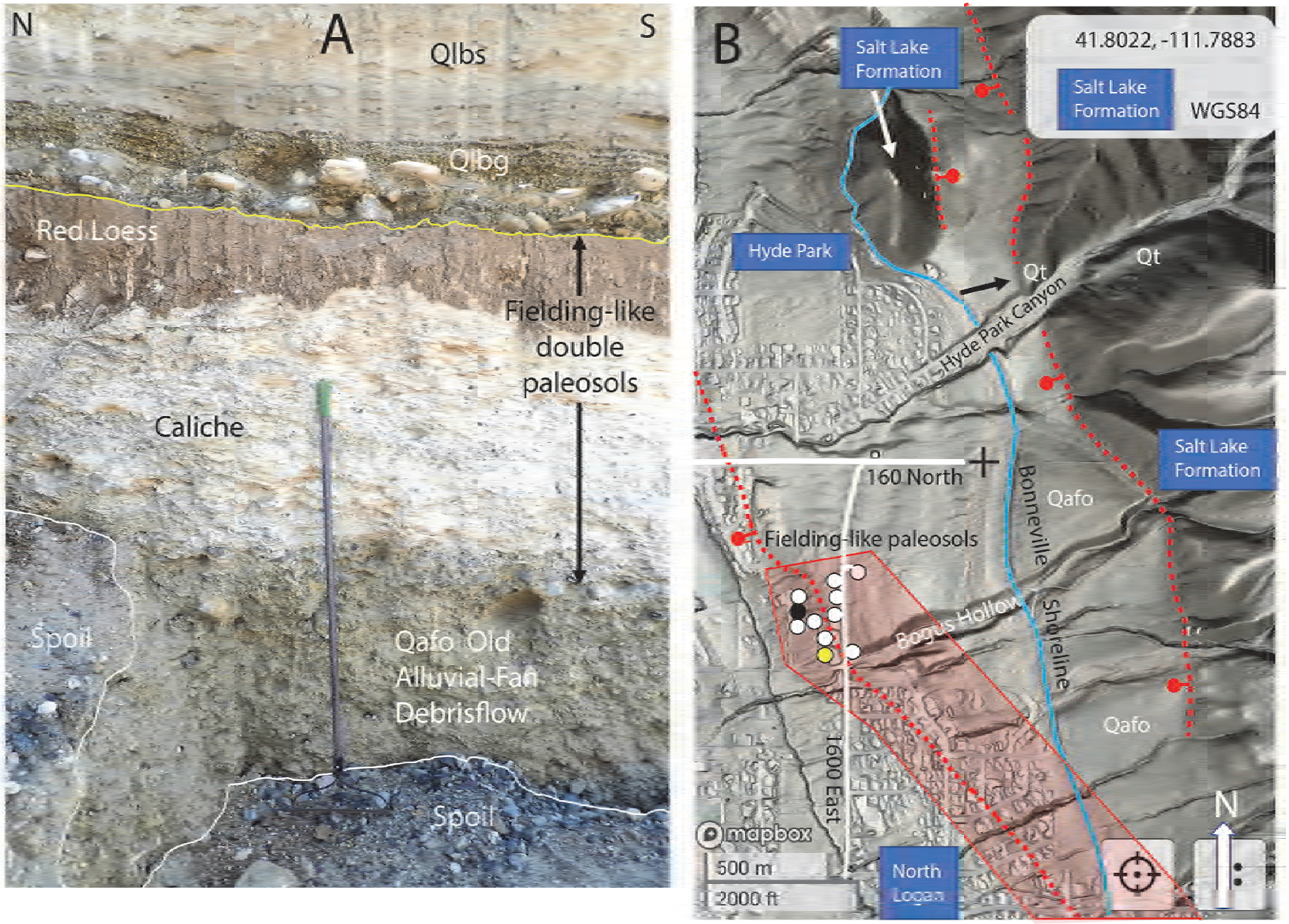

Figure 8. *A) Double paleosols in eastern Cache Valley (Figure 1B) that lithologically match our dated Qfg in the Newton Hill pit. Here they are overlain by Bonneville lag gravel (Qlbg) and sand (Qlbs). Underlying alluvial-fan deposits (Qafo) were not dated, so subaerial exposure and soil-forming could have begun before MIS 3. Location is at yellow dot in 8B. B) Lateral extent of exposures of double paleosols in east Cache Valley. Latitude and longitude indicate the mid-point of this image (+). Black dot marks site of ~143 ka OSL age (USU-2895) sampled within fine-grained Little Valley lake beds (Qlv) beneath a calcrete. Qt fluvial terrace is offset 9 m across a strand of the East Cache fault zone at the black arrow.*

Age Control (N=6)

Five exposures of pre-Bonneville lake gravels in the Newton Hill pit and one exposure in Hyde Park, Utah returned OSL and IRSL ages coeval with the Little Valley Lake cycle (MIS 6). The oldest age of ~169 ka (USU-2491) is from the north-central part of the Newton Hill pit, whereas the youngest age of ~143 ka (USU-2895) is from Hyde Park at ~1493 m. The latter is also the age determination from the highest elevation. The Little Valley lake cycle flooded Cache Valley to elevations well above ~1493 m, possibly as high as ~1530 m, and attained altitudes many tens of meters higher than expected (cf. Scott and others, 1983). The youngest beds dated in the Newton Hill pit (USU-1083; Table 1) are essentially the same age as that from Hyde Park.

Cutler Dam Lake Beds

Stratigraphic Relationships

In the south-central part of the Newton Hill pit, east-sloping foresets of sandy, well-rounded, pebble to cobble gravels underlie the Fielding geosols. The foresets there were >6 m high and extended horizontally about 200 m (Figure 6A). To the north, exposures of these spit gravels are about 6 to 10 m thick and flatten into finer bottomset beds (Figure 7B). There are sharp erosional contacts locally within the foresets (Figure 6A). The highest exposures reach ~1443 m, but early photos (Figure 6B) and projection in Figure 4D suggest that the highest lake beds may have reached ~1450 m (Appendix 5).

Bedding in the S-central part of the pit and the shape of the overlying pink marl (Figure 3) indicate that the spit probably was mainly east-plunging, yet part of this spit also extended northward (Figures 4A, 4B, 4D, 6B). Gravels to the north intertongue with underlying green, silty, fine-sandy laminated marl 2 m thick (Figure 7B). Most gravel lenses there thin downward and pinch out to the north between intercalated marl layers that thin upward and pinch out to the south. Two fault or slump surfaces offset the gravels in the north. These offset the contact between topsets and foresets (Figure 7B).

Age Control (N=2)

Two samples from this deposit in the south-central part of the Newton Hill pit yielded OSL dates of ~67 ka (USU-856, -858). These are coeval with the Cutler Dam lake cycle and MIS 4 (Figures 3, 4, 5; Table 1).

Ashy Channel Fill

Near the former west margin of the Newton Hill pit, a white reworked ashy fine sand filled a scour below thin surficial gravel and modern soil, ~1483 m. Satellite imagery (8-11-2011) in Google Earth Pro shows this narrow channel trended NNW-SSE. Probable Little Valley beds below this channel dip ~4° west and roll over eastward to dip gently east. The upper part of the probable Little Valley beds are truncated eastward at the pre-Cutler Dam erosional face (Figure 7A). This subaerial channel fill yielded an OSL age of ~54 ka (USU-1084), during MIS 3 (Table 1; Figures 3, 4C). This is older than the upper Fielding geosol but younger than the Cutler Dam gravels exposed lower in the Newton Hill pit and the shallow-water Cutler Dam muds in the type area southwest of Cutler Narrows (Figure 5).

Double Fielding Geosols In Newton Hill Pit

Stratigraphic Relationships

In the original south-central part of the pit, two successive geosols developed above and partly within the top of underlying gravel foresets of the Cutler Dam lake cycle (Figure 6A). This unit consists of an upper, humid-climate, red-weathering, loess-dominated interval and a lower, arid-climate, white caliche interval. The contact between the two geosols is primarily erosional, but locally gradational. In one place the upper geosol is separated from overlying deep-water Bonneville deposits by a thin gravel wedge up to 1 m thick (Figure 6C).

The lower of the two geosols typically has only an eroded lower Bk horizon, up to 1.5 m thick, above the Cutler Dam foreset gravels. This geosol pinches out east and west of the south-central part of the pit, and does not reach the east strand of the Dayton-Oxford fault westward in the pit (Figures 6B, 6C). Calcite in the lower geosol penetrated down into the Cutler Dam foreset gravels beneath (Figure 6A). It has amalgamated subhorizontal stringers of carbonate and amorphous nodules. Pieces of the eroded caliche are common in the lower part of the red geosol above (Figure 8A). The eroded upper contact of the caliche has distinct channels up to 15 cm deep filled with, and overlain by, as much as 2.5 m of the red geosol.

The upper geosol is mainly loess and slightly pebbly loess, although locally it contains abundant colluvium. It has considerable organic material, exhibits downward displacement of clay, has a distinctive reddish soil hue (10R5.5/4), displays little cementation, and has a few vertical calcite stringers, but lacks caliche nodules except those reworked into the base

(Figure 6C). Its top has a less prominent erosion surface than its base. This upper geosol thickens to 5 m or more westward, near the hanging wall of the Dayton-Oxford fault (Figures 6B, 7A), and locally on the north flank of the Cutler Dam spit, where the caliche geosol is absent (Figures 4A, 4D). There its upper part is colluvial gravelly mud overlying 2 to 3 layers of gravelly loess with weak subsoils. Locally in the north it pinches out eastward beneath a gray modern soil at the original surface of the pit.

Where absent in the east part of the pit, and locally in the north part of the pit, the upper contact of the double geosols is marked by a lag gravel or the green marl (Figures 4A, 4D) at the base of the Bonneville deposits above Cutler Dam foresets. Surveyed contacts of the top of the reddish geosol suggest that it probably rose at least to ~1463 m in the west part of the pit (Figures 4A, 4B, 4C). It descended to below ~1441 m in the SE part of the pit, and to below ~1444 m locally northward (Figures 3, 4D). Erosion probably removed these geosols from the lower and higher parts of the present Newton Hill pit before Bonneville deposits were laid down. The absence of the Fielding geosols in the footwall of the Dayton-Oxford fault makes it challenging to estimate the throw across the fault, although it must be >2 m.

Age Control (N = 1)

In the S-central part of the pit, the middle part of the red geosol, ~1444 m, contains a lens of sandy sediment that yielded an OSL age of ~39 ka (USU-855) (Figures 3, 4B, 6C). This dates to the penultimate interglacial, MIS 3c (Lisiecki and Raymo, 2005).

Double Geosols in Eastern Cache Valley

In Hyde Park and North Logan, Utah, in eastern Cache Valley, we found numerous examples of pre-Bonneville double paleosols in many trenches for utilities and in basement and landscape excavations (Figure 8B). These paleosols are essentially identical to those in the Newton Hill pit, with a red clay-rich paleosol over an eroded white caliche paleosol. Several of the lower exposures have only the eroded lower white Bk paleosol, locally with a very thin, eroded, red paleosol above. Detailed local mapping with an Abney hand level near sample site USU-2895 demonstrated an undulose paleotopography beneath the paleosol with lateral changes in the underlying sediments uphill and laterally. All exposures lie above the highest Cutler Dam deposits in the Newton Hill pit.

In eastern Cache Valley, either the double paleosol, loess deposits, or a gravel lag underlie the Bonneville offshore sand with snails (west, lower) and Bonneville gravel or post-Bonneville colluvial gravel (east, higher), respectively (Figure 8B). The white caliche paleosol overlies dated Little Valley marl (~143 ka; USU-2895) at ~1493 m in Hyde Park, and both paleosols overlie undated alluvial-fan debris flow deposits at ~1526 m in exposures farther east (Figure 8A). Exposures of these widespread double paleosols were recorded through a vertical range of at least 124 m and a horizontal separation of at least 2.7 km NNW -SSE (Figure 8B). The highest exposure, at ~1607 m, is above the Bonneville shoreline (41.78501, -111.77766). Our current concept of the spatial and stratigraphic relations of the lake cycles and intervening paleosols is shown in Figure 9.

Bonneville Lake Beds

Stratigraphic Relationships

Bonneville deposits originally blanketed the spit in the area of the Newton Hill pit (Figure 2). In the southern exposures, topsets and foresets of sandy pebble to cobble gravels of the Bonneville lake cycle (Figure 6A) grade downward into finer bottomsets that overlie more than 3 m of transgressive deep-water marls and laminated silty sand (Figure 6C). Northward, where the pre-Bonneville relief was lower, deposition included lower green marls and a single higher pink marl that form distinctive marker beds (Figures 3, 4) between thicker Bonneville gravels (Figure 10). The pink marl is a calcareous, very fine sandy, clay-rich silt. It is plastic, weakly laminated, and thin (tens of cm thick). It is either pink throughout (oxidized reddish orange (5R7/2) or greenish-gray to whitish color at the base. It might be Gilbert's "white marl", which dates from the highstand of Lake Bonneville. Its red stain may be due to iron supplied by the proximal Bear River.

Locally, a lower green Bonneville marl directly overlies Cutler Dam deposits where the Fielding geosols are absent (Figures 4A, 4D), but there are other traceable pale greenish marls higher in the Bonneville sequence. Several marls produced low-angle slip surfaces that repeat layers within the Bonneville deposits in small slumps and slides (Figure 10). These might have been triggered by earthquakes, the Bonneville flood, or both.

Age Control (N=4)

Near the south-center margin of the pit, gently east-dipping, gray, laminated silty sand yielded an OSL age of ~22 ka (USU-854) (Figures 3, 4B, 4C).

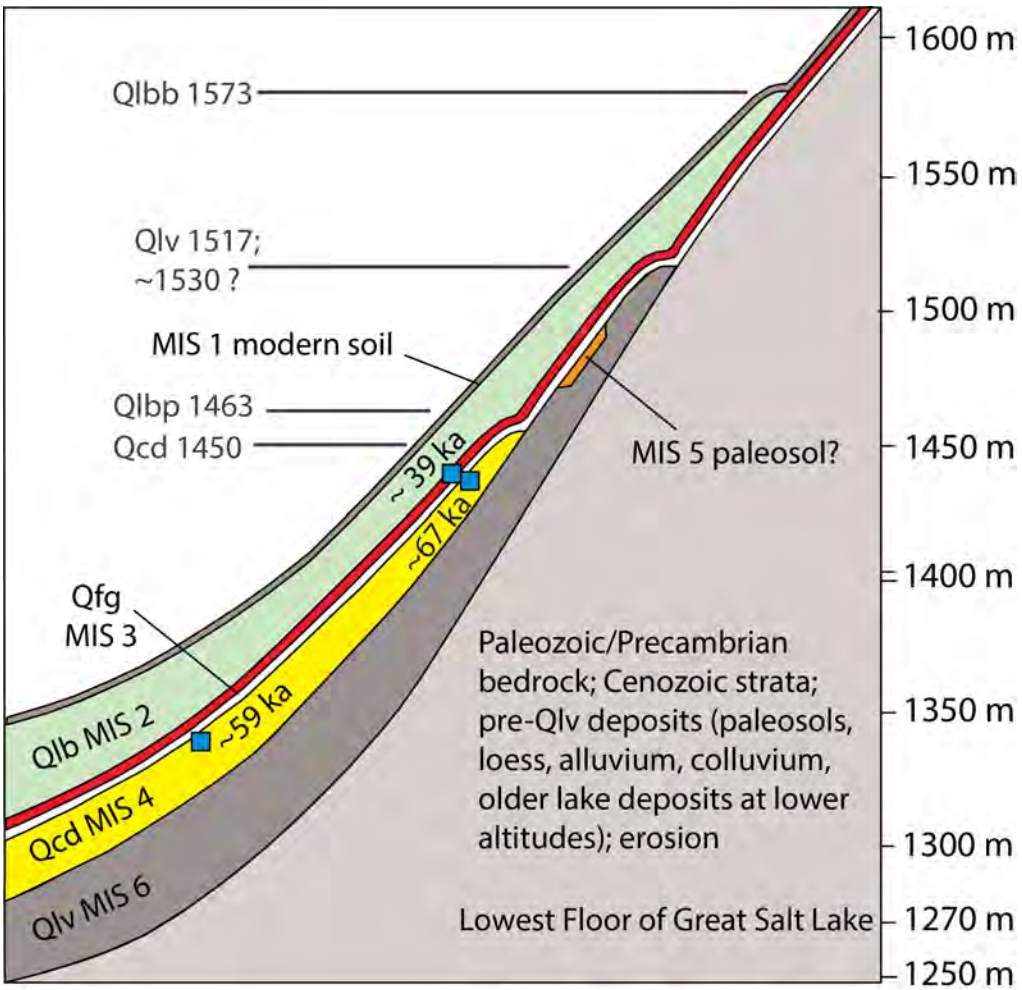

Figure 9. *Schematic cross section of the relative geometries of deposits of three pluvial lakes in Cache Valley, intervening double soils, the modern geosols, and the modern surface soil on the double paleosols above the Bonneville shoreline in eastern Cache Valley and the Newton Hill pit. Qlb = Bonneville lake cycle; Qlbb = Bonneville shoreline; Qlbp = Provo shoreline; Qfg = double Fielding geosols; Qcd = Cutler Dam lake cycle; Qlv = Little Valley lake cycle; MIS = marine oxygen-isotope stage. Although we found no distinct MIS 5 paleosol developed on Qlv, it might be incorporated in the base of Qfg above Qcd deposits. Above the Bonneville shoreline, modern soil is developing on and augmenting exposed Qfg. Horizontal scale is tens of kilometers. Concept from Oviatt and others (1987). Any paleosols within lake cycles are omitted. Altitudes are not corrected for rebound.*

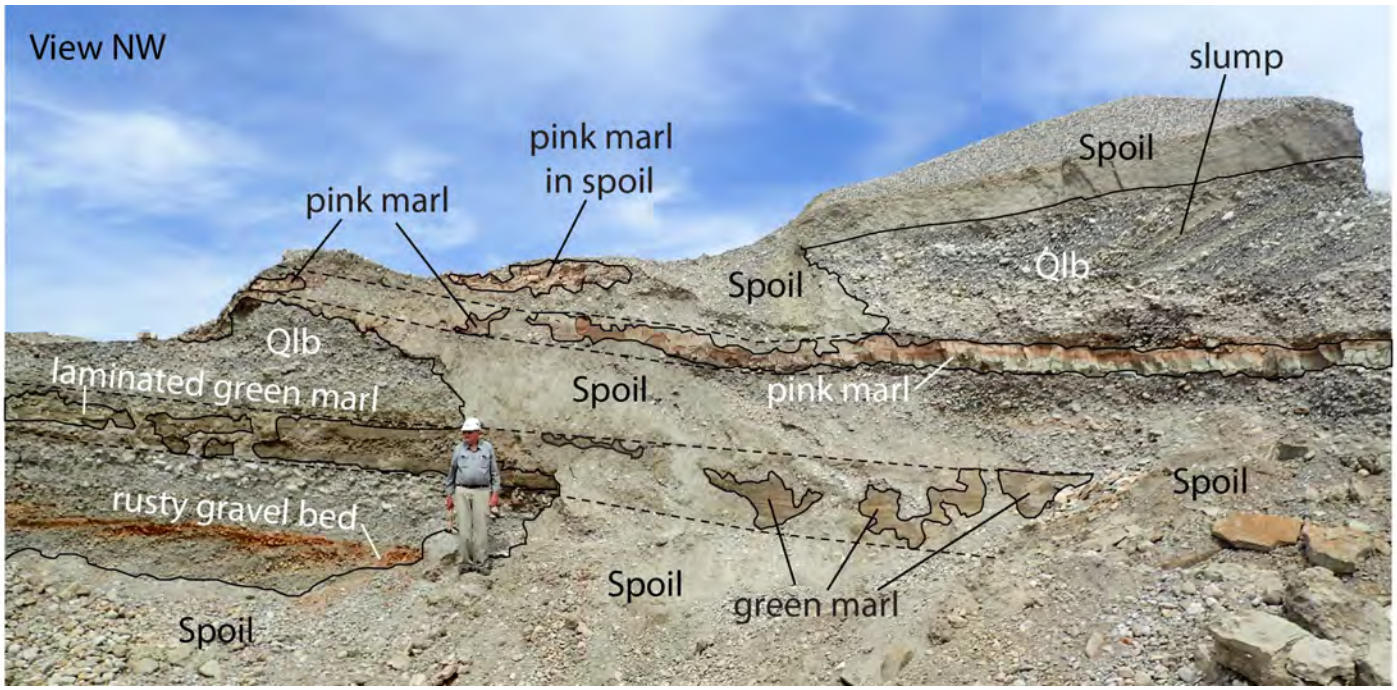

Figure 10. *Exposure of distinctive marls within Bonneville (Qlb) nearshore gravels in Newton pit. The pink marl is widespread in the Newton Hill pit whereas the underlying laminated green marl is more restricted. Thad Erickson = 1.8 m. NW part of pit. The stratigraphic position and gravel of the slump above the pink marl suggests a possible trigger by the Bonneville flood. The pink marl records the deepest water depths.*

These deep-water deposits sharply overlie an unconformity and the upper Fielding geosol (Figure 6B). A laminated silty sand lens in cobble gravel from the lower part of Bonneville deposits, in the central part of the pit, yielded a slightly younger OSL age of ~21 ka (USU-1082). There the Bonneville deposits directly overlie eroded Little Valley gravels (USU-1083) with no paleosol between (Figures 4B, 4D). A sand bed intertongued with northeast-dipping gravel beds in the north-central part of the pit yielded a post-flood Provo age of ~15 ka (USU-859) (Figure 3). At Muley Hill in Millville, Utah, gravel atop an eroded delta, at ~1550 m, between the Bonneville and Provo levels, yielded an age of ~21 ka (Table 1).

Subsurface Evidence of Pluvial Lakes

Drillers' logs from >1000 water wells across the center of Cache Valley southeast and east of Newton Hill document two gravelly layers and two clay-rich layers in the subsurface. An upper confining silty clay (marl?) unit ~18 m thick, an intervening, persistent gravel unit ~9 m thick, and a lower confining silty clay unit ~9 m thick, overlie thick underlying gravel and sand (Williams, 1962; Bjorklund and McGreevy, 1971; Clyde and others, 1984; Kariya and others, 1994; Robinson, 1999; Thomas and others, 2011). Figure 11 shows these relations along part of U.S. Highways 89/91 (Figure 1). Within the upper confining layer there are typically two horizons of non-persistent gravels associated laterally with oxidized brown silty clays. Gray, blue, or black silty clays lie both above and below these gravel and oxidized intervals. The lower confining layer also encloses lenses of gravels and related oxidized horizons. These clays overlie sandy gravels of Pleistocene age and underlying older gravels in the Salt Lake Formation that cumulatively reach ~150 m to 300 m thick between Smithfield, Wellsville, and Hyrum (Robinson, 1999) (Figure 1A). These coarse sediments are the Principal Aquifer in Cache Valley (Figure 11).

The unoxidized clays probably are deep-water lake deposits. They likely are coeval with the three lacustrine deposits in the Newton Hill pit, and perhaps earlier pluvial lakes in the main Bonneville basin (Williams, 1962), including older lake cycles identified in the Saltair and Burmester cores (Eardley and Gvosdetsky, 1960, Eardley and others, 1973; Williams, 1994; Oviatt and others, 1999). The gravels and oxidized muds at distinct levels within the unoxidized muds either indicate interglacial epochs or major oscillations within long pluvials (Williams, 1962; this study). In the southwest part of Figure 11, a persistent gravel within the upper confining layer may be a chance intersection laterally along a former stream channel.

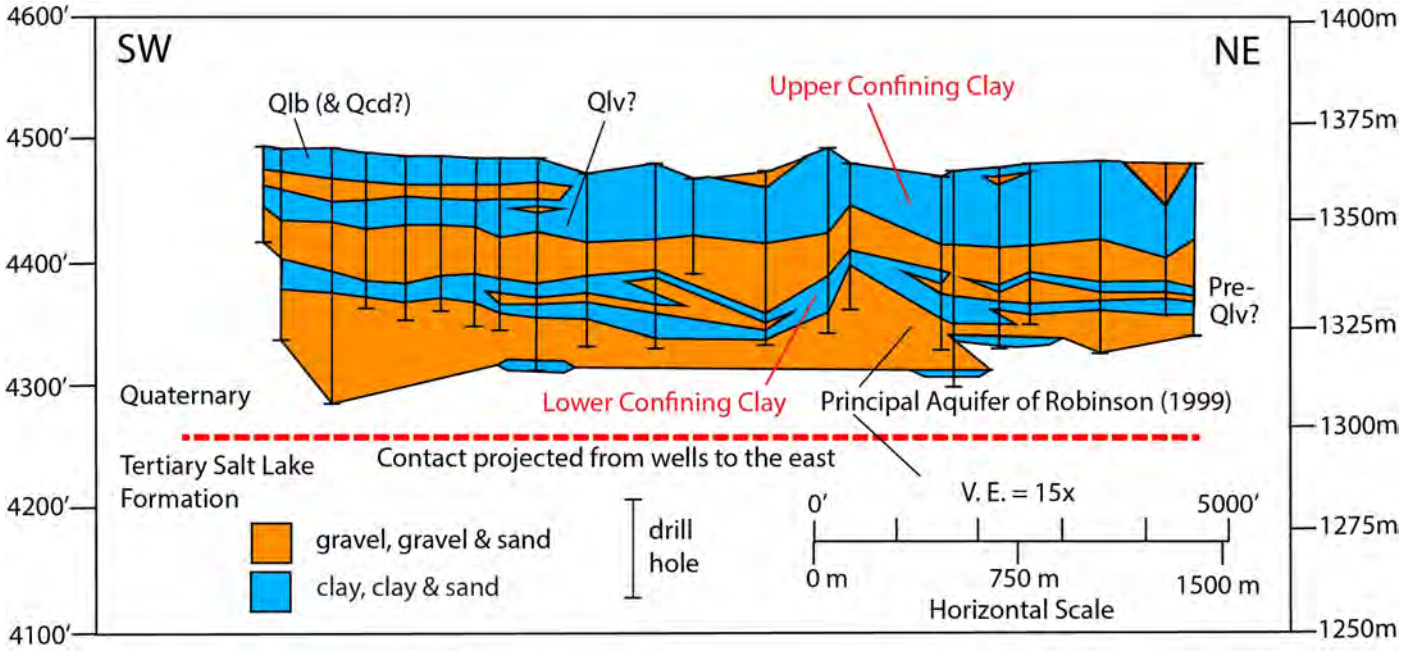

Figure 11. *Geologic cross section showing alternating pluvial fines (blue) and interglacial gravel and sand deposits (orange) beneath the low part of Cache Valley. This section is through College Ward in central Cache Valley, Utah, along U.S. Highways 89/91. Qlb = Bonneville; Qcd? = Cutler Dam; Qlv? = Little Valley. See Figure 1A for location. Question marks indicate that correlations with other lake cycles are possible. Williams (1962) first documented these repeating coarse and fine intervals of lacustrine and fluvial deposits in drill holes in five geologic cross sections across the Utah part of Cache Valley.*

Elsewhere in Cache Valley, the underlying Salt Lake Formation has many different lithologies. These include conglomerates, tuffaceous green (zeolite-bearing) to dark and light gray shales, sandstones, siltstones, thick to thin, pale brown very fine crystalline (micritic) limestones, oolitic limestones, and diabase (Adamson and others, 1955; Goessel and others, 1999; Oaks and others, 1999; Janecke and Evans, 1999; Janecke and others, 2003). These distinctive lithologies are repeated by extensional folds and normal faults, so that the Salt Lake Formation commonly exhibits tilts. Dips as high as 78° distinguish the Salt Lake Formation from the overlying Quaternary deposits (Oaks, 2000).

DISCUSSION

Correlations Related to the Hydrographs

Overview of the Hydrographs

Data for the hydrographs in Figure 5 are in Table 1 and Appendices 1 to 5. The hydrographs for Cache Valley and the main Bonneville basin show good correlation of lake highstands and lowstands in both basins and also with the O-isotope marine record of climatic fluctuations for MIS 6 through MIS 1. The Little Valley lake rose higher than the local Provo shoreline, whereas the Cutler Dam lake cycle did not rise quite as high (Figure 9).

The MIS 5 interglacial persisted for ~55 kyr, twice as long as the ~27 kyr- long MIS3 interglacial. The isotopic data also suggest that MIS 5 was warmer than MIS 3 (Figure 5). Yet there are no distinct, widespread soils associated with MIS 5 in Cache Valley, and the only possible exceptions elsewhere are the Promontory/Dimple Dell geosols in the Little Valley pit and other parts of the main Bonneville basin (Scott and others, 1983). It is noteworthy that well-dated Fielding humid soil and the underlying arid soil, both of which are widespread in Cache Valley, formed during the relatively short and mild interglacial MIS 3 before the Bonneville lake cycle, yet they are exceptionally thick and robust paleosols (Figures 3, 5, 6, 8).

The lake was at least 150 m deep during the 68 to 67 ka part of the Cutler Dam lake cycle, in the early part of MIS 4, yet it coincided with a relatively minor oscillation in the climate record (Lisiecki and Raymo, 2005). This seems anomalous compared with the climatic and hydrologic conditions that favored deep lakes during MIS 6 and MIS2. The oscillations of benthic marine isotopes are only about 60% as intense during MIS 4 as during MIS 6 and MIS2 (Figure 5).

Perhaps deep lakes can form with less Milankovitch forcing than glaciers. Alternatively, added water may have begun to flow across a waterfall in Oneida Narrows into Cache Valley then, followed ~20 kyr later by the complete, final diversion of the Bear River into the Bonneville basin (Pederson and others, 2016). A complex history of incision of Oneida Narrows is suggested by one or more widespread subsurface gravels below a mud layer under surficial gravel from Oneida Narrows through several kilometers downstream in drillers' logs of water wells (Oaks, 2010).

Little Valley Lake Cycle

The age and duration of the Little Valley lake cycle is constrained by our six new absolute ages, five published AAR estimates, one published TL age, and one extrapolation from the estimated rate of formation of the overlying Promontory paleosol (Figure 5; Table 1; Appendices 2, 3, 4). Combination of all the data for the main Bonneville basin (blue dashes in Figure 5) suggests that the Little Valley lake cycle might have persisted 20-30 ky into interglacial MIS 5. However, an end closer to 123 ka, at the end of MIS stage 6, is more likely based on the climate record and our new absolute ages (preferred model in Figure 5).

In the main Bonneville basin, altitude control for the Little Valley lake cycle is limited, with some corrected for rebound, others not (McCoy, 1981, 1987; Scott and others, 1982, 1983). The highest probable but undated Little Valley gravels in the main Bonneville basin are at ~1512 m in the Geneva quarry at Point of the Mountain, south of Salt Lake City (Scott and others, 1983) and at ~1517 m in the Little Valley pit, where they were initially misidentified as "Alpine" by Morrison (1965, 1966) and reinterpreted by Scott and others (1983). These older lake beds are about half way between the local Bonneville and Provo shorelines (Scott and others, 1983).

In Cache Valley the highest dated Little Valley deposits, at ~1493 m in Hyde Park are sandy, weakly laminated marl, and undated deposits traced uphill from dated beds in the upper Newton Hill pit, at ~1483 m. These also lie between the Bonneville and Provo shorelines. Thus, the highest level attained by the Little Valley pluvial lake is not certain, but elevation ranges are high and roughly similar in both basins (Appendix 5). Active tectonics in both basins may have raised or lowered individual sites, which is especially critical for older lakes. Further discovery of higher shoreline exposures and absolute ages are needed to determine if the actual highest water levels of the Little Valley lake cycle were the same or different across Cutler Narrows.

Cutler Dam Lake Cycle

Our ages of Cutler Dam deposits in Cache Valley confirm that this pluvial lake rose at least 110 m above that of marshy sediments in the type area (Oviatt and McCoy, 1988, 1992) in the main Bonneville basin SW of Cutler Narrows (Figures 1B, 6B; Appendix 5). Two IRSL ages from Cutler Dam deposits and two from the base of the Fielding geosol in the type area averaged ~59 ka (Kaufman and others, 2001). This is younger than the average of ~67 ka for two OSL ages near the higher level in Cache Valley. Although the error limits of the ages from both sites overlap slightly (Figure 5; Table 1; Appendix 2), the central ages differ. These data may indicate a drop to the lower level near the end of MIS 4, consistent with the climatic data (Figure 5).

Additional OSL age control from distal Cutler Dam beds in the Newton Hill pit would further constrain the hydrograph in Figure 5. Re-dating lake beds between those of the Little Valley and Bonneville lake cycles in Hansel Valley (Robison and McCalpin, 1987) with OSL might show that they are coeval with the Cutler Dam lake cycle, which seems likely.

Fielding Double Geosols

Our dated samples of the upper Fielding geosol and the ashy sand channel fill indicate that subaerial deposition replaced the Cutler Dam lake after the end of MIS 4, at ~56 ka. Our double geosols are similar to the sequence described by Kaufman and others (2001, p. 324) in the type area SW of Cutler Narrows. Their Figure 2 showed three successive geosols that comprise their Fielding geosol, described in the figure as: "Massive red-brown silt and clay; at least three petrocalcic horizons, each topped by a snail-rich horizon; oxidized rootlets on blocky weathered surfaces".

The similarity of our double geosols to descriptions of the Promontory and Dimple Dell double paleosols in the Little Valley pit (Morrison,1965) is also striking. There, a lower caliche geosol and an upper red (10YR) loess-derived geosol lie between Little Valley and Bonneville deposits. All exposures there are above the highest known Cutler Dam lake beds in Cache Valley.

Despite the similar lithologic features and nearly identical stratigraphic relationships, the Promontory and Dimple Dell geosols are interpreted to be much older, ~104 ka (Scott and others, 1983; their Table 5). If so, the Promontory and Dimple Dell palesols are significantly older than the Fielding geosols. Absolute ages are needed to resolve this puzzle.

An OSL age is needed in Hyde Park within the double paleosols there, to determine if these paleosols are definitely coeval with, or differ in age from, the dated upper Fielding geosol in the Newton Hill pit.

Bonneville Lake Cycle

The final diversion of the Bear River into Cache Valley ~ 45 to 55 ka (Pederson and others, 2016) was too late to raise the Cutler Dam lake, and all earlier lakes, above a divide ~2 km north of Red Rock Pass, at the north end of Cache Valley (Gilbert, 1890) (Figure 1A). Its final addition raised Lake Bonneville higher than earlier lakes, to overtop that divide (Bright, 1963; Hochberg, 1996; Bouchard and others, 1998; Link and others, 1999; Janecke and Oaks, 2014; Pederson and others, 2016; Utley, 2017). An earlier overflow across Oneida Narrows (Oaks, 2010) may have raised the Cutler Dam lake above that expected from the O-isotope data (Figure 5).

Our two OSL ages of ~21 ka in the Newton Hill pit, at ~1422 m and ~1447 m, lie within the wide envelope of ^{14}C dates with confidence intervals for the rising limb of the Bonneville transgression in the main Bonneville basin (cf. Oviatt, 2015, 2020). However, both are minimum depths for the lake level at those times. Furthermore, well-rounded gravels at Muley Hill, with an age of ~21 ka, at ~1550 m elevation, is close to the local Bonneville shoreline at ~1573 m (Figure 9), and above the Oviatt envelope of dates. Janecke and others (2013) obtained a ^{14}C age ~22 ka in nearshore sands at ~1500 m in a gravel pit at the mouth of Green Canyon in eastern Cache Valley, between Logan River and City Creek (Figure 1A), somewhat above the Oviatt envelope.

Thus, although the age-altitude data from Cache Valley plotted in Figure 5 might suggest a slightly earlier rise of Lake Bonneville during its transgression, the data do not differ enough from those compiled in Oviatt (2015, 2020) to be compelling. More precise and diverse age control is needed to improve the earlier curve for Lake Bonneville, which was compiled from ^{14}C age determinations.

We believe that a prolonged Bonneville highstand during oscillatory (?) overflow to the north, is needed to explain high, steep, wave-cut bedrock cliffs at the Bonneville shoreline throughout the Bonneville basin (Janecke and others, 2019). Significant time is also required to backfill Gem Valley, Oneida Narrows, lower Bear River-Mink Creek Canyon, and finally deposit the large Bonneville delta north of Preston, Idaho, with a surface area of >125 km^2 in Cache Valley (Figures 1A, 1B). The Bonneville delta of the Bear River back-filled a reach that was ~55 km long, between Gem Valley and northeast Cache Valley (Janecke and Oaks, 2011b).

Implications for Incision of Cutler Narrows

It is unclear if Cutler Narrows was incised well below the ~1450 m Cutler Dam gravels of Cache Valley before the Bonneville flood because the evidence is incomplete and inconclusive. Sr isotopes indicate likely entry of water of the Bear River west of Cutler Narrows during both the Little Valley and Cutler Dam lake cycles (Hart and others, 2004). The flow could have been through a fully incised Cutler Narrows, with lakes at the same or similar levels on both sides, or as flow across a lip near or slightly below the ~1450 m Cutler Dam gravel of Cache Valley that separated lakes with different levels. Although Oviatt and McCoy (1988, 1992), Oviatt and others (1987), and Kaufman and others (2001) found no deep-water Cutler Dam deposits in ~15 m of shallow-water Cutler Dam deposits west of Cutler Narrows, such could be present in the subsurface there.

Several arguments suggest that deep incision almost to the modern level of the Bear River is a reasonable interpretation of the existing data. These arguments include: (1) the ≥4 Ma age of the east side of the horst block, so that considerable time was available to incise the canyon at Cutler Narrows; (2) the short and low canyon in Cutler Narrows, compared to dozens of deeper and longer canyons cut by streams with a fraction of the discharge nearby (e.g. Logan Canyon), which include some carved by now minor and intermittent streams (e.g. Weston Canyon); and (3) subsurface fluvial (?) sand and gravel deposits, hundreds of meters thick, that alternate with clay and silt that settled from lakes (Williams, 1962). This facies pattern continues from the Quaternary units down into the underlying Pliocene Salt Lake Formation (~12 to ~2[?] Ma; Goessel and others, 1999; Oaks and others, 1999; Janecke and others, 2003) (Figure 11). The thick and laterally continuous fluvial (?) gravels beneath the center of Cache Valley suggest protracted external drainage because continuous playa and lake deposits would have formed if there had been a long-lived barrier in Cutler Narrows. Williams (1962) also argued that external drainage during most of the Pleistocene is required to produce the consistently thin Quaternary deposits beneath Cache Valley.

To determine if pre-Little Valley lakes extended through Cutler Narrows and how high they reached relative to those in the main Bonneville basin, absolute ages are needed from more lake beds between the Provo and Bonneville shorelines in both basins. A continuous core where the Quaternary deposits are thickest in Cache Valley, perhaps near the location of Figure 11, could provide further age control.

Altogether, we conclude that the narrow, low horst between Cache Valley and the main Bonneville basin was probably breached early because it is neither high enough nor wide enough to separate high pluvial lakes for an extended period of time (Figure 1). Much, possibly nearly all, of the excavation of Cutler Narrows in bedrock probably took place before the Little Valley lake cycle (Oaks and others, 2014, 2019, 2020; cf. Maw, 1968, Hunt, 1982).

Complete resolution could come from finding: (1) ~59 ka Cutler Dam shallow-water lake beds in Cache Valley near the same elevation as the Cutler Dam beds in the type section; or (2) high-elevation Cutler Dam beds in the main Bonneville basin that date from ~67 ka; or (3) that the dated Cutler Dam gravels between 1450 - 1410 m in Cache Valley are coeval with the low- elevation shallow-water deposits in the main Bonneville basin.

CONCLUSIONS

Our 14 new OSL and IRSL ages establish the first evidence of Cutler Dam lake deposits and double Fielding geosols, and provide the first absolute ages of Little Valley deposits in Cache Valley. Our quantitative hydrographs show firm correlation of deposits in Cache Valley with the Little Valley (MIS 6), Cutler Dam (MIS 4), Fielding (MIS 3), and Bonneville (MIS 2) units in the main Bonneville basin.

None of our contacts between dated sediment of the Little Valley and Cutler Dam lake cycles preserve paleosols. In contrast, our double Fielding geosols lie between well-dated Cutler Dam and Bonneville deposits up to the highest near-shore gravel deposits of the Cutler Dam lake cycle in the Newton Hill pit (Figures 6, 7A). Higher in the Newton Hill pit and in Hyde Park (Figure 8A) double paleosols lie between the Little Valley and Bonneville deposits. Above the Bonneville shoreline in North Logan (Figures 8B, 9) they lie above pre-Bonneville loess and alluvial-fan deposits. These paleosols consistently exhibit an eroded arid-climate white calcic Bk horizon overlain by a loessic humid-climate red soil, and thus are provisionally correlated here with the dated Fielding geosols in the Newton Hill pit despite the absence of additional geochronology.

Drillers' logs of water wells identify two thick, confining clay-rich layers separated by a continuous gravel layer. These overlie thick gravels of the gravels of the Principal Aquifer of Cache Valley (Figure 11). Each confining clay sequence contains local gravels with adjacent oxidized clays that may indicate emergence due to oscillations within protracted lake cycles or interglacial episodes between pluvials. Lake deposits older than Little Valley may be present here.

The majority of incision of Cutler Narrows proba-

bly predates the Little Valley lake cycle. Although the evidence for when Cutler Narrows was cut below the ~1450 m Cutler Dam deposits in Cache Valley is incomplete, we believe that the evidence supports early incision to near its present depth.

ACKNOWLEDGEMENTS

We thank reviewers Jeremiah Bernau, Paul Inkenbrandt, Daren Nelson, Jack Oviatt, an anonymous reviewer, and editor Hugh Hurlow for constructive suggestions for improvements to the text, figures, and tables, for pertinent references we had missed, and for valuable insights. James P. Evans aided us in many ways in addition to careful reviews. We benefited greatly from Staker-Parsons' permission to visit their Newton Hill pit repeatedly through 17 years, and thank Sam Waterman and Steve Tucker for their keen interest in our work, knowledge of layering in the pit before our first visit in 2006, and willingness on occasion to clean faces or excavate areas of interest between loading customers' trucks. Our colleague Alexis Ault discovered the double palesols in SE Hyde Park, Utah. Tomas Capaldi assisted in collecting sample USU-3243. Hugh Hurlow and Mike Vanden Berg deftly and kindly shepherded this manuscript to completion.

REFERENCES

Adamson, R.D., Hardy, C.T., and Williams, J.S., 1955, Tertiary rocks of Cache Valley, Utah and Idaho: Utah Geologic Association Guidebook 10, p. 1-22.

Auclair, M., Lamothe, M., and Huot, S., 2003. Measurement of anomalous fading for feldspar IRSL using SAR: Radiation Measurements, v. 37, p. 487-492.

Bjorklund, L.J., and McGreevy, L.J., 1971. Groundwater resources of Cache Valley, Utah and Idaho: Utah Department of Natural Resources, Technical Publication 36, 72 p.

Bouchard, D.P., Kaufman, D.S., Hochberg, A., and Quade, J., 1998, Quaternary history of the Thatcher Basin, Idaho, reconstructed from $^{87}Sr/^{86}Sr$ and amino acid composition of lacustrine fossils - Implications for the diversion of the Bear River into the Bonneville Basin: Palaeogeography, Palaeoclimatology, Palaeoecology, v. 141, p. 95-114.

Bright, R.C., 1963, Pleistocene Lakes Thatcher and Bonneville, southeastern Idaho: Ph.D. dissertation (unpublished), University of Minnesota, Minneapolis, 292 p.

Bright, R.C., 1967, Late-Pleistocene stratigraphy in Thatcher basin, southeastern Idaho: Tebiwa, v. 10, p. 1-17.

Buylaert, J.P., Murray A.S., Thomsen, K.J., and Jain, M., 2009, Testing the potential of an elevated temperature IRSL signal from K-feldspar: Radiation Measurements, v. 44, p. 560–565.

Carney, S.M., and Janecke, S.U., 2005, Excision and the original low dip of the Miocene-Pliocene Bannock detachment system, SE Idaho: Northern cousin of the Sevier Desert detachment?: Geological Society of America Bulletin, v. 117, p. 334-353.

Chen, C.Y., and Maloof, A.C., 2017, Revisiting the deformed highstand of Lake Bonneville: Quaternary Science Reviews, v. 159, p. 169-189.

Clyde, C.G., Jeppson, R.W., and Liu, Win-Kai, 1984, A groundwater model of Cache Valley, Utah. Utah Water Research Laboratory, Utah State University, Logan, Utah, Hydraulics and Hydrology Series, UWRL/H-84/04, 115 p.

Currey D.R., and Oviatt, C.G., 1985, Durations, average rates, and probable causes of Lake Bonneville expansions, still-stands, and contractions during the last deep-lake cycle, 32,000 to 10,000 years ago: Geographical Journal of Kore, v. 10, p. 1085-1099.

Eardley, A.J., and Gvosdetsky, V., 1960, Analysis of Pleistocene core from Great Salt lake, Utah: Geological Society of America Bulletin, v. 71, p. 1323 -1344.

Eardley, A.J., Shuey, R.T., Gvosdetsky, V., Nash, W.P., Picard, M.D., Grey, D.C., and Kukla, G.J., 1973, Lake cycles in the Bonneville basin, Utah: Geological Society of America Bulletin, v. 84, p. 211-216.

Ellis, N.R., and Jänecke, S.U. (advisor), 2018, LIDAR results in a revised map and analysis of active faults in West Cache fault zone, Utah: Senior thesis (unpublished), Utah State University, Logan, Utah, 32 p. https://works.bepress.com/susanne_janecke/228/

Evans, J.P., and Oaks, R.Q., Jr., 1996, Three-dimensional variation in extensional fault shape and basin form: The Cache Valley basin, eastern Basin and Range province, USA. Geological Society of America Bulletin, v. 108, p. 1580-1593.

Galbraith, R.F., and Roberts, R.G., 2012, Statistical aspects of equivalent dose and error calculation and display in OSL dating—an overview and some recommendations: Quaternary Geochronology, v. 11, p. 1–27.

Gansecki, C.A., Mahood, G.A., and McWilliams, M., 1998. New ages for the climactic eruptions at Yellowstone: Single-crystal $^{40}Ar/^{39}Ar$ dating identifies contamination: Geology, v. 26, p. 343-346.

Goessel, K.M., Oaks, R.Q., Jr., Perkins, M.E., and Janecke, S.U., 1999, Tertiary stratigraphy and structural Geology, Wellsville Mountains to Junction Hills, north-central Utah, in: Spangler, L.E. and C.J. Allen, editors, Geology of northern Utah: Utah Geological Association Publication 27, p. 45 -69.

Gilbert, G.K., 1875, Glacial epoch, in: Wheeler, G.M., Report upon geographical and geological exploration and surveys west of the one hundredth meridian, Volume III, Geology Part I, Report on the geology of portions of Nevada, Utah, California, and Arizona, examined in the years 1871 and 1872: U.S. Government Printing Office, Washington, D.C., p. 86-104.

Gilbert, G.K., 1890, Lake Bonneville: U.S. Geological Survey, Monograph 1, 438 p.

Guérin, G., Mercier, N., and Adamiec, G., 2011, Dose -rate conversion factors—update: Ancient TL, v. 29, p. 5-8.

Hart, W.S., Quade, J., Madsen, D.B., Kaufman, D.S., and Oviatt, C.G., 2004, The $^{87}Sr/^{86}Sr$ ratios of lacustrine carbonates and lake-level history of the Bonneville paleolake system: Geological Society of America Bulletin, v. 116, p. 1107-1119.

Hochberg, A., 1996, Aminostratigraphy of Thatcher basin, SE Idaho: Reassessment of Pleistocene lakes: M.S. Thesis (unpublished), Utah State University, Logan, Utah, 107 p.

Hunt, C.B., 1982, The anomalous transverse canyons of the Wasatch Range, in: Nielson, D.L., editor, Overthrust Belt of Utah: Utah Geological Association Publication 10, p.81-89.

Huntley, D.J., and Lamothe, M., 2001, Ubiquity of anomalous fading in K-feldspars and the measurement and correction for it in optical dating: Canadian Journal of Earth Sciences, v. 38, p. 1093–1106.

Janecke, S.U., and Evans, J.C., 1999, Folded and faulted Salt Lake Formation above the Miocene to Pliocene New Canyon and Clifton detachment faults, Malad and Bannock Ranges, Idaho: Field trip guide to the Deep Creek half graben and environs, in: Hughes, S. S., and G.D. Thackray, editors, Guidebook to the Geology of Eastern Idaho. Idaho Museum of National History, Pocatello, Idaho, p. 71-96.

Janecke, S.U., S.M. Carney, M.E. Perkins, J.C. Evans, P.K. Link, R.Q. Oaks, Jr., and B.P. Nash, 2003, Late Miocene-Pliocene detachment faulting and Pliocene-Pleistocene Basin-and-Range extension inferred from dismembered rift basins of the Salt Lake Formation, southeast Idaho, In R.G. Raynolds and R.M. Flores, eds., Cenozoic Systems of the Rocky Mountain Region: Rocky Mountain Section of the SEPM, p. 369-406.

Janecke, S.U., and Oaks, R.Q., Jr., 2011a, Reinterpreted history of latest Pleistocene Lake Bonneville — Geologic setting of threshold failure, Bonneville flood, deltas of the Bear River, and outlets for two Provo shorelines, southeastern Idaho, USA, in: Lee, J. and Evans, J.P., editors, Geological Field Trips to the Basin and Range, Rocky Mountains, Snake River Plain, and Terranes of the U.S. Cordillera: Geological Society of America Field Guide 21, p. 195-222.

Janecke, S.U., and Oaks, R.Q., Jr., 2011b, New insights into the outlet conditions of Late Pleistocene Lake Bonneville, southeastern Idaho, USA: Geosphere, v. 7, p. 1369-1391.

Janecke, S.U., Oaks, R.Q., Jr., Rittenour, T.M., Knight, A.J., and McNutt, D., 2013, Large liquefaction features and evidence for 4 earthquakes induced by Lake Bonneville in Cache Valley: A progress report: Presentation to Utah Fault Parameters working group, annual workshop, Salt Lake City.

Janecke, S.U., and Oaks, R.Q., Jr., 2014, Diversion[s] of the lower Bear River in Gem Valley, Idaho, by a tectono-volcanic valve: Late Cenozoic to Recent geologic and biotic history of the Snake River, Symposium volume with extended abstracts, p. 27 -28.

Jänecke, S.U., Oaks, R.Q., Jr., Rittenour. T.M., Knight, A.J., Oakeson, J., and Ellis, N., 2019, Cache Valley: A critical part of Lake Bonneville, records possible triggers of the Bonneville Flood, protracted Bonneville high stand, liquefaction, and clustered earthquakes on East and West Cache Fault Zones, in: Lund, W.R., McKean, A.P., and Bowman, S.D. (eds.), Proceedings Volume: 2018 Lake Bonneville Geologic Conference and Short Course. Day 2, Sessions 5-8; Utah Geological Survey. Miscellaneous Publication, MP-170-2, p. 68-134. 8 p. article and 58 p. of presentation. https://ugspub.nr.utah.gov/publications/misc_pubs/mp-170/mp-170-2.pdf

Kariya, K.A., Roark, D.M., and Hanson, K.M., 1994. Hydrogeology of Cache Valley, Cache County, Utah, and adjacent part of Idaho, with emphasis on simulation of ground-water flow. Utah Department of Natural Resources, Technical Publication 108, 120 p.

Kaufman, A., Broecker, W.S., Ku, T.-L., and Thurber, D.L., 1971, The status of U-series methods of mollusk dating: Geochimica et Cosmochimica Acta, v. 35, p. 1155-1183.

Kaufman, D.S., Forman, S.L., and Bright, J., 2001, Age of the Cutler Dam Alloformation (Late Pleistocene), Bonneville basin, Utah: Quaternary Research, v. 56, p. 322-344.

Link, P.K., Kaufman, D.S., and Thackray, G.D., 1999. Field guide to Pleistocene Lakes Thatcher and Bonneville and the Bonneville Flood, southeastern Idaho, in: Hughes, S.S., and Thackray, G.D., editors, Guidebook to the Geology of Eastern Idaho: Idaho Museum of Natural History, Pocatello, Idaho, p. 251-266.

Lisiecki, L.E., and Raymo, M.E., 2005, A Pliocene-Pleistocene stack of 57 globally distributed benthic ^{18}O records: Paleoceanography and Paleoclimatology, v. 20, n. 1, PA 1003, 17 p.

Marrero, S.M., 2009, Chlorine-36 production rate calibration using shorelines from Pleistocene Lake Bonneville: Ph.D. dissertation (unpublished), New Mexico Institute of Mining and Technology, Socorro, New Mexico, 201 p.

Maw, G.G., 1968, Lake Bonneville history in Cutler Dam quadrangle, Cache and Box Elder Counties, Utah: M.S. thesis (unpublished), Utah State University, Logan, Utah, 59 p.

McCoy, W.D., 1981, Quaternary aminostratigraphy of the Bonneville and Lahontan basins: Ph.D. dissertation (unpublished), University of Colorado, Boulder, 336 p.

McCoy, W.D., 1987, Quaternary aminostratigraphy of the Bonneville basin, western United States: Geological Society of America Bulletin, v. 98, p. 99-112.

Mejdahl, V., 1979, Thermoluminescence dating—beta-dose attenuation in quartz grains: Archaeometry, v. 21, p. 61–72.

Miller, D.M., 2016, The Provo shoreline of Lake Bonneville, in: Oviatt, C.G. and Shroder, J.F., editors, Lake Bonneville — a scientific update: Developments in Earth Surface Processes 20, Elsevier, New York, p. 127-144.

Morrison. R.B., 1965, New evidence on Lake Bonneville stratigraphy and history from southern Promontory Point, Utah: U.S. Geological Survey Professional Paper 525-C, p. C-110 – C-119.

Morrison, R.B., 1966, Predecessors of Great Salt Lake, in: Stokes, W.L., editor, The Great Salt Lake: Utah Geological Society, p.77-104.

Murray, A.S., and Wintle, A.G., 2000, Luminescence dating of quartz using an improved single aliquot regenerative-dose protocol: Radiation Measurements, v. 32, p. 57–73.

Nelson, D.T., 2012, Geomorphic and stratigraphic development of Lake Bonneville's intermediate paleoshorelines during the late Pleistocene: Ph.D. dissertation (unpublished), University of Utah, Salt Lake City, Utah, 213 p.

Nishizawa, S., 2010, The Bonneville Lake basin shoreline records of large lake and abrupt climate change events: Ph.D. dissertation (unpublished), University of Utah, Salt Lake City, Utah, 151 p.

Nishizawa, S., Currey, D.R., Brunelle, A., and Sack, D., 2013, Bonneville basin shoreline records of large lake intervals during marine isotope stage 3 and the latest glacial maximum: Palaeogeography, Palaeoclimatology, Palaeoecology, v. 386, p. 374-391.

Oaks, R.Q., Jr., 2000, Geologic history of Tertiary deposits between the Lower Bear River Drainage Basin and the Cache Valley Basin, north-central Utah, based on study of the Salt Lake Formation, the Collinston Conglomerate, and the Wasatch Formation, with applications to groundwater resources and fault-related geologic hazards: Final Report to Bear River Water Conservancy District, Box Elder County, and Utah Division of Water Resources, 116 p., Plates 5, 6A, and 6B, scale: 1:24,000. https://geodata.geology.utah.gov/pages/download.php?direct=1&noattach=true&ref=5845&ext=pdf&k=

Oaks, R.Q., Jr., 2010, Evaluation of the geologic setting and potential sites for water wells in the foothill region east, northeast, and southeast of Preston City, Franklin County, southeastern Idaho. Report (unpublished) for J-U-B Engineering and Preston City, 44 p, 9 Figures, 2 Tables, 2 Appendices.

Oaks, R.Q., Jr., 2012, Effect of structure and stratigraphy of the Salt Lake Formation on availability of groundwater immediately east of Paradise, Utah, and possible sources of springs along the Little Bear River farther west: Report for Mark Alexander and Chad Magnum, Paradise Hills Estates HOA, 20 p., 20 Figs. Report submitted to the Utah State Engineer.

Oaks, R.Q., Jr., Janecke, S.U., Rittenour, T.M., Nelson, M.S., and Erickson, T.L., 2014, Up to four deepwater pluvial lakes in Cache Valley, Utah-Idaho, including the Cutler Dam lake cycle at ~1445 m and possible Little Valley lake cycle at ~1485 m: Evidence for possible excavation of Cutler Narrows prior to 420 ka: Late Cenozoic to Recent Geologic and Biotic History of the Snake River: Abstracts for the workshop on Late Cenozoic to Recent geologic and biotic history of the Snake River, March 24-26, 2014, Pocatello, Idaho; http://geology.isu.edu/SnakeRiver/Proceedings.pdf (Symposium vol. with extended abstracts), p. 34-35.

Oaks, R.Q., Jr., Janecke, S.U., Rittenour, T.M., Erickson, T.L., and Nelson, M.S., 2019, OSL age dating of two, perhaps three, pre-Bonneville deepwater pluvial lakes in Cache Valley, Utah-Idaho: Implications of their unexpected high altitudes for excavation of Cutler Narrows from a level above

1494 m (4901'), down to the present 1314 m (4310') mainly during the Bonneville lake cycle: Utah Geological Survey Symposium on Lake Bonneville, 3-4 October, 2018.

Oaks, R.Q., Jr., Janecke, S.U., Rittenour, T.M., Erickson, T.L., and Nelson, M.S., 2020, Pre-Bonneville lakes in Cache Valley and excavation of Cutler Narrows across the Cache Butte Divide in the west, north-central Utah and southeastern Idaho: Rocky Mountain Section, Geological Society of America, 72nd Annual Meeting, Abstracts with Programs, v. 52, no. 3. https://doi: 10.1130/abs/2020RM-346804.

Oaks, R.Q., Jr., Smith, K.A., Janecke, S.U., Perkins, M.E., and Nash, W.P., 1999, Stratigraphy and tectonics of Tertiary strata of southern Cache Valley, north-central Utah, in: Spangler, L.E., and Allen, C.J., editors, Geology of Northern Utah: Utah Geological Association Publication 27, p. 71-110.

Oviatt, C.G., 1986a, Geologic Map of the Honeyville quadrangle, Box Elder and Cache Counties, Utah. Utah Geological Survey, Map 88, scale 1:24,000.

Oviatt, C.G., 1986b, Geologic Map of the Cutler Dam quadrangle, Box Elder and Cache Counties, Utah. Utah Geological Survey, Map 91, scale 1:24,000.

Oviatt, C.G., 2015, Chronology of Lake Bonneville, 30,000 to 10,000 yr B.P.: Quaternary Science Reviews, v. 110, p. 166-171.

Oviatt, C.G., 2020, G.K. Gilbert and the Bonneville shoreline: Geology of the Intermountain West, v. 7, p. 301-320. https://doi.org/10.31711/giw.v7.pp301-320.

Oviatt, C.G., Currey, D.R. and Sack, D., 1992, Radiocarbon chronology of Lake Bonneville, eastern Great Basin, USA: Palaeogeography, Palaeoclimatology, Palaeoecology, v. 99, p. 225-241.

Oviatt, C.G., Miller, D.M., Sack, D., and Kaufman, D.S., 1997, New explorations along the northern shore of Lake Bonneville, in: Link, P.K., and Kowalski, B.J., editors, Mesozoic to Recent Geology of Utah, Part 2: Brigham Young University Geology Studies, v. 42, p. 345-371.

Oviatt, C.G., and McCoy, W.D., 1988, The Cutler Dam Alloformation — Deposits of a probable early Wisconsin lake in the Bonneville basin, in: Machette, M.N., editor, In the footsteps of G.K. Gilbert — Lake Bonneville and neotectonics of the eastern Basin and Range Province: Geological Society of America Guidebook for field trip 12, the Geological Society of America 100th annual meeting, Denver, Colorado: Utah Geological and Mineral Survey Miscellaneous Publication 88-1, p. 21-26.

Oviatt, C.G., and McCoy, W.D., 1992, Early Wisconsin lakes and glaciers in the Great Basin, U.S.A., in: Clark, P.U. and Lee, P.D., editors, The last interglacial-glacial transition in North America: Geological Society of America Special Paper 270, p. 279-288.

Oviatt, C.G., McCoy, W.D. and Nash, W.P. 1994, Sequence stratigraphy of lacustrine deposits: A Quaternary example fromthe Bonneville basin, Utah: Geological Society of America Bulletin, v. 106, p. 133-144.

Oviatt, C.G., McCoy, W.D. and Reider, R.G., 1987, Evidence for a shallow early or middle Wisconsin lake in the Bonneville basin: Quaternary Research, v. 27, p. 248–262.

Oviatt, C.G., and Nash, W.P., 1989, Late Pleistocene volcanic ash and eruptions in the Bonneville basin, Utah: Geological Society of America Bulletin, v. 101, p.292-303.

Oviatt, C.G., Thompson, R.S., Kaufman, D.S., Bright, J., and Forester, R.M., 1999, Reinterpretation of the Burmester core, Bonneville basin, Utah: Quaternary Research, v. 52, p. 180-184.

Pederson, J.L., Janecke, S.U. Reheis, M.C., Kaufman, D.F., and Oaks, R.Q., Jr., 2016, The Bear River's history and diversion: Constraints, unsolved problems, and implications for Lake Bonneville's record, in: Oviatt, C.G., and Shroder, J.F., editors, Lake Bonneville: A Scientific Update: Developments in Earth Science Processes 20, Elsevier, Amsterdam, p. 28-59.

Pederson J.L., Rittenour, T.M., Jänecke, S.U., and Oaks, R.Q., Jr., 2018, The Bear River's diversion, the cutting of Oneida Narrows at 55-50 ka, and relations to the Lake Bonneville record; Utah Geological Survey Symposium on Lake Bonneville, 3 -4 October, 2018.

Rees-Jones, J., 1995. Optical dating of young sediments using fine-grain quartz. Ancient TL, v. 13, p. 9-14.

Robison, R.M., 1986, The surficial geology and neotectonics of Hansel Valley, Box Elder County, Utah: M.S. thesis (unpublished), Utah State University, Logan, Utah, 120 p.

Robison, R.M., and McCalpin, J.P., 1987, Surficial geology of Hansel Valley, Box Elder County, in: Kopp, R.S. and Cohenour, R.E., editors, Cenozoic geology of western Utah — Sites for precious metal and hydrocarbon accumulations: Utah Geological Association Publication 16, p. 335-350.

Robinson, J.M., 1999, Chemical and hydrostratigraphic characterization of ground water and surface water interaction in Cache Valley, Utah: M.S. thesis (unpublished), Utah State University, Logan, Utah, 172 p.

Scott, W.E., 1988, Deposits of the last two deep-lake cycles at Point of the Mountain, Utah, in: Ma-

chette, M.N., editor, In the footsteps of G.K. Gilbert — Lake Bonneville and neotectonics of the eastern Basin and Range Province: Geological Society of America Guidebook for field trip 12, the Geological Society of America 100th annual meeting, Denver, Colorado: Utah Geological and Mineral Survey Miscellaneous Publication 88-1, p. 86-88.

Scott, W.E, Machette, M.N., Shroba, R.R., and McCoy, W.D., 1982, Guidebook for the 1982 Friends of the Pleistocene Rocky Mountain Cell, Field Trip to Central Utah: modified from U.S. Geological Survey Open-File Reports 82-845 and 82-850, 100 p.

Scott, W.E., McCoy, W.D., Shroba, R.R., and Rubin, M., 1983, Reinterpretation of the last two cycles of Lake Bonneville, western United States: Quaternary Research, v. 20, p. 261-285.

Thomas, K., Oaks, R.Q., Jr., Inkenbrandt, P., Sabbah, W., and Lowe, M., 2011, Cache Valley principal aquifer storage and recovery, site assessment: Phase 1: Utah Geological Survey, Open-File Report 579, 34 p., appendices 23 p.

Utley, B.L., 2017, The Dynamic relationship between the Bear River, Quaternary basaltic center, normal faults, and the resulting rearrangement of rivers in the northeast edge of the Great Basin, southeast Idaho: M.S. Thesis (unpublished), Utah State University, Logan, Utah, 78 p.

Williams, S.K., 1994, Late Cenozoic tephrochronolgy of deep sediment cores from the Bonneville basin, northwest Utah: Geological Society of America Bulletin, v. 106, p. 1517-1530.

Williams, J.S., 1948, Geology of the Paleozoic rocks, Logan Quadrangle, Utah: Geological Society of America Bulletin, v. 59, p. 1121-1164.

Williams, J.S., 1958, Geologic Atlas of Utah, Cache County: Utah Geological and Mineral Survey Bulletin 64, 98 p.

Williams, J.S., 1962, Lake Bonneville — Geology of southern Cache Valley, Utah: U.S. Geological Survey Professional Paper 257-C, 152 p.

Appendix 1. *Optically Stimulated Luminescence (OSL) and Infrared Stimulated Luminescence (IRSL) age-date information, Newton Hill Pit, SE Hyde Park, and NE Millville, Cache County, Utah, March 2023.*

USU-Sample Number	Depth (m)	Number of aliquots[1]	Dose rate (Gy/ka)	D_E[2] ± 2σ (Gy)	Age[3] ± 2σ (ka)	In-situ H_2O (%)[3]	Grain size (μm)	K (%)[4]	Rb (ppm)[4]	Th (ppm)[4]	U (ppm)[4]	Cosmic (Gy/ka)	OSL/ IRSL[5]
859	16.2	22 (57)	1.76 ± 0.07	27.11 ± 2.17	15.42 ± 1.39	5.9 (15%)	90-150	1.14 ±0.03	52.0 ±2.1	6.2 ±0.6	1.7 ±0.1	0.05 ±0.01	OSL
3243	1	22 (30)	0.80 ± 0.04 [6]	16.74 ± 1.92	20.98 ± 3.04	1.81	150-250	0.59 ±0.01 0.26 ±0.01 0.51 ±0.01	15.0 ±0.15 5.9 ±0.06 11.7 ±0.12	1.76 ±0.2 0.67 ±0.07 1.32 ±0.1	1.0 ±0.1 0.7 ±0.04 1.0 ±0.1	0.25 ±0.02	OSL
1082	35.1	11 (42)	2.17 ± 0.09	46,31 ± 12.75 [4]	21.35 ± 3.48	7.4	150-250	1.48 ±0.04	66.5 ±2.7	8.8 ±0.8	1.9 ±0.1	0.02 ±0.00	OSL
854	11.3	24 (37)	2.98 ± 0.12	64.72 ± 9.88 [4]	21.72 ± 2.78	14.4	90-150	1.91 ±0.05	97.2 ±3.9	12.3 ±1.1	2.4 ±0.2	0.08 ±0.01	OSL
855	21.6	24 (49)	3.90 ± 0.16	153.29 ± 15.01	39.28 ± 3.72	10.2	63-150	2.41 ±0.06	119.5 ±4.8	14.6 ±1.3	3.4 ±0.2	0.04 ±0.00	OSL
1084	3.0	13 (32)	2.74 ± 0.11	146.65 ± 19.32	53.51 ± 6.44	12.7	75-150	1.72 ±0.04	74.3 ±3.0	10.5 ±1.0	1.8 ±0.1	0.19 ±0.02	OSL
856	24.7	20 (42)	1.77 ± 0.07	118.71 ± 8.36	66.82 ± 5.94	1.9	125-250	1.03 ±0.03	40.9 ±1.6	6.8 ±0.6	1.9 ±0.1	0.03 ±0.00	OSL
858	24.7	16 (57)	1.56 ± 0.06	92.17 ± 9.47	67.70 ± 6.46	3.2	150-250	1.27 ±0.03	34.7 ±1.4	4.4 ±0.4	1.1 ±0.1	0.03 ±0.00	OSL
2895	2.8	16 (29)	1.22 ± 0.05	173.72 ± 14.76	142.8 ± 13.1	-	150-250	0.69 ±0.02	24.9 ±1.0	3.5 ±0.3	1.2 ±0.1	0.19 ±0.02	OSL
1083	38.1	15 (34)	1.14 ± 0.05	164.12 ± 19.32	144.3 ± 14.5	3.3	150-250	0.85 ±0.02	29.7 ±1.2	3.9 ±0.4	0.9 ±0.1	0.02 ±0.00	OSL

USU-Sample Number	Depth (m)	Number of aliquots[1]	Dose rate (Gy/ka)	D_E[2] ± 2σ (Gy)	Age[3] ± 2σ (ka)	In-situ H_2O (%)[3]	Grain size (μm)	K (%)[4]	Rb (ppm)[4]	Th (ppm)[4]	U (ppm)[4]	Cosmic (Gy/ka)	OSL/ IRSL[5]
3202	59.4	19 (34)	1.39 ± 0.06 7	208.47 ± 31.80	150.0 ± 25.9	7.6	63-250	1.09 ±0.03 1.05 ±0.03 0.43 ±0.01	49.0 ±2.0 31.4 ±1.3 13.4 ±0.5	5.8 ±0.6 5.27 ±0.5 1.81 ±0.2	1.3 ±0.1 1.1 ±0.1 0.7 ±0.1	0.01 ±0.00	OSL
2490	32.0	15 (17)	2.29 ± 0.10 8,9	234.56 ± 25.82	155.6 ± 21.4	3.8	125-250	0.73 ±0.02 1.06 ±0.03	23.6 ±0.9 25.2 ±1.0	4.0 ±0.4 3.6 ±0.3	1.0 ±0.1 1.0 ±0.1	0.02 ±0.00	IRSL
857	13.4	20 (63)	0.94 ± 0.04	152.56 ± 19.30	161.5 ± 16.8	3.7	90-250	0.66 ±0.02	22.0 ±0.9	2.6 ±0.2	0.6 ±0.1	0.07 ±0.01	OSL
2491	38.7	23 (36)	1.13 ± 0.05	191.02 ± 28.12	169.4 ± 28.6	3.8	125-250	0.74 ±0.02	19.6 ±0.8	4.0 ±0.4	1.0 ±0.1	0.01 ±0.00	OSL

[1] Number of aliquots used in age calculation and number of aliquots analyzed in parentheses.

[2] Equivalent dose (D_E) calculated using the Central Age Model (CAM) of Galbraith and Roberts (2012), unless otherwise noted.

[3] Assumed 10±3% for moisture content over burial history for in-situ values <10%, excluding USU-859.

[4] Radioelemental concentrations determined using ICP-MS and ICP-AES techniques; dose rate is derived from concentrations by conversion factors from Guérin et al. (2011).

[5] OSL age analysis using the single-aliquot regenerative-dose procedure of Murray and Wintle (2000) on 1-2mm small-aliquots of quartz sand. IRSL age analysis using the two-temperature step (50°C, 225°C) pIR IRSL protocol of Buylaert et al. (2009) on 1-2 mm small-aliquots of potassium-rich feldspar. IRSL age on each aliquot corrected for fading following the method by Auclair et al.

[6] Grain-size based internal beta dose rate determined assuming 12.5% K and 400ppm Rb using Mejdahl (1979). Alpha contribution to IRSL dose rate determined using an efficiency factor, or 'a-value', of 0.09±0.01 after Rees-Jones (1995).

[7] Dose rate includes weighted average of radioelemental chemistry based on sand fraction (top value, 35%) and gravel fraction (bottom value, 65%).

Appendix 2. *Data for hydrographs. See Appendix 3 for AAR correlations supporting ~417 ka age for Qpp (Oviatt and others, 1999).*

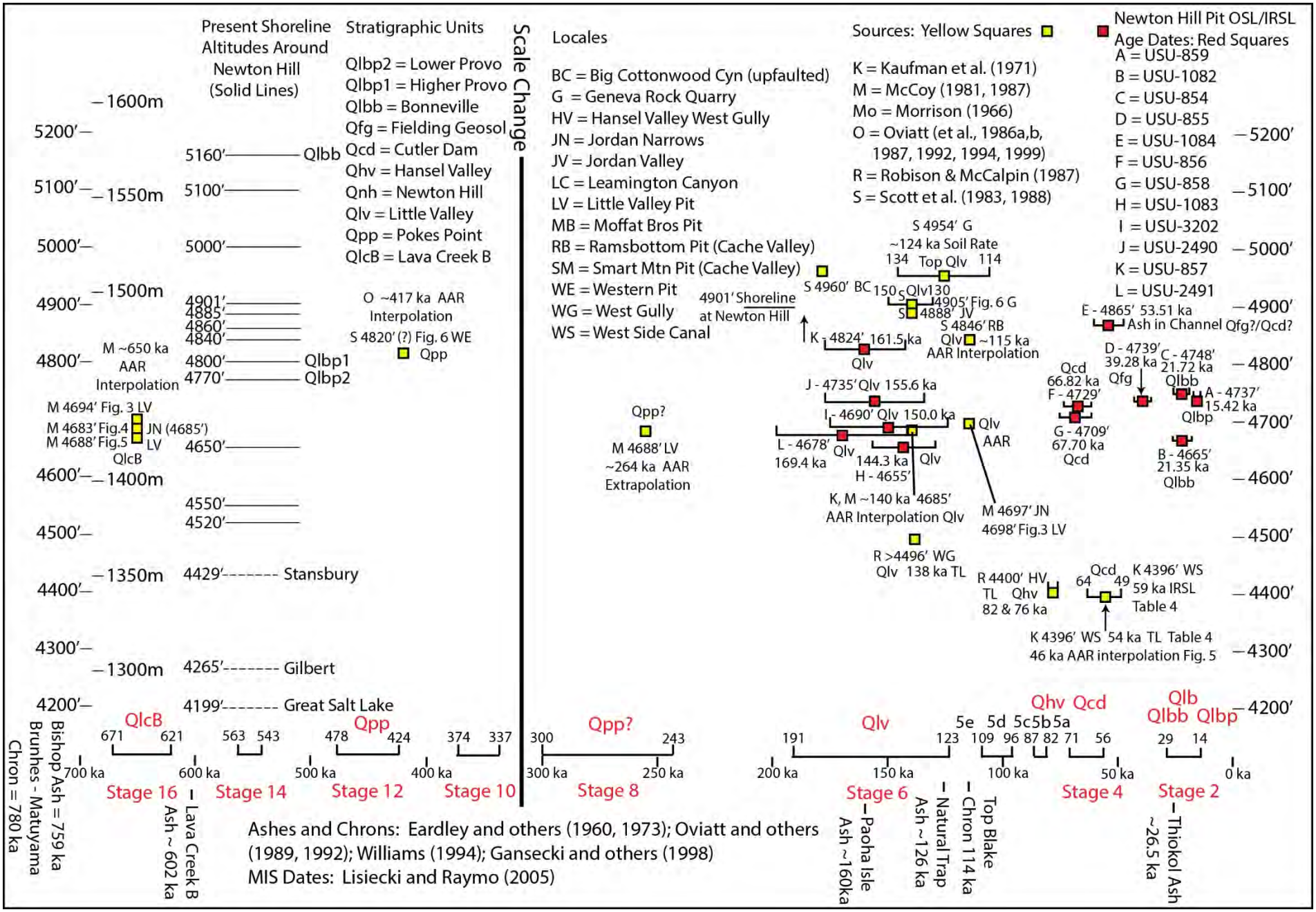

Appendix 3. *Amino-acid-racemization data interpolated betwen known ages of ashes, chrons and 14C and TL data in the Bonneville basin prior to our study. See Appendix 4 for data.*

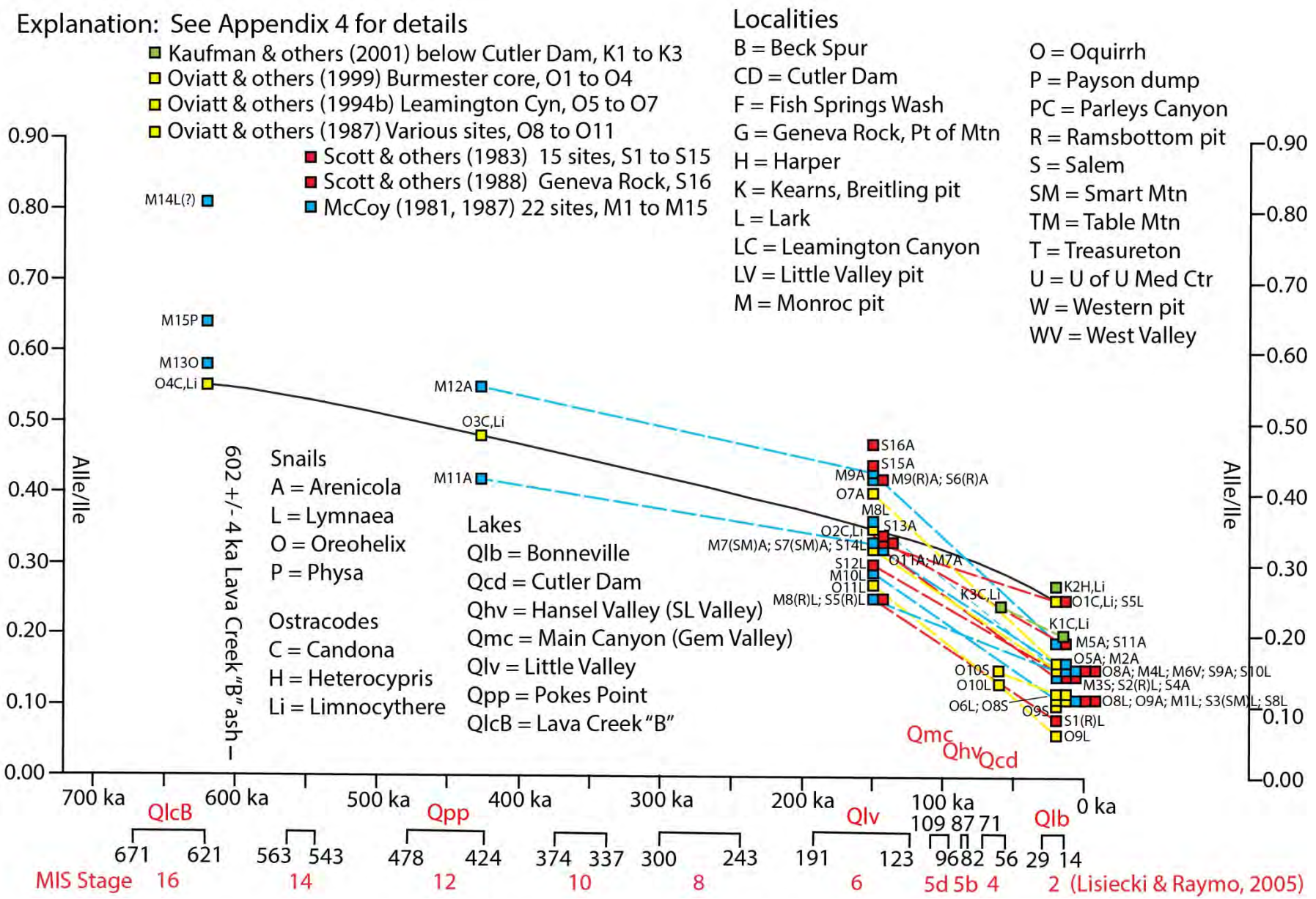

Appendix 4. *Sources for original AAR data used for Appendices 2 and 3.*

Kaufman and others (2001), West Side Canal; Thatcher Valley ID (Qmc); and Little Valley pit

Unit	Sample	Fossils (# of samples)	Racemization (D/L) Table 5 (Alle/Ile)	^{14}C age ka Calibrated Table 2	TL age ka 8 hr UV Table 4	IRSL age ka 3+ hr sun Table 4
Qlb	K-1 (#6)	C (8) Li (8)	0.202±0.009 0.154±0.014	14.5±0.4 [a]	12.2±1.3	12.0±1.2
Qlb	K-2 (#5)	H (8) Li (13)	0.184+0.011 0.221+0.016	~24 [b]	19±2	23±2
Qlb (?)	(#4)				63.0±6.0 25.4±3.6	32.4±3.1 (16 hr sun)
Qcd	(#3)			~43 [c]		
Qcd	K-3 (#2)	C (14) Li (9)	0.254±0.014 0.235±0.014		55.6±5.2	59.3±5.2
Qcd	K-4 (#1)					59.0±5.5
Qmc	K-5	C (12)	0.347±0.136	1.5 m above	St Helens ash	~110 ka
Qlb	K-6 (LV)	C (12)	0.237±0.015	20.2±0.3 [d]		
Qlv	K-7 (LV)	C (23)	0.414±0.021			

[a] Fluminicola sp. [b] Limnocythere spp. [c] Heliosoma sp. [d] Arenicola sp.

[e] Figure 5; interpolation based on Bouchard and others (1998) in Gem Valley near Thatcher ID

Oviatt and others (1999), Burmester core

Unit	Sample	Fossils (# of samples)	Racemization (D/L) (Alle/Ile)	Ages in ka and basis
Qlb	O-1	C, Li (5)	0.25±0.01	~20; numerous ^{14}C ages
Qlv	O-2	C, Li (52)	0.35±0.03	~150±20; Scott and others (1983); ^{230}Th & extrapolation from Ca accumulation rate
Qpp	O-3	C, Li (15)	0.48±0.02	~417±55; Interpolation between Qlv& QlcB
QlcB	O-4	C, Li (15)	0.55±0.02	~620; below ~602 Lava Creek B ash, above ~760 Brunhes Chron base

Oviatt and others (1994b), Leamington Canyon

Unit	Sample	Fossils (# of samples)	Racemization (D/L) (Alle/Ile)	Ages in ka and basis
Qlb	O-5	A (11)	0.16±0.03	14 ages between 14 & 21 (their Table 1)
Qlb	O-6	L (7)	0.12±0.02	
Qlv	O-7	A (4)	0.40±0.06	^{230}Th >90 ka & ~140 ka (their Table 1)

Oviatt and others (1987), West Side and Hammond Canals below Cutler Dam

Unit	Sample	Fossils Racemization (# of samples) (D/L) (Alle/Ile)
Qlb [f]	O-8	L 0.11±0.03 S 0.12±0.01 A 0.15±0.03
Qlb	O-9 (#3, 5)	L (1) 0.06 S (1) 0.011 A (5) 0.10±0.005
Qcd	O-10 (#5, 6)	L (2) 0.12±0.01 S (3) 0.15±0.01 H (3) 0.11±0.01 V (3) 0.14±0.01
Qlv [f]	O-11	L 0.27±0.03 A 0.32±0.03

[f] Average for Bonneville basin from McCoy (1981) and this paper

Scott and others (1983) Cache Valley (Table 2)

Unit	Sample	Location	Fossils Racemization (# of samples) (D/L) (Alle/Ile)
Qlb	S-1 [g]	R	L (?) 0.08±0.01
Qlb	S-2	R	L (?) 0.14±0.00
Qlb	S-3	SM	L (1) 0.11
Qlb	S-4	SM	A (1) 0.14
Qlv	S-5 [g]	R	L (?) 0.24±0.01
Qlv	S-6 [g]	R	A (?) 0.42±0.06
Qlv	S-7	SM	A (?) 0.33±0.01

R = Ramsbottom pit; SM = Smart Mountain

Scott and others (1983) Bonneville Basin and Cache Valley, combined averages (Table 1)
Locations: B, BC, G, JN, K, LC, LV, MC, MO, MU, OR, P, R, SM, W (See Appendix 3)

Unit	Sample	Fossils Racemization (# of samples) (D/L) (Alle/Ile)
Qlb	S-8	L (50) 0.11±0.03
Qlb	S-9	A (35) 0.15±0.04
Qlb	S-10 [gh]	L (33) 0.15±0.04
Qlb	S-11 [gh]	A (28) 0.19±0.04
Qlv	S-12	L (2) 0.30±0.02
Qlv	S-13	A (13) 0.34±0.03
Qlv	S-14 [gh]	L (10) 0.33±0.08
Qlv	S-15 [gh]	A (28) 0.44±0.06

[g] 1980 preparation differed from the other samples and resulted in higher values

[h] Table 5 and page 280: Assumed constant rate of addition of calcium to Promontory paleosol based on rate in post-Qlb soils = 70 ka to 120 ka plus 20 ka for burial by Qlb = 90 ka to 140 ka for top of Qlv. ^{230}Th Qlv age: > 105 ka from Kaufman and Broecker (1965, p. 4035). Oviatt and others (1999) assumed ~150±20 ka for average age of Qlv (see above).

Scott and others (1988)

Unit	Sample	Location	Fossils Racemization (# of samples) (D/L) (Alle/Ile)
Qlv	S-16	G	A (?) 0.47±0.02

McCoy (1981; 1987)

Unit	Sample	Location	# of sample s	Fossils Racemization (D/L) (Alle/Ile)
Qlb	M-1	JV, LC, LV, M, P, SM, TM, U	L (22)	0.11±0.01
Qlb	M-2	JV, LC, LV, M, SM	A (190	0.16±0.01
Qlb	M-3	LC	S (2)	0.14±0.02
Qlb	M-4 g	B, F, JN, L, O, P, PC, R, S, T	L (12)	0.15±0.02
Qlb	M-5 g	B, H, JN, K, LC, LV, O, P, S, T	A (12)	0.19±0.02
Qlb	M-6	S	V (3)	0.15±0.00
Qlv	M-7	B, LV, SM	A (13)	0.32±0.03
Qlv	M-7	SM	A (3)	0.33±0.01
Qlv	M-8 g	G, JN, K, LV, R	L (10)	0.36±0.04
Qlv	M-8 g	R	L (2)	0.25±0.01
Qlv	M-9 g	G, JN, K, LV, R, W	A (28)	0.43±0.02
Qlv	M-9 g	R	A (2)	0.42±0.02
Qlv	M-10	LV	L (2)	0.29±0.07
Qpp	M-11	LV	A (22)	0.42±0.06
Qpp	M-12 g	LV	A (12)	0.55±0.05
Qpp	M-13	LV	O (1)	0.58±0.05
QlcB	M-14 g	LV	L? (2)	0.81±0.04
QlcB	M-15 g	JN	P (5)	0.64±0.07

Correlations of matched samples for same fossils and same author(s) in Appendix 3.

Color	Qlb	Qcd	Qmc	Qlv	Qpp	QlcB	unused	Unmatched
Green	K1Li	K3Li					K2Li	K2H
Green	K1C	K3C	K5C	K7C			K6C	
Yellow	O9L	O10 L	O11L				O8L	
Yellow	O5A	O7A						
Yellow	O8A		O11A				O9A	
Yellow	O9S	O10 S						
Yellow	O1C, Li			O2C,Li	O3C,Li	O4C,Li		
Red	S1(R)L			S5(R)L	S2(R) L			S3(SM)L
Red	S4(SM)A			S7(SM)A				
Red	SSL			S14L				
Red	S9A			S13A			S11 A	S6(R)A
Red	S10L			S12L				
Red	S11A			S15A			S16 A	
Blue	M1L			M19L				M13O M15P
Blue	M2A			M7A	M11A			M34S M6V
Blue	M4L			M8L		M14L?		M8(R)L
Blue	M5A			M9A	M12A			M7(SM)A

Appendix 5. *Shoreline Altitudes of Lake Cycles in Main Bonneville Basin Compared to Coeval Shorelines in Cache Valley. Altitudes of Samples for These Lakes are Uncorrected for Isostatic Rebound.*

Main Bonneville Basin				**Cache Valley Bay**			
Lake Cycle	**Location; Source**	**Age in ka**	**Shoreline Altitude**	**Location; Source**	**Age in ka**	**Shoreline Altitude**	**Altitude Difference in Cache Valley**
Little Valley	Point of Mountain Scott and others, 1988	~124	~4954' ~1510 m	Hyde Park cut wall	~142.8	>4889' >1490 m	< -65' < -20 m
Little Valley	Big Cottonwood Canyon, Scott and others, 1983	~175	~4960' ~1512 m	Newton Hill Pit	~144.3 ~169.4	>4865' >1483 m	< -95' < -29 m
Little Valley?	Alpine under Promontory Geosol in Little Valley Pit Morrison, 1965b, 1966	Uncertain, probably Little Valley	~4986' ~1519 m'	Millville Eroded Delta Between Bonneville Highstand and Provo Delta; includes Muley Hill	Unknown; might be Little Valley	~4975' ~1516 m	~ -11' ~ -3 m
Hansel Valley	West Gully; Robison & McCalpin, 1987	~82 ~76	~4400' ~1341 m	Newton Hill Pit	None	None at pit level	None
Cutler Dam	Westside Canal; Kaufman and others, 1971	~59.4	~4396' ~1340 m	Newton Hill Pit	~66.82 ~67.70	~4733' [4757'] ~1443 m [1450 m]	+ 337' [361'] + 103 m [110 m]
Early Bonneville	Oviatt, 2015 Data Oviatt, 2020 Curve	~21	~4954' ~1510 m	Muley Hill, Millville	~20.98	~5085' ~1549 m	~+131' ~+40 m

Observations of Decadal-Scale Brine Chemistry Change at the Bonneville Salt Flats, Utah

Jeremiah A. Bernau[1,2], Brenda B. Bowen[1], Evan L. Kipnis[1], and Jory C. Lerback[1,3]

[1]*Department of Geology and Geophysics, University of Utah, Salt Lake City, Utah,* jeremiahbernau@gmail.com

[2]*Utah Geological Survey, Salt Lake City, Utah*

[3]*Department of Earth, Planetary and Space Sciences, University of California, Los Angeles*, California

10.31711/ugap.v51i.143

ABSTRACT

Over the past century, the Bonneville Salt Flats, which lies on the western edge of the Great Salt Lake watershed, has experienced changing environmental conditions and a unique history of land use, including resource extraction and recreation. The perennial halite salt crust has decreased in thickness since at least 1960. An experimental restoration project to return mined solutes began in 1997, but it has not resulted in anticipated salt crust growth. Here, primary observations of the Bonneville Salt Flats surface and subsurface brine chemistry and water levels collected from 2013 to 2023 are reported. Spatial and temporal patterns in chemistry, focused on density and water stable isotopes, are evaluated and compared with observations across seven periods of research spanning from 1925 to 2023. Declining salinity in the areas to the east of extraction ditches and south of Interstate 80 were observed. Brine extracted for potash production decreased in salinity as extraction rates increased. Between the years 1964 and 1997, brine in the shallow aquifer located beneath and to the east of the crust experienced a decrease in salinity. However, following this period, the salinity stabilized and subsequently increased. Salinity recovery was concurrent with declines in brine extraction and the salt restoration project, with the largest decrease in brine extraction being concurrent with the largest recovery in salinity. The specific impact of the restoration project on the brine salinity increase remains unclear. To the west, the shallow aquifer in the area between the Silver Island Mountains and the salt crust has increased in salinity. This increase is accompanied by a decline in groundwater levels, which enables the underground movement of solutes from east to west, following a salinity gradient away from the saline pan. Over the past 25 years, water levels in the alluvial-fan aquifer along the Silver Island Mountains have markedly declined, leading to the extraction of increasingly more saline and isotopically heavier basinal waters are intriguing landscapes for industrial use. This change is concurrent with the onset of the salt restoration project, which relies on alluvial-fan aquifer waters. This article's compilation of changes in groundwater chemistry provides an important resource for stakeholders working to understand and manage this dynamic and ephemeral evaporite system. It also offers an example of decadal-scale change in a highly managed Great Salt Lake watershed saline system.

INTRODUCTION

Saline pans, shallow depressions encrusted by evaporites where waters accumulate, provide an intriguing example where groundwater level and chemistry, climate, and anthropogenic activities converge. Here, several decades of chemical measurements, with a focus on density, are used to examine how the Bonneville Salt Flats (BSF) groundwater system changed in response to: 1) brine extraction for potash production, 2) alluvial-fan groundwater extraction for industrial uses, and 3) 25 years of an experimental brine "laydown" program to restore the saline pan (Figures 1 to 3) (Kipnis and Bowen, 2018). The laydown program uses alluvial-fan aquifer groundwater to dissolve the potash mine's halite (NaCl) byproduct and transport it to the saline pan in hopes of restoring saline pan thickness and extent. Multi-decadal analyses of satellite imagery and reoccurring measurements of salt crust thickness show long-term declines in crust thickness and extent (Bowen and others, 2017; Bowen and others, 2018; Radwin and Bowen, 2021). One-third of the crust consists of halite (NaCl) and two-thirds of it is gypsum ($CaSO_4 \cdot 2H_2O$). The multi-decadal nature of research on BSF and the uniquely involved mix of stakeholders including racing enthusiasts, recreational visitors, the potash industry, researchers, and governmental managers make this site well-suited for examining the evolution of brine chemistry. This landscape is dynamic with seasonal to decadal-scale changes in flooding and saline pan volume (Figure 2E and F) (Bowen and others, 2017). Here, this examination of long-term changes in brine chemistry, with groundwater levels as a secondary dataset, provides context for the relative impact of extraction and restoration

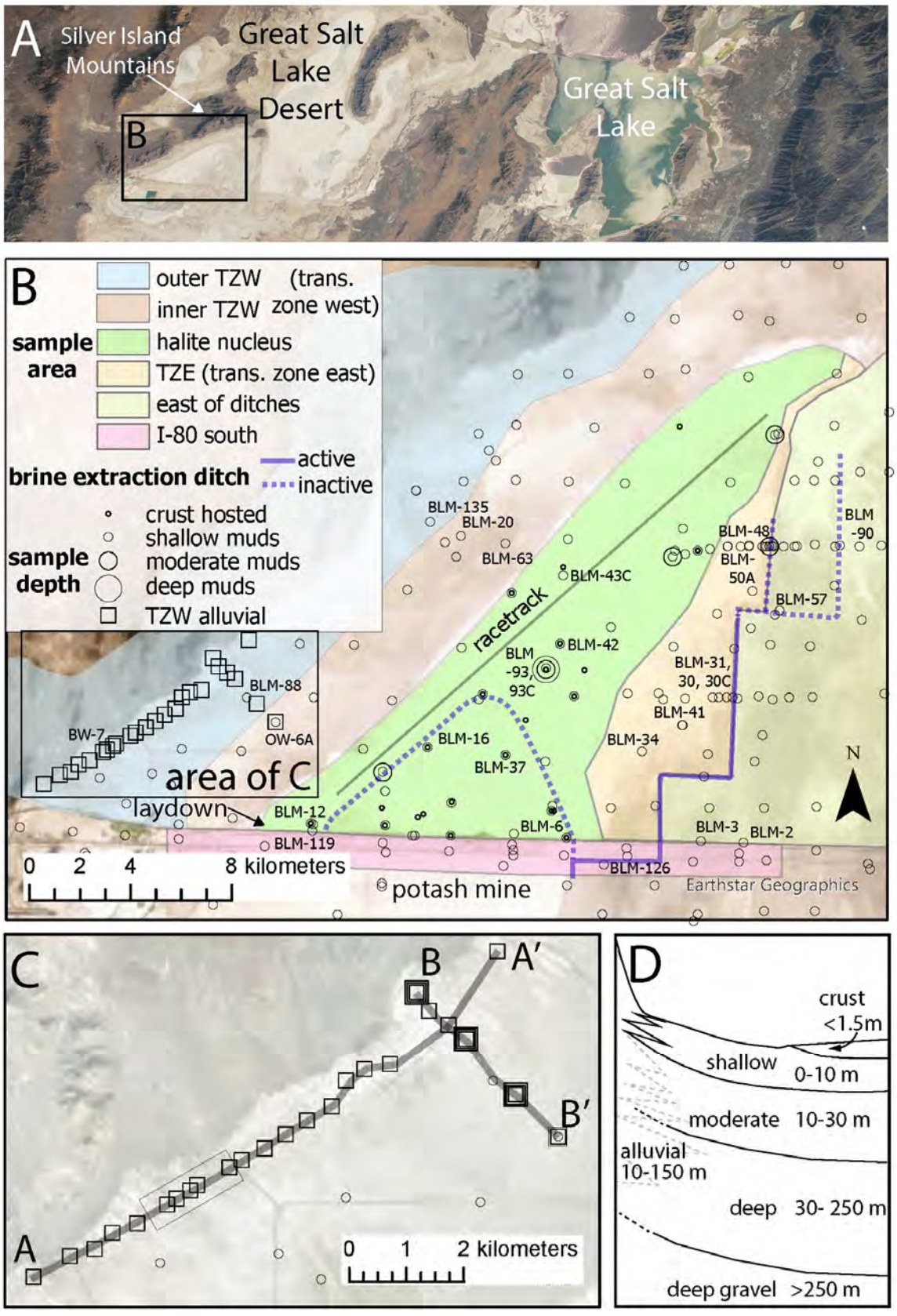

Figure 1. *Site overview. A. Off-angle International Space Station image of Bonneville Salt Flats, Great Salt Lake Desert, and Great Salt Lake (https://earthobservatory.nasa.gov/images/91765/bonneville-salt-flats). B) Areas of investigation. Sample areas (divided as zones moving east from west) and depths of different sampling wells noted in figure explanation. Inset C) shows locations of brackish water (BW) alluvial-fan aquifer production wells (A-A') and nested observational wells (OW) (B-B') along transects. Primary production wells outlined by box in the middle of A-A'. D) Schematic of investigated aquifer intervals (not to scale). Basemap imagery from Earthstar Geographics.*

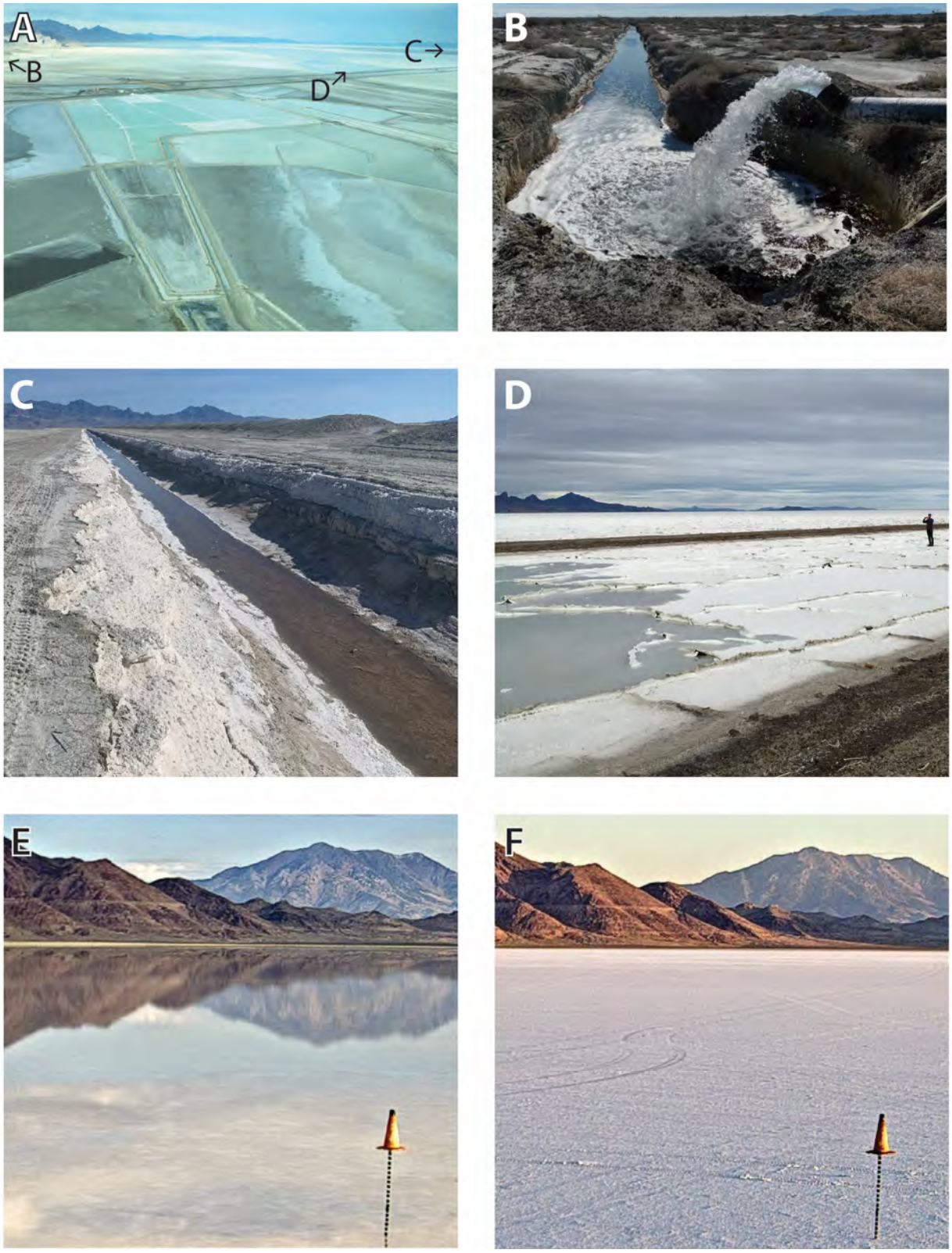

Figure 2. *Features influencing brine density and surface variation at BSF. A). Aerial photograph of potash mine looking north to BSF, letters denote relative locations of B to D. B) Alluvial-fan aquifer wells collect brackish water that is used in mine operations and to create salt laydown. C) Brine collection ditch (6 m deep) (Bingham, 1980) east of BSF (looking north). D) Laydown brine being introduced to BSF's southwest corner, person on right for scale. E and F) Time-lapse photos from BSF weather station on E) May 28, 2018, when the surface was flooded, and F) July 15, 2018, when the surface was desiccated. More field and aerial imagery of BSF is available with the Utah Geological Survey Data Archive system at https://geodata.geology.utah.gov/pages/search.php?search=%21collection129324.*

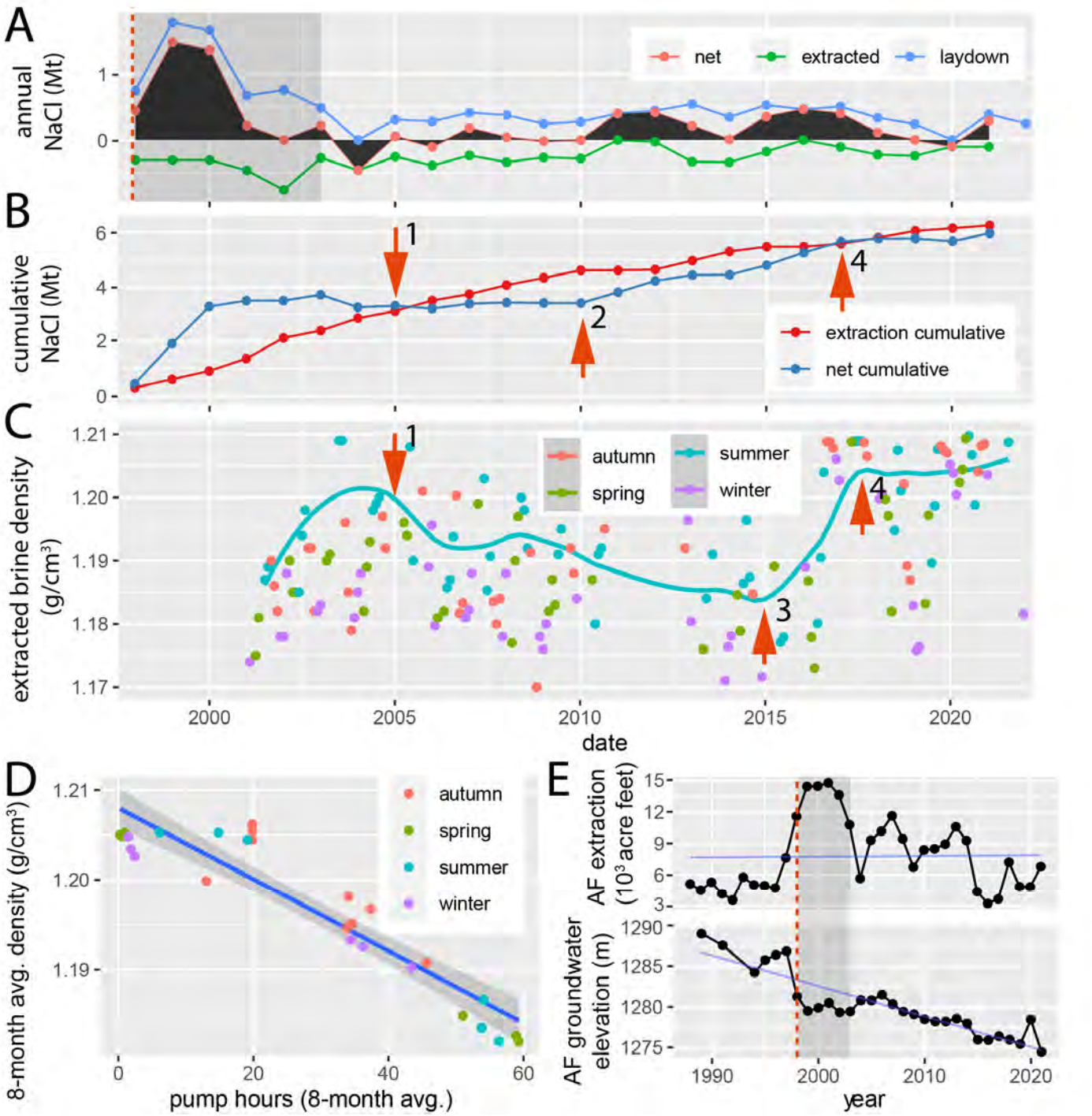

Figure 3. *Human activities (mining and laydown) that impact brine and solute mass through time. Changes in brine mass balance (A and B) in millions of tonnes (Mt) of NaCl (not brine), the density of extracted brines (C and D), and alluvial-fan aquifer (AF) groundwater extraction and groundwater levels (E). A) Annual values NaCl mass extracted from BSF's western ditches, added to the saline pan through the laydown, and net annual NaCl balance. B) Cumulative net movement of NaCl onto BSF from the laydown. C) Changes in extracted brine salinity over time. Note seasonality in density; summer values used for long-term trend. Numbered red arrows added to B) and C) highlight notable inflection points in data. In 2006 (point 1) the salinity of extracted brine began a long-term decline. Net cumulative brine contributions were neutral between 2005 and 2010 (point 2), and increased afterward; despite this increase, extracted brines did not begin to recover in salinity until 2015 (point 3). After 2017 (point 4) extracted brine salinity remains relatively high, while extraction is low. D) Correlation between pumping and extracted brine salinity (each dot represents the average of 8 months of pumping and brine density values) from Aug. 2018 to Dec. 2020 (these values are reported as hours of pumping, ~0.85 acre-ft/hour). E) Alluvial-fan annual groundwater extraction and groundwater elevation (meters above sea level) change over time (well located at 2.3 km in Figure 12) (10^3 acre-ft ≈ $1.23*10^6$ m^3). The vertical dashed red line shows when laydown began, and the gray area on (A) and (D) emphasizes the period with elevated laydown volumes and lower than anticipated (light blue line in lower E) groundwater levels. Alluvial-fan extraction data from https://www.waterrights.utah.gov/cgi-bin/wuseview.exe?Modinfo=WRUseage&wrnum=16-25.*

activities on changing saline pan extent and volume (Figure 3). This improved knowledge will help guide plans to optimize the sustained use, including both mining and racing, of this landscape.

METHODS

Brine chemistry was characterized and groundwater levels were measured at BSF between 2015 and 2023. Measurements prior to 2015 were compiled. This study involved extensive density measurement quality control, analyzing trends in individual wells, and analyzing data aggregated by area and aquifer. Here, groundwater levels are reported to provide context for observed changes; however, they are not the primary focus of this work.

Data Sources Over Time

Groundwater level and density data were divided over seven study periods that vary in length, intervals between periods, reported data, areas of investigation, and researchers (Figures 4 and 5). Nolan (1927) investigated the composition of Great Salt Lake Desert (GSLD) brines. In 1925, Nolan made shallow borings across the GSLD and reported sample total dissolved solids (TDS), major ions, and groundwater levels. Nolan made major-ion measurements in the field through titration (for chloride) and by measuring the volume of precipitate formed after adding chemicals to the solution (for potassium and sulfate). Several of these sites occur on the southern edge of BSF and the area between the Silver Island Mountains and the saline pan crust (Figure 4B).

Between 1946 and 1949, 23 alluvial-fan production wells (named BW for brackish water) were drilled to depths ranging between 32 and 111 m (Bernau and others, 2023a) (Figure 1C). BW wells flowed freely (1.1 to 9.5 m^3/second) when they were drilled, with reported potentiometric surfaces between 1.5 and 6 m above surface level. BW well water chemistry was reported in aggregate.

Two researchers investigated BSF chemistry between 1964 and 1972 (Figure 4C). In 1964 brine samples from shallow GSLD borings were analyzed for major ions, lithium, and TDS (Lindenburg, 1974). Between 1965 and 1967, Turk (1973) installed shallow (<9 m depth) wells across and adjoining BSF's crust, and measured groundwater levels and brine chemistry. In 1972, two brine chemistry samples from the alluvial-fan aquifer wells were collected (reported in the Water Quality Portal; Read and others, 2017).

Between 1975 and 1981 the U.S. Geological Survey performed two BSF studies (Figure 4D). Groundwater levels and chemistry were examined between 1975 and 1978 (Lines, 1978, 1979). In 1981 the U.S. Geological Survey Conservation Division measured brine chemistry from borings and wells (reported in White, 2002).

The next study period occurred leading up to the onset of the laydown in the autumn of 1997. Two groups collected measurements between 1991 and 1997 (Figure 4E). The U.S. Geological Survey measured BSF between 1991 and 1993 (Mason and others, 1995; Mason and Kipp, 1998). The Bureau of Land Management made annual measurements from a subset of wells between 1994 and 1997 (White, 2002).

Between 1998 and 2006 the Bureau of Land Management monitored brine chemistry and water levels in several wells to evaluate the laydown's impact (Figure 4F) (White, 2002). Some unpublished Bureau of Land Management measurements collected between 2003 and 2006 are compiled here (White, field notes and files including laboratory results, 1998 to 2014).

Between 2003 and 2018, Shaw Environmental, Inc. conducted biannual measurements of groundwater level and chemistry from various locations. These measurements, amounting to over 900 measurement sets, were gathered on behalf of the potash mine as part of its mine reclamation plan (Shaw Environmental, 2020). While most sites were within the potash mine, many samples were from the BSF study area. These include samples from the alluvial fan aquifer, east of the extraction ditch, and south of Interstate 80 (I-80) areas. The samples for the period spanning from 2007 to 2012 exclusively originate from this report.

Between 2015 and 2022, researchers from the University of Utah collected brine chemistry and groundwater level measurements, and between 2022 and 2023 the Utah Geological Survey collected similar measurements (Figure 4G) (Penrod, 2016; Bowen and others, 2018; Kipnis and Bowen, 2018; Lerback and others, 2019; Kipnis and others, 2020; Bernau and Bowen, 2021; Bernau and others, 2023a). The Bureau of Land Management made groundwater level and density measurements independently (White, field notes and files including laboratory results, 1998 to 2014) and in collaboration with the University of Utah in 2015.

Measurements

From May 2016 to May 2020, a precipitation sample collector with internal electrical heating was installed at the potash mine. Mine staff monitored and collected precipitation samples regularly, offering storm-event-level resolution for collected precipita-

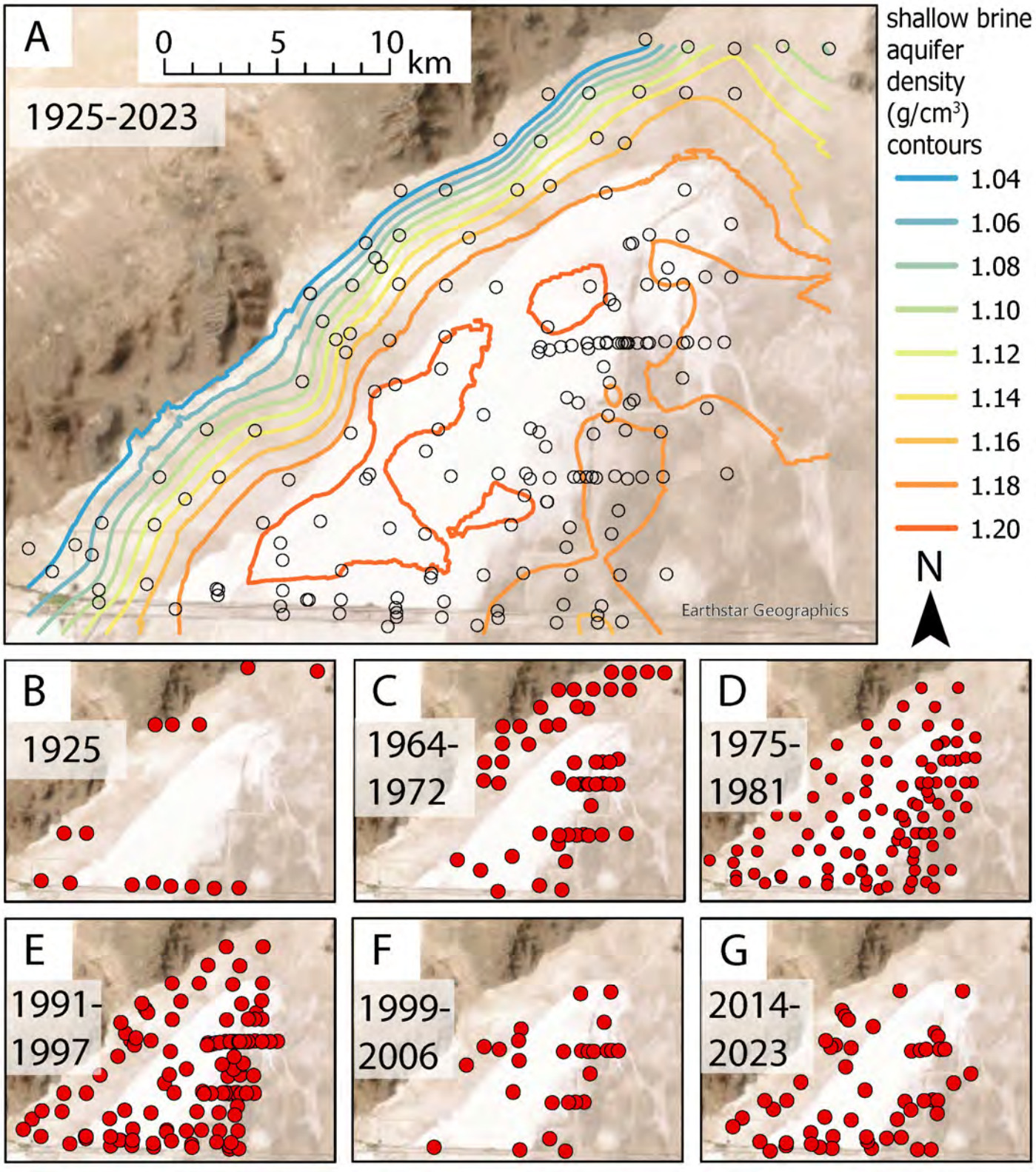

Figure 4. *Spatial distribution of shallow brine aquifer density measurements from the Bonneville Salt Flats and surrounding area. A) Compilation from density measurements between 1925 and 2023. B to G) Locations of shallow brine aquifer density measurements over time. Kriging done with Empirical Bayesian Kriging (Geostatistical Analyst) in ArcGIS.*

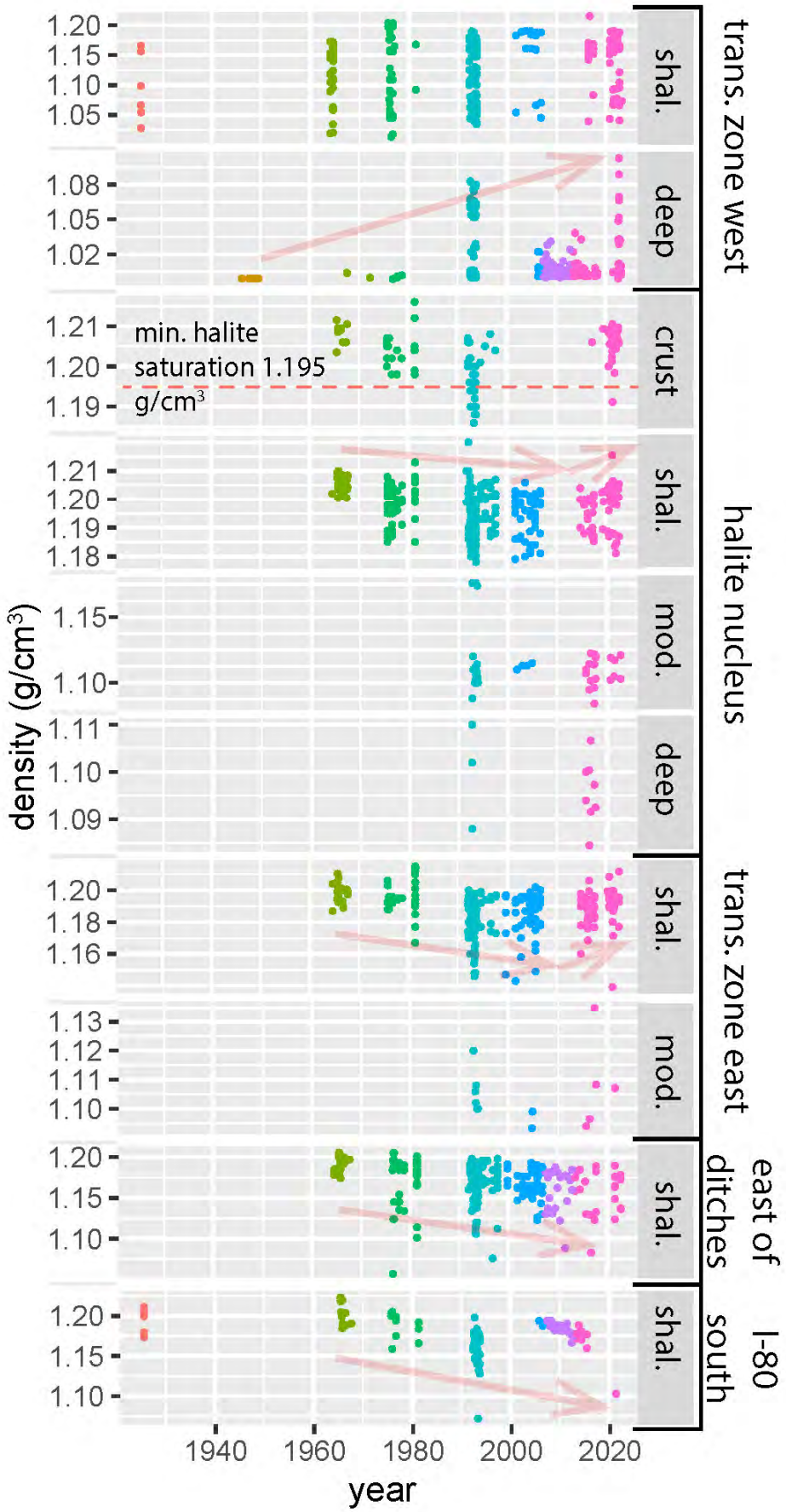

Figure 5. *Brine density measurements over time (~2000 data points). Measurements are separated by area and depth of investigation. Note the difference in vertical scales. Light red arrows added to highlight trends by area.*

tion. Stable water isotopes of hydrogen (δ^2H) and oxygen ($\delta^{18}O$) were measured at the SPATIAL Lab at the University of Utah with a Picarro L2130-i cavity ring-down spectrometer. Water isotope concentrations were calibrated to laboratory standards, and values were reported as per mil (‰) relative to the V-SMOW scale.

Between 2016 and 2021, ground and surface water samples were collected in acid-washed and deionized water-rinsed bottles and returned to the University of Utah for major ion and stable isotope analyses. A subset of samples was analyzed for major ion concentrations by external laboratories using inductively coupled plasma mass spectrometry (ICP-MS/AES) and ion chromatography as reported in Kipnis and others (2020). Samples collected in 2017 and 2020 were analyzed for major ion concentrations using a portable X-ray fluorescence spectrometer (pXRF) and calibrated to the methods described in Kipnis and others (2020). Calcium concentrations and total dissolved solids were excluded from pXRF results due to data calibration challenges. Additional samples were collected in 2017 and 2018 for chemical analyses including radiocarbon (C^{14}) and tritium ($^3H/^3He$) dating as reported in Lerback and others (2019). Samples collected in 2021 were measured for major ions using ICP-MS and ion chromatography at the University of Utah Earth Core Facility. Samples collected in 2022 were analyzed for major ion concentrations by external laboratories (Chemtech-Ford, Utah Public Health Laboratory). Brine density values were measured in field and lab settings with a Mettler-Toledo Densito 30PX. Laboratory measurements of density at 20°C were made following the procedures of Bernau and others (2023a) at 20 °C. Before 2022, when analyzing hydrogen (δ^2H) and oxygen ($\delta^{18}O$) stable isotopes from brine samples, solutes were removed through cryogenic vacuum extraction before stable isotope measurement. Starting in 2022, vacuum extraction was not used for brine samples analyzed for stable isotopes.

Data Quality Control

Due to the diversity in data vintages, care was taken in reviewing data quality. Because of this, changes in density were primarily focused on as density measurements are relatively robust over time and are less susceptible to methodological changes (Bernau and others, 2023a). Salinity is directly proportional to brine density and the two terms are used interchangeably here. In addition to data quality, seasonal changes in brine salinity were considered. Seasonal variations in brine density, as observed from monitoring well brines and brines extracted for potash production, indicate that samples collected during cooler and wetter winter to spring months are more likely to have depressed density measurements (Figure 6). Measurements with higher density from warmer, drier months (July to September, preferably August), are preferred for long-term evaluation. While the impact of temperature on density measurements was taken into account and corrected for whenever feasible (with a change of approximately 0.01 g/cm^3 observed between temperatures of 10 and 30 °C), it should be noted that warmer brines can dissolve more halite, resulting in higher densities (Bernau and others, 2023a). To mitigate the influence of dilution caused by flooding, it is advisable to utilize the highest recorded density at a site during a study period for long-term comparisons.

Brine chemistry reporting varied across studies. Some studies only reported field density, others reported major ion chemistry and periodically TDS, whereas others reported laboratory density measurements in addition to the measurements above. Field densities with reported temperature (if available) were corrected to the density at 20°C using Equation 11 in Bernau and others (2023a). Following the methods in Bernau and others (2023a), major ion data were used to model density using the SpecE8 module of Geochemists' Workbench® with the PHRQPITZ thermodynamic dataset (Pitzer, 1973; Harvie and others, 1980; Plummer and others, 1988; Bethke, 2013). Finally, available measurements were utilized to establish the correlation between TDS and density for BSF brines. Using the measured TDS data, a salinity for these brines was estimated. Chemical model-based estimates of density at BSF tend to underestimate density, indicating that major ion concentrations are typically underreported (Bernau and others, 2023a). When all of these measurement types and estimates of salinity were available, they were contrasted to delineate measurement quality. For long-term comparative analyses, laboratory density measurements were prioritized, then field density measurements, followed by chemically modeled density, and finally density estimated from TDS.

An additional step in data quality control was made using site-based knowledge to assess data quality and identify erroneous data to remove. For example, anomalously high density values (>1.22 g/cm^3) are not possible at BSF given its brine composition and suggest measurement errors, such as suspended sediment increasing field density measurements. An additional consideration was unusually low density measurements. For example, some samples from the years 1991 to 1993 have unusually low reported densities. Samples that contain higher levels of sodium

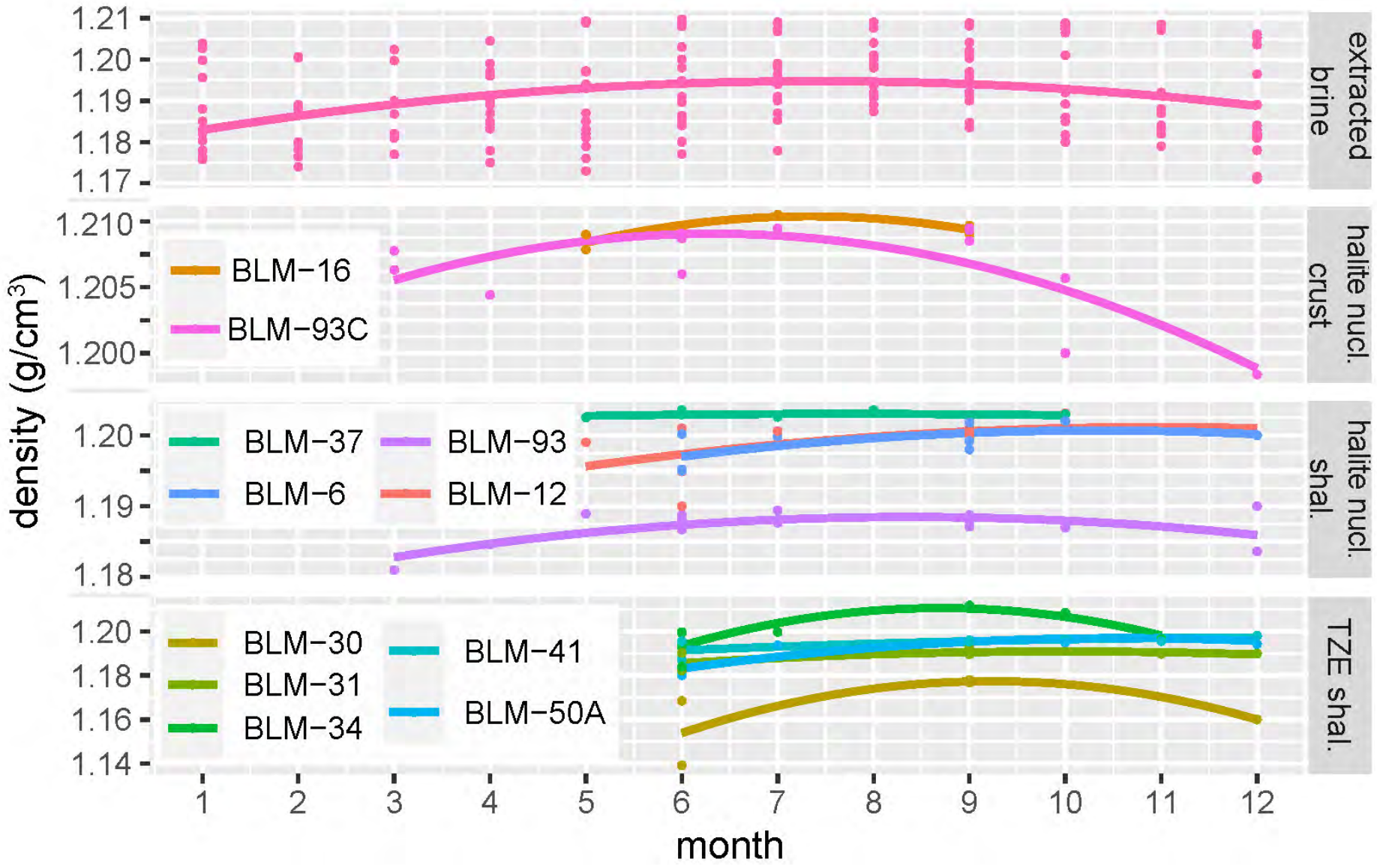

Figure 6. *Seasonality in density measurements across different sample areas. Data from 2000 to 2020 for extracted brines and 2015 to 2022 for well samples. Well locations are shown on Figure 1B. In general, brine salinity is highest and most consistent in August and September. Extracted brine density increases in the summer with peak evaporation and decreases in the winter with decreased evaporation and increased precipitation. Halite nucleus salinity reflects the impact of temperature on the solubility of halite. As the crust warms, it's brine can dissolve more halite, and increase in density. The halite nucleus shallow aquifer salinity is highest at the end of summer and lowest in the spring. Lower salinity in early spring may reflect the upward movement of deeper, less saline brine as the surface warms (Bernau and Bowen, 2021). Brine densities in the transitional zone east shallow aquifer generally peak in September, potentially reflecting evapoconcentration.*

and chloride ions exhibit greater densities. When these samples reach halite saturation, as they are when they are in contact with halite for a sustained period, any changes in density are limited by the process of halite dissolution or crystallization. In the case of brines in contact with halite, there have been instances where the reported densities were below the density of halite saturation. This was exceptionally clear in samples from the crust-hosted aquifer with reported densities below 1.18 g/cm^3, which is below halite saturation (1.195 g/cm^3 minimum at halite saturation at BSF) (Figure 5). These anomalously high and low measurements were omitted from analyses. The final step in data quality control used known spatial distributions of salinity to identify unusually high or low density measurements, which were then assessed and removed or kept if they were consistent with additional site measurements during that period.

Individual Well-Based Analysis

Given the spatial heterogeneity of the brine chemistry, it is important to evaluate this system at specific sites over time in addition to characterizing the overall system. Well sites were selected for individual well-based analysis if they had multiple measurements across several study periods (a site could include past borings and wells of similar depths at the same location). The Kendall test and linear regression (Kendall package and linear model function in the R© coding language) (Wilkinson and Rogers, 1973a; Hipel and McLeod, 1994; R Core Team, 2021; McLeod, 2022) were applied to site data to identify locations with statistically significant (p-value <0.05) long-term trends in density change. The Kendall test assumes that long-term trends are consistent and have not changed. Because measurements were not uniformly distributed over time they could not be used for Mann-Kendall or break-point analyses.

Areas of Investigation

To better describe changes and aggregate data, studied areas were divided spatially and by aquifer depth (Figure 1B and D).

Lateral Divisions

Areas of investigation were divided based on surface mineralogy, potential groundwater flows, fabricated structures (the interstate highway and drainage ditches), and lateral salinity (density) gradients (Figures 1B and 4A). Similar terminology based on hydrological fluxes and sedimentology has been used to establish lateral divisions in other saline pans (Munk and others, 2021). From west to east, these areas are the transition zone west (TZW), halite nucleus, transition zone east (TZE), east of ditches, and I-80 south (Figure 1).

The TZW area includes the region to the west of the persistent halite crust up to the Silver Island Mountain front. This area consists of a mudflat (inner TZW) which transitions into a higher-elevation mudflat with dunes and intermittent vegetation (outer TZW). The location of the inner and outer TZW is reflected in USDA soil maps, where the inner TZW area corresponds with a playa unit and the outer TZW area corresponds with a playa-saltair complex with 0 to 1% slope (Soil Survey Staff, accessed March 2023).

TZW waters flowed toward the saline pan in the past. Before 1946, at least two now-dormant springs near the mountain front flowed between 0.02 and 3.4 m^3/minute (Utah Division of Water Rights database). Lines (1979) reported a decline in hydraulic gradient between the alluvial fan and the saline pan. Mason and Kipp (1998) also reported outer TZW desiccation fractures (some >1 m wide) and no hydraulic gradient between the saline pan and TZW. Kipnis and Bowen (2018) also noted a decline in alluvial-fan aquifer groundwater levels beyond historical norms after 1998.

The halite nucleus consists of an area with a persistent halite crust (up to 1.5 m thick). The minimum halite extent, as mapped across several decades of aerial imagery, was interpreted as the halite nucleus' boundary. The salt crust aquifer only occurs beneath the halite nucleus. Nolan (1927) noted the halite nucleus extended south to the area of the current potash mine in 1925.

The TZE is between the halite nucleus and the eastern brine extraction ditches. This area is covered by ephemeral halite crust (precipitated from standing water) and efflorescent salts (primarily halite) overlying authigenic gypsum sand (Bernau and Bowen, 2021). The area to the east of the brine collection ditches is hydraulically connected to the greater GSLD. The east of ditches area is defined as the region that is closest to the drainage ditches and is likely to be impacted by brine extraction. The final area of investigation is the zone immediately to the south of I-80 that is impacted by brine extraction ditches and is isolated from the saline pan by I-80, which prevents overland flow and limits subsurface brine movement (Mason and Kipp, 1998). Before manmade structures were built at BSF, brines could flow from the southern and eastern parts of the GSLD to BSF. Evidence of this can be seen today in aerial and satellite imagery of seasonal ponds that develop to the

southeast of the potash mine (Radwin and Bowen, 2021).

Aquifer Divisions

Previous studies characterized basin-fill, alluvial-fan, and shallow brine aquifers by water chemistry and recharge rates (Turk, 1973; Lines, 1979; Mason and Kipp, 1998). Aquifers and samples are delineated by depth (Figure 1D); these include surficial samples, such as brine collected from extraction ditches and the laydown, and subsurface samples, which are the focus of this study. Depth intervals are described from shallowest to deepest. The crust-hosted wells occur in the halite nucleus, where they are screened within 1 m of the surface. Brine samples from this aquifer should be at halite saturation because the aquifer is hosted in halite. The shallow aquifer occurs directly under the crust-hosted aquifer in the halite nucleus and is in contact with the surface elsewhere. The shallow, moderate, and deep aquifers occur within lacustrine to saline sediments which consist of carbonate-rich mud and gypsum (with gypsum only occurring in deep basinal muds, >50 m depth) (Shuey, 1971; Stephens, 1974; Oviatt and others, 2020; Utah Division of Water Rights database).

The shallow basinal mud aquifer (reported as the shallow brine aquifer in other publications) occurs from ≥0 to <10 m depth. This aquifer ranges in salinity from 1.04 to 1.21 g/cm^3 (Figure 4A), is fractured, and contains brine-shrimp fecal pellet intervals, contributing to a higher hydraulic conductivity than anticipated from its mean grain size of silty clay (Turk and others, 1973; Lines, 1979). The aquifer's fractures occur in hexagonal patterns. Turk and others (1973) proposed that the fractures formed through osmotic desiccation or synaeresis. Where multiple wells exist in the same aquifer depth range at the same site, the shallower well or the well with a longer reporting span was used for multi-decadal single-well analyses. Turk (1973), Turk and others (1973), and Lines (1979) estimated the total thickness of this aquifer to be between 4.5 and 8 m. The largest source of recharge to the shallow brine aquifer is meteoric water infiltration through the surface (Mason and Kipp, 1998). Major aquifer discharge sources are the pumping of ditches along the eastern margin of the saline pan and subsurface flow south underneath I-80 (Mason and Kipp, 1998).

Wells screened in the moderate depth aquifer occur within ~10 to 30 m depth and only occur within the halite nucleus and TZE. Permeability in the moderate depth aquifer is far lower than the shallow aquifer (Mason and Kipp, 1998), possibly due to the absence of fractures and limited connection with overlying higher-permeability aquifers. Alluvial-fan brackick water (BW) aquifer wells (>10 to 150 m depth; measured wells occur between 22 and 111 m depth) are screened in muds (which occur from surface to 8 to ~70 m depth across BW wells) to alluvial-fan gravels (Stephens, 1974; Bernau and others, 2023b). The observation well (OW) alluvial-fan aquifer wells (Figure 1C) do not have any reported logs with them, but the OW wells closer to the Silver Island Mountain front reach depths known to intersect gravel lenses.

Two wells at BSF's center occur within deep (~30 to ~250 m depth) basinal muds and possibly bedded gypsum; this lithology interpretation is based on deep brine well logs from the potash mine to the south (Utah Division of Water Rights database; Bernau and others, 2023b). These deep basinal wells have 3-m-long screens at ~70 and 150 m depth. Underlying deep basinal muds are basinal gravels, which occur at depths of >250 m. The potash mine uses wells in basinal gravels as a source of potassium-rich brine. The basinal gravel aquifer consists of gravels, conglomerates, and Tertiary volcanic rocks (Stephens, 1974). Water rights reports and data reported in the potash mine reclamation plan (Shaw Environmental, 2020) of basinal gravel wells show the deep brine aquifer's potentiometric surface declined ~20 to 30 m between the 1950s and 2010s.

RESULTS

Here, chemical results are analyzed in a spatial and temporal context, progressing from west to east, covering the period from 1925 to 2023. Datasets with insufficient information to differentiate trends are not discussed. For example, most trace elements had insufficient data to identify spatial or temporal changes.

Transitional Zone West

Compositionally, many TZW samples differ markedly from other BSF samples (Figure 7). They have higher relative proportions of sulfate (SO_4^{2-}), alkalinity (as HCO_3^-), calcium (Ca^{2+}), and magnesium (Mg^{2+}) than other areas because they have lower concentrations of sodium (Na^+) and chloride (Cl^-) (especially in the alluvial-fan aquifer wells). Shallow aquifer TZW brines show a clear decrease in magnesium between the 1964–1972 and 1999–2006 periods, with increasing magnesium after the 1999–2006 period (Figure S1). Additionally, lithium (Li^+) concentrations are much lower in the TZW than in other areas (Figure S2).

Analysis of individual wells in the TZE shallow

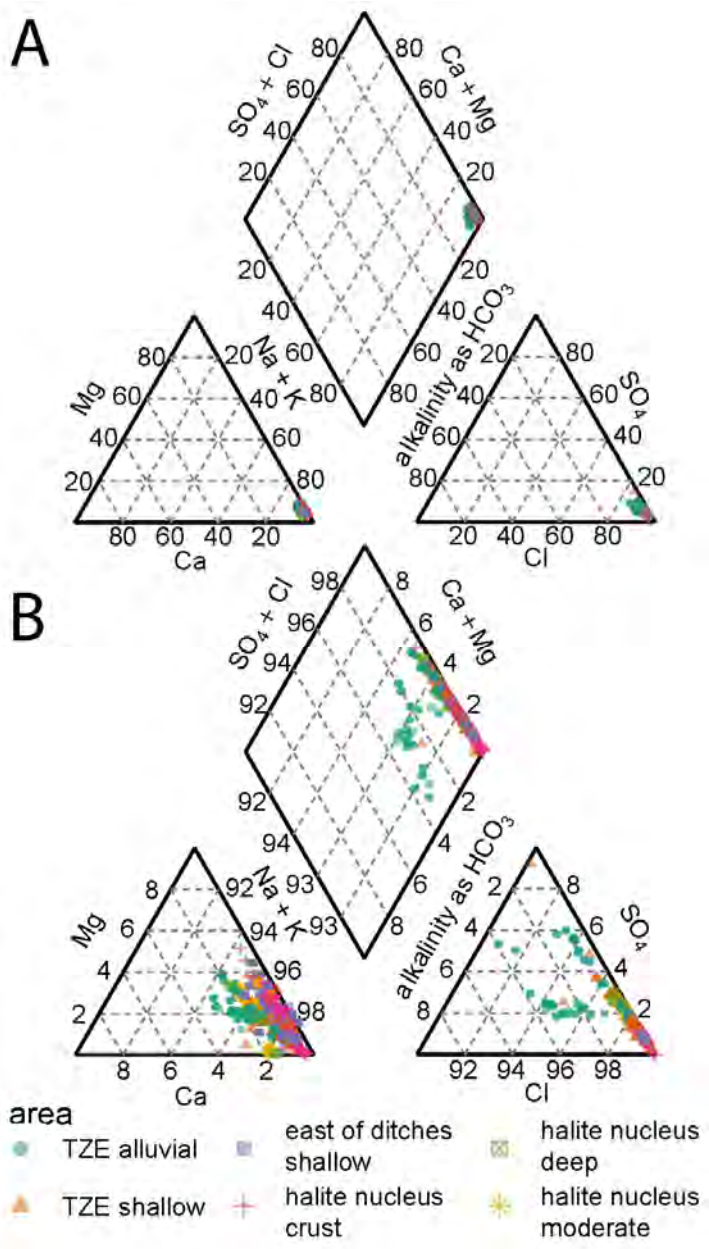

Figure 7. *Piper diagram of geochemistry measurements across BSF at A) normal scale, B) magnified scale. A) The high salinity system dominated by Na and Cl makes differentiating between sites based on relative ionic content challenging. B) Differentiation between sites when examined at the 90/10/10 percentile values.*

aquifer identified two areas of increasing salinity (Figures 8A and B). The first segment occurs near the OW transect (Figure 1C). The second segment occurs mid-way along the saline pan, where the inner TZW is wider because of a low-lying Silver Island Mountains pass connecting this area to Pilot Valley.

Aggregate analysis of the TZW shallow aquifer (Figure 9A) indicates that the outer TZW area has experienced an increase in salinity over time. In contrast, the inner TZW area does not exhibit consistent changes in salinity. The inner TZW aggregate results contrast with those of the individual well analyses, possibly from differences in sampling location across studies. Over time, the outer TZW area has had marked declines in groundwater levels; several shallow aquifer wells were persistently dry during the 2013–2023 study period.

Stable water isotope measurements from the TZW shallow aquifer indicate that it is isotopically lighter (meaning it originates from less evaporated waters or precipitation from cooler periods) relative to other shallow aquifer areas (Figures 10 and 11). Similar to the shallow aquifer in other areas, a negative shift in TZW shallow aquifer deuterium excess values (Dansgaard, 1964) suggests a change to more evaporated waters over time (Figure 11).

The alluvial-fan aquifer has had notable declines in groundwater levels since the early 1990s (Figure 3E) (Kipnis and Bowen, 2018). In addition to hydraulic head changes, between 1993 and 2022 there have been marked changes in brine density and δ^2H and $\delta^{18}O$ values. Furthermore, the spatial distribution of these values over time (Figures 12–15) reflects changing groundwater sourcing from mountain front sourced waters to more evaporated waters from the saline pan area.

The BW production well transect shows increasing density and a shift to heavier δ^2H and $\delta^{18}O$ isotopes over time (Figure 12). The largest density increase is concentrated at the center of the active production field (where produced waters now exceed a density of 1.05 g/cm^3), with smaller density increases occurring on the edge of the active field (wells at 1.8 and 4.2 km). There are some exceptions to the correlation between increased density and generally heavier water isotopes. Waters from a well at 4.2 km had relatively low densities, but heavier isotopic values. This indicates that some waters originate from precipitation under warmer conditions or from evaporated waters (as suggested by water isotopes) that do not have an elevated salinity.

Observations from the OW well transect, which spans the inner to outer parts of the alluvial-fan aquifer (Figure 1C), inform the interpretation of observed changes in BW chemistry (Figures 13 to 15). Figure 13A to C, a cross section of OW measurements over time shows an increased density gradient towards the basinward direction (to the east) with a transition in salinity between 1 and 2 km. Similarly, Figures 15A and D show a transitional zone between the alluvial-fan and basinal δ^2H and $\delta^{18}O$ values in the year 1993 occured between 1 and 2 km along the transect. The δ^2H, $\delta^{18}O$, and deuterium excess values observed in mountain front-adjacent alluvial-fan samples suggest these waters are sourced from winter precipitation that has undergone minimal evaporation and fractionation (Figure 11). The deuterium excess values of all

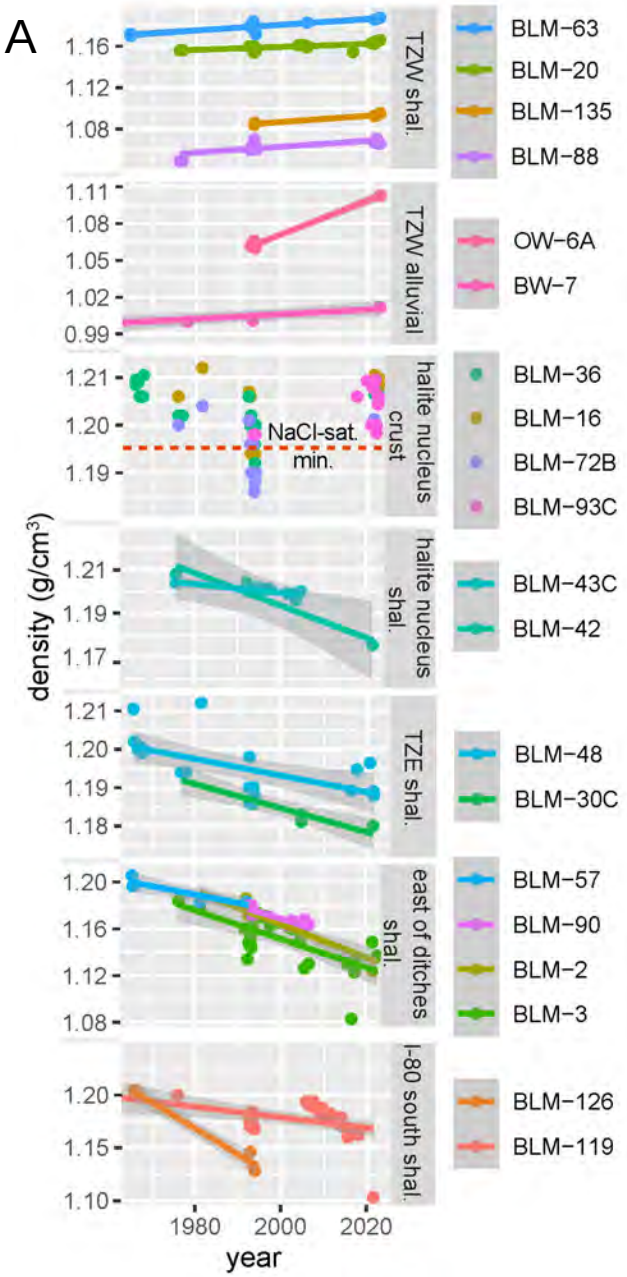

Figure 8. *A).* *Select well trends in density through time. Samples from east of ditches, TZE, and I-80 south areas are all from wells screened in the shallow aquifer. See Figure 1B well locations. B) Sites from Fig. 8A with a statistically significant change in salinity. Color is used to denote change in density. Size denotes the relative fit of change with time (higher r^2 shows a stronger correlation of change with time). All wells in B) are in the shallow aquifer except for the alluvial-fan aquifer well in the southwest corner of the map.*

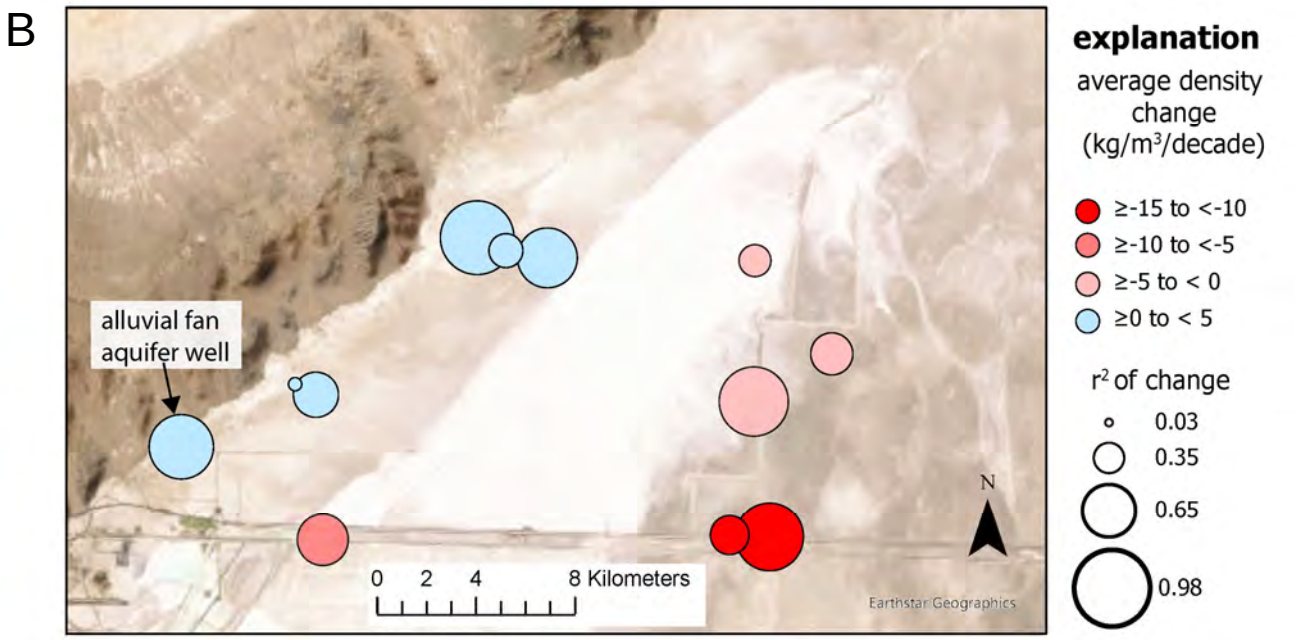

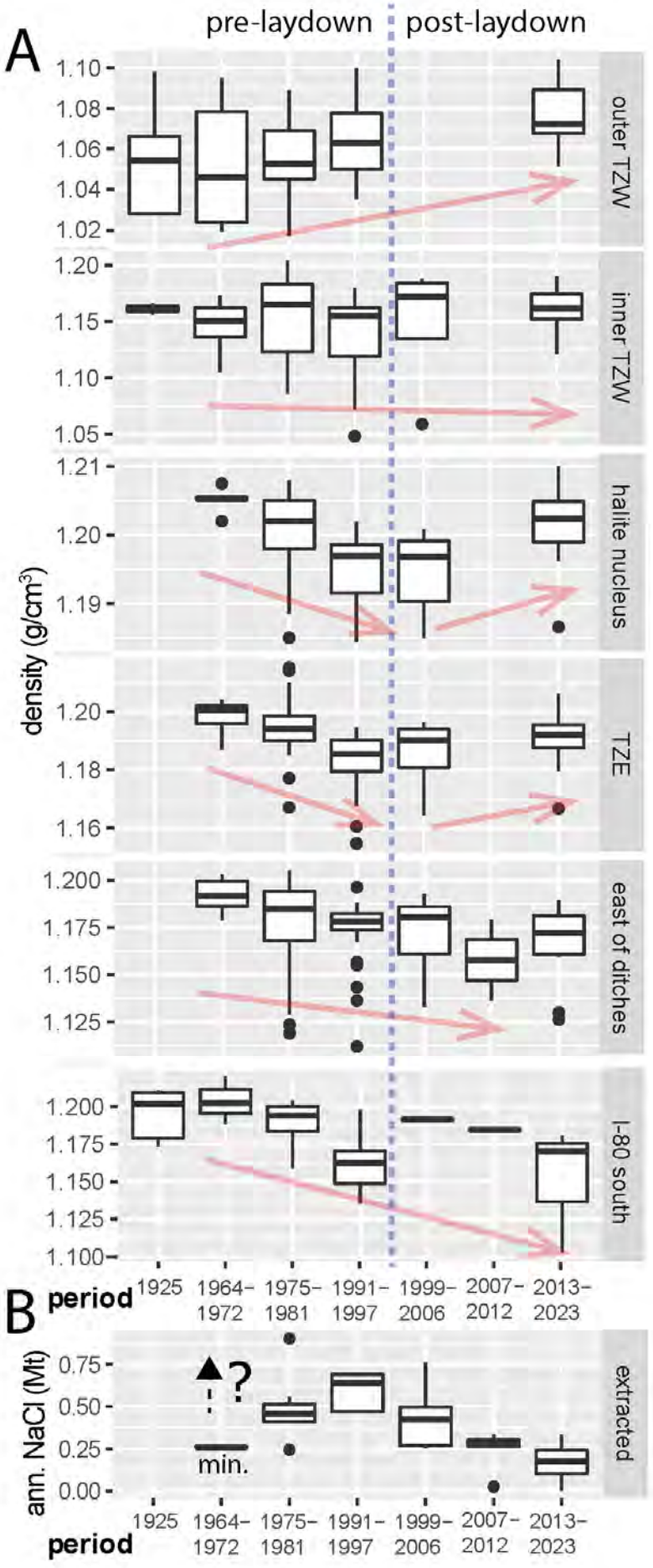

Figure 9. *Box and whisker plots of changes in (A) shallow aquifer brine density across different areas over time and in (B) brine extraction rates over time. Individual well data has been averaged for each sampling period to minimize the effect of sampling bias on results. Note that sampling has not been consistent at the same wells over time, making trends identified here different from those identified in Figure 8A. Extraction rates before 1991 are primarily estimated and have a high range of uncertainty.*

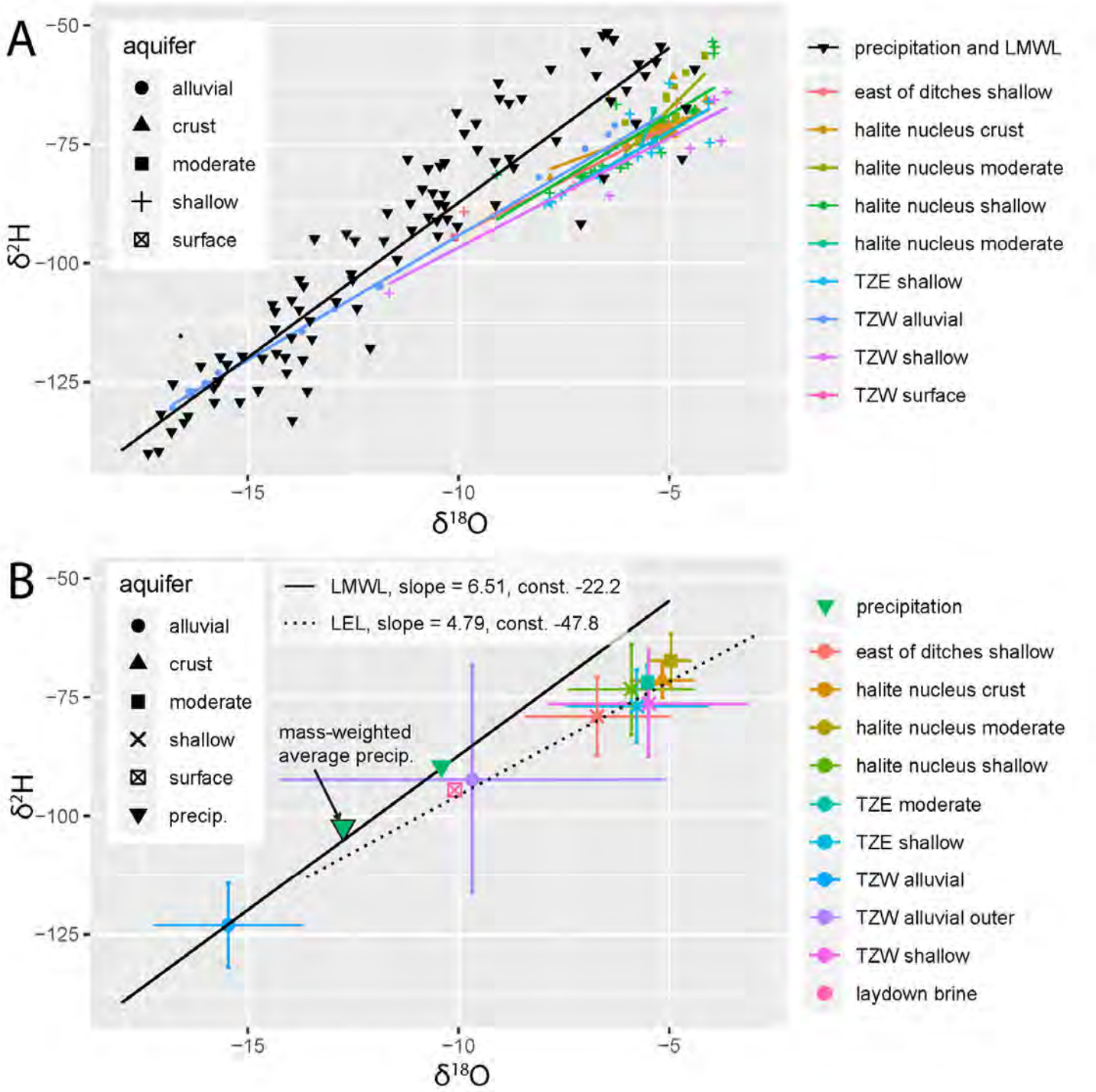

Figure 10. *Spatial changes in water δ^2H and $\delta^{18}O$. A) All isotope data. B) Average isotope values by area with standard deviation in error bars. TZE alluvial outer wells indicate OW wells located >1 km east of transect start. LMWL is the local meteoric water line. LEL is the local evaporation line.*

other areas suggest their composition was influenced by evaporation. Nevertheless, the absence of a proportional increase in deuterium excess values with increasing brine density implies that the salinity of the brine arises not only from evapoconcentration but also from the dissolution of salt (Figure 11D). These data strongly support the theory that high salinity in the halite nucleus is maintained by salt crust dissolution.

Between 1993 and 2022, the hydraulic gradient shifted to mountain front-directed flow with a 10 m change in the hydraulic head at 0 km in the OW transect (Figure 14A to F). Hydraulic head was corrected for density to assess the effect of density on groundwater flow by using Equation 1 (Figure 14D and E) (Post and others, 2007).

$$h_1 = \frac{\rho_2}{\rho_1} h_2 - \frac{\rho_2 - \rho_1}{\rho_1} z \qquad \text{(Equation 1)}$$

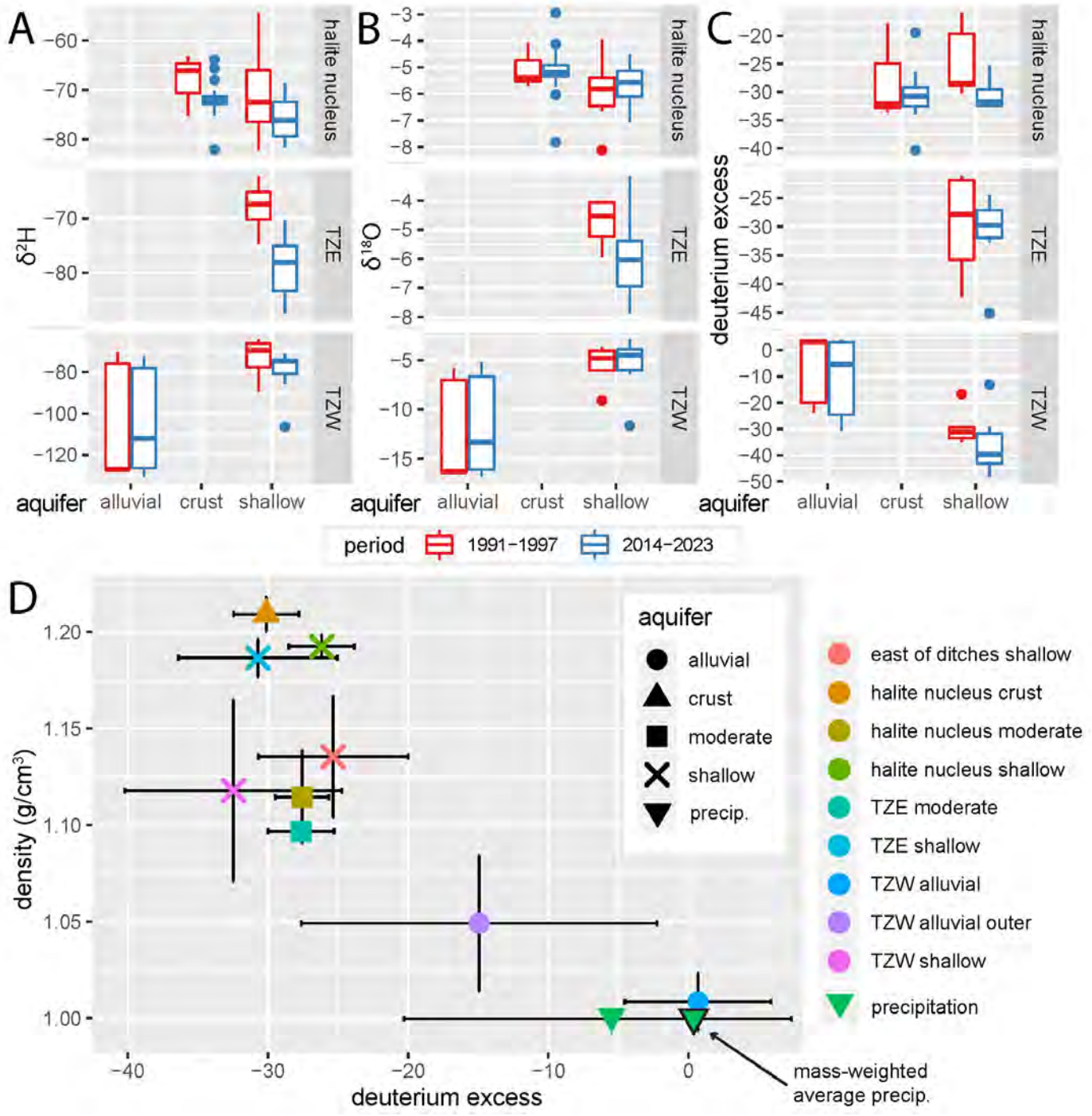

Figure 11. *Comparison of stable isotopes by area and aquifer over time. A) δ^2H, B) $\delta^{18}O$, C) deuterium excess, and D) deuterium excess relative to density.*

where ρ_1 is the reference density to adjust the sample to (freshwater density, 1.0 g/cm^3); ρ_2 is the density of the well-water (calculated from the average density of water's produced from a well in a period); h_2 is the height of the water level above a datum (mean sea level); z is the elevation (above the sea-level datum) of the mid-point of the well's screened interval; and h_1 is the equivalent head relative to the datum.

Between the years 1993 and 2022, there was an approximately 12-meter change in hydraulic head at the center of the BW production field. Interestingly, the basal head level observed in the OW wells (Figure 14b) for 2022 closely matches the head observed at the center of the production field in Figure 3E. This similarity in head change, despite a lateral offset of over 4 kilometers, indicates a high level of hydraulic connectivity across the BW alluvial-fan aquifer wells.

Correcting for the effect of density on hydraulic head has a significant impact on inferred water flow, as shown in Figure 14. In 1993, it becomes evident that groundwater primarily flows towards the west when the density correction is applied. Without this correction, groundwater flow would have been interpreted as moving towards an elevation of approxi-

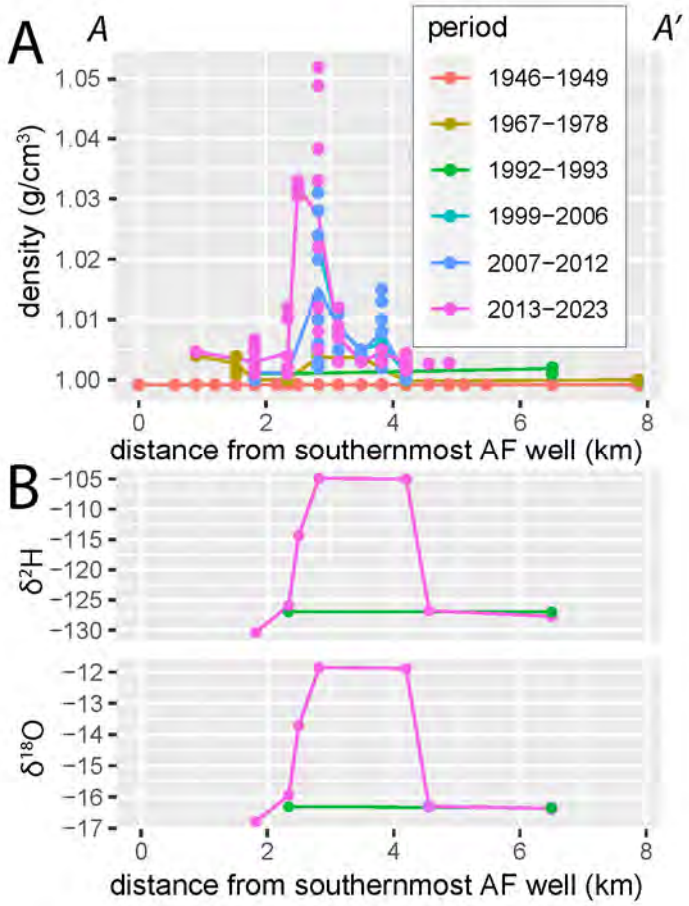

Figure 12. *BW well cross section with salinity and water stable isotopes over time. Location of A to A' is shown on Figure 1C.*

mately 1240 meters above sea level at 2 kilometers along the transect. In 2022, the density correction has a relatively smaller impact, but it still highlights that groundwater primarily flows in a westward direction, and downward vertical flow is less significant than what the uncorrected head measurement would suggest.

Changes in OW-brine density indicate that brine transports salt mass from the halite nucleus crust and underlying aquifers and towards the alluvial fan. Changes are concentrated on the basinward side of the OW cross section; where salinity has increased by 0.04 g/cm^3 at 2.6 km at ~1255 meters above sea level and by ~0.01 g/cm^3 at ~1215 meters above sea level. The cross-sectional view of salinity change (Figure 13C) shows a saline "nose" with brine migrating down and then west and upwards towards the alluvial fan (possibly along gravel lenses).

OW-transect wells have the largest stable-isotope changes of any area in the dataset. The largest change occurs at ~0.8 km at ~1245 meters above sea level (Figure 15C and F). This change reflects the movement of basinal water in the direction of the mountain front and is also shown in the 2022 cross-sectional view of isotope data (Figure 15B and E), which shows a blurring of the delineation between alluvial- and basinal-sourced water that was evident in the past (Figure 15A and D). These OW changes suggest that the BW well at 4.2 km has tapped basinal waters but has not yet sourced waters from areas with elevated salinity.

Halite Nucleus

Figure 5 illustrates declining halite nucleus brine density with depth. Crust aquifer brine is halite saturated (>1.195 g/cm^3); the shallow aquifer has high salinity (1.175 to >1.195 g/cm^3), and the moderate and deep aquifers have lower salinities (1.09 to 1.175 g/cm^3 and 1.08 to 1.11 g/cm^3, respectively). Mason and others (1995) showed this decline in salinity with depth by measuring pore water chemistry at multiple depths.

Individual well plots show no change in density over time in the halite nucleus crust samples (Figure 5). Past research suggested that the crust aquifer potassium concentrations decreased between the 1960s and the 1970s (Lines, 1979); subsequent analyses, however, show no long-term change in potassium from the 1960s baseline (Mason and Kipp, 1998; White, 2002) (Figure S3). Calcium concentrations decreased between the 1960s (from a high of ~1700 mg/L) to an observed low in the 1991–1997 period (~1100 mg/L) and then increased (Figure S4).

There is a notable isotopic lightening in the halite nucleus crust aquifer for δ^2H values between the periods of 1991–1997 and 2013–2023. Shallow aquifer samples show a similar change in δ^2H. This trend is not seen in the δ^{18}O values, which slightly increased in both aquifers.

Two wells showed decreasing halite nucleus shallow aquifer salinity over time (Figure 8). Aggregate data show a long-term density decrease with brines becoming halite undersaturated between 1964 and 1997 (Figure 9A). Afterward, density remained stable and then increased during the 2013–2023 period. Spatial differences in sampling location over time may influence this trend. In contrast to density measurements, the halite nucleus shallow aquifer sodium and chloride concentrations appear to consistently decrease over time (from 105 to 90 g/L and from 180 to 150 mg/L, respectively) (Figures S5 and S6), highlighting the problematic nature of accurately measuring high-salinity brines (Bernau and others, 2023a). Calcium concentrations are positively correlated to changes in density over time in the halite nucleus shallow aquifer while sulfate concentrations are negatively correlated to density changes (Figures 9, S4, and S7).

Moderate and deep halite nucleus aquifer wells

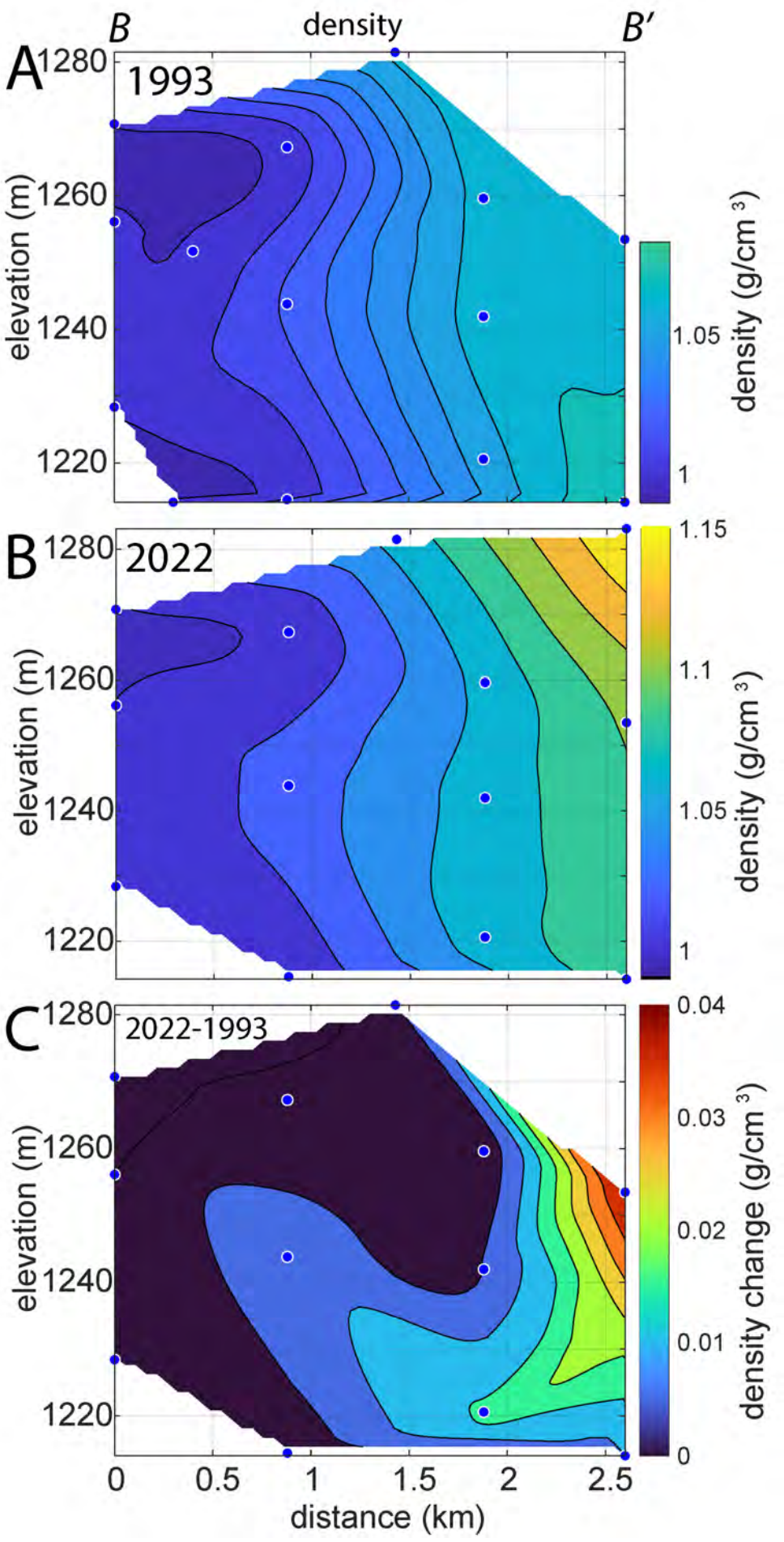

Figure 13. *OW cross section density. Density in (A) 1993, (B) 2022, and (C) change in density between 1993 and 2022. Each blue dot represents the midpoint of a well's screened interval. The location of B to B' is shown in Figure 1C. (~40x vertical exaggeration). Elevation is meters above sea level. Local surface elevation (not shown) is 1284.9 to 1293.0 m. Note that A & B use the same color scales with only the applicable range for each segment being shown.*

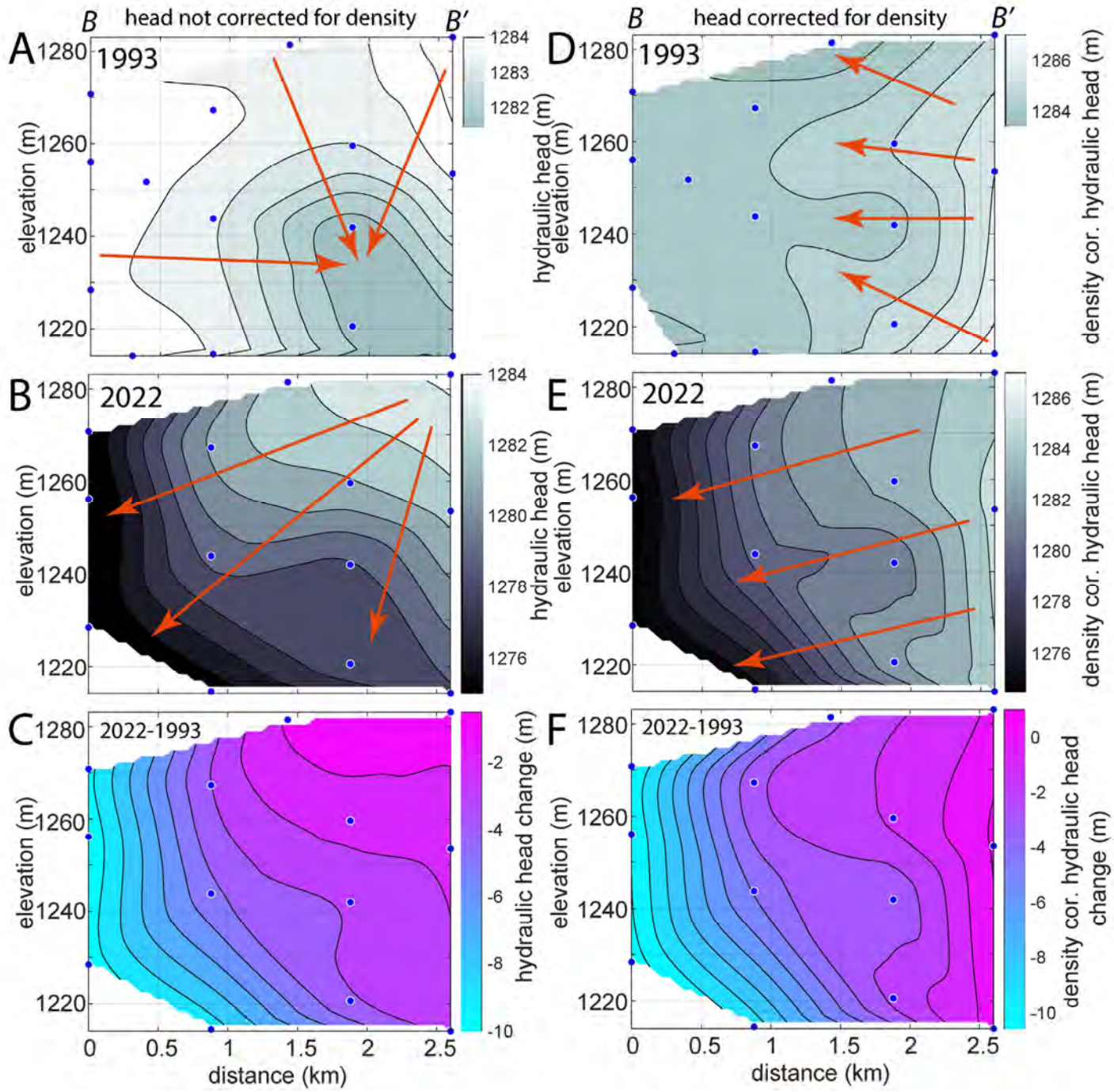

Figure 14. *OW cross section of hydraulic head over time. (A to C) Measured hydraulic head measurements and (D to F) hydraulic head measurements corrected for density. Note the impact of density correction on apparent flow direction (red arrows). Note that A & B, and D & E use the same color scales, respectively, with only the applicable range for each segment being shown. Each blue dot represents the midpoint of a well's screened interval. The location of B to B' is shown in Figure 1C. (~40x vertical exaggeration). Local surface elevation (not shown) is 1284.9 to 1293.0 m. Elevation is meters above sea level.*

have a limited sampling history over a small spatial extent, and no unequivocal changes in their composition were observed. The moderate depth aquifer had the highest observed sulfate concentrations of any area and aquifer (Figure S7).

Transitional Zone East

Two wells showed clear decreases in TZE shallow aquifer salinity over time (Figure 8). Aggregate TZE shallow aquifer measurements show salinity decreased through the 1991–1997 period and increased afterward. In contrast to density (and similar to the halite nucleus shallow aquifer), reported sodium and chloride concentrations have decreased over time. Magnesium concentrations at TZE reflect observed density changes. Similarly, TZE shallow aquifer potassium concentrations decreased up to the 1991–

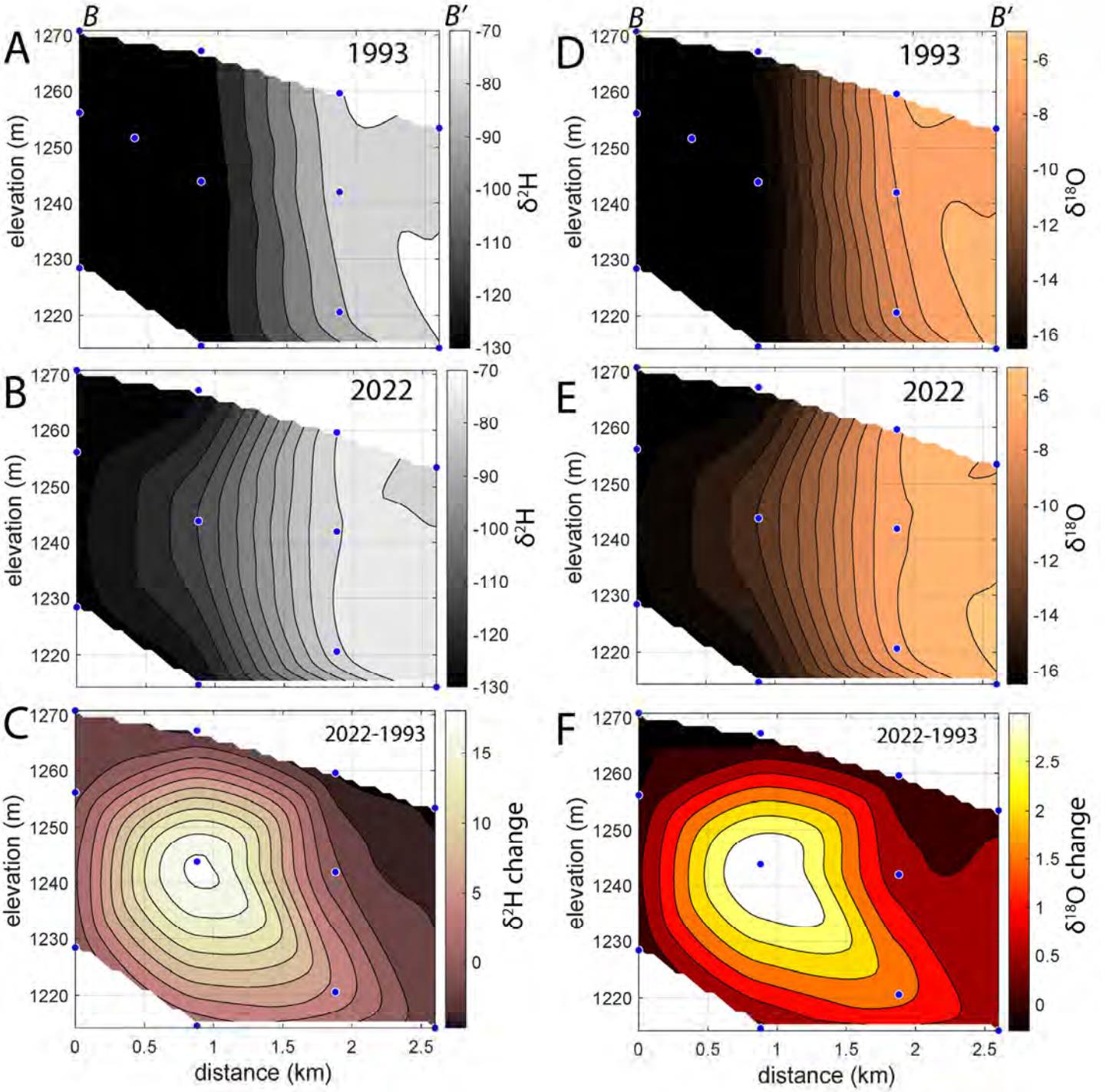

Figure 15. *OW cross section of water stable isotopes (δ^2H: A to C, and $\delta^{18}O$: D to F) over time. A & B and D & E use the same color scales, respectively, with only the applicable range for each segment being shown. Each blue dot represents the midpoint of a well's screened interval. The location of B to B' is shown in Figure 1C. Note the vertical scale differs from Figures 13 and 14. (~40x vertical exaggeration). Local surface elevation (not shown) is 1284.9 to 1293.0 m. Elevation is meters above sea level.*

1997 period; there were no changes in the following period. Measured δ^2H became lighter between the 1991–1997 and 2013–2023 periods (Figure 11A).

Extracted Brines

Here, changes in brine extracted from the eastern collection ditches are described. NaCl removal from subsurface flow to the south (Mason and Kipp, 1998) is not considered in these values. Sustained brine production at BSF began in 1939 (Bingham, 1980); since then, the location and volume of brine extraction for potash production at BSF have varied over time (Figure 9B). Before 1966, the Salduro Loop ditch at the center of BSF (Figure 1B) was used to harvest brine; this ditch was likely constructed after sustained production began in 1939, and it is present in 1946

aerial imagery. Hadzeriga (1964) reports an initial 1% KCl and 21% NaCl weight content of brines used for potash production. The mass of potassium produced annually from the shallow aquifer since 1968 is reported in the potash mine's estimated resources and reserves report (Agapito, 2022). Production from BSF area and the area south of I-80 was lumped together, as such these values can only be used to provide an estimate of brine extraction from BSF over time. The eastern ditches at BSF have been pumped intermittently since 1963 (Lines, 1979). An estimated 0.26 Mt NaCl/year was extracted from the eastern ditches between 1966 and 1972 (Stephens, 1974) (Figure 9B). Lines (1979) reports extraction of >0.25 Mt NaCl/year in 1976. Mason and Kipp (1998) estimated 0.47 Mt NaCl/year extraction. White (2004) reports that brine extraction between 1995 and 1998 was between 0.45 and 0.94 Mt NaCl/year. Brine extraction rates between 2001 and 2021 were highly variable (Todd Marks, Bureau of Land Management, written communication, 2023), ranging from almost none to nearly 0.8 Mt of NaCl extracted/year (Figure 3A). There was over twice as much annual average extracted mass in the 1996–2006 period (0.40 Mt/year) than in the 2013–2023 period (0.16 Mt/year). During at least the last part of the 1996–2023 period, the northern part of the extraction ditches was inactive (Figure 1B; potash mine personnel, verbal communication, 2022). Examination of the ratio of total KCl produced from the shallow aquifer (BSF and area south of I-80) and NaCl extracted from BSF over time shows that production became less reliant on BSF after the year 2000; with an average of 10 tonnes of NaCl extracted from BSF for every ton of KCl produced by the mine before 2000, and 5.5 tonnes of NaCl extracted from BSF for every ton of KCl produced afterward.

While seasonal precipitation and evaporation changes can impact the salinity of extracted brine (Figure 6), month-to-month analysis of density and extracted brine volumes show a clear decrease in extracted brine salinity with increased extraction rates (Figure 3D). The decrease in salinity with increased extraction suggests that deeper, less-saline waters rise upward (with reduced hydrostatic pressure) and contribute to the shallow aquifer.

From 2000 to 2004, the density of the extracted brine increased while the volume of brine extracted remained constant. From 2004 to 2015 the extracted brine density decreased; from 2004 to 2010 there was no net addition of NaCl to the salt flats. Following 2010, brine extraction greatly decreased, while laydown increased, leading to increased net volumes of brine contributed to BSF. Apparently, a 5-year lag occurred between decreased extraction with increased net brine contributions and the onset of salinity increase within the system. This is a much longer period than the salinity recovery period in the early 2000s, which was associated with a much larger pulse of input solutes over a shorter period. Following increasing density up to 2015, density remained high during the 2016–2020 period.

East of Ditches and I-80 South

Both the east of ditches and I-80 south areas have reduced hydraulic connection with the halite nucleus and are isolated from laydown brines. Furthermore, brine extraction ditches impact both of these areas. Accordingly, these areas provide an example of how the brine system may respond to extraction on decadal timescales without external solute sources.

In contrast to the halite nucleus and TZE shallow aquifers, brine samples from the east of ditches and I-80 south shallow aquifers show decreases in density across individual wells and in aggregate (Figures 8A and 9). Similar to the halite nucleus crust aquifer and TZE shallow aquifer, calcium concentrations in the east of ditches shallow aquifer decreased until the 1991–1997 period (from ~1500 to 1100 mg/L) and increased afterward (to ~1400 mg/L) (Figure S4).

DISCUSSION

Brine Chemistry Changes Over Time

BSF brine chemistry changes lie within three groups: 1) no change, 2) long-term decrease or increase, and 3) change in long-term trend following the 1991–1997 period. No long-term changes in the deep and moderate-depth aquifers underlying the halite nucleus and TZE were observed. Similarly, the inner TZW area, when taken in aggregate, did not show any change in density over time. However, analyses of several wells from the TZW area indicate parts of this area increased in density over time.

The shallow aquifer in the east of ditches and I-80 south areas show clear decreases in density over time, in contrast, the outer TZW area is the only shallow brine area to show long-term increases in density across several studies. The BW production well area in the TZW also shows consistent long-term increases in alluvial-fan aquifer density, but the east of ditches and I-80 south areas show long-term decreases in brine density, with the I-80 south area showing the largest salinity decrease. The changes in brine salinity in the I-80 south area also suggest that there is limited transport of solutes under I-80 from BSF to the I-80 south area. High connectivity between these areas would likely limit salinity decreases in the I-80 south

area as transported salt would replenish removed solutes.

The last group of chemical change, with changes in long-term trends after the 1991–1997 period, indicates a change in saline pan conditions. Long-term density decreases ceased and salinity increased after the 1991–1997 period in the halite nucleus and TZE shallow aquifer (Figure 9A). On smaller timescales, brine extracted for potash production shows an increase in salinity following the onset of the laydown in 1998. Later, an increase in salinity occurred when brine extraction greatly decreased as the laydown continued (Figure 3A to C).

The onset of the laydown coincides with a marked decrease in alluvial-aquifer groundwater levels. Declining levels, in turn, reversed hydraulic gradients, enabling basinal brine movement away from the saline pan (as seen in density and isotopic changes) (Figure 16). Careful consideration of the underlying forces driving changes in brine chemistry, primarily density and water stable isotopes (e.g., laydown, decrease in brine extraction, or long-term groundwater consumption trends), is needed to identify the core controls on change that will influence management decisions.

Potential Controls on Brine Chemistry Change

Laydown

A cessation in long-term density decreases and an increase in density in the halite nucleus and TZE shallow aquifers that is concurrent with the laydown was observed. Similarly, extracted brines for potash production showed increased density in the 3- to 5-year period after the laydown began. These observations support White's (2004) hypothesis that the laydown failed to lead to a 4–5 cm increase in halite thickness because it buffered salinity decreases in the shallow brine aquifer. Although increases in aquifer density are concurrent with the onset of the laydown, changing potash brine extraction rates may have had a larger impact on observed changes in groundwater density than the laydown.

An δ^2H isotopic lightening in both halite nucleus crust brines and shallow aquifer waters over time was observed; in the absence of other information, this lightening could be attributed to isotopically lighter laydown waters. However, isotopic measurements from the east of ditches area (which is isolated from

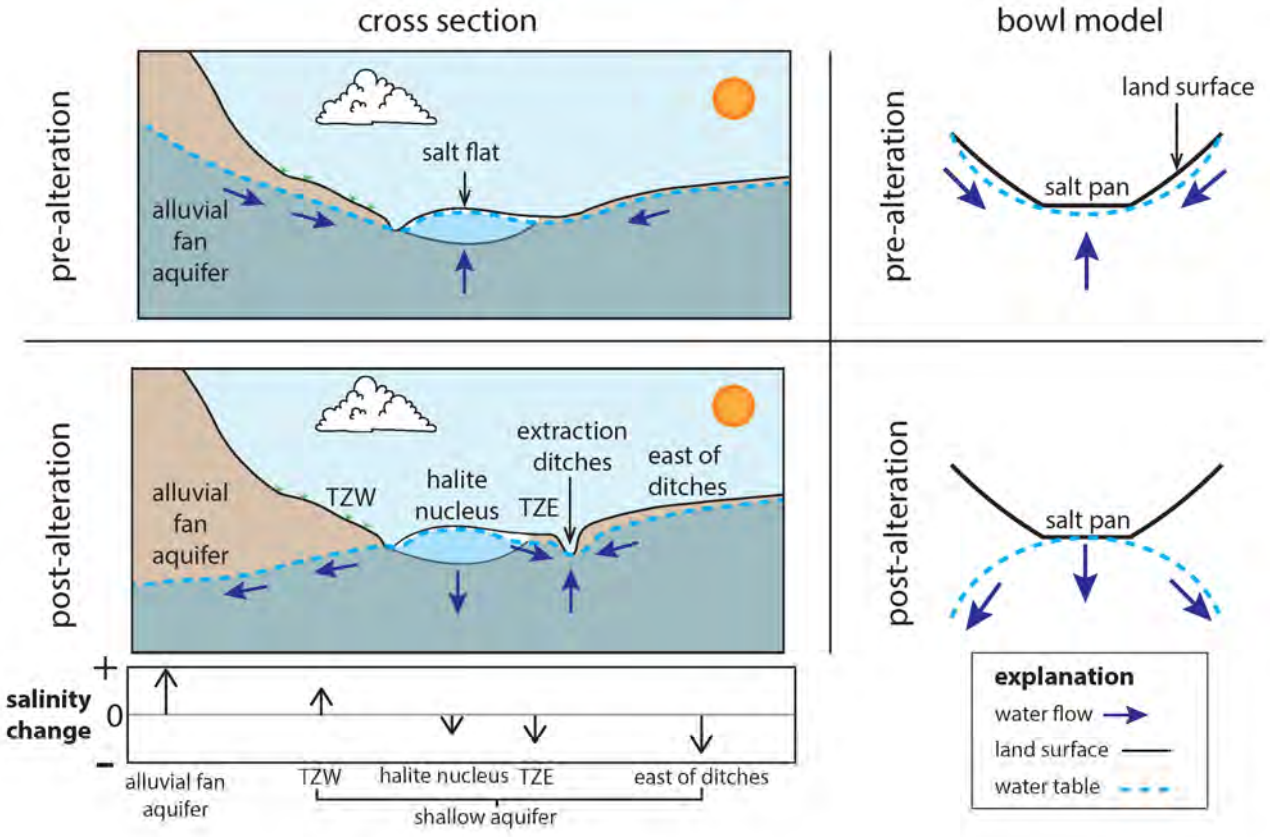

Figure 16. *Conceptual model for pre-alteration and modern groundwater (and brine) movement at BSF shown in cross section (left) and as a simplified conceptual model (right).*

laydown waters) show the same lightening over time. Therefore, a different mechanism, possibly increased infiltration of meteoric precipitation, may explain observed changes.

Changing Brine Extraction Rates

BSF brine extraction volumes before 1995 are poorly reported, leading to high uncertainty in estimated extraction volumes (Figure 9B). The average extraction volumes during the 1964–1972 and 1975–1981 periods may have been similar to or higher than those reported between 1995 and 1998. Measurements from 1999 to 2023 show stabilizing to increasing density in the halite nucleus and TZE shallow aquifers. There is a corresponding decrease in brine extraction during this period, with the largest increase in the halite nucleus shallow aquifer salinity corresponding to the greatest decrease in extraction rates. This relationship suggests that reduced extraction rates may contribute to some (and possibly most) of the observed density increases in these areas.

Examination of increasing sulfate concentrations over time relative to decreasing density in the halite nucleus and I-80 south areas shallow aquifers indicates these two values are related (Figures 9 and S7). This relationship suggests a mechanism for brine replacement after extraction. The moderate depth aquifer has elevated sulfate concentrations. When groundwater is extracted for mining, it lowers the constraining hydrostatic pressure, enabling deeper, less saline groundwater with higher sulfate concentrations to rise and replace extracted waters.

There is a positive correlation between extracted brine density and potash production brine extraction volumes (Figure 3D). Using that relationship, anticipated changes in density based on extracted brine volumes over time were modeled. While not reflecting observed density measurements (modeled density of 1.10 to 1.15 g/cm^3 between 2002 and 2010, when observed density was ~1.17 to 1.21 g/cm^3), modeled density did replicate trends in brine density change for some periods. The model replicates observed trends between 2002 and 2006 where it shows increasing and then decreasing density; it also shows increasing and then stabilized density between 2015 and 2021. Modeled and observed trends strongly differ between 2006 and 2015, where the model shows generally increasing density, while observations show generally decreasing density. These differences between observations and modeled changes suggest 1) extracted brine density may respond non-linearly to extraction rates (and accordingly, there is a lower limit for extracted brine salinity, potentially buffered from the dissolution of the halite crust); and possibly 2) under normal operating conditions (with some extraction and laydown volume of ~0.5 Mt NaCl/year) extracted brine salinity (and aquifer salinity) will decrease; additionally, 3) the large initial laydown pulse between 1998 and 2000 increased the salinity of extracted brines beyond their anticipated baseline.

Brine extraction can also depress local groundwater levels (Turk, 1973). These declines may enable infiltration of surface waters into the subsurface before they can evaporate. Isotopic lightening of the shallow aquifer (Figure 11A) may be attributed to the incorporation of isotopically lighter winter precipitation into the aquifer before significant evaporation occurred.

Given these observations, especially that changes in salinity can be attributed to extraction rates, the relative role of the laydown in increasing TZE and the halite nucleus shallow aquifer salinity remains unclear. It may be that a solute source (such as a halite crust or laydown brines) is necessary for density values to recover. Recent work on the sedimentology of BSF salt crusts documented extensive evidence of halite dissolution, suggesting that the diminishing crust is a likely source of these solutes (Bernau and Bowen, 2021).

Declining TZW Groundwater Levels

Two areas of increasing salinity were identified in the inner TZW shallow aquifer, and a long-term aggregate trend in increasing salinity in the outer TZW shallow aquifer was also found. Kipnis (2021) and Lines (1979) noted decreasing groundwater levels in these areas. Furthermore, several dry outer TZW shallow wells were noted during this investigation. Two mechanisms for increasing TZW shallow aquifer salinity are proposed: 1) the TZW inner area receives brine from the halite nucleus aquifers and surface precipitation, and 2) salinity that was once concentrated at the surface by efflorescence and then recycled basinward now accumulates in groundwater as the capillary fringe falls below the ground surface. Flow of halite nucleus brine to the inner TZW area may be enhanced by declining TZW hydraulic head. Furthermore, there is the potential for laydown brines (which accumulate on the western halite nucleus edge) to enter the TZW area.

Several observations, such as declining western halite nucleus shallow aquifer salinity and areas of inner TZW with increasing salinity, support the interpretation that westward movement of shallow aquifer brine contributes to recent declines in BSF crust thickness. Between the 2003 and 2016 salt crust thickness studies, the area on the southwestern side of BSF had some of the largest observed decreases in salt crust thickness. This area is also the closest part

of BSF to the alluvial-fan production wells. During the same period, the northernmost parts of the BSF crust reduced in volume; those declines may be attributable to their distance from the thickest part of the halite crust.

The alluvial-fan aquifer shows several significant changes over time. The decline in groundwater levels has reversed the hydrological gradient such that basinal waters now flow toward the mountain front. The movement of basinal waters toward the mountain front is demarcated by changes in brine density and δ^2H and $\delta^{18}O$ isotopes. Formerly fresh production wells now produce waters that exceed the salinity of the ocean (~35 ppt or 1.03 g/cm^3). These changes indicate that basinal brine (possibly the halite nucleus shallow and crust aquifer brine) is being removed from the saline pan area (Figure 16). Isotopic and density data should be considered to determine the relative sourcing of waters extracted by production wells to estimate how much brine will be removed from the halite nucleus area under different alluvial-fan extraction scenarios.

Climate Does Not Explain Observed Alluvial-Fan Groundwater Level Declines

Between 1993 and 2010, there were frequent drought periods, with the majority of years experiencing precipitation levels below the 25% quartile for precipitation based on data from 1910 to 2020 (Bernau, 2022). Before the 1990s, alluvial-fan aquifer levels varied but regularly returned to the land surface. In the period since then, they have shown a clear long-term decline that strongly differs from observations of similar alluvial-fan aquifer wells in the GSLD, which have remained relatively stable to slightly increasing over this period (NWIS, https://maps.waterdata.usgs.gov/mapper/index.html, sites 404757112582701 and 394905113354101). These data indicate that recent declines in the alluvial-fan aquifer are occurring because extraction rates have exceeded recharge rates for over two decades.

Impact of Laydown on Alluvial-Fan Aquifer Drawdown

Before 1997, the alluvial-fan groundwater level remained within 0 to 7 m of the surface (Kipnis and Bowen, 2018; Mason and Kipp, 1998). Following the laydown, groundwater levels never rose above 10 m below ground level and have continued to decline (Figure 3E). This suggests that groundwater levels have not yet reached a new equilibrium where inflow is equal to pumping rates and a larger area will be drained over time. The relative proportion of basinal water in produced alluvial aquifer waters will increase as this area expands. The laydown has led to as much as a doubling in alluvial groundwater extraction, and as such, plays a major role in decreasing alluvial-fan groundwater levels.

CONCLUSIONS

New chemical and groundwater level measurements and past research were compiled to examine multi-decadal changes at the Bonneville Salt Flats. Brine chemistry, most notably density and δ^2H and $\delta^{18}O$ water isotopes, has changed in response to anthropogenic activities (Figure 16). Shallow aquifer brine under and to the east of the crust declined in salinity between 1964 and 1997 and stabilized and increased in salinity afterward. Increased salinity may be due to decreased extraction rates in the past two decades, especially as the largest increase in salinity, during the 2013–2023 period, is concurrent with the largest decrease in extraction. However, this period is also concurrent with the experimental salt restoration laydown program. The relative role of the laydown in increasing aquifer salinity remains unclear. Alluvial aquifer groundwater levels have declined over time. This decline is linked to industrial water production, including the laydown. As a result, the hydraulic gradient has reversed, causing brine to flow away from the saline pan and towards the alluvial aquifer. This flow increases alluvial fan aquifer salinity and changes its isotopic composition. If alluvial-fan extraction rates remain the same, or if they rise with increases to the laydown, more salt will be removed from the Bonneville Salt Flats halite nucleus, potentially at volumes exceeding the laydown. These multi-decadal chemical changes inform the understanding of groundwater movement and halite crust changes in this system, which informs management for the sustained use of this landscape.

Supplemental Data

Supplemental data and figures are available at https://doi.org/10.5281/zenodo.8152647.

ACKNOWLEDGMENTS

The authors acknowledge that this study was conducted on traditionally Newe/Western Shoshone and Goshute lands. The authors would like to acknowledge Craig Peterson and Russ Draper with Intrepid Potash; Todd Marks, Roxanne Tea, Steve Allen and other past and current U.S. Bureau of Land

Management West Desert Field Office staff; Hannah Stinson, Lily Wetterlin, Olivia Watkins, Candace Penrod, Gabë Regenhardt, and Dr. Anna Cassell from the University of Utah; and Paul Inkenbrandt, Hugh Hurlow, and Greg Gavin of the Utah Geological Survey for assistance with data collection and sample analysis. This manuscript was improved through reviews and discussion with Greg Carling, Stephanie Carney, Scott Hynek, Michael Hylland, and Elliot Jagniecki. Torrie Duncan and John Good contributed to refining some of the figures in this report. Cryogenic vacuum extraction of brine samples was made possible by Suvankar Chakraborty, Dr. Jim Ehleringer, and Dr. Gabe Bowen at the University of Utah SIRFER Lab. Bill White provided unpublished field notes contributing to this work. Funding for this work was provided by an NSF Coupled Natural Human Systems Award #1617473, the United States Geological Survey, the Utah Geological Survey, the Utah State Legislature, the Bureau of Land Management, and the University of Utah Global Change and Sustainability Center Graduate Research Grants.

REFERENCES

Agapito Associates, Inc., 2022, Technical Report Summary of 2021 Estimated Resources and Reserves at Intrepid Potash-Wendover, 262 p.

Bernau, J.A., 2022, Spatial and temporal scales of water and salt movement at the Bonneville Salt Flats: Salt Lake City, University of Utah, Ph.D. dissertation, 195 p.

Bernau, J.A., and Bowen, B.B., 2021, Depositional and early diagenetic characteristics of modern saline pan deposits at the Bonneville Salt Flats, Utah, USA: Sedimentology, p. sed.12861.

Bernau, J.A., Jagniecki, E.A., Kipnis, E.L., and Bowen, B.B., 2023a, Applications and limitations of portable density meter measurements of Na-Ca-Mg-K-Cl-SO_4 brines: Chemical Geology, v. 616, p.121240

Bernau, J.A., Oviatt, C.G., Clark, D.L. and Bowen, B.B., 2023b, Sediment logs compiled from the Great Salt Lake Desert, western Utah, with a focus on the Bonneville Salt Flats area: Utah Geological Survey Open-File Report 754, 24 p., 3 appendices, https://doi.org/10.34191/OFR-754.

Bethke, C.M., 2013, Geochemical and biogeochemical reaction modeling: Cambridge University Press, Cambridge, UK, p.1689–1699.

Bingham, C.P., 1980, Solar production of potash from the brines of the Bonneville Salt Flats: Utah Geological and Mineral Survey Bulletin, v. 116.

Bowen, B.B., Kipnis, E.L., and Pechmann, J.M., 2018, Observations of salt crust thickness change at the Bonneville Salt Flats from 2003-2016, *in* Emerman, S.H., Bowen, B.B., Simmons, S., and Schamel, S. editors, Geofluids of Utah: Utah Geological Association Publication 47, p. 247–285.

Bowen, B.B., Kipnis, E.L., and Raming, L.W., 2017, Temporal dynamics of flooding, evaporation, and desiccation cycles and observations of salt crust area change at the Bonneville Salt Flats, Utah: Geomorphology, v. 299, p. 1–11.

Dansgaard, W., 1964, Stable isotopes in precipitation: Tellus, v. 16, no. 4, p. 436–468.

Hadzeriga, P., 1964, Some aspects of the physical chemistry of potash recovery by solar evaporation of brines: Society of Mining Engineers, v. 013, p. 169–174.

Harvie, C.E., Moller, N., and Weare, J.H., 1980, The prediction of mineral solubilities in natural waters—the Na-K-Mg-Ca-Cl-SO_4-H_2O system from zero to high concentration at 25°C: Geochimica et Cosmochimica Acta, v. 44, no. 7, p. 981–997.

Hipel, K.W., and McLeod, A.I., 1994, Time series modelling of water resources and environmental systems: Elsevier Science, Amsterdam, Netherlands.

Kipnis, E.L., 2021, Geologic change, hydrologic drivers, and resource use at the Bonneville Salt Flats, Utah, USA: Salt Lake City, University of Utah, Ph.D. dissertation, 100 p., 2 appendices.

Kipnis, E.L., and Bowen, B.B., 2018, Observations of salt crust change from 1960-2016 and the role of humans as geologic agents at the Bonneville Salt Flats, Utah, *in* Emerman, S.H., Bowen, B.B., Simmons, S., and Schamel, S. editors, Geofluids of Utah: Utah Geological Association Publication 47, p. 287–303.

Kipnis, E.L., Bowen, B.B., Hutchings, S.J., Hynek, S.A., and Benison, K.C., 2020, Major ion geochemistry in Na-Ca-Mg-K-Cl-SO_4 brines using portable X-ray fluorescence spectrometry: Chemical Geology, v. 558, no. September, p. 119865.

Lerback, J.C., Hynek, S.A., Bowen, B.B., Bradbury, C.D., Solomon, D.K., and Fernandez, D.P., 2019, Springwater provenance and flowpath evaluation in Blue Lake, Bonneville basin, Utah: Chemical Geology, v. 529, no. April, p. 119280.

Lindenburg, G.J., 1974, Factors contributing to the variance in the brines of the Great Salt Lake Desert and the Great Salt Lake: Salt Lake City, University of Utah, M.S. thesis, 70 p.

Lines, G.C., 1978, Selected ground-water data, Bonneville Salt Flats and Pilot Valley, western Utah: U.S. Geological Survey Utah Basin-Data Release, no. 30, 14 p.

Lines, G.C., 1979, Hydrology and surface morphology of the Bonneville Salt Flats and Pilot Valley playa, Utah: U.S. Geological Survey Geological

Survey Water-Supply, v. 2057, no. 2057, p. 1–107.

Mason, J.L., Brothers, W.C., Gerner, L.J., and Muir, P.S., 1995, Selected hydrologic data for the Bonneville Salt Flats and Pilot Valley, western Utah, 1991-93: U.S. Geological Survey Open-File Report, v. 95–104, p. 1–56.

Mason, J.L., and Kipp, K.L., 1998, Hydrology of the Bonneville Salt Flats, northwestern Utah, and simulation of ground-water flow and solute transport in the shallow-brine aquifer: U.S. Geological Survey Professional Paper, v. 1585, p. 108.

McLeod, A.I., 2022, Kendall Rank Correlation and Mann-Kendall Trend Test. R code

Munk, L.A., Boutt, D.F., Moran, B.J., McKnight, S. V., and Jenckes, J., 2021, Hydrogeologic and geochemical distinctions in freshwater-brine systems of an Andean salar: Geochemistry, Geophysics, Geosystems. v. 22, no. 3, 20 p. https://doi.org/10.1029/2020GC009345

Nolan, T.B., 1927, Potash brines in the Great Salt Lake Desert, Utah, Chapter B, *in* Contributions to economic geology (short papers and preliminary reports): U.S. Government Printing Office, p. 25–44.

Oviatt, C.G., Clark, D.L., Bernau, J.A., and Bowen, B.B., 2020, Data on the surficial deposits of the Great Salt Lake Desert, Bonneville Salt Flats and east part of the Wendover 30’ x 60’ quadrangles, Tooele County, Utah: Utah Geological Survey Open-File Report, 70 p.

Penrod, C.L., 2016, The geochemistry of meteoric water and surface-pond brines at Bonneville Salt Flats, UT: Salt Lake City, University of Utah, M.S. thesis, 30 p.

Pitzer, K.S., 1973, Thermodynamics of electrolytes–I—Theoretical basis and general equations: Journal of Physical Chemistry, v. 77, no. 2, p. 268–277.

Plummer, L.N., Parkhurst, D.L., Fleming, G.W., and Dunkle, S.A, 1988, A computer program incorporating Pitzer’s equations for calculation of geochemical reactions in brines: U.S. Geological Survey, Water-Resources Investigations Report, v. 88–4153, p. 707–720.

Post, V., Kooi, H., and Simmons, C., 2007, Using hydraulic head measurements in variable-density ground water flow analyses: Ground Water, v. 45, no. 6, p. 664–671.

R Core Team, 2021, R: A language and environment for statistical computing, R Foundation for Statistical Computing, Vienna, Austria. https://www.r-project.org/

Radwin, M.H., and Bowen, B.B., 2021, Mapping mineralogy in evaporite basins through time using multispectral Landsat data—Examples from the Bonneville basin, Utah, USA: Earth Surface Processes and Landforms, v. 46, no. 6, p. 1160–1176.

Read, E.K., Carr, L., De Cicco, L., Dugan, H.A., Hanson, P.C., Hart, J.A., Kreft, J., Read, J.S., and Winslow, L.A., 2017, Water quality data for national-scale aquatic research: The Water Quality Portal, Water Resources Research, v. 53, no. 2, p. 1735–1745.

Shaw Environmental, 2020, Intrepid Potash Mine and Reclamation Plan, submitted to Utah Division of Oil, Gas, and Mining: 1943 p., https://ut-dnr-ogm-prod-sf-public-bucket.s3.amazonaws.com/5624847.pdf

Shuey, R.T., 1971, Paleomagnetic chronology and correlation of Great Salt Lake basin sediments: Washington D.C., National Science Foundation, Final Technical Report for grant GA-16134, 15 p.

Soil Survey Staff, Natural Resources Conservation Service, United States Department of Agriculture, undated, Web Soil Survey. Available online: https://websoilsurvey.nrcs.usda.gov/app/WebSoilSurvey.aspx, accessed March 2023.

Stephens, J.C., 1974, Hydrologic reconnaissance of the northern Great Salt Lake Desert and summary hydrologic reconnaissance of northwestern Utah: United States Geological Survey, 55 p.

National Water Quality Monitoring Council, undated, The Water Quality Portal, https://www.waterqualitydata.us/, accessed November, 2022.

Turk, L.J., 1973, Hydrogeology of the Bonneville Salt Flats, Utah: Utah Geological and Mineral Survey, 82 p.

Turk, L.J., Davis, S.N., and Bingham, C.P., 1973, Hydrogeology of lacustrine sediments, Bonneville Salt Flats, Utah: Economic Geology, v. 68, no. 1, p. 65–78.

Utah Division of Natural Resources, undated, Water Rights database: https://www.waterrights.utah.gov/wrinfo/query.asp, accessed November, 2022.

White, W.W., 2002, Salt Laydown Project—Replenishment of Salt to the Bonneville Salt Flats, in Gwynn, J.W., editor, Great Salt Lake: An Overview of Change: Utah Geological Survey Special Publication, p. 433–486.

Wilkinson, G.N., and Rogers, C.E., 1973, Symbolic description of factorial models for analysis of variance: Journal of the Royal Statistical Society, Series C, v. 22, no. 3, p. 392–399.

Bonneville Basin Critical Zones: Spring Chemistry and Gastropod Ecology in Playa-Margin Wetlands

Jory C. Lerback [1], Brenda B. Bowen[2,4], Sam Bagge[2], Mikelia Heberer[2], Ryan Cocke[2], and Hayley L. Bricker[3]

[1]*Nuclear and Chemical Sciences Division, Lawrence Livermore National Laboratory, Livermore, California, lerback1@llnl.gov*

[2]*Department of Geology and Geophysics, University of Utah, Salt Lake City, Utah*

[3]*Department of Earth, Planetary and Space Sciences, University of California, Los Angeles*, California

[4]*Global Change and Sustainability Center, University of Utah, Salt Lake City, Utah*

10.31711/ugap.v51i.144

ABSTRACT

Playa margin wetlands in the Bonneville basin are sustained by groundwater-fed brackish springs, which transport salts and other solutes into the playa basin. These wetlands are sensitive to changing water availability and quality, which are impacted by changing climate and land use, and whose sediments also provide important records of changing environmental conditions. Gastropods building their shells in these springs provide important recorders of water chemistry and may reflect changing aqueous conditions. In this paper, we analyze spring water chemistry, gastropod ecology and gastropod shell chemistry of Blue Lake (BL) and Horseshoe Springs (HRS), two groundwater-fed wetlands in the Great Salt Lake watershed. We report the physical parameters including pH, temperature, and specific conductivity across the spring pond at Horseshoe springs. There was a slight but statistically significant variation in these physical characteristics between the deeper and shallower parts of the pool, providing evidence that there are different subsite microclimates, which may impact the populations and the isotopic composition of gastropod shells. We measured gastropod population diversity amongst nearly 12,000 shells sampled at Horseshoe springs, finding low population diversity (Shannon's Diversity Index of 0.432), although the populations of shallow and deep snails are slightly different. The dominant snail at HRS is the *Pyrgulopsis* which is imperiled, and we also note that we did not find living snails here. We evaluated the bulk shell variation of stable carbonate isotopes ($\delta^{13}C$, and $\delta^{18}O$) across sites and genera. We show that there were no significant subsite-level differences in gastropod $\delta^{13}C$ compositions, suggesting that water depth and productivity were not impacting the isotopic signal. We found subsite- and genera-specific differences in snail $\delta^{18}O$ compositions, which we interpret to be more dependent on the geography and microclimate of where the snail lived rather than the genera's physiology (pulmonate versus gil -breathing). We report concentrations of alkali metals (Li, Na, K, Rb, Cs), alkali earth metals (Be, Mg, Ca, Sr, Ba), and metals and metalloids (Al, Sc, Mn, Fe, Cu, Ni, Zn, As) at spring site waters and in bulk shells as potential baseline data for interpreting future or past environmental changes as recorded in shell material. We found trace element concentration and certain elemental ratio differences between genera at the same site (particularly of note were Li, Zn, Mn and Al) that will be important to constrain if these shells are to be applied as a paleoenvironmental proxy and are sometimes attributed to land use change.

Keywords: hydrology, isotopes, carbon, groundwater, gastropod, critical zone

INTRODUCTION

Earth's critical zone encompasses the interactions between the biosphere, atmosphere, hydrosphere, and lithosphere from the top of vegetation to the bedrock (U.S. National Research Council, 2001; Anderson and others, 2007; White and others, 2015). The critical zone is linked to anthropogenic activity, from soil formation's relationship with agricultural production to landscape modifications impacting the hydrologic cycle and water resources (Brantley and others, 2007; Fan and others, 2019; Fovet and others, 2021; Minor and others, 2020). Groundwater-fed wetlands are, like many critical zone ecosystems, susceptible to changes in climate, water quality, air quality, and other effects of human impacts including recreation, agriculture and urbanization (Miguez-Macho & Fan, 2012; Singha & Navarre-Sitchler, 2022; Torgeson and others, 2022). Groundwater-fed wetlands also provide sedimentary records of critical zone (particularly hydrological) processes over time, termed paleo-critical zones by Ashley (2020), which help to calibrate and extend the temporal scales by which we understand the feedbacks between groundwater and climate.

Playa margin wetlands in the Bonneville basin are sustained by brackish to saline springs, transporting salts into the playa basin (Lerback and others, 2019). Louderback and Rhode (2009) estimate the discharge rate of 1.6 cubic meters per second or $5x10^{10}$ L/yr at

Blue Lake (BL), one of the two springs in this study. Lerback and others (2019) reported a slightly lower annual discharge rate of $1.3x10^{10}$ L/yr, and report measured Na concentration ranging between 1400-1600 mg/L from 2016-2018. Using these values, and assuming no recirculation of playa solutes in these springs, we estimate that BL annually brings from 2.0×10^{13} - 7.5×10^{13} mg of sodium to the playa sediments annually (between 22,000-83,000 tons). Considering these salt accumulation rates and long timescales since glacial Lake Bonneville exposed these spring sites, brackish playa margin springs like BL may be an important component of Bonneville basin solute budgets. Thus, understanding the chemical history and sustainability of these spring wetlands is useful in future work describing the dynamic solute and water budgets sustaining the ecosystems and industries of the Bonneville basin.

In this paper, we describe two spring-fed wetlands in the relatively under-studied western side of the Great Salt Lake watershed and describe their spring water chemistry by measuring their physical parameters (total dissolved solids, pH, dissolved oxygen, and temperature) and chemical compositions (alkali metals, alkaline earth metals, select metals and metalloids) (Figure 1). We use these parameters to establish baseline chemistry for future monitoring of spring ecosystem functioning. Importantly, these wetlands foster gastropod (snail) populations, including some endemic genera. Gastropod community diversity can serve as a bioindicator of environmental changes, where an environmental change could lead to inhospitable conditions for a relatively homogenous gastropod population (Magurran, 1988; Hershler and others, 2014). Thus, we survey the gastropod communities in these two springs, and provide a baseline of population composition and diversity. Gastropod shell chemistry has been shown to record groundwater chemistry and changing aqueous conditions in the present, setting the stage for evaluating near-future environmental changes, and in the past to contextualize modern environmental change (Abell, 1985; Abell and Williams, 1989; Rosenthal and Katz, 1989; Ayliffe and others, 1996).

We provide some context for using gastropod shells as proxies for environmental change by investigating the variability of modern shell chemistry, using $\delta^{13}C$ and $\delta^{18}O$ and the trace elemental composition of shells (alkali metals, alkaline earth metals, select metals and metalloids) in comparison to water. $\delta^{13}C$ has been used to reflect changes in the carbon cycle, such as changes in carbon inputs (land-plant versus aquatic humus), photosynthesis, dissolved oxygen content (Keith and others, 1964; Aravena and others, 1992; Jin and others, 2021). $\delta^{18}O$ is often used to interpret the water temperatures at the time of carbonate formation (Anadon and others 2006; Immenhauser and others, 2016). While previous work highlights the complexities of using freshwater gastropods as direct stable isotopic proxies (Shanahan and others, 2005), we provide some additional context of differences by genera to understand differences in shell-building processes and potential disruptions to the isotopic utility as paleoenvironmental indicators. Shell chemical compositions, particularly trace elements, also have potential conservation applications as the rapidly building shells incorporate trace elements being introduced to the environment. If new material (particularly if containing heavy metals) is introduced (deposited and bioavailable) to the springs due to land use change, urbanization, air quality, or industry, the shell chemistry and ecology may record these changes, serving as sentinels of environmental change (Rainbow, 2007; Baroudi and others, 2020). Additionally, recent work highlights the potential for shells from gill-breathing gastropods preserved within spring sediments to record changes in groundwater chemistry through time using radiocarbon isotopes (Lerback and others, 2023).

MATERIALS AND METHODS

Site Description

This study describes two perennial spring wetland sites in northwestern Utah, on traditional and ancestral lands of the Newe/Western Shoshone, Goshute, and Ute peoples. The springs in this study are Blue Lake (BL) springs (40.502, -114.033) and Horseshoe Springs (HRS) (40.614, -112.709) in Toole County, Utah. As reported by Lerback and others (2023), BL and HRS spring systems are brackish (with specific conductance measurements above 7000 µS/cm) and mesothermal, with average temperatures between 20° C and 30°C depending on measurement location within the spring pools. These temperatures are higher than mean annual air temperatures of 12°C (Lerback and others, 2023).

Gastropod Physiology

Gastropod genera sampled in this study include *Melanoides, Pyrgulopsis*, *Physella, Tryonia*, *Planorbella*, and *Succineidae* (Figure 2).

Melanoides

M*elanoides* shells found in this study are of the species *tuberculate*. This paper will refer to *Mela-*

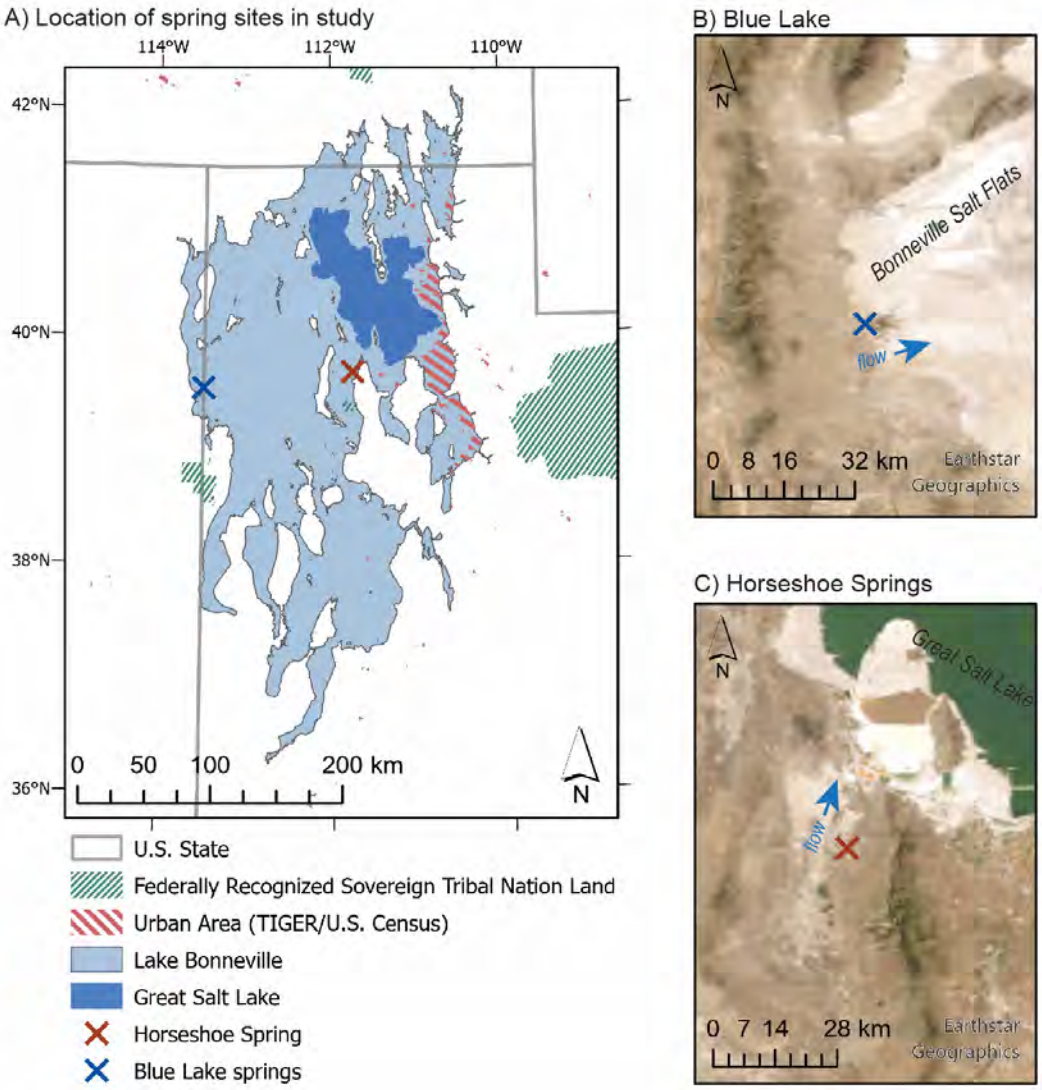

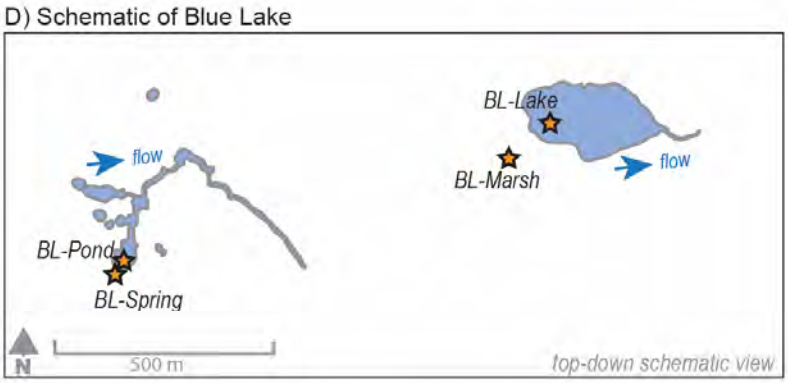

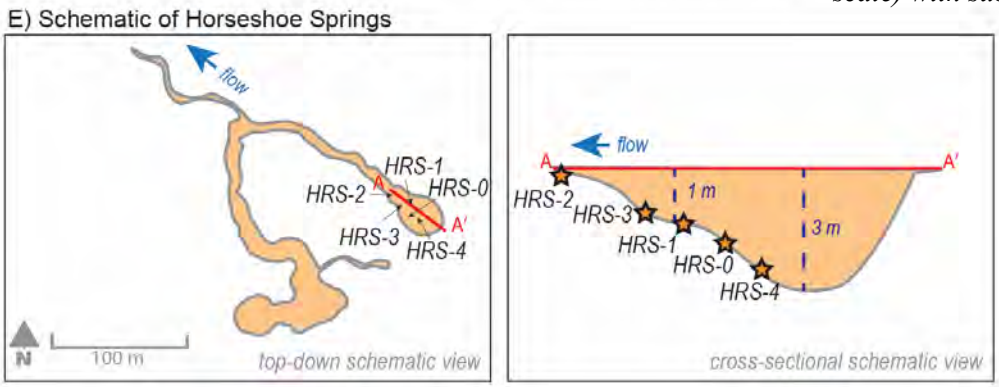

Figure 1. *Site Description. A) Location map of spring wetland sites. B) Satellite image of Blue Lake (BL) wetland at the playa margin. C) Satellite image of Horseshoe Springs (HRS) wetland at the playa margin with the southwest part of the Great Salt Lake. D) Schematic of Blue Lake (BL) from a top-down view with subsites marked. E) Schematic of Horseshoe Springs (HRS) from a top-down view (left) and cross-sectional schematic view (right, not to scale) with subsites marked.*

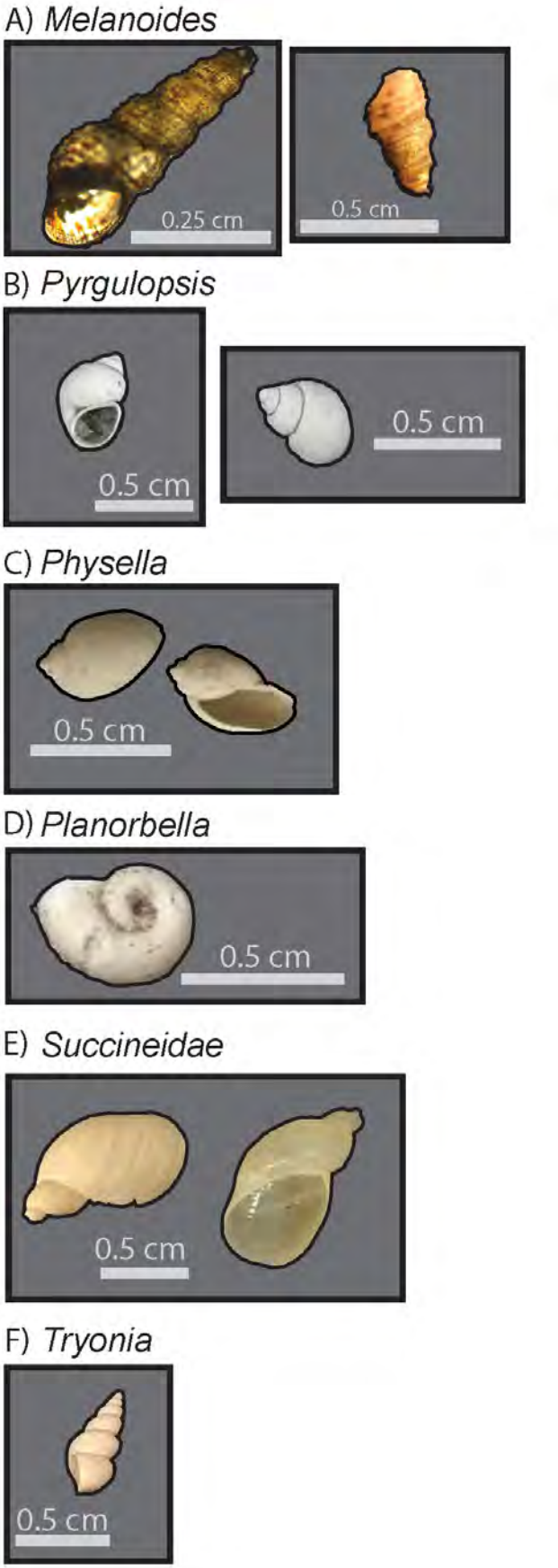

Figure 2. *Gastropod genera found in this study. A) Melanoides, B) Pyrgulopsis, C) Physella, D) Planorbella, E) Succineidae, and F) Tyronia.*

noides tuberculate as the genus only for consistency with the other genera described here. *Melanoides* is a prosobranch (gill-breathing), fully aquatic freshwater spring snail native to tropical Africa and Asia. *Melanoides* was first introduced to North America via the aquatic trade during the 1930s and has continued to spread across the continent into warm regions such as the Great Basin (Murray, 1971). *Melanoides* is an invasive species (Dudgeon, 1986; Facon and others, 2003; Raw and others, 2016). This species likes to burrow into the spring substrate during daylight hours and can therefore be difficult to detect in locations where it has recently been introduced (Subda Rao and Mitra, 1982). They may vary in size from 20 to 40 mm with a lifespan of about 2 – 3.5 years (Berry and Kadri, 1974; Dudgeon, 1982; Livshits and Fishelson, 1983; Pointier, 1989). *Melanoides* is less sensitive to salinity conditions than it is to temperature range, with an optimal growth range of 18 – 31^{o}C (Murray, 1971; Russo, 1973; Roessler and others, 1977; Neck, 1985; Bolaji and others, 2011). When optimal conditions are consistent and abundant, *Melanoides* may reach population densities of up to 6452 m^{-2}, as was found in a study conducted at Fish Springs National Wildlife Refuge by Rader et al. 2003. This is attributed to the species reproducing asexually (parthenogenetic), reproducing more than once in its lifetime as well as early in the life cycle (iteroparous), and by developing offspring internally (viviparous).

Pyrgulopsis

Pyrgulopsis sp. are one of the largest genera in the family Hydrobiidae, which are a family of prosobranch (gill-breathing) snails. They are the second most common Hydrobiidae genera in North America, specifically in Utah, Nevada, and Idaho, and are typically found in moist wetland areas such as the benthos of lakes and springs (Hershler, 1994). Measuring about 1 – 8 mm in shell length, individuals typically cluster with densities greater than 1000 m^{-2} (Hershler, 1994). They may grow to a length of 2.5 mm (Hershler and Sada, 1987). The temperature range of living specimens falls between 22 – 35^{o}C (Hershler, 1994). Individuals are typically found near spring groundwater discharge areas (Hershler and others, 2014). *Pyrgulopsis* sp. are very sensitive to climatic and environmental changes, which stem from members of this genus diversifying due to their regional separation and isolation; although individual species may live in a range of environments (e.g. temperatures, salinities, CO_2 concentrations), perturbations to these constant conditions can greatly disturb populations (Pearson and others, 2014). They are considered imperiled (Turgeon and others, 1998).

Tyronia

Tyronia sp. is another genera part of the Hydrobiidae family and is restricted to North America. Like its fellow Hydrobiid genera, *Tyronia* sp. are fully aquatic and typically prefer to inhabit thermal springs. Their dispersion is slow and may be linked to drainage history, making them key biogeographical indicator genera (Hershler and others, 1999). Some species may be quite salinity tolerant (Hershler and others, 1999). Shells can range between 1.2 – 7 mm in length (Hershler and Sada, 1987).

Physella

Physella sp. are part of subfamily Physinae, which are pulmonated (lung-breathing) freshwater spring snails. They are difficult to identify based on morphology alone (Young et al., 2021). *Physella* sp. are capable of self-fertilization (parthenogenesis), which may contribute to rapid evolution amplified by isolation or thermally different habitats (Perrin, 1986). They typically reproduce annually (Russell-Hunter, 1978). Observationally, *Physella* sp. have been known to inhabit waters with temperatures of 8 – 35^{o}C. Shell length can grow to 14 mm in very warm water temperatures, indicating that growth is temperature-dependent (McMahon, 1975).

Planorbella

Planorbella sp. are part of family Planorbidae and is a freshwater gastropod genus restricted to North America (Baker, 1945). Members of this genera are hermaphroditic and may rely on self-fertilization for reproduction (Martin and others, 2020). They have been shown in studies to be optimally active between 26 - 28^{o}C, with minimum and maximum optimal thresholds appearing to occur at 18^{o}C and 33^{o}C, respectively. (El-Emam and Madsen, 1982).

Succineidae

Succineidae are a family of minute taxa of pulmonated (lung-breathing) land snails that typically inhabit wetland areas worldwide (Pilsbry, 1948; Patterson, 1971). Genera are typically found on vegetations near streams or marshes, or where dew might be present. There may be extreme differences in morphological features such as size and shell shape, between genera within *Succineidae*. They are hermaphroditic and can reproduce through mutual fertilization or self-fertilization.

Experimental Design

We measured physical and chemical parameters using a multiparameter probe in the spring to understand circulation within the spring pond. We measured probe depth (m), Total Dissolved Solids (TDS in ppt), pH, Dissolved Oxygen (DO in mg/L) and temperature (°C) using an Aqua TROLL 600 Multiparameter Sonde. We recorded these basic physical and chemical parameters of the spring water along a NW-SE transect at HRS to understand the structure of flow and potential circulation within the northern spring pool and stream outlet (Figure 3). The probe recorded the time, which we marked and calibrated to locations marked at 0, 150s, 200s, 250s, 300s, and 345s. Time is used as a proxy for the distance along the transect, as it is not a linear transect. Water samples were collected at the water surface for trace element analyses in High-Density Polyethylene (HDPE) bottles that were washed with 5% HCl and rinsed three times with deionized water. Samples were filtered with a 0.45 μm polypropylene syringe filter and stored with minimal headspace.

At HRS, we sampled bulk sediment at sites HRS-1, HRS-2, HRS-3, and HRS-4 to measure the diversity and density of snail populations. At these four subsites in shallow and deeper waters, we filled one 0.25 L container with bulk sediment. Samples were cleaned at the University of Utah by sieving and rinsing bulk samples with deionized water and soaking the shells in 3% hydrogen peroxide for one hour which served to separate the sediment and organic material from the shells. Snails in sediment samples at each site were identified to the genus level and counted to understand the diversity of taxa across subsites at HRS. Gastropods were collected under a research agreement with the Utah Division of Wildlife Resources (4COLL10642). We used Shannon's Diversity Index to test the diversity of gastropods at HRS, which is a common metric of ecological diversity that takes into consideration the richness and evenness of each of the genera or species collected (Clarke and others, 2014). The equation from Shannon (1948) is

$$H = -\Sigma \frac{\text{number of individuals in species}}{\text{number of individuals in community}} \times ln\left(\frac{\text{number of individuals in species}}{\text{number of individuals in community}}\right) \quad (1)$$

Shells prepared for chemical analysis were cleaned with 3% hydrogen peroxide for one hour to remove organic material, rinsed with deionized water, and then sonicated to further remove organic matter and sediment. Bulk shells were homogenized individually using a mortar and pestle. Four shells were selected to be subsampled along transects from tip to

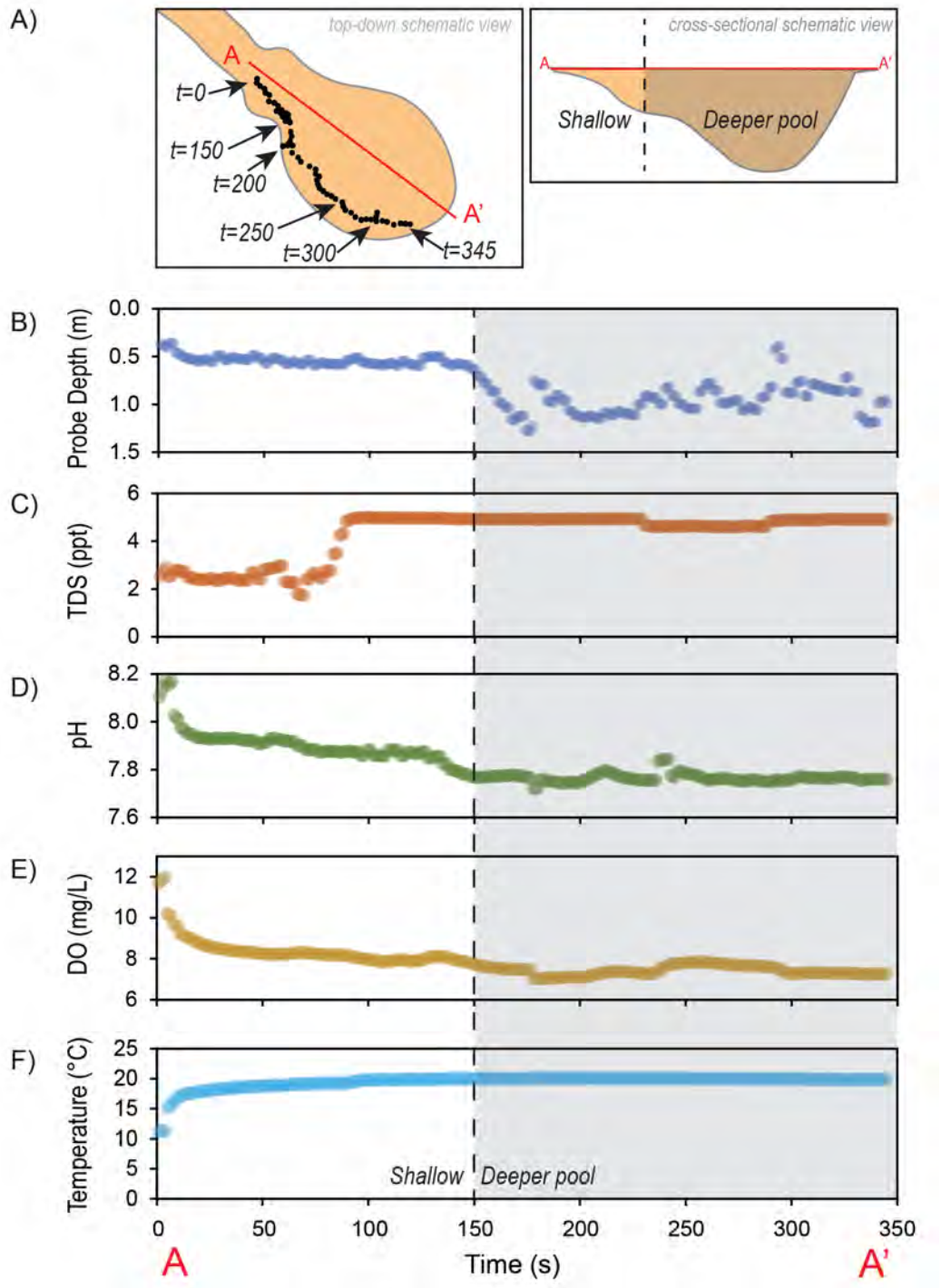

Figure 3. *Physical parameters of water along a transect at HRS. A) Schematic maps of HRS with probe transect locations and select times marked in the left panel, and the bathymetric distinction made between shallow and deep areas of the spring pool on the cross-sectional view in the right panel. B) Probe depth along transect. C) Total Dissolved Solids (TDS) along transect, D) pH along transect. E) Dissolved Oxygen (DO) along transect. F) Water temperature along transect.*

aperture ("intrashell transects") to assess variation in shell chemistry over the snail's lifetime. Intrashell transects were collected at four evenly spaced sub-sites along the long axis of the shell using a micro-drill. *Melanoides* shells from BL-Spring were selected for the intrashell transects due to their relatively larger size.

A total of sixty-four whole gastropod shells (37 from BL and from 27 HRS) and four sub-sampled shells from BL were analyzed at the SIRFER laboratory at the University of Utah. Samples were reacted with orthophosphoric acid and analyzed as CO_2 after cryogenic purification. Samples were analyzed on a Finnigan MAT 252 mass spectrometer. Data are reported using delta notation relative to the Vienna Pee Dee belemnite (VPDB) standard for carbonates and water $\delta^{13}C$ and the Vienna standard mean ocean water (VSMOW) for water $\delta^{18}O$, where analytical precision for $\delta^{13}C$ and $\delta^{18}O$ was ~0.1‰. $\delta^{18}O$-VSMOW values were converted to $\delta^{18}O$-VPDB to directly compare $\delta^{18}O$ of water and shells. An additional 22 shell samples (17 from BL and from five HRS) were added to the dataset here from Lerback and others (2023), where their data were made using the same methods. Analyses including calculation of mean and standard deviations (SD), and statistical tests including analy-

sis of variance (ANOVA) and Tukey's Honestly Significant Difference (HSD) were performed in R v3.6 in RStudio. Comparisons between water and shell isotope values evaluated the fractionation (ε), which is the difference between shell and water isotope values.

Eight shells (four *Succineidae* from BL, three *Pyrgulopsis* and one *Tryonia* from HRS) and four water samples (two from BL and two from HRS) were analyzed for trace element concentrations at the University of Utah's Strontium Isotopes Laboratory using an Agilent 7500ce quadrupole inductively coupled plasma mass spectrometer (ICP-MS).

RESULTS AND DISCUSSION

Spring Water

We evaluated the multiparameter probe data from HRS to understand how the aquatic environment varies within the spring system. We divided the HRS multiparameter probe data from HRS into shallow and deep sections of the pond at time 150s (of a total of 345s recorded) due to the relatively steady depth of the probe measurements (0.5 m depth in the NW section, and 1-1.5 m depth in the SE part of the transect where the shore edge became steep) and the variable depths of the spring pond (Table 1). Over the transect, TDS ranged from 1.7 in the shallow pool to 5.0 ppt in the deeper pool. Average TDS values were 3.6 ppt (SD = 1.2) for the shallow pool and 4.8 ppt (SD = 0.1) for the deeper pool. This difference was significant where ($t(151) = 12.6$; $p < 0.01$). The decrease in TDS values downstream (from shallower to deeper) within the spring may result from fresh water discharging to the shallower spring pool or evapoconcentration in the deep pool. The water pH increased through the transect, with a total mean of 7.8 (SD = 0.08), ranging from a low of 7.7 in the deep section to a high of 8.2 in the shallow areas. The average of the deep section was 7.8 (SD = 0.01), and the shallow section was 7.9 (SD = 0.07), with a significant difference ($t(162) = -22.5$; $p < 0.01$). DO content gradually increased from 7.45 mg/L (SD = 0.22) to 8.1 (SD = 0.78) as the water flowed into the shallower region. This difference was significant where ($t(170) = -15.5$; $p < 0.01$). The temperature was relatively elevated through the transect around 19.5°C (SD = 1.19). The water temperature in the shallow section of the spring was an average of 18.8°C (SD= 1.59. The deep section of the pond water 20.0°C (SD = 0.08), which is warmer than the shallower section ($t(148) = 9.0$; $p < 0.001$). Data for these measurements are provided in Appendix 1.

We measured alkali metals (Li, Na, K, Rb, and Cs), alkaline earth metals (Be, Mg, Ca, Sr, and Ba), and select metals and metalloids (Al, Mn, Fe, Zn) in spring waters (Figure 4 and Appendix 2). Overall, alkali metal concentrations were more abundant at BL than at HRS and were highest at the BL-Marsh site, which is likely due to evapoconcentration in the shallow standing water. Al, Mn, and Fe concentrations in HRS and BL were the 0.04 mg/L detection limit. Although this water is not designated for human consumption, it is worth contextualizing these values as below the National Secondary Drinking Water Standards of 0.05-0.2 mg/L, 0.05 and 0.3 mg/L, respectively (U.S. Environmental Protection Agency, 2009). Although these natural brackish springs are not used for drinking water, we note that these analyses did not have high enough resolution to detect whether the concentrations were below the National Primary Drinking Water Regulations maximum contaminant level for As of 0.01 mg/L (U.S. Environmental Protection Agency, 2009).

Gastropods

Ecological Diversity

Biodiversity is important for protecting the stability of the community which can aid in the overall recovery time from ecological harm that may threaten an ecosystem (e.g., natural disasters, famine, and diseases) (Magurran, 1988). We counted nearly 12,000 gastropod shells across four subsites at HRS, and we note that we did not find any living specimens with organic tissues which needed to be cleaned. We believe that the sampled shells are relatively modern

Table 1. *Water Physical Parameters: Probe Transect Data Summary.*

Parameter	Shallow	Deep	Total
Probe Depth (m)	mean = 0.54	mean = 0.95	mean = 0.77
TDS (ppt)	mean = 3.6, SD = 1.21	mean = 4.8, SD = 0.14	mean = 4.3, SD = 1.01
pH	mean = 7.9, SD = 0.07	mean = 7.8, SD = 0.02	mean = 7.8, SD = 0.08
DO (mg/L)	mean = 8.4, SD = 0.73	mean = 7.4, SD = 0.23	mean = 7.8, SD = 0.69
Temperature (°C)	mean = 18.8, SD = 1.59	mean = 20, SD = 0.08	mean = 19.5, SD = 1.2

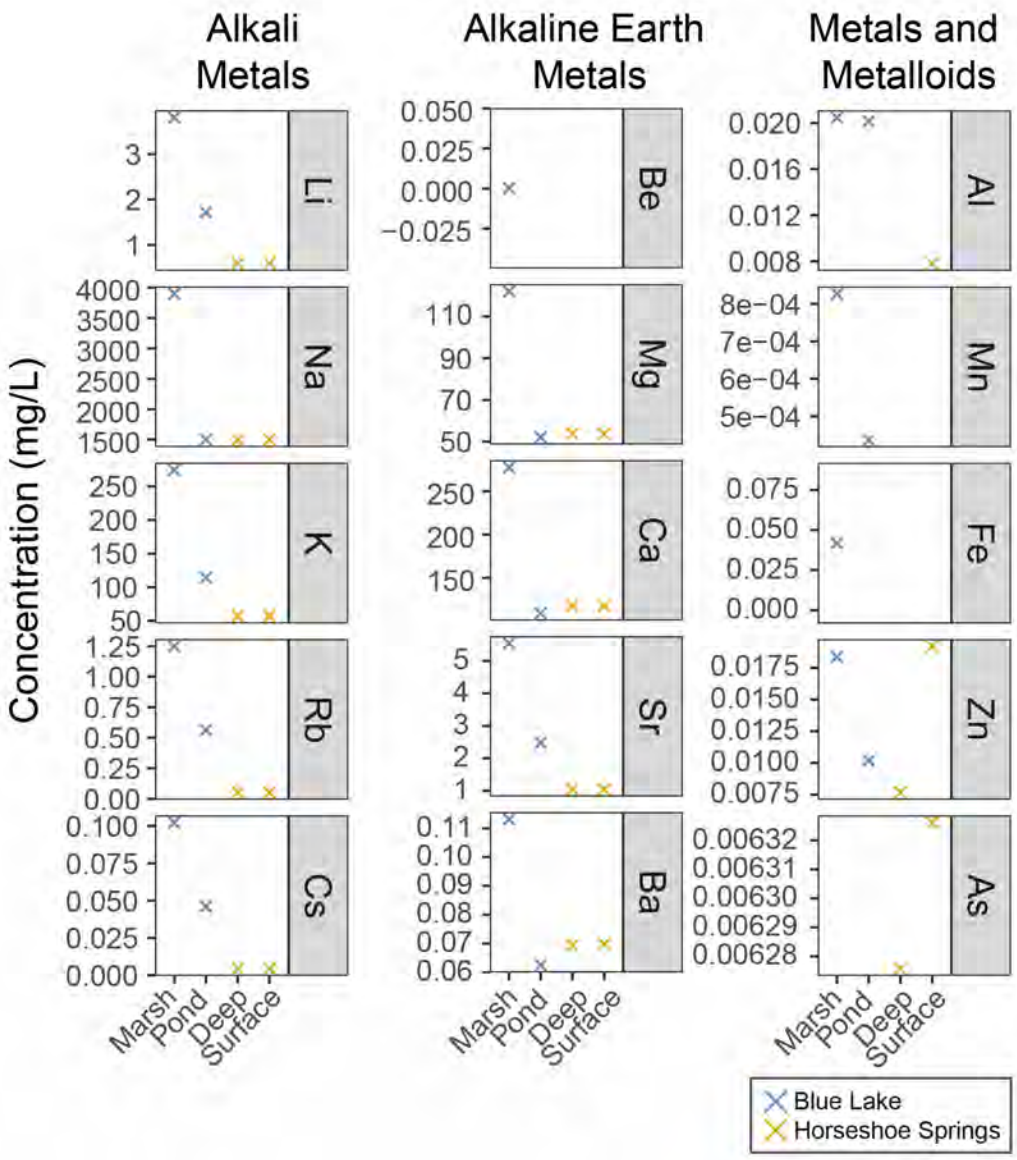

Figure 4. *Trace element concentrations of springwaters. Marsh waters have relatively higher elemental concentrations due to evaporation and relatedly less water input.*

(i.e., not representing shells last alive thousands or hundreds of years ago) based on their sampling location at the surface of the spring sediments but recognize some might represent older shells that could have been brought to the surface by sediment disturbances, e.g., fish burrows in the spring sediments. We counted the number of individuals in each genus to measure the diversity of genera in the ecosystem (Table 2).

The Shannon's Diversity Index at HRS (combining subsites) was 0.432. While the index theoretically ranges from zero to infinity, this value is low compared to other studies where Shannon's Diversity Index often ranges from 1.5-3.5 (Magurran and McGill, 2011; Ifo and others, 2016).

We measured gastropod population diversity differences between the subsites (Figure 1E), which we further grouped into the shallow and deep sections following the distinctions shown in Figure 3A. Subsites HRS-2 and HRS-3 are considered shallow, and subsites HRS-0, HRS-1, and HRS-4 are considered deep (although HRS-0 was not sampled to characterize gastropod diversity). The shallow sediment samples yielded a higher density of shells, where 76% (n = 9087) of individual shells counted were from the shallow samples and both shallow and deep samples had the same volume of sediment collected. *Pyrgulopsis* and *Tyronia* were the most common genera found, with a few *Physella* (n = 18) found in both shallow and deep subsites. While different genera, *Pyrgulopsis* and *Tyronia* are both members of the same gastropod family, and their joint presence may be due to shared preference for similar environmental conditions. A chi-squared (χ^2) analysis of the ob-

Table 2. *Gastropod Population: Count of Individuals in Sampled Community.*

Genera	HRS-1 (Deep)	HRS-2 (Shallow)	HRS-3 (Shallow)	HRS-4 (Deep)
Pyrgulopsis	2404	2149	5253	334
Tyronia	112	72	1596	47
Physella	1	0	17	0

served number of *Pyrgulopsis*, *Tyronia*, and *Physella* genera counted from the shallow versus deep subsites resulted in a χ^2 of 219 ($p < 0.05$), thus indicating a statistically significant difference (albeit small) between populations in the small and deep parts of the HRS pond.

$\delta^{13}C$ and $\delta^{18}O$

Shells were analyzed for $\delta^{13}C$ and $\delta^{18}O$ and compared to Total Dissolved Inorganic Carbon (TDIC) $\delta^{13}C$ and water $\delta^{18}O$ to understand the potential effects of environmentally related and biomediated carbon isotope fractionation (Appendix 3). $\delta^{13}C$ and $\delta^{18}O$ metrics can be representative of environmental conditions during the time of snail activity and can be used as an indicator of source carbon and source water, useful for evaluating environmental changes in the past (recorded in sedimentary records), and in future collections.

Shell samples were aggregated by subsite at BL and HRS (Figure 5A, Table 3). At BL, the subsite av-

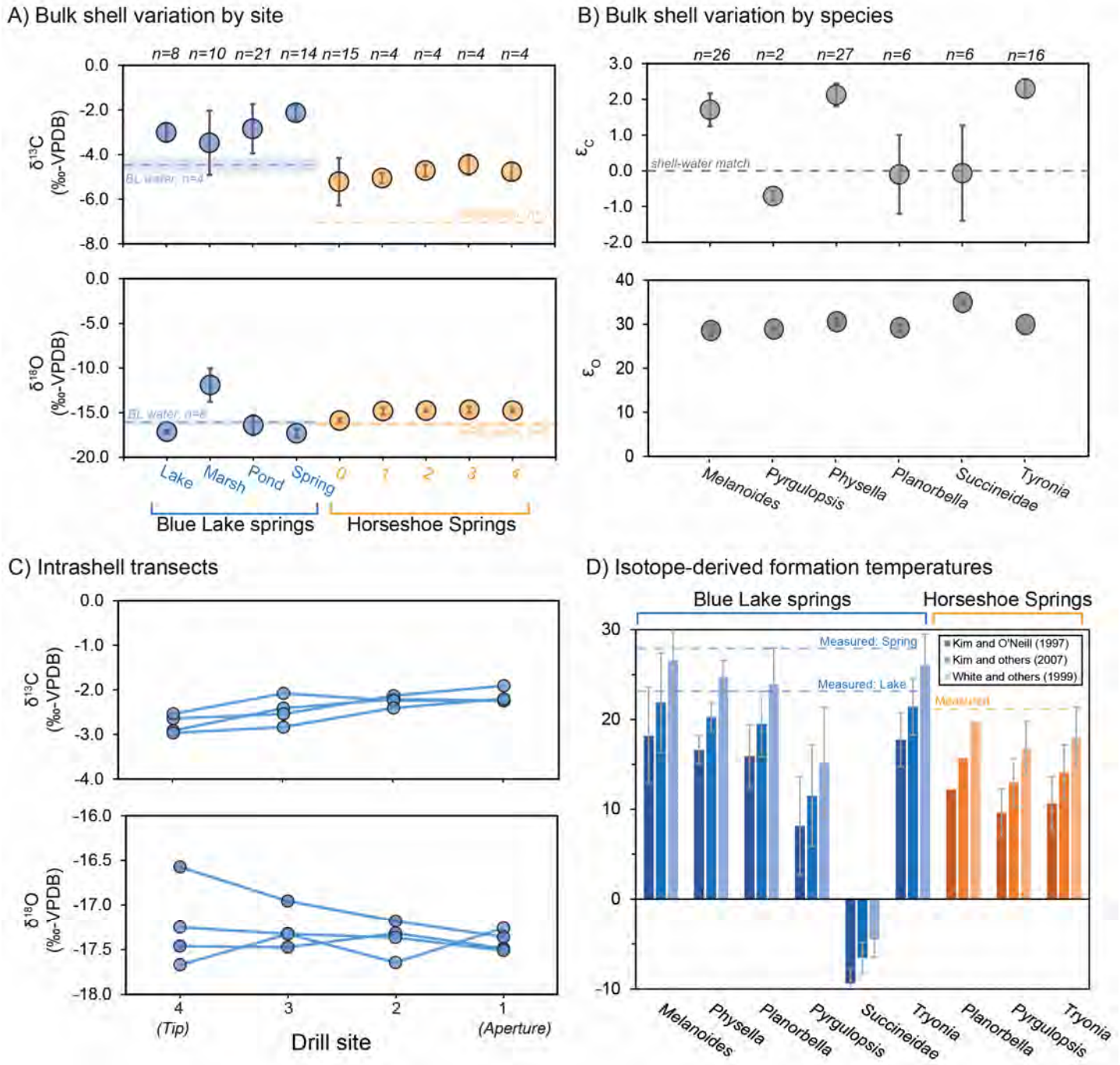

Figure 5. *Stable isotope measurements of gastropod shells. A) $\delta^{13}C$ and $\delta^{18}O$ measurements of bulk, homogenized shells by site and subsite. B) ε_C and ε_o of bulk, homogenized shells by genera. C) $\delta^{13}C$ and $\delta^{18}O$ variation within intrashell transects on Melanoides shells. D) Modelled shell formation (ambient water) temperatures based on $\delta^{18}O$ composition by site and genera.*

Table 3. Gastropod Shell $\delta^{13}C$ and $\delta^{18}O$ Data by Site.

Site	Average of $\delta^{13}C$	SD of $\delta^{13}C$	Count of $\delta^{13}C$	Average of $\delta^{18}O$	SD of $\delta^{18}O$	Count of $\delta^{18}O$
BL-Lake	-3.01	0.41	8	-17.13	0.16	8
BL-Marsh	-3.48	1.44	10	-11.91	1.85	10
BL-Pond	-2.85	1.10	21	-16.41	1.12	21
BL-Spring	-2.13	0.33	14	-17.31	0.46	14
HRS-Subsite-00	-5.22	1.06	15	-15.89	0.20	15
HRS-Subsite-01	-5.06	0.23	4	-14.82	0.41	4
HRS-Subsite-02	-4.72	0.25	4	-14.77	0.14	4
HRS-Subsite-03	-4.46	0.45	4	-14.68	0.35	4
HRS-Subsite-04	-4.77	0.38	4	-14.79	0.17	4

erage $\delta^{13}C$ values of shells ranged from -2.1 to -3.5‰ (a range of by 1.4‰), whereas the $\delta^{13}C_{TDIC}$ values in water samples at BL averaged -4.2‰ (SD = 0.43, n=4) (Lerback and others, 2023). An ANOVA shows that there are no significant differences between subsite $\delta^{13}C_{shell}$ values ($F = 0.765$, $p = 0.519$). At BL, the subsite shell averages of $\delta^{18}O$ values ranged from -11.9 to -17.3‰ (a range of by 5.4‰). Subsites had statistically different values (ANOVA $F= 36.18$, $p < 0.01$), where a Tukey's HSD test showed that pairwise, the BL-Marsh was different than every other site at $p < 0.01$ with a difference of more than 4‰). This is likely because the marsh had shallow standing water which may have had significant evaporative effects. Water samples (converted to VPBD from VSMOW) of BL discharge averaged -45.5‰ (SD = 0.1, n=12). Data for water stable isotopes at these sites is provided in Appendix 4.

At HRS, the subsite averages of $\delta^{13}C$ ranged from -4.5 to -5.2‰ (a range of 0.8‰), whereas $\delta^{13}C_{TDIC}$ values from water at HRS yielded a value of 7.2‰ (n = 1) (Lerback and others, 2019). The $\delta^{13}C_{TDIC}$ values were not statistically different across sites (ANOVA $F = 0.479$, $p = 0.75$). At HRS, the shell subsite averages of $\delta^{18}O$ (VPDB) values ranged from -14.7 to -15.9‰ (a range of 2.6‰). The $\delta^{18}O$ of shells at HRS was statistically different between sites (ANOVA $F = 32.28$, $p < 0.01$), where a Tukey's HSD test showed that pairwise, the HRS-0 was different than the other sites at $p < 0.01$, with a difference of 1‰).Water at HRS had a measured value (converted to VPBD from VSMOW) of -45.5‰ (SD=0.1, n=8).

$\delta^{13}C$ values of bulk sediment were -26.6 and -20.7‰ at BL-pond and HRS-0, respectively (Lerback and others, 2023), which are within the range of values expected of plant material in the region (Hart and others, 2010). Shell $\delta^{13}C$ values are more reflective of water $\delta^{13}C$ (TDIC) than sediment, similar to findings by Fritz and Poplowski (1974).

Stable isotope data of shells were also aggregated by genera (Figure 5B, Table 4) $\delta^{13}C$ (VPDB) values in shells ranged from -1.7‰ of a *Tryonia* at BL to -9.0‰ from a *Planorbella* at HRS. Significant differences existed in $\delta^{13}C$ between genera (ANOVA $F = 7.172$, $p < 0.01$), where the Tukey HSD found a difference of greater than 1‰ between *Melanoides* and all other genera ($p < 0.1$) but no significant differences between the four other genera ($p > 0.1$). $\delta^{18}O$ (VPDB) values in shells range from -10.0‰ of a *Succineidae* at BL-Marsh at BL to -17.5‰ of a *Melanoides* at BL-Spring. We found differences between the genera $\delta^{18}O$ (ANOVA $F = 45.41$, $p < 0.01$), where the Tukey HSD showed a pairwise difference between *Melanoides* and *Tyronia* (difference of 1.3‰, $p < 0.01$), and between *Melanoides* and *Pyrgulopsis* (difference of 1.9‰, $p < 0.01$). There was a difference of at least 4‰ between *Succineidae* and all other genera including *Melanoides* ($p < 0.01$). Lastly, there was also a difference of 1.3‰ between *Planorbella* and *Pyrgulopsis* ($p < 0.1$).

The fractionation between the measured shell and the spring waters is represented by epsilon (ε) for shell-TDIC in carbon and for shell-H_2O in oxygen stable isotope values (element denoted with a subscript). Water $\delta^{18}O$ for BL and HRS was reported relative to a VSMOW standard, which we convert to the VPDB standard before calculating the fractionation values for oxygen (ε_O). *Planorbella* and *Succineidae* have ε_C near 0, while the other shells (*Melanoides*, *Physella*, and *Tyronia*) show ε_C of greater than 1.5‰. All genera but *Succineidae*, had an average ε_O of 29.6 (SD = 1.2, n = 57). The elevated ε_O of +34‰ (SD = 0.44, n = 6) found in *Succineidae* is unsurprising because *Succineidae* is a genus only found at BL-

Table 4. *Gastropod Shell $\delta^{13}C$ and $\delta^{18}O$ Data by Genera.*

Genera	Average of $\delta^{13}C$	SD of $\delta^{13}C$	Count of $\delta^{13}C$	Average of $\delta^{18}O$	SD of $\delta^{18}O$	Count of $\delta^{18}O$
Melanoides	1.71	0.46	26	-0.95	1.19	15
Physella	-0.70	NA	2	-0.64	NA	2
Pyrgulopsis	2.13	0.31	27	1.03	0.81	19
Planorbella	-0.10	1.10	6	-0.31	0.75	5
Succineidae	-0.06	1.33	6	5.41	0.44	6
Tryonia	2.30	0.26	16	0.41	0.89	16

Marsh, where evaporation is occurring in shallow standing water (Morgan, 1970). Shanahan and others (2005) posit that *Succineidae* and *Physella* are pulmonates (lung-breathing), enabling them to live in these shallow areas where more evaporation is occurring and seasonally changing the water $\delta^{18}O$.

Following the methodologies provided by Shanahan and others (2005), we also evaluated the variation within the whorls of a single shell. The within-shell (intrashell) isotopic variation here may be due to biomediated fractionation or due to seasonal variation in waters during stages of growth. We examined the isotopes in intrashell transects along the long axis of growth from shell aperture to tip (Figure 5C, Appendix 5). These variations are otherwise averaged by homogenizing bulk shells. Variation of $\delta^{13}C$ was less than 1‰ through the shell, where three out of four shells increased by almost 1‰ overall. For $\delta^{18}O$ (VSMOW) values, the maximum variation observed was a linear decrease in one shell from -16.5‰ to -17.5‰ along the transect, whereas the other three shells did not vary more than 0.3‰. The variation within shells indicates that intrashell variation is minimal compared to the variation between bulk shells. This likely reflects the stable conditions provided by the mesothermal, seasonally stable discharge at BL.

We used the measured shell $\delta^{18}O$ values and measured average water $\delta^{18}O$ (which are assumed in paleoclimate studies) to calculate the expected shell formation temperatures (Figure 5D, Appendix 6). Like Shanahan and others (2005), we compare these estimated temperatures to measured temperatures of the springs reported by Lerback and others (2023). The fractionation equation from Kim and O'Neil (1997) estimates temperatures for synthetic calcite, where Kim and others (2007) estimate the formation temperature for synthetic aragonite, and finally, the equation by White and others (1999) estimates the formation temperature for aragonitic molluscs. Each of these equations predicts a temperature lower than the measured discharge temperatures of 28°C at BL and 21°C at HRS, but predicted temperatures for the genera *Melanoides*, *Physella*, *Planorbella*, and *Tryonia* by White and others (1997) are within the range found at BL between the Spring subsite discharge and the Lake subsite, and this equation also is closer to the mesothermal temperatures at HRS as well. Because *Physella, Planorbella* and *Succinidae* are all pulmonates, we might expect these to have more similar predicted temperatures, and different as compared to the gil-breathing genera. However, *Physella* and *Planorbella* predicted temperatures are more closely aligned with the gil-breathing genera, so the $\delta^{18}O$ may be more dependent on the microclimate associated with the location than the genera-specific vital effects that Shanahan and others (2005) discussed.

Trace Elements

We measured alkali metals (Li, Na, K, Rb, and Cs), alkaline earth metals (Be, Mg, Ca, Sr, and Ba), and select metals and metalloids (Al, Mn, Fe, Zn) in gastropod shells from HRS and BL to understand how shell chemistry may represent water or environmental chemistry (Figure 6, Appendix 7). On average, higher concentrations of Li, K, Rb, Be, Sr, Mn, Zn, and As were found in shells from BL than HRS. We provide these data to develop some baseline values as shells can be used as bioindicators of environmental change but note these associations need to be studied in more detail for genera-specific biases. Notably, the single *Tyronia* shell from HRS had concentrations of Na, Rb, Cs, Mg, Ba, Al, and Mn distinctly higher than shells from the same location, although the data are too sparse to draw statistical significance. However, the difference in trace element concentration may indicate there may be phyla- and genera-specific differences in how elements will bioaccumulate in body materials (including shells) (Langston and others, 1998; Rainbow, 2007). Bolotov and others, (2015) showed that freshwater bivalve trace element concentrations are significantly impacted by biological shell-building processes and geography (water elemental concentrations as related to the proximity of chemical sources). Land snail shell incorporation of environmental trace elements have also been discussed as bi-

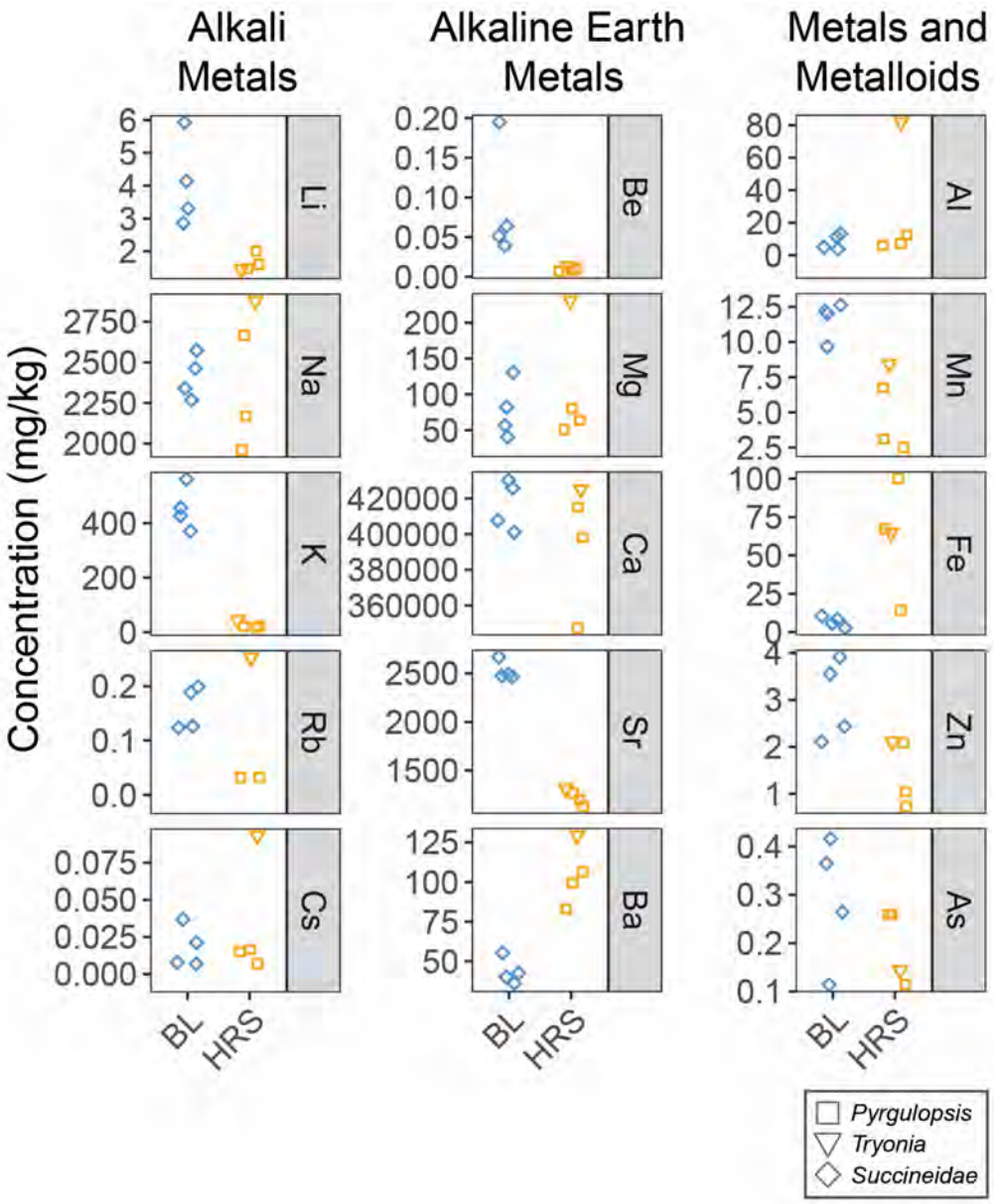

Figure 6. *Trace element concentrations measured in gastropod shells.*

omonitors for changing environmental conditions (de Vaufleury and Pihan, 1999; Madejon and others, 2013; Pauget and others, 2013), but need to be more carefully studied because of high soil variability and complexity of ecosystems. We show that spring snails throughout HRS ponds live in relatively chemically homogeneous environments, and thus we believe aquatic snail shells may be represent more consistent environmental proxies (within same-genera groups) than land snails.

We calculated the elemental ratios (mol/mol) of shells and water that have been evaluated in gastropod shells for paleoclimate reconstructions (Figure 7). These include Mg/Ca which have been used for temperature reconstruction in marine and lake foraminifera collections (Nurenberg and others, 1996; Lea and others, 1999; Elderfield and Ganssen, 2000; Dekens and others, 2002; Anand and others, 2003; Tripati and others, 2003Khider and others, 2015; Gray and Evans, 2019; Saenger and Evans, 2019). The study of Mg/Ca ratios in bivalves and gastropods have been limited and focus primarily on marine systems (Wanamaker and others, 2008; García-Escárzaga and others, 2015). Ulrich and others (2021) found that there was strong association between biomineral elemental chemistry and shell-building genera relatedness and that amongst the marine gastropods that were studied, element incorporation patterns arose at the class level. Our data test whether the Mg/Ca relationship works in the select freshwater gastropod taxa. At BL, waters had higher Mg/Ca ratios than were observed in *Succineidae* shells (approximately 0.8 mmol/mol in water, and 0.0 mmol/mol in shells), whereas in HRS shell the Mg/Ca values were all very low, less than 2.0 mmol/mol. Dellinger and others (2018) show data for marine mollusks that confirm lower Mg/Ca ratios (0.3-8 mmol/mol) than can be expected for more aragonitic materials. Using the calibration equation from Anand and others (2003) (which was derived for marine foraminifera which incorporates source water

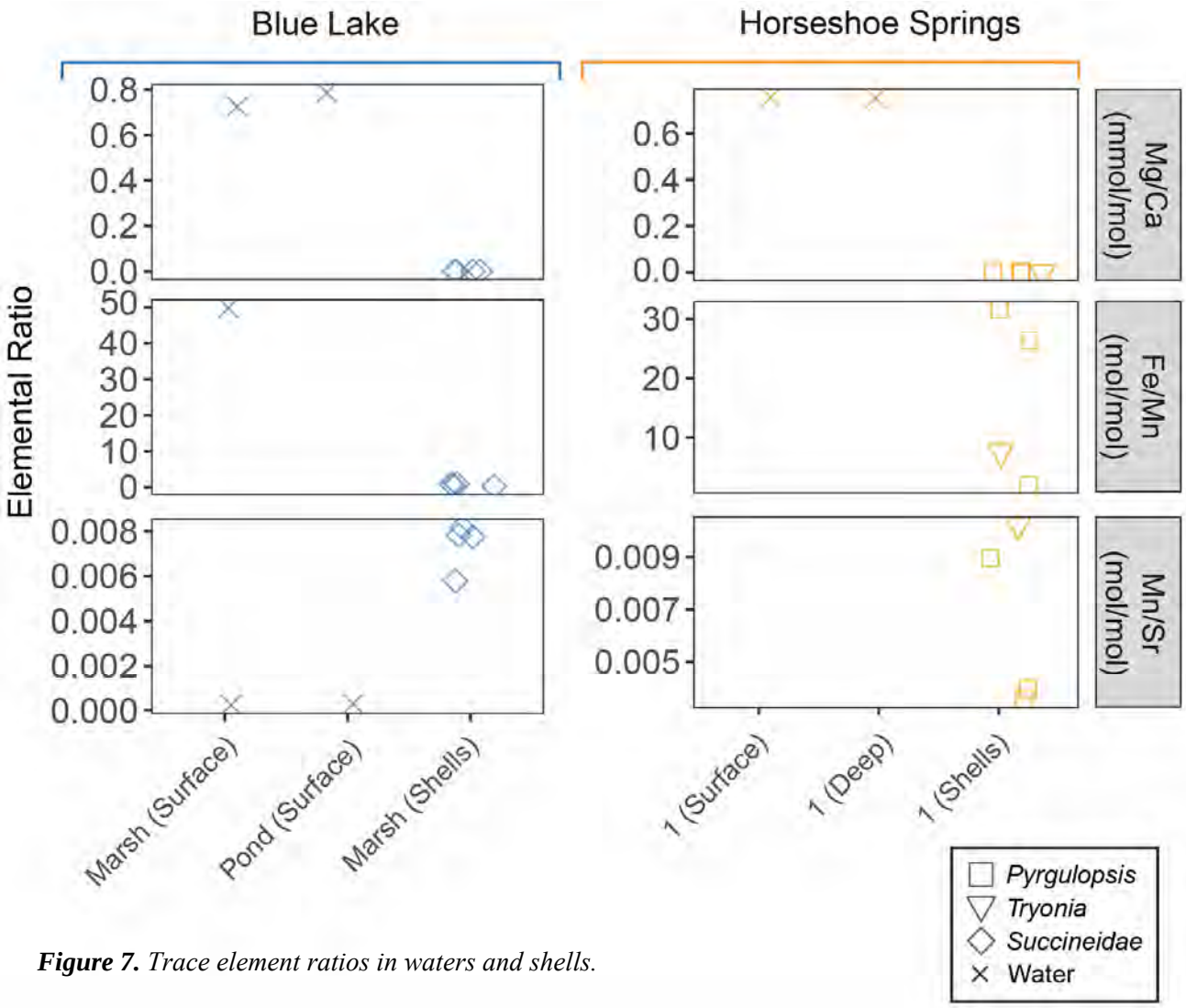

Figure 7. *Trace element ratios in waters and shells.*

Mg/Ca geochemistry), the expected Mg/Ca ratio for these shells is 3.011 and 2.515 mmol/mol, respectively (using the water temperatures of 23°C at BL and 21°C at HRS reported by Lerback and others, 2023). Given the measured ratios of 3.1 and 4.3 mmol/mol for BL and HRS, these spring water gastropod genera record very different Mg/Ca ratios that may reflect the gastropod shell-building processes partitioning of elemental species, especially in comparison to the marine foraminiferal calibrations that have been previously reported. Therefore, freshwater gastropods are likely unsuitable for temperature reconstruction with the Mg/Ca paleothermometer without further study.

Gastropod elemental ratios of Fe/Mn and Mn/Sr have been used as a proxy for a variety of processes, such as changes in water chemistry including sediment input, redox conditions, and water balance fluctuations (Rosenthal and Katz, 1989; Wanamaker Jr and others, 2008; Korponai and others, 2010). More specifically, Fe/Mn and Mn/Sr have been used in sedimentary records as indicators of redox conditions at the time of deposition and may also indicate potential alteration via diagenesis (Templeton and others, 2000). Examples of such factors affecting Fe/Mn and Mn/Sr ratios are changing mixing regimes, erosional input of sediment, aquatic productivity, soil leaching, and eutrophication. Water Fe/Mn ratios were not reported because concentrations were below the instrument detection limit. The Fe/Mn values of *Succineidae* shells found at BL range from 0.21 to 0.85 mol/mol, whereas the Fe/Mn values of *Pyrgulopsis* and single *Tryonia* collected at HRS range from 2.08 to 31.56 mol/mol (Figure 7, Table 8). We observed within-genera variability even within the same site; one *Pyrgulopsis* shell from HRS has Fe/Mn and Mn/Sr values that show an elevated signal compared to the two other *Pyrgulopsis* samples, falling nearer that *Tryonia* sample from the same site. We also observed some subsite variation; the *Succineidae* samples from BL show a depleted Fe/Mn signal relative to sampled marsh surface water, and an elevated Mn/Sr signal when compared to both marsh surface and pond surface water. This elevated Mn/Sr may reflect preferential uptake or more bioavailability of the trace element Mn as compared to the more abundant elements.

CONCLUSIONS

Wetland critical zones are important sites to monitor for changes to water resources and biodiversity and are sites for sedimentological preservation of wetland critical zone processes. The water chemistry shapes wetland critical zones over long time periods, and the chemistry provides solutes that contribute to the saline ecosystems of the Bonneville basin. Aspects of the water chemistry are preserved in gastropod shells, which can (1) provide an ongoing observational metric as "sentinel" organisms, rapidly capturing chemical changes to the system, and (2) also which are preserved in sediments, providing historical records of the magnitude of change in spring chemistries which contextualize modern environmental changes. We provide chemical characteristics of modern water from two mesothermal, playa-margin springs in the western Bonneville basin, and evaluate gastropod chemistry as providing potential records of spring chemistry changes through time.

The Shannon's Diversity Index at four HRS subsites indicates that the ecological diversity is low, with one snail genera, *Pyrgulopsis* (an imperiled genera) being the dominant shell found (Magurran, 1988; Magurran and McGill, 2011). While more research (particularly into paleoenvironmental conditions and past population distributions) can clarify a baseline diversity in these springs, the low diversity index reported here may reflect that the ecosystem's overall stability may be sensitive to environmental changes, including land use change that impacts the geochemical profile of the water. The modern chemistry of the shells can also be used as a baseline to compare with sedimentary shell records or future shell collections as bioindicators of environmental change. We present isotopic and trace element data among subsites and genera to constrain the variables relevant to scientists interested in using shells as proxies for spring water changes through time. We found genera and subsite differences in $\delta^{13}C$ and $\delta^{18}O$ variations and trace element chemistry of modern water and shells, which will need to be better constrained in order to effectively use these chemical relationships to interpret past environments. Our data did not find evidence for significant physiological differences based on pulmonate versus gil-breathing genera in the stable isotope data.

Overall, this paper describes wetland critical zone chemistry and metrics of biodiversity in a system of ecological importance in the Great Salt Lake watershed. As gastropods deposited in spring sediments can be used as recorders of environmental change, we evaluate the factors that may impact geochemical preservation and thus environmental reconstructions.

ACKNOWLEDGMENTS

Thanks to Kate Holcomb, Lisbeth Louderback, Don Sada, and Saxon Sharp for assistance with gastropod identification. Thank you to reviewers Jay Quade and Jesse Bateman for their helpful comments, which greatly improved this paper. This work is partially supported by the Global Changes and Sustainability Center at the University of Utah, the NSF/GSA Graduate Student Geoscience Grant #12745-20, which is funded by NSF Award #1949901, and by the UC Presidential Postdoctoral Fellowship Program. Part of this work was performed under the auspices of the U.S. Department of Energy by Lawrence Livermore National Laboratory under Contract DE-AC52-07NA27344, release number LLNL-JRNL-855225.

REFERENCES

Abell, P.I., 1985, Oxygen Isotope Ratios In Modern African Gastropod Shells: A Database For Paleoclimatology: Chemical Geology, 58, 183–193.

Abell, P.I., and Williams, M.A.J., 1989, Oxygen and carbon isotope ratios in gastropod shells as indicators of paleoenvironments in the Afar region of Ethiopia: Palaeogeography, Palaeoclimatology, Palaeoecology, 74(3–4), 265–278. https://doi.org/10.1016/0031-0182(89)90065-5

Anadon, P., Moscariello, A., Rodríguez-Lázaro, J., and Filippi, M.L., 2006, Holocene environmental changes of Lake Geneva (Lac Léman) from stable isotopes (δ13C, δ18O) and trace element records of ostracod and gastropod carbonates: Journal of Paleolimnology, 35, 593-616.

Anand, P., Elderfield, H., and Conte, M.H., 2003, Calibration of Mg/Ca thermometry in planktonic foraminifera from a sediment trap time series: Calibration of Mg/Ca Thermometry in Planktonic Foraminifera: Paleoceanography, 18(2), https://doi.org/10.1029/2002PA000846

Anderson, S.P., von Blanckenburg, F., and White, A.F., 2007, Physical and Chemical Controls on the Critical Zone: Elements, 3(5), 315–319.

Aravena, R., Warner, B.G., MacDonald, G.M., and Hanf, K.I., 1992, Carbon isotope composition of lake sediments in relation to lake productivity and radiocarbon dating: Quaternary Research, 37(3), 333-345.

Ashley, G.M., 2020, Paleo-Critical Zones, windows into the changing life and landscapes during the Quaternary Period: Quaternary Research, 96, 53–65. https://doi.org/10.1017/qua.2020.49

Ayliffe, D., Williams, M.A.J., and Sheldon, F., 1996, Stable carbon and oxygen isotopic composition of

early-Holocene gastropods from Wadi Mansurab, north-central Sudan: The Holocene, 6(2), 157–169. https://doi.org/10.1177/095968369600600203

Baker, F.C., 1945, The molluscan family Planorbidae: University of Illinois Press, Urbana, IL.

Baroudi, F., Al Alam, J., Fajloun, Z., and Millet, M., 2020, Snail as sentinel organism for monitoring the environmental pollution; a review: Ecological indicators, 113, 106240.

Berry, A.J., and Kadri, A.B.H., 1974, Reproduction in the Malayan freshwater cerithiacean gastropod Melanoides tuberculate: Journal of Zoology, 172 (3), 369-381.

Bolaji, D.A., Edokpayi, C.A., Samuel, O.B., Akinnigbagbe, R.O., and Ajulo, A.A., 2011, Morphological characteristics and Salinity tolerance of Melanoides tuberculatus (Muller, 1774): World Journal of Biological Research, 004(2).

Bolotov, I.N., Pokrovsky, O.S., Auda, Y., Bespalaya, J.V., Vikhrev, I.V., Gofarov, M.Y., and Zouiten, C., 2015, Trace element composition of freshwater pearl mussels Margaritifera spp. across Eurasia: Testing the effect of species and geographic location: Chemical Geology, 402, 125-139.

Brantley, S.L., Goldhaber, M.B., and Ragnarsdottir, K.V., 2007, Crossing Disciplines and Scales to Understand the Critical Zone: Elements, 3(5), 307–314. https://doi.org/10.2113/gselements.3.5.307

Clarke, K.R., Gorley, R.N., Somerfield, P.J., and Warwick, R.M., 2014, Change in marine communities: An approach to statistical analysis and interpretation (3rd ed.): PRIMER-E: Plymouth.

Dekens, P.S., Lea, D.W., Pak, D.K., and Spero, H.J., 2002, Core top calibration of Mg/Ca in tropical foraminifera: Refining paleotemperature estimation: Geochemistry, Geophysics, Geosystems, 3 (4), 1–29. https://doi.org/10.1029/2001GC000200

Dellinger, M., West, A.J., Paris, G., Adkins, J.F., von Strandmann, P.A.P., Ullmann, C.V., Eagle, R.A., Freitas, P., Bagard, M.L., Ries, J.B. and Corsetti, F.A., 2018, The Li isotope composition of marine biogenic carbonates: Patterns and mechanisms: Geochimica et Cosmochimica Acta, 236, 315-335.

De Vaufleury, A.G., and Pihan, F., 2000, Growing snails used as sentinels to evaluate terrestrial environment contamination by trace elements: Chemosphere, 40(3), 275-284.

Dudgeon, D., 1982, Aspects of the desiccation tolerance of four species of benthic mollusca from Plover Cove Reservoir, Hong Kong: The Veliger, 24(3), 267- 271.

Dudgeon, D., 1986, The life cycle, population dynamics and productivity of Melanoides tuberculata (Muller, 1774) (Gastropoda: Prosobranchia: Thiaridae) in Hong Kong: Journal of Zoology, 208(1), 37–53. https://doi.org/10.1111/j.1469-7998.1986.tb04707.x

Elderfield, H., and Ganssen, G., 2000, Past temperature and $\delta^{18}O$ of surface ocean waters inferred from foraminiferal Mg/Ca ratios: Nature, 405, 442–445.

El-Emam, M.A., and Madsen, H., 1982, The effect of temperature, darkness, starvation and various food types on growth, survival and reproduction of Helisoma duryi, Biomphalaria alexandrina and Bulinus truncatus (Gastropoda: Planorbidae): Hydrobiologia, 88, 265-275.

Facon, B., Jarne, P., Pointier, J.P., and David, P., 2005, Hybridization and invasiveness in the freshwater snail Melanoides tuberculata: Hybrid vigour is more important than increase in genetic variance: Hybrid vigour in an invasive snail: Journal of Evolutionary Biology, 18(3), 524–535. https://doi.org/10.1111/j.1420-9101.2005.00887.x

Facon, B., Pointier, J.P., Glaubrecht, M., Poux, C., Jarne, P., and David, P., 2003, A molecular phylogeography approach to biological invasions of the New World by parthenogenetic Thiarid snails: Molecular Ecology, 12(11), 3027–3039. https://doi.org/10.1046/j.1365-294X.2003.01972.x

Fan, Y., Grant, G., and Anderson, S.P., 2019, Water within, moving through, and shaping the Earth's surface: Introducing a special issue on water in the critical zone: Hydrological Processes, 33(25), 3146–3151. https://doi.org/10.1002/hyp.13638

Fritz, P., and Poplawski, S, 1974, 18O and 13C in the shells of freshwater molluscs and their environments: Earth and Planetary Science Letters, 24(1), 91-98.

Fovet, O., Belemtougri, A., Boithias, L., Braud, I., Charlier, J., Cottet, M., Daudin, K., Dramais, G., Ducharne, A., Folton, N., Grippa, M., Hector, B., Kuppel, S., Le Coz, J., Legal, L., Martin, P., Moatar, F., Molénat, J., Probst, A., and Datry, T., 2021, Intermittent rivers and ephemeral streams: Perspectives for critical zone science and research on socio-ecosystems: WIREs Water, 8(4). https://doi.org/10.1002/wat2.1523

García-Escárzaga, A., Moncayoa, S., Gutiérrez-Zugasti, I., González-Morales, M.R., Martín-Chivelet, J., and Cáceres, J.O., 2015, Mg/Ca ratios measured by Laser Induced Breakdown Spectroscopy (LIBS): A new approach to decipher environmental conditions: Journal of Analytical Atomic Spectrometry.

Gray, W.R., and Evans, D., 2019, Nonthermal Influences on Mg/Ca in Planktonic Foraminifera: A Review of Culture Studies and Application to the Last Glacial Maximum: Paleoceanography and

Paleoclimatology, 34(3), 306–315. https://doi.org/10.1029/2018PA003517

Hart, R., Nelson, S.T., and Eggett, D., 2010, Uncertainty in ^{14}C model ages of saturated zone waters: The influence of soil gas in terranes dominated by C3 plants: Journal of Hydrology, 392(1–2), 83–95. https://doi.org/10.1016/j.jhydrol.2010.08.001

Hershler, R., 1994, A review of the North American freshwater snail genus Pyrgulopsis (Hydrobiidae): Smithsonian Contributions to Zoology, 554.

Hershler, R., 1999, A systematic review of the hydrobiid snails (Gastropoda: Rissoidea) of the Great Basin, western United States. Part II. Genera Colligyrus, Fluminicola, Pristinicola, and Tryonia: The Veliger.

Hershler, R., Liu, H.P., and Howard, J., 2014, Springsnails: a new conservation focus in western North America. BioScience, 64(8), 693-700.

Hershler, R., and Sada, D., 1987, Springsnails (Gastropoda: Hydrobiidae) of Ash Meadows, Amargosa Basin, California-Nevada: Proceedings of the Biological Society of Washington.

Ifo, S.A., Moutsambote, J.M., Koubouana, F., Yoka, J., Ndzai, S.F., Bouetou-Kadilamio, L.N. O., Mampouya, H., Jourdain, C., Bocko, Y., Mantota, A.B., Mbemba, M., Mouanga-Sokath, D., Odende, R., Mondzali, L.R., Wenina, Y.E.M., Ouissika, B.C., and Joel, L.J., 2016, Tree Species Diversity, Richness, and Similarity in Intact and Degraded Forest in the Tropical Rainforest of the Congo Basin: Case of the Forest of Likouala in the Republic of Congo: International Journal of Forestry Research, 2016, 1–12. https://doi.org/10.1155/2016/7593681

Immenhauser, A., Schoene, B.R., Hoffmann, R., and Niedermayr, A., 2016, Mollusc and brachiopod skeletal hard parts: Intricate archives of their marine environment: Sedimentology, 63(1), 1-59.

Jin, Z., Zhang, F., Li, X., Wang, J., and Jin, C., 2021, Seasonal/Interannual Variation and Controlling Factors for Oxygen and Carbon Isotopes of Ostracod Shells Collected From a Time-Series Sediment Trap in Lake Qinghai: Frontiers in Earth Science, 9, 727330.

Keith, M.L., Anderson, G.M., and Eichler, R., 1964, Carbon and oxygen isotopic composition of mollusk shells from marine and fresh-water environments: Geochimica et cosmochimica acta, 28(10-11), 1757-1786.

Khider, D., Huerta, G., Jackson, C., Stott, L.D., and Emile-Geay, J., 2015, A Bayesian, multivariate calibration for G lobigerinoides ruber Mg/Ca: G. ruber Mg/Ca Calibration: Geochemistry, Geophysics, Geosystems, 16(9), 2916–2932. https://doi.org/10.1002/2015GC005844

Kim, S.T. and O'Neil, J.R., 1997, Equilibrium and nonequilibrium oxygen isotope effects in synthetic carbonates: Geochimica et cosmochimica acta, 61 (16), 3461-3475.

Kim, S.T., O'Neil, J.R., Hillaire-Marcel, C., and Mucci, A., 2007, Oxygen isotope fractionation between synthetic aragonite and water: Influence of temperature and Mg2+ concentration: Geochimica et Cosmochimica Acta, 71(19), 4704-4715.

Korponai, J., Braun, M., Buczkó, K., Gyulai, I., Forró, L., Nédli, J., and Papp, I., 2010, Transition from shallow lake to a wetland: A multi-proxy case study in Zalavári Pond, Lake Balaton, Hungary. Hydrobiologia, 641(1), 225–244. https://doi.org/10.1007/s10750-009-0087-0

Langston, W.J., Bebianno, M.J., and Burt, G.R., 1998, Metal handling strategies in molluscs: Metal metabolism in aquatic environments, 219-283.

Lea, D.W., Mashiotta, T.A., and Spero, H.J., 1999, Controls on magnesium and strontium uptake in planktonic foraminifera determined by live culturing: Geochimica et Cosmochimica Acta, 63(16), 2369–2379. https://doi.org/10.1016/S0016-7037(99)00197-0

Lerback, J.C., Bagge, S., and Bowen, B.B., 2023, Evaluation of Aqueous Gastropod Shells as Groundwater Radiocarbon Proxies Across Species and Sites: Radiocarbon, 1–20. https://doi.org/10.1017/RDC.2022.103

Lerback, J.C., Hynek, S.A., Bowen, B.B., Bradbury, C.D., Solomon, D.K., and Fernandez, D.P., 2019, Springwater provenance and flowpath evaluation in Blue Lake, Bonneville basin, Utah: Chemical Geology, 529, 119280. https://doi.org/10.1016/j.chemgeo.2019.119280

Livshits, G., and Fishelson, L., 1983, Biology and Reproduction of The Freshwater Snail Melanoides Tubercolata (Gastropoda: Prosobranchia) in Israel: Israel Journal of Ecology and Evolution, 32(1), 21–35. https://doi.org/10.1080/00212210.1983.10688532

Louderback, L.A., and Rhode, D.E., 2009, 15,000 Years of vegetation change in the Bonneville basin: The Blue Lake pollen record: Quaternary Science Reviews, 28(3–4), 308–326. https://doi.org/10.1016/j.quascirev.2008.09.027

Madejón, P., Arrébola, J., Madejón, E., Burgos, P., López-Garrido, R., Cárcaba, A., and Murillo, J.M., 2013, The snail Theba pisana as an indicator of soil contamination by trace elements: potential exposure for animals and humans: Journal of the Science of Food and Agriculture, 93(9), 2259-2266.

Magurran, A.E., 1988, Ecological diversity and its measurement: Princeton University Press.

Magurran, A.E., and McGill, B.J. (Eds.), 2011, Biological diversity: Frontiers in measurement and assessment: Oxford University Press.

Martin, K.R., Johnson, P.T., Bowerman, J., and Li, J., 2020, Biogeography of the freshwater gastropod, Planorbella trivolvis, in the western United States: Plos one, 15(7), e0235989.

McMahon, R.F., 1975, Effects of artificially elevated water temperatures on the growth, reproduction and life cycle of a natural population of Physa virgata Gould: Ecology, 56(5), 1167-1175.

Miguez-Macho, G., and Fan, Y., 2012, The role of groundwater in the Amazon water cycle: 1. Influence on seasonal streamflow, flooding and wetlands: Journal of Geophysical Research, 117 (D15113). https://doi.org/10.1029/2012JD017539

Minor, J., Pearl, J.K., Barnes, M.L., Colella, T.R., Murphy, P.C., Mann, S., and Barron-Gafford, G.A., 2020, Critical Zone Science in the Anthropocene: Opportunities for biogeographic and ecological theory and praxis to drive earth science integration: Progress in Physical Geography: Earth and Environment, 44(1), 50–69. https://doi.org/10.1177/0309133319864268

Morgan, C.M.P., 1970, Taxonomic Studies of the Land Snail Family Succineidae (Doctoral dissertation, University of Michigan).

Murray, H.D., 1971, The introduction and spread of thiarids in the United States: The Biologist 53, 1333-135

Neck, R.W., 1985, Melanoides tuberculata in extreme southern Texas: Texas Conchologist 21(4): 150-15.

Nurenberg, D., Bijma, J., and Hemleben, C., 1996, Assessing the reliability of magnesium in foraminiferal calcite as a proxy for water mass temperatures: Geochimica et Cosmochimica Acta, 60(5), 803–814.

Patterson, C.M., 1971, Taxonomic studies on the land snail family Succineidae: Malacol. Rev., 4, 131-202.

Pauget, B., Gimbert, F., Coeurdassier, M., Crini, N., Pérès, G., Faure, O., and De Vaufleury, A., 2013, Assessing the in situ bioavailability of trace elements to snails using accumulation kinetics: Ecological indicators, 34, 126-135.

Pearson, D., Wells, S., Sprankle, T., Sorensen, J., and Martinez, M., 2014, Reproductive Seasonality and Developmental Characteristics of the Page Springsnail (Pyrgulopsis morrisoni): Journal of the Arizona-Nevada Academy of Science, 45(2), 64–69. https://doi.org/10.2181/036.045.0202

Perrin, N., 1986, The life history parameters of Physa acuta (Gastropoda, Mollusca) in experimental conditions: Revue Suisse Zoologique 93, 725–736.

Pilsbry, H.A., 1948, Land Mollusca of North America (north of Mexico), Volume II, Part 2: Academy of Natural Sciences of Philadelphia Monographs, 3, 521–1113.

Pointier, J.P., 1989, Comparison between two biological control trials of Biomphalaria glabrafa in a pond in Guadeloupe, French West Indies: Journal of Medical and Applied Malacology, 27233-95.

Rader, R.B., Belk, M.C., and Keleher, M.J., 2003, The Introduction of an Invasive Snail (Melanoides tuberculata) to Spring Ecosystems of the Bonneville Basin, Utah: Journal of Freshwater Ecology, 18 (4), 647–657. https://doi.org/10.1080/02705060.2003.9664007

Rainbow, P.S., 2007, Trace metal bioaccumulation: models, metabolic availability and toxicity: Environment international, 33(4), 576-582.

Raw, J., Perissinotto, R., Miranda, N., and Peer, N., 2016, Diet of Melanoides tuberculata (Müller, 1774) from subtropical coastal lakes: Evidence from stable isotope ($\delta^{13}C$ and $\delta^{15}N$) analyses: Limnologica, 59, 116–123. https://doi.org/10.1016/j.limno.2016.05.004

Roessler, M.A., Beardsley, G.L., and Tabb, D.C., 1977, New records of the introduced snail, Melanoides tuberculata (Mollusca: Thiaridae) in south Florida: Florida Scientist 40(1): 87-94.

Rosenthal, Y., and Katz, A., 1989, The applicability of trace elements in freshwater shells for paleogeochemical studies: Chemical Geology, 78(1), 65–76. https://doi.org/10.1016/0009-2541(89)90052-1

Russell-Hunter, W.D., 1978, Ecology of freshwater pulmonates. *In* Fretter, V., and Peake, J., (eds.), Pulmonates. Volume 2A. Systematics, Evolution and Ecology. Chapter 8. Academic Press, New York, New York.

Russo, T.N., 1973, Discovery of the gastropod snail Melanoides (Thiara) tuberculata (Miiller) in Forida: Florida Scientist 36(2-4):2 12-2 13.

Saenger, C.P., and Evans, M.N., 2019, Calibration and Validation of Environmental Controls on Planktic Foraminifera Mg/Ca Using Global Core-Top Data: Paleoceanography and Paleoclimatology, 34(8), 1249–1270. https://doi.org/10.1029/2018PA003507

Shannon, C.E., 1948, A Mathematical Theory of Communication: Bell System Technical Journal, 27(3), 379–423. https://doi.org/10.1002/j.1538-7305.1948.tb01338.x

Shanahan, T.M., Pigati, J.S., Dettman, D.L., and Quade, J., 2005, Isotopic variability in the aragonite shells of freshwater gastropods living in springs with nearly constant temperature and isotopic composition: Geochimica et Cosmochimica Acta, 69(16), 3949-3966.

Singha, K., and Navarre-Sitchler, A., 2022, The Importance of Groundwater in Critical Zone Science: Groundwater, 60(1), 27–34. https://doi.org/10.1111/gwat.13143

Subba Rao, N.V., and Mitra, S.C., 1982, Bioecology of two melaniid snails (Mollusca: Gastropoda) in ponds near Calcutta: J Zool Soc (India) 1&2, 21-32.

Templeton, D.M., Ariese, F., Cornelis, R., Danielsson, L.G., Muntau, H., and Leeuwen, H.P.V., 2000, Guidelines for terms related to chemical speciation and fractionation of elements. Definitions, structural aspects, and methodological approaches (IUPAC Recommendations 2000): Pure and Applied Chemistry, 72(8), 1453–1470.

Torgeson, J.M., Rosenfeld, C.E., Dunshee, A.J., Duhn, K., Schmitter, R., O'Hara, P.A., Ng, G.H.C., and Santelli, C.M., 2022, Hydrobiogechemical interactions in the hyporheic zone of a sulfate-impacted, freshwater stream and riparian wetland ecosystem: Environmental Science: Processes & Impacts, 24(9), 1360–1382. https://doi.org/10.1039/D2EM00024E

Tripati, A.K., Delaney, M.L., Zachos, J.C., Anderson, L.D., Kelly, D.C., and Elderfield, H., 2003, Tropical sea-surface temperature reconstruction for the early Paleogene using Mg /Ca ratios of planktonic foraminifera: Paleoceanography, 18(4), 1101. https://doi.org/10.1029/2003PA000937

Turgeon, D.D., Quinn, J.F., Bogan, A.E., Coan, E.V., Hochberg, F.G., Lyons, W.G., Mikkelsen, P.M., Neves, R.J., Roper, C.F.E., Rosenberg, G., Roth, B., Scheltema, A., Thompson, F. G., Vecchione, M., and Williams, J.D., 1998, Common and scientific names of aquatic invertebrates from the United States and Canada: Mollusks (2nd ed.): American Fisheries Society; USGS Publications Warehouse. http://pubs.er.usgs.gov/publication/70162654

U.S. Environmental Protection Agency, 2009, National primary drinking water regulations. 816-F-09-004. https://www.nrc.gov/docs/ML1307/ML13078A040.pdf

U.S. National Research Council, 2001, Basic research opportunities in the Earth sciences.

Wanamaker Jr., A.D., Kreutz, K.J., Wilson, T., Borns Jr., H.W., Introne, D.S., and Feindel, S., 2008, Experimentally determined Mg/Ca and Sr/Ca ratios in juvenile bivalve calcite for Mytilus edulis: Implications for paleotemperature reconstructions: Geo-Marine Letters, 28(5–6), 359–368. https://doi.org/10.1007/s00367-008-0112-8

White, R.M.P., Dennis, P.F., and Atkinson, T.C., 1999, Experimental calibration and field investigation of the oxygen isotopic fractionation between biogenic aragonite and water: Rapid Communications in Mass Spectrometry, 13(13), 1242-1247.

White, T., Brantley, S., Banwart, S., Chorover, J., Dietrich, W., Derry, L., Lohse, K., Anderson, S., Aufdendkampe, A., Bales, R., Kumar, P., Richter, D., and McDowell, B., 2015, The Role of Critical Zone Observatories in Critical Zone Science: Developments in Earth Surface Processes, Vol. 19, 15–78. Elsevier. https://doi.org/10.1016/B978-0-444-63369-9.00002-1

Young, M.K., Smith, R., Pilgrim, K.L., and Schwartz, M.K., 2021, Molecular species delimitation refines the taxonomy of native and nonnative physinine snails in North America: Scientific reports, 11(1), 21739.

Oviatt, C. G., Thompson, R. S., Kaufman, D. S., Bright, J., and Forester, R. M., 1999, Reinterpretation of the Burmester core, Bonneville basin, Utah: Quaternary Research, v. 52, p. 180-184.

Pedone, V.A., Oviatt, C.G., and McGee, D., 2023, Late Quaternary carbonate microbialite complex on the west shore of Great Salt Lake Utah, USA: Journal of Quaternary Science, v. 38, no. 3, p. 319-332.

Reynard, E., and Brilha, J., 2018, Geoheritage: Assessment, Protection, and Management, Elsevier, 482 p.

Sandberg, P.A., 1975, New interpretations of Great Salt Lake ooids of ancient non-skeletal carbonate mineralogy: Sedimentology, v. 22, p. 497-537. https://doi.org/10.1111/j.1365-3091.1975.tb00244.x

Stegner, W., 1954, Beyond the Hundredth Meridian: John Wesley Powell and the Second Opening of the West: Houghton Mifflin, Boston, MA, 438 p.

Vanden Berg, M.D., 2019, Domes, rings, ridges, and polygons: Characteristics of microbialites from Utah's Great Salt Lake: Sedimentary Record, v. 17, no. 1, p. 4–10.

Weir, K., 2020, Nurtured by nature: American Psychological Association, v. 51, p. 50. https://www.apa.org/monitor/2020/04/nurtured-nature

Wilcock, L., Frantz, C.M., and Vanden Berg, M.D., 2023, Use of remote imagery to map microbialite distribution at Great Salt Lake, Utah: Implications for microbialite exposure, in Vanden Berg, M.D., Ford, R., Frantz, C. Hurlow, H., Gunderson, K., and Atwood, G. (eds.), Great Salt Lake and the Bonneville Basin: Geologic History and Anthropocene Issues: Utah Geological Association Publication 51.

Appendix 1. *Water physical parameter data from probe transect.*

Time	Group	Depth (m)	Temperature (°C)	Total Dissolved Solids (ppt)	pH	RDO Concentration (mg/L)	Specific Conductivity (µS/cm)
1	Shallow	0.373	11.27	2.5	8.1	11.68	3852.72
2	Shallow	0.383	11.27	2.64	8.13	11.78	4067.68
3	Shallow	0.393	11.28	2.78	8.15	11.88	4282.65
4	Shallow	0.403	11.28	2.92	8.17	11.99	4497.62
5	Shallow	0.362	15.12	2.52	8.15	10.2	3869.74
6	Shallow	0.363	15.32	2.55	8.16	10.14	3916.6
7	Shallow	0.365	15.53	2.58	8.17	10.08	3963.46
8	Shallow	0.461	16.38	2.79	8.03	9.7	4286.13
9	Shallow	0.465	16.5	2.78	8.02	9.64	4282.09
10	Shallow	0.469	16.62	2.78	8.01	9.58	4278.05
11	Shallow	0.5	17.22	2.73	7.98	9.21	4197.18
12	Shallow	0.504	17.26	2.73	7.97	9.19	4199.55
13	Shallow	0.508	17.3	2.73	7.97	9.17	4201.92
14	Shallow	0.526	17.5	2.5	7.95	9.03	3849.93
15	Shallow	0.527	17.52	2.49	7.95	9.01	3828.27
16	Shallow	0.528	17.54	2.47	7.95	9	3806.61
17	Shallow	0.53	17.55	2.46	7.95	8.99	3784.95
18	Shallow	0.546	17.76	2.41	7.93	8.83	3700.48
19	Shallow	0.547	17.77	2.4	7.93	8.82	3688.59
20	Shallow	0.548	17.78	2.39	7.93	8.81	3676.71
21	Shallow	0.53	17.95	2.39	7.93	8.69	3684.06
22	Shallow	0.529	17.97	2.39	7.93	8.68	3683.68
23	Shallow	0.528	17.98	2.39	7.93	8.67	3683.31
24	Shallow	0.554	18.06	2.44	7.93	8.61	3746.17
25	Shallow	0.555	18.07	2.44	7.93	8.6	3750.11
26	Shallow	0.555	18.07	2.44	7.93	8.6	3754.06
27	Shallow	0.497	18.2	2.37	7.93	8.51	3643.82
28	Shallow	0.494	18.21	2.37	7.93	8.51	3638.84
29	Shallow	0.491	18.22	2.36	7.93	8.5	3633.87
30	Shallow	0.488	18.23	2.36	7.93	8.5	3628.89
31	Shallow	0.532	18.3	2.44	7.93	8.48	3758.54
32	Shallow	0.533	18.31	2.45	7.93	8.48	3763
33	Shallow	0.534	18.32	2.45	7.93	8.47	3767.47
34	Shallow	0.511	18.44	2.46	7.93	8.4	3780
35	Shallow	0.511	18.45	2.46	7.93	8.39	3783.48
36	Shallow	0.511	18.46	2.46	7.93	8.39	3786.96
37	Shallow	0.524	18.53	2.37	7.93	8.37	3649.47
38	Shallow	0.524	18.54	2.37	7.93	8.37	3641.83
39	Shallow	0.524	18.54	2.36	7.93	8.37	3634.18
40	Shallow	0.531	18.63	2.38	7.92	8.35	3661.48
41	Shallow	0.531	18.63	2.38	7.92	8.34	3660.27
42	Shallow	0.532	18.64	2.38	7.92	8.34	3659.06

43	Shallow	0.533	18.65	2.38	7.92	8.34	3657.85
44	Shallow	0.49	18.69	2.68	7.92	8.31	4119
45	Shallow	0.488	18.7	2.69	7.92	8.31	4144.63
46	Shallow	0.486	18.7	2.71	7.92	8.31	4170.27
47	Shallow	0.516	18.74	2.43	7.91	8.27	3738.22
48	Shallow	0.516	18.74	2.42	7.91	8.27	3723.76
49	Shallow	0.517	18.75	2.41	7.91	8.27	3709.3
50	Shallow	0.563	18.78	2.8	7.91	8.24	4312.73
51	Shallow	0.566	18.79	2.82	7.91	8.24	4336.27
52	Shallow	0.569	18.79	2.83	7.91	8.24	4359.8
53	Shallow	0.522	18.86	2.86	7.93	8.21	4407.27
54	Shallow	0.52	18.87	2.87	7.93	8.21	4422.75
55	Shallow	0.518	18.87	2.88	7.93	8.21	4438.23
56	Shallow	0.516	18.87	2.89	7.93	8.21	4453.71
57	Shallow	0.535	18.82	2.96	7.92	8.24	4550.99
58	Shallow	0.535	18.82	2.96	7.92	8.24	4555.91
59	Shallow	0.534	18.82	2.96	7.92	8.24	4560.83
60	Shallow	0.572	18.96	2.32	7.92	8.22	3570.09
61	Shallow	0.574	18.97	2.29	7.92	8.22	3517.96
62	Shallow	0.577	18.97	2.25	7.92	8.22	3465.82
63	Shallow	0.554	19.02	2.28	7.92	8.26	3510.2
64	Shallow	0.553	19.03	2.27	7.92	8.26	3493.2
65	Shallow	0.553	19.03	2.26	7.92	8.26	3476.19
66	Shallow	0.577	19.06	1.8	7.9	8.29	2773.32
67	Shallow	0.578	19.06	1.78	7.9	8.3	2738.19
68	Shallow	0.579	19.07	1.76	7.9	8.3	2703.05
69	Shallow	0.579	19.07	1.73	7.9	8.3	2667.92
70	Shallow	0.538	19.13	2.38	7.88	8.29	3666.19
71	Shallow	0.536	19.13	2.41	7.88	8.29	3705.42
72	Shallow	0.535	19.13	2.43	7.88	8.29	3744.64
73	Shallow	0.586	19.19	2.63	7.88	8.25	4041.07
74	Shallow	0.588	19.19	2.65	7.88	8.25	4078.32
75	Shallow	0.59	19.19	2.68	7.88	8.25	4115.56
76	Shallow	0.565	19.23	2.48	7.87	8.22	3819.99
77	Shallow	0.565	19.23	2.47	7.87	8.21	3806.91
78	Shallow	0.565	19.23	2.47	7.87	8.21	3793.82
79	Shallow	0.577	19.25	2.74	7.88	8.2	4218.14
80	Shallow	0.577	19.25	2.75	7.88	8.2	4234.77
81	Shallow	0.577	19.25	2.76	7.88	8.2	4251.4
82	Shallow	0.577	19.25	2.77	7.88	8.2	4268.03
83	Shallow	0.58	19.27	3.44	7.88	8.19	5288.08
84	Shallow	0.58	19.27	3.48	7.88	8.19	5352.31
85	Shallow	0.581	19.27	3.52	7.88	8.19	5416.53
86	Shallow	0.581	19.22	4.24	7.87	8.19	6517.24
87	Shallow	0.581	19.22	4.29	7.87	8.19	6596.06
88	Shallow	0.581	19.21	4.34	7.87	8.19	6674.87
89	Shallow	0.54	19.26	4.82	7.88	8.17	7421.89

90	Shallow	0.538	19.26	4.86	7.88	8.16	7481.36
91	Shallow	0.535	19.26	4.9	7.88	8.16	7540.84
92	Shallow	0.519	19.54	4.95	7.87	8.07	7613.5
93	Shallow	0.517	19.56	4.96	7.87	8.07	7627.92
94	Shallow	0.515	19.57	4.97	7.87	8.06	7642.34
95	Shallow	0.514	19.59	4.98	7.87	8.06	7656.77
96	Shallow	0.554	19.7	4.98	7.86	8.02	7661.11
97	Shallow	0.556	19.71	4.98	7.86	8.01	7660.43
98	Shallow	0.558	19.72	4.98	7.86	8.01	7659.74
99	Shallow	0.571	19.77	4.99	7.88	7.97	7680.29
100	Shallow	0.573	19.77	4.99	7.88	7.97	7681.31
101	Shallow	0.574	19.78	4.99	7.88	7.96	7682.32
102	Shallow	0.578	19.8	4.97	7.86	7.94	7650.34
103	Shallow	0.579	19.81	4.97	7.86	7.94	7649.01
104	Shallow	0.579	19.81	4.97	7.86	7.94	7647.67
105	Shallow	0.585	19.84	4.98	7.86	7.86	7658.82
106	Shallow	0.586	19.84	4.98	7.86	7.86	7658.77
107	Shallow	0.586	19.84	4.98	7.86	7.85	7658.71
108	Shallow	0.587	19.84	4.98	7.86	7.85	7658.65
109	Shallow	0.571	19.83	4.98	7.88	7.87	7657.5
110	Shallow	0.57	19.83	4.98	7.88	7.87	7657.75
111	Shallow	0.57	19.83	4.98	7.88	7.87	7657.99
112	Shallow	0.589	19.81	4.97	7.88	7.93	7648.08
113	Shallow	0.59	19.81	4.97	7.88	7.93	7647.5
114	Shallow	0.59	19.8	4.97	7.88	7.94	7646.92
115	Shallow	0.55	19.84	4.97	7.86	7.94	7647.9
116	Shallow	0.548	19.85	4.97	7.86	7.94	7647.75
117	Shallow	0.547	19.85	4.97	7.86	7.95	7647.61
118	Shallow	0.58	19.89	4.97	7.87	7.89	7643.28
119	Shallow	0.581	19.89	4.97	7.87	7.89	7643.09
120	Shallow	0.582	19.89	4.97	7.87	7.89	7642.9
121	Shallow	0.583	19.9	4.97	7.87	7.89	7642.71
122	Shallow	0.594	19.87	4.97	7.87	7.89	7642.89
123	Shallow	0.595	19.87	4.97	7.87	7.89	7642.82
124	Shallow	0.596	19.87	4.97	7.87	7.89	7642.74
125	Shallow	0.517	19.92	4.97	7.87	7.95	7639.41
126	Shallow	0.513	19.93	4.97	7.87	7.96	7639.25
127	Shallow	0.509	19.93	4.97	7.87	7.96	7639.08
128	Shallow	0.502	19.85	4.96	7.85	8.08	7632.75
129	Shallow	0.5	19.85	4.96	7.85	8.09	7632.33
130	Shallow	0.498	19.85	4.96	7.85	8.1	7631.92
131	Shallow	0.502	19.94	4.96	7.85	8.09	7636.98
132	Shallow	0.502	19.95	4.96	7.85	8.09	7637.16
133	Shallow	0.503	19.95	4.96	7.85	8.09	7637.33
134	Shallow	0.503	19.96	4.96	7.85	8.09	7637.5
135	Shallow	0.559	19.94	4.95	7.83	8.1	7608.89
136	Shallow	0.562	19.95	4.94	7.82	8.1	7607.48

137	Shallow	0.565	19.95	4.94	7.82	8.1	7606.07
138	Shallow	0.587	20.04	4.94	7.8	8	7601.13
139	Shallow	0.59	20.04	4.94	7.8	8	7600.29
140	Shallow	0.592	20.04	4.94	7.8	7.99	7599.45
141	Shallow	0.576	20.03	4.94	7.79	7.93	7592.73
142	Shallow	0.575	20.03	4.94	7.79	7.92	7592.35
143	Shallow	0.574	20.03	4.93	7.79	7.91	7591.96
144	Shallow	0.588	20.02	4.93	7.78	7.86	7586.62
145	Shallow	0.588	20.02	4.93	7.78	7.86	7586.22
146	Shallow	0.588	20.01	4.93	7.78	7.86	7585.82
147	Shallow	0.589	20.01	4.93	7.78	7.85	7585.42
148	Shallow	0.629	20.01	4.93	7.77	7.77	7578.26
149	Shallow	0.631	20.01	4.93	7.77	7.77	7577.78
150	Deep	0.634	20.01	4.93	7.77	7.76	7577.3
151	Deep	0.704	20.02	4.93	7.77	7.69	7576.95
152	Deep	0.708	20.02	4.92	7.77	7.68	7576.81
153	Deep	0.713	20.02	4.92	7.77	7.67	7576.66
154	Deep	0.774	20	4.92	7.77	7.62	7576.71
155	Deep	0.779	19.99	4.92	7.77	7.62	7576.73
156	Deep	0.784	19.99	4.92	7.77	7.62	7576.75
157	Deep	0.856	19.99	4.92	7.77	7.57	7572.97
158	Deep	0.861	19.99	4.92	7.77	7.57	7572.77
159	Deep	0.866	19.99	4.92	7.77	7.56	7572.56
160	Deep	0.871	19.98	4.92	7.77	7.56	7572.35
161	Deep	0.977	19.98	4.92	7.77	7.52	7569.69
162	Deep	0.984	19.98	4.92	7.77	7.52	7569.47
163	Deep	0.991	19.98	4.92	7.77	7.52	7569.25
164	Deep	1.028	19.99	4.92	7.77	7.5	7567.25
165	Deep	1.032	19.99	4.92	7.77	7.5	7567.09
166	Deep	1.035	19.99	4.92	7.77	7.5	7566.94
167	Deep	1.154	19.98	4.92	7.78	7.49	7572.95
168	Deep	1.161	19.98	4.92	7.78	7.49	7573.25
169	Deep	1.167	19.98	4.92	7.78	7.49	7573.55
170	Deep	1.123	19.98	4.92	7.77	7.49	7572.76
171	Deep	1.123	19.98	4.92	7.77	7.49	7572.84
172	Deep	1.123	19.98	4.92	7.77	7.48	7572.92
173	Deep	1.122	19.98	4.92	7.77	7.48	7572.99
174	Deep	1.268	19.98	4.93	7.77	7.46	7583.29
175	Deep	1.275	19.98	4.93	7.77	7.46	7583.81
176	Deep	1.281	19.98	4.93	7.77	7.45	7584.33
177	Deep	1.225	19.97	4.93	7.77	7.46	7581.18
178	Deep	0.745	20.23	4.91	7.72	7.04	7546.57
179	Deep	0.773	20.24	4.9	7.72	7.03	7545.79
180	Deep	0.802	20.24	4.9	7.72	7.02	7545.01
181	Deep	0.784	20.14	4.91	7.76	7.03	7551.84
182	Deep	0.793	20.13	4.91	7.76	7.03	7552.02
183	Deep	0.802	20.12	4.91	7.76	7.03	7552.19

184	Deep	0.959	20.08	4.92	7.75	7.06	7570.66
185	Deep	0.966	20.08	4.92	7.75	7.06	7571.86
186	Deep	0.973	20.07	4.92	7.75	7.06	7573.06
187	Deep	0.979	20.07	4.92	7.75	7.07	7574.27
188	Deep	0.908	20.07	4.93	7.75	7.07	7578.24
189	Deep	0.907	20.07	4.93	7.75	7.07	7578.83
190	Deep	0.906	20.07	4.93	7.75	7.07	7579.42
191	Deep	0.954	20.05	4.92	7.74	7.09	7576.65
192	Deep	0.955	20.05	4.92	7.74	7.09	7576.53
193	Deep	0.956	20.05	4.92	7.74	7.09	7576.41
194	Deep	1.06	20.08	4.94	7.75	7.1	7594.5
195	Deep	1.067	20.08	4.94	7.75	7.1	7595.42
196	Deep	1.074	20.08	4.94	7.75	7.1	7596.35
197	Deep	1.112	20.1	4.93	7.75	7.1	7590.61
198	Deep	1.116	20.1	4.93	7.75	7.1	7590.65
199	Deep	1.12	20.1	4.93	7.74	7.1	7590.69
200	Deep	1.124	20.1	4.93	7.74	7.1	7590.72
201	Deep	1.135	20.11	4.92	7.75	7.11	7572.66
202	Deep	1.136	20.11	4.92	7.76	7.11	7571.53
203	Deep	1.138	20.11	4.92	7.76	7.11	7570.39
204	Deep	1.121	20.08	4.93	7.77	7.17	7583.62
205	Deep	1.121	20.08	4.93	7.77	7.17	7584
206	Deep	1.12	20.08	4.93	7.77	7.17	7584.38
207	Deep	1.143	20.07	4.93	7.78	7.25	7584.39
208	Deep	1.144	20.06	4.93	7.78	7.26	7584.7
209	Deep	1.145	20.06	4.93	7.78	7.26	7585.02
210	Deep	1.146	20.06	4.93	7.78	7.27	7585.33
211	Deep	1.088	20.04	4.93	7.79	7.32	7583.78
212	Deep	1.086	20.04	4.93	7.8	7.32	7583.68
213	Deep	1.083	20.04	4.93	7.8	7.33	7583.58
214	Deep	1.108	20.03	4.93	7.79	7.38	7588.5
215	Deep	1.108	20.03	4.93	7.79	7.38	7588.74
216	Deep	1.109	20.03	4.93	7.79	7.38	7588.97
217	Deep	1.075	20.04	4.93	7.77	7.37	7590.77
218	Deep	1.074	20.04	4.93	7.77	7.38	7590.97
219	Deep	1.073	20.04	4.93	7.77	7.38	7591.17
220	Deep	1.095	20.06	4.93	7.77	7.36	7590.4
221	Deep	1.095	20.06	4.93	7.77	7.36	7590.37
222	Deep	1.096	20.06	4.93	7.76	7.36	7590.35
223	Deep	1.096	20.07	4.93	7.76	7.36	7590.33
224	Deep	1.11	20.05	4.94	7.76	7.34	7592.75
225	Deep	1.111	20.05	4.94	7.76	7.34	7592.85
226	Deep	1.113	20.05	4.94	7.76	7.34	7592.96
227	Deep	1.008	20.05	4.94	7.76	7.31	7595.79
228	Deep	1.002	20.05	4.94	7.76	7.3	7595.99
229	Deep	0.997	20.05	4.94	7.76	7.3	7596.19
230	Deep	0.919	20.05	4.68	7.76	7.27	7197.13

231	Deep	0.912	20.05	4.66	7.76	7.27	7175.5
232	Deep	0.906	20.05	4.65	7.76	7.27	7153.87
233	Deep	0.928	20.05	4.62	7.76	7.27	7114.05
234	Deep	0.928	20.05	4.62	7.76	7.27	7104.11
235	Deep	0.928	20.05	4.61	7.76	7.27	7094.18
236	Deep	0.928	20.05	4.6	7.76	7.27	7084.24
237	Deep	0.99	20.05	4.61	7.83	7.47	7099.62
238	Deep	0.994	20.05	4.62	7.84	7.48	7100.44
239	Deep	0.998	20.05	4.62	7.84	7.49	7101.27
240	Deep	0.833	20.04	4.63	7.84	7.64	7130.42
241	Deep	0.825	20.04	4.64	7.84	7.65	7132.41
242	Deep	0.817	20.04	4.64	7.84	7.66	7134.39
243	Deep	0.909	20.03	4.62	7.78	7.76	7105.67
244	Deep	0.911	20.03	4.62	7.77	7.77	7104.64
245	Deep	0.912	20.03	4.62	7.77	7.78	7103.6
246	Deep	0.987	20.03	4.63	7.79	7.77	7116.45
247	Deep	0.993	20.03	4.63	7.79	7.77	7116.51
248	Deep	0.999	20.03	4.63	7.79	7.77	7116.57
249	Deep	1.006	20.03	4.63	7.79	7.77	7116.64
250	Deep	1.04	20.03	4.64	7.78	7.82	7131.62
251	Deep	1.043	20.02	4.64	7.78	7.82	7132.73
252	Deep	1.046	20.02	4.64	7.78	7.82	7133.84
253	Deep	1.044	20.02	4.64	7.78	7.82	7136.56
254	Deep	1.044	20.01	4.64	7.78	7.82	7136.98
255	Deep	1.044	20.01	4.64	7.78	7.82	7137.4
256	Deep	0.87	20.01	4.63	7.77	7.84	7121.68
257	Deep	0.86	20.01	4.63	7.77	7.84	7120.84
258	Deep	0.85	20.01	4.63	7.77	7.84	7120
259	Deep	0.792	20	4.61	7.76	7.82	7094.36
260	Deep	0.786	20	4.61	7.76	7.82	7092.63
261	Deep	0.779	20	4.61	7.76	7.82	7090.9
262	Deep	0.773	20	4.61	7.76	7.82	7089.17
263	Deep	0.85	20.01	4.6	7.76	7.77	7078.52
264	Deep	0.853	20.01	4.6	7.76	7.77	7077.45
265	Deep	0.856	20.01	4.6	7.76	7.77	7076.38
266	Deep	0.979	20.01	4.61	7.76	7.76	7099.24
267	Deep	0.988	20.01	4.62	7.76	7.76	7100.3
268	Deep	0.996	20.01	4.62	7.76	7.75	7101.37
269	Deep	0.981	20.01	4.6	7.76	7.73	7081.11
270	Deep	0.982	20.01	4.6	7.76	7.73	7080.49
271	Deep	0.984	20.01	4.6	7.76	7.73	7079.86
272	Deep	0.963	20	4.6	7.76	7.69	7077.37
273	Deep	0.961	20	4.6	7.76	7.69	7076.78
274	Deep	0.959	20	4.6	7.76	7.69	7076.19
275	Deep	0.957	20	4.6	7.76	7.68	7075.59
276	Deep	1.056	19.98	4.62	7.75	7.67	7104.38
277	Deep	1.061	19.98	4.62	7.75	7.66	7105.89

278	Deep	1.066	19.97	4.62	7.75	7.66	7107.39
279	Deep	1.029	19.96	4.65	7.76	7.66	7147.6
280	Deep	1.029	19.96	4.65	7.76	7.66	7150.33
281	Deep	1.029	19.96	4.65	7.76	7.65	7153.06
282	Deep	1.057	19.95	4.61	7.76	7.65	7098.87
283	Deep	1.057	19.95	4.61	7.76	7.65	7096.65
284	Deep	1.058	19.95	4.61	7.76	7.65	7094.42
285	Deep	0.932	19.95	4.62	7.75	7.63	7101.76
286	Deep	0.926	19.95	4.62	7.75	7.62	7100.99
287	Deep	0.92	19.95	4.62	7.75	7.62	7100.22
288	Deep	0.913	19.95	4.61	7.75	7.62	7099.45
289	Deep	0.83	19.95	4.83	7.75	7.59	7426.1
290	Deep	0.823	19.95	4.84	7.75	7.59	7443.64
291	Deep	0.816	19.95	4.85	7.75	7.58	7461.18
292	Deep	0.431	19.95	4.85	7.76	7.54	7465.86
293	Deep	0.409	19.95	4.86	7.76	7.53	7472.57
294	Deep	0.387	19.95	4.86	7.76	7.53	7479.27
295	Deep	0.519	19.95	4.88	7.75	7.46	7502.56
296	Deep	0.519	19.95	4.88	7.75	7.45	7503.16
297	Deep	0.871	19.95	4.89	7.76	7.29	7522.43
298	Deep	0.879	19.95	4.89	7.76	7.29	7522.81
299	Deep	0.879	19.94	4.89	7.76	7.28	7524.61
300	Deep	0.879	19.94	4.89	7.76	7.28	7524.72
301	Deep	0.879	19.94	4.89	7.76	7.28	7524.82
302	Deep	0.776	19.94	4.89	7.77	7.29	7520.93
303	Deep	0.768	19.94	4.89	7.77	7.29	7520.66
304	Deep	0.761	19.94	4.89	7.77	7.29	7520.39
305	Deep	0.754	19.94	4.89	7.77	7.29	7520.13
306	Deep	0.907	19.91	4.89	7.77	7.3	7527.86
307	Deep	0.913	19.91	4.89	7.77	7.3	7528.18
308	Deep	0.919	19.91	4.89	7.76	7.3	7528.49
309	Deep	0.791	19.91	4.89	7.77	7.32	7528.08
310	Deep	0.787	19.9	4.89	7.77	7.32	7528.22
311	Deep	0.783	19.9	4.89	7.77	7.32	7528.36
312	Deep	0.805	19.9	4.89	7.76	7.32	7523.26
313	Deep	0.803	19.9	4.89	7.76	7.32	7522.95
314	Deep	0.802	19.9	4.89	7.76	7.32	7522.63
315	Deep	0.829	19.89	4.92	7.76	7.31	7563.5
316	Deep	0.831	19.89	4.92	7.76	7.3	7565.7
317	Deep	0.834	19.88	4.92	7.76	7.3	7567.89
318	Deep	0.836	19.88	4.92	7.76	7.3	7570.08
319	Deep	0.85	19.86	4.92	7.76	7.29	7569.92
320	Deep	0.851	19.86	4.92	7.76	7.29	7570.78
321	Deep	0.853	19.86	4.92	7.76	7.29	7571.64
322	Deep	0.859	19.84	4.92	7.77	7.29	7573.14
323	Deep	0.86	19.84	4.92	7.77	7.29	7573.11
324	Deep	0.861	19.84	4.92	7.77	7.29	7573.08

325	Deep	0.726	19.82	4.91	7.77	7.29	7558.29
326	Deep	0.718	19.82	4.91	7.77	7.29	7557.48
327	Deep	0.711	19.82	4.91	7.77	7.29	7556.68
328	Deep	0.858	19.84	4.91	7.76	7.28	7558.94
329	Deep	0.863	19.84	4.91	7.76	7.28	7558.79
330	Deep	0.869	19.85	4.91	7.76	7.28	7558.63
331	Deep	0.874	19.85	4.91	7.76	7.28	7558.48
332	Deep	1.114	19.86	4.91	7.75	7.26	7556.52
333	Deep	1.13	19.86	4.91	7.75	7.26	7556.5
334	Deep	1.146	19.86	4.91	7.75	7.26	7556.49
335	Deep	1.182	19.87	4.92	7.76	7.25	7563.37
336	Deep	1.188	19.88	4.92	7.76	7.25	7563.71
337	Deep	1.194	19.88	4.92	7.76	7.25	7564.04
338	Deep	1.184	19.87	4.91	7.76	7.27	7561.04
339	Deep	1.183	19.87	4.91	7.76	7.27	7561.01
340	Deep	1.182	19.87	4.91	7.76	7.27	7560.98
341	Deep	0.987	19.87	4.91	7.76	7.26	7559.3
342	Deep	0.976	19.87	4.91	7.76	7.26	7559.13
343	Deep	0.964	19.87	4.91	7.76	7.26	7558.95
344	Deep	0.953	19.87	4.91	7.76	7.26	7558.78
345	Deep	0.988	19.86	4.91	7.76	7.27	7557.15

Appendix 2. *Water Trace Element Data (mg/L).*

Site	subsite	Li	Na	K	Rb	Cs	Be	Mg	Ca	Sr	Ba	Al	Sc	Mn	Fe	Cu	Ni	Zn	As
BL	Marsh	3.81	3897	274	1.25	0.102	0.0002	122.1	278	5.5	0.11	0.02	<0.0002	0	0.042	<0.5	0	0.02	<0.04
BL	Pond	1.71	1501	114	0.56	0.046	<0.000006	52.1	109	2.5	0.06	0.02	0.0002	0	<0.008	<0.5	0	0.01	<0.04
HRS	Deep	0.59	1496	57	0.05	0.004	<0.00005	53.9	118	1.1	0.07	<0.005	<0.0004	<0.003	<0.04	<0.0007	<0.0002	0.01	<0.04
HRS	Surface	0.59	1498	58	0.05	0.004	<0.00005	53.8	117	1	0.07	0.01	<0.0004	<0.003	<0.04	0	<0.0002	0.02	<0.04

Appendix 3. *Bulk shell stable isotope data.*

Sample Name	Site	Sample Type	Genera	Sub-site	$\delta^{13}C$ (‰-VPDB)	$\delta^{18}O$ (‰-VSMOW)	Data Source	Lab
BL-M-T6-1	BL	Shell	*Succineidae*	BL-Marsh	-3.4	-10.017	this study	SIRFER
BL-M-T6-2	BL	Shell	*Succineidae*	BL-Marsh	-3.33	-10.017	this study	SIRFER
BL-M-T6-6	BL	Shell	*Succineidae*	BL-Marsh	-4.23	-10.546	this study	SIRFER
BL-M-T6-3	BL	Shell	*Succineidae*	BL-Marsh	-3.07	-10.703	this study	SIRFER
BL-M-T6-4	BL	Shell	*Succineidae*	BL-Marsh	-5.18	-10.812	this study	SIRFER
BL-M-T6-5	BL	Shell	*Succineidae*	BL-Marsh	-6.49	-11.096	this study	SIRFER
BL-P-T5-8	BL	Shell	*Melanoides*	BL-Pond	-1.84	-12.646	this study	SIRFER
BL-M-T2-1	BL	Shell	*Pyrgulopsis*	BL-Marsh	-2.34	-13.182	this study	SIRFER
BL-M-T2-3	BL	Shell	*Pyrgulopsis*	BL-Marsh	-2.52	-13.894	this study	SIRFER
BL-M-T2-4	BL	Shell	*Pyrgulopsis*	BL-Marsh	-2.14	-14.243	this study	SIRFER
HRS-01-PP-O1	HRS	Shell	*Pyrgulopsis*	HRS-Subsite-01	-5.24	-14.343	this study	SIRFER
HRS-03-PP-O1	HRS	Shell	*Pyrgulopsis*	HRS-Subsite-03	-4.85	-14.361	this study	SIRFER
HRS-03-PP-O2	HRS	Shell	*Pyrgulopsis*	HRS-Subsite-03	-3.95	-14.406	this study	SIRFER
HRS-02-TP-O2	HRS	Shell	*Tryonia*	HRS-Subsite-02	-4.39	-14.568	this study	SIRFER
HRS-04-TP-O1	HRS	Shell	*Tryonia*	HRS-Subsite-04	-4.42	-14.578	this study	SIRFER
BL-M-T2-2	BL	Shell	*Pyrgulopsis*	BL-Marsh	-2.09	-14.634	this study	SIRFER
HRS-04-TP-O2	HRS	Shell	*Tryonia*	HRS-Subsite-04	-4.48	-14.733	this study	SIRFER
HRS-01-TP-O2	HRS	Shell	*Tryonia*	HRS-Subsite-01	-4.76	-14.776	this study	SIRFER
HRS-02-PP-O1	HRS	Shell	*Pyrgulopsis*	HRS-Subsite-02	-4.67	-14.795	this study	SIRFER
HRS-01-PP-O2	HRS	Shell	*Pyrgulopsis*	HRS-Subsite-01	-5.23	-14.83	this study	SIRFER
HRS-02-PP-O2	HRS	Shell	*Pyrgulopsis*	HRS-Subsite-02	-4.86	-14.851	this study	SIRFER
HRS-02-TP-O1	HRS	Shell	*Tryonia*	HRS-Subsite-02	-4.97	-14.858	this study	SIRFER
HRS-04-PP-O1	HRS	Shell	*Pyrgulopsis*	HRS-Subsite-04	-5	-14.879	this study	SIRFER
HRS-03-TP-O1	HRS	Shell	*Tryonia*	HRS-Subsite-03	-4.82	-14.88	this study	SIRFER
HRS-04-PP-O2	HRS	Shell	*Pyrgulopsis*	HRS-Subsite-04	-5.18	-14.959	this study	SIRFER
HRS-03-TP-O2	HRS	Shell	*Tryonia*	HRS-Subsite-03	-4.2	-15.059	this study	SIRFER
BL-P-T4-2	BL	Shell	*Planorbella*	BL-Pond	-4.82	-15.295	this study	SIRFER
HRS-01-TP-O1	HRS	Shell	*Tryonia*	HRS-Subsite-01	-5.01	-15.349	this study	SIRFER
HRS-T2-4	HRS	Shell	*Pyrgulopsis*	HRS-Subsite-00	-5.14	-15.565	this study	SIRFER
HRS-T4-1	HRS	Shell	*Planorbella*	HRS-Subsite-00	-8.96	-15.67	this study	SIRFER
HRS-T2-1	HRS	Shell	*Pyrgulopsis*	HRS-Subsite-00	-5.19	-15.718	this study	SIRFER
HRS-T2-5	HRS	Shell	*Pyrgulopsis*	HRS-Subsite-00	-5.19	-15.778	this study	SIRFER
HRS-T2-2	HRS	Shell	*Pyrgulopsis*	HRS-Subsite-00	-5.08	-15.788	this study	SIRFER
HRS-T2-3	HRS	Shell	*Pyrgulopsis*	HRS-Subsite-00	-5.03	-15.883	this study	SIRFER
HRS-T1-3	HRS	Shell	*Tryonia*	HRS-Subsite-00	-4.95	-15.98	this study	SIRFER
BL-P-T2-2	BL	Shell	*Pyrgulopsis*	BL-Pond	-1.92	-16.045	this study	SIRFER
HRS-T1-4	HRS	Shell	*Tryonia*	HRS-Subsite-00	-4.98	-16.068	this study	SIRFER
HRS-T1-1	HRS	Shell	*Tryonia*	HRS-Subsite-00	-4.57	-16.085	this study	SIRFER
HRS-T1-5	HRS	Shell	*Tryonia*	HRS-Subsite-00	-5.02	-16.131	this study	SIRFER
HRS-T1-2	HRS	Shell	*Tryonia*	HRS-Subsite-00	-4.96	-16.158	this study	SIRFER
BL-P-T2-1	BL	Shell	*Pyrgulopsis*	BL-Pond	-1.72	-16.282	this study	SIRFER
BL-P-T3-2	BL	Shell	*Physella*	BL-Pond	-5.02	-16.341	this study	SIRFER
BL-S-T1-1	BL	Shell	*Tryonia*	BL-Spring	-1.92	-16.374	this study	SIRFER
BL-P-T1-1	BL	Shell	*Tryonia*	BL-Pond	-1.71	-16.524	this study	SIRFER
BL-P-T4-5	BL	Shell	*Planorbella*	BL-Pond	-4.5	-16.641	this study	SIRFER
BL-P-T3-1	BL	Shell	*Physella*	BL-Pond	-4.82	-16.819	this study	SIRFER
BL-P-T4-1	BL	Shell	*Planorbella*	BL-Pond	-3.65	-16.823	this study	SIRFER
BL-P-T5-6	BL	Shell	*Melanoides*	BL-Pond	-2.24	-16.858	this study	SIRFER
BL-L-T5-4	BL	Shell	*Melanoides*	BL-Lake	-2.93	-16.893	this study	SIRFER
BL-P-T4-4	BL	Shell	*Planorbella*	BL-Pond	-3.71	-16.916	this study	SIRFER
BL-P-T5-3	BL	Shell	*Melanoides*	BL-Pond	-2.48	-17.015	this study	SIRFER
BL-P-T5-4	BL	Shell	*Melanoides*	BL-Pond	-2.15	-17.058	this study	SIRFER
BL-P-T5-1	BL	Shell	*Melanoides*	BL-Pond	-2.44	-17.084	this study	SIRFER
BL-P-T5-7	BL	Shell	*Melanoides*	BL-Pond	-2.49	-17.125	this study	SIRFER
BL-P-T5-2	BL	Shell	*Melanoides*	BL-Pond	-2.46	-17.135	this study	SIRFER
BL-L-T5-3	BL	Shell	*Melanoides*	BL-Lake	-2.99	-17.162	this study	SIRFER
BL-L-T5-1	BL	Shell	*Melanoides*	BL-Lake	-3.02	-17.238	this study	SIRFER
BL-L-T5-2	BL	Shell	*Melanoides*	BL-Lake	-2.38	-17.238	this study	SIRFER
BL-S-T5-4	BL	Shell	*Melanoides*	BL-Spring	-2.23	-17.343	this study	SIRFER
BL-S-T5-1	BL	Shell	*Melanoides*	BL-Spring	-2.1	-17.516	this study	SIRFER
BL-S-T5-5	BL	Shell	*Melanoides*	BL-Spring	-2.29	-17.519	this study	SIRFER
BL-S-T1-2	BL	Shell	*Tryonia*	BL-Spring	-1.91	-17.541	this study	SIRFER
BL-S-T5-2	BL	Shell	*Melanoides*	BL-Spring	-2.13	-17.549	this study	SIRFER
BL-P-T4-3	BL	Shell	*Planorbella*	BL-Pond	-3.08	-	this study	SIRFER
BL-Spring-Shell-2019-1	BL	Shell	*Melanoides*	BL-Spring	-2.21	-	Lerback and others, 2023	NOSAMS
BL-Spring-Shell-2019-2	BL	Shell	*Melanoides*	BL-Spring	-2.26	-	Lerback and others, 2023	NOSAMS
BL-Spring-Shell-2019-3	BL	Shell	*Melanoides*	BL-Spring	-	-	Lerback and others, 2023	NOSAMS
BL-Spring-Shell-2019-4	BL	Shell	*Melanoides*	BL-Spring	-3.08	-	Lerback and others, 2023	NOSAMS
BL-Pond-Shell-2019-1	BL	Shell	*Melanoides*	BL-Pond	-2.17	-	Lerback and others, 2023	NOSAMS
BL-Pond-Shell-2019-2	BL	Shell	*Melanoides*	BL-Pond	-2.09	-	Lerback and others, 2023	NOSAMS
BL-Pond-Shell-2019-3	BL	Shell	*Melanoides*	BL-Pond	-2.37	-	Lerback and others, 2023	NOSAMS
BL-Pond-Shell-2019-4	BL	Shell	*Melanoides*	BL-Pond	-2.14	-	Lerback and others, 2023	NOSAMS
BL-Lake-Shell-2018-1	BL	Shell	*Melanoides*	BL-Lake	-3.06	-	Lerback and others, 2023	NOSAMS
BL-Lake-Shell-2018-2	BL	Shell	*Melanoides*	BL-Lake	-2.85	-	Lerback and others, 2023	NOSAMS
BL-Lake-Shell-2018-3	BL	Shell	*Melanoides*	BL-Lake	-2.98	-	Lerback and others, 2023	NOSAMS

BL-Lake-Shell-2018-4	BL	Shell	*Melanoides*	BL-Lake	-3.89	-	Lerback and others, 2023	NOSAMS
HRS-Pond-Shell-2020-1	HRS	Shell	*Pyrgulopsis*	HRS-Subsite-00	-5.18	-	Lerback and others, 2023	NOSAMS
HRS-Pond-Shell-2020-2	HRS	Shell	*Pyrgulopsis*	HRS-Subsite-00	-4.43	-	Lerback and others, 2023	NOSAMS
HRS-Pond-Shell-2020-3	HRS	Shell	*Pyrgulopsis*	HRS-Subsite-00	-4.77	-	Lerback and others, 2023	NOSAMS
HRS-Pond-Shell-2020-4	HRS	Shell	*Pyrgulopsis*	HRS-Subsite-00	-4.79	-	Lerback and others, 2023	NOSAMS
BL-Spring-Shell-2020-5	BL	Shell	*Pyrgulopsis*	BL-Spring	-1.82	-	Lerback and others, 2023	NOSAMS
BL-Spring-Shell-2020-6	BL	Shell	*Pyrgulopsis*	BL-Spring	-1.97	-	Lerback and others, 2023	NOSAMS
BL-Spring-Shell-2020-7	BL	Shell	*Pyrgulopsis*	BL-Spring	-1.94	-	Lerback and others, 2023	NOSAMS
BL-Spring-Shell-2020-8	BL	Shell	*Pyrgulopsis*	BL-Spring	-1.83	-	Lerback and others, 2023	NOSAMS
BL-Pond-Sediment-2020-1	BL	Sediment	-	BL-Pond	-26.61	-	Lerback and others, 2023	NOSAMS
HRS-Pond-Sediment-2020-1	HRS	Sediment	-	HRS-Subsite-00	-20.65	-	Lerback and others, 2023	NOSAMS

Appendix 4 . *Water stable isotope data.*

Site	Type	$\delta^{18}O$ (‰-VSMOW)	$\delta^{18}O$ (‰-VPDB converted)	$\delta^{13}C$ (‰-VPDB)	$\delta^{13}C$ Source	Lab	Source	Subsite
BL	Water	-	-	-3.73	Measured	NOSAMS	Lerback and others, 2023	BL-Lake
BL	Water	-	-	-4	Measured	NOSAMS	Lerback and others, 2023	BL-Pond
BL	Water	-	-	-4.5	Measured	NOSAMS	Lerback and others, 2019 Supplementary Data. "Lookout Point, 6/2/2017"	BL-Spring
BL	Water	-	-	-4.65	Measured	NOSAMS	Lerback and others, 2023	BL-Spring
HRS	Water	-	-	-7.02	Measured	NOSAMS	Lerback and others, 2023	HRS-Subsite-00
BL	Water	-15.9	-45.42	-		SIRFER	Lerback and others, 2019	BL-Spring
BL	Water	-16.05	-45.56	-		SIRFER	Lerback and others, 2019	BL-Spring
BL	Water	-15.92	-45.43	-		SIRFER	Lerback and others, 2019	BL-Spring
BL	Water	-15.99	-45.5	-		SIRFER	Lerback and others, 2019	BL-Spring
BL	Water	-16	-45.51	-		SIRFER	Lerback and others, 2019	BL-Spring
BL	Water	-16.1	-45.61	-		SIRFER	Lerback and others, 2019	BL-Spring
BL	Water	-15.86	-45.37	-		SIRFER	Lerback and others, 2019	BL-Lake
BL	Water	-15.74	-45.26	-		SIRFER	Lerback and others, 2019	BL-Lake
HRS	Water	-16.23	-45.73	-		SIRFER	Lerback and others, 2023	HRS-Subsite-00
HRS	Water	-16.06	-45.57	-		SIRFER	Lerback and others, 2023	HRS-Subsite-00
HRS	Water	-15.98	-45.49	-		SIRFER	Lerback and others, 2023	HRS-Subsite-00
HRS	Water	-16.04	-45.55	-		SIRFER	Lerback and others, 2023	HRS-Subsite-00
HRS	Water	-16	-45.51	-		SIRFER	Lerback and others, 2023	HRS-Subsite-00
HRS	Water	-15.89	-45.41	-		SIRFER	Lerback and others, 2023	HRS-Subsite-00
HRS	Water	-16.01	-45.52	-		SIRFER	Lerback and others, 2023	HRS-Subsite-00

Appendix 5. *Gastropod Intrashell $\delta^{13}C$ and $\delta^{18}O$ Transect Data.*

Sample Name	Drill site Number	$\delta^{13}C$	$\delta^{18}O$
BL-S-T5-9-4	4	-2.91	-17.46
BL-S-T5-9-3	3	-2.41	-17.48
BL-S-T5-9-2	2	-2.21	-17.32
BL-S-T5-9-1	1	-2.24	-17.49
BL-S-T5-8-4	4	-2.64	-17.25
BL-S-T5-8-3	3	-2.54	-17.33
BL-S-T5-8-2	2	-2.13	-17.37
BL-S-T5-8-1	1	-1.91	-17.51
BL-S-T5-7-4	4	-2.54	-17.67
BL-S-T5-7-3	3	-2.08	-17.33
BL-S-T5-7-2	2	-2.24	-17.65
BL-S-T5-7-1	1	-2.25	-17.26
BL-S-T5-6-4	4	-2.97	-16.57
BL-S-T5-6-3	3	-2.84	-16.96
BL-S-T5-6-2	2	-2.41	-17.18
BL-S-T5-6-1	1	-2.2	-17.36

Appendix 6. *Calculated formation temperatures of gastropod shells*

Sample Name	Genera	Sub-site	T (°C; Kim and O'Neill, 1997)	T (°C; Kim and others, 2007)	T (°C; White and others, 1999)
BL-M-T6-1	*Succineidae*	BL-Marsh	-11.4	-8.6	-6.8
BL-M-T6-2	*Succineidae*	BL-Marsh	-11.4	-8.6	-6.8
BL-M-T6-6	*Succineidae*	BL-Marsh	-9.3	-6.5	-4.5
BL-M-T6-3	*Succineidae*	BL-Marsh	-8.7	-5.9	-3.8
BL-M-T6-4	*Succineidae*	BL-Marsh	-8.3	-5.4	-3.3
BL-M-T6-5	*Succineidae*	BL-Marsh	-7.2	-4.3	-2.1
BL-P-T5-8	*Melanoides*	BL-Pond	-0.8	2.2	5
BL-M-T2-1	*Pyrgulopsis*	BL-Marsh	1.4	4.5	7.5
BL-M-T2-3	*Pyrgulopsis*	BL-Marsh	4.5	7.7	11
BL-M-T2-4	*Pyrgulopsis*	BL-Marsh	6	9.2	12.7
BL-M-T2-2	*Pyrgulopsis*	BL-Marsh	7.7	11	14.6
BL-P-T4-2	*Planorbella*	BL-Pond	10.7	14.1	18
BL-P-T2-2	*Pyrgulopsis*	BL-Pond	14.1	17.7	21.9
BL-P-T2-1	*Pyrgulopsis*	BL-Pond	15.2	18.8	23.2
BL-P-T3-2	*Physella*	BL-Pond	15.5	19.1	23.5
BL-S-T1-1	*Tryonia*	BL-Spring	15.7	19.2	23.7
BL-P-T1-1	*Tryonia*	BL-Pond	16.4	20	24.5
BL-P-T4-5	*Planorbella*	BL-Pond	16.9	20.5	25.1
BL-P-T3-1	*Physella*	BL-Pond	17.8	21.4	26.1
BL-P-T4-1	*Planorbella*	BL-Pond	17.8	21.4	26.1
BL-P-T5-6	*Melanoides*	BL-Pond	17.9	21.6	26.3
BL-L-T5-4	*Melanoides*	BL-Lake	18.1	21.8	26.5
BL-P-T4-4	*Planorbella*	BL-Pond	18.2	21.9	26.6
BL-P-T5-3	*Melanoides*	BL-Pond	18.7	22.4	27.1
BL-P-T5-4	*Melanoides*	BL-Pond	18.9	22.6	27.4
BL-P-T5-1	*Melanoides*	BL-Pond	19	22.7	27.5
BL-P-T5-7	*Melanoides*	BL-Pond	19.2	22.9	27.7
BL-P-T5-2	*Melanoides*	BL-Pond	19.3	23	27.8
BL-L-T5-3	*Melanoides*	BL-Lake	19.4	23.1	27.9
BL-L-T5-1	*Melanoides*	BL-Lake	19.8	23.5	28.4
BL-L-T5-2	*Melanoides*	BL-Lake	19.8	23.5	28.4
BL-S-T5-4	*Melanoides*	BL-Spring	20.3	24	28.9
BL-S-T5-1	*Melanoides*	BL-Spring	21.1	24.9	29.9
BL-S-T5-5	*Melanoides*	BL-Spring	21.1	24.9	29.9
BL-S-T1-2	*Tryonia*	BL-Spring	21.2	25	30
BL-S-T5-2	*Melanoides*	BL-Spring	21.3	25.1	30.1
HRS-01-PP-O1	*Pyrgulopsis*	HRS-Subsite-01	6.3	9.5	13
HRS-03-PP-O1	*Pyrgulopsis*	HRS-Subsite-03	6.3	9.6	13.1
HRS-03-PP-O2	*Pyrgulopsis*	HRS-Subsite-03	6.5	9.8	13.3
HRS-02-TP-O2	*Tryonia*	HRS-Subsite-02	7.3	10.6	14.1
HRS-04-TP-O1	*Tryonia*	HRS-Subsite-04	7.3	10.6	14.2
HRS-04-TP-O2	*Tryonia*	HRS-Subsite-04	8	11.3	15
HRS-01-TP-O2	*Tryonia*	HRS-Subsite-01	8.2	11.5	15.2
HRS-02-PP-O1	*Pyrgulopsis*	HRS-Subsite-02	8.3	11.6	15.3
HRS-01-PP-O2	*Pyrgulopsis*	HRS-Subsite-01	8.4	11.8	15.4
HRS-02-PP-O2	*Pyrgulopsis*	HRS-Subsite-02	8.5	11.9	15.6
HRS-02-TP-O1	*Tryonia*	HRS-Subsite-02	8.5	11.9	15.6
HRS-04-PP-O1	*Pyrgulopsis*	HRS-Subsite-04	8.6	12	15.7
HRS-03-TP-O1	*Tryonia*	HRS-Subsite-03	8.6	12	15.7
HRS-04-PP-O2	*Pyrgulopsis*	HRS-Subsite-04	9	12.4	16.1
HRS-03-TP-O2	*Tryonia*	HRS-Subsite-03	9.4	12.8	16.6
HRS-01-TP-O1	*Tryonia*	HRS-Subsite-01	10.8	14.2	18.1
HRS-T2-4	*Pyrgulopsis*	HRS-Subsite-00	11.7	15.2	19.2
HRS-T4-1	*Planorbella*	HRS-Subsite-00	12.2	15.7	19.8
HRS-T2-1	*Pyrgulopsis*	HRS-Subsite-00	12.4	15.9	20
HRS-T2-5	*Pyrgulopsis*	HRS-Subsite-00	12.7	16.2	20.3
HRS-T2-2	*Pyrgulopsis*	HRS-Subsite-00	12.8	16.3	20.4
HRS-T2-3	*Pyrgulopsis*	HRS-Subsite-00	13.2	16.7	20.9
HRS-T1-3	*Tryonia*	HRS-Subsite-00	13.6	17.2	21.4
HRS-T1-4	*Tryonia*	HRS-Subsite-00	14.1	17.6	21.8
HRS-T1-1	*Tryonia*	HRS-Subsite-00	14.1	17.7	21.9
HRS-T1-5	*Tryonia*	HRS-Subsite-00	14.4	17.9	22.2
HRS-T1-2	*Tryonia*	HRS-Subsite-00	14.5	18	22.3

Appendix 7. *Gastropod Shell Trace Element Data (mg/kg)*

Site	Taxa	Li	Na	K	Rb	Cs	Be	Mg	Ca	Sr	Ba	Al	Sc	Mn	Fe	Cu	Ni	Zn	As
BL	*Succineidae*	3.3	2573	370	0.12	0.008	0.0392	56.7	407754	2486.8	40.07	4.86	0.0268	12.19	2.611	5.4	0.21	2.44	0.11
BL	*Succineidae*	5.93	2268	456	0.19	0.037	0.195	130.5	425888	2666.1	55.38	13.16	0.032	9.67	8.333	3.7	0.22	3.91	0.36
BL	*Succineidae*	2.86	2464	561	0.2	0.021	0.0516	82.2	430344	2473.6	42.62	11.31	0.0398	12.02	10.424	3.4	0.15	2.11	0.42
BL	*Succineidae*	4.14	2340	427	0.13	0.007	0.064	40.6	401159	2463.8	36.12	3.7	0.0271	12.63	5.667	11.2	0.35	3.55	0.26
HRS	*Pyrgulopsis*	1.6	2170	21	0.03	0.017	0.007	80.6	398182	1263.9	99.39	5.95	0.09	3.12	100.026	<11	1.9	2.09	0.26
HRS	*Pyrgulopsis*	2	2667	22	<0.03	0.007	0.0105	51.1	415211	1200.8	106.43	7.12	0.0949	6.75	14.235	<11	2.2	1.05	0.11
HRS	*Pyrgulopsis*	1.47	1960	18	0.03	0.015	0.0077	63.9	347402	1131.3	83.02	12.29	0.0812	2.51	67.234	<9	1.67	0.74	0.26
HRS	*Tryonia*	1.44	2879	45	0.25	0.093	0.0134	230.9	425229	1317.5	129.36	81.88	0.1146	8.45	64.693	<20	2.25	2.11	0.14

Great Salt Lake Desert Landscape Change Over Multiple Temporal Scales—A Field Trip Guide Covering the Bonneville Salt Flats and Knolls Sand Dunes

Jeremiah A. Bernau[1,3], Brenda B. Bowen[1], Charles G. Oviatt[2], and Donald L. Clark[3]
[1]*Department of Geology and Geophysics, University of Utah, Salt Lake City, Utah,* jeremiahbernau@gmail.com
[2]*Department of Geology, Kansas State University, Manhattan, Kansas*
[3]*Utah Geological Survey, Salt Lake City, Utah*

10.31711/ugap.v51i.145

TRIP OVERVIEW

This one-day (~260-mile) field trip guide provides an overview of the late Pleistocene to Holocene history of the Great Salt Lake Desert. Stops include Knolls Sand Dunes and areas on or surrounding the Bonneville Salt Flats, such as Juke Box trench, the Bonneville Salt Flats International Speedway, and the saline pan center and edge (Figure 1). We cover the post-Lake Bonneville geomorphic evolution of the Great Salt Lake Desert including changes in land cover over the past century. The Great Salt Lake Desert area provides unique access to saline landscape features including gypsum dunes and a perennial saline pan. We discuss the origin of these features and how they fit within the area's broader geologic context. The accessibility of sites discussed here depends on surface conditions. In general, late summer to early fall is the most opportune time to visit this area. *Vehicular travel to any of the off-road sites is discouraged when there is standing water or high near-surface moisture (wet mud with little traction). Surface conditions can change rapidly, and we recommend researching current conditions before initiating this trip. This desert is hot and dry during the summer and there is no shade and limited access to water; please plan accordingly.*

Past and current Great Salt Lake Desert depositional changes provide an analog for the modern Great Salt Lake with changing water availability, potential dust production, competing priorities, and rapidly changing land cover. The information presented here impacts understanding natural and geologic heritage, changing management strategies, and landscape dynamism over multiple spatial and temporal scales.

DEPOSITIONAL AND EROSIONAL HISTORY

This trip features a landscape in the heart of the Great Basin, the Bonneville basin in northwestern Utah, which includes classic examples of Basin and Range topography. While traveling between Salt Lake City and the Great Salt Lake Desert, we will cross several mountain ranges that have excellent fault-block tilting and Lake Bonneville shoreline exposures. The Bonneville Salt Flats and Knolls dune field areas are bounded by grabens with <300 ft of deposition in the past 600,000 to 800,000 years (Shuey, 1971). The Bonneville Salt Flats is located within the Wendover Graben; this area has >1000 ft of laminated carbonate muds and gypsum beds that are underlain by conglomerates (Stephens, 1974; Bernau and others, 2023b). The Wendover and other nearby grabens began forming in the Miocene (Miller and others, 2021). Although faulting and seismic activity are thought to have largely ceased in this area, we discuss evidence for late Pleistocene to Holocene fault movement and soft sediment deformation features (the cause of these features, whether seismicity, decompression dewatering, or compaction, is unknown). In addition to this field trip guide, several maps provide more insights into the geologic history of this area (Cook and others, 1964; Doelling, 1964; Stifel, 1964; Doelling and others, 1994; Clark and others, 2020; Bernau and others, 2023; Clark and others, in progress).

Late Pleistocene to Holocene Geological Record

Late Pleistocene Lake Bonneville provides the geologic backdrop for this trip. Based on radiocarbon dating, Lake Bonneville was persistent between 30,000 and 13,000 calibrated radiocarbon years before present (cal yr B.P.) (Figure 2) (Oviatt, 2015). At its peak, it was almost as big as Lake Michigan and extended over one-third of the state of Utah. Lake Bonneville extended from the Wasatch Range to the Utah-Nevada state line area and from Soda Springs in

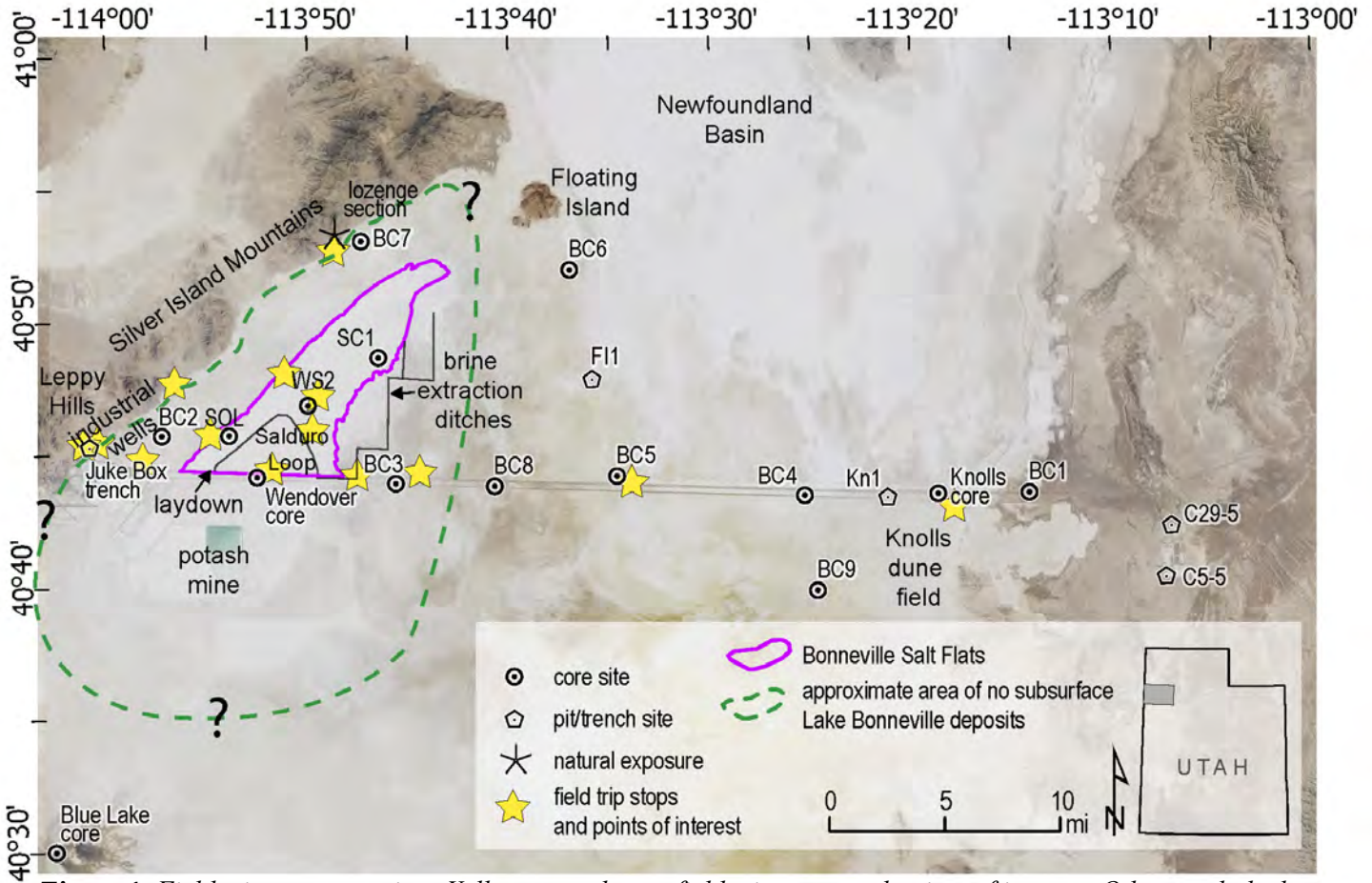

Figure 1. *Field trip area overview. Yellow stars denote field trip stops and points of interest. Other symbols denote sites used to interpret the Great Salt Lake Desert depositional record in Figure 3. Figure modified from Clark and others (in progress). Basemap imagery from Earthstar Geographics.*

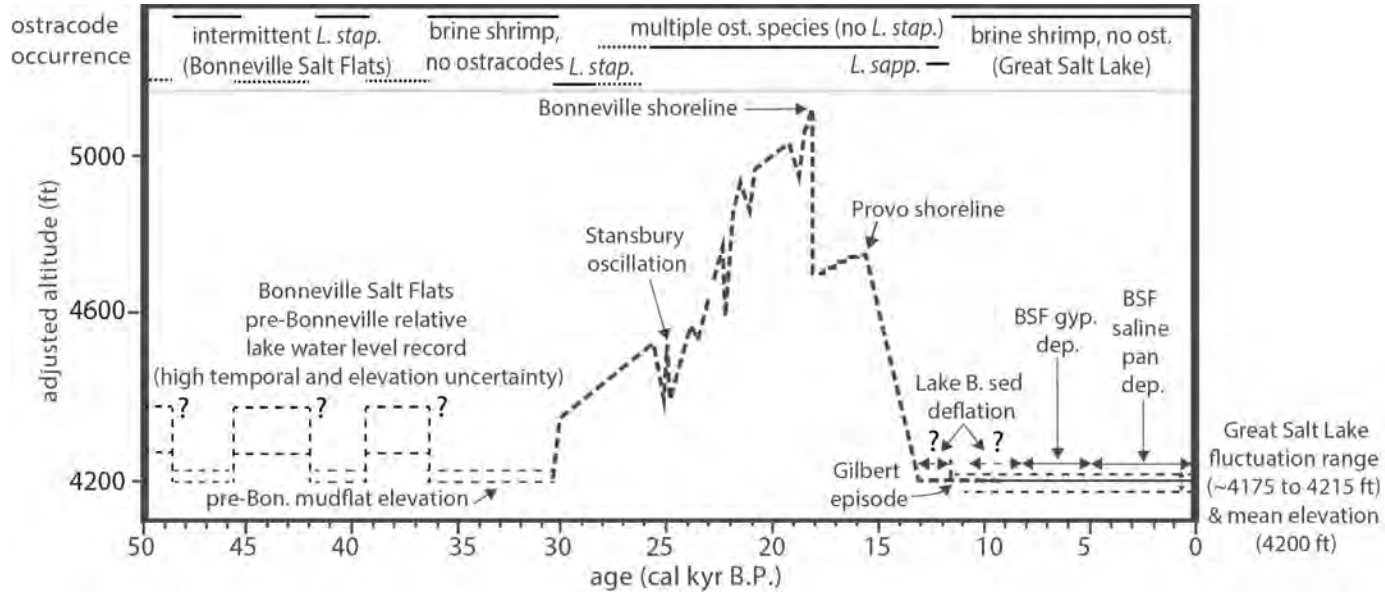

Figure 2. *Lake Bonneville hydrograph with depositional history from Bonneville Salt Flats cores added. Modified from Oviatt (2015).*

southern Idaho south to Parowan, Utah (making it nearly twice as long as it was wide) (Gilbert, 1890). In addition to its shorelines, Lake Bonneville left a regular stratigraphic succession of marl across its basin (~1–6 ft thick in most areas).

Erosion of the Great Salt Lake Desert

The Great Salt Lake and Bonneville Salt Flats have long been considered saline remnants of Lake Bonneville (Eardley, 1962). Analysis of Great Salt Lake Desert shallow cores, pits, trenches, and other exposures indicates that story is more complicated (Oviatt and others, 2020; Bernau, 2022; Bernau and others, 2023b; Clark and others, in progress). The Bonneville Salt Flats, rather than forming from Lake Bonneville's remnant waters, began forming at ~8,000 cal yr B.P., about 5,000 years after Lake Bonneville's final retreat to modern Great Salt Lake levels. After Lake Bonneville desiccated, an estimated 3–6 ft of Lake Bonneville sediments were deflated (eroded by wind) from the area surrounding the site of the modern Bonneville Salt Flats. This past deflation provides an analog for potential Great Salt Lake sediment deflation that may occur if its water levels continue to decline.

The Great Salt Lake Desert depositional record along Interstate Highway 80 (I-80) is summarized in Figure 3 (Louderback and Rhode, 2009; Oviatt and others, 2018; Oviatt and others, 2020; Bernau, 2022). Surprisingly, because of the deflation of Lake Bonneville sediments, the Bonneville Salt Flats—a Great Salt Lake Desert depositional area with up to 5 ft of Holocene deposition—has a less complete geologic record than the adjoining mudflat, which has had little, if any Holocene deposition but has retained all to some of the Lake Bonneville marl deposits. This depositional difference highlights the potential for topographic lows in arid climates to have less complete geologic records, making this an important consideration when planning and interpreting investigations of paleoenvironmental records.

Research on modern deflation at Owens Lake, California, provides a model that explains observed Great Salt Lake Desert deflationary patterns (Figure 4) (Reynolds and others, 2007). Deflation in arid settings is strongly influenced by groundwater level and salinity. Playas become deflationary surfaces when groundwater levels fall far below the surface (Rosen, 1994). This fact alone, however, does not explain observed deflationary patterns. The Bonneville Salt Flats, as a regional topographic low, should have higher groundwater levels than adjoining Great Salt Lake Desert basin floor areas, which do not have the same degree of deflation. Salinity explains this apparent contradiction. The Bonneville Salt Flats area would have had higher groundwater salinity as water flowed in and evapoconcentrated from surface waters

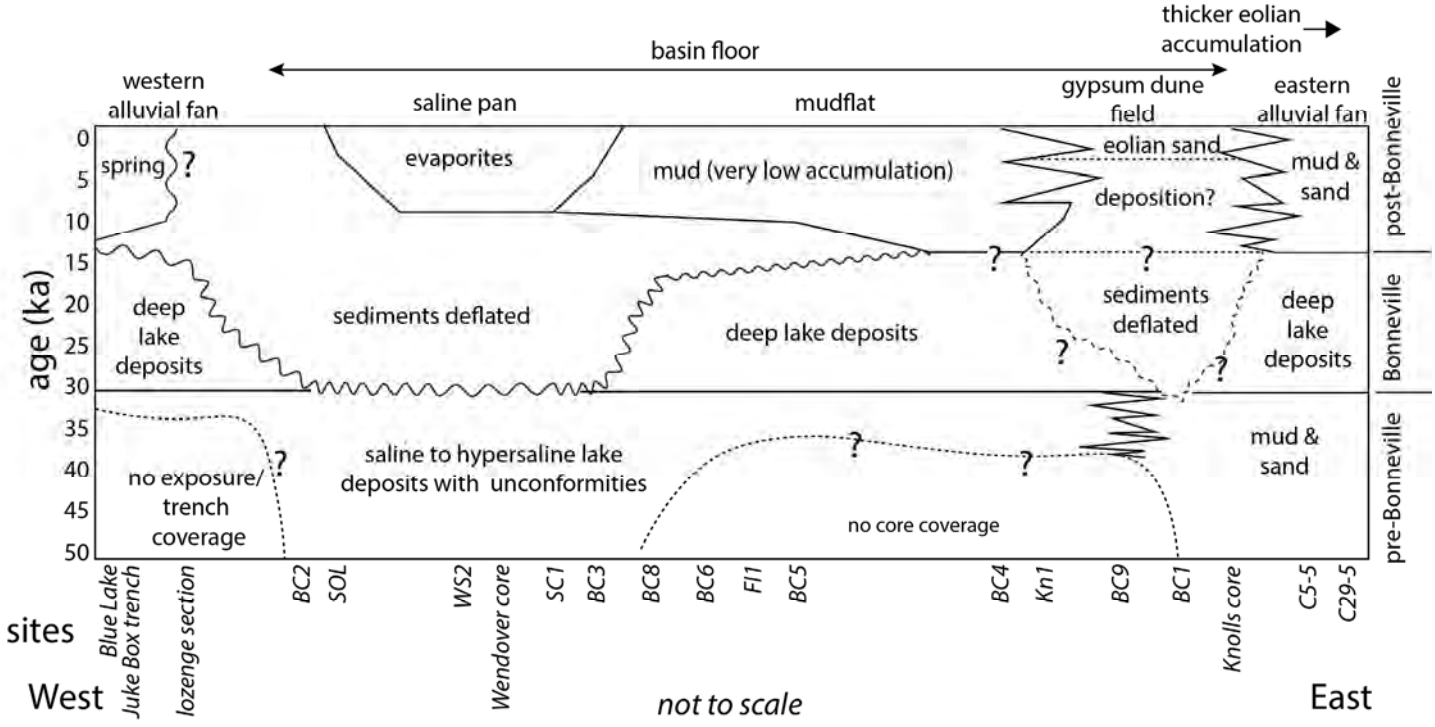

Figure 3. *Chronostratigraphic cross section of shallow Great Salt Lake Desert deposits. Figure is based on information from Great Salt Lake Desert core and pit sites shown in Figure 1 (Louderback and Rhode, 2009; Oviatt and others, 2018; Oviatt and others, 2020; Bernau, 2022) and the information supporting this figure is described in Bernau and others, 2023b.*

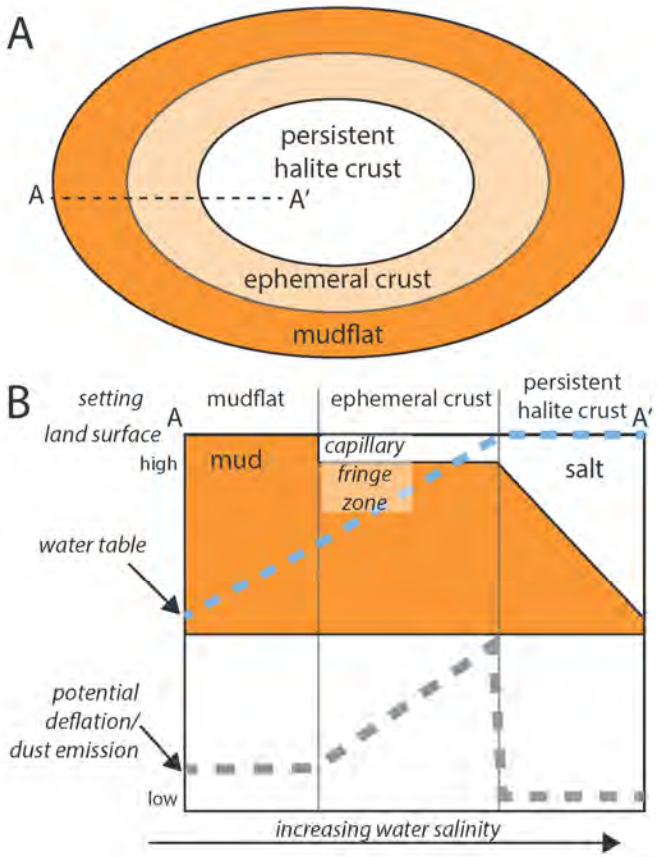

Figure 4. *Deflation model for the Great Salt Lake Desert, modified from Reynolds and others (2007). (A) The saline pan and surrounding area. (B) Cross section A - A' shows deflation is highest in the area immediately adjacent to the persistent halite crust (Figure from Bernau and others, 2023b).*

or groundwaters. Surficial salts, depending on their thickness and composition, greatly alter a surface's erodibility. Thick salt layers crystallized from standing water are very resistant to erosion. Ephemeral crusts created from groundwater evaporation, however, are highly unstable; they easily break up and act as abrasives. Similarly, displacive evaporite growth, commonly gypsum, may alter the properties of near-surface mud. Areas with minor salinity (groundwater table so low that the capillary fringe is below the surface, or they have continuous freshwater input) can form relatively stable surfaces that limit deflation.

Using the model in Figure 4, it is likely that before saline pan formation at the Bonneville Salt Flats that this area had an ephemeral crust that accelerated deflation, enabling Lake Bonneville sediments to be locally removed. As climate shifted at ~8,000 cal yr B.P., gypsum sands began accumulating at the saline pan, limiting deflation. Finally, saline pan deposition with bedded halite deposits began to accumulate around 5,500 cal yr B.P. as the climate became cooler and wetter (Bernau, 2022). These cooler and wetter conditions enabled more surface water, and potentially, groundwater, to flow into the saline pan and for deeper and longer-lived surface ponding to occur. Thicker, bedded halite deposits, like the halite layers seen at the modern surface of the Bonneville Salt Flats were then able to form.

FIELD TRIP ROAD LOG

Begin by driving west along I-80 from Salt Lake City for ~80 miles to Exit 41 (Knolls). You will pass through several mountain ranges and basins of the eastern Basin and Range physiographic province. The Great Salt Lake Desert, because of its remoteness, hosts hazardous waste facilities and military testing. Much of the Great Salt Lake Desert hass limited to public access due to military testing and training activities. Near Aragonite, as you enter the Great Salt Lake Desert (near Exit 49), smokestacks from a hazardous waste incineration plant to the south become visible. A low-level nuclear and mixed waste landfill is west of this facility near Clive (Exit 49). A hazardous waste landfill is also located northwest of the Clive exit.

Knolls Sand Dunes

Take Exit 41, drive to the south, and follow the road as it bends west. After ~1 mile, you will be in the dunes (40.7244° N, 113.2821° W; all coordinates in WGS84 datum). Several places on the side of the road provide some distance from the road and are safer than the road for parking. This road can be busy with ATVs and UTVs, particularly on weekends.

Site Description

The Knolls dune field and other Great Salt Lake Desert gypsum dunes have been investigated since the 1950s (Jones, 1953; Eardley, 1962; Dean, 1978; Jewell and Nicoll, 2011; Boden, 2016; Fitzgerald, 2019). These dunes and salt pans are considered excellent analogs for aspects of the Martian landscape and may help us better understand Mars' surface evolution and past potential for the existence and preservation of life (Benison and Karmanocky, 2014). Gypsum dunes have low preservation potential. Most documented gypsum dunes are less than a few tens of thousands of years old (Warren, 2006).

Gypsum dunes on the eastern side of the Great Salt Lake Desert are concentrated along a change in slope (Doelling, 1964). Dunes consist of predominantly medium- to very fine sand (Figure 5) and may

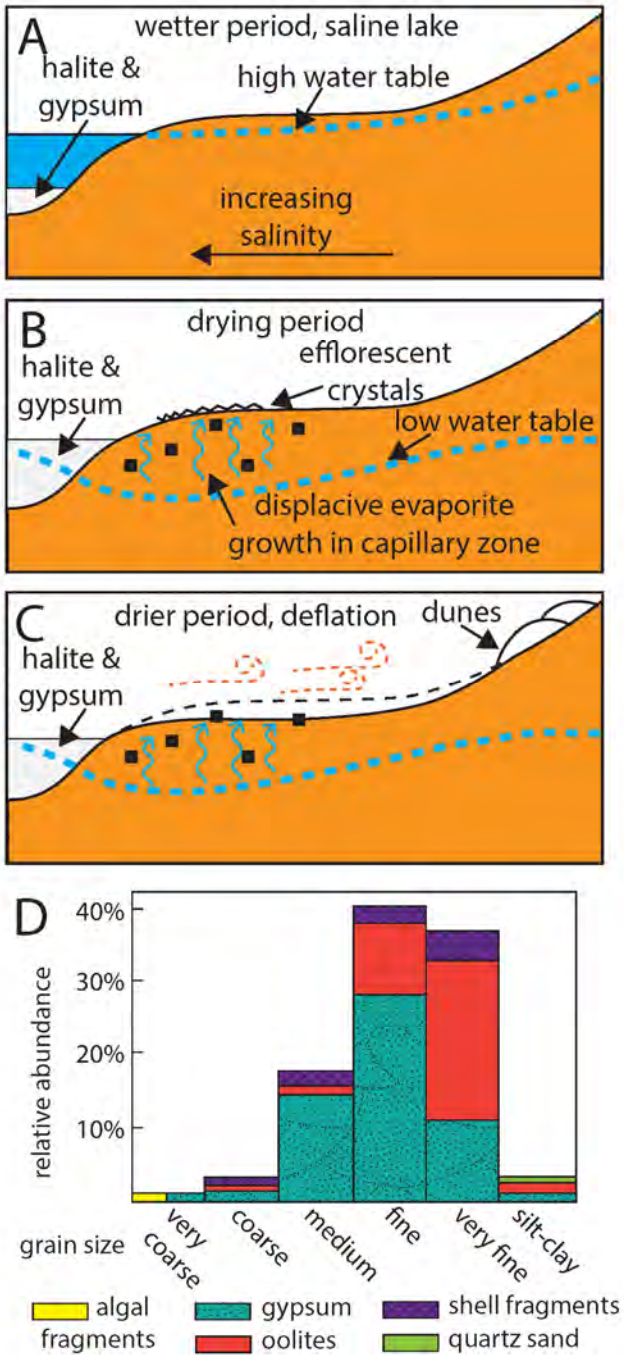

Figure 5. *Schematic model for gypsum dune origin (A to C) and grain size composition of dunes at Knolls (D). (A to C) is based on Bowler (1986) and (D) is modified from Jones (1953).*

be >30 ft high (Boden, 2016). Most grains are gypsum (up to 60%), with oolites being the second most common grain. Trace shell fragments (predominantly ostracodes), algal fragments, and quartz sand also occur (Jones, 1953). Quartz and oolitic dunes occur in other Great Salt Lake Desert areas (Dean, 1978). In addition to these eastern gypsum dunes, there are several smaller dune areas to the west, approaching the Bonneville Salt Flats (Boden, 2016).

Gypsum dunes are evidence of a drying saline landscape. Gypsum forms in arid environments 1) as bottom growth crystals at the bottom of a shallow saline lake, or 2) displacively in subsurface sediments from the evaporation of groundwaters. Great Salt Lake Desert gypsum dunes are thought to mostly originate from displacive growths. Drying conditions and falling groundwater levels enable gypsum crystals to be transported (Figure 5). Deflation of fine-grained sediments exposes displacive crystals which then are redistributed by wind and accumulate downwind along changes in slope. In the modern Great Salt Lake Desert, predominant winds are from the west/southwest (Jewell and Nicoll, 2011). Dunes are stabilized by vadose zone moisture (wetter conditions), when available, or vegetation, or they stabilize where prevailing winds meet.

Analyses of cores reveals that Lake Bonneville sediments were partially to fully deflated at and near Knolls (Eardley, 1962; Oviatt and others, 2020). Similarly, Lake Bonneville marl has been truncated in the area to the west of Knolls, indicating deflation was concentrated here (relative to the mudflats to the west) before gypsum deposition. Optically stimulated luminescence dating of gypsum crystals (an atypical material for this technique) suggested that gypsum dune formation has been constant since >2,300 yr B.P. and is ongoing (Fitzgerald, 2019). Gypsum was deposited at the Bonneville Salt Flats between 3,500 and 1,700 cal yr B.P. (Bernau, 2022). Analyses of aerial photography from the years 1953, 1972, and 2015 indicate that many dunes in the Knolls area are still active, with some dunes moving by several miles in that period (Fitzgerald, 2019). Similarly, our observations of sediment caught by a snow fence running parallel to old Highway 40 (south of I-80) indicate Great Salt Lake Desert deflation is still actively occurring. Sediments stopped by the snow fence consisted of mud, gypsum crystals, and carbonate lumps.

Transit To Juke Box Trench

Return to I-80 and continue west for 37 miles to Exit 4. The interstate mile markers below note areas of interest along this route.

Mile Marker 25

The unimproved road leading to the northwest from here connects to Floating Island. Floating Island's name stems from the mirage that occurs on hot days, creating an illusion that the small mountain is suspended or floating in the air. *Note: Traversing the Floating Island Dike Road is only advisable with a heavy-duty high-clearance vehicle.* This elevated road

on an earthen dike was constructed to limit the extent of the West Pond, a large lake created in the Great Salt Lake Desert by the West Desert Pumping Project in the 1980s (Wold and Waddell, 1994; Kohler, 2002). During this wet period, rising Great Sale Lake levels had the potential to flood infrastructure, commercial facilities, and homes. To address this, large pumps ~11 miles west of Lakeside, Utah, were constructed and used to pump Great Sale Lake water into the Great Salt Lake Desert, specifically the Newfoundland Evaporation Basin (the area directly to the north and east of mile marker 25) (Figure 1). When pumped waters evaporated, they created a saline pan that exceeds the modern Bonneville Salt Flats in extent. Over time the saline pan has decreased in size (Radwin and Bowen, 2021). Due to the absence of a saline pan in the Newfoundland Basin before the pumping project, it is unlikely that the hydrological conditions in the area would naturally support the long-term persistence of a saline pan.

Mile Marker 15

Analyses of aerial imagery and past reports of the Bonneville Salt Flats' extent indicate that the Bonneville Salt Flats' surface halite once extended to this location (Nolan, 1927). The past thickness of halite between mile markers 15 and 13, however, was thin (<1 inch).

Mile Marker 13.5

The ditch (which has adjoining tailings berms) stretching to the north is used to collect briny groundwater for potash production. The ditch extends under the highway and to the south where it connects to large evaporation ponds used to concentrate brine at the potash mine. These evaporation ponds are a local source of gypsum sand in the Great Salt Lake Desert. There is another set of berms between this and the next stop; they are from a brine collection ditch that has been inactive since the 1960s (the Salduro Loop).

Note: The ditches are located on private property and a fence along the road limits the pull-over area, ***do not stop here or enter the ditches***.

Mile Marker 10

Many people know the Bonneville Salt Flats from the I-80 rest stop. This stop has public restrooms and is the best place to explore the Bonneville Salt Flats' surface morphology for salt polygons. More discussion of salt polygons is available under the Bonneville Salt Flats surface morphology section of this guide.

Exit 4

Take Exit 4. Near Exit 4, there is a gas station with public restrooms, the remaining stops do not have any facilities. This stop is also an option to refuel before continuing or returning to Salt Lake City. Continue north on Leppy Pass Road for ~0.2 miles and take a left onto the paved I-80 frontage road. Continue on the I-80 frontage road for 1.4 miles until the road reaches a T intersection. Take a right. Continue for 0.8 miles towards the alluvial fan until there is another T in the road, take a left and continue for ~200 ft, and park. Walk to Juke Box trench (40.7549° N, 114.0102° W) (elevation ~4255 ft) ~150 ft southeast of here.

Please be aware that the roads beyond the I-80 frontage road are not regularly maintained. In the event of recent precipitation or insufficient evaporation to dry the surface, these roads can become impassable. Exercise caution and consider the weather conditions before venturing onto these roads. Under sustained dry conditions, all sites described in the rest of this guide are accessible in 2-wheel-drive vehicles with standard clearance. Accessibility is markedly reduced under wet conditions. ***Proceed with caution.***

Juke Box Trench

Juke Box trench is located at the site of a past spring. Because of the archeological significance of this area (see discussion of Juke Box Cave and Danger Cave), a trench was excavated and investigated by archeologist David Madsen and colleagues in the 1980s. It was enlarged in 2009 and revisited for paleoenvironmental interpretation (Oviatt and others, 2018).

This stop has an excellent example of pre-Bonneville, Lake Bonneville, and post-Bonneville deposits. The depositional section is (1) base: pre-Bonneville oolitic sand and carbonate-cemented gravel and sand; (2) Lake Bonneville offshore fine-grained sediments (marl); (3) an unconformity that cuts the Bonneville section; (4) a gravel lens at the base of the post-Bonneville sequence (possibly deposited during the Gilbert episode); and (5) Holocene wetland deposits.

Depositional record

Three main strata in Lake Bonneville marl correspond to different stages in the lake's levels. During the lake's rising (transgressive) stage, it left laminated marls (Figure 6). The laminae are interpreted as evi-

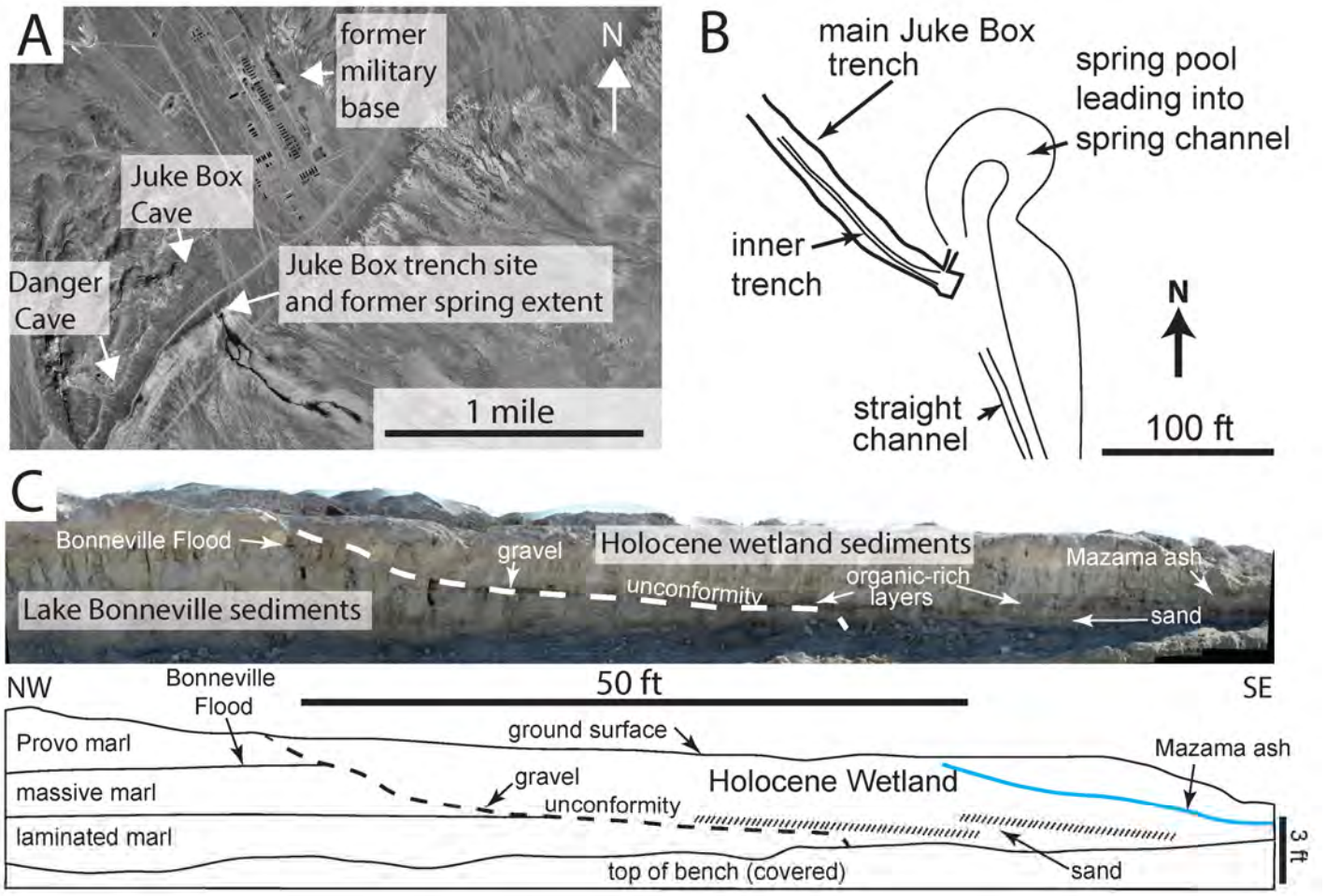

Figure 6. *Overview of Juke Box trench. (A) 1946 aerial imagery overview of the area. Danger and Juke Box caves, former military base, and past extent of spring noted. (B) Map overview of Juke Box trench. (C) Juke Box trench sediments. Note lateral change in deposition locally with little to no Holocene deposition and Lake Bonneville (Provo marl, massive marl, and laminated marl) sediments being preserved to the northwest (coincident with a notable change in surface morphology), and deflated area covered by Holocene wetland sediments. This wetland was active as recently as 1946. (B and C) modified from Oviatt and others (2018).*

dence of little bioturbation and more-rapid deposition. As Lake Bonneville approached its maximum size and formed the Bonneville level shoreline, a more massive (layerless) marl was deposited. This layer is interpreted as originating from slower depositional rates and more bioturbation. The top of this interval is denoted by a sharp change in lithology associated with the Bonneville flood. As the lake decreased in size, the color of the marl changed, reflecting changes in mineralogy associated with the evapoconcentration of lake waters (Provo level and post-Provo). Across these stages, ostracode species also change, creating a regular sequence that can be used to aid stratigraphic interpretation (Figure 2) (Oviatt, 2015, 2017).

Based on radiocarbon dating, deflation (wind erosion) of Lake Bonneville sediments occurred between the terminal desiccation of Lake Bonneville (~13,000 cal yr B.P.) and the Gilbert episode (~11,600 cal yr B.P.) (Oviatt and others, 2018). Radiocarbon dating and tephra indicate sustained wetland deposition since ~10,500 cal yr B.P. A significant stratigraphic marker in these deposits is the Mazama ash (7,600 yr B.P.), which was deposited during the last significant eruption of the volcano at Crater Lake National Park in Oregon.

Juke Box Cave and Danger Cave (Optional Stop)

This optional stop is located to the west of Juke Box trench. Juke Box Cave and nearby Danger Cave are important archeological sites. Furthermore, the vista from Juke Box Cave's entrance provides an excellent overview of the area.

Continue along the road from where you parked for ~150 ft, take the road to the right and head up the alluvial fan until you reach a large turnaround area,

and park there. From here the road extends up to Juke Box Cave (40.7570° N, 114.0130° W) (elevation ~4446 ft). This is a short, but steep, hike. To reach Danger Cave (40.7490° N, 114.0182° W) continue ~0.6 mi southwest along the dirt road from where you parked. A short path leads to the gated cave entrance.

Archeological Significance

Juke Box Cave is believed to have acquired its name because during World War II soldiers from the nearby military barracks (Figure 6A) used the cave to socialize and even went so far as to construct concrete dance floor in its confines. Danger Cave holds the distinction of being Utah's first State Monument. It also holds a place on the National Register of Historic Places and is recognized as a National Historic Landmark. Major excavations were conducted at Juke Box and Danger caves in the 1940s and 1950s by University of Utah researchers (Jennings and others, 1956). Since then, intermittent work has been conducted on the caves, taking advantage of new archaeological techniques as they have become available (Madsen, 2014). The initial excavation of Danger Cave was important in helping establish the utility of radiocarbon dating as a valid chronological tool when it proved to be one of the oldest archeological sites in North America known at the time.

These caves were occupied repeatedly by indigenous people between about 12,500 cal yr B.P. to historic times (Jennings and others, 1956; Madsen and Rhode 1990; Rhode and Madsen, 1998; Rhode and others, 2005; Rhode and others, 2006; Goebbel and others, 2007). Early people were present here intermittently from ~12,500 to 8,000 cal yr B.P. This area was later used by Desert Archaic people (~1,500 cal yr B.P.), the Fremont (~1,500 to 700 cal yr B.P.), and proto-historic Shoshonean groups (~700 cal yr B.P. – present). The extremely good preservation in the dry caves, coupled with their detailed stratigraphy, has provided some of the best evidence of prehistoric lifeways of Great Basin peoples, as well as records of ecosystem change and paleoclimate. Textiles, baskets, pottery, animal bones, plant remains, weapons, chipped stones, coprolites, quids (chewed bits of fibrous food), arrowheads, and leather scraps have all been found in the caves.

Paleoenvironmental Record

Juke Box Cave is located near the Stansbury shoreline and Stansbury shoreline tufas are visible near the cave's entrance. Plant and animal remains left by the cave's inhabitants record changes in the surrounding environments, including the Juke Box spring marshland that existed below the cave and nearby desert and mountain ecosystems. Additional paleoenvironmental information from pollen analyzed from cores taken in the marsh and from woodrat nests found in nearby caves containing well-preserved plants, insects, and vertebrate remains supplement the cave records (Rhode and Madsen, 1998; Madsen and others, 2001). These woodrat "middens" can be preserved for tens of thousands of years, providing ecological snapshots of the past, making them invaluable paleoenvironmental tools.

Bonneville Salt Flats

Return to the I-80 frontage road and continue for 1.4 miles until you reach Leppy Pass Road. Take a left. Continue for 5 miles (at the bend in the road, turn right/east towards the Bonneville Salt Flats). At the end of the pavement, there is a large turn-around area. Park here (40.7625° N, 113.8958° W). Depending on events and surface conditions you may be able to access the salt crust (stops in these areas are described in the geomorphology section below).

Access to Bonneville Salt Flats crust is limited seasonally by surface flooding. In general, if there is surface moisture at the end of the access road, stay off the salt flats. Ignoring this guideline may rip up and damage the crust for years to come (Figure 7). In addition, the salt can be thin. It is easy to get stuck in the underlying mud and it is expensive and damaging to be towed out. Only drive on the salt when it is dry and when your tires do not leave a track. Furthermore, access is limited during events such as Speed Week. The Bonneville Salt Flats is on public land managed by the Bureau of Land Management. A schedule of Bonneville Salt Flats events is available at https://www.blm.gov/visit/bonneville-salt-flats.

When on the salt flats, be careful to watch out for cross-traffic. ***Fatal crashes have happened here before****. Also, be aware of the state of the crust. If your vehicle is leaving tracks, keep momentum, turn around, and return to the stable crust!*

The vast expansive landscape of the Bonneville Salt Flats is treasured for different uses by many groups of people. The brines underlying the saline pan are enriched in potassium and have been mined continuously since 1939 (Bingham, 1980). The landscape is valued by tourists and artists for its sharp contrasts and stark beauty (Zajchowski and others, 2020; Bowen and Wischer, 2023). The hard flat surface is treasured by the vehicular land-speed racing community for its flatness, mechanical properties, and length (Francisco, 1965). Social and physical scientists also value this landscape, which provides an example of saline processes influenced by human action

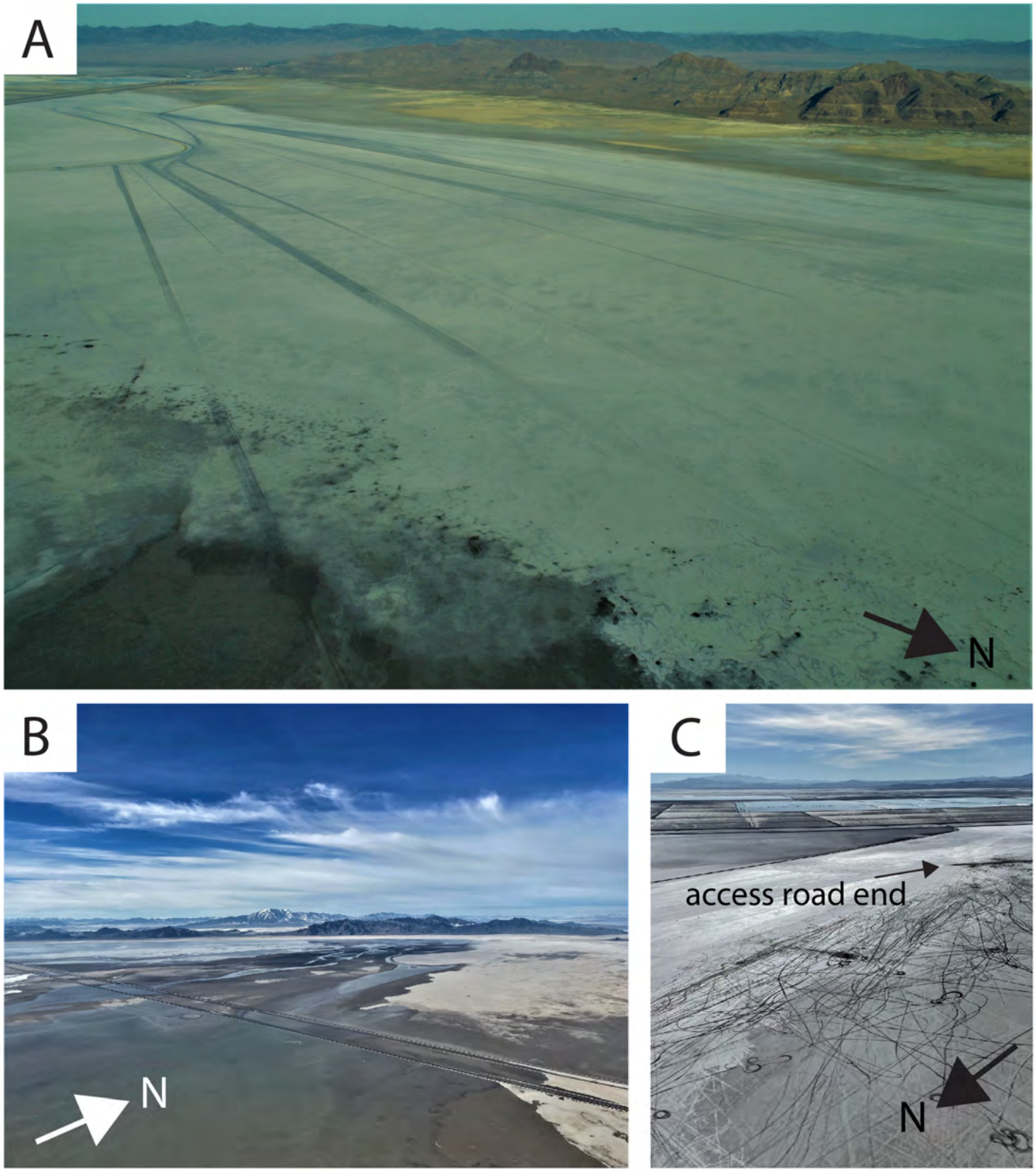

Figure 7. *Aerial imagery of the Bonneville Salt Flats. (A) Racetracks and view of Silver Island Mountains. (B) Water input from south of Interstate 80. (C) Car tracks left near the end of the access road, view of potash mine to the south. Note that tracks are more evident to the west, towards the edge of the saline pan where the crust is thinner. North arrows added to show orientation. Images taken with pilot Dr. Gabe Bowen on (A) August 17, 2019, (B) February 19, 2023, and (C) October 30, 2022. These and other Bonneville Salt Flats aerial imagery available at: https://geodata.geology.utah.gov/pages/search.php?search=%21collection129324.*

(e.g., Christiansen, 1963; Zajchowski and others, 2020). Here, we describe a century of changes at the Bonneville Salt Flats and provide context for these changes through the window of the Bonneville Salt Flats' depositional history. We then describe the surface expression of the crust and how it varies spatially and temporally.

Recent change

The Bonneville Salt Flats' recent history is characterized by changes in salt crust area and thickness (Figure 8). Furthermore, the geochemistry of Bonneville Salt Flats brines has changed over time in response to changing management (Bernau and others, 2023a, this volume). Anthropogenic activities during this period are strong contributors to this change. The saline pan has been dissected by industrial activity and an interstate highway, and its waters have been collected for mineral production. These changes have upset and limited the ability of multiple stakeholders to use the site, spurring several salt crust thickness studies, research, and lobbying for action (Francisco, 1965; Kipnis and Bowen, 2018).

For a quarter century, restoration efforts at the Bonneville Salt Flats have focused on a brine "laydown" program. To the north of Juke Box trench, there are alluvial-fan aquifer production wells. These brackish water wells are used to provide the potash mine with water for its operations. They have also been used to supply water for the laydown program since 1997. The laydown uses alluvial-fan water to dissolve waste halite from mine operations, the resulting brine then floods the Bonneville Salt Flats' surface. This project has not had anticipated results, and the crust has continued to decrease in area and thickness (Figure 8B and D) (White, 2004; Bowen and others, 2017; Kipnis and Bowen, 2018).

Alluvial-fan aquifer extraction may be exacerbating long-term crust declines (Bernau and others, 2023a, this volume). Since the onset of the laydown, groundwater levels in the alluvial fan have steadily fallen, leading hydraulic gradients to reverse; instead of water flowing towards the saline pan as it used to, it now flows away from the saline pan. This is evidenced by the salinity of the waters the wells now produce–they used to be fresh, but several wells now produce brine that is saltier than the ocean (Bernau and others, 2023a, this volume). A portion of this water likely comes from groundwaters underlying the saline pan. Dewatering from lowering alluvial-fan water levels (from surface to ~50 ft below the surface in 2021) has created >3-ft-wide desiccation fractures in areas near the mountain front (Mason and Kipp, 1998).

Depositional history

The depositional history of the Bonneville Salt Flats' site provides insights and perspective on modern change. Before Lake Bonneville, there were intermittent shallow saline lakes similar to the modern Great Sale Lake (>45,000 to >28,000 cal yr B.P.) (Figure 2; Bernau, 2022). These lake deposits have small faults and soft sediment deformation features, suggesting past seismic activity; an alternative interpretation of these features is that they are dewatering structures that developed as lake levels fell, and water was released from sediments as the overlying pressure of lake waters was removed. A fault with ~1.5 ft of Holocene offset along the southeastern Silver Island Mountains in a former spring area suggests that seismic activity may be ongoing (Hecker, 1993; Madsen, D., personal communication, 2022) (further investigation and interpretation of these sediments is needed). From the Bonneville Salt Flats you can see shorelines left by Lake Bonneville on the Silver Island Mountains and the Leppy Hills (Figure 7A).

The Bonneville Salt Flats salt crust consists of layers of gypsum sand and halite crystals. The gypsum sand becomes coarser with increasing depth, indicating the displacive growth of crystals after deposition (Bowen and others, 2018; Bernau and Bowen, 2021). Bonneville Salt Flats' gypsum deposition began at ~8,000 cal yr B.P. (Bernau, 2022). The origin of the gypsum sand is likely in-situ growth, which is seen in some modern sediments. Some grains may originate from displacive crystals that were later reworked with deflation. Radiocarbon dating of pollen, and similarly sized material from bedded Bonneville Salt Flats evaporites, indicates that the Bonneville Salt Flats is much younger than previously thought. The Bonneville Salt Flats likely resembled today's saline pan by 5,500 cal yr B.P., not immediately after Lake Bonneville (13,000 to 11,000 cal yr B.P.), as was previously thought. This new evidence indicates the saline pan may be a much more ephemeral feature than assumed. Similarly, the Bonneville Salt Flats' depositional history with respect to regional changes in climate indicates that halite is deposited under wetter conditions whereas gypsum is deposited under drier conditions. Recent records suggest this region is becoming drier (Williams and others, 2022), making the Bonneville Salt Flats likely to shift towards more gypsum accumulation even in the absence of direct anthropogenic alteration.

Crust surface morphology

You can view a timeline of surface conditions from this location in photos collected by citizen scien-

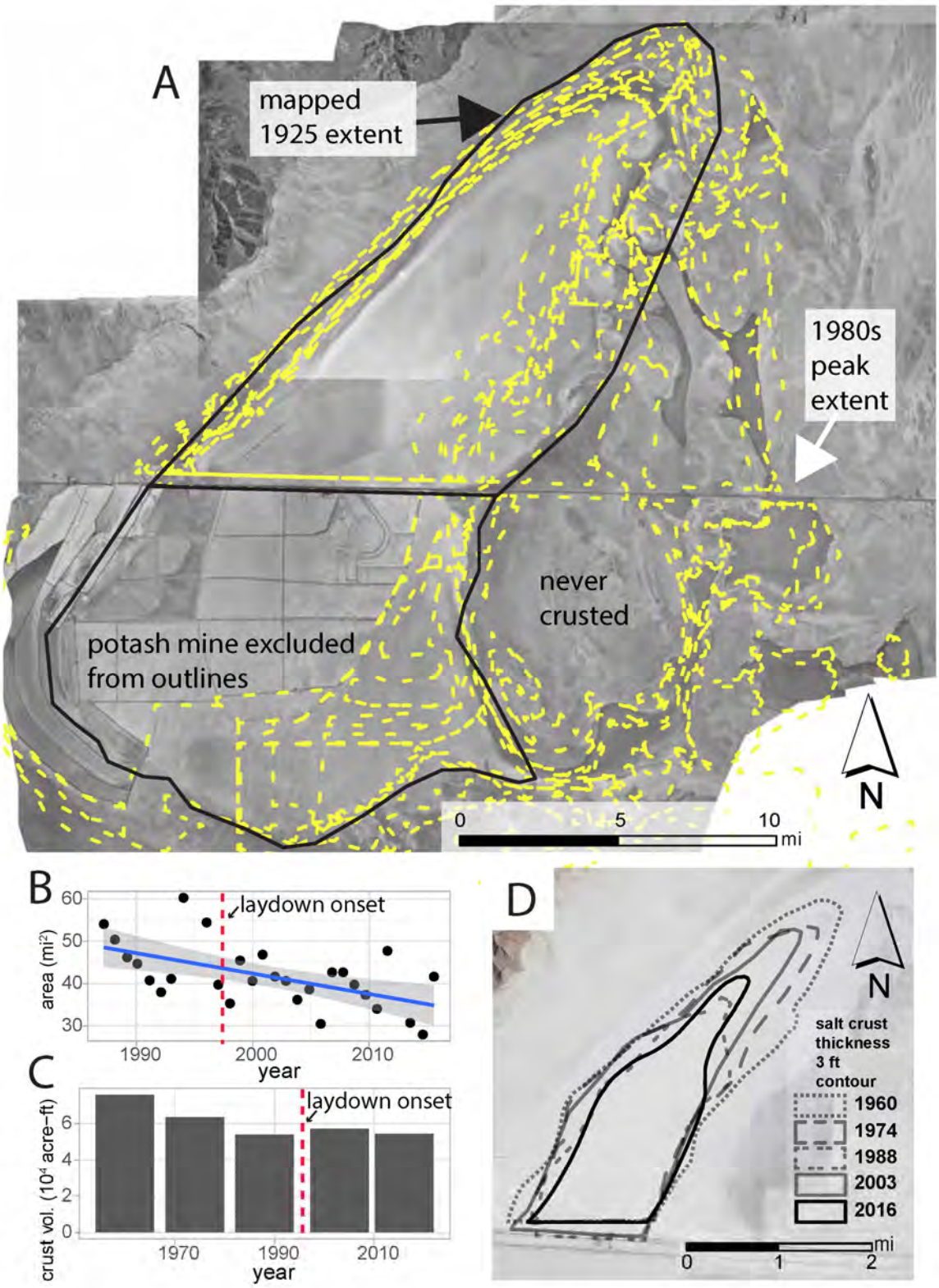

Figure 8. *Overview of change at the Bonneville Salt Flats. (A) Photomosaic of 1953 aerial imagery giving an overview of the Bonneville Salt Flats. Dashed yellow lines show the extent of surface halite from aerial imagery and black outline shows the oldest mapped extent of surface halite (Nolan, 1927). Aerial imagery is available in non-photomosaic form at https://imagery.geology.utah.gov/pages/home.php and in photomosaic form at https://geodata.geology.utah.gov/pages/search.php?search=%21collection129324. (B) A consistent long-term trend of declining saline extent is evident in analyzed Landsat data mapping the areal extent of end-desiccation surface halite over the Bonneville Salt Flats area north of I-80 (Bowen and others, 2017). (C) Recalculated (to adjust for differences in methodology) crust volume across salt crust thickness studies (1960 to 2016) (Kipnis and Bowen, 2018). (D) Change in the area of 3 ft crust thickness contour at the Bonneville Salt Flats across studies (modified from Kipnis and Bowen, 2018).*

tists here: https://www.chronolog.io/site/BSF101. These images highlight how variable the surface of the crust can be seasonally, or from week to week. Less than 1 cm of precipitation has led to >20 cm of flooding at this location. Heavy summer precipitation can rapidly alter conditions and event plans. Storms and deteriorating crust conditions led to the cancellation of racing events in 1993, 1994, 2014, 2015, and 2022 (Kipnis and Bowen, 2018).

The surface expression of evaporites at the Bonneville Salt Flats is dynamic and changes in response to cycles of flooding, evapoconcentration, and desiccation (Figure 9) (Lowenstein and Hardie, 1985; Bernau and Bowen, 2021). During the flooding stage, rainfall contributes to the full or partial dissolution of halite (Figure 9). This is apparent in dissolution pits that expose darker, gypsum and microbial-rich mud that underlies surface halite layers (Figure 10A1 and A2). During the evaporation stage, salt crystals begin to crystallize on the surface of the brine as rafts or at the sediment-water interface as bottom-growth crystals (Figure 10B1 and B2). One unique feature at the Bonneville Salt Flats is salt blisters (Figure 10B3), these may form from the remobilization of trapped air under a crust after flooding. Most people know the Bonneville Salt Flats from its appearance during the desiccation stage. The crust is in this stage when surface water is completely removed by evaporation. Many surface morphologies form during this period, with the most rapid growth occurring immediately after the surface enters the desiccation stage when near-surface pores are larger (not filled by crystal growth) and contain water. One diagnostic feature of this period is efflorescent (or popcorn) halite (Figure 10C). These aptly named crystals effloresce, or bloom, from the ground.

During the desiccation stage, efflorescent growth causes the crust's morphology to change. On the salt flats, we will cover the transition from the thin-crusted, pressure-buckled crust at the western edge of the Bonneville Salt Flats to the smooth-crusted transitional zone near the raceway and weather station (Figure 11). Finally, we will move towards the Salduro Loop, an area covered by polygonal crust. The surface expression of the crust is influenced by its thickness and history (Figures 11E, 12, and 13). For more information about the surface expression of halite crusts and other surface features in similar settings see Christiansen (1963), Lines (1979), Goodall and others (2000), Wang and others (2014), El-Maarry and others (2015), Nield and others (2015), Milewski and others (2017), Lasser and others (2020), Bernau and Bowen (2021), and Zhang and others (2021).

Buckled crust

Our first stop on the Bonneville Salt Flats' crust occurs on its western edge. Drive onto the saline pan and follow the main traffic area (salt crust is smoother) to the northeast for 4.5 miles (40.8054° N, 113.8309° W). Then turn west towards the Silver Island Mountains and continue until you see buckled crust (Figure 11A).

Note: If you approach this area in the mid-summer or early fall and there has not been a recent flooding event you will see pressure-buckled crust. You may opt to stop and walk to this area if the surface is becoming less stable and you are beginning to create tracks. ***Avoid getting stuck – turn around if the surface is unstable!***

The buckled crust is underlain by a thin layer of gypsum sand over carbonate mud. It is located near the salt-flat to mudflat transition, so wind-blown sediment may easily accumulate on these buckles. The buckled morphology forms as the crust bends to accommodate increases in crust volume. As the crust buckles it may transport sediment on its underside as well as sediments deposited by wind on its surface to-

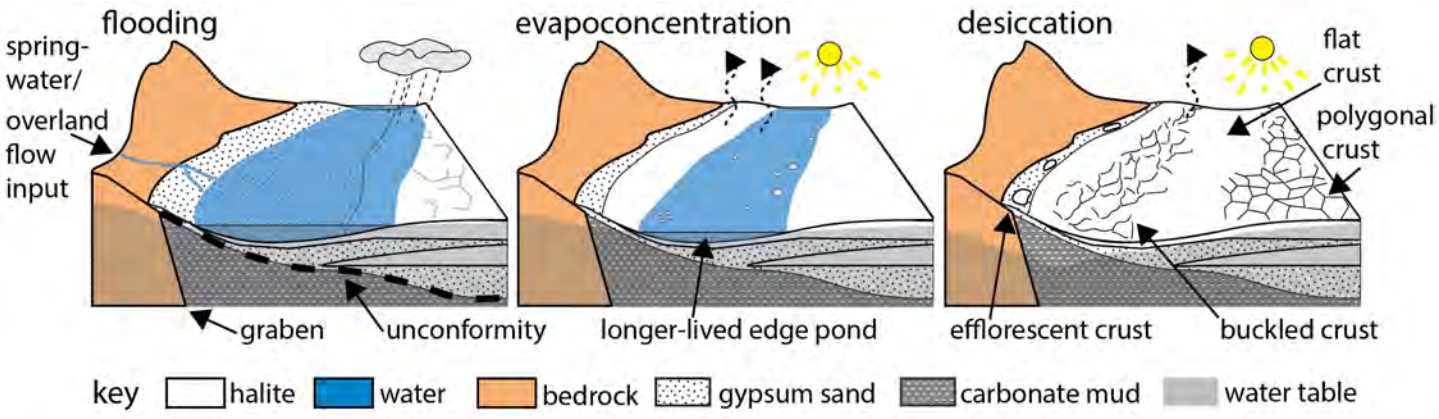

Figure 9. *Flooding, evapoconcentration, and desiccation periods at the Bonneville Salt Flats (modified from Bernau and Bowen, 2021).*

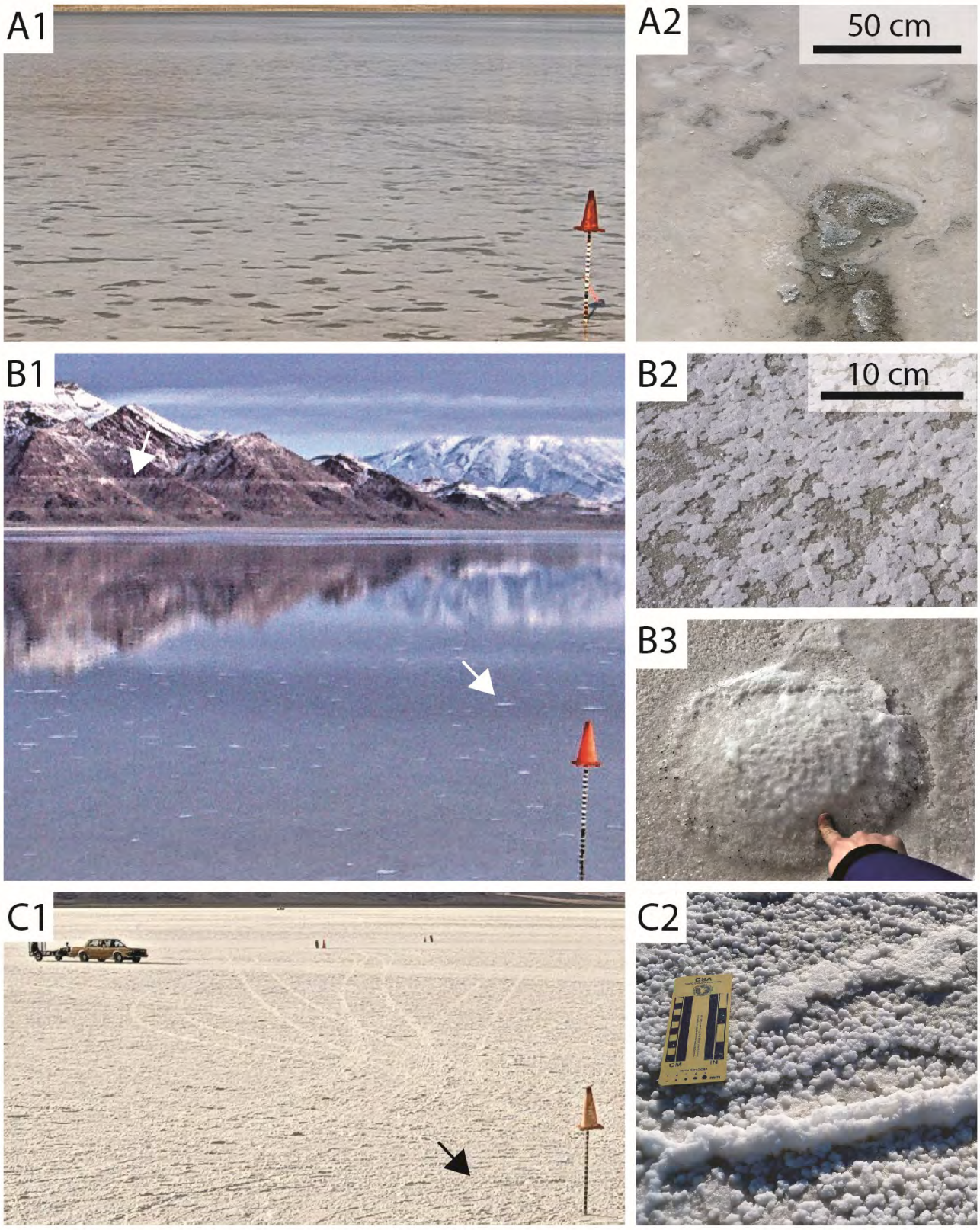

Figure 10. *Surficial expression of the Bonneville Salt Flats across flooding, evaporation, and desiccation periods (modified from Bernau and Bowen, 2021). (A) Flooding features include halite-undersaturated brine and partial (dissolution pits [A2]) to full dissolution of the surface crust. (B) Evaporation stage, where halite crystalizes on the water surface as rafts (white arrow) (B1 and B2). (B1) View to west of prominent Lake Bonneville shorelines looking west. (B3) Halite blister feature where halite has bulged up after flooding. This feature is surrounded by insects, which accumulated at the water level line and bottom-growth halite. Halite blisters often occur in the southern racetrack area in the autumn after the surface has desiccated after flooding. Blisters are shown forming in Figure 11. (C) As the surface shifts from the flooding to the desiccation period efflorescent (or popcorn) halite (black arrow) (C2) forms.*

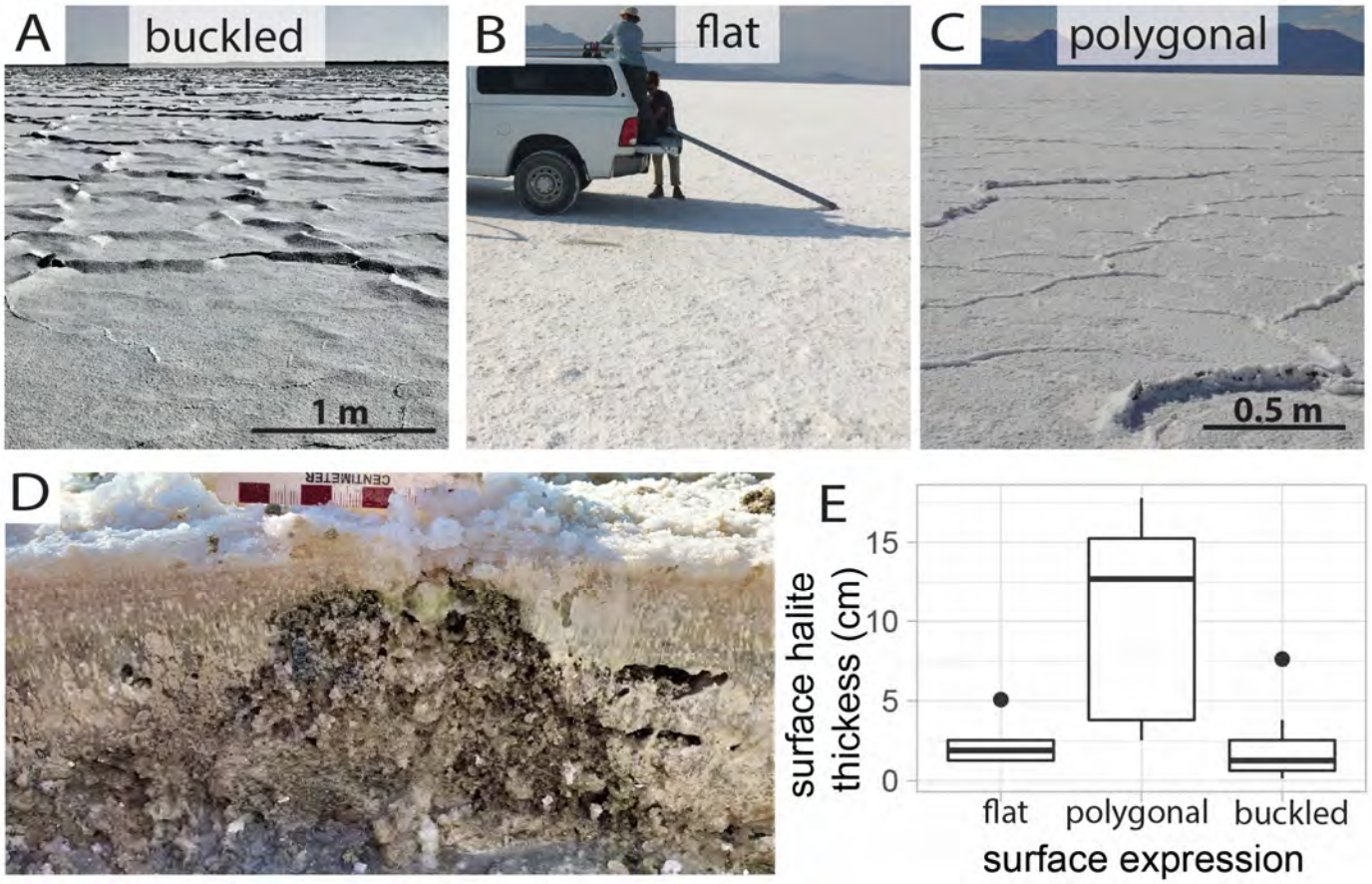

Figure 11. *Surface and subsurface expression of halite crust (modified from Bernau and Bowen, 2021). Surficial halite can vary widely, but generally is (A) buckled, (B) flat, or (C) polygonal. (D) Cross section across a polygon similar to that shown in (C). (E) Surface expression of halite crust in relation to surface halite thickness. Pressure buckles consistently occur near saline pan's edges. Flat areas coincide with southern and central racetrack areas where seasonal ponding is persistent (Bowen and others, 2017; Craft and Horel, 2019). The polygonal crust is concentrated within and to the northeast of the Salduro Loop.*

ward the area of buckling. This may lead to the formation of a small detrital sediment ridge; this ridge creates a preferred area for buckling to occur in the future because crusts deposited over the ridge will be thinner and easier to break, creating a feedback loop for buckling to regularly occur in the same area and for more sediment to accumulate at the same spot (Figure 12 left) (Lokier and Steuber, 2009; Lokier, 2012). Observations of other areas of the saline pan indicate that the surface expression of buckling can be highly variable in height, spacing, and shape (polygonal vs. orthogonal), potentially depending on the thickness of surface halite, mineralogy, and other factors (for example, buckles often form where car tracks have created a preferential break point).

Flat crust

Our next stop is near the center of the Bonneville Salt Flats at the BFLAT weather station. Drive south for ~1.5 miles (40.7846° N, 113.8297° W). The weather station should become visible as you near it; it has a chain link fence surrounding it.

Note: Watch for cross traffic, this route cuts across several racetracks and high traffic areas.

You may notice as you travel towards the saline pan center that the crust's morphology changes and is generally flatter. In areas where the racetrack has been prepped even efflorescent crystals become subdued. The racetrack is prepared by dragging heavy steel beams behind a vehicle to crush and homogenize the crust (Morgan, 1985). If the crust is too thin or if conditions are too moist, preparing the racetrack can rip the crust, degrading its quality and limiting the ability to safely race.

In addition to racetrack preparation, regular flooding of this area (a seasonal pond is concentrated on the Bonneville Salt Flats' western edge, a topographic low point) and salt crust thickness likely contribute to its flatness. Seasonal flooding at the Bonneville Salt Flats is one of the features that makes it so ideal for land-speed racing. Flooding removes any buckles in the crust and redistributes sediment, and when the pond desiccates it leaves a new flat crust. Areas that

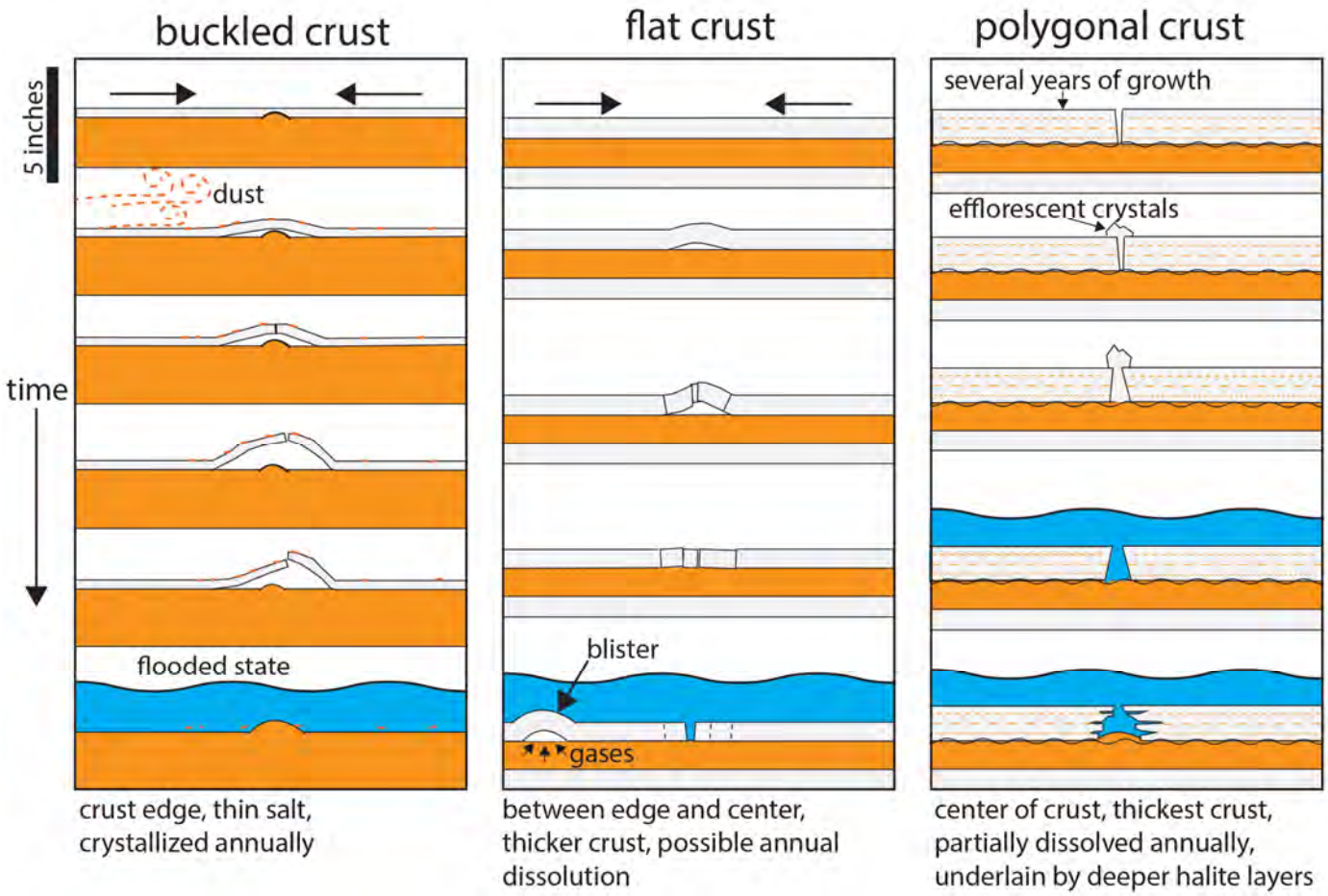

Figure 12. *Schematic of processes leading to the formation of different surface morphologies. The upper (first) section shows the surface at beginning of the desiccation stage. (Left) Formation of buckled crust, which typically occurs in thin salt at saline pan edge. Note the accumulation of sediment at the buckle location as halite crust expands with efflorescent growth (modified from Lokier, 2012; Lokier and Steuber, 2009). (Center) Formation of flat crust and blisters. The flat crust is generally thicker, limiting its ability to buckle or reach heights seen in thinner crust areas. Blisters are thought to form after flat areas flood, the lack of surface buckles and breaks in these areas limit off-gassing, enabling trapped gases to move laterally, accumulate, and bubble up in an area, deforming the crust in the process (based on the description in Bernau and Bowen [2021] and similar to microbial mat gas domes in other settings [Goodall and others, 2000; Noffke and others, 2002]). (Right) Polygonal crust development occurs in areas where halite crust is persistent across flooding events; although a contractional origin of polygons has been proposed, the features at the Bonneville Salt Flats may be explained by repeated cycles of flooding with preferred dissolution occurring along polygonal edges (either pre-existing or formed by buckling). The gaps then become preferred areas of dissolution (see Figure 11D and Bernau and Bowen [2021] for further reference). Note that under extended flooding periods, the surface halite can completely dissolve near the Bonneville Salt Flats' center; during these periods, remnant gypsum becomes rippled from wave action.*

flood less frequently, such as Death Valley and Salar de Atacama, can have rough surfaces that develop as the crust deforms during the desiccation stage (Bobst and others, 2001). The crust in this flat area is generally thicker than the buckled crust area. A thicker crust may be harder to buckle because of its mechanical properties. Similarly, the thicker crust has more pore space that efflorescent crystals could develop within, vertically distributing crystal growth and reducing lateral deformational pressures (Figures 11E and 12 center).

The site of the BFLAT weather station (operated by the Utah Geological Survey after 2021 and by the University of Utah from 2016 to 2021) highlights some of the long-term research performed on the Bonneville Salt Flats. The weather station measures precipitation and evaporation, enabling researchers to understand how water is moving in and out of the crust. It also collects time-lapse images and logs data every 5 minutes, enabling anyone to see current surface conditions on the saline pan (https://meso1.chpc.utah.edu/station_cameras/bflat_cam/bflat_cam_current.jpg). Similarly, several groundwater monitoring wells with multiple depths are present here. These wells are used to understand how groundwater levels change in response to climate and human actions. They also enable researchers to determine if shallow groundwater at the saline pan is moving up to

moving up to feed the crust or if it is moving down and removing salts from the saline pan.

Polygonal crust

Our final stop on the Bonneville Salt Flats' crust visits the polygonal crust. Head 1 mile south from BFLAT towards the berm of the Salduro Loop (40.7700° N, 113.8283° W). The Salduro Loop was a brine collection ditch. The crust next to it can be soft, in some areas inside the loop you can see where the ditch filled in with halite by identifying deep brine-filled holes in the salt. *To minimize the chances of getting stuck, do not drive within 100 ft of the loop. Furthermore, the salt where the ditch has filled in with halite may be fragile and could collapse beneath you, step with care*!

This site has some of the thickest surface crust at the Bonneville Salt Flats. It also has a distinctive polygonal fracture system. The polygons are highlighted by vertical ridges of efflorescent halite. The efflorescent halite is very porous and dissolves during flooding, inverting the local topography (leaving a crack where a ridge once was). This crust is persistent across multiple flooding events. Under extended flooding periods, the surface halite can completely dissolve near the saline pan's center and remnant gypsum becomes rippled. Although a contractional origin of salt polygons has been proposed (Tucker, 1981), the features at the Bonneville Salt Flats can be explained by repeated cycles of flooding with preferred dissolution occurring along polygonal edges (either pre-existing or formed by buckling) and the growth of efflorescent salt at the surface (Bernau and Bowen, 2021) (Figures 11D and 12 right).

The polygonal geometries at the Bonneville Salt Flats occur at multiple scales, ranging from less than a meter to over 300 meters across. The multiple scales of polygons can be seen in person, in aerial imagery (Figure 13), and, at the largest scale, in multispectral satellite (resolution up to ~100 ft/pixel) spectral index images. Using different methods and examining polygons at a much smaller scale, Lasser and others (2020) present evidence for convection occurring beneath polygonal crusts, indicating a strong relationship between the surface expression of saline pans and groundwater movement beneath them.

You may now enjoy exploring the rest of the Bonneville Salt Flats' crust or return to Salt Lake City. To return to the access road head west and follow the Salduro Loop berm (~4 miles), then return west towards the access road which will become be visible (40.7625° N, 113.8958° W).

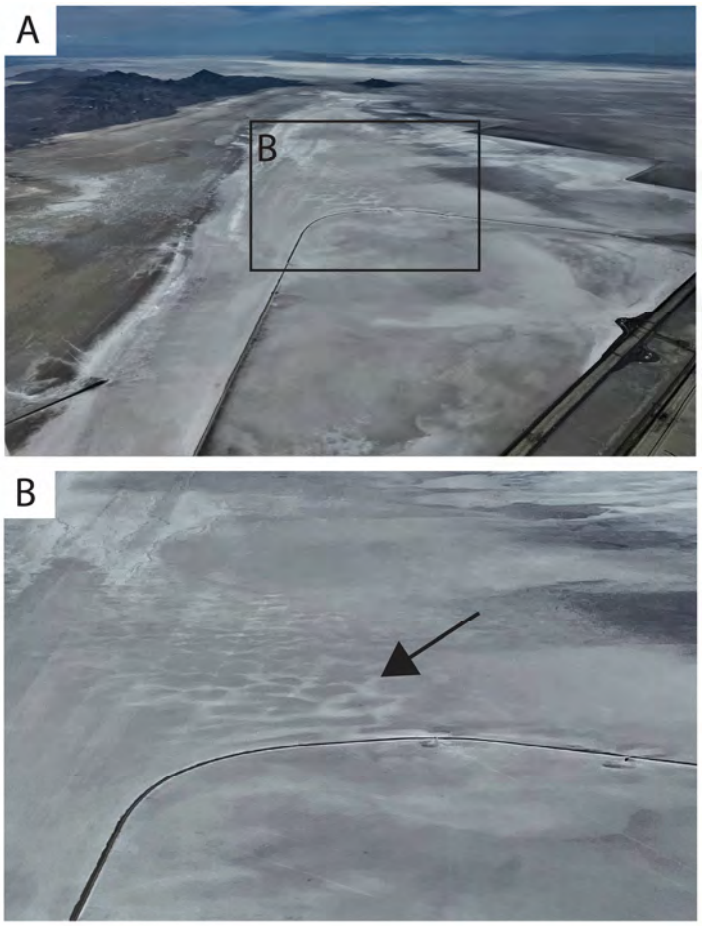

Figure 13. *Aerial imagery of the Bonneville Salt Flats on June 9, 2022. (A) View looking north. (B) Large polygonal features (black arrow). Images taken with pilot Dr. Gabe Bowen.*

Silver Island Mountains Access Road (Optional Extension)

The Silver Island Mountains access road provides another great perspective on this area, specifically on the contact between deflated and non-deflated surfaces. To access it, go west from the end of the access road for 3.8 miles. At the T in the road, go right. Continue for 0.8 miles and take a slight right onto Silver Island Road (unmarked) and continue north for ~14.5 miles (40.8926° N, 113.7978° W). *Note: This road is periodically maintained and may have heavily rutted or muddy areas that require a high clearance vehicle.*

The exposed gravel bar here is enhanced by erosion; it is known as the lozenge section and highlights the sharp contact between preserved and deflated areas. The lozenge section is capped by Lake Bonneville's late-regressive-phase well-rounded gravels. Lake Bonneville sediments are likely preserved here because the gravels limited deflation (Figure 14A). Below the gravels are reddish, silty, sandy beds that

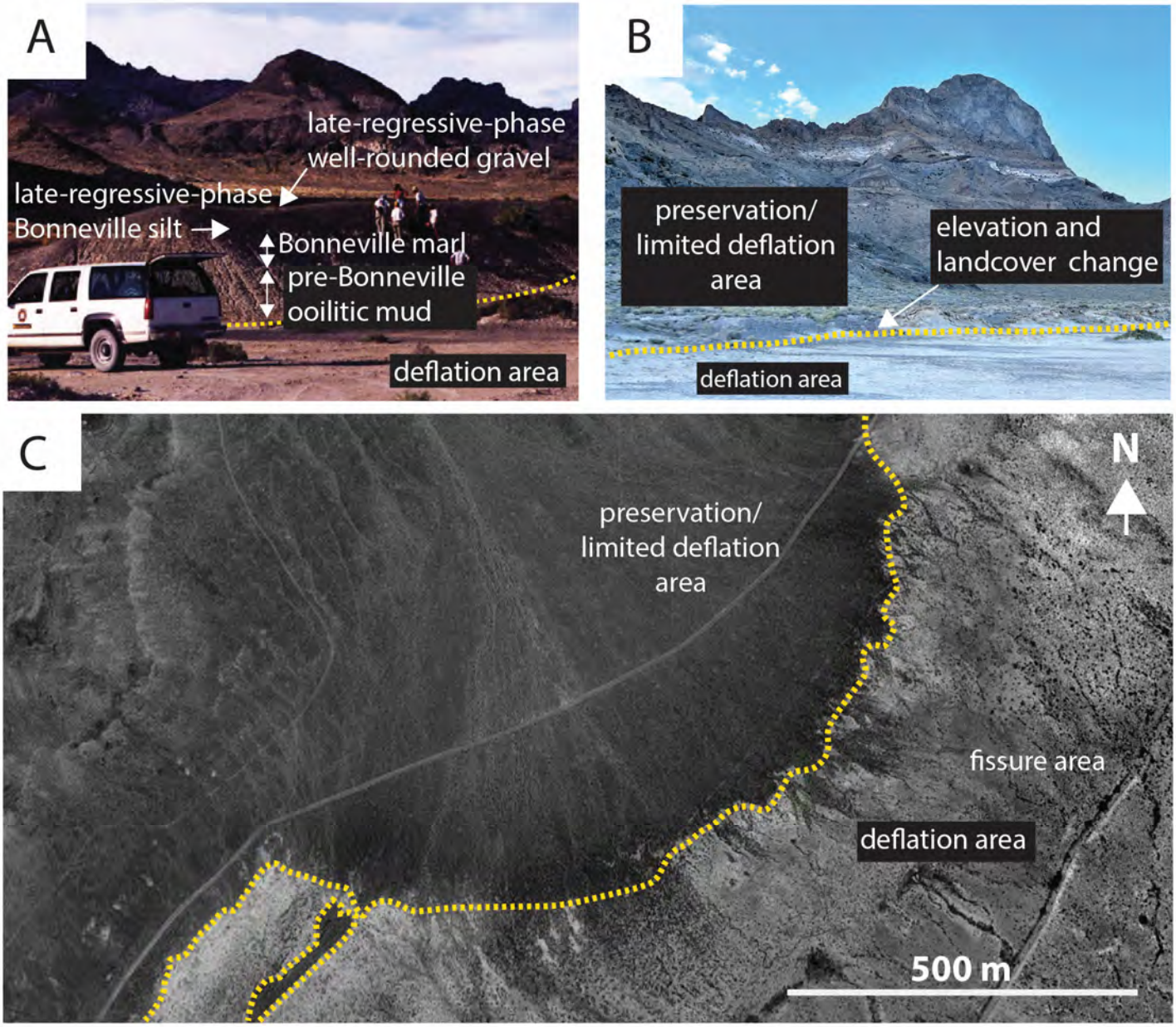

Figure 14. *Edge of deflation along the Silver Island Mountains' alluvial-fan edge. (A) The lozenge section (image modified from Munroe and others [2015] and site further described in Oviatt and others [2020]). (B and C) Preservation and deflation areas are delineated by changes in elevation and land cover. Note that the preservation of Lake Bonneville sediments delineated by surface cover is also evident at Juke Box trench (Figure 6). (C) is a USGS National Aerial Photography Program (NAPP) photo from July 1997. Dashed yellow line delineates between the areas of preservation (alluvium and gravel bars) and deflation.*

overlie Lake Bonneville and underlying pre-Lake Bonneville sediments. The eroded mudflat is to the east and the alluvial-fan deposits, which have limited erosion, are to the west (Figure 14B).

If you continue northeast on this road, you will see similar erosional features and will reach a road that connects with Floating Island (40.9295° N, 113.7189° W). Turn around and retrace your route. The final stop is an alluvial fan that demonstrates the erosional contact between deflated and preserved Lake Bonneville sediments. This stop coincides with the furthest northern extent of groundwater extraction, a now-dormant spring, and desiccation fissures. Return south along Silver Island Road for 11 miles. Stop just after the promontory (40.7960° N, 113.9395° W).

To the east of this area is a former spring (40.7947° N, 113.9325° W). The eastern linear feature is a now inactive freshwater collection ditch for the northernmost extent of now inactive brackish water production wells (Figure 12C). The mudflat area between the former collection ditch and the alluvial fan has many large, deep (several feet) desiccation fissures (Mason and Kipp, 1998). *There are no trails here so choose your steps carefully.*

Directions Back To Salt Lake City

Return to I-80 and head east (~120 miles). If you drove on the salt flats you may wish to wash your vehicle in Wendover or back in Salt Lake City. Salt accumulation depends on surface conditions; for example, salt may more easily accumulate on your vehicle if the Bonneville Salt Flats has flooded recently or if groundwater levels are near the surface, as they are in the mid-summer (Bernau, 2022). The crust is driest in the fall to winter, when groundwater levels decline if there has been no precipitation (salt accumulation on your vehicle will be lower under these conditions). Salt will cake onto the surface and get onto ledges and crannies beneath a vehicle. We recommend using a self-service carwash (with hot water if possible) to ensure salt has been removed and to limit potential corrosion.

ACKNOWLEDGMENTS

We acknowledge that this study was conducted on traditionally Newe/Western Shoshone and Goshute lands. We thank Craig Peterson and Russ Draper with Intrepid Potash; Bureau of Land Management West Desert District's current and former office staff, including Kevin Oliver, Matt Preston, Mike Nelson, Cheryl Johnson, Steve Allen, Roxanne Tea, and Todd Marks; University of Utah researchers Jory Lerback, Evan Kipnis, and Mark Radwin; and Utah Geological Survey geologists Paul Inkenbrandt, Hugh Hurlow, Bill Keach, and Elliot Jagniecki. Isaac Hart and Andrea Brunelle (University of Utah), and Stephanie Carnie and Mike Hylland (Utah Geological Survey) are appreciated for their helpful reviews and comments, and Genevieve Atwood is thanked for acting as the editor of this paper. We also thank Steve Bowman for help scanning past Bonneville Salt Flats' files and setting up the GeoData archive and David Madsen for enriching our discussion of Danger and Juke Box caves. We also thank Dr. Gabe Bowen for piloting several flights over the Great Salt Lake Desert, enabling us to collect aerial imagery. Funding for this work was provided by an NSF Coupled Natural Human Systems Award #1617473, the Utah Geological Survey, the Utah State Legislature, the Bureau of Land Management, an American Association of Petroleum Geologists Grant-In-Aid, and University of Utah Global Change and Sustainability Center Graduate Research Grants. Funding for geologic mapping in the area is by the STATEMAP and FEDMAP components of the National Cooperative Geologic Mapping Program.

REFERENCES

Benison, K.C., and Karmanocky, F.J., 2014, Could microorganisms be preserved in Mars gypsum? Insights from terrestrial examples: Geology, v. 42, no. 7, p. 615–617.

Bernau, J.A., 2022, Spatial and temporal scales of water and salt movement at the Bonneville Salt Flats: Salt Lake City, University of Utah, Ph.D. dissertation, 195 p.

Bernau, J.A., and Bowen, B.B., 2021, Depositional and early diagenetic characteristics of modern saline pan deposits at the Bonneville Salt Flats, Utah, USA: Sedimentology, p. sed.12861.

Bernau, J.A., Bowen, B.B., Leback, J., Kipnis, E.L., 2023a, Observations of decadal-scale brine geochemical change at the Bonneville Salt Flats: *in* Vanden Berg, M., Frantz, C., Ford, R., Hurlow, H., Gunderson, K., and Atwood, G., editors, Great Salt Lake & the Bonneville Basin—Geologic History & Anthropocene Issues: Utah Geological Association Publication 51, p. xx.

Bernau, J.A., Oviatt, C.G., Clark, D.L. and Bowen, B.B., 2023b, Sediment logs compiled from the Great Salt Lake Desert, western Utah, with a focus on the Bonneville Salt Flats area: Utah Geological Survey Open-File Report 754, 24 p., 3 appendices, *https://doi.org/10.34191/OFR-754*

Bingham, C.P., 1980, Solar Production of Potash from the Brines of the Bonneville Salt Flats: Utah Geological and Mineral Survey Bulletin, v. 116, p. 229–242.

Bobst, A.L., Lowenstein, T.K., Jordan, T.E., Godfrey, L. V., Ku, T.-L., and Luo, S., 2001, A 106 ka paleoclimate record from drill core of the Salar de Atacama, northern Chile: Paleogeography, Palaeoclimatology, Palaeoecology, v. 173, no. 1–2, p. 21–42.

Boden, H.T., 2016, Gypsiferous sand dune deposits on SITLA lands in the Great Salt Lake Desert project area, Tooele County, Utah: *in* Comer, J.B., Inkenbrandt, P.C., Krahulec, K.A., and Pinnell, M., editors, Resources and geology of Utah's West Desert: Utah Geological Association Publication 45, p. 105–130.

Bowen, B.B., Bernau, J.A., Kipnis, E.L., Lerback, J.C., Wetterlin, L., and Kleba, B., 2018, The making of a perfect racetrack at the Bonneville Salt Flats: The Sedimentary Record, v. 16, no. 2, p. 4–11.

Bowen, B.B., Kipnis, E.L., and Raming, L.W., 2017, Temporal dynamics of flooding, evaporation, and desiccation cycles and observations of salt crust area change at the Bonneville Salt Flats, Utah:

Geomorphology, v. 299, p. 1–11.
Bowen, B.B., and Wischer, W., 2023, Evaporated—Explorations in Art, Science and Salt: Leonardo, p. 1–18.
Bowler, J.M., 1986, Spatial variability and hydrologic evolution of Australian lake basins— Analogue for Pleistocene hydrologic change and evaporite formation: Palaeogeography, Palaeoclimatology, Palaeoecology, v. 54, no. 1–4, p. 21–41.
Christiansen, F.W., 1963, Polygonal fracture and fold systems in the Salt Crust, Great Salt Lake Desert: Science, v. 139, no. 3555, p. 607–609.
Clark, D.L., Oviatt, C.G., Hardwick, C., and Page, D., 2020, Interim geologic map of the Bonneville Salt Flats and east part of the Wendover 30' x 60' quadrangles, Tooele County, Utah - Year 3: Utah Geological Survey Open-File Report 731, 1–30 p., 2 plates, scale 1:62,500.
Clark, D.L., Oviatt, C.G., Miller, D.M., Felger, T.J., Hardwick, C.L., Langenheim, V.E., Bowen, B.B., Vernaur, J.A., and Page, D., in progress, Geologic map of the Bonneville Salt Flats and east part of the Wendover 30' x 60' quadrangles, Tooele County, Utah: Utah Geological Survey Map, scale 1:62,500.
Cook, K.L., Halverson, M.O., Stepi, J.C., and Berg, J.W., 1964, Regional gravity survey of the northern Great Salt Lake Desert and adjacent areas in Utah, Nevada, and Idaho: Geological Society of America Bulletin, v. 75, p. 715–740.
Craft, K.M., and Horel, J.D., 2019, Variations in surface albedo arising from flooding and desiccation cycles on the Bonneville Salt Flats, Utah: Journal of Applied Meteorology and Climatology, v. 58, no. 4, p. 773–785.
Dean, L., 1978, Eolian sand dunes of the Great Salt Lake Basin: Utah Geology, v. 2, p. 103–111.
Doelling, H.H., 1964, Geology of the northern Lakeside Mountains and the Grassy Mountains and vicinity, Tooele and Box Elder Counties, Utah: Salt Lake City, University of Utah, Ph.D. dissertation, 354 p., geologic map and cross sections (map sheets 1–5), scale 1:31,680.
Doelling, H.H., Solomon, B.J., and Davies, S.F., 1994, Geologic map of the Grayback Hills quadrangle, Tooele County, Utah: Utah Geological Survey Map 166, 22 p., 2 plates, scale 1:24,000.
Eardley, A.J., 1962, Gypsum dunes and evaporite history of the Great Salt Lake Desert: Utah Geological and Mineral Survey, Utah Geological and Mineralogical Survey Special Studies 2, 27 p.
El-Maarry, M.R., Watters, W.A., Yoldi, Z., Pommerol, A., Fischer, D., Eggenberger, U., and Thomas, N., 2015, Field investigation of dried lakes in western united states as an analogue to desiccation fractures on Mars: Journal of Geophysical Research: Planets, v. 120, p. 2241–2257.
Fitzgerald, V., 2019, Chronology of gypsum dunes at Knolls, Utah—refining OSL techniques and timing of Holocene eolian processes: Kansas State University, M.S. thesis, 95 p.
Francisco, D., 1965, Save the salt!: Popular Hot Rodding, p. 2.
Gilbert, G.K., 1890, Lake Bonneville: U.S. Geological Survey Monograph 1, 438 p.
Goebbel, T., Graf, K., Hockett, B., and Rhode, D.E., 2007, The Paleoindian occupations at Bonneville Estates Rockshelter, Danger Cave, and Smith Creek Cave (eastern Great Basin, USA)—Interpreting their radiocarbon chronologies: *in* BAR International Series, p. 3–9.
Goodall, T.M., North, C.P., and Glennie, K.W., 2000, Surface and subsurface sedimentary structures produced by salt crusts: Sedimentology, v. 47, no. 1, p. 99–118.
Hecker, S., 1993, Quaternary tectonics of Utah with emphasis on earthquake-hazard characterization: Utah Geological Survey Bulletin 127, 157 p., 6 pls., scale 1:500,000.
Jennings, J.D., Reed, E.K., Griffin, J.B., Kelley, J.C., Meighan, C.W., Stubbs, S., Wheat, J. Ben, and Taylor, D.C., 1956, The American Southwest—A problem in cultural isolation: Memoirs of the Society for American Archaeology, no. 11, p. 59–127.
Jewell, P.W., and Nicoll, K., 2011, Wind regimes and aeolian transport in the Great Basin, U.S.A.: Geomorphology, v. 129, no. 1–2, p. 1–13.
Jones, D.J., 1953, Gypsum-oolite dunes, Great Salt Lake Desert, Utah: American Association of Petroleum Geologists Bulletin, v. 37, p. 2530–2538.
Kipnis, E.L., and Bowen, B.B., 2018, Observations of salt crust change from 1960-2016 and the role of humans as geologic agents at the Bonneville Salt Flats, Utah: *in* Emerman, S.H., Bowen, B.B., Simmons, S., and Schamel, S. editors, Geofluids of Utah: Utah Geological Association Publication 47, p. 287–303.
Kohler, J.J.F., 2002, Effects of the West Desert Pumping Project on the near-surface brines in a portion of the Great Salt Lake Desert, Tooele and Box Elder Counties, Utah—Great Salt Lake—An overview of change: Utah Department of Natural Resources Special Publication, p. 487–496.
Lasser, J., Nield, J.M., and Goehring, L., 2020, Surface and subsurface characterization of salt pans expressing polygonal patterns: Earth System Science Data Discussions, p. 1–31.
Lines, G.C., 1979, Hydrology and surface morphology of the Bonneville Salt Flats and Pilot Valley

playa, Utah: Geological Survey Water-Supply, v. 2057, p. 1–107.
Lokier, S.W., 2012, Development and evolution of subaerial halite crust morphologies in a coastal sabkha setting: Journal of Arid Environments, v. 79, p. 32–47.
Lokier, S.W., and Steuber, T., 2009, Large-scale intertidal polygonal features of the Abu Dhabi coastline: Sedimentology, v. 56, no. 3, p. 609–621.
Louderback, L.A., and Rhode, D.E., 2009, 15,000 Years of vegetation change in the Bonneville basin—the Blue Lake pollen record: Quaternary Science Reviews, v. 28, no. 3–4, p. 308–326.
Lowenstein, T.K., and Hardie, L.A., 1985, Criteria for the recognition of salt-pan evaporites: Sedimentology, v. 32, no. 5, p. 627–644.
Madsen, D.B., 2014, Eight decades eating dust: *in* Archaeology in the Great Basin and Southwest—Papers in Honor of Don D. Fowler, p. 191–203.
Madsen, D.B., Broughton, J.M., Livingston, S.D., Hunt, J., Quade, J., Schmitt, D.N., Shaver, I.M.W., Rhode, D.E., and Grayson, D.K., 2001, Late Quaternary environmental change in the Bonneville basin, western USA: Palaeogeography, Palaeoclimatology, Palaeoecology, v. 167, no. 3–4, p. 243–271.
Madsen, D.B., and Rhode, D.E., 1990, Early Holocene pinyon (Pinus monophylla) in the northeastern Great Basin: Quaternary Research, v. 33, no. 1, p. 94–101.
Mason, J.L., and Kipp, K.L., 1998, Hydrology of the Bonneville Salt Flats, northwestern Utah, and simulation of ground-water flow and solute transport in the shallow-brine aquifer: U.S. Geological Survey Professional Paper, v. 1585, 108 p.
Milewski, R., Chabrillat, S., and Behling, R., 2017, Analyses of recent sediment surface dynamic of a Namibian Kalahari salt pan based on multitemporal Landsat and hyperspectral Hyperion data: Remote Sensing, v. 9, no. 2., p. 24.
Miller, D.M., Felger, T.J., and Langenheim, V.E., 2021, Geologic and geophysical maps of the Newfoundland Mountains and part of the adjacent Wells 30' x 60' quadrangles, Box Elder County, Utah: Utah Geological Survey Miscellaneous Publication 173DM, 27 p., 2 plates, scale 1:62,500, https://doi.org/10.34191/MP-173DM.
Morgan, G.B., 1985, Recreation Management Plan for the Bonneville Salt Flats Special Recreation Management Area and Area of Critical Environmental Concern, Utah: Bureau of Land Management.
Munroe, J.S., Laabs, B.J.C., Oviatt, C.G., and Jewell, P.W., 2015, Trip 1. New Investigations of Pleistocene Pluvial and Glacial Records from the Northeastern Great Basin: *in* Field Trip Guidebook, Sixth International Limnogeology Congress, Reno, Nevada, June 15–19, 2015, p. 1–30.
Nield, J.M., Bryant, R.G., Wiggs, G.F.S., King, J., Thomas, D.S.G., Eckardt, F.D., and Washington, R., 2015, The dynamism of salt crust patterns on playas: Geology, v. 43, no. 1, p. 31–34.
Noffke, N., Gerdes, G., Klenke, T., and Krumbein, W.E., 2002, Microbially induced sedimentary structures—a new category within the classification of primary sedimentary structures-reply: Journal of Sedimentary Research, v. 72, no. 4, p. 589–590.
Nolan, T.B., 1927, Potash brines in the Great Salt Lake Desert, Utah—Chapter B in Contributions to economic geology (short papers and preliminary reports): U.S. Government Printing Office, p. 25–44.
Oviatt, C.G., 2015, Chronology of Lake Bonneville, 30,000 to 10,000 yr BP.: Quaternary Science Reviews, v. 110, p. 166–171.
Oviatt, C.G., 2017, Ostracodes in Pleistocene Lake Bonneville, eastern Great Basin, North America: Hydrobiologia, v. 786, no. 1, p. 125–135.
Oviatt, C.G., Clark, D.L., Bernau, J.A., and Bowen, B.B., 2020, Data on the surficial deposits of the Great Salt Lake Desert, Bonneville Salt Flats and east part of the Wendover 30’ x 60’ Quadrangles, Tooele County, Utah: Utah Geological Survey Open-File Report 724, p. 1–70, 2 appendices.
Oviatt, C.G., Pigati, J.S., Madsen, D.B., Rhode, D.E., and Bright, J., 2018, Juke Box trench—a valuable archive of late Pleistocene and Holocene stratigraphy in the Bonneville basin, Utah: Utah Geological Survey Miscellaneous Publication MP-18-1, p. 1–15.
Radwin, M.H., and Bowen, B.B., 2021, Mapping mineralogy in evaporite basins through time using multispectral Landsat data—Examples from the Bonneville basin, Utah, USA: Earth Surface Processes and Landforms, v. 46, no. 6, p. 1160–1176.
Reynolds, R.L., Yount, J.C., Reheis, M., Goldstein, H.L., Chavez, P., Fulton, R.S., Whitney, J., Fuller, C.C., and Forester, R.M., 2007, Dust emission from wet and dry playas in the Mojave Desert, USA: Earth Surface Processes and Landforms, v. 34, no. March, p. 613–628.
Rhode, D.E., Goebel, T., Graf, K.E., Hockett, B.S., Jones, K.T., Madsen, D.B., Oviatt, C.G., and Schmitt, D.N., 2005, Latest Pleistocene-early Holocene human occupation and paleoenvironmental change in the Bonneville Basin, Utah-Nevada: GSA Field Guides, v. 6, no. January 2005, p. 211–230.

Rhode, D.E., and Madsen, D.B., 1998, Pine nut use in the Early Holocene and beyond—The Danger Cave archaeobotanical record: Journal of Archaeological Science, v. 25, no. 25, p. 1199–1210.

Rhode, D.E., Madsen, D.B., and Jones, K.T., 2006, Antiquity of early Holocene small-seed Danger Cave: Antiquity, v. 80, no. January, p. 328–339.

Rosen, M.R., 1994, The importance of groundwater in playas—A review of playa classifications and the sedimentology and hydrology of playas: Geological Society of America Special Papers, v. 289, no. January 1994, p. 1–18.

Shuey, R.T., 1971, Paleomagnetic chronology and correlation of Great Salt Lake basin sediments: Washington D.C., National Science Foundation, Final Technical Report for grant GA-16134, 15 p.

Stephens, J.C., 1974, Hydrologic reconnaissance of the northern Great Salt Lake Desert and summary hydrologic reconnaissance of northwestern Utah: Utah Geological and Mineral Survey, p. 5–24.

Stifel, P.B., 1964, Geology of the Terrace and Hogup Mountains, Box Elder County, Utah: Salt Lake City, University of Utah, Ph.D. dissertation, 173 p.

Tucker, R.M., 1981, Giant polygons in the Triassic salt of Cheshire, England; a thermal contraction model for their origin: Journal of Sedimentary Research, v. 51, no. 3, p. 779–786.

Wang, L., Gong, H., Shao, Y., and Li, B., 2014, Analysis of elevation discrepancies along the Lop Nur ear-shaped stripes observed using GLAS and DGPS data: International Journal of Remote Sensing, v. 35, no. 4, p. 1466–1480.

Warren, J.K., 2006, Evaporites: Sediments, resources and hydrocarbons, p. 1–1035.

White, W.W., 2004, Replenishment of salt to the Bonneville Salt Flats–Results of the 5-year experimental Salt Laydown Project: Betting on Industrial Minerals, Proceedings of the 39th Forum on the geology of Industrial Minerals, v. 80, no. May 2002, p. 243–262.

Williams, A.P., Cook, B.I., and Smerdon, J.E., 2022, Rapid intensification of the emerging southwestern North American megadrought in 2020–2021: Nature Climate Change, v. 12, no. 3, p. 232–234.

Wold, S.R., and Waddell, K.M., 1994, Salt Budget for West Pond, Utah, April 1987 to June 1989: Water-Resources Investigations Report 93-4028, no. April 1987, p. 1–20.

Zajchowski, C.A.B., Brownlee, M.T.J., Blacketer, M.P., Peterson, B.A., Craft, K., and Bowen, B.B., 2020, Rapid resource change and visitor-use management—Social–ecological connections at the Bonneville Salt Flats: Environmental Management, v. 66, no. 2, p. 263–277.

Zhang, G., Xiao, Y., Xiang, M., Hong, C., Zhang, B.T., Liu, L., Shi, P., and Liu, J., 2021, Structure and morphological characteristics of polygonal salt crust, the West Juyan Lake, China: Geosciences Journal, p. 1-12.